

SEP 30 1996

# SANDIA REPORT

SAND96-1326/1 • UC-721  
Unlimited Release  
Printed August 1996

RECEIVED

OCT 15 1996

OSTI

## Waste Isolation Pilot Plant Shaft Sealing System Compliance Submittal Design Report

### Volume 1 of 2: Main Report Appendices A, B, C, and D

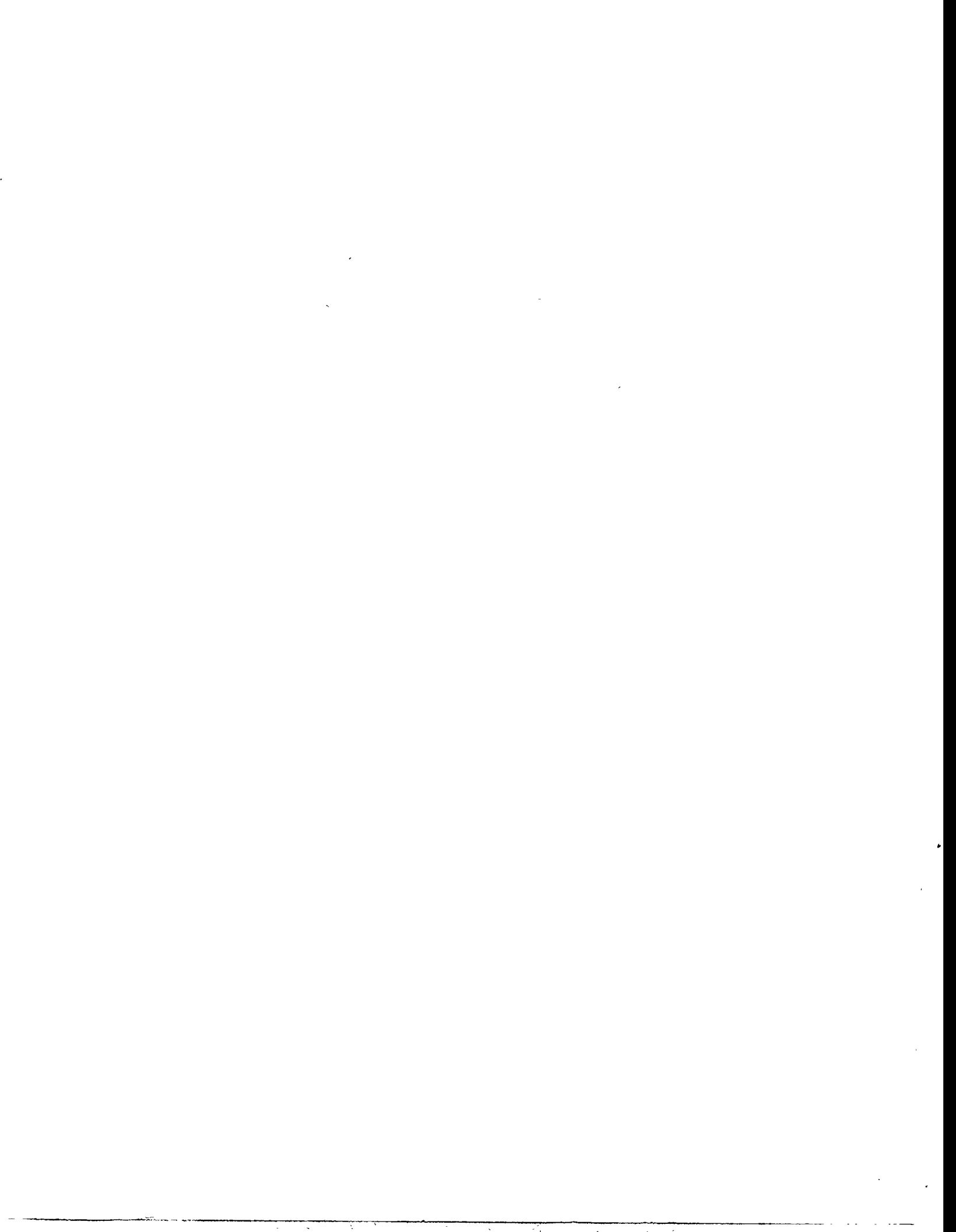
Repository Isolation Systems Department

Prepared by  
Sandia National Laboratories  
Albuquerque, New Mexico 87185 and Livermore, California 94550  
for the United States Department of Energy  
under Contract DE-AC04-94AL85000

Approved for public release; distribution is unlimited.

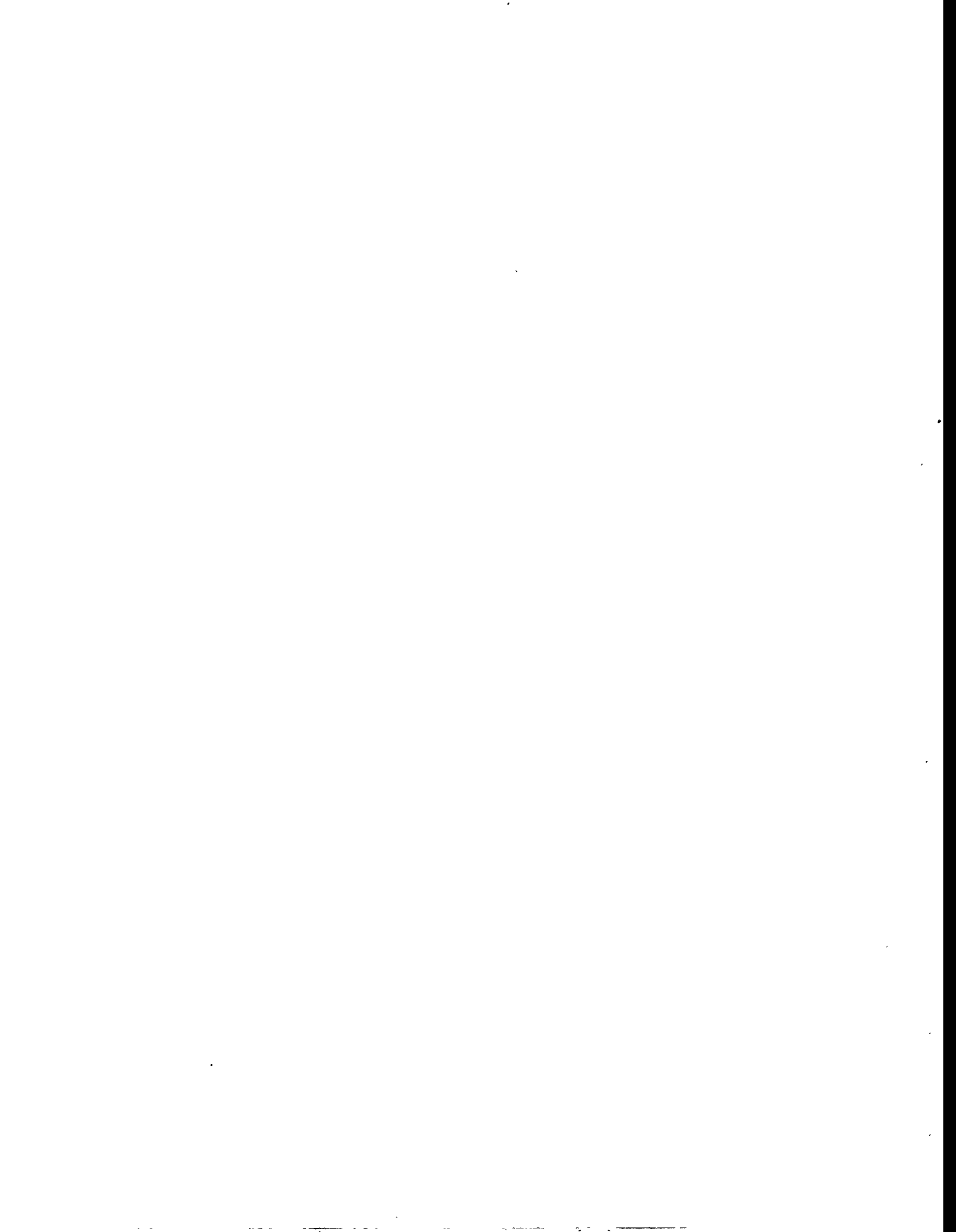
MASTER

DISTRIBUTION OF THIS DOCUMENT IS UNLIMITED



**DISCLAIMER**

**Portions of this document may be illegible  
in electronic image products. Images are  
produced from the best available original  
document.**



## **DISCLAIMER**

This report was prepared as an account of work sponsored by an agency of the United States Government. Neither the United States Government nor any agency thereof, nor any of their employees, makes any warranty, express or implied, or assumes any legal liability or responsibility for the accuracy, completeness, or usefulness of any information, apparatus, product, or process disclosed, or represents that its use would not infringe privately owned rights. Reference herein to any specific commercial product, process, or service by trade name, trademark, manufacturer, or otherwise does not necessarily constitute or imply its endorsement, recommendation, or favoring by the United States Government or any agency thereof. The views and opinions of authors expressed herein do not necessarily state or reflect those of the United States Government or any agency thereof.



SAND96-1326/1  
Unlimited Release  
Printed August 1996

Distribution  
Category UC-721

# **Waste Isolation Pilot Plant Shaft Sealing System Compliance Submittal Design Report**

## **Volume 1 of 2: Main Report Appendices A, B, C, and D**

Repository Isolation Systems Department  
Sandia National Laboratories  
Albuquerque, NM 87185

### **ABSTRACT**

This report describes a shaft sealing system design for the Waste Isolation Pilot Plant (WIPP), a proposed nuclear waste repository in bedded salt. The system is designed to limit entry of water and release of contaminants through the four existing shafts after the WIPP is decommissioned. The design approach applies redundancy to functional elements and specifies multiple, common, low-permeability materials to reduce uncertainty in performance. The system comprises 13 elements that completely fill the shafts with engineered materials possessing high density and low permeability. Laboratory and field measurements of component properties and performance provide the basis for the design and related evaluations. Hydrologic, mechanical, thermal, and physical features of the system are evaluated in a series of calculations. These evaluations indicate that the design guidance is addressed by effectively limiting transport of fluids within the shafts, thereby limiting transport of hazardous material to regulatory boundaries. Additionally, the use or adaptation of existing technologies for placement of the seal components combined with the use of available, common materials assure that the design can be constructed.

## Acknowledgments

The work presented in this document represents the combined effort of a number of individuals at Sandia National Laboratories, Parsons Brinckerhoff (under contract AG-4909), INTERA (under contract AG-4910), RE/SPEC (under contract AG-4911), and Tech Reps. The Sandian responsible for the preparation of each section of the report and the lead individual(s) at firms under contract to Sandia that provided technical expertise are recognized below.

Section	Author(s)
Executive Summary	F.D. Hansen, Sandia
Section 1, Introduction	J.R. Tillerson, Sandia
Section 2, Site Geologic, Hydrologic, & Geochemical Setting	A.W. Dennis and S.J. Lambert, Sandia
Section 3, Design Guidance	A.W. Dennis, Sandia
Section 4, Design Description	A.W. Dennis, Sandia
Section 5, Material Specifications	F.D. Hansen, Sandia
Section 6, Construction Techniques	E.H. Ahrens, Sandia
Section 7, Structural Analyses of Shaft Seals	L.D. Hurtado, Sandia; M.C. Loken and L.L. Van Sambeek, RE/SPEC
Section 8, Hydrologic Evaluation of the Shaft Seal System	M.K. Knowles, Sandia; V.A. Kelley, INTERA
Section 9, Conclusions	J.R. Tillerson and A.W. Dennis, Sandia
Appendix A, Material Specifications	F.D. Hansen, Sandia
Appendix B, Shaft Sealing Construction Procedures	E.H. Ahrens, Sandia, with the assistance of Parsons Brinckerhoff Construction and Scheduling staff
Appendix C, Fluid Flow Analyses	M.K. Knowles, Sandia; V.A. Kelley, INTERA
Appendix D, Structural Analyses	L.D. Hurtado, Sandia; M.C. Loken and L.L. Van Sambeek, RE/SPEC
Appendix E, Design Drawings	A.W. Dennis, Sandia; C.D. Mann, Parsons Brinckerhoff, with the assistance of the Parsons Brinckerhoff Design staff

Design reviews provided by Malcolm Gray, Atomic Energy Canada Ltd., Whiteshell Laboratory; Stephen Phillips, Phillips Mining, Geotechnical & Grouting, Inc.; and John Tinucci, Itasca Consulting Group, Inc. are appreciated, as are document reviews provided by Don Galbraith, U.S. Department of Energy Carlsbad Area Office; William Thompson, Carlsbad Area Office Technical Assistance Contractor; Robert Stinebaugh, Palmer Vaughn, Deborah Coffey, and Wendell Weart, Sandia.

T.P. Peterson and S.B. Kmetz, Tech Reps, served as technical editors of this document.

## Contents

EXECUTIVE SUMMARY .....	vii
Introduction .....	vii
Site Setting.....	vii
Design Guidance.....	viii
Design Description .....	viii
Structural Analysis .....	ix
Hydrologic Evaluations .....	xi
Concluding Remarks .....	xiii
1. INTRODUCTION .....	1
1.1 Purpose of Compliance Submittal Design Report.....	1
1.2 WIPP Description.....	1
1.3 Performance Objective for WIPP Shaft Seal System.....	1
1.4 Sealing System Design Development Process .....	3
1.5 Organization of Document .....	4
1.6 Systems of Measurement.....	5
2. SITE GEOLOGIC, HYDROLOGIC, AND GEOCHEMICAL SETTING.....	7
2.1 Introduction .....	7
2.2 Site Geologic Setting.....	7
2.2.1 Regional WIPP Geology and Stratigraphy.....	7
2.2.2 Local WIPP Stratigraphy .....	10
2.2.3 Rock Mechanics Setting.....	10
2.3 Site Hydrologic Setting .....	12
2.3.1 Hydrostratigraphy.....	12
2.3.2 Observed Vertical Gradients .....	16
2.4 Site Geochemical Setting.....	17
2.4.1 Regional and Local Geochemistry in Rustler Formation and Shallower Units .....	17
2.4.2 Regional and Local Geochemistry in the Salado Formation.....	19
3. DESIGN GUIDANCE.....	23
3.1 Introduction .....	23
3.2 Design Guidance and Design Approach.....	23
4. DESIGN DESCRIPTION.....	25
4.1 Introduction .....	25
4.2 Existing Shafts.....	25
4.3 Sealing System Design Description .....	28
4.3.1 Salado Seals.....	29
4.3.2 Rustler Seals.....	34
4.3.3 Near-Surface Seals .....	34
5. MATERIAL SPECIFICATION .....	37
5.1 Longevity.....	38
5.2 Materials .....	39
5.2.1 Mass Concrete.....	39

5.2.2	Compacted Clay .....	40
5.2.3	Asphalt .....	41
5.2.4	Compacted Salt Column .....	41
5.2.5	Cementitious Grout .....	42
5.2.6	Earthen Fill .....	43
5.3	Concluding Remarks .....	43
6.	CONSTRUCTION TECHNIQUES.....	45
6.1	Multi-Deck Stage.....	45
6.2	Salado Mass Concrete (Shaft Station Monolith and Shaft Plugs).....	45
6.3	Compacted Clay Columns (Salado and Rustler Formations).....	50
6.4	Asphalt Waterstops and Asphaltic Mix Columns.....	50
6.5	Compacted WIPP Salt .....	50
6.6	Grouting of Shaft Walls and Removal of Liners.....	51
6.7	Earthen Fill .....	51
6.8	Schedule.....	53
7.	STRUCTURAL ANALYSES OF SHAFT SEALS .....	55
7.1	Introduction .....	55
7.2	Analysis Methods .....	55
7.3	Models of Shaft Seals Features .....	55
7.3.1	Seal Material Models .....	56
7.3.2	Intact Rock Lithologies .....	56
7.3.3	Disturbed Rock Zone Models .....	56
7.4	Structural Analyses of Shaft Seal Components.....	56
7.4.1	Salado Mass Concrete Seals.....	56
7.4.2	Crushed Salt Seals.....	58
7.4.3	Compacted Clay Seals.....	59
7.4.4	Asphalt Seals .....	59
7.5	Disturbed Rock Zone Considerations.....	60
7.5.1	General Discussion of DRZ .....	60
7.5.2	Structural Analyses .....	60
7.6	Other Analyses .....	61
7.6.1	Asphalt Waterstops .....	61
7.6.2	Shaft Pillar Backfilling.....	62
8.	HYDROLOGIC EVALUATION OF THE SHAFT SEAL SYSTEM.....	63
8.1	Introduction .....	63
8.2	Performance Models.....	63
8.3	Downward Migration of Rustler Groundwater.....	63
8.3.1	Analysis Method .....	64
8.3.2	Summary of Results .....	64
8.4	Gas Migration and Consolidation of Compacted Salt Column .....	65
8.4.1	Analysis Method .....	66
8.4.2	Summary of Results .....	66
8.5	Upward Migration of Brine .....	69
8.6	Intra-Rustler Flow.....	69

9. CONCLUSIONS.....	71
10. REFERENCES .....	73
Appendix A — Material Specification .....	A-1
Appendix B — Shaft Sealing Construction Procedures .....	B-1
Appendix C — Fluid Flow Analyses.....	C-1
Appendix D — Structural Analyses .....	D-1
Appendix E — Design Drawings .....	Volume 2

### Figures

Figure 1-1. View of the WIPP underground facility.....	2
Figure 2-1. Location of the WIPP in the Delaware Basin. ....	8
Figure 2-2. Chart showing major stratigraphic divisions, southeastern New Mexico.....	9
Figure 2-3. Generalized stratigraphy of the WIPP site showing repository level.....	11
Figure 4-1. Arrangement of the Air Intake Shaft sealing system. ....	30
Figure 6-1. Multi-deck stage illustrating dynamic compaction. ....	46
Figure 6-2. Multi-deck stage illustrating excavation for asphalt waterstop.....	47
Figure 6-3. Drop pattern for 6-m-diameter shaft using a 1.2-m-diameter tamper. ....	48
Figure 6-4. Plan and section views of downward spin pattern of grout holes. ....	49
Figure 6-5. Plan and section views of upward spin pattern of grout holes. ....	52
Figure 8-1. Example of calculation of an effective salt column permeability from the depth-dependent permeability at a point in time.....	68
Figure 8-2. Effective permeability of the compacted salt column using the 95% certainty line. ....	68

### Tables

Table 2-1. Salado Brine Seepage Intervals <sup>(1)</sup> .....	14
Table 2-2. Permeability and Thickness of Hydrostratigraphic Units in Contact with Seals .....	15
Table 2-3. Freshwater Head Estimates in the Vicinity of the Air Intake Shaft .....	17
Table 2-4. Chemical Formulas, Distributions, and Relative Abundance of Minerals in the Rustler and Salado Formations (after Lambert, 1992).....	18
Table 2-5. Major Solutes in Selected Representative Groundwater from the Rustler Formation and Dewey Lake Redbeds, in mg/L (after Lambert, 1992).....	19
Table 2-6. Variations in Major Solutes in Brines from the Salado Formation, in mg/L (after Lambert, 1992).....	21
Table 3-1. Shaft Sealing System Design Guidance .....	23
Table 4-1. Drawings Showing Configuration of Existing WIPP Shafts (Drawings are in Appendix E) .....	26
Table 4-2. Summary of Information Describing Existing WIPP Shafts.....	27
Table 4-3. Drawings Showing the Sealing System for Each Shaft (Drawings are in Appendix E).....	31
Table 4-4. Drawings Showing the Shaft Station Monoliths (Drawings are in Appendix E).....	33
Table 8-1. Summary of Results from Performance Model.....	67

## Acronyms

AIS	Air Intake Shaft
AMM	asphalt mastic mix
CFR	Code of Federal Regulations
DOE	Department of Energy
DRZ	disturbed rock zone
EPA	Environmental Protection Agency
HMAC	hot mix asphalt concrete
MDCF	Multimechanism Deformation Coupled Fracture
MD	Munson-Dawson
NMVP	No Migration Variance Petition
PA	performance assessment
PTM	Plug Test Matrix
QA	quality assurance
SMC	Salado Mass Concrete
SPVD	Site Preliminary Design Validation
SSSPT	Small Scale Seal Performance Test
SWCF	Sandia WIPP Central Files
TRU	transuranic
WIPP	Waste Isolation Pilot Plant

## **EXECUTIVE SUMMARY**

### **Introduction**

This report documents a shaft seal system design developed as part of a submittal to the Environmental Protection Agency (EPA) that will demonstrate regulatory compliance of the Waste Isolation Pilot Plant (WIPP) for disposal of transuranic waste. The shaft seal system limits entry of water into the repository and restricts the release of contaminants. Shaft seals address fluid transport paths through the opening itself, along the interface between the seal material and the host rock, and within the disturbed rock surrounding the opening. The entire shaft seal system is described in this report and its five appendices, which include seal material specifications, construction methods, rock mechanics analyses, fluid flow evaluations, and the design drawings. The design represents a culmination of several years of effort that has most recently focused on providing to the EPA a viable shaft seal system design. Sections of this report and the appendices explore function and performance of the WIPP shaft seal system and provide well documented assurance that such a shaft seal system could be constructed using available materials and methods.

The purpose of the shaft seal system is to limit fluid flow within four existing shafts after the repository is decommissioned. Such a seal system would not be implemented for several decades, but to establish that regulatory compliance can be achieved at that future date, a shaft seal system has been designed that exhibits excellent durability and performance and is constructable using existing technology. The design approach is conservative, applying redundancy to functional elements and specifying various common, low-permeability materials to reduce uncertainty in performance. It is recognized that changes in the design described here will occur before construction and that this design is not the only possible combination of materials and construction strategies that would adequately limit fluid flow within the shafts.

### **Site Setting**

One of the Department of Energy's (DOE's) site selection criteria is a favorable geologic setting which minimizes fluid flow as a transport mechanism. Groundwater hydrology in the proximity of the WIPP site is characterized by geologic strata with low transmissivity and low hydrologic gradients, both very positive features with regard to sealing shafts. For purposes of performance evaluations, hydrological analyses divide lithologies and requirements into the Rustler Formation (and overlying strata) and the Salado Formation, comprised mostly of salt. The principal design concern is fluid transport phenomena of seal materials and lithologies within the Salado Formation.

The rock mechanics setting is an important consideration in terms of system performance. Rock properties affect hydrologic response of the shaft seal system. The stratigraphic section contains lithologies that exhibit brittle and ductile behavior. A zone of rock around the shafts is disturbed owing to the creation of the opening. The disturbed rock zone (DRZ) is an important design consideration because it possesses higher permeability than intact rock. Host rock response and its potential to fracture, flow, and heal around WIPP shaft openings are relevant to the performance of the shaft seal system.

## Design Guidance

Use of both engineered and natural barriers to isolate wastes from the accessible environment is required by 40 CFR 191.14(d), and the use of engineered barriers to prevent or substantially delay movement of water or radionuclides toward the accessible environment is required by 40 CFR 194.44. Hazardous constituent release limits are specified in 40 CFR 191 for the entire repository system (EPA, 1996a; 1996b).

Design guidance for the shaft seal system addresses the need for the WIPP to comply with system requirements and to follow accepted engineering practices using demonstrated technology. Design guidance is categorized below:

- limit hazardous constituents reaching regulatory boundaries,
- restrict groundwater flow through the sealing system,
- use materials possessing mechanical and chemical compatibility,
- protect against structural failure of system components,
- limit subsidence and prevent accidental entry, and
- utilize available construction methods and materials.

Discussions of the design presented in the text of this report and the details presented in the appendices respond to these qualitative design guidelines. The shaft seal system design was completed under a Quality Assurance program that includes review by independent, qualified experts to assure the best possible information is provided to the DOE on selection of engineered barriers (40 CFR 194.27). Technical reviewers examined the complete design including conceptual, mathematical, and numerical models and computer codes (40 CFR 194.26). The design reduces the impact of uncertainty associated with any particular element by using multiple sealing system components and by using components constructed from different materials.

## Design Description

The shaft sealing system comprises 13 elements that completely fill the shaft with engineered materials possessing high density and low permeability. Salado Formation components provide the primary regulatory barrier by limiting fluid transport along the shaft during and beyond the 10,000-year regulatory period. Components within the Rustler Formation limit commingling between brine-bearing members, as required by state regulations. Components from the Rustler to the surface fill the shaft with common materials of high density, consistent with good engineering practice. A synopsis of each component is given below.

**Shaft Station Monolith.** At the bottom of each shaft a salt-saturated concrete monolith supports the local roof. A salt-saturated concrete, called Salado Mass Concrete (SMC), is specified and is placed using a conventional slickline construction procedure where the concrete is batched at the surface. SMC has been tailored to match site conditions. The salt-handling shaft and the waste-handling shaft have sumps which also will be filled with salt-saturated concrete as part of the monolith.

**Clay Columns.** A sodium bentonite is used for three compacted clay components in the Salado and Rustler Formations. Although alternative construction specifications are viable, labor-

intensive placement of compressed blocks is specified because of proven performance. Clay columns effectively limit brine movement from the time they are placed to beyond the 10,000-year regulatory period. Stiffness of the clay is sufficient to promote healing of fractures in the surrounding rock salt near the bottom of the shafts, thus removing the proximal DRZ as a potential pathway. The Rustler clay column limits brine communication between the Magenta and Culebra Members of the Rustler Formation.

**Concrete-Asphalt Waterstop Components.** Concrete-asphalt waterstop components comprise three elements: an upper concrete plug, a central asphalt waterstop, and a lower concrete plug. Three such components are located within the Salado Formation. These concrete-asphalt waterstop components provide independent shaft cross-section and DRZ seals that limit fluid transport, either downward or upward. Concrete fills irregularities in the shaft wall, while use of the salt-saturated concrete assures good bonding with salt. Salt creep against the rigid concrete components establishes a compressive stress state and promotes early healing of the salt DRZ surrounding the concrete plugs. The asphalt intersects the shaft cross section and the DRZ.

**Compacted Salt Column.** Each shaft seal includes a column of compacted WIPP salt with 1.5 percent weight water added to the natural material. Construction demonstrations have shown that mine-run WIPP salt can be dynamically compacted to a density equivalent to approximately 90% of the average density of intact Salado salt. The remaining void space is removed through consolidation caused by creep closure. The salt column becomes less permeable as density increases. The location of the compacted salt column near the bottom of the shaft assures the fastest achievable consolidation of the compacted salt column after closure of the repository. Analyses indicate that the salt column becomes an effective long-term barrier in under 100 years.

**Asphalt Column.** An asphalt-aggregate mixture is specified for the asphalt column, which bridges the Rustler/Salado contact and provides a seal essentially impermeable to brine for the shaft cross-section and the shaft wall interface. All asphalt is placed with a heated slickline.

**Concrete Plugs.** A concrete plug is located just above the asphalt column and keyed into the surrounding rock. Mass concrete is separated from the cooling asphalt column with a layer of fibercrete, which permits work to begin on the overlying clay column before the asphalt has completely cooled. Another concrete plug is located near the surface, extending downward from the top of the Dewey Lake Redbeds.

**Earthen Fill.** The upper shaft is filled with locally available earthen fill. Most of the fill is dynamically compacted (the same method used to construct the salt column) to a density approximating the surrounding lithologies. The uppermost earthen fill is compacted with a sheepsfoot roller or vibratory plate compactor.

### **Structural Analysis**

Structural issues pertaining to the shaft seal system have been evaluated. Mechanical, thermal, physical, and hydrological features of the system are included in a broad suite of structural calculations. Conventional structural mechanics applications would normally calculate load on system elements and compare the loads to failure criteria. Several such conventional calculations have been performed and show that the seal elements exist in a favorable, compressive stress state that is low in comparison to the strength of the seal materials. Thermal analyses have been

performed to examine the effects of concrete heat of hydration and heat transfer for asphalt elements. Coupling between damaged rock and fluid flow and between the density and permeability of the consolidating salt column is evaluated within the scope of structural calculations.

The appendices provide descriptions of various structural calculations conducted as part of the design study. The purpose of each calculation varies; however, the calculations generally address one or more of the following concerns: (1) stability of the component, (2) influences of the component on hydrological properties of the seal and surrounding rock, or (3) construction methods. Stability calculations address:

- potential for thermal cracking of concrete;
- structural loads on seal components resulting from salt creep, gravity, swelling clay, dynamic compaction, or possible repository-generated gas pressures.

Structural calculations defining input conditions to hydrological calculations include:

- spatial extent of the DRZ within the Salado Formation salt beds as a function of depth, time, and seal material;
- fracturing and DRZ development within Salado Formation interbeds;
- shaft-closure induced consolidation of compacted salt columns;
- impact of pore pressures on salt consolidation.

Construction analyses examine:

- placement and structural performance of asphalt waterstops,
- potential subsidence reduction through backfilling the shaft station areas.

Structural calculations model shaft features including representation of the host rock and its damaged zone as well as the seal materials themselves. Two important structural calculations discussed below are unique to shaft seal applications.

**DRZ Behavior.** The development and subsequent healing of a disturbed rock zone (DRZ) that forms in the rock mass surrounding the WIPP shafts is a significant concern in the seal design. It is well known that a DRZ will develop in rock salt adjacent to the shaft upon excavation. Placement of rigid components in the shaft promotes healing within the salt DRZ as seal elements restrain inward creep and reduce the stress difference. Two computer models to calculate development and extent of the salt DRZ are used. The first model uses a ratio of stress invariants to predict fracture; the second approach uses a damage stress criterion. The temporal and spatial extent of the DRZ along the entire shaft length is evaluated.

Several analyses are performed to examine DRZ behavior of the rock salt surrounding the shaft. The time-dependent DRZ development and subsequent healing in the Salado salt surrounding each of the four seal materials are considered. All seal materials below a depth of about 300 m provide sufficient rigidity to heal the DRZ, a phenomenon that occurs quickly around rigid components near the shaft bottom. An extensive calculation is made of construction effects on the DRZ during placement of the asphalt-concrete waterstops. The time-dependent development of the DRZ within anhydrite and polyhalite interbeds of the Salado Formation is calculated. For

all interbeds, the factor of safety against shear or tensile fracturing increases with depth into the rock surrounding the shaft wall. These results indicate that a continuous DRZ will not develop in nonsalt Salado rocks. Rock mechanics analysis also determines which of the near surface lithologies fracture in the proximity of the shaft. Results from these rock mechanics analyses are used as input conditions for the fluid-flow analyses.

**Compacted Salt Behavior.** Unique application of crushed salt as a seal component required development of a constitutive model for salt reconsolidation. The model developed includes a nonlinear elastic component and a creep consolidation component. The nonlinear elastic modulus is density-dependent, based on laboratory test data performed on WIPP crushed salt. Creep consolidation behavior of crushed salt is based on three candidate models whose parameters are obtained from model fitting to hydrostatic and shear consolidation test data gathered for WIPP crushed salt. The model for consolidating crushed salt is used to predict permeability of the salt column.

The seal system prevents fluid transport to the consolidating salt column to ensure that pore pressure does not unacceptably inhibit the reconsolidation process. Calculations made to estimate fractional density of the crushed salt seal as a function of time, depth, and pore pressure show consolidation time increases as pore pressure increases, as expected. At a constant pore pressure of one atmosphere, compacted salt will increase from its initial fractional density of 90% to 96% within 40, 80, and 120 years after placement at the bottom, middle, and top of the salt component, respectively. At a fractional density of 96%, the permeability of reconsolidating salt is approximately  $10^{-18} \text{ m}^2$ . A pore pressure of 2 MPa increases times required to achieve a fractional density of 96% to 92 years, 205 years, and 560 years at the bottom, middle, and top of the crushed salt column, respectively. A pore pressure of 4 MPa would effectively prevent reconsolidation of the crushed salt within 1,000 years. Fluid flow calculations show only minimal transport of fluids to the salt column, so pore pressure equilibrium in the consolidating salt does not occur before low permeabilities ( $\sim 10^{-18} \text{ m}^2$ ) are achieved.

## Hydrologic Evaluations

The ability of the shaft seal system to satisfy design guidance is determined by the performance of the actual seal components within the physical setting in which they are constructed. Important elements of the physical setting are hydraulic gradients of the region, properties of the lithologic units surrounding a given seal component, and potential gas generation within the repository. Hydrologic evaluations focus on processes that could result in fluid flow through the shaft seal system and the ability of the seal system to limit any such flow. Transport of radiological or hazardous constituents will be limited if the carrier fluids are similarly limited.

Physical processes that could impact seal system performance have been incorporated into four models. These models evaluate: (1) downward migration of groundwater from the Rustler Formation, (2) gas migration and reconsolidation of the crushed salt seal component, (3) upward migration of brines from the repository, and (4) flow between water-bearing zones in the Rustler Formation.

**Downward Migration of Rustler Groundwater.** The shaft seal system is designed to limit groundwater flowing into and through the shaft sealing system. The principal source of groundwater to the seal system is the Culebra Member of the Rustler Formation. No significant

sources of groundwater exist within the Salado Formation; however, brine seepage has been noted at a number of the marker beds and is included in the models. Downward migration of Rustler groundwater is limited to ensure that liquid saturation of the compacted salt column does not impact the consolidation process and to limit quantities of brine reaching the repository horizon.

Consolidation of the compacted salt column will be most rapid immediately following seal construction. Simulations conducted for the 200-year period following closure demonstrate that, during this initial period, downward migration of Rustler groundwater is insufficient to impact the consolidation process. Rock mechanics analyses show that this period encompasses the reconsolidation process. Lateral migration of brine through the marker beds is quantified in the analysis and shown to be inconsequential.

At steady-state, the flow rate is most dependent on permeability of the system. Potential flow paths within the seal system consist of the seal material, an interface with the surrounding rock, and the host rock DRZ. Low permeability is specified for the engineered materials, and construction methods ensure a tight interface. Thus the flow path most likely to impact performance is the DRZ. Effects of the DRZ and sensitivity of the seal system performance to both engineered and host rock barriers show that the DRZ is successfully mitigated by the proposed design.

**Gas Migration and Salt Column Consolidation.** A multi-phase flow model of the lower seal system evaluates the performance of components extending from the middle concrete-asphalt waterstop located at the top of the salt column to the repository horizon for 200 years following closure. During this time period, the principal fluid sources to the model consist of potential gas generated by the waste and lateral brine migration within the Salado Formation. The predicted downward migration of a small quantity of Rustler groundwater (discussed above) is included in this analysis.

Effects of gas generation are evaluated for three different repository repressurization scenarios, which simulate pressures as high as 14 MPa. Model results predict that high repository pressures do not produce appreciable differences in the volume of gas migration over the 200-year simulation period. Relatively low gas flow is a result of the low permeability and rapid healing of the DRZ around the lower concrete-asphalt waterstop.

**Upward Migration of Brine.** The Salado Formation is overpressurized with respect to the measured heads in the Rustler, and upward migration of contaminated brines could occur through an inadequately sealed shaft. Results from the model discussed above demonstrate that the crushed salt seal will reconsolidate to a very low permeability within 100 years following repository closure. Structural results show that the DRZ surrounding the long-term clay and crushed salt seal components will completely heal within the first several decades. Model calculations predict that very little brine flows from the repository to the Rustler/Salado contact.

**Intra-Rustler Flow.** Based on head differences between the various members of the Rustler Formation, nonhydrostatic conditions exist within the Rustler Formation. Therefore, the potential exists for vertical flow within water-bearing strata within the Rustler. The two units with the greatest transmissivity within the Rustler are the Culebra and the Magenta dolomites, which have the greatest potential for interflow. The relatively low undisturbed permeabilities of

the mudstone and anhydrite units separating the Culebra and the Magenta naturally limit crossflow. However, the construction and subsequent closure of the shaft provide a potentially permeable vertical conduit connecting water-bearing units.

The primary motivation for limiting formation crossflow within the Rustler is to prevent mixing of formation waters within the Rustler, as required by State of New Mexico statute. Commonly, such an undertaking would limit migration of higher dissolved solids (high-density) groundwater into lower dissolved solids groundwater. In the vicinity of the WIPP site, the Culebra has a higher density groundwater than the Magenta, and the potential for fluid migration between the two most transmissive units is from the unit with the lower total dissolved solids to the unit with the higher dissolved solids. This calculation shows that potential flow rates between the Culebra and the Magenta are insignificant. Under expected conditions, intra-Rustler flow is expected to be of such a limited quantity that (1) it will not affect either the hydraulic or chemical regime within the Culebra or the Magenta and (2) it will not be detrimental to the seal system itself.

### **Concluding Remarks**

The principal conclusion is that an effective, implementable shaft seal system has been designed for the WIPP. Design guidance is addressed by limiting any transport of fluids within the shaft, thereby limiting transport of hazardous material to regulatory boundaries. The application or adaptation of existing technologies for placement of seal components combined with the use of available, common materials provide confidence that the design can be constructed. The structural setting for seal elements is compressive, with shear stresses well below the strength of seal materials. Because of the favorable hydrologic regime coupled with the low intrinsic permeability of seal materials, long-term stability of the shaft seal system is expected. Credibility of these conclusions is bolstered by the basic design approach of using multiple components to perform each sealing function and by using extensive lengths within the shafts to effect a sealing system. The shaft seal system adequately meets design requirements and can be constructed.

Page intentionally blank.

# 1. INTRODUCTION

## 1.1 Purpose of Compliance Submittal Design Report

This report documents the detailed design of the shaft sealing system for the Waste Isolation Pilot Plant (WIPP). The design documented in this report builds on the concepts and preliminary evaluations presented in the Sealing System Design Report issued in 1995 (DOE, 1995). The report contains a detailed description of the design and associated construction procedures, material specifications, analyses of structural and fluid flow performance, and design drawings. The design documented in this report forms the basis for shaft sealing discussions in the Compliance Certification Application (CCA) to the Environmental Protection Agency (EPA), for shaft sealing simulations in the associated performance assessments, and for ongoing evaluations of the sealing system associated with the no-migration variance petition.

## 1.2 WIPP Description

The WIPP is designed as a full-scale, mined geological repository for the safe management, storage, and disposal of transuranic (TRU) radioactive wastes generated by US government defense programs. The facility is located near Carlsbad, New Mexico, in the southeastern portion of the state. The underground facility (Figure 1-1) consists of a series of shafts, drifts, panels, and disposal rooms. Four shafts, ranging in diameter from 3.5 to 6.1 m, connect the disposal horizon to the surface. Sealing of these four shafts is the focus of this report.

The disposal horizon is at a depth of approximately 655 m in bedded halite within the Salado Formation. The Salado is a sequence of bedded evaporites approximately 600 m thick that were deposited during the Permian Period, which ended about 225 million years ago. Salado salt has been identified as a good geologic medium to host a nuclear waste repository because of several favorable characteristics. The characteristics present at the WIPP site include very low permeability, vertical and lateral stratigraphic extent, tectonic stability, and the ability of salt to creep and ultimately entomb material placed in excavated openings. Creep closure also plays an important role in the shaft sealing strategy.

The WIPP facility must be determined to be in compliance with applicable regulations prior to the disposal of waste. After the facility meets the regulatory requirements, disposal rooms will be filled with containers holding TRU wastes of various forms. Wastes placed in the drifts and disposal rooms will be at least 150 m from the shafts. Regulatory requirements include use of both engineered and natural barriers to limit migration of hazardous constituents from the repository to the accessible environment. The shaft seals are part of the engineered barriers.

## 1.3 Performance Objective for WIPP Shaft Seal System

Each of the four shafts from the surface to the underground repository must be sealed to limit hazardous material release to the accessible environment and to limit groundwater flow into the repository. Although the seals will be permanent, the regulatory period applicable to the repository system analyses is 10,000 years.

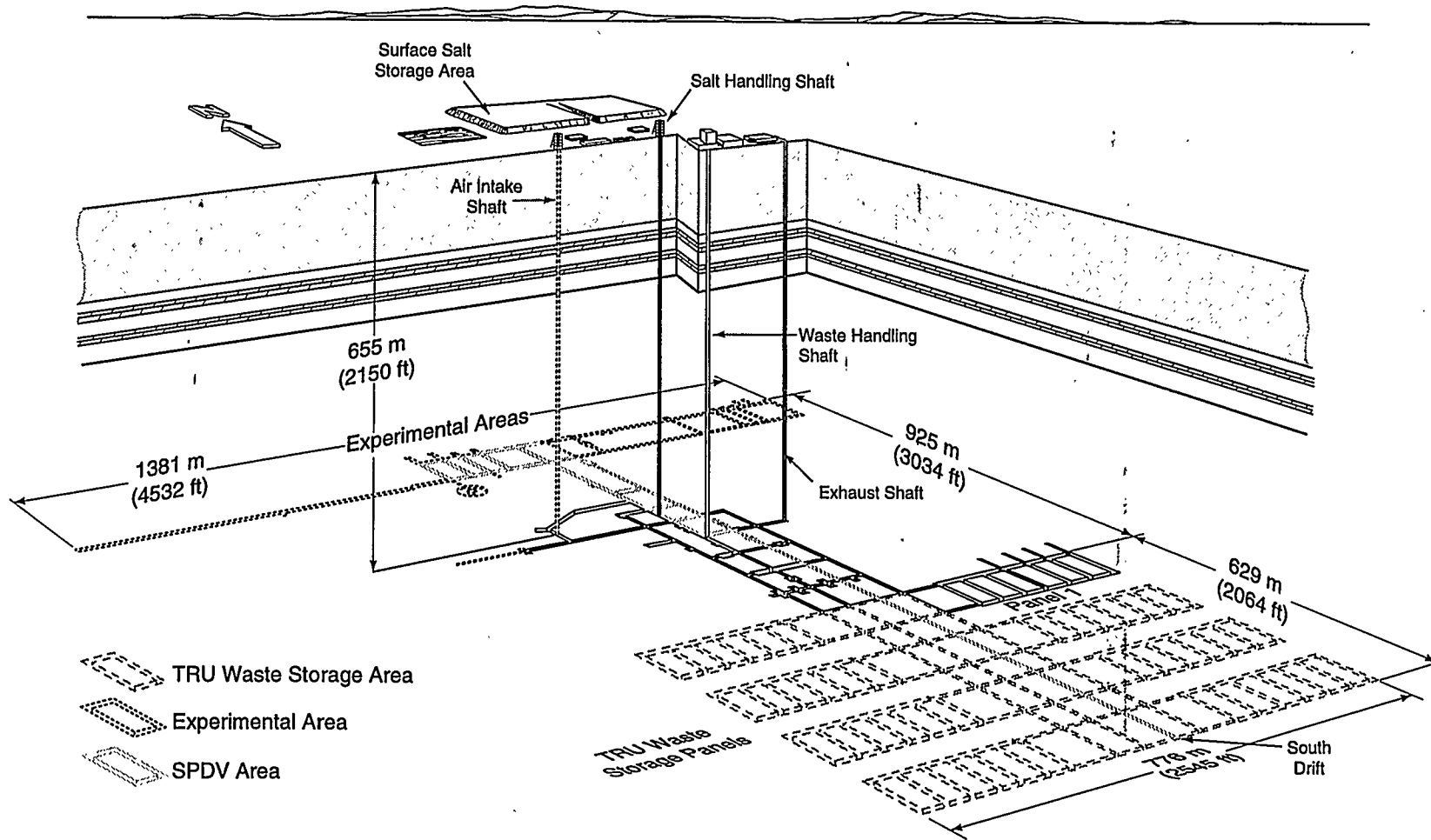


Figure 1-1. View of the WIPP facility.

## 1.4 Sealing System Design Development Process

This report presents a conservative approach to shaft sealing system design. Shaft sealing system performance plays a crucial role in meeting regulatory radionuclide and hazardous constituents release requirements. Although all engineering materials have uncertainties in properties, a combination of available, low-permeability materials can provide an effective sealing system. To reduce the impact of system uncertainties and to provide a high level of assurance of compliance, numerous components are used in this sealing system. Components in this design include long columns of clay, densely compacted crushed salt, a waterstop of asphaltic material sandwiched between massive low-permeability concrete plugs, a column of asphalt, and a column of earthen fill. Different materials perform identical functions within the design, thereby adding confidence in the system performance through redundancy.

The design is based on common materials and construction methods that utilize available technologies. When choosing materials, emphasis was given to permeability characteristics and mechanical properties of seal materials. However, the system is also chemically and physically compatible with the host formations, enhancing long-term performance.

Recent laboratory experiments, construction demonstrations, and field test results have been added to the broad and credible database and have supported advances in modeling capability. Results from a series of multi-year, in situ, small-scale seal performance tests show that bentonite and concrete seals maintain very low permeabilities and show no deleterious effects in the WIPP environment. A large-scale dynamic compaction demonstration established that crushed salt can be successfully compacted. Laboratory tests show that compacted crushed salt consolidates through creep closure of the shaft from initial conditions achieved in dynamic compaction to a dense salt mass with regions where permeability approaches that of in situ salt. These technological advances have allowed more credible analysis of the shaft sealing system.

The design was developed through an interactive process involving a design team consisting of technical specialists in the design and construction of underground facilities, materials behavior, rock mechanics analysis, and fluid flow analysis. The design team included specialists drawn from the staff of Sandia National Laboratories, Parsons Brinckerhoff Quade and Douglas, Inc. (contract number AG-4909), INTERA, Inc. (contract number AG-4910), and RE/SPEC Inc. (contract number AG-4911), with management by Sandia National Laboratories. The contractors developed a quality assurance program consistent with the Sandia National Laboratories Quality Assurance Program Description for the WIPP project. All three contractors received quality assurance support visits and were audited through the Sandia National Laboratories audit and assessment program. Quality assurance (QA) documentation is maintained in the Sandia National Laboratories WIPP Central Files. Access to project files for each contractor can be accomplished using the contract numbers specified above. In addition to the contractor support, technical input was obtained from consultants in various technical specialty areas.

Formal preliminary and final design reviews have been conducted on the technical information documented in the report. In addition, technical, management, and QA reviews have been performed on this report. Documentation is in the WIPP Central File.

It is recognized that additional information, such as on specific seal material or formation characteristics, on the sensitivity of system performance to component properties, on placement effectiveness, and on long-term performance, could be used to simplify the design and perhaps reduce the length or number of components. Such design optimization and associated simplifications are left to future research that may be used to update the compliance evaluations completed between now and the time of actual seal emplacement.

## **1.5 Organization of Document**

This report contains an Executive Summary, 10 sections, and 5 appendices. The body of the report does not generally contain detailed backup information; this information is incorporated by reference or in the appendices.

The Executive Summary is a synopsis of the design and the supporting discussions related to seal materials, construction procedures, structural analyses, and fluid flow analyses. Introductory material in Section 1 sets the stage for and provides a "road map" to the remainder of the report.

Site characteristics that detail the setting into which the seals would be placed are documented in Section 2. These characteristics include the WIPP geology and stratigraphy for both the region and the shafts as well as a brief discussion of rock mechanics considerations of the site that impact the sealing system. Regional and local characteristics of the hydrologic and geochemical settings are also briefly discussed.

Section 3 presents the design guidance used for development of the shaft sealing system design. Seal-related guidance from applicable regulations is briefly described. The design guidance is then provided along with the design approach used to implement the guidance. The guidance forms the basis both for the design and for evaluations of the sealing system presented in other sections.

The shaft sealing system is documented in Section 4; detailed drawings for the design are provided in Appendix E. The seal components, their design, and their functions are discussed for the Salado, the Rustler, and the overlying formations.

The sealing materials are described briefly in Section 5, with more detail provided in the materials specifications (Appendix A). The materials used in the various seal components are discussed along with the reasons they are expected to function as intended. Material properties including permeability, strength, and mechanical constitutive response are given for each material. Brief discussions of expected compatibility, performance, construction techniques, and other characteristics relevant to the WIPP setting are also given.

Section 6 contains a brief description of the construction techniques proposed for use. General site and sealing preparation activities are discussed, including construction of a multi-deck stage for use throughout the placement of the components. Construction procedures to be used for the various types of components are then summarized based on the more detailed discussions provided in Appendix B.

Section 7 summarizes structural analyses performed to assess the ability of the shaft sealing system to function in accordance with the design guidance provided in Section 3 and to

provide input to hydrological calculations. The methods and computer programs, the models used to simulate the behavior of the seal materials and surrounding salt, and the results of the analyses are discussed. Particular emphasis is placed on the evaluations of the behavior of the disturbed rock zone. Details of the structural analyses are presented in Appendix D.

Section 8 summarizes fluid flow analyses performed to assess the ability of the shaft sealing system to function in accordance with the design guidance provided in Section 3. Hydrologic evaluations are focused on processes that could result in fluid flow through the shaft seal system and the ability of the seal system to limit such flow. Processes evaluated are downward migration of groundwater from the overlying formation, gas migration and reconsolidation of the crushed salt component, upward migration of brines from the repository, and flow between water-bearing zones in the overlying formation. Hydrologic models are described and the results are discussed as they relate to satisfying the design guidance, with extensive reference to Appendix C that documents details of the flow analyses.

Conclusions drawn about the performance of the WIPP shaft sealing system are described in Section 9. The principal conclusion that an effective, implementable design has been presented is based on the presentations in the previous sections. A reference list that documents principal references used in developing this design is then provided.

The five appendices that follow provide details related to the following subjects:

Appendix A — Material Specification

Appendix B — Shaft Sealing Construction Procedures

Appendix C — Fluid Flow Analyses

Appendix D — Structural Analyses

Appendix E — Design Drawings (separate volume)

## 1.6 Systems of Measurement

Two systems of measurement are used in this document and its appendices. Both the System International d'Unites (SI) and English Gravitational (*fps* units) system are used. This usage corresponds to common practice in the United States, where SI units are used for scientific studies and *fps* units are used for facility design, construction materials, codes, and standards. Dual dimensioning is used in the design description and other areas where this use will aid the reader.

Page intentionally blank.

## **2. SITE GEOLOGIC, HYDROLOGIC, AND GEOCHEMICAL SETTING**

The site characteristics relevant to the sealing system are discussed in this section. The location and geologic setting of the WIPP are discussed first to provide background. The geology and stratigraphy, which affect the shafts, are then discussed. The hydrologic and geochemical settings, which influence the seals, are described last.

### **2.1 Introduction**

The WIPP site is located in an area of semiarid rangeland in southeastern New Mexico. The nearest major population center is Carlsbad, 42 km west of the WIPP. Two smaller communities, Loving and Malaga, are about 33 km to the southwest. Population density close to the WIPP is very low: fewer than 30 permanent residents live within a 16-km radius.

### **2.2 Site Geologic Setting**

Geologically the WIPP is located in the Delaware Basin, an elongated depression that extends from just north of Carlsbad southward into Texas. The Delaware Basin is bounded by the Capitan Reef (see Figure 2-1). The basin covers over 33,000 km<sup>2</sup> and is filled with sedimentary rocks to depths of 7,300 m (Hills, 1984). Rock units of the Delaware Basin (representing the Permian System through the Quaternary System) are listed in Figure 2-2.

Minimal tectonic activity has occurred in the region since the Permian Period (Powers et al., 1978). Faulting during the late Tertiary Period formed the Guadalupe and Delaware Mountains along the western edge of the basin. The most recent igneous activity in the area occurred during the mid-Tertiary Period about 35 million years ago and is evidenced by a dike in the subsurface 16 km northwest of the WIPP. Major volcanic activity last occurred more than 1 billion years ago during Precambrian time (Powers et al., 1978). None of these processes affected the Salado Formation at the WIPP. Therefore, seismic-related design criteria are not included in the current seal systems design guidelines.

#### **2.2.1 Regional WIPP Geology and Stratigraphy**

The Delaware Basin began forming with crustal subsidence during the Pennsylvanian Period approximately 300 million years ago. Relatively rapid subsidence over a period of about 14 million years resulted in the deposition of a sequence of deep-water sandstones, shales, and limestones rimmed by shallow-water limestone reefs such as the Capitan Reef (see Figure 2-1). Subsidence slowed during the late Permian Period. Evaporite deposits of the Castile Formation and the Salado Formation (which hosts the WIPP underground workings) filled the basin and extended over the reef margins. The evaporites, carbonates, and clastic rocks of the Rustler Formation and the Dewey Lake Redbeds were deposited above the Salado Formation near the end of the Permian Period. The Santa Rosa and Gatuña Formations were deposited after the close of the Permian Period.

From the surface downward to the repository horizon the stratigraphic units are the Quaternary surface sand sediments, Gatuña Formation, Santa Rosa Formation, Dewey Lake Redbeds, Rustler Formation, and Salado Formation. Three principal stratigraphic units (the Dewey Lake Redbeds, the Rustler Formation, and the Salado Formation) comprise all but the upper 15 to 30 m (50 to 100 ft) of the geologic section above the WIPP facility.

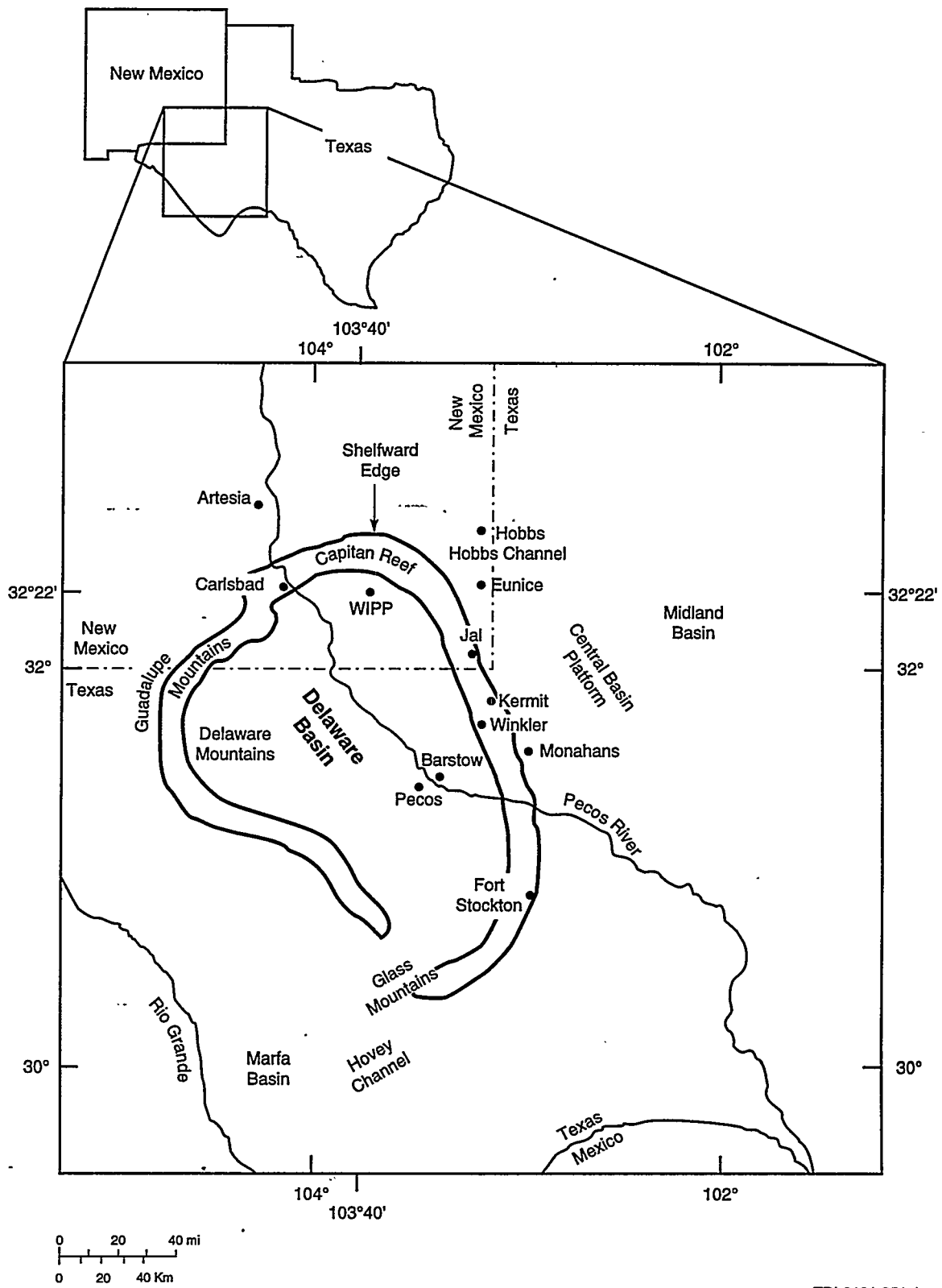


Figure 2-1. Location of the WIPP in the Delaware Basin.

Erathem	System	Series	Lithostratigraphic Unit	Age Estimate (yr)		
Cenozoic	Quaternary	Holocene	Windblown sand			
		Pleistocene	Mescalero caliche	~500,000		
			Gatufia Formation	~600,000		
	Tertiary	Pliocene		Ogallala Formation	5.5 million	
			Miocene		24 million	
		Oligocene	Absent in southeastern New Mexico			66 million
				Eocene		
				Paleocene		
		Cretaceous	Upper	Absent in southeastern New Mexico	144 million	
			Lower	Detritus preserved		
Mesozoic	Jurassic	Absent in southeastern New Mexico	208 million			
	Triassic	Upper	Dockum Group	245 million		
		Lower	Absent in southeastern New Mexico			
Paleozoic	Upper	Ochoan	Dewey Lake Redbeds Rustler Formation Salado Formation Castile Formation	286 million		
		Permian	Guadalupian		Capitan Limestone and Bell Canyon Formation	
	Lower		Leonardian		Bone Springs	
			Wolfcampian		Wolfcamp (informal)	

Modified from Bachman, 1987

Figure 2-2. Chart showing major stratigraphic divisions, southeastern New Mexico.

The Dewey Lake Redbeds consist of alternating layers of reddish-brown, fine-grained sandstone and siltstone cemented with calcite and gypsum (Vine, 1963). The Rustler Formation lies below the Dewey Lake Redbeds; this formation, the youngest of the Late Permian evaporite sequence, includes units that provide potential pathways for radionuclide migration from the WIPP. The five units of the Rustler, from youngest to oldest, are: (1) the Forty-niner Member, (2) the Magenta Dolomite Member, (3) the Tamarisk Member, (4) the Culebra Dolomite Member, and (5) an unnamed lower member.

The 250-million-year-old Salado Formation lies below the Rustler Formation. This unit is about 600 m thick and consists of three informal members. From youngest to oldest, they are: (1) an upper member (unnamed) composed of reddish-orange to brown halite interbedded with polyhalite, anhydrite, and sandstone, (2) a middle member (the McNutt Potash Zone) composed of reddish-orange and brown halite with deposits of sylvite and langbeinite; and (3) a lower member (unnamed) composed of mostly halite with lesser amounts of anhydrite, polyhalite, and glauberite, with some layers of fine clastic material. These lithologic layers are nearly horizontal at the WIPP, with a regional dip of less than one degree. The WIPP repository is located in the unnamed lower member of the Salado Formation, approximately 655 m (2150 ft) below the ground surface.

### **2.2.2 Local WIPP Stratigraphy**

The generalized stratigraphy of the WIPP site, with the location of the repository, is shown in Figure 2-3. To establish the geologic framework required for the design of the WIPP facility shaft sealing system, an evaluation was performed to assess the geologic conditions existing in and between the shafts, where the individual shaft sealing systems will eventually be emplaced (DOE, 1995: Appendix A). The study evaluated shaft stratigraphy, regional groundwater occurrence, brine occurrence in the exposed Salado Formation section, and the consistency between recorded data and actual field data.

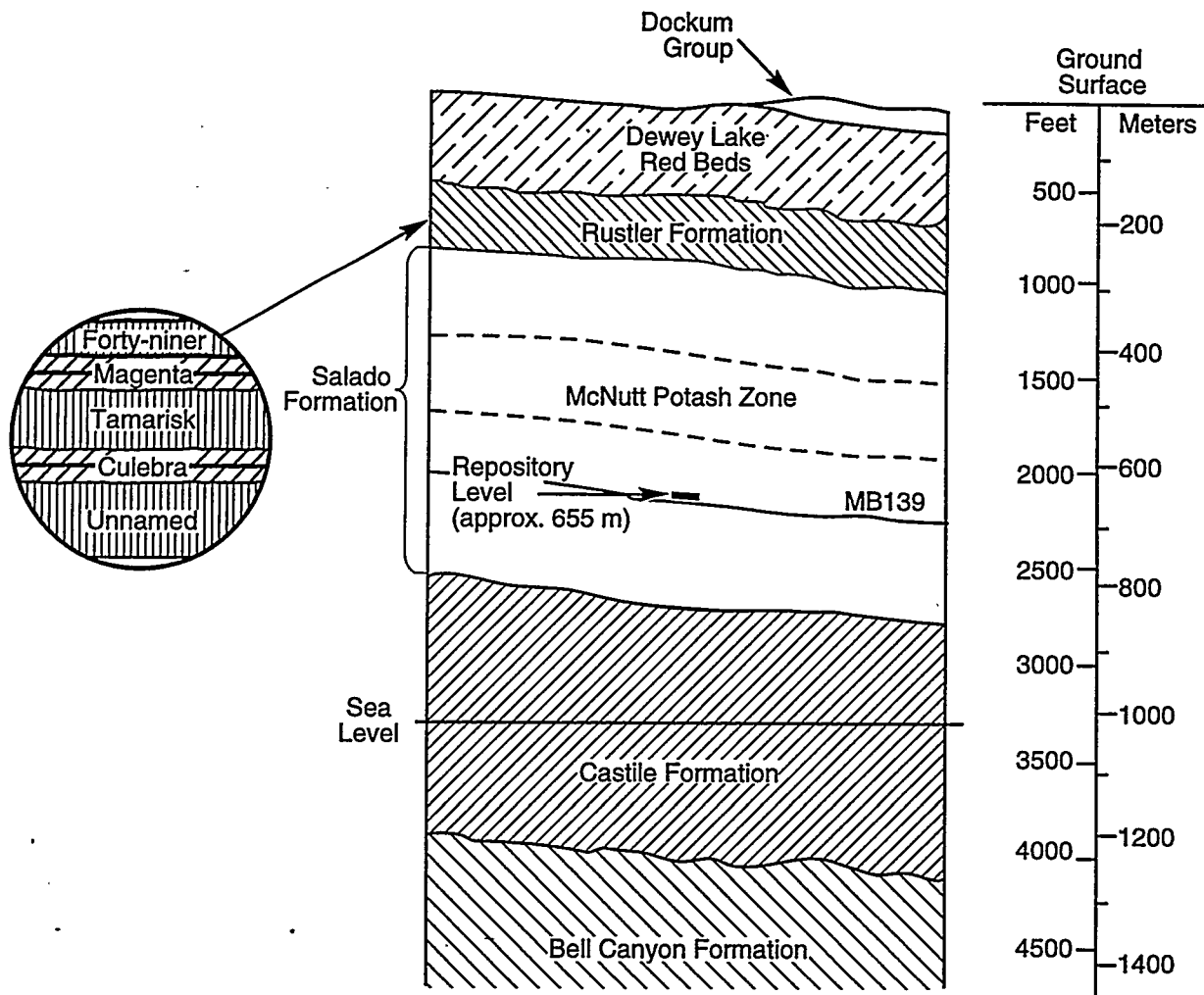
Four shafts connect the WIPP underground workings to the surface, the (1) Air Intake Shaft (AIS), (2) Exhaust Shaft, (3) Salt Handling Shaft, and (4) Waste Shaft. Stratigraphic correlation and evaluation of the unit contacts show that lithologic units occur at approximately the same levels in all four shaft locations. Some stratigraphic contact elevations vary because of regional structure and stratigraphic thinning and thickening of units. However, the majority of the stratigraphic contacts used to date are suitable for engineering design reference because they intersect all four shafts.

### **2.2.3 Rock Mechanics Setting**

The WIPP stratigraphy includes rock types that exhibit both brittle and ductile behaviors. The majority of the stratigraphy intercepted by the shafts consists of the Salado Formation, which is predominantly halite. The primary mechanical behavior of halitic rocks is creep. Except near free surfaces (such as the shaft wall), the salt rocks will remain tight and undisturbed despite the long-term creep deformation they sustain. The other rock types within the Salado Formation are anhydrites and polyhalites. These two rock types are typically brittle, stiff, and exhibit high strength in laboratory tests. The structural strength of particular anhydritic rock layers, however, depends on the thickness of the layers, which range from thin (<1 m) to fairly

thick (10 m or more). Brittle failure of these noncreeping rocks can occur as they restrain, or attempt to restrain, the creep of the salt above and below the stiff layer. Although thick layers can resist the induced stresses, thin layers are fractured in tension by the salt creep. Because the deformation in the bounding salt is time dependent, the damage in the brittle rock is also time dependent.

Above the Salado Formation, the Rustler Formation stratigraphy consists of relatively strong limestones and siltstones. The shaft excavation is the only significant disturbance to these rocks. Any subsurface subsidence (deformation) or loading induced by the presence of the repository are negligible in a rock mechanics sense.



TRI-6121-352-0

Figure 2-3. Generalized stratigraphy of the WIPP site showing repository level.

Regardless of rock type, the shafts create a disturbed zone in the surrounding rock. Microfracturing will occur in the rock adjacent to the shaft wall, where confining stresses are low or nonexistent. The extent of the zone depends on the rock strength and the prevailing stress state, which is depth dependent. In the salt rocks, microfracturing occurs to form the disturbed zone both at the time of excavation and later as dilatant creep deformations occur. In the brittle rocks, the disturbance occurs at the time of excavation and does not worsen with time. The extent of disturbed zones in the salt and brittle rocks can be calculated, as will be described in Section 7 and Appendix D.

Preventing the salt surrounding the shafts from creeping causes reintroduction of stresses that reverse the damage process and cause healing (Van Sambeek et al., 1993). The seal system design relies on this principle for sealing the disturbed zone in salt. In the brittle rocks, grouting of the damage is a viable means of reducing the interconnected fractures that increase the permeability of the rock.

## **2.3 Site Hydrologic Setting**

The WIPP shafts penetrate approximately 655 m (2150 ft) of sediments and rocks. From a hydrogeologic perspective, relevant information includes the permeability of the water-bearing units, the thickness of the water-bearing units, and the observed vertical pressure (head) gradients expected to exist after shaft construction and ambient pressure recovery. This section will discuss these three aspects of the site hydrogeology. The geochemistry of the pore fluids adjacent to the shaft system is also important hydrogeologic information and will be provided in Section 2.4.

### **2.3.1 Hydrostratigraphy**

The WIPP shafts penetrate Quaternary surface sediments, the Gatuña Formation, the Santa Rosa Formation, the Dewey Lake Redbeds, the Rustler Formation, and the Salado Formation. The Rustler Formation contains the only laterally-persistent water-bearing units in the WIPP vicinity. As a result, flow-field characterization, regional flow-modeling, and performance assessment off-site release scenarios focus on the Rustler Formation. The hydrogeology of the stratigraphic units in contact with the upper portion of the AIS sealing system is fairly well known from detailed hydraulic testing of the Rustler Formation at well H-16 located 17 m from the AIS (Beauheim, 1987). The H-16 borehole was drilled in July and August 1987 to monitor the hydraulic responses of the Rustler members to the drilling and construction of the AIS. During the drilling of H-16, each member of the Rustler Formation was cored. In addition, detailed drill-stem, pulse, and slug hydraulic tests were performed in H-16 on the members of the Rustler. Through the detailed testing program at H-16, the permeability of each of the Rustler members was estimated. Detailed mapping of the AIS by Holt and Powers (1990) and other investigators provided information on the location of wet zones and weeps within the Salado Formation. This information will be summarized below. The reader, unless particularly interested in this subject, should proceed to Section 2.3.2.

Water-bearing zones have been observed in units above the Rustler Formation in the WIPP site vicinity. However, drilling in the Dewey Lake Redbeds has not identified any continuous saturated units at the WIPP site. Water-bearing units within stratigraphic intervals

above the Rustler are typically perched saturated zones of very low yield. Thin perched groundwater intervals have been encountered in WIPP wells H-1, H-2, and H-3 (Mercer and Orr, 1979). The only Dewey Lake Redbed wells that have sufficient yields for watering livestock are the James Ranch wells, the Pocket well, and the Fairfield well (Brinster, 1991). These wells are located to the south of the WIPP and are not in the immediate vicinity of the WIPP shafts.

The Dewey Lake Redbeds overlie the Rustler Formation. The Rustler is composed of five members defined by lithology. These are, in ascending order, the unnamed lower member, the Culebra dolomite, the Tamarisk, the Magenta dolomite, and the Forty-niner (see Figure 2-3). Of these five members, the unnamed lower member, the Culebra, and the Magenta are the most transmissive units in the Rustler. The Tamarisk and the Forty-niner are aquitards within the Rustler and have very low permeabilities relative to the three members listed above.

To the east of the shafts in Nash Draw, the Rustler/Salado contact has been observed to be permeable and water-bearing. This contact unit has been referred to as the "brine aquifer" (Mercer, 1983). The brine aquifer is not reported to exist in the vicinity of the shafts. The hydraulic conductivity of the Rustler/Salado contact in the vicinity of the shafts is reported to be approximately  $4 \times 10^{-11}$  m/s, which is equivalent to a permeability of  $6 \times 10^{-18}$  m<sup>2</sup> using reference brine fluid properties (Brinster, 1991). The unnamed lower member was hydraulic tested at well H-16 in close proximity to the AIS. The maximum permeability of the unnamed lower member was interpreted to be  $2.2 \times 10^{-18}$  m<sup>2</sup> and was attributed to the unnamed lower member claystone by Beauheim (1987), which correlates to the transition and bioturbated clastic zones of Holt and Powers (1990).

The Culebra Dolomite Member is the most transmissive member of the Rustler Formation in the vicinity of the WIPP site and is the most transmissive saturated unit in contact with the shaft sealing system. The Culebra is an argillaceous dolomiticite which contains secondary porosity in the form of abundant vugs and fractures. The permeability of the Culebra varies greatly in the vicinity of the WIPP and is controlled by the condition of the secondary porosity (fractures). The permeability of the Culebra in the vicinity of the shafts is approximately  $2.1 \times 10^{-14}$  m<sup>2</sup>.

The Tamarisk Member is composed primarily of massive, lithified anhydrite, including anhydrite 2, mudstone 3, and anhydrite 3. Testing of the Tamarisk at H-16 was unsuccessful. The estimated transmissivity of the Tamarisk at H-16 is one to two orders of magnitude lower than the least-transmissive unit successfully tested at H-16, which results in a permeability range from  $4.6 \times 10^{-20}$  to  $4.6 \times 10^{-19}$  m<sup>2</sup>. Anhydrites in the Rustler have an approximate permeability of  $1 \times 10^{-19}$  m<sup>2</sup>. The permeability of mudstone 3 is  $1.5 \times 10^{-19}$  m<sup>2</sup> (Brinster, 1991).

The Magenta is a dolomite that is typically less permeable than the Culebra. The Magenta Dolomite Member overlies the Tamarisk Member. The Magenta is an indurated, gypsiferous, arenaceous, dolomite that Holt and Powers (1990) classify as a dolarenite. The dolomite grains are primarily composed of silt to fine sand-sized clasts. Wavy to lenticular bedding and ripple cross laminae are prevalent through most of the Magenta. Holt and Powers (1990) estimate that inflow to the shaft from the Magenta during shaft mapping was less than 1 gal/min. The Magenta has a permeability of approximately  $1.5 \times 10^{-15}$  m<sup>2</sup> (Saulnier and Avis, 1988).

The Forty-niner Member is divided into three informal lithologic units. The lowest unit is anhydrite 4, a laminated anhydrite having a gradational contact with the underlying Magenta. Mudstone 4 overlies anhydrite 4 and is composed of multiple units containing mudstones, siltstones, and very fine sandstones. Anhydrite 5 is the uppermost informal lithologic unit of the Forty-niner Member. The permeability of mudstone 4, determined from the pressure responses in the Forty-niner interval of H-16 to the drilling of the AIS, is  $3.9 \times 10^{-16} \text{ m}^2$  (referred to as the Forty-niner claystone by Avis and Saulnier, 1990).

The Salado Formation is a very low permeability formation that is composed of bedded halite, polyhalite, anhydrite, and mudstones. Inflows in the shafts have been observed over select intervals during shaft mapping, but flows are below the threshold of quantification. In some cases these weeps are individual, lithologically distinct marker beds, and in some cases they are not. Directly observable brine flow from the Salado Formation into excavated openings is a short-lived process. Table 2-1 lists the brine seepage intervals identified by Holt and Powers (1990) during their detailed mapping of the AIS. Seepage could be indicated by a wet rockface or by the presence of precipitate from brine evaporation on the shaft rockface. The zones listed in Table 2-1 make up less than 10% of the Salado section that is intersected by the WIPP shafts.

Table 2-1. Salado Brine Seepage Intervals<sup>(1)</sup>

Stratigraphic Unit	Lithology	Thickness (m)
Marker Bed 103	Anhydrite	5.0
Marker Bed 109	Anhydrite	7.7
Vaca Triste	Mudstone	2.4
Zone A	Halite	2.9
Marker Bed 121	Polyhalite	0.5
Union Anhydrite	Anhydrite	2.3
Marker Bed 124	Anhydrite	2.7
Zone B	Halite	0.9
Zone C	Halite	2.7
Zone D	Halite	3.2
Zone E	Halite	0.6
Zone F	Halite	0.9
Zone G	Halite	0.6
Zone H	Halite	1.8
Marker Bed 129	Polyhalite	0.5
Zone I	Halite	1.7
Zone J	Halite	1.2

(1) After US DOE, 1995.

To gain perspective into the important stratigraphic units from a hydrogeologic view, the permeability and thickness of the units adjacent to the shafts can be compared. Table 2-2 lists the lithologic units in the Rustler and the Salado Formations with their best estimate permeabilities and their thickness as determined from the AIS mapping. The stratigraphy of the units overlying the Rustler is not considered in Table 2-2 because these units are typically not saturated in the vicinity of the WIPP shafts. The overlying sediments account for approximately 25% of the stratigraphy column adjacent to the shafts.

Because permeability varies over several orders of magnitude, the log of the permeability is also listed to simplify comparison between units. Table 2-2 shows that by far the two most transmissive zones occur in the Rustler Formation; these are the Culebra and Magenta dolomites. These units are relatively thin when compared to the combined Rustler and Salado thickness adjacent to the shafts (3% of Rustler and Salado combined thickness). The Magenta and the Culebra are the only two units that are known to possess permeabilities higher than  $1 \times 10^{-18} \text{ m}^2$ .

Table 2-2. Permeability and Thickness of Hydrostratigraphic Units in Contact with Seals

Formation	Member/ Lithology	Undisturbed Permeability ( $\text{m}^2$ )	Thickness (m)
Rustler	Anhydrite <sup>(1)</sup>	$1.0 \times 10^{-19}$	46.7
Rustler	Mudstone 4	$3.9 \times 10^{-16}$	4.4
Rustler	Magenta	$1.5 \times 10^{-15}$	7.8
Rustler	Mudstone 3	$1.5 \times 10^{-19}$	2.9
Rustler	Culebra	$2.1 \times 10^{-14}$	8.9
Rustler	Transition/ Bioturbated Clastics	$2.2 \times 10^{-18}$	18.7
Salado	Halite	$1.0 \times 10^{-21}$	356.6
Salado	Polyhalite	$3.0 \times 10^{-21}$	10.9
Salado	Anhydrite	$1.0 \times 10^{-19}$	28.2

(1) Anhydrite 5, Anhydrite 4, Anhydrite 3, and Anhydrite 2

The vast majority (97%) of the rocks adjacent to the shaft in the Rustler and the Salado Formations are low permeability ( $< 1 \times 10^{-18} \text{ m}^2$ ). The conclusion that can be drawn from reviewing Table 2-2 is that the shafts are located hydrogeologically in a low permeability, low groundwater flow regime. Inflow measurements have historically been made at the shafts, and observable flow is attributed to leakage from the Rustler Formation.

Flow modeling of the Culebra has demonstrated that depressurization has occurred as a result of the sinking of the shafts at the site. Maximum estimated head drawdown in the Culebra at the centroid of the shafts was estimated by Haug et al. (1987) to be 33 m in the mid-1980s. This drawdown in the permeable units intersected by the shafts is expected because the shafts act as long-term constant pressure (atmospheric) sinks. Measurements of fluid flow into the WIPP

shafts when they were unlined show a range from a maximum of 0.11 L/s (3,469 m<sup>3</sup>/yr) measured in the Salt Handling Shaft on September 13, 1981 to a minimum of 0.008 L/s (252 m<sup>3</sup>/yr) measured at the Waste Handling Shaft on August 6, 1987 (LaVenue et al., 1990).

The following summary of shaft inflow rates from the Rustler is based on a review of LaVenue et al. (1990) and Cauffman et al. (1990). Shortly after excavation and prior to grouting and liner installation, the inflow into the Salt Handling Shaft was 0.11 L/s (3,469 m<sup>3</sup>/yr). The average flow rate measured after shaft lining for the period from mid-1982 through October 1992 was 0.027 L/s (851 m<sup>3</sup>/yr). The average flow rate into the Waste Handling Shaft during the time when the shaft was open and unlined was about 0.027 L/s (851 m<sup>3</sup>/yr). Between the first and second grouting events (July 1984 to November 1987) the average inflow rate was 0.016 L/s (505 m<sup>3</sup>/yr). No estimates were found after the second grouting. Inflow to the pilot holes for the Exhaust Shaft averaged 0.028 L/s (883 m<sup>3</sup>/yr). In December 1984 a liner plate was grouted across the Culebra. After this time, a single measurement of inflow from the Culebra was 0.022 L/s (694 m<sup>3</sup>/yr). After liner plate installation, three separate grouting events occurred at the Culebra. No measurable flow was reported after the third grouting event in the summer of 1987. Flow into the AIS when it was unlined and draining averaged 0.044 L/s (1,388 m<sup>3</sup>/yr). Since the Rustler has been lined, flow into the AIS has been negligible.

The majority of the flow represented by these shaft measurements originates from the Rustler. This is clearly evident by the fact that lining of the WIPP shafts was found to be unnecessary in the Salado Formation below the Rustler/Salado contact. When the liners were installed, flow rates diminished greatly. Under sealed conditions, hydraulic gradients in rocks adjacent to the shaft will diminish as the far-field pressures approach ambient conditions. The low-permeability materials sealing the shaft combined with the reduction in lateral hydraulic gradients will likely result in flow rates into the shaft that are several orders of magnitude less than observed under open shaft or lined shaft conditions.

### **2.3.2 Observed Vertical Gradients**

Hydraulic heads within the Rustler and between the Rustler and Salado Formations are not in hydrostatic equilibrium. Mercer (1983) recognized that heads at the Rustler Salado transition (referred to as the brine aquifer and not present in the vicinity of the WIPP shafts) indicate an upward hydraulic gradient from that zone to the Culebra. Later, with the availability of more head measurements within the Salado and Rustler members, Beauheim (1987) provided additional insight into the potential direction of vertical fluid movement within the Rustler. He reported that the hydraulic data indicate an upward gradient from the Salado to the Rustler.

Formation pressures in the Salado Formation have been decreased in the near vicinity of the WIPP underground facility. The highest, and thought to be least disturbed, estimated formation fluid pressure from hydraulic testing is 12.55 MPa estimated from interpretation of testing within borehole SCP01 in Marker Bed 139 (MB139) just below the underground facility horizon (Beauheim et al., 1993). The fresh-water head within MB139, based on the estimated static formation pressure of 12.55 MPa, is 1,663.6 m (5,458 ft) above mean sea level (msl).

Hydraulic heads in the Rustler have also been impacted by the presence of the WIPP shafts. Impacts in the Culebra were significant in the 1980s with a large drawdown cone extending away from the shafts in the Culebra (Haug et al., 1987). The undisturbed head of the

Rustler Salado contact in the vicinity of the AIS is estimated to be about 936.0 m (3,071 ft) msl (Brinster, 1991). The undisturbed head in the Culebra is estimated to be approximately 926.9 m (3,041 ft) msl in the vicinity of the AIS (LaVenue et al., 1990). The undisturbed head in the Magenta is estimated to be approximately 960.1 m (3,150 ft) msl (Brinster, 1991).

The disturbed and undisturbed heads in the Rustler are summarized in Table 2-3. Also included is the freshwater head of MB139 based on hydraulic testing in the WIPP underground. Consistent with the vertical flow directions proposed by previous investigators, estimated vertical gradients in the vicinity of the AIS before the shafts were drilled indicate a hydraulic gradient from the Magenta to the Culebra and from the Rustler/Salado contact to the Culebra. There is also the potential for flow from the Salado Formation to the Rustler Formation.

Table 2-3. Freshwater Head Estimates in the Vicinity of the Air Intake Shaft

Hydrologic Unit	Freshwater Head (m asl)		Reference
	Undisturbed	Disturbed	
Magenta Member	960.1 <sup>1</sup>	948.8 <sup>2</sup> (H-16)	Brinster (1991) Beauheim (1987)
Culebra Member	926.9 <sup>1</sup>	915.0 <sup>2</sup> (H-16)	LaVenue et al. (1990) Beauheim (1987)
Lower Unnamed Member	—	953.4 <sup>2</sup> (H-16)	Beauheim (1987)
Rustler/Salado Contact	936.0 - 940.0 <sup>1</sup>	—	Brinster (1991)
Salado MB139	1,663.6 <sup>2</sup>	—	Beauheim et al. (1993)

1 Estimated from a contoured head surface plot based principally on well data collected prior to shaft construction.

2 Measured through hydraulic testing and/or long-term monitoring.

## 2.4 Site Geochemical Setting

### 2.4.1 Regional and Local Geochemistry in Rustler Formation and Shallower Units

The Rustler Formation, overlying the Salado Formation, consists of interbedded anhydrite/gypsum, mudstone/siltstone, halite east of the WIPP site, and two layers of dolomite. Principal occurrences of NaCl/MgSO<sub>4</sub> brackish to briny groundwater in the Rustler at the WIPP site and to the north, west, and south are found (1) at the lower member near its contact with the underlying Salado and (2) in the two dolomite members having a variable fracture-induced secondary porosity. The mineralogy of the Rustler Formation is summarized in Table 2-4.

The five members of the Rustler Formation are described as follows: (1) The Forty-niner Member is similar in lithology to the other non-dolomitic units but contains halite east of the WIPP site. (2) The Magenta Member is another variably fractured dolomite/sulfate unit containing sporadic occurrences of groundwater near and west of the WIPP site. (3) The Tamarisk Member is dominantly anhydrite (locally altered to gypsum) with subordinate fine-

grained clastics, containing halite to the east of the WIPP site. (4) The Culebra Dolomite Member is dominantly dolomite with subordinate anhydrite and/or gypsum, having a variable fracture-induced secondary porosity containing regionally continuous occurrences of groundwater at the WIPP site and to the north, west, and south. (5) An unnamed lower member consists of sandstone, siltstone, mudstone, claystone, and anhydrite locally altered to gypsum, and containing halite under most of the WIPP site and occurrences of brine at its base, mostly west of the WIPP site.

Table 2-4. Chemical Formulas, Distributions, and Relative Abundance of Minerals in the Rustler and Salado Formations (after Lambert, 1992)

Mineral	Formula	Occurrence/ Abundance
Amesite	$(Mg_4Al_2)(Si_2Al_2)O_{10}(OH)_8$	S, R
Anhydrite	$CaSO_4$	SSS, RRR
Calcite	$CaCO_3$	S, RR
Carnallite	$KMgCl_3 \cdot 6H_2O$	SS†
Chlorite	$(Mg,Al,Fe)_{12}(Si,Al)_8O_{20}(OH)_{16}$	S‡, R‡
Corrensite	Mixed-layer chlorite/smectite	S‡, R‡
Dolomite	$CaMg(CO_3)_2$	RR
Feldspar	$(K,Na,Ca)(Si,Al)_4O_8$	S‡, R‡
Glauberite	$Na_2Ca(SO_4)_2$	S
Gypsum	$CaSO_4 \cdot 2H_2O$	S, RRR
Halite	$NaCl$	SSS, RRR
Illite	$K_{1-1.5}Al_4(Si_{7-6.5}Al_{1-1.5}O_{20})(OH)_4$	S‡, R‡
Kainite	$KMgClSO_4 \cdot 3H_2O$	SS†
Kieserite	$MgSO_4 \cdot H_2O$	SS†
Langbeinite	$K_2Mg_2(SO_4)_3$	S*
Magnesite	$MgCO_3$	S, R
Polyhalite	$K_2Ca_2Mg(SO_4)_4 \cdot 2H_2O$	SS, R
Pyrite	$FeS_2$	S, R
Quartz	$SiO_2$	S‡, R‡
Serpentine	$Mg_3Si_2O_5(OH)_4$	S‡, R‡
Smectite	$(Ca_{1/2},Na)_{0.7}(Al,Mg,Fe)_4(Si,Al)_8O_{20}(OH)_4 \cdot nH_2O$	S‡, R‡
Sylvite	$KCl$	SS*

Key to Occurrence/Abundance notations:

S = Salado Formation; R = Rustler Formation; 3× = abundant, 2× = common, 1× = rare or accessory;

\* = potash-ore mineral (never near surface); † = potash-zone non-ore mineral; ‡ = in claystone interbeds.

The Dewey Lake Redbeds, overlying the Rustler Formation, are the uppermost Permian unit; they consist of siltstones and claystones locally transected by concordant and discordant fractures that may contain gypsum. The Dewey Lake Redbeds contain sporadic occurrences of groundwater that may be locally perched, mostly in the area south of the WIPP site. The Triassic Dockum Group (undivided) rests on the Dewey Lake Redbeds in the eastern half of the WIPP site and thickens eastward; it is a locally important source of groundwater for agricultural and domestic use.

The Gatuña Formation, overlying the Dewey Lake Redbeds, occurs locally as channel and alluvial pond deposits (sands, gravels, and boulder conglomerates). The pedogenic Mescalero caliche is commonly developed on top of the Gatuña Formation and on many other erosionally truncated rock types. Surficial dune sand, which may be intermittently damp, covers virtually all outcrops at and near the WIPP site. Siliceous alluvial deposits southwest of the WIPP site also contain potable water. The geochemistry of groundwater found in the Rustler Formation and Dewey Lake Redbeds is summarized in Table 2-5.

Table 2-5. Major Solutes in Selected Representative Groundwater from the Rustler Formation and Dewey Lake Redbeds, in mg/L (after Lambert, 1992)

Well	Date	Zone	Ca	Mg	Na	K	SO <sub>4</sub>	Cl
WIPP-30	July 1980	R/S	955	2770	121,000	2180	7390	192,000
WIPP-29	July 1980	R/S	1080	2320	36,100	1480	12,000	58,000
H-5B	June 1981	Cul	1710	2140	52,400	1290	7360	89,500
H-9B	November 1985	Cul	590	37	146	7	1900	194
H-2A	April 1986	Cul	743	167	3570	94	2980	5310
P-17	March 1986	Cul	1620	1460	28,300	782	6020	48,200
WIPP-29	December 1985	Cul	413	6500	94,900	23,300	20,000	179,000
H-3B1	July 1985	Mag	1000	292	1520	35	2310	3360
H-4C	November 1986	Mag	651	411	7110	85	7100	8460
Ranch	June 1986	DL	420	202	200	4	1100	418

Key to Zone:

R/S = "basal brine aquifer" near the contact between the Rustler and Salado Formations;

Cul = Culebra Member, Rustler Formation;

Mag = Magenta Member, Rustler Formation;

DL = Dewey Lake Redbeds.

#### 2.4.2 Regional and Local Geochemistry in the Salado Formation

The Salado Formation consists dominantly of halite, interrupted at intervals of meters to tens of meters by beds of anhydrite, polyhalite, mudstone, and local potash mineralization (sylvite or langbeinite, with or without accessory carnallite, kieserite, kainite and glauberite, all in a halite matrix). Some uniquely identifiable non-halite units, 0.1 to 10 m thick, have been

numbered from the top down (100 to 144) for convenience as marker beds to facilitate cross-basinal stratigraphic correlation. The WIPP facility was excavated just above Marker Bed 139 in the Salado Formation at a depth of about 655 m.

Although the most common Delaware Basin evaporite mineral is halite, the presence of less soluble interbeds (dominantly anhydrite, polyhalite, and claystone) and more soluble admixtures (e.g. sylvite, glauberite, kainite) has resulted in chemical and physical properties significantly different from those of pure NaCl. Under differential stress produced near excavations, brittle interbeds (anhydrite, polyhalite, magnesite, dolomite) may fracture, whereas under a similar stress regime pure NaCl would undergo plastic deformation. Fracturing of these interbeds has locally enhanced the permeability, allowing otherwise nonporous rock to carry groundwater (e.g., the fractured polyhalitic anhydrite of Marker Bed 139 under the floor of the WIPP excavations).

Groundwater in evaporites represents the exposure of chemical precipitates to fluids that may be agents (as in the case of dissolution) or consequences of postdepositional alteration of the evaporites (as in the cases of dehydration of gypsum and diagenetic dewatering of other minerals). Early in the geological studies of the WIPP site, groundwater occurrences that could be hydrologically characterized were identified.

Since the beginning of conventional mining in the Delaware Basin, relatively short-lived seeps (pools on the floor, efflorescences on the walls, and stalactitic deposits on the ceiling) have been known to occur in the Salado Formation where excavations have penetrated. These brine occurrences are commonly associated with the non-halitic interbeds whose porosity is governed either by fracturing (as in brittle beds) or mineralogical discontinuities (as in "clay" seams).

The geochemistry of brines encountered in the Salado Formation is summarized in Table 2-6. The relative abundance of minerals was summarized in Table 2-4.

Table 2-6. Variations in Major Solutes in Brines from the Salado Formation, in mg/L  
(after Lambert, 1992)

Source of Brine	Date	Ca	Mg	K	Na	Cl	SO <sub>4</sub>
Room G Seep							
	Sep-87	278	14800	15800	99000	188000	29500
	Nov-87	300	18700	15400	97100	190000	32000
	Feb-88	260	18200	17100	94100	186000	36200
	Mar-88	280	17000	16200	92100	187000	34800
	Jul-88	292	13000	14800	96600	188000	29300
	Sep-88	273	14700	13700	86500	185000	28000
	Apr-91	240	14400	12900	95000	189000	28000
	Jul-91	239	14100	13100	93000	190000	27700
	Oct-91	252	14700	14100	95000	189000	27100
Marker Bed 139 (under repository)							
		300	18900	14800	67700	155900	14700
		300	17100	15600	72700	158900	13400
		300	17600	15800	71600	182200	14700
Room J							
		230	17700	13500	63600	167000	15100
		210	27400	22400	56400	168000	19600
		220	17900	15600	73400	165000	9300
		250	22200	18300	63000	165000	31100
		190	31000	19900	46800	170000	24600
		100	35400	27800	40200	173000	30000
		270	18900	14500	59900	166000	16200
		280	20200	17000	70400	165000	10600
Room Q							
		279	31500	22600	68000	205000	19400
		288	31100	24100	68000	203000	19200
		257	34000	26300	63000	205000	23500
AIS Sump (accumulation in bottom of sump)							
	Jul-88	960	1040	1720	118000	187000	6170
	May-89	900	500	600	83100	122700	7700
	May-89	1000	800	1100	82400	114200	8800
McNutt Potash Zone							
Duval mine		640	55400	30000	27500	236500	3650
Miss. Chem. mine		200	44200	45800	43600	226200	12050

Page intentionally blank.

### 3. DESIGN GUIDANCE

#### 3.1 Introduction

The WIPP is subject to regulatory requirements contained in 40 CFR 191 and 40 CFR 194. The use of both engineered and natural barriers to isolate wastes from the accessible environment is required by 40 CFR 191.14(d), and the use of engineered barriers to prevent or substantially delay the movement of water or radionuclides toward the accessible environment is required by 40 CFR 194.44. Quantitative requirements for potential releases of radioactive and other hazardous materials from the repository system are specified in 40 CFR 191 and 40 CFR 268. The regulations impose quantitative release requirements on the total repository system, not on individual subsystems of the repository system, for example, the shaft sealing subsystem.

#### 3.2 Design Guidance and Design Approach

The guidance described for the design of the shaft sealing system addresses the need for the WIPP to comply with system requirements and to follow accepted engineering practices using demonstrated technology. The design guidance addresses the need to limit:

1. radiological or other hazardous constituents reaching the regulatory boundaries,
2. groundwater flow into and through the sealing system,
3. chemical and mechanical incompatibility,
4. structural failure of system components,
5. subsidence and accidental entry, and
6. development of new construction technologies and/or materials.

For each element of design guidance, a design approach has been developed. Table 3-1 contains qualitative design guidance and the design approach used to implement it.

Table 3-1. Shaft Sealing System Design Guidance

<b>Qualitative Design Guidance</b>	<b>Design Approach</b>
<i>The shaft sealing system shall limit:</i>	<i>The shaft sealing system shall be designed to meet the qualitative design guidance in the following ways:</i>
1. the migration of radiological or other hazardous constituents from the repository horizon to the regulatory boundary during the 10,000-year regulatory period following closure;	1. In the absence of human intrusion, brine migrating from the repository horizon to the Rustler Formation must pass through a low permeability sealing system.
2. groundwater flowing into and through the shaft sealing system;	2. In the absence of human intrusion, groundwater migrating from the Rustler Formation to the repository horizon must pass through a low permeability sealing system.

Table 3-1. Shaft Sealing System Design Guidance

Qualitative Design Guidance	Design Approach
3. chemical and mechanical incompatibility of seal materials with the seal environment;	3. Brine contact with seal elements is limited and materials possess acceptable mechanical properties.
4. the possibility for structural failure of individual components of the sealing system;	4. State of stress from forces expected from rock creep and other mechanical loads is favorable for seal materials.
5. subsidence of the ground surface in the vicinity of the shafts and the possibility of accidental entry after sealing;	5. The shaft is completely filled with low-porosity materials, and construction equipment would be needed to gain entry.
6. the need to develop new technologies or materials for construction of the shaft sealing system.	6. Construction of the shaft sealing system is feasible using available technologies and materials.

## 4. DESIGN DESCRIPTION

### 4.1 Introduction

The design presented in this section was developed based on (1) the design guidance outlined in Section 3.0, (2) past design experience, and (3) a desire to reduce uncertainties associated with the performance of the WIPP sealing system. The WIPP shaft sealing system design has evolved over the past decade from the initial concepts presented by Stormont (1984) to the design concepts presented in this document. The past designs are:

- the plugging and sealing program for the WIPP (Stormont, 1984),
- the initial reference seal system design (Nowak et al., 1990),
- the seal design alternative study (Van Sambeek et al., 1993),
- the WIPP sealing system design (DOE, 1995).

The present design changes were implemented to take advantage of knowledge gained from small-scale seals tests conducted at the WIPP (Knowles and Howard, 1996), advances in the ability to predict the time-dependent mechanical behavior of compacted salt rock (Callahan et al., 1996), large-scale dynamic salt compaction tests and associated laboratory determination of the permeability of compacted salt samples (Hansen and Ahrens, 1996; Brodsky et al., 1996), field tests to measure the permeability of the DRZ surrounding the WIPP AIS (Dale and Hurtado, 1996), and around seals (Knowles et al., 1996). A summary paper (Hansen et al., 1996) describing the design has been prepared.

The shaft sealing system is composed of seals within the Salado Formation, the Rustler Formation, and the Dewey Lake Redbeds and overlying units. All components of the sealing system are designed to meet Items 3, 4, and 6 of the Design Guidance (Table 3-1.); that is, all sealing system components are designed to be chemically and mechanically compatible with the seal environment, structurally adequate, and constructable using currently available technology and materials. The seals in the Salado Formation are also designed to meet Items 1 and 2 of the Design Guidance. These seals will limit fluid migration upward from the repository to the Rustler Formation and downward from the Rustler Formation to the repository. Migration of brine upward and downward is discussed in Sections 8.5 and 8.4 respectively. The seals in the Rustler Formation are designed to meet Item 2 in addition to Items 3, 4, and 6 of the Design Guidance. The seals in the Rustler Formation limit migration of Rustler brines into the shaft cross-section and also limit cross-flow between the Culebra and Magenta members. The principal function of the seals in the Dewey Lake Redbeds and overlying units is to meet Item 5 of the Design Guidance, that is, to limit subsidence of the ground surface in the vicinity of the shafts and to prevent accidental entry after repository closure. Entry of water (surface water and any groundwater that might be present in the Dewey Lake Redbeds and overlying units) into the sealing system is limited by restraining subsidence and by placing high density fill in the shafts.

### 4.2 Existing Shafts

The WIPP underground facilities are accessed by four shafts commonly referred to as the Waste, Air Intake, Exhaust, and Salt Handling Shafts. These shafts were constructed between 1981 and 1988. All four shafts are lined from the surface to just below the contact of the Rustler

and Salado Formations. The lined portion of the shafts terminates in a substantial concrete structure called the “key,” which is located in the uppermost portion of the Salado Formation. Drawings showing the configuration of the existing shafts are included in Appendix E and listed below in Table 4-1. Table 4-2 contains a summary of information describing the existing shafts.

The upper portions of the WIPP shafts are lined. The Waste, Air Intake, and Exhaust shafts have concrete linings; the Salt Handling Shaft has a steel lining with grout backing. In addition, during shaft construction, steel liner plates, wire mesh, and pressure grouting were used to stabilize portions of the shaft walls in the Rustler Formation and overlying units. Seepage of groundwater into the lined portions of the shafts has been observed. This seepage was expected; in fact, the shaft keys (massive concrete structures located at the base of each shaft liner) were designed to collect the seepage and transport it through a piping system to collection points at the repository horizon. In general, the seepage originates in the Magenta and Culebra members of the Rustler Formation and in the interface zone between the Rustler and Salado formations. It flows along the interface between the shaft liner and the shaft wall and through the DRZ immediately adjacent to the shaft wall. In those cases where seepage through the liner occurred, it happened where the liner offered lower resistance to flow than the interface and DRZ, for example, at construction joints. Maintenance grouting, in selected areas of the WIPP shafts, has been utilized to reduce seepage.

Table 4-1. Drawings Showing Configuration of Existing WIPP Shafts  
(Drawings are in Appendix E)

Shaft	Drawing Title	Sheet Number of Drawing SNL-007
Waste	Near-Surface/Rustler Formation Waste Shaft Stratigraphy & As-Built Elements	2 of 28
Waste	Salado Formation Waste Shaft Stratigraphy & As-Built Elements	3 of 28
AIS	Near-Surface/Rustler Formation Air Intake Shaft Stratigraphy & As-Built Elements	7 of 28
AIS	Salado Formation Air Intake Shaft Stratigraphy & As-Built Elements	8 of 28
Exhaust	Near-Surface/Rustler Formation Exhaust Shaft Stratigraphy & As-Built Elements	12 of 28
Exhaust	Salado Formation Exhaust Shaft Stratigraphy & As-Built Elements	13 of 28
Salt Handling	Near-Surface/Rustler Formation Salt Handling Shaft Stratigraphy & As-Built Elements	17 of 28
Salt Handling	Salado Formation Salt Handling Shaft Stratigraphy & As-Built Elements	18 of 28

Table 4-2. Summary of Information Describing Existing WIPP Shafts

	Shafts			
	Salt Handling	Waste	Air Intake	Exhaust
<b>A. Construction Method</b>				
i. Sinking method	Blind bored	Initial 6' pilot hole slashed by drill & blast (smooth wall blasting)	Raise bored	Initial 6' pilot hole slashed by drill & blast (smooth wall blasting)
ii. Dates of shaft sinking	7/81-10/81	Drilled 12/81-2/82 Slashed 10/83-6/84	12/87-8/88	9/83-11/84
iii. Ground treatment in water-bearing zone	Grout behind steel liner during construction	Grouted 1984 & 1988	Grouted 1993	Grouted 1985, 1986, & 1987
iv. Sump construction	Drill & blast	Drill & blast	No sump	No sump
<b>B. Upper Portion of Shaft *</b>				
i. Type of liner	Steel	Concrete	Concrete	Concrete
ii. Lining diameter (ID)	10'-0"	19'-0"	18'-0"/16'-7"	14'-0"
iii. Excavated diameter	11'-10"	20'-8" to 22'-4"	20'-3"	15'-8" to 16'-8"
iv. Installed depth of liner	838.5'	812'	816'	846'
<b>C. Key Portion of Shaft *</b>				
i. Construction material	Reinf. conc. w/chem. seals	Reinf. concrete w/chem. seals	Reinf. concrete w/chem. seals	Reinf. concrete w/chem. seals
ii. Liner diameter (ID)	10'-0"	19'-0"	16'-7"	14'-0"
iii. Excavated diameter	15'-0" to 18'-0"	27'-6" to 31'-0"	29'-3" to 35'-3"	21'-0" to 26'-0"
iv. Depth-top of Key	844'	836'	834'	846'
v. Depth-bottom of Key	883'	900'	897'	910'
vi. Dow Seal #1 depth	846' to 848'	846' to 849'	839' to 842'	853' to 856'
vii. Dow Seal #2 depth	853' to 856'	856' to 859'	854' to 857'	867' to 870'
viii. Dow Seal #3 depth	868 to 891'	NA	NA	NA
ix. Top of salt (Rustler/Salado contact)	851'	843'	841'	853'
<b>D. Lower Shaft (Unlined) *</b>				
i. Type of support	Unlined	Chain link mesh	Unlined	Chain link mesh
ii. Excavated diameter	11'-10"	20'-0"	20'-3"	15'-0"
iii. Depth-top of "unlined"	882'	900'	904'	913'
iv. Depth-bottom of "unlined"	2144'	2142'	2128'	2148'
<b>E. Station *</b>				
i. Type of support	Wire mesh		Wire mesh	Wire mesh
ii. Principal dimensions	21H x 31W	12H x 30W	25H x 36W	12H x 23W
iii. Depth-top of station	2144'	2142'	2128'	2148'
iv. Depth-floor of station	2162'	2160'	2150'	2160'
<b>F. Sump *</b>				
Depth-top of sump	2162'	2160'	No sump	No sump
Depth-bottom of sump	2272'	2286'		
<b>G. Shaft Duty</b>	Construction hoisting of excavated salt; personnel hoisting	Hoisting shaft for lowering waste containers; personnel hoisting until waste receipt	Ventilation shaft for intake (fresh) air; personnel hoisting	Exhaust air ventilation shaft

\*This information is from the Westinghouse WID drawings identified on Sheets 2, 3, 7, 8, 12, 13, 17, and 18 of Drawing SNL-007 (see Appendix E).

### 4.3 Sealing System Design Description

This section describes the shaft sealing system design, components, and functions. The shaft sealing system consists of three essentially independent parts:

1. The seals in the Salado Formation provide the primary regulatory barrier. They will limit fluid flow into and out of the repository throughout the 10,000-year regulatory period.
2. The seals in the Rustler Formation will limit flow from the water-bearing members of the Rustler Formation and limit commingling of Magenta and Culebra groundwaters.
3. The seals in the Dewey Lake Redbeds and the near-surface units will limit infiltration of surface water and preclude accidental entry through the shaft openings.

The same sealing system is used in all four shafts. Therefore an understanding of the sealing system for one shaft is sufficient to understand the sealing system in all shafts. Only minor differences exist in the lengths of the components, and the component diameters differ to accommodate the existing shaft diameters.

The shaft liner will be removed in four locations in each shaft. All of these locations are within the Rustler Formation. Additionally, the upper portion of each shaft key will be eliminated. The portion of the shaft key that will be eliminated spans the Rustler/Salado interface and extends into the Salado Formation. The shaft liner removal locations are

1. from 10 ft above the Magenta Member to the base of the Magenta (removal distances vary from 34–39 ft because of different member thickness at shaft locations),
2. for a distance of 10 ft in the anhydrite of the Tamarisk Member,
3. through the full height of the Culebra (17–24 ft), and
4. from the top anhydrite unit in the unnamed lower member to the top of the key (67–85 ft).

Additionally, the concrete will be removed from the top of the key to the bottom of the key's lower chemical seal ring (23 to 29 ft). Drawing SNL-007, Sheets 4, 9, 14, and 19 in Appendix E show shaft liner removal plans, and Sheet 23 shows key removal plans.

The decision to abandon portions of the shaft lining and key in place is based on two factors. First, no improvements in the performance of the sealing system associated with removal of these isolated sections of concrete have been identified. Second, because the keys are thick and heavily reinforced, their removal would be costly and time consuming. No technical problems are associated with the removal of this concrete; thus, if necessary, its removal can be incorporated in any future design.

The DRZ will be pressure grouted throughout the liner and key removal areas and for a distance of 10 ft above and below all liner removal areas. The pressure grouting will stabilize the DRZ during liner removal and shaft sealing operations. The grouting will also control groundwater seepage during and after liner removal. The pressure grouting of the DRZ has not been assigned a sealing function beyond the construction period. It is likely that this grout will seal the DRZ for an extended period of time. However, past experience with grout in the mining and tunneling industries demonstrates that groundwater eventually opens alternative pathways through the media and reestablishes seepage patterns (maintenance grouting is common in both

mines and tunnels). Therefore, post-closure sealing of the DRZ in the Rustler Formation has not been assumed in the design.

The compacted clay sealing material (bentonite) will seal the shaft cross-section in the Rustler Formation. In those areas where the shaft liner has been removed, the compacted clay will confine the vertical movement of groundwater in the Rustler to the DRZ. Sealing the shaft DRZ is accomplished in the Salado Formation. It is achieved initially through the interruption of the halite DRZ by concrete-asphalt waterstops and on a long-term basis through the natural process of healing the halite DRZ. The properties of the compacted clay are discussed in Section 5.3.2. The concrete-asphalt waterstops and DRZ healing in the Salado are discussed in Sections 7.6.1 and 7.5.2 respectively.

Reduction of the uncertainty associated with long-term performance is addressed by replacing the upper and lower Salado Formation salt columns used in some of the earlier designs with compacted clay columns and by adding asphalt sealing components in the Salado Formation. Use of disparate materials for sealing components reduces the uncertainty associated with a common-mode failure.

The compacted salt column provides a seal with an initial permeability several orders of magnitude higher than the clay or asphalt columns; however, its long-term properties will approach those of the host rock. The permeability of the compacted salt, after consolidation, will be several orders of magnitude lower than that of the clay and comparable to that of the asphalt. The clay provides seals of known low permeability at emplacement, and asphalt provides an independent low permeability seal of the shaft cross-section and the shaft wall interface at the time of installation. Sealing of the DRZ in the Rustler Formation during the construction period is accomplished by grouting, and initial sealing of the DRZ in the Salado Formation is accomplished by three concrete-asphalt waterstops.

In the following sections, each component of each of the three shaft segments is identified by name and component number (see Figure 4-1 for nomenclature). Associated drawings in Appendix E are also identified. Drawings showing the overall system configurations for each shaft are listed in Table 4-3.

#### **4.3.1 Salado Seals**

The seals placed in the Salado Formation are composed of (1) consolidated salt, clay, and asphalt components that will function for very long periods, exceeding the 10,000-year regulatory period; and (2) salt saturated concrete components that will function for extended periods. The specific components that comprise the Salado seals are described below.

##### **4.3.1.1 Compacted Salt Column**

The compacted salt column (Component 10 in Figure 4-1, and shown in Drawing SNL-007, Sheet 25) will be constructed of crushed salt taken from the Salado Formation. The length of the salt column varies from 170 to 172 m (556 to 564 ft) in the four shafts. The compacted salt column is sized to allow the column and concrete-asphalt waterstops at either end to be placed between the Vaca Triste Unit and Marker Bed 136. The salt will be placed and

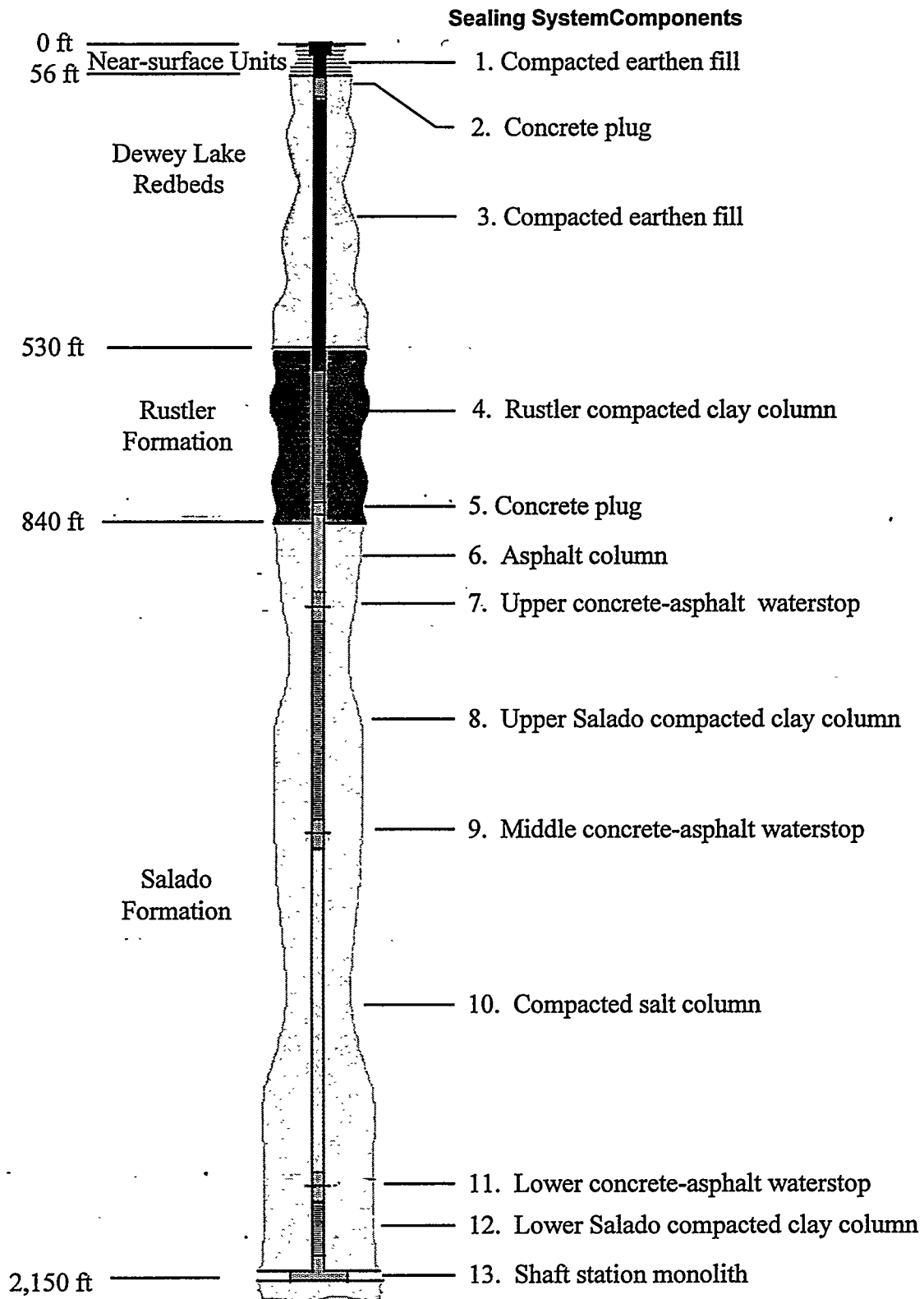


Figure 4-1. Arrangement of the Air Intake Shaft sealing system.

**Table 4-3. Drawings Showing the Sealing System for Each Shaft  
(Drawings are in Appendix E)**

<b>Shaft</b>	<b>Drawing Title</b>	<b>Sheet Number of Drawing SNL 007</b>
Waste	Near-Surface/Rustler Formation Waste Shaft Stratigraphy & Sealing Subsystem Profile	4 of 28
Waste	Salado Formation Waste Shaft Stratigraphy & Sealing Subsystem Profile	5 of 28
AIS	Near-Surface/Rustler Formation Air Intake Shaft Stratigraphy & Sealing Subsystem Profile	9 of 28
AIS	Salado Formation Air Intake Shaft Stratigraphy & Sealing Subsystem Profile	10 of 28
Exhaust	Near-Surface/Rustler Formation Exhaust Shaft Stratigraphy & Sealing Subsystem Profile	14 of 28
Exhaust	Salado Formation Exhaust Shaft Stratigraphy & Sealing Subsystem Profile	15 of 28
Salt Handling	Near-Surface/Rustler Formation Salt Handling Shaft Stratigraphy & Sealing Subsystem Profile	19 of 28
Salt Handling	Salado Formation Salt Handling Shaft Stratigraphy & Sealing Subsystem Profile	20 of 28

compacted to a density approaching 90% of the average density of intact Salado salt. The effects of creep closure will cause this density to increase with time, further reducing permeability.

The salt column will offer limited resistance to fluid migration immediately after emplacement, but it will become less permeable as creep closure further compacts the salt. Salt creep increases rapidly with depth; therefore, at any time, creep closure of the shaft will be greater at greater depth. The location and initial compaction density of the compacted salt column were chosen to assure consolidation of the compacted salt column in the 100 years following repository closure. The state of salt consolidation, results of analyses predicting the creep closure of the shaft, consolidation and healing of the compacted salt, and healing of the DRZ surrounding the compacted salt column are presented in Sections 7.5 and 8.4 of this document. These results indicate that the salt column will become an effective long-term barrier within 100 years.

#### 4.3.1.2 Upper and Lower Salado Compacted Clay Columns

The upper and lower Salado compacted clay columns (Components 8 and 12 respectively in Figure 4-1) are shown in detail on Drawing SNL-007, Sheet 24. A commercial well-sealing grade sodium bentonite will be used to construct the upper and lower Salado clay columns. These clay columns will effectively limit fluid movement from the time they are placed and will provide an effective barrier to fluid migration throughout the 10,000-year regulatory period and thereafter. The upper clay column ranges in length from 102 to 107 m (335 to 351 ft), and the lower clay column ranges in length from 29 to 33 m (94 to 107 ft) in the four shafts. The locations for the upper and lower clay columns were selected based on the need to limit fluid migration into the compacting salt column. The lower clay column stiffness is sufficient to promote early healing of the DRZ, thus removing the DRZ as a potential pathway for fluids (Appendix D, Section 5.2.1).

#### 4.3.1.3 Upper, Middle, and Lower Concrete-Asphalt Waterstops

The upper, middle, and lower concrete-asphalt waterstops (Components 7, 9, and 11 respectively in Figure 4-1) are identical and are composed of three elements: an upper concrete plug, a central asphalt waterstop, and a lower concrete plug. These components are also shown on Drawing SNL-007, Sheet 22. The concrete specified is a specially developed salt-saturated concrete called Salado Mass Concrete (SMC). In all cases the component's overall design length is 15 m (50 ft).

The upper and lower concrete plugs of the concrete-asphalt waterstop are identical. They fill the shaft cross-section and have a design length of 7 m (23 ft). The plugs are keyed into the shaft wall to provide positive support for the plug and overlying sealing materials. The interface between the concrete plugs and the surrounding formation will be pressure grouted. The upper plug in each component will support dynamic compaction of the overlying sealing material if compaction is specified. Dynamic compaction of the salt column is discussed in Section 6.

The asphalt waterstop is located between the upper and lower concrete plugs. In all cases a kerf extending one shaft radius beyond the shaft wall is cut in the surrounding salt to contain the waterstop. The kerf is 0.3 m (1 ft) high at its edge and 0.6 m (2 ft) high at the shaft wall. The kerf, which cuts through the existing shaft DRZ, will result in the formation of a new DRZ along its perimeter. This new DRZ will heal shortly after construction of the waterstop, and thereafter the waterstop will provide a very low permeability barrier to fluid migration through the DRZ. The formation and healing of the DRZ around the waterstop are addressed in Section 7.6.1. The asphalt fill for the waterstop extends two feet above the top of the kerf to assure complete filling of the kerf. The construction procedure used assures that shrinkage of the asphalt from cooling will not result in the creation of voids within the kerf and will minimize the size of any void below the upper plug.

Concrete-asphalt waterstops are placed at the top of the upper clay column, the top of the compacted salt column, and the top of the lower clay column. The concrete-asphalt waterstops provide independent seals of the shaft cross-section and the DRZ. The SMC plugs (and grout) will fill irregularities in the shaft wall, bond to the shaft wall, and seal the interface. Salt creep against the rigid concrete components will place a compressive load on the salt and promote

early healing of the salt DRZ surrounding the SMC plugs. The asphalt waterstop will seal the shaft cross-section and the DRZ.

The position of the concrete components was first determined by the location of the salt and clay columns. The components were then moved upward or downward from their initial design location to assure the components were located in regions where halite was predominant. This positioning, coupled with variations in stratigraphy, is responsible for the variations in the lengths of the salt and clay columns.

#### 4.3.1.4 Asphalt Column

An asphalt-aggregate mixture is specified for the asphalt column (Component 6 in Figure 4-1). This column is 42 to 44 m (138 to 143 ft) in length in the four shafts, as shown in Drawing SNL-007, Sheet 23. The asphalt column is located above the upper concrete-asphalt waterstop; it extends approximately 5 m (16 ft) above the Rustler/Salado interface. A 6-m (20-ft) long concrete plug (part of the Rustler seals) is located just above the asphalt column.

The existing shaft linings will be removed from a point well above the top of the asphalt column to the top of the shaft keys. The concrete shaft keys will be removed to a point just below the lowest chemical seal ring in each key. The asphalt column is located at the top of the Salado Formation and provides an essentially impermeable seal for the shaft cross section and along the shaft wall interface. The length of the asphalt column will decrease slightly as the column cools. The procedure for placing the flowable asphalt-aggregate mixture is described in Section 6.

#### 4.3.1.5 Shaft Station Monolith

A shaft station monolith (Component 13) is located at the base of the each shaft. Because the configurations of each shaft differ, drawings of the shaft station monoliths for each shaft were prepared. These drawings are identified in Table 4-4. The shaft station monoliths will be constructed with SMC. The monoliths function to support the shaft wall and adjacent drift roof, thus preventing damage to the seal system as the access drift closes from natural processes.

Table 4-4. Drawings Showing the Shaft Station Monoliths (Drawings are in Appendix E)

Shaft	Drawing Title	Sheet Number of Drawing SNL-007
Waste	Waste Shaft Shaft Station Monolith	6 of 28
AIS	Air Intake Shaft Shaft Station Monolith	11 of 28
Exhaust	Exhaust Shaft Shaft Station Monolith	16 of 28
Salt Handling	Salt Handling Shaft Shaft Station Monolith	21 of 28

## **4.3.2 Rustler Seals**

The seals in the Rustler Formation are composed of the Rustler compacted clay column and a concrete plug. The concrete plug rests on top of the asphalt column of the Salado seals. The clay column extends from the concrete plug through most of the Rustler Formation and terminates above the Rustler's highest water-bearing zone in the Forty-niner Member.

### **4.3.2.1 Rustler Compacted Clay Column**

The Rustler compacted clay column (Component 4 in Figure 4-1) is shown on Drawing SNL-007, Sheet 27 for each of the four shafts. A commercial well-sealing-grade sodium bentonite will be used to construct the Rustler clay column, which will effectively limit fluid movement from the time of placement and provide an effective barrier to fluid migration throughout the 10,000-year regulatory period and thereafter. Design length of the Rustler clay column is about 71 m (234 to 235 ft) in the four shafts.

The location for the Rustler clay columns was selected to limit fluid migration into the shaft cross-section and along the shaft wall interface and to limit mixing of Culebra and Magenta waters. The clay column extends from above the Magenta Member to below the Culebra Member of the Rustler Formation. The Magenta and Culebra are the water-bearing units of the Rustler. The members above the Magenta (the Forty-niner), between the Magenta and Culebra (the Tamarisk), and below the Culebra (the unnamed lower member) are aquitards in the vicinity of the WIPP shafts.

### **4.3.2.2 Rustler Concrete Plug**

The Rustler concrete plug (Component 5 in Figure 3-1) is constructed of SMC. The plugs for the four shafts are shown on Drawing SNL-007, Sheet 26. The plug is 6 m (20 ft) long and will fill the shaft cross-section. The plug is placed directly on top of the asphalt column of the Salado seals. The plug will be keyed into the surrounding rock and grouted. The plug permits work to begin on the overlying clay column before the asphalt has completely cooled. The option of constructing the overlying clay columns using dynamic compaction (present planning calls for construction using compressed clay blocks) is also maintained by keying the plug into the surrounding rock.

## **4.3.3 Near-Surface Seals**

The near-surface region is composed of dune sand, the Mescalero caliche, the Gatuña Formation, the Santa Rosa Formation, and the Dewey Lake Redbeds. This region extends from the ground surface to the top of the Rustler Formation—a distance of about 160 m (525 ft). All but about 15 m (50 ft) of this distance is composed of the Dewey Lake Redbeds Formation. The near-surface seals are composed of two earthen fill columns and a concrete plug. The upper earthen fill column (Component 1) extends from the shaft collar through the surficial deposits downward to the top of the Dewey Lake Redbeds. The concrete plug (Component 2) is placed in the top portion of the Dewey Lake Redbeds, and the lower earthen fill column (Component 3) extends from the concrete plug into the Rustler Formation. These components are shown on Drawing SNL-007, Sheet 28.

This seal will limit the amount of surface water entering the shafts and will limit the potential for any future groundwater migration into the shafts. The near surface seals will also completely close the shafts and prevent accidental entry and excessive subsidence in the vicinity of the shafts. As discussed in Section 4.3.2, the existing shaft linings will be abandoned in place throughout the near-surface region.

#### 4.3.3.1 Near-Surface Upper Compacted Earthen Fill

This component (Component 1 in Figure 3-1) will be constructed using locally available fill. The fill will be compacted to a density near that of the surrounding material to inhibit the migration of surface waters into the shaft cross-section. The length of this column varies from 17 to 28 m (56 to 92 ft) in the four shafts. In all cases, this portion of the WIPP sealing system may be modified as required to facilitate decommissioning of the WIPP surface facilities.

#### 4.3.3.2 Near-Surface Concrete Plug

Current plans call for an SMC plug (Component 2 in Figure 4-1). However, freshwater concrete may be used if found to be desirable at a future time. The plug extends 12 m (40 ft) downward from the top of the Dewey Lake Redbeds. It is placed inside the existing shaft lining, and the interface is grouted.

#### 4.3.3.3 Near-Surface Lower Compacted Earthen Fill

This component (Component 3 in Figure 4-1) will be constructed using locally available fill, which will be placed using dynamic compaction (the same method used to construct the salt column). The fill will be compacted to a density equal to or greater than the surrounding materials to inhibit the migration of surface waters into the shaft cross-section. The length of this column varies from 136 to 148 m (447 to 486 ft) in the four shafts.

Page intentionally blank.

## 5. MATERIAL SPECIFICATION

Appendix A provides a body of technical information for each of the WIPP shaft seal materials. The materials specification characterizes each seal material, establishes the adequacy of its function, states briefly the method of component placement, and quantifies expected characteristics (particularly permeability) pertinent to a WIPP-specific shaft seal design. The goal of the materials specifications is to substantiate why materials used in this seal system design will limit fluid flow within the shafts and thereby limit releases of hazardous constituents from the WIPP site at the regulatory boundary.

This section summarizes materials characteristics for shaft seal system components designed for the WIPP. The shaft seal system will not be constructed for decades; however, if it were to be constructed in the near term, materials specified could be placed in the shaft and meet performance specifications without unreasonable advances in either material development or construction techniques. Construction methods are described in Appendix B. Materials specifications and construction specifications are not to be construed as the only materials or methods that would suffice to seal the shafts effectively. Undoubtedly, the design will be modified, perhaps simplified, and construction alternatives may prove to be advantageous during the years before seal construction proceeds. Nonetheless, a materials specification is necessary to establish a frame of reference for shaft seal design and analysis, to guide construction specifications, and to provide a basis for seal material parameters.

Design detail and other characteristics of the geologic, hydrologic, and chemical setting are provided in the text, appendices, and references. The four shafts will be entirely filled with dense materials possessing low permeability and other desirable engineering and economic attributes. Seal materials include concrete, clay, asphalt, and compacted salt. Other construction and fill materials include cementitious grout and earthen fill. Concrete, clay, and asphalt are common construction materials used extensively in sealing applications. Their descriptions, drawn from literature and site-specific references, are given in Appendix A. Compaction and natural reconsolidation of crushed salt are uniquely applied here. Therefore, crushed salt specification includes discussion of constitutive behavior and sealing performance, specific to WIPP applications. Cementitious grout is also specified in some detail. Only rudimentary discussion of earthen fill is given here and in Appendices A and B. Specifications for each material are discussed in the following order:

- functions,
- material characteristics,
- construction,
- performance requirements,
- verification methods.

Seal system components are materials possessing high durability and compatibility with the host rock. The system contains functional redundancy and uses differing materials to reduce uncertainty in performance. All materials used in the shaft seal system are expected to maintain their integrity for very long periods. Some sealing components reduce fluid flow soon after placement while other components are designed to function well beyond the regulatory period.

## 5.1 Longevity

A major environmental advantage of the WIPP locale is an overall lack of groundwater to seal against. Even though very little regional water is present in the geologic setting, the seal system reflects great concern for groundwater's potential influence on the shaft seal system. If the hydrologic system sustained considerable fluid flow, brine geochemistry could impact engineered materials. Brine would not chemically change the compacted salt column, but mechanical effects of pore pressure are of concern to reconsolidation. The geochemical setting, as further discussed in Section 2.4, will have little influence on concrete, asphalt, and clay shaft seal materials. Each material is durable because the potential for degradation or alteration is very low.

Materials used to form the shaft seals are the same as those identified in the scientific and engineering literature as appropriate for sealing deep geologic repositories for radioactive wastes. Durability or longevity of seal components is a primary concern for any long-term isolation system. Issues of possible degradation have been studied throughout the international community and within waste isolation programs in the USA. Specific degradation studies are not detailed in this document because longevity is one of the over-riding attributes of the materials selected and degradation is not perceived to be likely. However, it is acknowledged here that microbial degradation, seal material interaction, mineral transformation, such as silicification of bentonite, and effects of a thermal pulse from asphalt or hydrating concrete are areas of continuing investigations.

Among longevity concerns, degradation of concrete is the most recognized. At this stage of the design, it is established that only small volumes of brine ever reach the concrete elements (see Section C4). Further analysis concerned with borehole plugging using cementitious materials shows that at least 100 pore volumes of brine in an open system would be needed to begin degradation processes. In a closed system, such as the hydrologic setting in the WIPP shafts, phase transformations create a degradation product of increased volume. Net volume increase owing to phase transformation in the absence of mass transport would decrease rather than increase permeability of concrete seal elements.

Asphalt has existed for thousands of years as natural seeps. Longevity studies specific to DOE's Hanford site have utilized asphalt artifacts buried in ancient ceremonies to assess long-term stability (Wing and Gee, 1994). Asphalt used as a seal component deep in the shaft will inhabit a benign environment, devoid of ultraviolet light or an oxidizing atmosphere. Additional assurance against possible microbial degradation in asphalt elements is provided with addition of lime. For these reasons, it is believed that asphalt components will possess their design characteristics well beyond the regulatory period.

Natural bentonite is a stable material that generally will not change significantly over a period of ten thousand years. Bentonitic clays have been widely used in field and laboratory experiments concerned with radioactive waste disposal. As noted by Gray (1993), three internal mechanisms, illitization, silicification and charge change, could affect sealing properties of bentonite. Illitization and silicification are thermally driven processes and, following discussion by Gray (1993), are not possible in the environment or time-frame of concern at the WIPP. The naturally occurring Wyoming bentonite which is the specified material for the WIPP shaft seal is

well over a million years old. It is, therefore, highly unlikely that the metamorphism of bentonite enters as a design concern.

## 5.2 Materials

### 5.2.1 Mass Concrete

Concrete has low permeability and is widely used for hydraulic applications. The specification for mass concrete presents a special design mixture of a salt-saturated concrete called Salado Mass Concrete (SMC). Performance of SMC and similar salt-saturated mixtures has been established through analogous industrial applications and in laboratory and field testing. The documentation substantiates adequacy of SMC for concrete applications within the WIPP shafts.

The function of the concrete is to provide durable components with small void volume, adequate structural compressive strength, and low permeability. SMC is used as massive plugs, a monolith at the base of each shaft, and in tandem with asphalt waterstops. Concrete is a rigid material that will support overlying seal components while promoting natural healing processes within the salt DRZ. Concrete is one of the redundant components that protects the reconsolidating salt column. The salt column will achieve low permeabilities in fewer than 100 years, and concrete will no longer be needed at that time. However, concrete will continue to provide good sealing characteristics for a very long time.

Salt-saturated concrete contains sufficient salt as an aggregate to saturate hydration water with respect to NaCl. Salt-saturated concrete is required for all uses within the Salado Formation because fresh water concrete would dissolve part of the host rock. The concrete specified for the shaft seal system has been tailored for the service environment and includes all the engineering properties of high quality concrete, as described in Appendix A. Among these are low heat of hydration, high compressive strength, and low permeability. Because SMC provides material characteristics of high-performance concrete, it will likely be the concrete of choice for all seal applications at the WIPP.

Construction involves surface preparation and slickline placement. A batching and mixing operation on the surface will produce a wet mixture having low initial temperatures. Placement uses a tremie line, where the fresh concrete exits the slickline below the surface level of the concrete being placed. Placed in this manner, the SMC will have low porosity (about 5%) with or without vibration. Tremie line placement is a standard construction method in mining operations.

Specifications of concrete properties include mixture proportions and characteristics before and after hydration. SMC strength is much greater than required for shaft seal elements, and the state of stress within the shafts is compressional with little shear stress developing. Volume stability of the SMC is also excellent; this, combined with salt-saturation, assures a good bond with the salt. Permeability of SMC is very low, consistent with most concrete (Pfeifle et al., 1996). Because of a favorable state of stress and isothermal conditions, the SMC will remain intact. Because little brine is available to alter concrete elements, minimal degradation is possible. These favorable attributes combine to assure concrete elements within the Salado will remain structurally sound and possess very low permeability (between  $2 \times 10^{-21}$  and  $1 \times 10^{-17}$  m<sup>2</sup>)

for exceedingly long periods. A permeability distribution function and associated discussion are given in Appendix A.

Standard ASTM specifications are made for the green and hydrated concrete properties. Quality control and a history of successful use in both civil construction and mining applications assure proper placement and performance.

### **5.2.2 Compacted Clay**

Compacted clays are commonly proposed as primary sealing materials for nuclear waste repositories and have been extensively investigated against rigorous performance requirements. Advantages of clays for sealing purposes include low permeability, demonstrated longevity in many types of natural environments, deformability, sorptive capacity, and demonstrated successful utilization in practice for a variety of sealing purposes.

Compacted clay as a shaft sealing component functions as a barrier to brine flow and possibly to gas flow (see alternative construction methods in Appendix B). Compacted bentonitic clay can generate swelling pressure and clays have sufficient rigidity to promote healing of any DRZ in the salt. Wetted swelling clay will seal fractures as it expands into available space and will ensure tightness between the clay seal component and the shaft walls.

The Rustler and Salado compacted clay columns are specified to be constructed of dense sodium bentonite blocks. An extensive experimental data base exists for the permeability of sodium bentonites under a variety of conditions. Many other properties of sodium bentonite, such as strength, stiffness, and chemical stability, are established. Bentonitic clays heal when fractured and can penetrate small fractures or irregularities in the host rock. Further, bentonite is stable in the seal environment. These properties, noted by international waste isolation programs, make bentonite a widely accepted seal material.

From the bottom clay component to the top earthen fill, different methods will be used to place clay materials in the shaft. Seal performance within the Salado Formation is far more important to regulatory compliance of the seal system than is performance of clay and earthen fill in the overlying formations. Therefore, more time and effort will be expended on placement of Salado clay components. Three potential construction methods could be used to place clay in the shaft, as discussed in Appendix B: compacted blocks, vibratory roller, and dynamic compaction. Construction of Salado clay components specifies block assembly.

Required sealing performance of compacted clay elements varies with location. For example, Component 4 provides separation of water-bearing zones, while the lowest clay column (Component 12) limits fluid flow to the reconsolidating salt column. If liquid saturation in the clay column of 85% can be achieved, it would serve as a gas barrier. In addition, compacted clay seal components promote healing of the salt DRZ. To achieve low permeabilities, the dry density of the emplaced bentonite should be about  $1.8 \text{ g/cm}^3$ . A permeability distribution function for performance assessment and the logic for its selection are given in Appendix A.

Verification of specified properties such as density, moisture content, permeability, or strength of compacted clay seals can be determined by direct measurement during construction. However, indirect methods are preferred because certain measurements, such as permeability, are

likely to be time consuming and invasive. Methods used to verify the quality of emplaced seals will include quality of block production and field measurements of density.

### **5.2.3 Asphalt**

Asphalt is used to prevent water migration down the shaft in two ways: as an asphalt column near the Rustler/Salado contact and as a "waterstop" sandwiched between concrete plugs at three locations within the Salado Formation. Asphalt components of the WIPP seal design add assurance that minimal transport of brine down the sealed shaft will occur.

Asphalt is a widely used construction material because of its many desirable engineering properties. Asphalt is a strong cement, readily adhesive, highly waterproof, and durable. Furthermore, it is a plastic substance that is readily mixed with mineral aggregates. A range of viscosity is achievable for asphalt mixtures. It is highly resistant to most acids, salts, and alkalis. These properties are well suited to the requirements of the WIPP shaft seal system.

Construction of the seal components containing asphalt can be accomplished using a slickline process where low-viscosity heated material is effectively pumped into the shaft. The technology to apply the asphalt in this manner is available as described in the construction procedures in Appendix B.

The asphalt components are required to endure for about 100 years and limit brine flow down the shaft to the compacted salt component. Since asphalt will not be subjected to ultraviolet light or an oxidizing environment, it is expected to provide an effective seal for centuries. Air voids less than 2% ensure low permeability. The permeability of the massive asphalt column is expected to have an upper limit  $1 \times 10^{-18} \text{ m}^2$ .

Sufficient construction practice and laboratory testing information is available to assure performance of the asphalt component. Laboratory validation tests to optimize viscosity may be desirable before final installation specifications are prepared. In general, verification tests would add quantitative documentation to expected performance values and have direct application to WIPP.

### **5.2.4 Compacted Salt Column**

A reconsolidated column of natural WIPP salt will seal the shafts permanently. If salt reconsolidation is unimpeded by fluid pore pressures, the material will eventually achieve extremely low permeabilities approaching those of the native Salado Formation. Recent developments in support of the WIPP shaft seal system have produced confirming experimental results, constitutive material models, and construction methods that substantiate use of a salt column to create a low permeability seal component. Reuse of salt excavated in the process of creating the underground openings has been advocated since its initial proposal in the 1950s. Replacing the natural material in its original setting ensures physical, chemical, and mechanical compatibility with the host formation.

The function of the compacted and reconsolidated salt column is to limit transmission of fluids into or out of the repository for the statutory period of 10,000 years. The functional period starts within a hundred years and lasts essentially forever. After a period of consolidation, the salt column will almost completely retard gas or brine migration within the former shaft opening.

A completely consolidated salt column will achieve flow properties indistinguishable from natural Salado salt.

The salt component is composed of crushed Salado salt with additional small amounts of water. The total water content of the crushed salt will be adjusted to 1.5 wt% before it is tamped into place. Field and laboratory tests have verified that natural salt can be compacted to significant fractional density ( $\rho \geq 0.9$ ) with addition of these moderate amounts of water.

Dynamic compaction is the specified construction procedure to tamp crushed salt in the shaft. Deep dynamic compaction provides great energy to the crushed salt, is easy to apply, and has an effective depth of compactive influence greater than lift thickness. Dynamic compaction is relatively straightforward and requires a minimal work force in the shaft. Compaction itself will follow procedures developed in a large-scale compaction demonstration, as outlined in Appendix B.

Numerical models of the shaft provide density of the compacted salt column as a function of depth and time. Many calculations comparing models for consolidation of crushed salt were performed to quantify performance of the salt column, as discussed in Appendix D and the references (Callahan et al., 1996; Brodsky et al., 1996). From the density-permeability relationship of reconsolidating crushed salt, permeability of the compacted salt seal component is calculated. In general, results show that the bottom of the salt column consolidates rapidly, achieving permeability of  $1 \times 10^{-19} \text{ m}^2$  in about 50 years. By 100 years, the middle of the salt column reaches similar permeability.

Results of the large-scale dynamic compaction demonstration suggest that deep dynamic compaction will produce a sufficiently dense starting material. As with other seal components, testing of the material in situ will be difficult and probably not optimal to ensure quality of the seal element. This is particularly apparent for the compacted salt component because the compactive effort produces a finely powdered layer on the top of each lift. It was demonstrated (Hansen and Ahrens, 1996) that the fine powder is very densely compacted upon tamping the superincumbent lifts. The best means to ensure that the crushed salt element is placed properly is to establish performance through verification of quality assurance/quality control procedures. If crushed salt is placed with a reasonable uniformity of water and compacted with sufficient energy, long-term performance can be assured.

### **5.2.5 Cementitious Grout**

Cementitious grouting is specified for all concrete members. Grouting is also used in advance of liner removal to stabilize the ground and to limit water inflow during shaft seal construction. Cementitious grout is specified because of its proven performance, nontoxicity, and previous use at the WIPP.

The function of grout is to stabilize the surrounding rock before existing concrete liners are removed. Grout will fill fractures within adjacent lithologies, thereby adding strength and reducing permeability and, hence, water inflow during shaft seal construction. Grout around concrete members of the concrete asphalt waterstop will be employed in an attempt to tighten the interface and fill microcracks in the DRZ. Efficacy of grouting will be determined during construction.

An ultrafine cementitious grout has been specifically developed for use at the WIPP (Ahrens and Onofrei, 1996). This grout consists of Type 5 portland cement, pumice as a pozzolanic material, and superplasticizer. The average particle size is approximately 2 microns. The ultrafine grout is mixed in a colloidal grout mixer, with a water to components ratio (W:C) of 0.6:1.

Drilling and grouting sequences provided in Appendix B follow standard procedures. Grout will be mixed on the surface and transported by slickline to the middle deck on the multi-deck stage (galloway). Grout pressures are specified below lithostatic to prevent hydrofracturing.

Performance of grout is not a consideration for compliance issues. Grouting of concrete elements is an added assurance to tighten interfaces. Grouting is used to facilitate construction by stabilizing any loose rock behind the concrete liner.

No verification of the effectiveness of grouting is currently specified. If injection around concrete plugs is possible, an evaluation of quantities and significance of grouting will be made during construction. Procedural specifications will include measurements of fineness and determination of rheology in keeping with processes established during the WIPP demonstration grouting (Ahrens et al., 1996).

#### **5.2.6 Earthen Fill**

A brief description of the earthen fill is provided in Appendix A, and construction is summarized in Appendix B. Compacted fill can be obtained from local borrow pits, or material excavated during shaft construction can be returned to the shaft. There are minimal design requirements for earthen fill and none that are related to WIPP regulatory performance.

### **5.3 Concluding Remarks**

Materials specifications in Appendix A provide descriptions of seal materials along with reasoning on their expected reliability in the WIPP setting. The specification follows a framework that states the function of the seal component, a description of the material, and a summary of construction techniques. The performance requirements for each material are detailed. Materials chosen for use in the shaft seal system have several common desirable attributes: low permeability, high density, compatibility, longevity, low cost, constructability, availability, and supporting documentation.

Page intentionally blank.

## 6. CONSTRUCTION TECHNIQUES

Construction of the shaft sealing system is feasible. The described procedures utilize currently available technology, equipment, and materials to satisfy shaft sealing system design guidance. Although alternative methods are possible, those described satisfy the design guidance requirements listed in Table 3-1 and detailed in the appendices. Construction feasibility is established by reference to comparable equipment and activities in the mining, petroleum, and food industries and test results obtained at the WIPP. Equipment and procedures for emplacement of sealing materials are described below.

### 6.1 Multi-Deck Stage

A multi-deck stage (Figures 6-1 and 6-2) consisting of three vertically connected decks will be the conveyance utilized during the shaft sealing operation. Detailed sketches of the multi-deck stage appear in Appendix E. The stage facilitates installation and removal of utilities and provides a working platform for the various sealing operations. A polar crane attached to the lower deck provides the mechanism required for dynamic compaction and excavation of the shaft walls. Additionally, the header at the bottom of the slickline is supported by a reinforced steel shelf, which is securely bolted to the shaft wall during emplacement of sealing materials. The multi-deck stage can be securely locked in place in the shaft whenever desired (e.g., during dynamic compaction, excavation of the salt walls of the shaft, grouting, liner removal, etc.). The multi-deck stage is equipped with floodlights, remotely aimed closed-circuit television, fold-out floor extensions, a jib crane, and range-finding devices. Similar stages are commonly employed in shaft sinking operations.

The polar crane can be configured for dynamic compaction (Figure 6-1) or for excavation of salt (Figure 6-2); a man cage or bucket can be lowered through the stage to the working surface below. Controlled manually or by computer, the crane and its trolley utilize a geared track drive. The crane can swiftly position the tamper (required for dynamic compaction) in the drop positions required (Figure 6-3) or accommodate the undercutter required for excavation of the shaft walls. The crane incorporates a hoist on the trolley and an electromagnet, enabling it to position, hoist, and drop the tamper. A production rate of one drop every two minutes during dynamic compaction is possible.

### 6.2 Salado Mass Concrete (Shaft Station Monolith and Shaft Plugs)

Salado Mass Concrete, described in Appendix A, will be mixed on surface at 20°C and transferred to emplacement depth through a slickline (i.e., a steel pipe fastened to the shaft wall and used for the transfer of sealing materials from surface to the fill horizon) minimizing air entrainment and ensuring negligible segregation. Existing sumps will be filled to the elevation of the floor of the repository horizon, and emplacement of the shaft station monolith is designed to eliminate voids at the top (back) of the workings.

When excavating salt for waterstops or plugs in the Salado Formation, an undercutter attached to the trolley of the polar crane will be forced into the shaft wall by a combination of geared trolley and undercutter drives. Full circumferential cuts will be accomplished utilizing the torque developed by the geared polar crane drive.

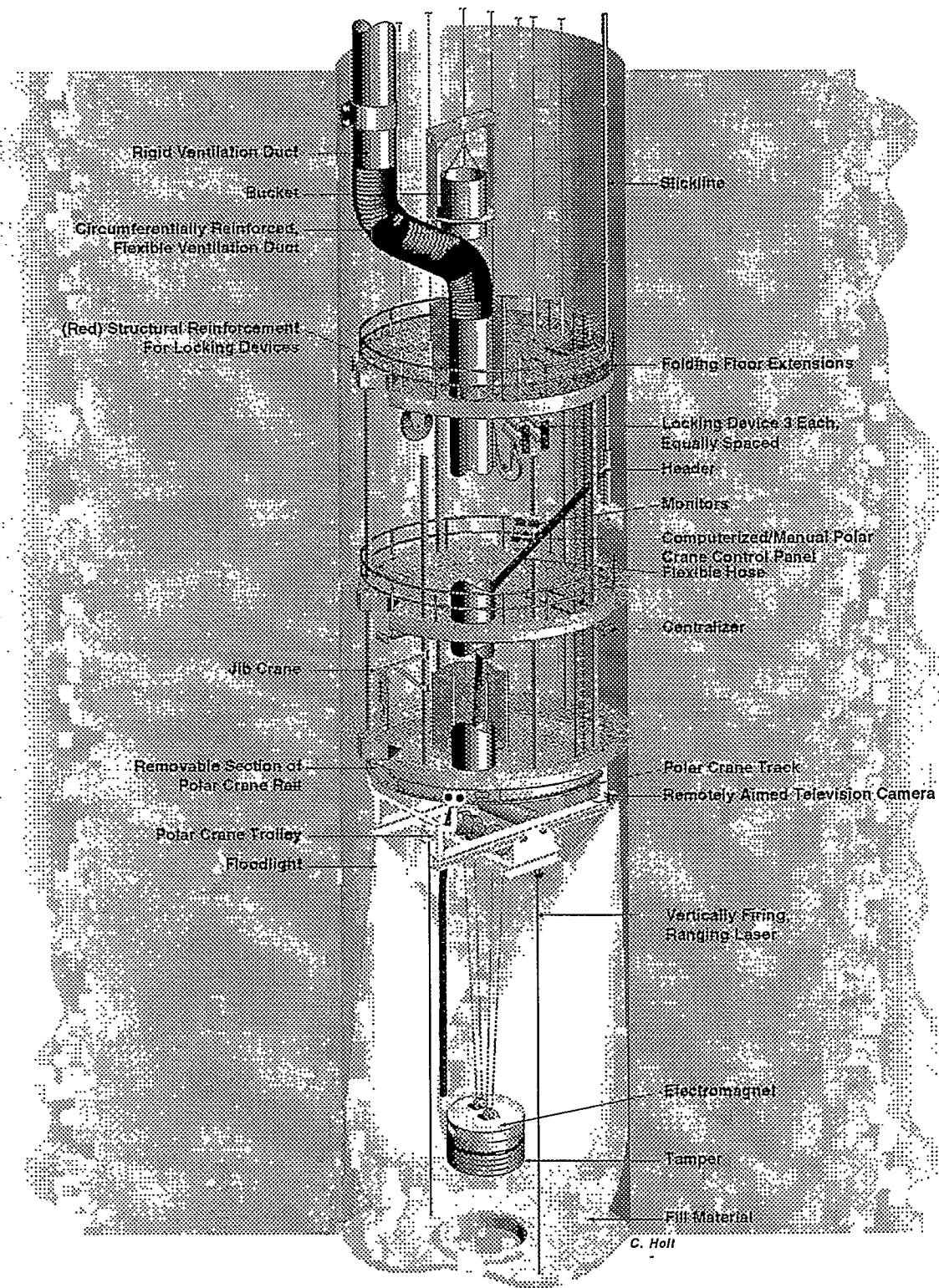


Figure 6-1. Multi-deck stage illustrating dynamic compaction.

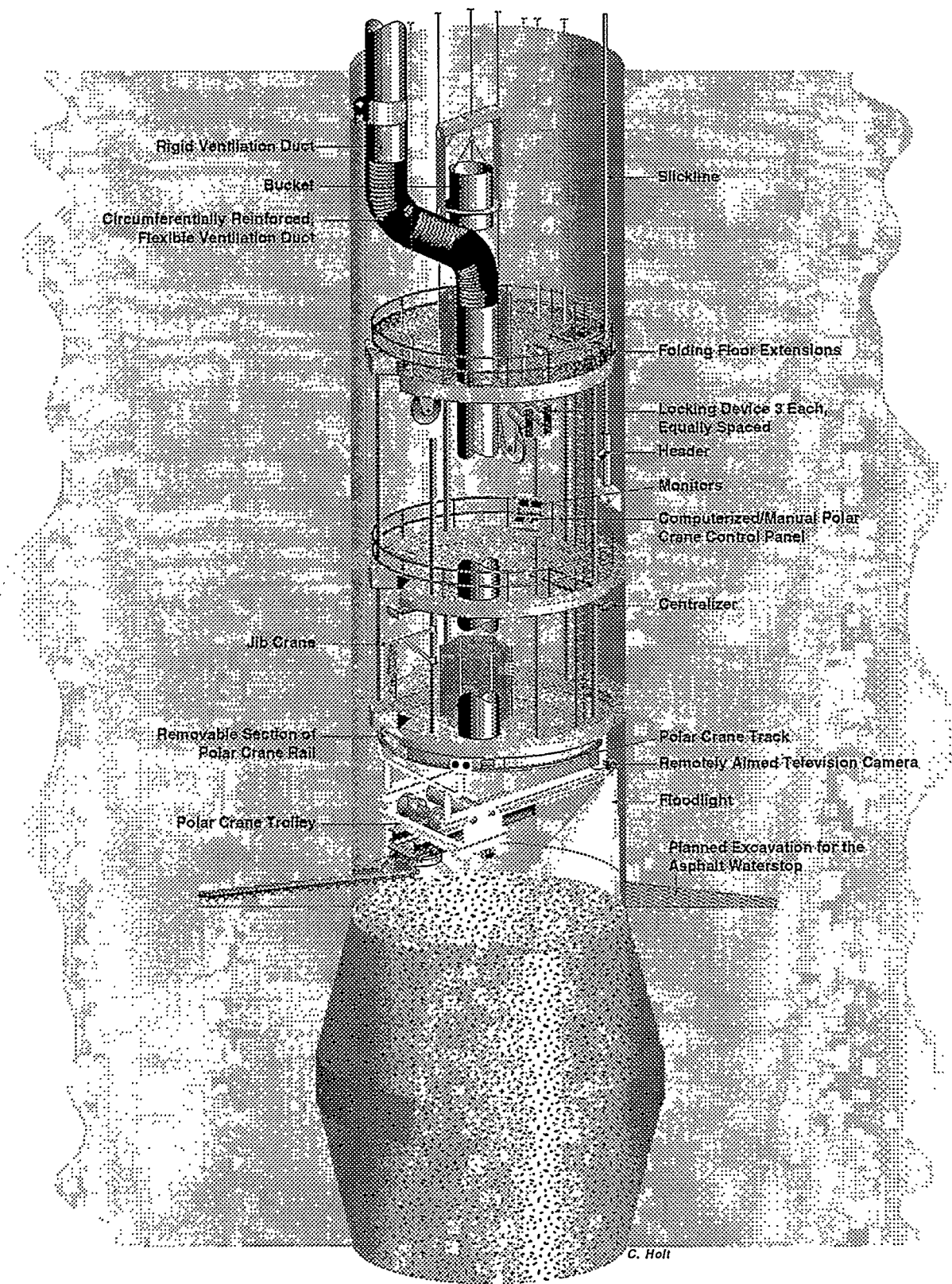
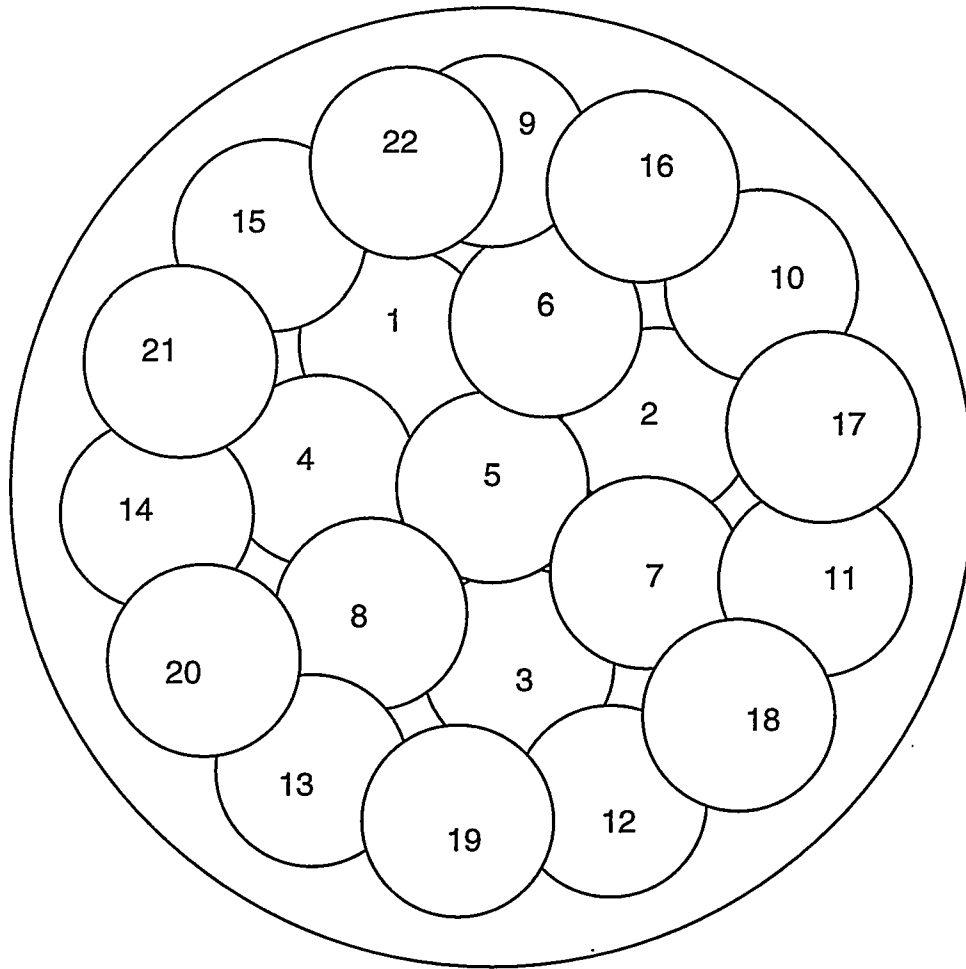


Figure 6-2. Multi-deck stage illustrating excavation for asphalt waterstop.



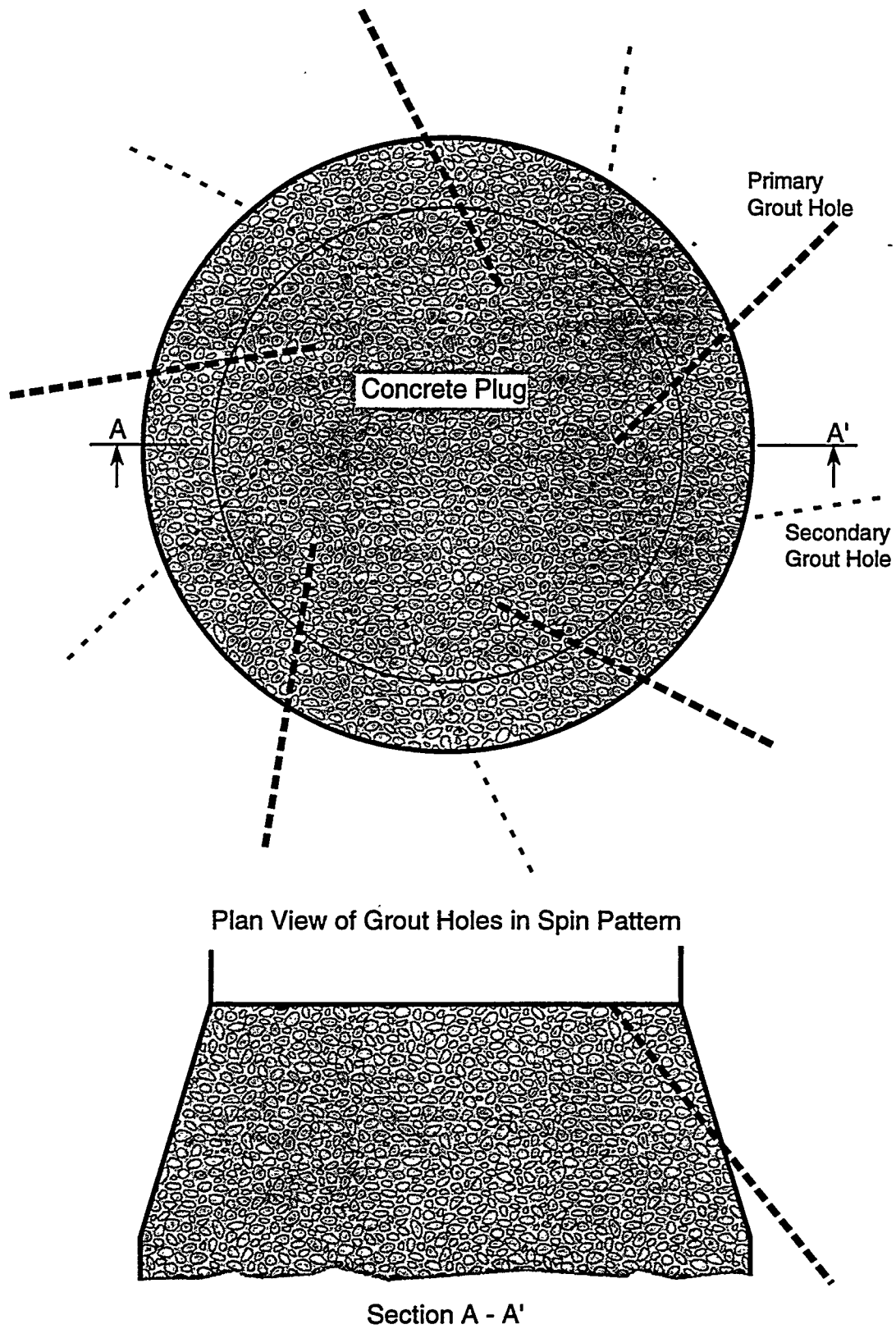
Scale: 1" = 4'

TRI-6121-376-0

Figure 6-3. Drop pattern for 6-m-diameter shaft using a 1.2-m-diameter tamper.

The undercutter proposed is a modified version of those currently in use in salt and coal mines, where their performance is proven. Such modifications and applications have been judged feasible by the manufacturer.

The concrete-salt interface and DRZ around concrete plugs in the Salado Formation (and the one at the base of the Rustler Formation) will be grouted with ultrafine grout. Injection holes will be collared in the top of the plug and drilled downward at 45° below horizontal. The holes will be drilled in a “spin” pattern describing a downward opening cone designed to intercept both vertical and horizontal fractures (Figure 6-4). The holes will be stage grouted (i.e., primary holes will be drilled and grouted, one at a time). Secondary holes will then be drilled and grouted, one at a time, on either side of primaries that accepted grout.



TRI-6121-373-0

Figure 6-4. Plan and section views of downward spin pattern of grout holes.

### **6.3 Compacted Clay Columns (Salado and Rustler Formations)**

Cubic blocks of sodium bentonite, 20.8 cm on the edge and weighing approximately 18 kg, will be precompacted on surface to a density between 1.8 and 2.0 gm/cm<sup>3</sup> and emplaced manually. The blocks will be transferred from surface on the man cage. Block surfaces will be moistened with a fine spray of potable water, and the blocks will be manually placed so that all surfaces are in contact. Peripheral blocks will be trimmed to fit irregularities in the shaft wall, and remaining voids will be filled with a thick mortar of sodium bentonite and potable water. Such blocks have been produced at the WIPP and used in the construction of 0.9-m-diameter seals, where they performed effectively (Knowles and Howard, 1996). Alternatives, which may be considered in future design evaluations, are discussed in Appendix B.

### **6.4 Asphalt Waterstops and Asphaltic Mix Columns**

Neat asphalt is selected for the asphalt waterstops, and an asphaltic mastic mix (AMM) consisting of neat asphalt, fine silica sand, and hydrated lime will be the sealing material for the columns. Both will be fluid at emplacement temperature and remotely emplaced. Neat asphalt (or AMM, prepared in a pug mill near the shaft collar) will be heated to 180°C and transferred to emplacement depth via an impedance-heated, insulated tremie line (steel pipe) suspended from slips (pipe holding device) at the collar of the shaft.

This method of line heating is common practice in the mining and petroleum industries. This method lowers the viscosity of the asphalt so that it can be pumped easily. Remote emplacement by tremie line eliminates safety hazards associated with the high temperature and gas produced by the hot asphalt. Fluidity ensures that the material will flow readily and completely fill the excavations and shaft. Slight vertical shrinkage will result from cooling (calculations in Appendix D), but the material will maintain contact with the shaft walls and the excavation for the waterstop. Vertical shrinkage will be counteracted by the emplacement of additional material.

### **6.5 Compacted WIPP Salt**

Dynamic compaction of mine-run WIPP salt has been demonstrated (Ahrens and Hansen, 1995). The surface demonstration produced salt compacted to 90% of in-place rock salt density, with a statistically averaged permeability of  $1.65 \times 10^{-15} \text{ m}^2$ . Additional laboratory consolidation of this material at 5 MPa confining pressure (simulating creep closure of the salt) resulted in increased compaction and lower permeability (Brodsky, 1994). Dynamic compaction was selected because it is simple, robust, proven, has excellent depth of compaction, and is applicable to the vertical WIPP shafts.

The compactive effect expanded laterally and downward in the demonstration, and observation during excavation of the compacted salt revealed that the lateral compactive effect will fill irregularities in the shaft walls. Additionally, the depth of compaction, which was greater than that of the three lifts of salt compacted, resulted in the bottom lift being additionally compacted during compaction of the two overlying lifts. This cumulative effect will occur in the shafts.

Construction of the salt column will proceed in the following manner:

- Crushed and screened salt will be transferred to the fill elevation via slickline. Use of slicklines is common in the mining industry, where they are used to transfer backfill materials or concrete to depths far greater than those required at the WIPP. Potable water will be added via a fine spray during emplacement at the fill surface to adjust the moisture content to  $1.5 \pm 0.3$  wt%, accomplished by electronically coordinating the weight of the water with that of the salt exiting the hose.
- Dynamic compaction will then be used to compact the salt by dropping the tamper in specific, pre-selected positions such as those shown in Figure 6-3.

## **6.6 Grouting of Shaft Walls and Removal of Liners**

The procedure listed below is a common mining practice which will be followed at each elevation where liner removal is specified. If a steel liner is present, it will be cut into manageable pieces and hoisted to the surface for disposal, prior to initiation of grouting.

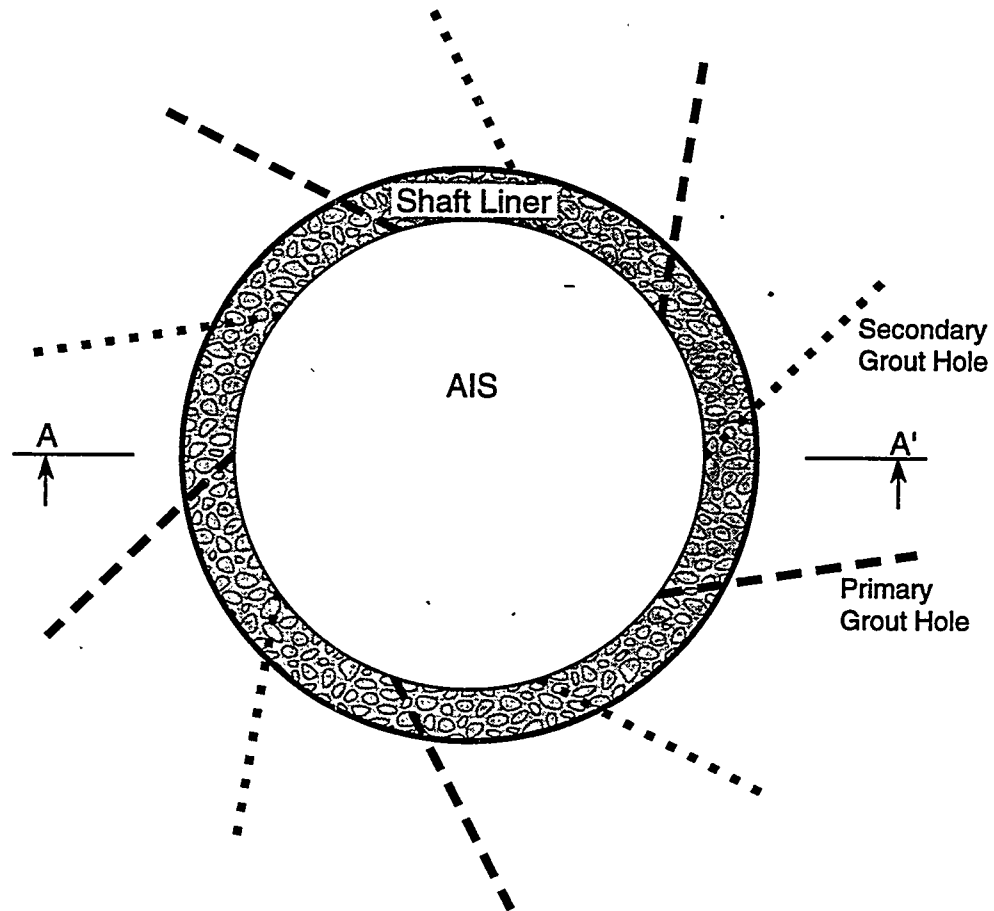
Upward opening cones of diamond drill holes will be drilled into the shaft walls in a spin pattern (Figure 6-5) to a depth ensuring complete penetration of the Disturbed Rock Zone (DRZ) surrounding the shaft. For safety reasons, no major work will be done from the top deck; all sealing activities will be conducted from the bottom deck. The ends of the holes will be 3 m apart, and the fans will be 3 m apart vertically, covering the interval from 3 m below to 3 m above the interval of liner removal. Tests at the WIPP demonstrated that the ultrafine cementitious grout penetrated more than 2 m from the injection holes (Ahrens et al., 1996).

Injection holes will be drilled and grouted one at a time, as is the practice in stage grouting. Primary holes are grouted first, followed by the grouting of secondary holes on either side of primaries that accepted grout. Ultrafine grout will be injected below lithostatic pressure to avoid hydrofracturing the rock, proceeding from the bottom fan upward. Grout will be mixed on surface and transferred to depth via the slickline.

Radial, horizontal holes will then be drilled on a 0.3-m grid, covering the interval to be removed. These will be drilled to a depth sufficient to just penetrate the concrete liner. A chipping hammer will be used to break a hole through the liner at the bottom of the interval. This hole, approximately 0.3 m in diameter, will serve as "free face," to which the liner can be broken. Hydraulically-actuated steel wedges will then be used in the pre-drilled holes to break out the liner in manageable pieces, beginning adjacent to the hole and proceeding upward. Broken concrete will be allowed to fall to the fill surface, where it will be gathered and hoisted to the surface for disposal. Chemical seal rings will be removed as encountered.

## **6.7 Earthen Fill**

Local soil, screened to produce a maximum particle dimension of approximately 15 mm, will be the seal material. This material will be transferred to the fill surface via the slickline and emplaced in the same manner as the salt. After adjusting the moisture content of the earthen fill below the concrete plug in the Dewey Lake Redbeds to achieve maximum compaction, the fill will be dynamically compacted, achieving a permeability as low as that of the enclosing formation.



Plan View of Grout Holes in Spin Pattern



Section A - A'

TRI-6121-374-0

Figure 6-5. Plan and section views of upward spin pattern of grout holes.

The portion of the earthen fill above the plug will be compacted with a vibratory-impact sheepsfoot roller, a vibratory sheepsfoot roller, or a walk-behind vibratory plate compactor, because of insufficient height for dynamic compaction.

### **6.8 Schedule**

For discussion purposes, it has been assumed that the shafts will be sealed two at a time. This results in the four shafts being sealed in approximately six and a half years. The schedules presented in Appendix B are based on this logic. Sealing the shafts sequentially would require approximately eleven and a half years.

Page intentionally blank.

## **7. STRUCTURAL ANALYSES OF SHAFT SEALS**

### **7.1 Introduction**

The shaft seal system was designed in accordance with design guidance described in Section 3.2. To be successful, seal system components must exhibit desired structural behavior. The desired structural behavior can be as simple as providing sufficient strength to resist imposed loads. In other cases, structural behavior is critical to achieving desired hydrological properties. For example, permeability of compacted salt depends on the consolidation induced by shaft closure resulting from salt creep. In this example, results from structural analyses feed directly into fluid-flow calculations, which are described in Section 8, because structural behavior affects both time-dependent permeabilities of the compacted salt and pore pressures within the compacted salt. In other structural considerations, thermal effects are analyzed as they affect the constructability and schedule for the seal system. Thus a series of analyses, loosely termed structural analyses, were performed to accomplish three purposes:

1. to determine loads imposed on components and to assess both structural stability based on the strength of the component and mechanical interaction between components;
2. to estimate the influence of structural behavior of seal materials and surrounding rock on hydrological properties; and
3. to provide structural and thermal related information on construction issues.

For the most part, structural analyses rely on information and design details presented in the Design Description (Section 4), the Design Drawings (Appendix E), and Material Specification (Section 5 and Appendix A). Some analyses are generic, and calculation input and subsequent results are general in nature.

### **7.2 Analysis Methods**

Finite-element modeling was the primary numerical modeling technique used to evaluate structural performance of the shaft seals and surrounding rock mass. Well documented finite-element computer programs, SPECTROM-32 and SPECTROM-41, were used in structural and thermal modeling, respectively. The computer program SALT\_SUBSID was used in the subsidence modeling over the backfilled shaft-pillar area. Specific details of these computer programs as they relate to structural calculations are listed in Appendix D, Section D2.

### **7.3 Models of Shaft Seals Features**

Structural calculations require material models to characterize the behavior of (1) each seal material (concrete, crushed salt, compacted clay, and asphalt); (2) the intact rock lithologies in the near-surface, Rustler, and Salado formations; and (3) any DRZ within the surrounding rock. A general description of the material models used in characterizing each of these materials and features is given below. Details of the models and specific values of model parameters are given in Appendix D, Section D3.

### **7.3.1 Seal Material Models**

The SMC thermal properties required for the structural analyses (thermal conductivity, density, specific heat, and volumetric heat generation rate) were obtained from SMC test data. Concrete was assumed to behave as a viscoelastic material, based on experimental data, and the elastic modulus of SMC was modeled as age-dependent. Strength properties of SMC were specified in the design (see Appendix A).

For crushed salt, the deformational model included a nonlinear elastic component and a creep consolidation component. The nonlinear elastic modulus was assumed to be density-dependent, based on laboratory test data performed on WIPP crushed salt. Creep consolidation behavior of crushed salt was based on three candidate models whose parameters were obtained from model fitting to hydrostatic and shear consolidation test data performed on WIPP crushed salt. Creep consolidation models include functional dependencies on density, mean stress, stress difference, temperature, grain size, and moisture content.

Compacted clay was assumed to behave according to a nonlinear elastic model in which shear stiffness is negligible, and asphalt was assumed to behave as a weak elastic material. Thermal properties of asphalt were taken from literature.

### **7.3.2 Intact Rock Lithologies**

Salado salt was assumed to be argillaceous salt that is governed by the Multimechanism Deformation Coupled Fracture (MDCF) model, which is an extension of the Munson-Dawson (M-D) creep model. A temperature-dependent thermal conductivity was necessary.

Salado interbeds were assumed to behave elastically. Their material strength was assumed to be described by a Drucker-Prager yield function, consistent with values used in previous WIPP analyses.

Deformational behavior of the near-surface and Rustler Formation rock types was assumed to be time-invariant, and their strength was assumed to be described by a Coulomb criterion, consistent with literature values.

### **7.3.3 Disturbed Rock Zone Models**

Two different models were used to evaluate the development and extent of the DRZ within intact salt. The first approach used ratios of time-dependent stress invariants to quantify the potential for damage or healing to occur. The second approach used the damage stress criterion according to the MDCF model for WIPP salt.

## **7.4 Structural Analyses of Shaft Seal Components**

### **7.4.1 Salado Mass Concrete Seals**

Five analyses related to structural performance of SMC seals were performed, including (1) a thermal analysis, (2) a structural analysis, (3) a thermal stress analysis, (4) a dynamic compaction analysis, and (5) an analysis of the effects of clay swelling pressure. This section presents these analyses and evaluates the results in terms of the performance of the SMC seal. Details of these calculations are given in Appendix D, Section D4.

(0, 2, and 4 MPa). Results indicate that times required to consolidate the crushed salt increase as the pore pressure increases, as expected. For example, for a pore pressure of 2 MPa, the times required to achieve a fractional density of 96% are about 90 years, 205 years, and 560 years at the bottom, middle, and top of the crushed salt column, respectively. A pore pressure of 4 MPa would effectively prevent reconsolidation of the crushed salt within a reasonable period (<1,000 years). The results of this calculation were used in the fluid flow calculations, and the impact of these pore pressures on the permeability of the crushed salt seal is described in Section 8 and Appendix C.

### **7.4.3 Compacted Clay Seals**

One analysis was performed to determine the structural response of compacted clay seals. The objective of this calculation was to determine stresses in the upper Salado compacted clay component and the lower Salado compacted clay component as a result of creep of the surrounding salt. Details of this calculation are given in Appendix D, Section D4. Results of this calculation indicate that after 50 years the compressive stresses in the upper Salado compacted clay component are about 0.7 MPa; not including the effects of swelling pressures. Similarly, after 50 years the stresses in the lower Salado compacted clay component are approximately 2.6 MPa. Based on these results, the compacted clay component will provide some restraint to the creep of salt and induce a back (radial) stress in the clay seal, which will promote healing of the DRZ in the surrounding intact salt (see discussion about DRZ in Section 7.5.1).

### **7.4.4 Asphalt Seals**

Three analyses were performed related to structural performance of the asphalt seals, including (1) a thermal analysis, (2) a structural analysis, and (3) a shrinkage analysis. This section presents the results of these analyses and evaluates the results in terms of the performance of the asphalt seal. Details of these analyses are given in Appendix D, Section D4.

#### **7.4.4.1 Thermal Analysis**

The objectives of this calculation were (1) to determine temperature histories within the asphalt seal and the surrounding salt and (2) to determine effects of the length of the waterstop.

Results indicate that the center of the asphalt column will cool from its emplaced temperature of 180°C to 83°C, 49°C, 31°C, and 26°C at times 0.1 year, 0.2 year, 0.5 year, and 1.0 year, respectively. Similarly, the asphalt/salt interface temperatures at corresponding times are 47°C, 38°C, 29°C, and 26°C. The time required for a waterstop to cool is significantly less than that required to cool the asphalt column. Based on these results, about 40 days are required for asphalt to cool to an acceptable working environment temperature. The thermal impact on enhanced creep rate of the surrounding salt is considered to be negligible.

#### **7.4.4.2 Structural Analysis**

The objective of this analysis was to calculate pressures in asphalt that result from restrained creep of the surrounding salt and to evaluate stresses induced on the concrete seal component by such pressurization.

Results indicate that pressures in the waterstops after 100 years are 1.8 MPa, 2.5 MPa, and 3.2 MPa for the upper, middle, and lower waterstops, respectively. Based on these results, the structural integrity of concrete components will not be compromised by imposed pressures, and the rock surrounding the asphalt will not be fractured by the pressure. The pressure from asphalt is enough to initiate healing of the DRZ surrounding the waterstop.

#### **7.4.4.3 Shrinkage Analysis**

The objective of this analysis was to calculate shrinkage of the asphalt column as it cools from its emplaced temperature to an acceptable working environment temperature. Results of this analysis indicate that the 42-m asphalt column will shrink 0.9 m in height as the asphalt cools from its emplaced temperature of 180°C to 38°C.

### **7.5 Disturbed Rock Zone Considerations**

#### **7.5.1 General Discussion of DRZ**

Microfracturing leading to a DRZ occurs within salt whenever excavations are made. Laboratory and field measurements show that a DRZ has enhanced permeability. The body of evidence strongly suggests that induced fracturing is reversible and healed when deviatoric stress states created by the opening are reduced. Rigid seal components in the shaft provide a restraint to salt creep closure, thereby inducing healing stress states in the salt. A more detailed discussion of the DRZ is included in Appendix D.

#### **7.5.2 Structural Analyses**

Three analyses were performed to determine the behavior of the DRZ in the rock mass surrounding the shaft. The first analysis considered time-dependent DRZ development and subsequent healing of intact Salado salt surrounding each of the four seal materials. The second analysis considered time-dependent development of the DRZ within anhydrite and polyhalite interbeds within the Salado Formation. The last analysis considered time-independent DRZ development within the near-surface and Rustler formations. These analyses are discussed below and given in more detail in Appendix D, Section D5. Results from these analyses were used as input conditions for the fluid flow analysis presented in Section 8 and Appendix C.

##### **7.5.2.1 Salado Salt**

The objective of this calculation was to determine time-dependent extent of the DRZ in salt, assuming no pore pressure effects, for each of the four shaft seal materials (i.e., concrete, crushed salt, compacted clay, and asphalt). The seal materials below a depth of about 300 m provide sufficient rigidity to heal the DRZ within 100 years. Asphalt, modeled as a weak elastic material, will not create a stress state capable of healing the DRZ because it is located high in the Salado.

##### **7.5.2.2 Salado Anhydrite Beds**

The objective of this calculation was to determine the extent of the DRZ within the Salado anhydrite and polyhalite interbeds as a result of creep of surrounding salt.

For all interbeds, the factor of safety against failure (shear or tensile fracturing) increases with depth into the rock surrounding the shaft wall. These results indicate that, with the exception of Marker Bed 117 (MB117), the factor of safety is greater than 1 (no DRZ will develop) for all interbeds. For MB117, the potential for fracturing is localized to within 1 m of the shaft wall.

### 7.5.2.3 Near-Surface and Rustler Formations

The objective of this calculation was to determine the extent of the DRZ surrounding the shafts in the near-surface and Rustler formations.

Rock types in near-surface and Rustler formations are anhydrite, dolomite, and mudstone. These rock types exhibit time-independent behavior. Results indicate that no DRZ will develop in anhydrite and dolomite (depths between 165 and 213 m). For mudstone layers, the radial extent of the DRZ increases with depth, reaching a maximum of 2.6 shaft radii at a depth of 223 m.

## 7.6 Other Analyses

This section discusses two structural analyses performed in support of design concerns, namely (1) the asphalt waterstops constructability and (2) benefits from shaft station backfilling. Analyses performed in support of these efforts are discussed below and given in more detail in Appendix D, Section D6.

### 7.6.1 Asphalt Waterstops

The DRZ is a major contributor to fluid flows through a low permeability shaft seal system, regardless of the materials emplaced within the shaft. Therefore, to increase the confidence in the overall shaft seal, low permeability layers (termed radial waterstops) were included to intersect the DRZ surrounding the shaft. These waterstops are emplaced to alter the flow direction either inward toward the shaft seal or outward toward intact salt. Asphalt-filled waterstops will be effective soon after emplacement. The objectives of these structural calculations were to evaluate performance of the waterstops in terms of (1) intersecting the DRZ around the shaft, (2) inducing a new DRZ because of special excavation, and (3) promoting healing of the DRZ.

Results indicate that the DRZ from the shaft extends to a radial distance of less than one shaft radius (3.04 m). Waterstop excavation extends the DRZ radially to about 1.4 shaft radii (4.3 m). However, this extension is localized within the span of the concrete component and extends minimally past the waterstop edge. The DRZ extent reduced rapidly after the concrete and asphalt restrained creep of the surrounding salt. After 20 years, the spatial extent of the DRZ is localized near the asphalt-concrete interface, extending spatially into the salt at a distance of less than 2 m. Based on these results, construction of waterstops is possible without substantially increasing the DRZ. Furthermore, the waterstop extends well beyond the maximum extent of the DRZ surrounding the shaft and effectively blocks this flow path (within 2 years after emplacement), albeit over only a short length of the flow path.

### **7.6.2 Shaft Pillar Backfilling**

The objective of this calculation was to assess potential benefits from backfilling a portion of the shaft pillar to reduce subsurface subsidence and thereby decrease the potential for inducing fractures along the shaft wall. The calculated subsidence without backfilling is less than one foot, due to the relatively low extraction ratio at the WIPP. Based on the results of this analysis, backfilling portions of the shaft pillar would result in only 10% to 20% reduction in surface subsidence. This reduction in subsidence from backfilling is not considered enough to warrant backfilling the shaft pillar area. The shaft seals within the Salado are outside the angle-of-draw for any horizontal displacements caused by the subsidence over the waste panels. Moreover, horizontal strains caused by subsidence induced by closures within the shaft pillar are compressive in nature and insignificant in magnitude to induce fracturing along the shaft wall.

## **8. HYDROLOGIC EVALUATION OF THE SHAFT SEAL SYSTEM**

### **8.1 Introduction**

The design guidance in Section 3 presented the rationale for sealing the shaft seal system with low permeability materials, but it did not provide specific performance measures for the seal system. This section compares the hydrologic behavior of the system to several performance measures that are directly related to the ability of the seal system to limit liquid and gas flows through the seal system. The hydrologic evaluation is focused on the processes that could result in fluid flow through the shaft seal system and the ability of the seal system to limit any such flow. Transport of radiological or hazardous constituents will be limited if the carrier fluids are similarly limited.

The hydrologic performance models are fully described in Appendix C. The analyses presented are deterministic. Quantitative values for those parameters that are considered uncertain and that may significantly impact the primary performance measures have been varied, and the results are presented in Appendix C. This section summarizes the seal system performance analyses and discusses results within the context of the design guidance of Section 3. The results demonstrate that (1) fluid flows will be limited within the shaft seal system and (2) uncertainty in the conceptual models and parameters for the seal system are mitigated by redundancy in component function and materials.

### **8.2 Performance Models**

The physical processes that could impact seal system performance are presented in detail in Appendix C. These processes have been incorporated into four performance models. These models evaluate (1) downward migration of groundwater from the Rustler Formation, (2) gas migration and consolidation of the crushed salt seal component, (3) upward migration of brines from the repository, and (4) flow between water-bearing zones in the Rustler Formation. The first three are analyzed using numerical models of the Air Intake Shaft (AIS) seal system and the finite-difference codes SWIFT II and TOUGH28W. These codes are extensively used and well documented within the scientific community. A complete description of the models is provided in Appendix C. The fourth performance model uses a simple, analytical solution for fluid flow. Results from the analyses are summarized in the following sections and evaluated in terms of the design guidance presented in Section 3.

Material properties and conceptual models that may significantly impact seal system performance have been identified, and uncertainty in properties and models have been addressed through variation of model parameters. These parameters include (1) the effective permeability of the DRZ, (2) those describing salt column consolidation and the relationship between compacted salt density and permeability, and (3) repository gas pressure applied at the base of the shaft seal system.

### **8.3 Downward Migration of Rustler Groundwater**

The shaft seal system is designed to limit groundwater flowing into and through the shaft sealing system (see Section 3). The principal source of groundwater to the seal system is the Culebra Member of the Rustler Formation. The Magenta Member of this formation is also

considered a groundwater source, albeit a less significant source than the Culebra. No significant sources of groundwater exist within the Salado Formation; however, brine seepage has been noted at a number of the marker beds. The modeling includes the marker beds, as discussed in Appendix C. Downward migration of Rustler groundwater must be limited so that liquid saturation of the compacted salt column does not impact the consolidation process and to ensure that significant quantities of brine do not reach the repository horizon. Because it is clear that limitation of liquid flow into the salt column necessarily limits liquid flow to the repository, the volumetric flux of liquid into and through the salt column were selected as performance measures for this model.

Consolidation of the compacted salt column will be most rapid immediately following seal construction. Simulations were conducted for the 200-year period following closure to demonstrate that, during this initial period, downward migration of Rustler groundwater will be insufficient to impact the consolidation process. Lateral migration of brine through the marker beds is also quantified in the analysis and shown to be nondetrimental to the function of the salt column.

### **8.3.1 Analysis Method**

Seal materials will not, in general, be fully saturated with liquid at the time of construction. The host rock surrounding the shafts will also be partially desaturated at the time of seal construction. The analysis presented in this section assumes a fully saturated system. The effects of partial saturation of the shaft seal system are favorable in terms of system performance, as will be discussed in Section 8.3.2.

Seal material and host rock properties used in the analyses are discussed in Appendix C, Section C3. Appendix A contains a detailed discussion of seal material properties. A simple perspective on the effects of material and host rock properties may be obtained from Darcy's Law. At steady-state, the flow rate in a fully saturated system depends directly on the system permeability. The seal system consists of the component material and host rock DRZ. Low permeability is specified for the engineered materials; thus the system component most likely to impact performance is the DRZ. Rock mechanics calculations presented in Appendix D predict that the DRZ in the Salado Formation will not be vertically continuous because of the intermittent layers of stiff anhydrites (marker beds). Asphalt waterstops are included in the design to minimize DRZ impacts. The effects of the marker beds and the asphalt waterstops on limiting downward migration are explicitly simulated through variation of the permeability of the layers of Salado DRZ.

Initial, upper, and lateral boundary conditions for the performance model are consistent with field measurements for the physical system. At the base of the shaft a constant atmospheric pressure is assumed.

### **8.3.2 Summary of Results**

The initial pore volumes in the filled repository and the AIS salt column are approximately 460,000 m<sup>3</sup> and 250 m<sup>3</sup>, respectively. The performance model predicts a maximum cumulative flow of less than 5 m<sup>3</sup> through the sealed shafts for the 200 years following closure. If the marker beds have a disturbed zone immediately surrounding the shaft,

the maximum flow is less than  $10 \text{ m}^3$  during the same period. Assuming the asphalt waterstops are not effective in interrupting the vertical DRZ, the volumetric flow increases but is still less than  $30 \text{ m}^3$  for the 200 years following closure. These volumes are less than 1/100 of 1% of the pore volume in the repository and less than 20% of the initial pore volume of the salt column.

Two additional features of the model predictions should also be considered. The first of these is that flow rates fall from less than  $1 \text{ m}^3 / \text{year}$  in the first five years to negligible values within 10 years of seal construction. Therefore most of the cumulative flow occurs within a few years following closure. The second feature is the model prediction that the system returns to nearly ambient undisturbed pressures within two years. The repressurization occurs quickly within the model due to the assumption of a fully saturated flow regime because of brine incompressibility. As will be discussed in Section 8.4, the pore pressure in the compacted salt column is a critical variable in the analysis. The pressure profiles predicted by the model are an artifact of the assumption of full liquid saturation and do not apply to the pore pressure analysis of the salt column.

The magnitude of brine flow that can reach the repository through a sealed shaft is minimal and will not impact repository performance. The flow that reaches the salt column must be assessed with regard to the probable impacts on the consolidation process. Although the volume of flow to the salt column is a small percentage of the available pore volume, the saturation state and fluid pore pressure of this component are the variables of significance. These issues cannot be addressed by a fully saturated model. Instead it is necessary to include these findings in a multi-phase model that includes the salt column. This is the topic of Section 8.4.

The results of the fully saturated model will over-predict the flow rates through the sealed shaft. This analysis does not take credit for the time required for the system to resaturate, nor does it take credit for the sorptive capabilities of the clay components. The principal source of groundwater to the system is the Rustler Formation. The upper clay component is located below the Rustler and above the salt column and will be emplaced at a liquid saturation state of approximately 80%. Bentonite clays exhibit strong hydrophilic characteristics, and it is expected that the upper clay component will have these same characteristics. As a result, it is possible that a significant amount of the minimal Rustler groundwater that reaches the clay column will be absorbed and retained by this seal component. Although this effect is not directly included in the present analysis, the installation of a partially saturated clay component provides assurance that the flow rates predicted by the model are maximum values.

#### **8.4 Gas Migration and Consolidation of Compacted Salt Column**

The seal system is designed to limit the flow of gas from the disposal system through the sealed shafts. Migration of gas could impact performance if this migration substantially increases the fluid pore pressure of the compacted salt column. The initial pore pressure of the salt column will be approximately atmospheric. The sealed system will interact with the adjacent desaturated host rock as well as the far-field formation. Natural pressurization will occur as the system returns to an equilibrium state. This pressurization, coupled with seepage of brine through the marker beds, will also result in increasing fluid pore pressure within the compacted salt column. The analysis presented in this section addresses the issue of fluid pore pressure in the compacted salt column resulting from the effects of gas generation at the repository horizon

and natural repressurization from the surrounding formation. A brief discussion on the impedance to gas flow afforded by the lower compacted clay column is also presented.

#### **8.4.1 Analysis Method**

A multi-phase flow model of the lower seal system was developed to evaluate the performance of components extending from the middle SMC component to the repository horizon.

Rock mechanics calculations presented in Section 7 and Appendix D predict that the compacted salt column will consolidate for a period of approximately 400 years if the fluid-filled pores of the column do not produce a backstress. Within the physical setting of the compacted salt column, three processes have been identified which may result in a significant increase in pore pressure: groundwater flow from the Rustler Formation, gas migration from the repository, and natural fluid flow and repressurization from the Salado Formation. The first two processes were incorporated into the model as initial and boundary conditions, respectively. The third process was captured in all simulations through modeling of the lithologies surrounding the shaft. Simulations were conducted for 200 years following closure to evaluate any effects these processes might have on the salt column during this initial period.

As discussed in Section 8.3.1, the host rock DRZ is an important consideration in seal system performance. A vertically continuous DRZ could exist in both the Rustler and Salado Formations. Concrete-asphalt waterstops are included in the design to add assurance that a DRZ will not adversely impact seal performance. The significance of a continuous DRZ and waterstops will be evaluated based on results of the performance model.

A detailed description of the model grid, assumptions, and parameters is presented in Appendix C.

#### **8.4.2 Summary of Results**

The consolidation process is a function of both time and depth. The resultant permeability of the compacted salt column will similarly vary. To simplify the evaluation, an effective permeability of the salt component was calculated. This permeability is calculated by analogy to electrical circuit theory. The permeability of each model layer is equated to a resistor in a series of resistors. The equivalent resistance (i.e., permeability) of a homogeneous column of identical length is derived in this manner. Figure 8-1 illustrates this process.

Results of the performance model simulations are summarized in Table 8-1. The effective permeabilities were calculated by the model assuming that, as the salt consolidated, permeability was reduced pursuant to the best-fit line through the experimental data (Figure A-7). From Table 8-1 it is clear that, for all simulated conditions, the salt column consolidates to very low values in 200 years. Differences in the effective permeability because of increased repository gas pressure and a vertically continuous DRZ were negligible. The DRZ around concrete components is predicted to heal (Appendix D) within 25 years. If the asphalt waterstops do not function as intended, the DRZ in this region will still heal in 25 years, as compared to 2 years for effective waterstops. The effective permeability of the compacted salt column increases by about a factor of two for this condition. However, the resultant permeability is sufficiently

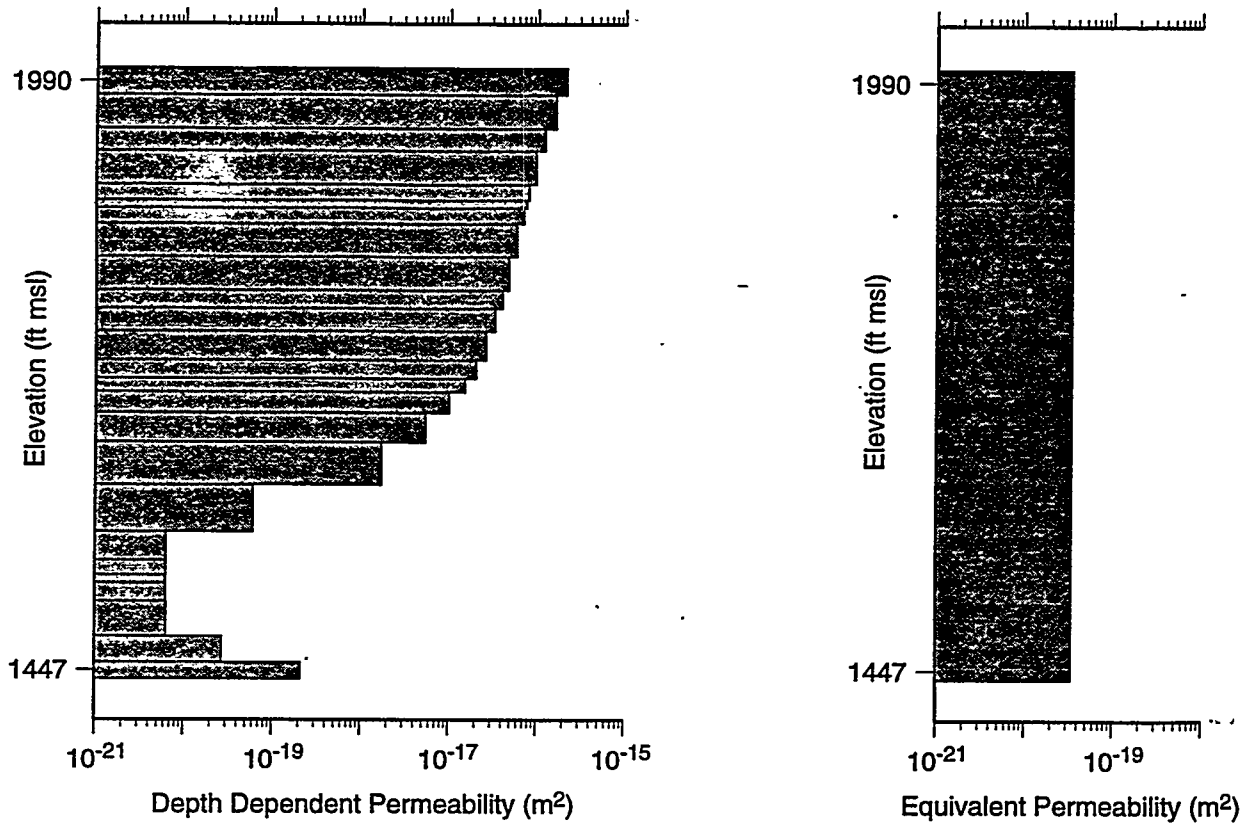
low that the compacted salt columns will comprise permanent effective seals within the WIPP shafts.

Table 8-1. Summary of Results from Performance Model

Repository Pressure	Rustler Flow (m <sup>3</sup> )	Continuous DRZ (Yes/No)	Concrete-Asphalt Waterstop Healing Time (Years)	Effective Permeability at 200 Years (m <sup>2</sup> )
7 MPa in 100 Years	0	No	2	3.3×10 <sup>-20</sup>
14 MPa in 200 Years	0	No	2	3.3×10 <sup>-20</sup>
7 MPa in 100 Years	2.7	Yes	2	3.4×10 <sup>-20</sup>
7 MPa in 100 Years	17.2	Yes	25	6.0×10 <sup>-20</sup>

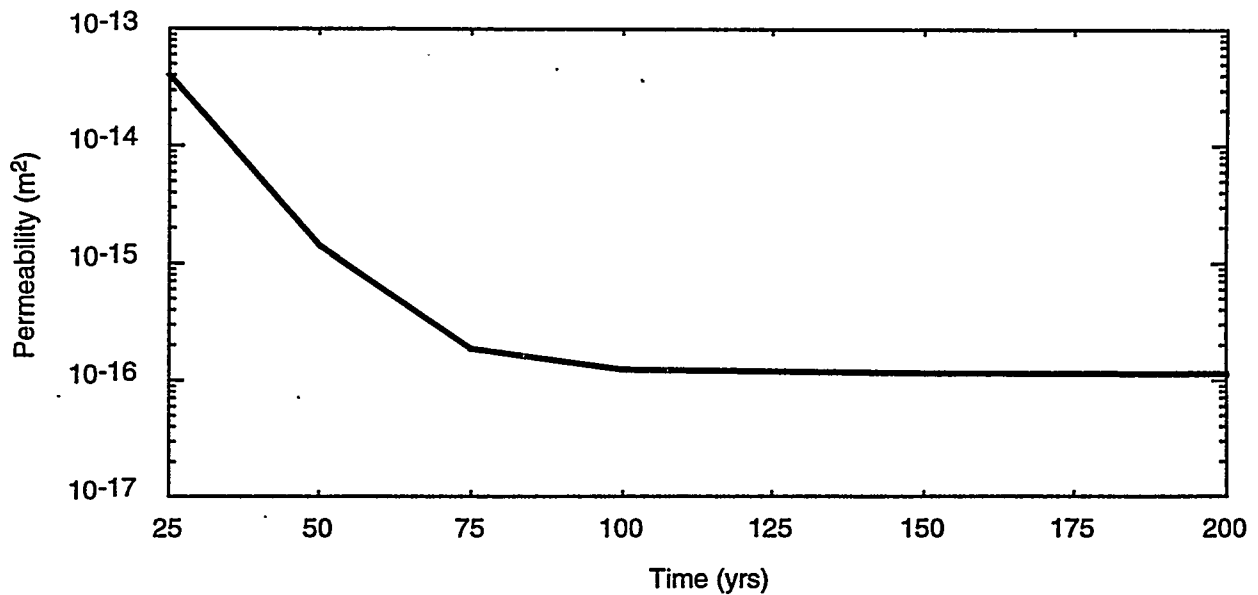
The relationship between the fractional density (i.e., consolidation state) of the compacted salt column and permeability is uncertain, as discussed in Appendix A. Lines drawn through the experimental data (Figure A-7) provide a means to quantify this uncertainty but do not capture the actual physical process of consolidation. As observed through microscopy, consolidation is dominated by pressure solution and redeposition, a mechanism of mass movement facilitated by the presence of moisture on grain boundaries (Hansen and Ahrens, 1996). As this process continues, the connected porosity and hence permeability of the composite mass will reduce at a rate that has not been characterized by the data collected in WIPP experiments. The results of the multi-phase performance model presented in Table 8-1 used a best-fit line through the data. Additional simulations were conducted using a line that represents a 95% certainty that the permeability is less than or equal to values taken from this line. Model simulations that used the 95% line are not considered representative of the consolidation process. However, these results provide an estimation of the significance that this uncertainty may have on the seal system performance.

Figure 8-2 depicts the effective permeability of the salt column as a function of time using the 95% line. The consolidation process, and hence permeability reduction, essentially stopped at 75 years for this simulation. Although the model predicts that the fractional density at the base of the salt column will reach approximately 97% of the density of intact halite, the permeability remains several orders of magnitude higher than that of the surrounding host rock. As a result, repressurization occurs rapidly throughout the vertical extent of the compacted salt column, and consolidation ceases. Laboratory experiments have shown that permeability to brine should decrease to levels of 10<sup>-18</sup> to 10<sup>-20</sup> m<sup>2</sup> at the fractional densities predicted by the performance model. The transport of brine within the consolidating salt will reduce the permeability even further (Brodsky et al., 1995). The predicted permeability of 10<sup>-16</sup> m<sup>2</sup> is still sufficiently low that brine migration would be limited (DOE, 1995). However, the results of this analysis are more valuable in terms of demonstrating the coupled nature of the mechanical and hydrological behavior of consolidating crushed salt.



TRI-6121-380-0

Figure 8-1. Calculation of an effective salt column permeability from the depth-dependent permeability at a point in time.



TRI-6121-354-0

Figure 8-2. Effective permeability of the Salado salt column using the 95% certainty line.

A final consideration within this performance model relates to the lower compacted clay column. This clay column is included in the design to provide a barrier to both gas and brine migration from the repository horizon. The ability of the clay to prevent gas migration will depend upon its liquid saturation state (Section 5 and Appendix A). The lower clay component has an initial liquid saturation of about 80%, and portions of the column achieve brine saturations of nearly 100% during the 200 year simulation period. If the clay component performs as designed, gas migration through this component should be minimal. An examination of the model gas saturations indicates that, for all runs, gas flow occurs primarily through the DRZ prior to healing. These model predictions are consistent with field demonstrations that brine-saturated bentonite seals will prevent gas flow at differential pressures of up to 4 MPa (Knowles and Howard, 1996).

### **8.5 Upward Migration of Brine**

The performance model discussed in Section 8.3 was modified to simulate undisturbed equilibrium pressures. As discussed in Appendix C, the Salado Formation is overpressurized with respect to the measured heads in the Rustler, and upward migration of contaminated brines could occur through an inadequately sealed shaft. Sections 8.3 and 8.4 demonstrated that the compacted salt column will consolidate to a low permeability following repository closure. Appendix D and Section 7 show that the DRZ surrounding the long-term clay and crushed salt seal components will completely heal within the first several decades. As a result, upward migration at the base of the Salado salt is predicted to be approximately  $1 \text{ m}^3$  over the regulatory period. At the Rustler/Salado contact, a total of approximately  $20 \text{ m}^3$  migrates through the sealed AIS over the regulatory period. The only brine sources between these two depths are the marker beds. It can therefore be concluded that most of the brine flow reaching the Rustler/Salado contact originates in marker beds above the repository horizon. The seal system effectively limits the flow of brine and gas from the repository through the sealed shafts throughout the regulatory period.

### **8.6 Intra-Rustler Flow**

The potential exists for vertical flow within water-bearing strata of the Rustler Formation. Flow rates were estimated using a closed form solution of the steady-state saturated flow equation (Darcy's Law). The significance of the calculated flow rates can be assessed in terms of the width of the hydraulic disturbance (i.e., plume half-width) generated in the recipient flow field. The plume half-width was calculated to be minimal for all expected conditions (Section C7). Intra-Rustler flow is therefore concluded to be of such a limited quantity that (1) it will not affect either the hydraulic or chemical regime in the Rustler and (2) it will not be detrimental to the seal system.

**Page intentionally blank.**

## 9. CONCLUSIONS

The principal conclusion drawn from discussions in the previous sections and details provided in the appendices is that an effective, implementable design has been documented for the WIPP shaft sealing system. Specifically, the six elements of the Design Guidance, Table 3-1, are implemented in the design in the following manner:

1. The shaft sealing system shall limit the migration of radiological or other hazardous constituents from the repository horizon to the regulatory boundary during the 10,000-year regulatory period following closure.

Based on the analysis presented in Section 8.5, it was determined that this shaft sealing system effectively limits the migration of radiological or other hazardous constituents from the repository horizon to the regulatory boundary during the 10,000-year regulatory period following closure.

2. The shaft sealing system shall limit groundwater flowing into and through the shaft sealing system.

The combination of the seal components in the Salado Formation, the Rustler Formation, and above the Rustler combine to produce a robust system. Based on analysis presented in Section 8.3, it was concluded that the magnitude of brine flow that can reach the repository through the sealed shaft is minimal and will not impact repository performance.

3. The shaft sealing system shall limit chemical and mechanical incompatibility of seal materials with the seal environment.

The sealing system components are constructed of materials possessing high durability and compatibility with the host rock. Engineered materials including salt-saturated concrete, bentonite, clays, and asphalt are expected to retain their design properties over the regulatory period.

4. The shaft sealing system shall limit the possibility for structural failure of individual components of the sealing system.

Analysis of components has determined that: (a) the structural integrity of concrete components will not be compromised by induced radial stress, imposed vertical stress, temperature gradients, dynamic compaction of overlying materials, or swelling pressure associated with bentonite (Section 7.4.1); (b) the thermal impact of asphalt on the creep rate of the salt surrounding the asphalt waterstops is negligible (Section 7.4.4); and (c) the pressure from the asphalt element of the concrete-asphalt waterstops is sufficient to initiate healing of the surrounding DRZ within two years of emplacement (Section 7.6.1). The potential for structural failure of sealing components is minimized by the favorable compressive stress state that will exist in the sealed WIPP shafts.

5. The shaft sealing system shall limit subsidence of the ground surface in the vicinity of the shafts and the possibility of accidental entry after sealing.

The use of high density sealing materials that completely fill the shafts eliminates the potential for shaft wall collapse, eliminates the possibility of accidental entry after closure, and assures that local surface depressions will not occur at shaft locations.

6. The shaft sealing system shall limit the need to develop new technologies or materials for construction of the shaft sealing system.

The shaft sealing system utilizes existing construction technologies (identified in Section 6) and materials (identified in Section 5).

The design guidance can be summarized as focusing on two principal questions: Can you build it, and will it work? The use or adaptation of existing technologies for the placement of the seal components combined with the use of available, common materials assure that the design can be constructed. Performance of the sealing system has been demonstrated in the hydrologic analyses that show very limited flows of gas or brine, in structural analyses that assure acceptable stress and deformation conditions, and in the use of low permeability materials that will function well in the environment in which they are placed. Confidence in these conclusions is bolstered by the basic design approach of using multiple components to perform each intended sealing function and by using extensive lengths within the shafts to effect a sealing system. Additional confidence is added by the results of field and lab tests in the WIPP environment that support the data base for the seal materials.

## 10. REFERENCES

- Ahrens, E.H., and F.D. Hansen. 1995. *Large-Scale Dynamic Compaction Demonstration Using WIPP Salt: Fielding and Preliminary Results*. SAND95-1941. Albuquerque, NM: Sandia National Laboratories. (Copy on file in the Sandia WIPP Central Files, Sandia National Laboratories, Albuquerque, NM [SWCF] as WPO31104.)
- Ahrens, E.H., and M. Onofrei. 1996. "Ultrafine Cement Grout for Sealing Underground Nuclear Waste Repositories," *2nd North American Rock Mechanics Symposium (NARMS 96), Montreal, Quebec, June 19-21, 1996*. SAND96-0195C. Albuquerque, NM: Sandia National Laboratories. (Copy on file in the SWCF as WPO31251.)
- Ahrens, E.H., T.F. Dale, and R.S. Van Pelt. 1996. *Data Report on the Waste Isolation Pilot Plant Small-Scale Seal Performance Test, Series F Grouting Experiment*. SAND93-1000. Albuquerque, NM: Sandia National Laboratories. (Copy on file in the SWCF as WPO37355.)
- Andersen, P.J., M.E. Andersen, and D. Whiting. 1992. *A Guide to Evaluating Thermal Effects in Concrete Pavements*. SHRP-C/FR-92-101. Washington, DC: Strategic Highway Research Program, National Research Council. (Copy on file in the SWCF.)
- Avis, J.D., and G.J. Saulnier, Jr. 1990. *Analysis of the Fluid-Pressure Responses of the Rustler Formation at H-16 to the Construction of the Air-Intake Shaft at the Waste Isolation Pilot Plant (WIPP) Site*. SAND89-7067. Albuquerque, NM: Sandia National Laboratories. (Copy on file in the SWCF as WPO24168.)
- Bachman, G.O. 1987. *Karst in Evaporites in Southeastern New Mexico*. SAND86-7078. Albuquerque, NM: Sandia National Laboratories. (Copy on file in the SWCF as WPO24006.)
- Beauheim, R.L. 1987. *Interpretations of Single-Well Hydraulic Tests Conducted at and Near the Waste Isolation Pilot Plant (WIPP) Site, 1983-1987*. SAND87-0039. Albuquerque, NM: Sandia National Laboratories. (Copy on file in the SWCF as WPO27679.)
- Beauheim, R.L., R.M. Roberts, T.F. Dale, M.D. Fort, and W.A. Stensrud. 1993. *Hydraulic Testing of Salado Formation Evaporites at the Waste Isolation Pilot Plant Site: Second Interpretive Report*. SAND92-0533. Albuquerque, NM: Sandia National Laboratories. (Copy on file in the SWCF as WPO23378.)
- Brinster, K.F. 1991. *Preliminary Geohydrologic Conceptual Model of the Los Medaños Region Near the Waste Isolation Pilot Plant for the Purpose of Performance Assessment*. SAND89-7147. Albuquerque, NM: Sandia National Laboratories. (Copy on file in the SWCF as WPO27781.)
- Brodsky, N.S. 1994. *Hydrostatic and Shear Consolidation Tests with Permeability Measurements on Waste Isolation Pilot Plant Crushed Salt*. SAND93-7058. Albuquerque, NM: Sandia National Laboratories.

- Brodsky, N.S., D.H. Zeuch, and D.J. Holcomb. 1995. "Consolidation and Permeability of Crushed WIPP Salt in Hydrostatic and Triaxial Compression," *Rock Mechanics Proceedings of the 35th U.S. Symposium, University of Nevada, Reno, NV, June 5-7, 1995*. Eds. J.J.K. Daemen and R.A. Schultz. Brookfield, VT: A.A. Balkema. 497-502. (Copy on file in the SWCF as WPO22432.)
- Brodsky, N.S., F.D. Hansen, and T.W. Pfeifle. 1996. "Properties of Dynamically Compacted WIPP Salt," *4th International Conference on the Mechanical Behavior of Salt, Montreal, Quebec, June 17-18, 1996*. SAND96-0838C. Albuquerque, NM: Sandia National Laboratories. (Copy on file at the Technical Library, Sandia National Laboratories, Albuquerque, NM.)
- Callahan, G.D., M.C. Loken, L.D. Hurtado, and F.D. Hansen. 1996. "Evaluation of Constitutive Models for Crushed Salt," *4th International Conference on the Mechanical Behavior of Salt, Montreal, Quebec, June 17-18, 1996*. SAND96-0791C. Albuquerque, NM: Sandia National Laboratories. (Copy on file in the SWCF as WPO36449.)
- Cauffman, T.L., A.M. LaVenue, and J.P. McCord. 1990. *Ground-Water Flow Modeling of the Culebra Dolomite. Volume II: Data Base*. SAND89-7068/2. Albuquerque, NM: Sandia National Laboratories. (Copy on file in the SWCF as WPO10551.)
- Dale, T., and L.D. Hurtado. 1996. "WIPP Air-Intake Shaft Disturbed-Rock Zone Study," *4th International Conference on the Mechanical Behavior of Salt, Montreal, Quebec, June 17-18, 1996*. SAND96-1327C. Albuquerque, NM: Sandia National Laboratories. (Copy on file in the SWCF.)
- DOE (U.S. Department of Energy). 1995. *Waste Isolation Pilot Plant Sealing System Design Report*. DOE/WIPP-95-3117. Carlsbad, NM: U.S. Department of Energy, Waste Isolation Pilot Plant. (Copy on file in the SWCF as WPO29062.)
- EPA (Environmental Protection Agency). 1996a. *Criteria for the Certification and Re-Certification of the Waste Isolation Pilot Plant's Compliance with the 40 CFR Part 191 Disposal Regulations. Response to Comments Document for 40 CFR Part 194*. EPA 402-R-96-001. Washington, DC: U.S. Environmental Protection Agency, Office of Radiation and Indoor Air. (Copy on file in the Nuclear Waste Management Library, Sandia National Laboratories, Albuquerque, NM.)
- EPA (Environmental Protection Agency). 1996b. *Criteria for the Certification and Re-Certification of the Waste Isolation Pilot Plant's Compliance with the 40 CFR Part 191 Disposal Regulations. Background Information Document for 40 CFR Part 194*. EPA 402-R-96-002. Washington, DC: U.S. Environmental Protection Agency, Office of Radiation and Indoor Air. (Copy on file in the Nuclear Waste Management Library, Sandia National Laboratories, Albuquerque, NM.)
- Gray, M.N. 1993. *OECD/NEA International Stripa Project. Overview Volume III: Engineered Barriers*. Stockholm, Sweden: SKB, Swedish Nuclear Fuel and Waste Management Company. (Copy on file in the Nuclear Waste Management Library, Sandia National Laboratories, Albuquerque, NM as TD898.2.G73 1993.)

- Hansen, F.D., and E.H. Ahrens. 1996. "Large-Scale Dynamic Compaction of Natural Salt," *4th International Conference on the Mechanical Behavior of Salt, Montreal, Quebec, June 17-18, 1996*. SAND96-0792C. Albuquerque, NM: Sandia National Laboratories. (Copy on file in the SWCF as WPO39544.)
- Hansen, F.D., E.H. Ahrens, A.W. Dennis, L.D. Hurtado, M.K. Knowles, J.R. Tillerson, T.W. Thompson, and D. Galbraith. 1996. "A Shaft Seal System for the Waste Isolation Pilot Plant," *Proceedings of SPECTRUM '96, Nuclear and Hazardous Waste Management, International Topical Meeting, American Nuclear Society/Department of Energy Conference, Seattle, WA, August 18-23, 1996*. SAND96-1100C. Albuquerque, NM: Sandia National Laboratories. (Copy on file in the SWCF as WPO39369.) . . . .
- Haug, A., V.A. Kelley, A.M. LaVenue, and J.F. Pickens. 1987. *Modeling of Ground-Water Flow in the Culebra Dolomite at the Waste Isolation Pilot Plant (WIPP) Site: Interim Report*. SAND86-7167. Albuquerque, NM: Sandia National Laboratories. (Copy on file in the SWCF as WPO28486.)
- Hills, J.M. 1984. "Sedimentation, Tectonism, and Hydrocarbon Generation in [the] Delaware Basin, West Texas and Southeastern New Mexico," *American Association of Petroleum Geologists Bulletin*. Vol. 68, no. 3, 250-267. (Copy on file in the SWCF.)
- Holt, R.M., and D.W. Powers. 1990. *Geologic Mapping of the Air Intake Shaft at the Waste Isolation Pilot Plant*. DOE-WIPP 90-051. Carlsbad, NM: Westinghouse Electric Corporation for U.S. Department of Energy. (Copy on file in the Nuclear Waste Management Library, Sandia National Laboratories, Albuquerque, NM.)
- Knowles, M.K., and C.L. Howard. 1996. "Field and Laboratory Testing of Seal Materials Proposed for the Waste Isolation Pilot Plant," *Proceedings of the Waste Management 1996 Symposium, Tucson, AZ, February 25-29, 1996*. SAND95-2082C. Albuquerque, NM: Sandia National Laboratories. (Copy on file in the SWCF as WPO30945.)
- Knowles, M.K., D. Borns, J. Fredrich, D. Holcomb, R. Price, D. Zeuch, T. Dale, and R.S. Van Pelt. 1996. "Testing the Disturbed Zone Around a Rigid Inclusion in Salt," *4th Conference on the Mechanical Behavior of Salt, Montreal, Quebec, June 17-18, 1996*. SAND95-1151C. Albuquerque, NM: Sandia National Laboratories. (Copy on file in the SWCF.)
- Lambert, S.J. 1992. "Geochemistry of the Waste Isolation Pilot Plant (WIPP) Site, Southeastern New Mexico, U.S.A.," *Applied Geochemistry*. Vol. 7, no. 6, 513-531. (Copy on file in the SWCF as WPO26361.)
- LaVenue, A.M., T.L. Cauffman, and J.F. Pickens. 1990. *Ground-Water Flow Modeling of the Culebra Dolomite. Volume I: Model Calibration*. SAND89-7068/1. Albuquerque, NM: Sandia National Laboratories. (Copy on file in the SWCF as WPO24085.)
- Mercer, J.W. 1983. *Geohydrology of the Proposed Waste Isolation Pilot Plant Site, Los Medanos Area, Southeastern New Mexico*. Water-Resources Investigations Report 83-4016. Albuquerque, NM: U.S. Geological Survey, Water Resources Division. (Copy on file in the Nuclear Waste Management Library, Sandia National Laboratories, Albuquerque, NM.) (Copy on file in the SWCF.)

- Mercer, J.W., and B.R. Orr. 1979. *Interim Data Report on the Geohydrology of the Proposed Waste Isolation Pilot Plant Site, Southeast New Mexico*. Water-Resources Investigations Report 79-98. Albuquerque, NM: U.S. Geological Survey, Water Resources Division. (Copy on file in the SWCF.)
- Nowak, E.J., J.R. Tillerson, and T.M. Torres. 1990. *Initial Reference Seal System Design: Waste Isolation Pilot Plant*. SAND90-0355. Albuquerque, NM: Sandia National Laboratories. (Copy on file in the SWCF as WPO23981.)
- Pfeifle, T.W., F.D. Hansen, and M.K. Knowles. 1996. "Salt-Saturated Concrete Strength and Permeability," *4th Materials Engineering Conference, ASCE Materials Engineering Division, Washington, DC, November 11-18, 1996*. Albuquerque, NM: Sandia National Laboratories.)
- Powers, D.W., S.J. Lambert, S-E. Shaffer, L.R. Hill, and W.D. Weart, eds. 1978. *Geological Characterization Report Waste Isolation Plant (WIPP) Site, Southeastern New Mexico*. SAND78-1596. Albuquerque, NM: Sandia National Laboratories. Vols. I-II. (Copy on file in the SWCF as WPO5448, WPO26829-26830.)
- Saulnier, G.J., Jr., and J.D. Avis. 1988. *Interpretation of Hydraulic Tests Conducted in the Waste-Handling Shaft at the Waste Isolation Pilot Plant (WIPP) Site*. SAND88-7001. Albuquerque, NM: Sandia National Laboratories. (Copy on file in the SWCF as WPO24164.)
- Stormont, J.C. 1984. *Plugging and Sealing Program for the Waste Isolation Pilot Plant (WIPP)*. SAND84-1057. Albuquerque, NM: Sandia National Laboratories. (Copy on file in the SWCF as WPO24698.)
- Van Sambeek, L.L., D.D. Luo, M.S. Lin, W. Ostrowski, and D. Oyenuga. 1993. *Seal Design Alternatives Study*. SAND92-7340. Albuquerque, NM: Sandia National Laboratories. (Copy on file in the SWCF as WPO23445.)
- Vine, J.D. 1963. *Surface Geology of the Nash Draw Quadrangle, Eddy County, New Mexico*. Geological Survey Bulletin 1141-B. Washington, DC: U.S. Government Printing Office. (Copy on file in the SWCF as WPO39558.)
- Wing, N.R., and G.W. Gee. 1994. "Quest for the Perfect Cap," *Civil Engineering*. Vol. 64, no. 10, 38-41. (Copy on file in the SWCF as WPO21158.)

# **Appendix A**

## **Material Specification**

### **Appendix A Abstract**

This appendix specifies material characteristics for shaft seal system components designed for the Waste Isolation Pilot Plant. The shaft seal system will not be constructed for decades; however, if it were to be constructed in the near term, materials specified here could be placed in the shaft and meet performance specifications. A material specification is necessary today to establish a frame of reference for design and analysis activities and to provide a basis for seal material parameters. This document was used by three integrated working groups: (1) the architect/engineer for development of construction methods and supporting infrastructure, (2) fluid flow and structural analysis personnel for evaluation of seal system adequacy, and (3) technical staff to develop probability distribution functions for use in performance assessment. The architect/engineers provide design drawings, construction methods and schedules as appendices to the final shaft seal system design report, called the *Compliance Submittal Design Report*. Similarly, analyses of structural aspects of the design and fluid flow calculations comprise other appendices to the final design report. These products together are produced to demonstrate the adequacy of the shaft seal system to independent reviewers, the EPA, and stakeholders. It is recognized that actual placement of shaft seals is many years in the future, so design, planned construction method, and components will almost certainly change between now and the time that detailed construction specifications are prepared for the bidding process. Specifications provided here are likely to guide future work between now and the time of construction, perhaps benefiting from optimization studies, technological advancements, or experimental demonstrations.

Page intentionally blank.

## Contents

A1. INTRODUCTION .....	5
A1.1 Sealing Strategy .....	8
A1.2 Longevity .....	8
A2. MATERIAL SPECIFICATIONS .....	10
A2.1 Mass Concrete .....	10
A2.1.1 Functions .....	11
A2.1.2 Material Characteristics .....	11
A2.1.3 Construction .....	13
A2.1.4 Performance Requirements .....	14
A2.1.5 Verification Methods .....	16
A2.2 Compacted Clay .....	18
A2.2.1 Functions .....	18
A2.2.2 Material Characteristics .....	18
A2.2.3 Construction .....	20
A2.2.4 Performance Requirements .....	20
A2.2.5 Verification Methods .....	23
A2.3 Asphalt Components .....	24
A2.3.1 Functions .....	24
A2.3.2 Material Characteristics .....	24
A2.3.3 Construction .....	25
A2.3.4 Performance Requirements .....	26
A2.3.5 Verification Methods .....	27
A2.4 Compacted Salt Column .....	27
A2.4.1 Functions .....	28
A2.4.2 Material Characteristics .....	29
A2.4.3 Construction .....	29
A2.4.4 Performance Requirements .....	30
A2.4.5 Verification Methods .....	33
A2.5 Cementitious Grout .....	34
A2.5.1 Functions .....	34
A2.5.2 Material Characteristics .....	34
A2.5.3 Construction .....	35
A2.5.4 Performance Requirements .....	35
A2.5.5 Verification Methods .....	36
A2.6 Earthen Fill .....	36
A2.6.1 Functions .....	36
A2.5.2 Material Characteristics .....	36
A2.5.3 Construction .....	36
A2.5.4 Performance Requirements .....	36
A2.5.6 Verification .....	36
A3. CONCLUDING REMARKS .....	36
A4. REFERENCES .....	37

## Figures

Figure A-1. Schematic of the WIPP shaft seal design. ....	6
Figure A-2. Cumulative distribution function for SMC. ....	16
Figure A-3. Sodium bentonite permeability versus density. ....	22
Figure A-4. Cumulative frequency distribution for compacted bentonite. ....	23
Figure A-5. Asphalt permeability cumulative frequency distribution function. ....	27
Figure A-6. Fractional density of the consolidating salt column. ....	31
Figure A-7. Permeability of consolidated crushed salt as a function of fractional density. ....	32
Figure A-8. Compacted salt column permeability cumulative frequency distribution function at seal midpoint 100 years following closure. ....	33

## Tables

Table A-1. Concrete Mixture Proportions .....	12
Table A-2. Standard Specifications for Concrete Materials .....	12
Table A-3. Chemical Composition of Expansive Cement.....	13
Table A-4. Requirements for Salado Mass Concrete Aggregates.....	14
Table A-5. Target Properties for Salado Mass Concrete .....	15
Table A-6. Test Methods Used for Measuring Concrete Properties During and After Mixing....	17
Table A-7. Test Methods Used for Measuring Properties of Hardened Concrete .....	17
Table A-8. Representative Bentonite Composition. ....	19
Table A-9. Asphalt Component Specifications .....	25
Table A-10. Ultrafine Grout Mix Specification.....	35

## A1. INTRODUCTION

This appendix provides a body of technical information for each of the WIPP shaft seal system materials identified in the text of the *Compliance Submittal Design Report*. This material specification characterizes each seal material, establishes why it will function adequately, states briefly how each component will be placed, and quantifies expected characteristics, particularly permeability, pertinent to a WIPP-specific shaft seal design. Each material is first described from an engineering viewpoint, then appropriate properties are summarized in tables and figures which emphasize permeability parameter distribution functions used in performance calculations. Materials are discussed beyond limits normally found in conventional construction specifications. Descriptive elements focus on stringent shaft seal system requirements that are vital to regulatory compliance demonstration. Information normally contained in an engineering *performance specification* is included because more than one construction method, or even a completely different material, may function adequately. Content that would eventually be included contractually in *specifications for materials* or *specifications for workmanship* are not included in detail. The goal of these specifications is to substantiate why materials used in this seal system design will limit fluid flow and thereby adequately limit releases of hazardous constituents from the WIPP site at the regulatory boundary.

Figure A-1 is a schematic drawing of the proposed WIPP shaft sealing system. Design detail and other characteristics of the geologic, hydrologic and chemical setting are provided in the main body of the report, other appendices, and references. The four shafts will be entirely filled with dense materials possessing low permeability and other desirable engineering and economic attributes. Seal materials include concrete, clay, asphalt, and compacted salt. Other construction and fill materials include cementitious grout and earthen fill. The level of detail included for each material, and the emphasis of detail, vary among the materials. Concrete, clay, and asphalt are common construction materials used extensively in hydrologic applications. Their descriptions will be rather complete, and performance expectations will be drawn from the literature and site-specific references. Portland cement concrete is the most common structural material being proposed for the WIPP shaft seal system and its use has a long history. Considerable specific detail is provided for concrete because it is salt-saturated. Clay is used extensively in the seal system. Clay is often specified in industry as a construction material, and bentonitic clay has been widely specified as a low permeability liner for hazardous waste sites. Therefore, a considerable body of information is available for clay materials, particularly bentonite. Asphalt is a widely used paving and waterproofing material, so its specification here reflects industry practice. It has been used to seal shaft linings as a filler between the concrete and the surrounding rock, but has not been used as a full shaft seal component. Compaction and natural reconsolidation of crushed salt are uniquely applied here. Therefore, the crushed salt specification provides additional information on its constitutive behavior and sealing performance. Cementitious grout is also specified in some detail because it has been developed and tested for WIPP-specific applications and similar international waste programs. Earthen fill will be given only cursory specifications here because it has little impact on the shaft seal performance and placement to nominal standards is easily attained.

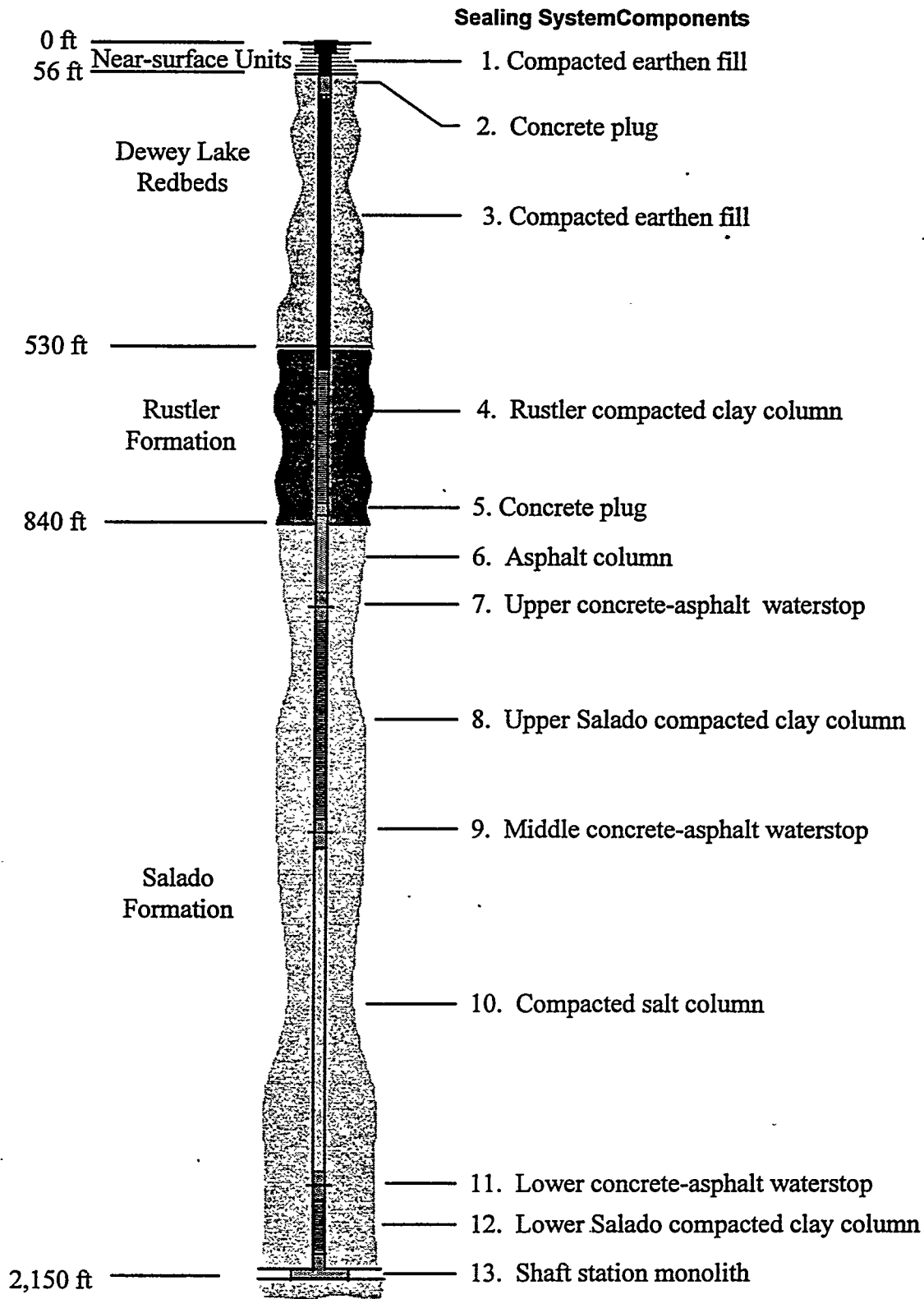


Figure A-1. Schematic of the WIPP shaft seal design.

Discussion of each material is divided into sections, which are described in the annotated bullets below:

- **Functions**

A general summary of functions of specific seal components is presented. Each seal component must function within a natural setting, so design considerations embrace naturally occurring characteristics of the surrounding rock.

- **Material Characteristics**

Constitution of the seal material is described and key physical, chemical, mechanical, hydrological, and thermal features are discussed.

- **Construction**

A brief mention is made regarding construction, which is more thoroughly treated in Appendix B of the *Compliance Submittal Design Report*. Construction, as discussed in this section, is primarily concerned with proper placement of materials. A viable construction procedure that will attain placement specifications is identified, but such a specification does not preclude other potential methods from use when the seal system is eventually constructed.

- **Performance Requirements**

Regulations to which the WIPP must comply do not provide quantitative specifications applicable to seal design. Performance of the WIPP repository is judged against potential releases of hazardous constituents at the regulatory boundary, which is a probabilistic calculation. To this end, probability distribution functions for permeabilities (referred to as PDFs) of each material have been derived for performance assessment of the WIPP system and are included within this subsection on performance requirements.

- **Verification Methods**

It must be assured that seal materials placed in the shaft meet specifications. Both design and selection of materials reflect this principal concern. Assurance is provided by quality control procedures, quality assurance protocol, real-time testing, demonstrations of technology before construction, and personnel training. Materials and construction procedures are kept relatively simple, which creates robustness within the overall system. In addition, elements of the seal system often are extensive in length, and construction will require years to complete. If atypical placement of materials is detected, corrections can be implemented without impacting performance. These specifications limit in situ testing of seal material as it is constructed although, if it is later determined to be desirable, certain in situ tests can be amended in construction specifications. Invasive testing has the potential to compromise the material, add cost, and create logistic and safety problems. Conventional specifications are made for property testing and quality control.

- **References**

These specifications draw on a wealth of information available for each material. Reference to literature values, existing data, anecdotal information, similar applications, laboratory and field testing, and other applicable supportive documentation is made.

## A1.1 Sealing Strategy

The shaft seal system design is an integral part of compliance with 40 CFR 191. The EPA has also promulgated 40 CFR 194, entitled "Criteria for the Certification and Recertification of the Waste Isolation Pilot Plant's Compliance with the 40 CFR Part 191," to which this design and these specifications are responsive. Other seal design requirements, such as State of New Mexico regulations, apply to stratigraphy above the Salado.

Compliance of the site with 40 CFR 191 will be determined in part by the ability of the seal system to limit migration of hazardous constituents to the regulatory boundary. Both natural and engineered barriers may combine to form the isolation system, with the shaft seal system forming an engineered barrier in a natural setting. Seal system materials possess high durability and compatibility with the host rock. All materials used in the shaft seal system are expected to maintain their integrity for very long periods. The system contains functional redundancy and uses differing materials to reduce uncertainty in performance. Some sealing components are used to retard fluid flow soon after placement, while other components are designed to function well beyond the regulatory period. International programs engaged in research and demonstration of sealant technology provide significant information on longevity of materials similar to those proposed for this shaft seal system (Gray, 1993). When this information is applied to the setting and context of the WIPP, there is strong evidence that the materials specified will maintain their positive attributes for defensibly long periods.

## A1.2 Longevity

Longevity of materials is considered within the site geologic and hydrologic setting as summarized in the main body of this report and described in the Seal System Design Report (DOE, 1995). A major environmental advantage of the WIPP locality is an overall lack of groundwater to seal against. In terms of sealing the WIPP site, the stratigraphy can be conveniently divided into the Salado Formation and the superincumbent formations comprising primarily the Rustler Formation and the Dewey Lake Redbeds. The Salado Formation, composed mainly of evaporite sequences dominated by halite, is nearly impermeable. Transmissivity of engineering importance in the Salado Formation is lateral along anhydrite interbeds, basal clays, and fractured zones near underground openings. Neither the Dewey Lake Redbeds nor the Rustler Formation contains regionally productive sources of water, although seepage near the surface in the Exhaust Shaft has been observed. Permeability of materials placed in the Salado below the contact with the Rustler, and their effects on the surrounding disturbed rock zone, are the primary engineering properties of concern. Even though very little regional water is present in the geologic setting, the seal system reflects great concern for groundwater's potential influence on materials comprising the shaft seal system.

Shaft seal materials have been selected in part because of their exceptional durability. However, it is recognized that brine chemistry *could* impact engineered materials if conditions permitted. Highly concentrated saline solutions can, under severe circumstances, affect performance of cementitious materials and clay. Concrete has been shown to degrade under certain conditions, and clays can be more transmissive to brine than to potable water. Asphalt and compacted salt are essentially chemically inert to brine. Although stable in naturally occurring seeps such as those in the Santa Barbara Channel (California), asphalt can degrade

when subjected to ultraviolet light or through microbial activity. Brine would not chemically change the compacted salt column, but mechanical effects of pore pressure are of concern to reconsolidation. Mechanical influences of brine on the reconsolidating salt column are discussed in Sections 7 and 8 of the main report, which summarize Appendices D and C, respectively.

Because of limited volumes of brine, low hydraulic gradients, and low permeability materials, the geochemical setting will have little influence on shaft seal materials. Each material is durable, though the potential exists for degradation or alteration under extreme conditions. For example, the three major components of portland cement concrete, portlandite ( $\text{Ca}(\text{OH})_2$ ), calcium-aluminate-hydrate (CAH) and calcium-silicate-hydrate (CSH), are not thermodynamically compatible with WIPP brines. If large quantities of high ionic strength brine were available and transport of mass was possible, degradation of cementitious phases would certainly occur. Such a localized phenomenon was observed on a construction joint in the liner of the Waste Handling Shaft at the WIPP site. Within the shaft seal system, however, the hydrologic setting does not support such a scenario. Locally brine will undoubtedly contact the surface of mass placements of concrete. A low hydrologic gradient will limit mass transport, although degradation of paste constituents is expected where brine contacts concrete.

Among longevity concerns, degradation of concrete is the most recognized. At this stage of the design, it is established that only small volumes of brine ever reach the concrete elements (see Section 8). Further analysis concerned with borehole plugging using cementitious materials shows that at least 100 pore volumes of brine in an open system would be needed to begin degradation processes. In a closed system, such as the hydrologic setting in the WIPP shafts, phase transformations create a degradation product of increased volume. Net volume increase owing to phase transformation in the absence of mass transport would decrease rather than increase permeability of concrete seal elements.

Mechanical and chemical stability of clays, in this case the emphasis is on bentonitic clay, is particularly favorable in the WIPP geochemical and hydrological environment. A compendium of recent work associated with the Stripa project in Sweden (Gray, 1993) provides field-scale testing results, supportive laboratory experimental data, and thermodynamic modeling that lead to a conclusion that negligible transformation of the bentonite structure will occur over the regulatory period of the WIPP. In fact, very little brine penetration into clay components is expected, based on intermediate-scale experiments at WIPP. Any wetting of bentonite will result in development of swelling pressure, a favorable situation that would accelerate return to a uniform stress state within the clay component.

Natural bentonite is a stable material that generally will not change significantly over a period of ten thousand years. Bentonitic clays have been widely used in field and laboratory experiments concerned with radioactive waste disposal. As noted by Gray (1993), three internal mechanisms, illitization, silicification and charge change, could affect sealing properties of bentonite. Illitization and silicification are thermally driven processes and, following discussion by Gray (1993), are not possible in the environment or time-frame of concern at the WIPP. The naturally occurring Wyoming bentonite which is the specified material for the WIPP shaft seal is well over a million years old. It is, therefore, highly unlikely that metamorphism of bentonite enters as a design concern.

Asphalt has existed for thousands of years as natural seeps. Longevity studies specific to DOE's Hanford site have utilized asphalt artifacts buried in ancient ceremonies to assess long-term stability (Wing and Gee, 1994). Asphalt used as a seal component deep in the shaft will inhabit a benign environment, devoid of ultraviolet light or an oxidizing atmosphere. Additional assurance against possible microbial degradation in asphalt elements is mitigated with addition of lime. For these reasons, it is thought that design characteristics of asphalt components will endure well beyond the regulatory period.

Materials being used to form the shaft seals are the same as those being suggested in the scientific and engineering literature as appropriate for sealing deep geologic repositories for radioactive wastes. This fact was noted during independent technical review. Durability or longevity of seal components is a primary concern for any long-term isolation system. Issues of possible degradation have been studied throughout the international community and within waste isolation programs in the USA. Specific degradation studies are not detailed in this document because longevity is one of the over-riding attributes of the materials selected and degradation is not perceived to be likely. However, it is acknowledged here that microbial degradation, seal material interaction, mineral transformation, such as silicification of bentonite, and effects of a thermal pulse from asphalt or hydrating concrete remain areas of continued study.

## **A2. MATERIAL SPECIFICATIONS**

The WIPP shaft seal system plays an important role in meeting regulatory requirements. A combination of available, durable materials which can be emplaced with low permeability is proposed as the seal system. Components include mass concrete, asphalt waterstops sandwiched between concrete plugs, a column of asphalt, long columns of compacted clay, and a column of compacted crushed WIPP salt. The design is based on common materials and construction technologies that could be implemented using today's technology. In choosing materials, emphasis was given to permeability characteristics and mechanical properties. The function, constitution, construction, performance, and verification of each material are given in the following sections.

### **A2.1 Mass Concrete**

Concrete has exceptionally low permeability and is widely used for hydraulic applications such as water storage tanks, water and sewer systems, and massive dams. Salt-saturated concrete has been used successfully as a seal material in potash and salt mining applications. Upon hydration, unfractured concrete is nearly impermeable, having a permeability less than  $10^{-20} \text{ m}^2$ . In addition, concrete is a primary structural material used for compression members in countless applications. Use of concrete as a shaft seal component takes advantage of its many attributes and the extensive documentation of its use.

This specification for mass concrete will discuss a special design mixture of a salt-saturated concrete called Salado Mass Concrete or SMC (Wakeley et al., 1995). Performance of SMC and similar salt-saturated mixtures is established and will be completely adequate for concrete applications within the WIPP shafts. Because concrete is such a widely used material, it has been written into specifications many times. Therefore, the specification for SMC contains

recognized standard practices, established test methods, quality controls, and other details that are not available at a similar level for other seal materials. Use of salt-saturated concrete, especially SMC, is backed by extensive laboratory and field studies that establish performance characteristics far exceeding requirements of the WIPP shaft seal system.

### **A2.1.1 Functions**

The function of the concrete is to provide a durable component with small void volume, adequate structural compressive strength, and low permeability. Concrete components appear within the shaft seal system at the very bottom, the very top, and several locations in between where they provide a massive plug that fills the opening and a tight interface between the plug and host rock. In addition, concrete is a rigid material that will support overlying seal components while promoting natural healing processes within the salt disturbed rock zone (the DRZ is discussed further in Appendix D).

Concrete is one of the redundant components that protects the reconsolidating salt column. Since the salt column will achieve low permeabilities in fewer than 100 years (see Section 2.4.4 of this specification), concrete would no longer be needed after that time. For purposes of performance assessment calculations, a change in concrete permeability to degraded values is "allowed" to occur. However, concrete within the Salado Formation is likely to endure throughout the regulatory period with sustained engineering properties.

All concrete sealing elements, with the exception of a possible concrete cap, are unreinforced. In conventional civil engineering design, reinforcement is used to resist tensile stresses since concrete is weak in tension and reinforcement bar (rebar) balances tensile stresses in the steel with compressive stresses in concrete. However, concrete has exceptional compressive strength, and all the states of stress within the shaft will be dominated by compressive stress. Mass concrete, by definition, is related to any volume of concrete where heat of hydration is a design concern. SMC is tailored to minimize heat of hydration and overall differential temperature. An analysis of hydration heat distribution is included in Appendix D. Boundary conditions are favorable for reducing any possible thermally induced tensile cracking during the hydration process.

### **A2.1.2 Material Characteristics**

Salt-saturated concrete contains sufficient salt as an aggregate to saturate hydration water with respect to NaCl. Salt-saturated concrete is required for all uses within the Salado Formation because fresh water concrete would dissolve part of the host rock. Dissolution would cause a poor bond and perhaps a more porous interface, at least initially.

Dry materials for SMC include cementitious materials, fine and coarse aggregates, and sodium chloride. Concrete mixture proportions of materials for one cubic yard of concrete appear in Table A-1.

Table A-1. Concrete Mixture Proportions

Material	lb/yd <sup>3</sup>
Portland cement	278
Class F fly ash	207
Expansive cement	134
Fine aggregate	1292
Coarse aggregate	1592
Sodium chloride	88
Water	225

$\text{kg/m}^3 = (\text{lb/yd}^3) * (0.59)$ . Water : Cement Ratio is weight of water divided by all cementitious materials.

Table A-2 is a summary of standard specifications for concrete materials. Further discussion of each specification is presented in subsequent text, where additional specifications pertinent to particular concrete components are also given.

Table A-2. Standard Specifications for Concrete Materials

Material	Applicable Standard Tests and Specifications	Comments
Class H oilwell cement	American Petroleum Institute Specification 10	Chemical composition determined according to ASTM C 114
Class F fly ash	ASTM C 618, Standard Specification for Fly Ash	Composition and properties determined according to ASTM C 311
Expansive cement	Similar to ASTM C 845	Composition determined according to ASTM C 114
Salt	ASTM E 534, Chemical Analysis of Sodium Chloride	Batched as dry ingredient, not as an admixture
Coarse and fine aggregates	ASTM C 33, Standard Specification for Concrete Aggregates; ASTM C 294 and C 295 also applied	Moisture content determined by ASTM C 566

**Portland cement** shall conform to American Petroleum Institute (API) Specification 10 Class G or Class H. Additional requirements for the cement are that the fineness as determined according to ASTM C 204 shall not exceed  $300 \text{ m}^2/\text{kg}$ , and the cement must meet the requirement in ASTM C 150 for moderate heat of hydration.

**Fly Ash** shall conform to ASTM C 618, Class F, with the additional requirement that the percentage of Ca cannot exceed 10 %.

**Expansive cement** for shrinkage-compensation shall have properties so that, when used with portland cement, the resulting blend is shrinkage compensating by the mechanism described in ASTM C 845 for Type K cement. Additional requirements for chemical composition of the shrinkage compensating cement appear in Table A-3.

Table A-3. Chemical Composition of Expansive Cement

Chemical composition	Weight %
Magnesium oxide, max	1.0
Calcium oxide, min	38.0
Sulfur trioxide, max	28.0
Aluminum trioxide (AL <sub>2</sub> O <sub>3</sub> ), min	7.0
Silicon dioxide, min	7.0
Insoluble residue, max	1.0
Loss on ignition, max	12.0

**Sodium Chloride** shall be of a technical grade consisting of a minimum of 99.0 % sodium chloride as determined according to ASTM E 534, and shall have a maximum particle size of 600 µm.

**Aggregate** proportions are reported here on saturated surface-dry basis. Specific gravity of coarse and fine aggregates used in these proportions were 2.55 and 2.58, respectively. Absorptions used in calculations were 2.25 (coarse) and 0.63 (fine) % by mass. Concrete mixture proportions will be adjusted to accommodate variations in the materials selected, especially differences in specific gravity and absorptions of aggregates. Fine aggregate shall consist of natural silica sand. Coarse aggregate shall consist of gravel. The quantity of flat and elongated particles in the separate size groups of coarse aggregates, as determined by ASTM D 4791, using a value of 3 for width-thickness ratio and length-width ratio, shall not exceed 25 % in any size group. Moisture in the fine and coarse aggregate shall not exceed 0.1 % when determined in accordance with ASTM C 566. Aggregates shall meet the requirements listed in Table A-4.

### A2.1.3 Construction

Construction techniques include surface preparation of mass concrete and slickline (a drop pipe from the surface) placement at depth within the shaft. A batching and mixing operation on the surface will produce a wet mixture having initial temperatures not exceeding 20°C. Placement uses a tremie line, where the fresh concrete exits the slickline below the surface level of the concrete being placed. This procedure will minimize entrained air. Placement requires no vibration and, except for the large concrete monolith at the base of each shaft, no form work. No special curing is required for the concrete because its natural environment ensures retention of humidity and excellent hydration conditions. It is desired that each concrete pour be continuous, with the complete volume of each component placed without construction joints. However, no perceivable reduction in performance is anticipated if, for any reason,

concrete placement is interrupted. A free face or cold joint could allow lateral flow but would remain perpendicular to flow down the shaft. Further discussion of concrete construction is presented in Appendix B.

Table A-4. Requirements for Salado Mass Concrete Aggregates

Property	Fine Aggregate	Coarse Aggregate
Specific Gravity (ASTM C 127, ASTM C 128)	2.65, max.	2.80, max
Absorption (ASTM C 127, ASTM C 128)	1.5 percent, max	3.5 percent, max
Clay Lumps and Friable Particles (ASTM C 142)	3.0 percent, max	3.0 percent, max
Material Finer than 75- $\mu$ m (No. 200) Sieve (ASTM C 117)	3.0 percent, max	1.0 percent, max
Organic Impurities (ASTM C 40)	No. 3, max	N/A
L.A. Abrasion (ASTM C 131, ASTM C 535)	N/A	50 percent, max
Petrographic Examination (ASTM C 295)	Carbonate mineral aggregates shall not be used	Carbonate rock aggregates shall not be used
Coal and Lignite, less than 2.00 specific gravity (ASTM C 123)	0.5 percent, max	0.5 percent, max

#### A2.1.4 Performance Requirements

Specifications of concrete properties include characteristics in the green state as well as the hardened state. Properties of hydrated concrete include conventional mechanical properties and projections of permeabilities over hundreds of years, a topic discussed at the end of this section. Table A-5 summarizes target properties for SMC. Attainment of these characteristics has been demonstrated (Wakeley et al., 1995). SMC has a strength of about 40 MPa at 28 days and continues to gain strength after that time, as is typical of hydrating cementitious materials. Concrete strength is naturally much greater than required for shaft seal elements because the state of stress within the shafts is compressional with little shear stress developing. In addition, compressive strength of SMC increases as confining pressure increases (Pfeifle et al., 1996). Volume stability of the SMC is also excellent, which assures a good bond with the salt.

Thermal and constitutive models for the SMC are described in Appendix D. Thermal properties are fit to laboratory data and used to calculate heat distribution during hydration. An isothermal creep law and an increasing modulus are used to represent the concrete in structural calculations. The resistance established by concrete to inward creep of the Salado Formation accelerates healing of microcracks in the salt. The state of stress impinging on concrete elements within the Salado Formation will approach a lithostatic condition.

Table A-5. Target Properties for Salado Mass Concrete

Property	Comment
Initial slump $10 \pm 1.0$ in. Slump at 2 hr $8 \pm 1.5$ in.	ASTM C 143, high slump needed for pumping and placement
Initial temperature $\leq 20^\circ\text{C}$	ASTM C 1064, using ice as part of mixing water
Air content $\leq 2.0\%$	ASTM C 231 (Type B meter), tight microstructure and higher strength
Self-leveling	Restrictions on underground placement may preclude vibration
No separately batched admixtures	Simple and reproducible operations
Adiabatic temperature rise $\leq 16^\circ\text{C}$ at 28 days	To reduce thermally induced cracking
30 MPa (4500 psi) compressive strength	ASTM C 39, at 180 days after placement
Volume stability	ASTM C 157, length change between +0.05 and -0.02% through 180 days

Permeability of SMC is very low, consistent with most concretes. Owing to a favorable state of stress and isothermal conditions, the SMC will remain intact. Because little brine is available to alter concrete elements, minimal degradation is possible. Resistance to phase changes of salt-saturated concretes and mortars within the WIPP setting has been excellent. These favorable attributes combine to assure concrete elements within the Salado will remain structurally sound and possess very low permeability for exceedingly long periods.

Permeabilities of SMC and other salt-saturated concretes have been measured in Small-Scale Seal Performance Tests (SSSPT) and Plug Test Matrix (PTM) at the WIPP for a decade and are corroborated by laboratory measurements (e.g., Knowles and Howard, 1996; Pfeifle et al., 1996). From these tests, values and ranges of concrete permeability have been developed. For performance assessments calculations, permeability of SMC seal components is treated as a random variable defined by a log triangular distribution with a best estimator of  $1.78 \times 10^{-19} \text{ m}^2$  and lower and upper limits of  $2.0 \times 10^{-21}$  and  $1.0 \times 10^{-17} \text{ m}^2$ , respectively.

The probability distribution function is shown in Figure A-2. Further, it is recognized that concrete function is required for only a relatively short-term period as salt reconsolidates. Concrete is expected to function adequately beyond its design life. For calculational expediency, a higher, very conservative permeability of  $1.0 \times 10^{-14}$  is assigned to concrete after 400 years. This abrupt change in permeability does not imply degradation, but rather reflects system redundancy and the fact that concrete is no longer relied on as a seal component.

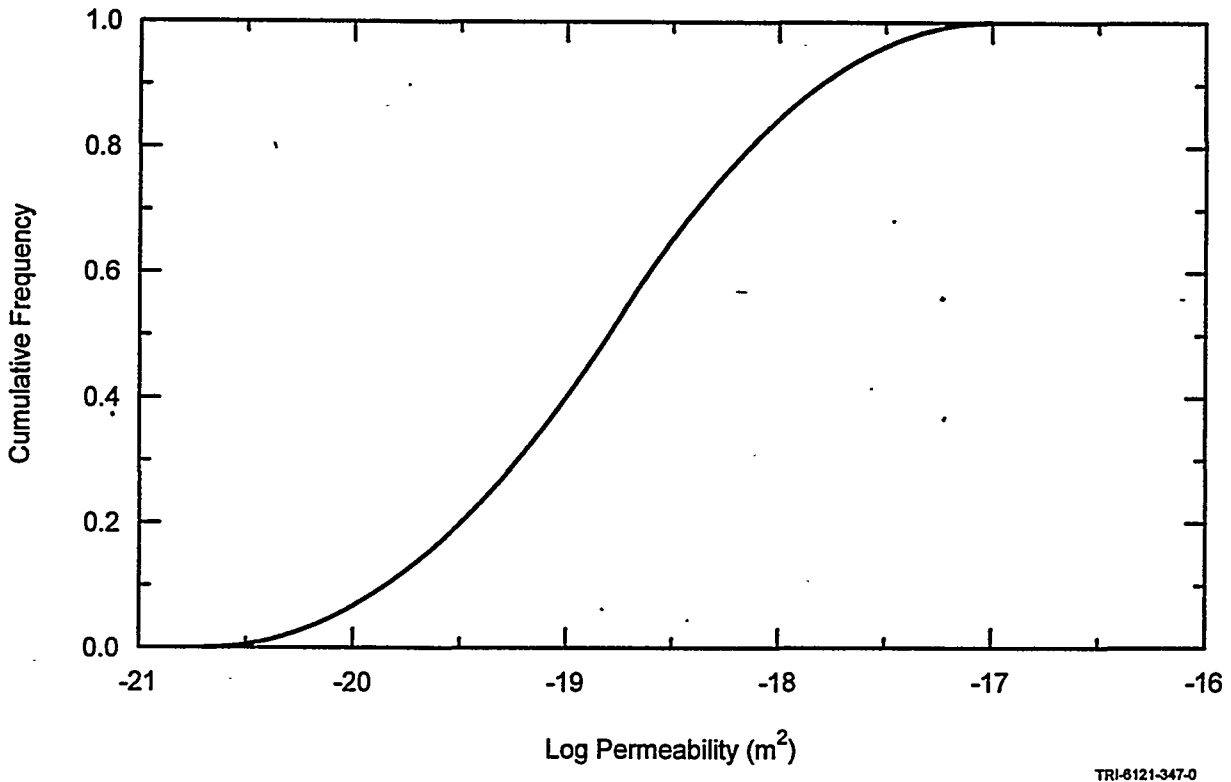


Figure A-2. Cumulative distribution function for SMC.

### A2.1.5 Verification Methods

The concrete supplier shall perform the inspection and tests described below (Tables A-6 and A-7) and, based on the results of these inspections and tests, shall take appropriate action. The laboratory performing verification tests shall be on-site and shall conform with ASTM C 1077. Individuals who sample and test concrete or the constituents of concrete as required in this specification shall have demonstrated a knowledge and ability to perform the necessary test procedures equivalent to the ACI minimum guidelines for certification of Concrete Laboratory Testing Technicians, Grade I. The Buyer will inspect the laboratory, equipment, and test procedures for conformance with ASTM C 1077 prior to start of dry materials batching operations and prior to restarting operations.

#### A2.1.5.1 Fine Aggregate

(A) *Grading.* Dry materials will be sampled while the batch plant is operating; there shall be a sieve analysis and fineness modulus determination in accordance with ASTM C 136.

(B) *Fineness Modulus Control Chart.* Results for fineness modulus shall be grouped in sets of three consecutive tests, and the average and range of each group shall be plotted on a control chart. The upper and lower control limits for average shall be drawn 0.10 units above and below the target fineness modulus, and the upper control limit for range shall be 0.20 units above the target fineness modulus.

Table A-6. Test Methods Used for Measuring Concrete Properties During and After Mixing

Property	Test Method	Title
Slump	ASTM C 143	Slump of Portland Cement Concrete
Unit weight	ASTM C 138	Unit Weight, Yield, and Air Content (Gravimetric) of Concrete
Air content	ASTM C 231	Air Content of Freshly Mixed Concrete by the Pressure Method
Mixture temperature	ASTM C 1064	Temperature of Freshly Mixed Concrete

Table A-7. Test Methods Used for Measuring Properties of Hardened Concrete

Property	Test Method	Title
Compressive strength	ASTM C 39	Compressive Strength of Cylindrical Concrete Specimens
Modulus of elasticity	ASTM C 469	Static Modulus of Elasticity and Poisson's Ratio of Concrete in Compression
Volume stability	ASTM C 157	Length Change of Hardened Cement Mortar and Concrete

(C) *Corrective Action for Fine Aggregate Grading.* When the amount passing any sieve is outside the specification limits, the fine aggregate shall be immediately resampled and retested. If there is another failure for any sieve, the fact shall be immediately reported to the Buyer. Whenever a point on the fineness modulus control chart, either for average or range, is beyond one of the control limits, the frequency of testing shall be doubled. If two consecutive points are beyond the control limits, the process shall be stopped and stock discarded if necessary.

(D) *Moisture Content Testing.* There shall be at least two tests for moisture content in accordance with ASTM C 566 during each 8-hour period of dry materials batch plant operation.

(E) *Moisture Content Corrective Action.* Whenever the moisture content of fine aggregate exceeds 0.1 % by weight, the fine aggregate shall be immediately resampled and retested. If there is another failure the batching shall be stopped.

#### A2.1.5.2 Coarse Aggregate

(A) *Grading.* Coarse aggregate shall be analyzed in accordance with ASTM C 136.

(B) *Corrective Action for Grading.* When the amount passing any sieve is outside the specification limits, the coarse aggregate shall be immediately resampled and retested. If the second sample fails on any sieve, that fact shall be reported to the Buyer. Where two consecutive averages of five tests are outside specification limits, the dry materials batch plant operation shall be stopped, and immediate steps shall be taken to correct the grading.

(C) *Moisture Content Testing.* There shall be at least two tests for moisture content in accordance with ASTM C 566 during each 8-hour period of dry materials batch plant operation.

(D) *Moisture Content Corrective Action.* Whenever the moisture content of coarse aggregate exceed 0.1 % by weight, the coarse aggregate shall be immediately resampled and retested. If there is another failure, batching shall be stopped.

#### **A2.1.5.3 Batch-Plant Control**

The measurement of all constituent materials including cementitious materials, each size of aggregate, and granular sodium chloride shall be continuously controlled. The aggregate batch weights shall be adjusted as necessary to compensate for their nonsaturated surface-dry condition.

#### **A2.1.5.4 Concrete Products**

Concrete products will be tested during preparation and after curing as summarized in Tables A-6 and A-7 for preparation and hydrated concrete, respectively.

### **A2.2 Compacted Clay**

Compacted clays are commonly proposed as primary sealing materials for nuclear waste repositories and have been extensively investigated (e.g., Gray, 1993). Compacted clay as a shaft sealing component provides a barrier to brine and possibly to gas flow into or out of the repository and supports the shaft with a high density material to minimize subsidence. In the event that brine does contact the compacted clay columns, bentonitic clay can generate a beneficial swelling pressure. Swelling would increase internal supporting pressure on the shaft wall and accelerate healing of any disturbed rock zone. Wetted, swelling clay will seal fractures as it expands into available space and will ensure tightness between the clay seal component and the shaft walls.

#### **A2.2.1 Functions**

In general, clay is used to prevent fluid flow either down or up the shaft. In addition, clay will stabilize the shaft opening and provide a backstress within the Salado Formation that will enhance healing of microfractures in the disturbed rock. Bentonitic clays are specified for Components 4, 8, and 12. In addition to limiting brine migration down the shafts, a primary function of a compacted clay seal through the Rustler Formation (Component 4) is to provide separation of water bearing units. The primary function of the upper Salado clay column (Component 8) is to limit groundwater flow down the shaft, thereby adding assurance that the reconsolidating salt column is protected. The lower Salado compacted clay column (Component 12) will act as a barrier to brine and possibly to gas flow (see construction alternatives in Appendix B) soon after placement and remain a barrier throughout the regulatory period.

#### **A2.2.2 Material Characteristics**

The Rustler and Salado compacted clay columns will be constructed of a commercial well-sealing grade sodium bentonite blocks compacted to between 1.8 and 2.0 g/cm<sup>3</sup>. An extensive experimental data base exists for the permeability of sodium bentonites under a variety

of conditions. Many other properties of sodium bentonite, such as strength, stiffness, and chemical stability also have been thoroughly investigated. Advantages of clays for sealing purposes include low permeability, demonstrated longevity in many types of natural environments, deformability, sorptive capacity, and demonstrated successful utilization in practice for a variety of sealing purposes.

A variety of clays could be considered for WIPP sealing purposes. For WIPP, as for most if not all nuclear waste repository projects, bentonite has been and continues to be a prime candidate as the clay sealing material. Bentonite clay is chosen here because of its overwhelming positive sealing characteristics. Bentonite is a highly plastic swelling clay material (e.g., Mitchell, 1993), consisting predominantly of smectite minerals (e.g., IAEA, 1990). Montmorillonite, the predominant smectite mineral in most bentonites, has the typical plate-like structure characteristic of most clay minerals.

The composition of a typical commercially available sodium bentonite (e.g. Volclay, granular sodium bentonite) contains over 90% montmorillonite and small portions of feldspar, biotite, selenite, etc. A typical sodium bentonite has the chemical composition summarized in Table A-8 (American Colloid Company, 1995). This chemical composition is close to that reported for MX-80 which was used successfully in the Stripa experiments (Gray, 1993). Sodium bentonite has a tri-layer expanding mineral structure of approximately  $(Al Fe_{1.67} Mg_{0.33}) Si_4O_{10} (OH)_2 Na^+ Ca^{++}_{0.33}$ . Specific gravity of the sodium bentonite is about 2.5. The dry bulk density of granular bentonite is about  $1.04 g/cm^3$ .

Densely compacted bentonite (of the order of  $1.75g/cm^3$ ), when confined, can generate a swelling pressure up to 20 MPa when permeated by water (IAEA, 1990). The magnitude of the swelling pressure generated depends on the chemistry of the permeating water. Laboratory and field measurements suggest that the bentonite specified for shaft seal materials in the Salado may achieve swell pressures of 3 to 4 MPa, and likely substantially less. Swelling pressure in the bentonite column is not expected to be appreciable because little contact with brine fluids is conceivable. Further considerations of potential swelling of bentonite within the Rustler Formation may be appropriate, however.

Table A-8. Representative Bentonite Composition.

Chemical Compound	Weight %
SiO <sub>2</sub>	63.0
Al <sub>2</sub> O <sub>3</sub>	21.1
Fe <sub>2</sub> O <sub>3</sub>	3.0
FeO	0.4
MgO	2.7
Na <sub>2</sub> O	2.6
CaO	0.7
H <sub>2</sub> O	5.6
Trace Elements	0.7

Mixtures of bentonite and water can range in rheological characteristics from a virtually Newtonian fluid to a stiff solid, depending on water content. Bentonite can form stiff seals at low moisture content, and can penetrate fractures and cracks when it has a higher water content. Under the latter conditions it can fill void space in the seal itself and disturbed rock zones. Bentonite with dry density of  $1.75 \text{ g/cm}^3$  has a cohesion of 5-50 kPa, and a friction angle of 5 to  $15^\circ$  (IAEA, 1990). At density greater than  $1.6\text{-}1.7 \text{ g/cm}^3$ , swelling pressure of bentonite is less affected by the salinity of groundwater providing better chemical and physical stabilities.

### **A2.2.3 Construction**

Seal performance within the Salado Formation is far more important to regulatory compliance than is performance of earthen fill in the overlying formations. Three potential construction methods might be used to place clay in the shaft, as discussed in Appendix B. Construction of bentonite clay components specifies block assembly procedures demonstrated successfully at the WIPP site (Knowles and Howard, 1996) and in a considerable body of work by Roland Pusch (see summary in Gray, 1993). To achieve low permeabilities, dry density of the bentonite blocks should be about  $2.0 \text{ g/cm}^3$ , although a range of densities is discussed in Section 2.2.4. A high density of clay components is also desirable to carry the weight of overlying seal material effectively and to minimize subsidence.

Placement of clay in the shaft is one area of construction that might be made more cost and time effective through optimization studies. An option to construct clay columns using dynamic compaction will likely prove to be efficient, so it is specified for earthen fill in the Dewey Lake Redbeds (as discussed later) and may prove to be an acceptable placement method for other components. Dynamic compaction would use equipment developed for placement of crushed salt. The Canadian nuclear waste program has conducted extensive testing, both in situ and in large scale laboratory compaction of clay-based barrier materials with dynamic hydraulically powered impact hammers (e.g., Kjartanson et al, 1992). The Swedish program similarly has investigated field compaction of bentonite-based tunnel backfill by means of plate vibrators (e.g., Nilsson, 1985). Both studies demonstrated the feasibility of in situ compaction of bentonite-based materials to a high density. Near surface, conventional compaction methods will be used because insufficient space remains for dynamic compaction using the multi-deck work stage.

### **A2.2.4 Performance Requirements**

The proven characteristics of bentonite assure attainment of very low permeability seals. It is recognized that the local environment contributes to the behavior of compacted clay components. Long-term material stability is a highly desired sealing attribute. Clay components located in brine environments will have to resist cation exchange and material structure alteration. Clay is geochemically mature, reducing likelihood of alteration and imbibition of brine is limited to isolated areas. Compacted clay is designed to withstand possible pressure gradients and to resist erosion and channeling that could conceivably lead to groundwater flow through the seal. Compacted clay seal components support the shaft walls and promote healing of the salt DRZ. Volume expansion or swelling would accelerate healing in the salt. A barrier to gas flow could be constructed if moisture content of approximately 85% of saturation could be achieved.

Permeability of bentonite is inversely correlated to dry density. Figure A-3 plots bentonite permeability as a function of reported sample density for sodium bentonite samples. The permeability ranges from approximately  $1 \times 10^{-21}$  to  $1 \times 10^{-17} \text{ m}^2$ . In all cases, the data in Figure A-3 are representative of low ionic strength permeant waters. Data provided in this figure are limited to sodium bentonite and bentonite/sand mixtures with clay content greater than or equal to 50 %. Cheung et al. (1987) report that in bentonite/sand mixtures, sand acts as an inert fraction which does not alter the permeability of the mixture from that of a 100 % bentonite sample at the same equivalent dry density. Also included in Figure A-3 are the three point - estimates of permeability at dry densities of 1.4, 1.8, and  $2.1 \text{ g/cm}^3$  provided by Jaak Daemen of the University of Nevada, Reno, who is actively engaged in WIPP-specific bentonite testing.

A series of in situ tests (SSSPTs) that evaluated compacted bentonite as a sealing material at the WIPP site corroborate data shown in Figure A-3. Test Series D tested two 100 % bentonite seals in vertical boreholes within the Salado Formation at the repository horizon. The diameter of each seal was 0.91 m, and the length of each seal was 0.91 m. Cores of the two bentonite seals had initial dry densities of 1.8 and  $2.0 \text{ g/cm}^3$ . Pressure differentials of 0.72 and 0.32 MPa were maintained across the bentonite seals with a brine reservoir on the upstream (bottom) of the seals for several years.

Over the course of the seal test, no visible brine was observed at the downstream end of the seals. Upon decommissioning the SSSPT, brine penetration was found to be only 15 cm. Determination of the absolute permeability of the bentonite seal was not precise; however, a bounding calculation of  $1 \times 10^{-19} \text{ m}^2$  was made by Knowles and Howard (1996).

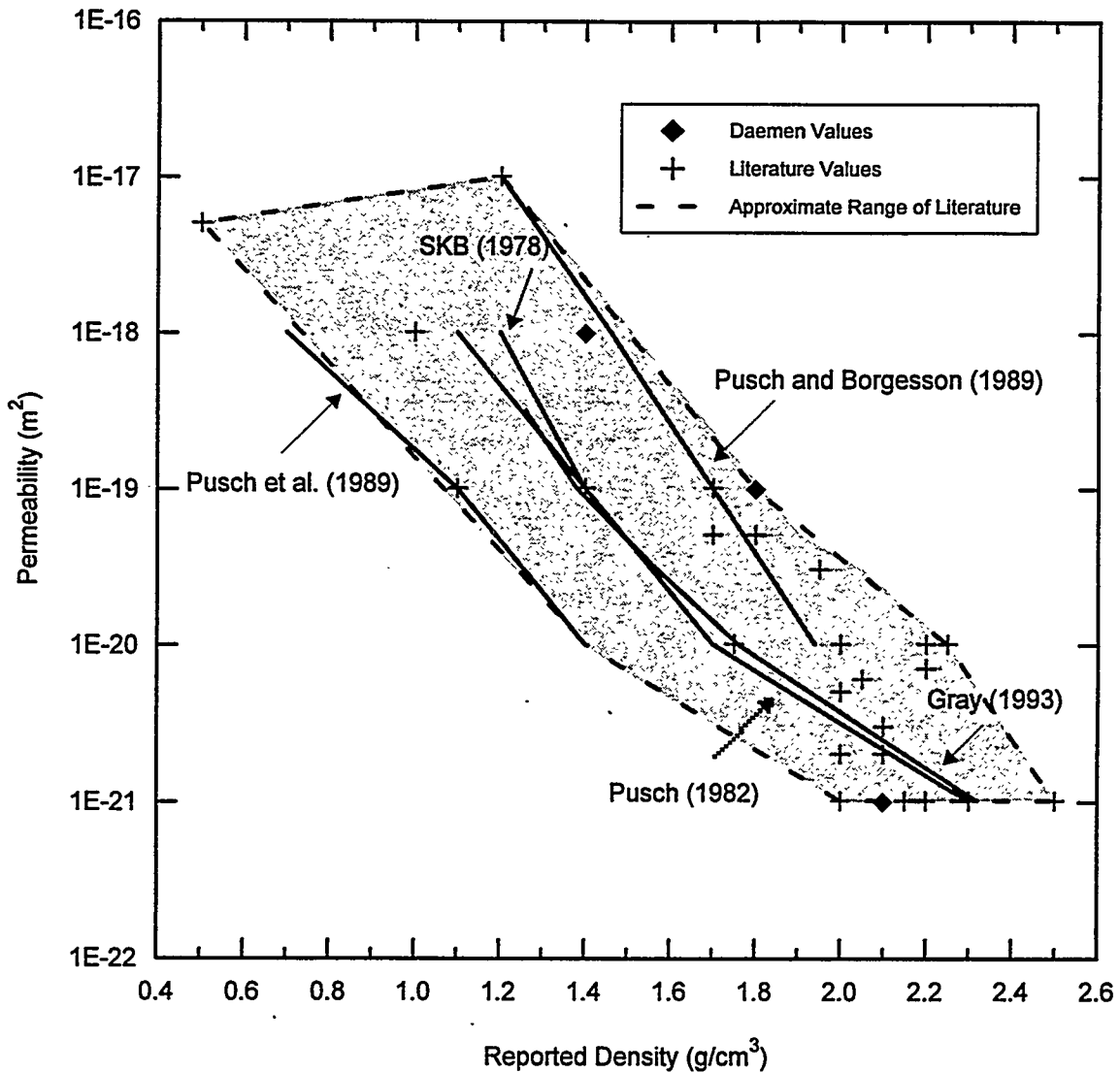
Beginning with a specified dry density of 1.8 to  $2.0 \text{ g/cm}^3$  and Figure A-3, a distribution function for clay permeability was developed and is provided in Figure A-4. Parameter distribution reflects some conservative assumptions pertaining to WIPP seal applications. The following provide rationale behind the distribution presented in Figure A-4.

1. A practical minimum for the distribution can be specified at  $1 \times 10^{-21} \text{ m}^2$ .
2. If effective dry density of the bentonite emplaced in the seals only varies from 1.8 to  $2.0 \text{ g/cm}^3$ , then a maximum expected permeability can be extrapolated from Figure A-3 as  $1 \times 10^{-19} \text{ m}^2$ .
3. Uncertainty exists in being able to place massive columns of bentonite to design specifications. To address this uncertainty in a conservative manner, it is assumed that the compacted clay be placed at a dry density as low as  $1.6 \text{ g/cm}^3$ . At  $1.6 \text{ g/cm}^3$ , the maximum permeability for the clay would be approximately  $5 \times 10^{-19} \text{ m}^2$ . Therefore, neglecting salinity effects, a range of permeability from  $1 \times 10^{-21}$  to  $5 \times 10^{-19} \text{ m}^2$  with a best estimate of less than  $1 \times 10^{-19} \text{ m}^2$  could be reasonably defined (assuming a best estimate emplacement density of  $1.8 \text{ g/cm}^3$ ). It could be argued, based on Figure A-3, that a best estimate could be as low as  $2 \times 10^{-20} \text{ m}^2$ .

Salinity increases bentonite permeability; however, these effects are greatly reduced at the densities specified for the shaft seal. At seawater salinity, Pusch et al. (1989) report the effects on permeability could be as much as a factor of 5 (one-half order of magnitude). To account for salinity effects in a conservative manner, the maximum permeability is increased from  $5 \times 10^{-19}$  to  $5 \times 10^{-18} \text{ m}^2$ . The best estimate permeability is increased by one-half order of magnitude to

$5 \times 10^{-19} \text{ m}^2$ . The lower limit is held at  $1 \times 10^{-21} \text{ m}^2$ . Because salinity effects are greatest at lower densities, the maximum is adjusted one full order of magnitude while the best estimate (assumed to reside at a density of  $1.8 \text{ g/cm}^3$ ) is adjusted one-half of an order.

The four arguments presented above give rise to the permeability cumulative frequency distribution plotted in Figure A-4, which summarizes the performance specification for bentonite columns.



TRI-6121-360-1

Figure A-3. Sodium bentonite permeability versus density.

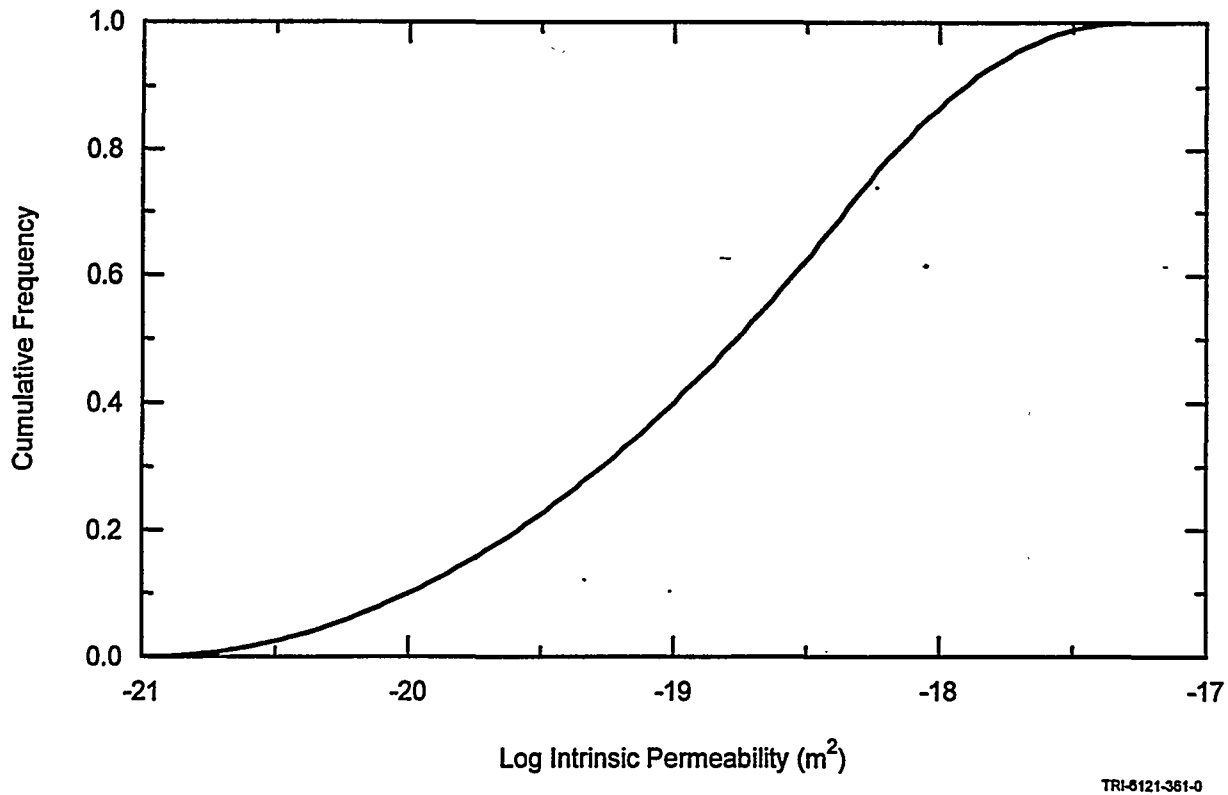


Figure A-4. Cumulative frequency distribution for compacted bentonite.

### A2.2.5 Verification Methods

Verification of specified properties such as density, moisture content or strength of compacted clay seals can be determined by direct access during construction. However, indirect methods are preferred because certain measurements, such as permeability, are likely to be time consuming and invasive. Methods used to verify the quality of emplaced seals will include quality of block production and field measurements of density. As a minimum, standard quality control procedures recommended for compaction operations will be implemented including visual observation, in situ density measurements, and moisture content measurements. Visual observation accompanied by detailed record keeping will assure design procedures are being followed. In situ testing will confirm design objectives are accomplished in the field.

Density measurements of compacted clay shall follow standard procedures such as ASTM D 1556, D 2167, and D 2922. The moisture content of clay blocks shall be calculated based on the water added during mixing and can be confirmed by following ASTM Standard procedures D 2216 and D 3017. It is probable that verification procedures will require modifications to be applicable within the shaft. As a minimum, laboratory testing to certify the above referenced quality control measures will be performed to assure that the field measurements provide reliable results.

## **A2.3 Asphalt Components**

Asphalt is used to prevent water migration down the shaft in two ways: an asphalt column bridging the Rustler/Salado contact and a "waterstop" sandwiched between concrete plugs at three locations within the Salado Formation, two above the salt column and one below the salt column. An asphalt mastic mix (AMM) that contains aggregate is specified for the column while the specification for the waterstop layer is pure asphalt.

Asphalt is a widely used construction material with many desirable properties. Asphalt is a strong cement, is readily adhesive, highly waterproof, and durable. Furthermore, it is a plastic substance that provides controlled flexibility to mixtures of mineral aggregates with which it is usually combined. It is highly resistant to most acids, salts, and alkalis. A number of asphalts and asphalt mixes are available that cover a wide range of viscoelastic properties which allows the properties of the mixture to be designed for a wide range of requirements for each application. These properties are well suited to the requirements of the WIPP shaft seal system.

### **A2.3.1 Functions**

The generic purpose of asphalt seal components above the salt column is to eliminate water migration downward. The asphalt waterstops above the salt column are designed to intersect the DRZ and limit fluid flow. Asphalt is not the lone component preventing flow of brine downward; it functions in tandem with concrete and a compacted clay column. Waterstop Component # 11 located below the salt column would naturally limit upward flow of brine or gas. Concrete abutting the asphalt waterstops provides a rigid element that creates a backstress upon the inward creeping salt, promoting healing within the DRZ. Asphalt is included in the WIPP shaft seal system to reduce uncertainty of system performance by providing redundancy of function while using an alternative material type. The combination of shaft seal components restricts fluid flow up or down to allow time for the salt column to reconsolidate and form a natural fluid-tight seal.

The physical and thermal attributes of asphalt combine to reduce fluid flow processes. The placement fluidity permits asphalt to flow into uneven interstices or fractures along the shaft wall. Asphalt will self-level into a nearly voidless mass. As it cools, the asphalt will eventually cease flowing. The elevated temperature and thermal mass of the asphalt will enhance creep deformation of the salt and promote healing of the DRZ surrounding the shaft. Asphalt adheres tightly to most materials, eliminating flow along the interface between the seal material and the surrounding rock.

### **A2.3.2 Material Characteristics**

The asphalt column specified for the WIPP seal system is an AMM commonly used for hydraulic structures. The AMM is a mixture of asphalt, sand, and hydrated lime. The asphalt content of AMM is higher than those used in typical hot mix asphalt concrete (pavements). High asphalt contents (10-20% by weight) and fine, well-graded aggregate (sand and mineral fillers) are used to obtain a near voidless mix. A low void content ensures a material with extremely low water permeability because there are a minimum number of connected pathways for brine migration.

A number of different asphaltic construction materials, including hot mix asphalt concrete (HMAC), neat asphalt, and AMMs, were evaluated for use in the WIPP seal design. HMAC was eliminated because of construction difficulty that might have led to questionable performance. An AMM is selected as a preferred alternative for the asphalt columns because it has economic and performance advantages over the other asphaltic options. Aggregate and mineral fines in the AMM increase rigidity and strength of the asphalt seal component, thereby enhancing the potential to heal the DRZ and reducing shrinkage relative to neat asphalt.

Viscosity of the AMM is an important physical property affecting construction and performance. The AMM is designed to have low enough viscosity to be pumpable at application temperatures and able to flow readily into voids. High viscosity of the AMM at operating temperatures prevents long-term flow, although none is expected. Hydrated lime is included in the mix design to increase the stability of the material, decrease moisture susceptibility, and act as an anti-microbial agent. Table A-9 details the mix design specifications for the AMM.

The asphalt used in the waterstop is AR-4000, a graded asphalt of intermediate viscosity. The waterstop uses pure, or neat, asphalt because it is a relatively small volume when compared to the column.

### **A2.3.3 Construction**

Construction of asphalt seal components can be accomplished using a slickline process where the molten material is effectively pumped into the shaft. The AMM will be mixed at ground level in a pug mill at approximately 180°C. At this temperature the material is readily pourable. The AMM will be slicklined and placed using a heated and insulated tremie line. The AMM will easily flow into irregularities in the surface of the shaft or open fractures until the AMM cools. After cooling, flow into surface irregularities in the shaft and DRZ will slow considerably because of the sand and mineral filler components in the AMM and the temperature dependence of the viscosity of the asphalt. AMM requires no compaction in construction. Neat asphalt will be placed in a similar fashion.

The technology to pump AMM is available as described in the construction procedures in Appendix B. One potential problem with this method of construction is ensuring that the slickline remains heated throughout the construction phase. Impedance heating (a current construction technique) can be used to ensure the pipe remains at temperatures sufficient to promote flow. The lower section (say 10 m) of the pipe may not need to be heated, and it may not be desirable to heat it as it is routinely immersed in the molten asphalt during construction to minimize air entrainment. Construction using large volumes of hot asphalt would be facilitated by placement in sections. After several meters of asphalt are placed, the slickline would be retracted by two lengths of pipe and pumping resumed. Once installed, the asphalt components will cool; the column will require several months to approach ambient conditions. Calculations of cooling times and plots of isotherms for the asphalt column are given in Appendix D. It should be noted that a thermal pulse into the surrounding rock salt could produce positive rock mechanics conditions. Fractures will heal much faster owing to thermally activated dislocation motion and diffusion. Salt itself will creep inward at a much greater rate as well.

Table A-9. Asphalt Component Specifications

AMM Composition:		20 wt% asphalt (AR-4000 graded asphalt) 70 wt% aggregate (silicate sand) 10 wt% hydrated lime
Aggregate (% passing by weight)		
US Sieve Size		Specification Limits
2.36 mm	(No. 8)	100
1.18 mm	(No. 16)	90
600	(No. 30)	55-75
300	(No. 50)	35-50
150	(No. 100)	15-30
75	(No. 200)	5-15
Mineral Filler: Hydrated Lime Chemical Composition:		
Total active lime content (% by weight) .....		min. 90.0%
Unhydrated lime weight (% by weight CaO).....		max. 5.0%
Free water (% by weight H <sub>2</sub> O).....		max. 4.0%
Residue Analysis:		
Residue retained on No. 6 sieve .....		max. 0.1%
Residue retained on No. 30 sieve .....		max. 3.0%

#### A2.3.4 Performance Requirements

Asphalt components are required to endure for about 100 years as an interim seal while the compacted salt component reconsolidates to create a very low permeability seal component. Since asphalt will not be subjected to ultraviolet light or an oxidizing environment, it is expected to provide an effective brine seal for several centuries. Air voids should be less than 2% to ensure low permeability. Asphalt mixtures do not become measurably permeable to water until voids approach 8% (Brown, 1990).

At Hanford, experiments are ongoing on the development of a passive surface barrier designed to isolate wastes (in this case to prevent downward flux of water and upward flux of gases) for 1000 years with no maintenance. The surface barrier uses asphalt as one of many horizontal components because low-air-void, high-asphalt-content materials are noted for low permeability and improved mechanically stable compositions. The design objective of this asphalt concrete was to limit infiltration to  $1.6 \times 10^{-9}$  cm/s ( $1.6 \times 10^{-11}$  m/s, or for fresh water, an intrinsic permeability of  $1.6 \times 10^{-18}$  m<sup>2</sup>). The asphalt component of the barrier is composed of a 15 cm layer of asphaltic concrete overlain with a 5-mm layer of fluid-applied asphalt. The reported hydraulic conductivity of the asphalt concrete is estimated to be  $1 \times 10^{-9}$  m/s (equivalent

to an intrinsic permeability of approximately  $1 \times 10^{-16} \text{ m}^2$  assuming fresh water). Myers and Duranceau (1994) report that the hydraulic conductivity of fluid-applied asphalt is estimated to be  $1.0 \times 10^{-11}$  to  $1.0 \times 10^{-10} \text{ cm/s}$  (equivalent to an intrinsic permeability of approximately  $1.0 \times 10^{-20}$  to  $1.0 \times 10^{-19} \text{ m}^2$  assuming fresh water).

Consideration of published values results in a lowest practical permeability of  $1 \times 10^{-21} \text{ m}^2$ . The upper limit of the asphalt seal permeability is assumed to be  $1 \times 10^{-18} \text{ m}^2$ . Intrinsic permeability of the asphalt column is defined as a log triangular distributed parameter, with a best estimate value of  $1 \times 10^{-20} \text{ m}^2$ , a minimum value of  $1 \times 10^{-21} \text{ m}^2$ , and a maximum value of  $1 \times 10^{-18} \text{ m}^2$ , as shown in Figure A-5. It is recognized that the halite DRZ in the uppermost portion of the Salado Formation is not likely to heal because creep of salt is relatively slow.

These values are used in performance assessment of regulatory compliance analyses and in fluid flow calculations (Appendix C) pertaining to seal system functional evaluation. Other calculations pertaining to rock mechanics and structural considerations of asphalt elements are discussed in Appendix D.

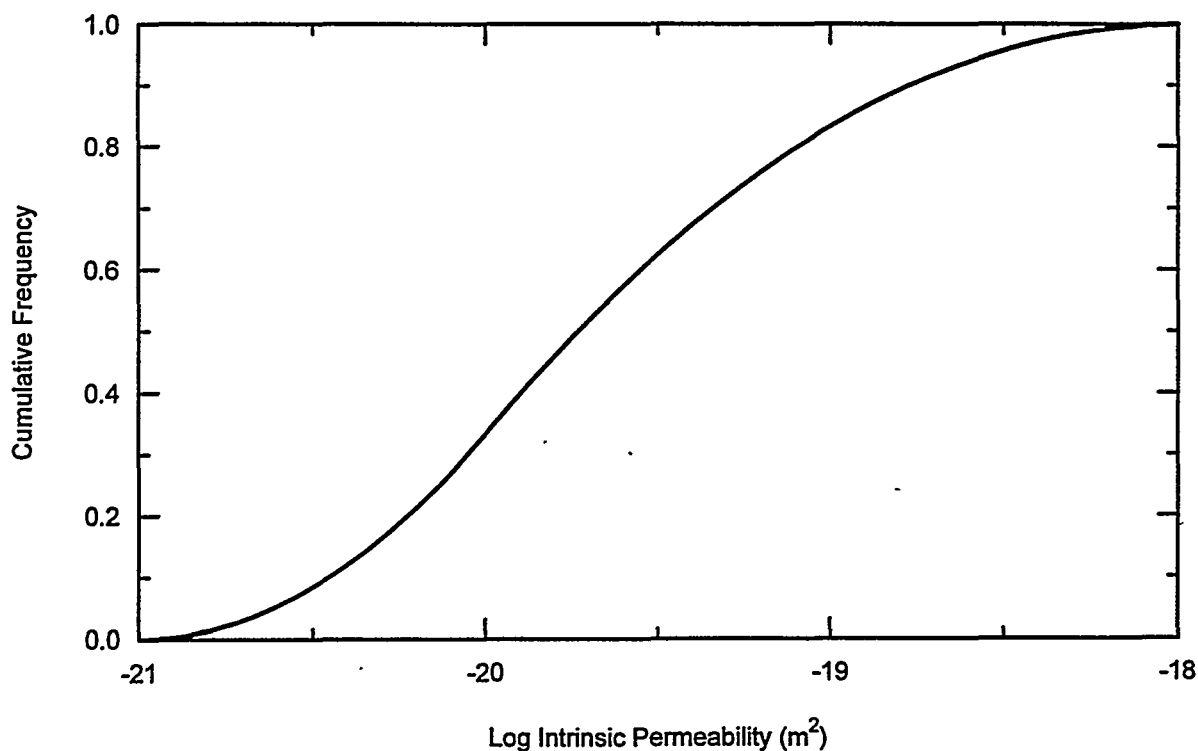


Figure A-5. Asphalt permeability cumulative frequency distribution function.

### **A2.3.5 Verification Methods**

Viscosity of the AMM must be low enough for easy delivery through a heated slickline. Sufficient text book information is available to assure performance of the asphalt component; however, laboratory validation tests may be desirable before installation. There are no plans to test asphalt components after they are placed. With that in mind, some general tests identified below would add quantitative documentation to expected performance values and have direct application to WIPP. The types and objectives of the verification tests are:

*Mix Design.* A standard mix design which evaluates a combination of asphalt and aggregate mixtures would quantify density, air voids, viscosity, and permeability. Although the specified mixture will function adequately, studies could optimize the mix design.

*Viscoelastic Properties at Service Temperatures.* Viscoelastic properties over the range of expected service temperatures would refine the rheological model.

*Accelerated Aging Analysis.* Asphalt longevity issues could be further addressed by using the approach detailed in PNL-Report 9336 (Fréeman and Romine, 1994).

*Brine Susceptibility Analysis.* The presumed inert nature of the asphalt mix can be demonstrated through exposure to groundwater brine solutions found in the Salado Formation. Potential for degradation will be characterized by monitoring the presence of asphalt degradation products in WIPP brine or brine simulant as a function of time. Effects on hydraulic conductivity can be measured during these experiments.

### **A2.4 Compacted Salt Column**

A reconstituted salt column has been proposed as a primary means to isolate for several decades those repositories containing hazardous materials situated in evaporite sequences. Reuse of salt excavated in the process of creating the underground openings has been advocated since the initial proposal by the NAS in the 1950s. Replacing the natural material to its original setting ensures physical, chemical, and mechanical compatibility with the host formation. Recent developments in support of the WIPP shaft seal system have produced confirming experimental results, constitutive material laws, and construction methods that substantiate use of a salt column for a low permeability, perfectly compatible seal component.

Numerical models of the shaft and seal system have been used to provide information on the mechanical processes that affect potential pathways and overall performance of the seal system. Several of these types of analyses are developed in Appendix D. Simulations of the excavated shaft and the compacted salt seal element behavior after placement show that as time passes, the host salt creeps inward, the compacted salt is loaded by the host formation and consolidates, and a back pressure is developed along the shaft wall. The back pressure imparted to the host formation by the compacted salt promotes healing of any microcracks in the host rock. As compacted salt consolidates, density and stiffness increase and permeability decreases.

#### **A2.4.1 Functions**

The function of the compacted and reconsolidated salt column is to limit transmission of fluids into or out of the repository for the statutory period of 10,000 years. The functional period

starts within a hundred years and lasts essentially forever. After a period of consolidation, the salt column will almost completely retard gas or brine migration within the former shaft opening. A completely consolidated salt column will achieve flow properties indistinguishable from natural Salado salt.

#### **A2.4.2 Material Characteristics**

The salt component comprises crushed Salado salt with addition of small amounts of water. No admixtures other than water are needed to meet design specifications. Natural Salado salt (also called WIPP salt) is typical of most salts in the Permian Basin: it has an overall composition approaching 90-95 % halite with minor clays, carbonate, anhydrite, and other halite minerals. Secondary minerals and other impurities are of little consequence to construction or performance of the compacted salt column as long as the halite content is approximately 90 %.

The total water content of the crushed salt should be approximately 1.5 wt% as it is tamped into place. Field and laboratory testing verified that natural salt can be compacted to significant density ( $\rho \geq 0.9$ ) with addition of these modest amounts of water. In situ WIPP salt contains approximately 0.5 wt% water. After it is mined, transported, and stored, some of the connate water is lost to evaporation and dehydration. Water content of the bulk material that would be used for compaction in the shaft is normally quite small, on the order of 0.25 wt%, as measured during compaction demonstrations (Hansen and Ahrens, 1996). Measurements of water content of the salt will be necessary periodically during construction to calibrate the proper amount of water to be added to the salt as it is placed.

Water added to the salt will be sprayed in a fine mist onto the crushed salt as it is cast in each lift. Methods similar to those used in the large-scale compaction demonstration will be developed such that the spray visibly wets the salt grain surfaces. General uniformity of spray is desired. The water has no special chemical requirements for purity. It can be of high quality (drinkable) but need not be potable. Brackish water would suffice because water of any quality would become brackish upon application to the salt.

The mined salt will be crushed and screened to a nominal maximum diameter of 5 mm. Gradation of particles smaller than 5 mm is not of concern because the crushing process will create relatively few fines compared to the act of dynamic compaction. Based on preliminary large-scale demonstrations, excellent compaction was achieved without optimization of particle sizes. It is evident from results of the large compaction demonstration coupled with laboratory studies that initial density can be increased and permeability decreased beyond existing favorable results. Further demonstrations of techniques, including crushing and addition of water may be undertaken in ensuing years between compliance certification and beginning of seal placement.

#### **A2.4.3 Construction**

Dynamic compaction is the specified procedure to tamp crushed salt in the shaft. Other techniques of compaction have potential, but their application has not been demonstrated. Deep dynamic compaction provides the greatest energy input to the crushed salt, is easy to apply, and has an effective depth of compactive influence far greater than lift thickness. Dynamic compaction is relatively straightforward and requires a minimal work force. If the number of drops remains constant, diameter and weight of the tamper increases in proportion to the

diameter of the shaft. The weight of the tamper is a factor in design of the infrastructure supporting the hoisting apparatus. Larger, heavier tampers require equally stout staging. The construction method outlined in Appendix B balances these opposing criteria. Compaction itself will follow the successful procedure developed in the large-scale compaction demonstration (Hansen and Ahrens, 1996).

Transport of crushed salt to the working level can be accomplished by dropping it down a slickline. As noted, additional water will be sprayed onto the crushed salt at the bottom of the shaft as it is placed. Lift heights of approximately 2 m are specified, though greater depths could be compacted effectively using dynamic compaction. Uneven piles of salt can be hand leveled.

#### **A2.4.4 Performance Requirements**

Compacted crushed salt is a unique seal material because it consolidates naturally as the host formation creeps inward. As the crushed salt consolidates, void space diminishes, density increases, and permeability decreases. Thus, sealing effectiveness of the compacted salt column will improve with time. Laboratory testing over the last decade has shown that pulverized salt specimens can be compressed to high densities and low permeabilities (Brodsky et al., 1996). In addition, consolidated crushed salt uniquely guarantees chemical and mechanical compatibility with the host salt formation. Therefore, crushed salt will provide a seal that will function ..... essentially forever once the consolidation process is completed. Primary performance results of these analyses include plots of fractional density as a function of depth and time for the crushed salt column and permeability distribution functions that will be used for performance assessment calculations. These performance results are summarized near the end of this section, following a limited background discussion.

To predict performance, a constitutive model for crushed salt is required. To this end, a technical evaluation of potential crushed salt constitutive models was completed (Callahan et al., 1996). Ten potential crushed salt constitutive models were identified in a literature search to describe the phenomenological and micromechanical processes governing consolidation of crushed salt. Three of the ten potential models were selected for rigorous comparisons to a specially developed, although somewhat limited, database. The database contained data from hydrostatic and shear consolidation laboratory experiments. The experiments provide deformation (strain) data as a function of time under constant stress conditions. Based on volumetric strain measurements from experiments, change in crushed salt density and porosity are known. In some experiments, permeability was also measured, which provides a relationship between density and permeability of crushed salt. Models were fit to the experimental database to determine material parameter values and the model that best represents experimental data.

Modeling has been used to predict consolidating salt density as a function of time and position in the shaft. Position or depth of the calculation is important because creep rates of intact salt and crushed salt are strong functions of stress difference. Analyses made use of a "pineapple" slice structural model at the top (430 m), middle (515 m), and bottom (600 m) of the compacted salt column. Initial fractional density of the compacted crushed salt was 0.90 (1944 kg m<sup>-3</sup>). The structural model, constitutive material models, boundary conditions, etc. are described in Appendix D. Modeling results coupled with laboratory-determined relationships

between density and permeability were used to develop distribution functions for permeability of the compacted crushed salt column for centuries after seal emplacement.

Analyses used reference engineering values for parameters in the constitutive models (e.g., the creep model for intact salt and consolidation models for crushed salt). Some uncertainty associated with model parameters exists in these constitutive models. Consolidating salt density was quantified by predicting density at specific times using parameter variations. Many of these types of calculations comparing three models for consolidation of crushed salt were performed to quantify performance of the salt column, and the reader is referred to Appendix D for more detail.

Predictions of fractional density as a function of time and depth are shown in Figure A-6. Performance calculations of the seal system require quantification of the resultant salt

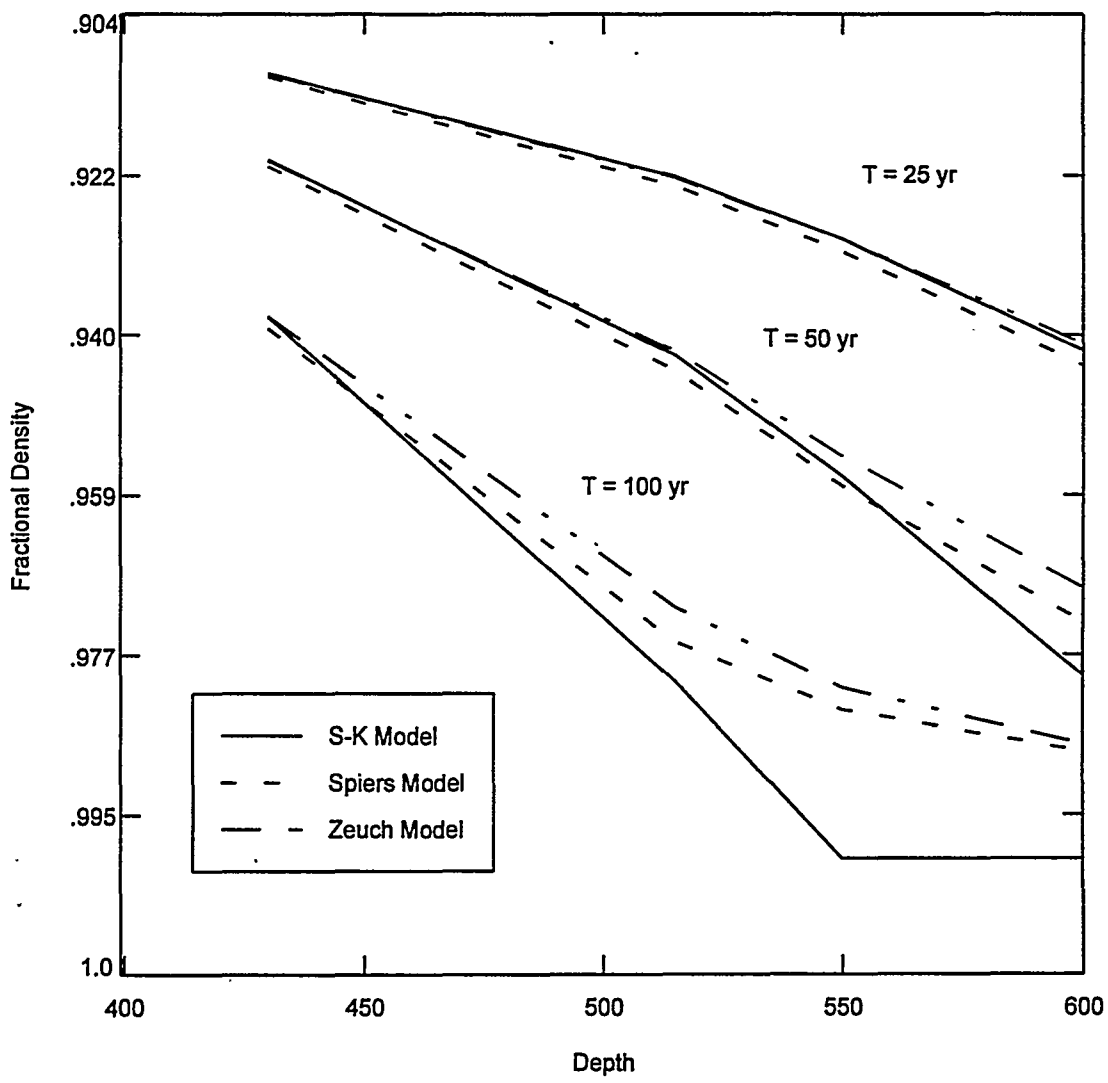


Figure A-6. Fractional density of the consolidating salt column.

permeability. The permeability can be derived from the experimental data presented in Figure A-7. This plot depicts probabilistic lines through the experimental data. From these lines, distribution functions can be derived. Permeability of the compacted salt column is treated as a transient random variable defined by a log triangular distribution. Distribution functions were provided for 0, 50, 100, 200, and 400 years after seal emplacement, assuming that fluids in the salt column pores spaces would not produce a backstress. The resultant cumulative frequency distribution for seal permeability at the seal mid-height is shown in Figure A-8. This method predicts permeabilities ranging from  $1 \times 10^{-23} \text{ m}^2$  to  $1 \times 10^{-16} \text{ m}^2$ . Because crushed salt consolidation will be affected by both mechanical and hydrological processes, detailed calculations were performed. These calculations are presented in Appendices C and D.

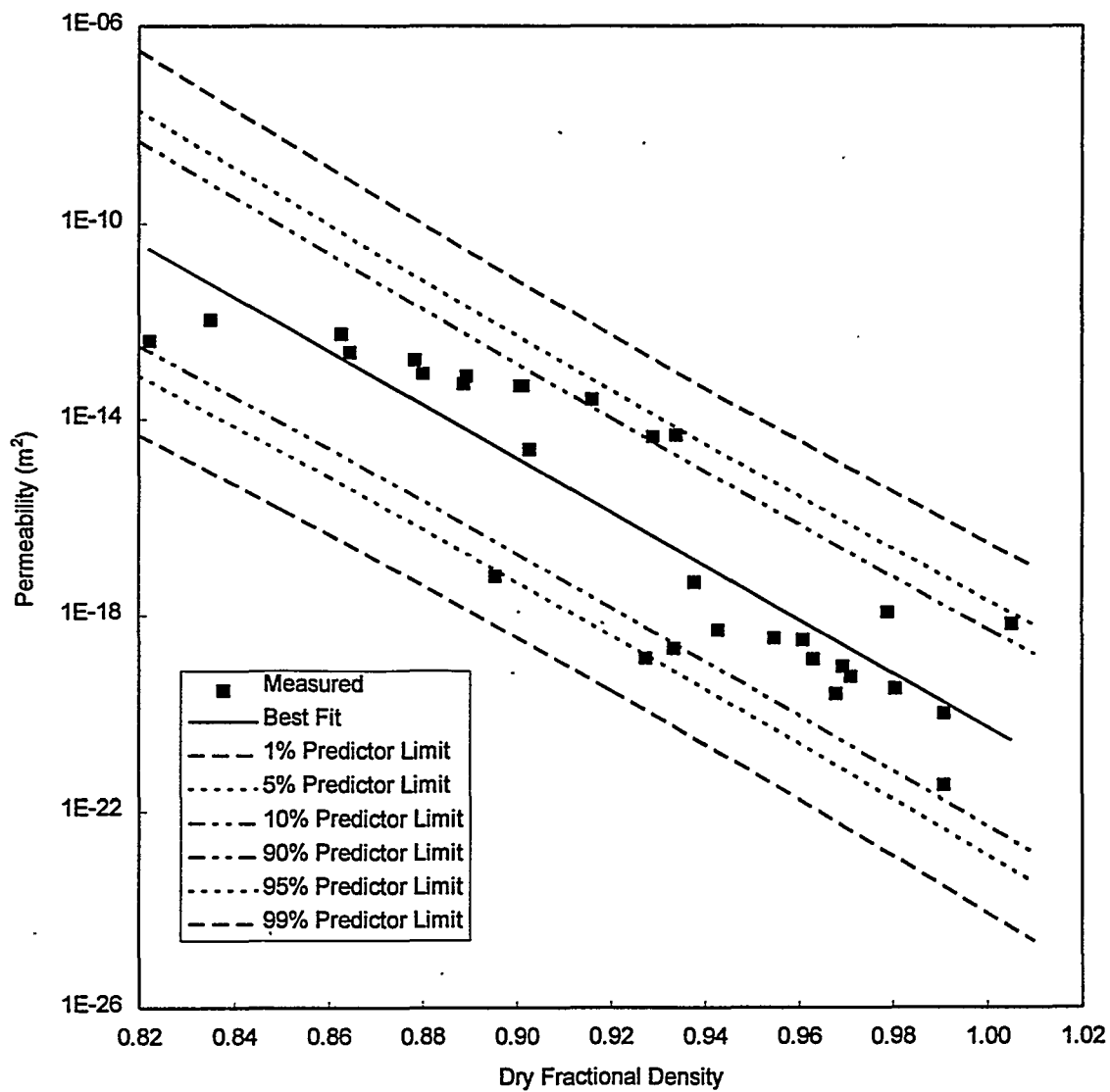


Figure A-7. Permeability of consolidated crushed salt as a function of fractional density.

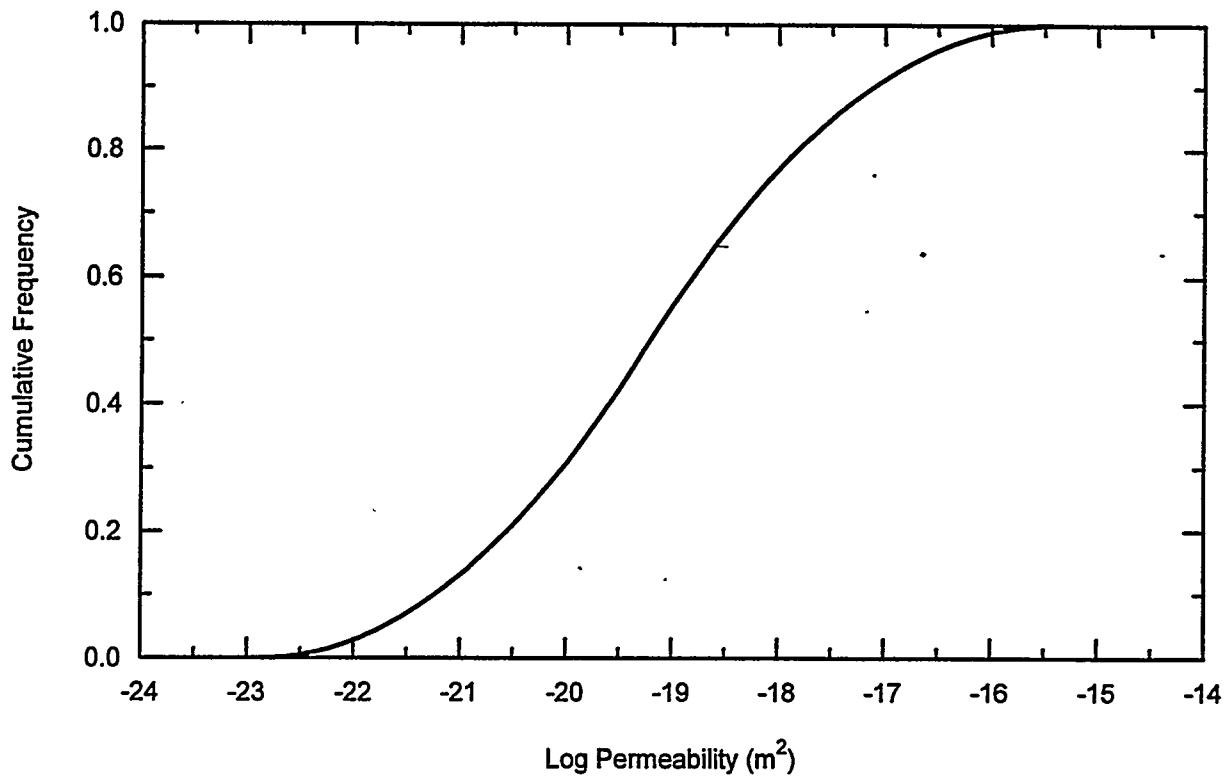


Figure A-8. Compacted salt column permeability cumulative frequency distribution function at seal midpoint 100 years following closure.

Numerical models of the shaft provide density of the compacted salt column as a function of depth and time. From the density-permeability relationship, permeability of the compacted salt seal component can be calculated. Similarly, the extent of the disturbed rock zone around the shaft is provided by numerical models. From field measurements of the halite DRZ, permeability of the DRZ is known as a function of depth and time. These spatial and temporal permeability values provide information required to assess the potential for brine and gas movement in and around the consolidating salt column.

#### A2.4.5 Verification Methods

Results of the large-scale dynamic compaction demonstration suggest that deep dynamic compaction will produce a dense starting material, and laboratory work and modeling show that compacted salt will reconsolidate within several decades to an essentially impermeable mass. As with other seal components, testing of the material in situ will be difficult and probably not the best way to ensure quality of the seal element. This is particularly apparent for the compacted salt component because the compactive effort produces a finely powdered layer on the top of each lift. It turns out that the fine powder compacts into a very dense material when the next lift is compacted. The best way to ensure that the crushed salt element functions properly is to establish performance through QA/QC procedures. If crushed salt is placed with a reasonable

uniformity of water and is compacted with sufficient energy, long-term performance can be assured.

Periodic measurements of the water content of loose salt as it is placed in lifts will be used for verification and quality control. Thickness of lifts will be controlled. Energy imparted to each lift will be documented by logging drop patterns and drop height. If deemed necessary, visual inspection of the tamped salt can be made by human access. The powder layer can be shoveled aside and hardness of underlying material can be qualitatively determined or tested. Overall geometric measurements made from the original surface of each lift could be used to approximate compacted density.

## **A2.5 Cementitious Grout**

Cementitious grouting is specified for all concrete members in response to external review suggestions. Grouting is also used in advance of liner removal to stabilize the ground. Cementitious grout is specified because of its proven performance, nontoxicity, and previous use at the WIPP.

### **A2.5.1 Functions**

The function of grout is to stabilize the surrounding rock before existing concrete liners are removed. Grout will fill fractures within adjacent lithologies, thereby adding strength and reducing permeability. Grout around concrete members of the concrete asphalt waterstop will be employed in an attempt to tighten the interface and fill microcracks in the DRZ. Efficacy of grouting will be determined during construction. In addition, reduction of local permeability will further limit groundwater influx into the shaft during construction. Concrete plugs are planned for specific elevations in the lined portion of each shaft. The formation behind the concrete liner will be grouted from approximately 3 m below to 3 m above the plug positions to ensure stability of any loose rock.

### **A2.5.2 Material Characteristics**

The grout developed for use in the shaft seal system has the following characteristics:

- no water separation upon hydration,
- low permeability paste,
- fine particle size,
- low hydrational heat,
- no measurable agglomeration subsequent to mixing,
- two hours of injectability subsequent to mixing,
- short set time,
- high compressive strength, and
- competitive cost.

A cementitious grout developed by Ahrens and coworkers (Ahrens et al., 1996) is specified for application in the shaft seal design. This grout consists of portland cement, pumice

as a pozzolanic material, and superplasticizer in the proportions listed in Table A-10. The ultrafine grout is mixed in a colloidal grout mixer, with a water to components ratio (W:C) of 0.6:1. Grout has been produced with 90 % of the particles smaller than 5 microns and an average particle size of 2 microns. The extremely small particle size enables the grout to penetrate fractures with apertures as small as 6 microns.

Table A-10. Ultrafine Grout Mix Specification

Component	Weight Percent (wt%)
Type 5 portland cement	45
Pumice	55
Superplasticizer	1.5

### A2.5.3 Construction

Grout holes will be drilled in a spin pattern that extends from 3 m below to 3 m above that portion of the lining to be removed. The drilling and grouting sequence will be defined in the workmanship specifications prior to construction. Grout will be mixed on surface and transferred to the work deck via the slick line. Maximum injection pressure will be lithostatic, less 50 psig. It is estimated that four holes can be drilled and grouted per shift.

### A2.5.4 Performance Requirements

Performance of grout is not a consideration for compliance issues. Grouting is used to facilitate construction by stabilizing any loose rock behind the concrete liner. If the country rock is fractured, grouting will reduce the permeability of the DRZ significantly. Application at the WIPP demonstrated permeability reduction in an anhydrite marker bed of two to three orders of magnitude (Ahrens et al., 1996). Reduction of local permeability adds to longevity of the grout itself and reduces the possibility of brine contacting seal elements. Because grout does not influence compliance issues, a model for it is not used and has not been developed. General performance achievements are:

- filled fractures as small as 6 microns,
- no water separation upon hydration,
- no evidence of halite dissolution,
- no measurable agglomeration subsequent to mixing,
- one hour of injectability,
- initial Vicat needle set in 2.5 hours,
- compressive strength 40 MPa at 28 days, and
- competitive cost.

### **A2.5.5 Verification Methods**

No verification of the effectiveness of grouting is currently specified. If injection around concrete plugs is possible, an evaluation of quantities and significance of grouting will be made during construction. Procedural specifications will include measurements of fineness and determination of rheology in keeping with processes established during the WIPP demonstration grouting (Ahrens et al., 1996).

## **A2.6 Earthen Fill**

Compacted earthen fill comprise approximately 150 m of shaft fill in the Dewey Lake Redbeds and near surface stratigraphy.

### **A2.6.1 Functions**

There are minimal performance requirements imposed for Components 1 and 3 and none that affect regulatory compliance of the site. Specifications for Components 1 and 3 are general: fill the shaft with relatively dense material to reduce subsidence.

### **A2.5.2 Material Characteristics**

Fill can utilize material that was excavated during shaft sinking and stored at the WIPP site, or a borrow pit may be excavated to secure fill material. The bulk fill material may include bentonite additive, if deemed appropriate.

### **A2.5.3 Construction**

Dynamic compaction is specified for the clay column in the Dewey Lake Formation because of its perceived expediency. Vibratory compaction will be used near surface when there is no longer space for the three stage construction deck.

### **A2.5.4 Performance Requirements**

Care will be taken to compact the earthen fill with an energy of twice Modified Proctor energy, which has been shown to produce a dense, uniform fill.

### **A2.5.6 Verification**

Materials placed will be documented, with density measurements as appropriate.

## **A3. CONCLUDING REMARKS**

Material specifications in this appendix provide descriptions of seal materials along with reasoning about why they are expected to function well in the WIPP setting. The specification follows a framework that states the function of the seal component, a description of the material, and a summary of construction techniques that could be implemented without resorting to extensive development efforts. Discussion of performance requirements for each material is the most detailed section because design of the seal system requires analysis of performance to ascertain compliance with regulations. Successful design of the shaft seal system is

demonstrated by an evaluation of how well the design performs, rather than by comparison with a predetermined quantity.

Materials chosen for use in the shaft seal system have several common desirable attributes: low permeability, availability, high density, longevity, low cost, constructability, and supporting documentation. Functional redundancy using different materials provides an economically and technologically feasible shaft seal system that limits fluid transport.

#### A4. REFERENCES

- Ahrens, E.H., T.F. Dale, and R.S. Van Pelt. 1996. *Data Report on the Waste Isolation Pilot Plant Small-Scale Seal Performance Test, Series F Grouting Experiment*. SAND93-1000. Albuquerque, NM: Sandia National Laboratories. (Copy on file in the Sandia WIPP Central Files, Sandia National Laboratories, Albuquerque, NM [SWCF] as WPO37355.)
- American Colloid Company. 1995. "Technical Data Sheet. Volclay GPG 30." Arlington Heights, IL: Industrial Chemical Division, American Colloid Company. 1 p. (Copy on file in the SWCF as WPO39636.)
- American Petroleum Institute. 1990. "Specification for Materials and Testing for Well Cements." API Specification 10. 5th ed. Washington, DC: American Petroleum Institute. (Available from American Petroleum Institute, 1220 L St. NW, Washington, DC 20005, 202/682-8375.)
- ASTM C 33 - 93. "Specification for Concrete Aggregates," *Annual Book of ASTM Standards, Volume 04.02, Concrete and Aggregates*. Philadelphia, PA: American Society for Testing and Materials. (Available from American Society for Testing and Materials, 1916 Race Street, Philadelphia, PA 19103-1187, 215/299-5400.)
- ASTM C 39 - 94. "Test Method for Compressive Strength of Cylindrical Concrete Specimens," *Annual Book of ASTM Standards, Volume 04.02, Concrete and Aggregates*. Philadelphia, PA: American Society for Testing and Materials. (Available from American Society for Testing and Materials, 1916 Race Street, Philadelphia, PA 19103-1187, 215/299-5400.)
- ASTM C 40 - 92. "Test Method for Organic Impurities in Fine Aggregates for Concrete," *Annual Book of ASTM Standards, Volume 04.02, Concrete and Aggregates*. Philadelphia, PA: American Society for Testing and Materials. (Available from American Society for Testing and Materials, 1916 Race Street, Philadelphia, PA 19103-1187, 215/299-5400.)
- ASTM C 114 - 94. "Test Methods for Chemical Analysis of Hydraulic Cement," *Annual Book of ASTM Standards, Volume 04.01, Cement; Lime; Gypsum*. Philadelphia, PA: American Society for Testing and Materials. (Available from American Society for Testing and Materials, 1916 Race Street, Philadelphia, PA 19103-1187, 215/299-5400.)
- ASTM C 117 - 95. "Test Method for Material Finer Than 75- $\mu$ m (No. 200) Sieve in Mineral Aggregates by Washing," *Annual Book of ASTM Standards, Volume 04.02, Concrete and Aggregates*. Philadelphia, PA: American Society for Testing and Materials. (Available from American Society for Testing and Materials, 1916 Race Street, Philadelphia, PA 19103-1187, 215/299-5400.)

- ASTM C 123 - 94. "Test Method for Lightweight Pieces in Aggregate," *Annual Book of ASTM Standards, Volume 04.02, Concrete and Aggregates*. Philadelphia, PA: American Society for Testing and Materials. (Available from American Society for Testing and Materials, 1916 Race Street, Philadelphia, PA 19103-1187, 215/299-5400.)
- ASTM C 127 - 88 (1993). "Test Method for Specific Gravity and Absorption of Coarse Aggregate," *Annual Book of ASTM Standards, Volume 04.02, Concrete and Aggregates*. Philadelphia, PA: American Society for Testing and Materials. (Available from American Society for Testing and Materials, 1916 Race Street, Philadelphia, PA 19103-1187, 215/299-5400.)
- ASTM C 128 - 93. "Test Method for Specific Gravity and Absorption of Fine Aggregate," *Annual Book of ASTM Standards, Volume 04.02, Concrete and Aggregates*. Philadelphia, PA: American Society for Testing and Materials. (Available from American Society for Testing and Materials, 1916 Race Street, Philadelphia, PA 19103-1187, 215/299-5400.)
- ASTM C 131 - 89. "Test Method for Resistance to Degradation of Small-Size Coarse Aggregate by Abrasion and Impact in the Los Angeles Machine," *Annual Book of ASTM Standards, Volume 04.02, Concrete and Aggregates*. Philadelphia, PA: American Society for Testing and Materials. (Available from American Society for Testing and Materials, 1916 Race Street, Philadelphia, PA 19103-1187, 215/299-5400.)
- ASTM C 136 - 95a. "Test Method for Sieve Analysis of Fine and Coarse Aggregates," *Annual Book of ASTM Standards, Volume 04.02, Concrete and Aggregates*. Philadelphia, PA: American Society for Testing and Materials. (Available from American Society for Testing and Materials, 1916 Race Street, Philadelphia, PA 19103-1187, 215/299-5400.)
- ASTM C 138 - 92. "Test Method for Unit Weight, Yield, and Air Content (Gravimetric) of Concrete," *Annual Book of ASTM Standards, Volume 04.02, Concrete and Aggregates*. Philadelphia, PA: American Society for Testing and Materials. (Available from American Society for Testing and Materials, 1916 Race Street, Philadelphia, PA 19103-1187, 215/299-5400.)
- ASTM C 142 - 78 (1990). "Test Method for Clay Lumps and Friable Particles in Aggregates," *Annual Book of ASTM Standards, Volume 04.02, Concrete and Aggregates*. Philadelphia, PA: American Society for Testing and Materials. (Available from American Society for Testing and Materials, 1916 Race Street, Philadelphia, PA 19103-1187, 215/299-5400.)
- ASTM C 143 - 90a. "Test Method for Slump of Hydraulic Cement Concrete," *Annual Book of ASTM Standards, Volume 04.02, Concrete and Aggregates*. Philadelphia, PA: American Society for Testing and Materials. (Available from American Society for Testing and Materials, 1916 Race Street, Philadelphia, PA 19103-1187, 215/299-5400.)
- ASTM C 150 - 95. "Specification for Portland Cement," *Annual Book of ASTM Standards, Volume 04.01, Cement; Lime; Gypsum*. Philadelphia, PA: American Society for Testing and Materials. (Available from American Society for Testing and Materials, 1916 Race Street, Philadelphia, PA 19103-1187, 215/299-5400.)

- ASTM C 157 - 93. "Test Method for Length Change of Hardened Hydraulic-Cement Mortar and Concrete," *Annual Book of ASTM Standards, Volume 04.02, Concrete and Aggregates*. Philadelphia, PA: American Society for Testing and Materials. (Available from American Society for Testing and Materials, 1916 Race Street, Philadelphia, PA 19103-1187, 215/299-5400.)
- ASTM C 204 - 94a. "Test Method for Fineness of Hydraulic Cement by Air Permeability Apparatus," *Annual Book of ASTM Standards, Volume 04.01, Cement; Lime; Gypsum*. Philadelphia, PA: American Society for Testing and Materials. (Available from American Society for Testing and Materials, 1916 Race Street, Philadelphia, PA 19103-1187, 215/299-5400.)
- ASTM C 231 - 91b. "Test Method for Air Content of Freshly Mixed Concrete by the Pressure Method," *Annual Book of ASTM Standards, Volume 04.02, Concrete and Aggregates*. Philadelphia, PA: American Society for Testing and Materials. (Available from American Society for Testing and Materials, 1916 Race Street, Philadelphia, PA 19103-1187, 215/299-5400.)
- ASTM C 294 - 86 (1991). "Descriptive Nomenclature for Constituents of Natural Mineral Aggregates," *Annual Book of ASTM Standards, Volume 04.02, Concrete and Aggregates*. Philadelphia, PA: American Society for Testing and Materials. (Available from American Society for Testing and Materials, 1916 Race Street, Philadelphia, PA 19103-1187, 215/299-5400.)
- ASTM C 295 - 90. "Guide for Petrographic Examination of Aggregates for Concrete," *Annual Book of ASTM Standards, Volume 04.02, Concrete and Aggregates*. Philadelphia, PA: American Society for Testing and Materials. (Available from American Society for Testing and Materials, 1916 Race Street, Philadelphia, PA 19103-1187, 215/299-5400.)
- ASTM C 311 - 94b. "Test Methods for Sampling and Testing Fly Ash or Natural Pozzolans for Use as a Mineral Admixture in Portland-Cement Concrete," *Annual Book of ASTM Standards, Volume 04.02, Concrete and Aggregates*. Philadelphia, PA: American Society for Testing and Materials. (Available from American Society for Testing and Materials, 1916 Race Street, Philadelphia, PA 19103-1187, 215/299-5400.)
- ASTM C 469 - 94. "Test Method for Static Modulus of Elasticity and Poisson's Ratio of Concrete in Compression," *Annual Book of ASTM Standards, Volume 04.02, Concrete and Aggregates*. Philadelphia, PA: American Society for Testing and Materials. (Available from American Society for Testing and Materials, 1916 Race Street, Philadelphia, PA 19103-1187, 215/299-5400.)
- ASTM C 534 - 94. "Specification for Preformed Flexible Elastomeric Cellular Thermal Insulation in Sheet and Tubular Form," *Annual Book of ASTM Standards, Volume 04.06, Thermal Insulation; Environmental Acoustics*. Philadelphia, PA: American Society for Testing and Materials. (Available from American Society for Testing and Materials, 1916 Race Street, Philadelphia, PA 19103-1187, 215/299-5400.)

- ASTM C 535 - 89. "Test Method for Resistance to Degradation of Large-Size Coarse Aggregate by Abrasion and Impact in the Los Angeles Machine," *Annual Book of ASTM Standards, Volume 04.02, Concrete and Aggregates*. Philadelphia, PA: American Society for Testing and Materials. (Available from American Society for Testing and Materials, 1916 Race Street, Philadelphia, PA 19103-1187, 215/299-5400.)
- ASTM C 566 - 95. "Test Method for Total Moisture Content of Aggregate by Drying," *Annual Book of ASTM Standards, Volume 04.02, Concrete and Aggregates*. Philadelphia, PA: American Society for Testing and Materials. (Available from American Society for Testing and Materials, 1916 Race Street, Philadelphia, PA 19103-1187, 215/299-5400.)
- ASTM C 618 - 95. "Specification for Coal Fly Ash and Raw or Calcined Natural Pozzolan for Use as a Mineral Admixture in Portland Cement Concrete," *Annual Book of ASTM Standards, Volume 04.02, Concrete and Aggregates*. Philadelphia, PA: American Society for Testing and Materials. (Available from American Society for Testing and Materials, 1916 Race Street, Philadelphia, PA 19103-1187, 215/299-5400.)
- ASTM C 845 - 90. "Specification for Expansive Hydraulic Cement," *Annual Book of ASTM Standards, Volume 04.01, Cement; Lime; Gypsum*. Philadelphia, PA: American Society for Testing and Materials. (Available from American Society for Testing and Materials, 1916 Race Street, Philadelphia, PA 19103-1187, 215/299-5400.)
- ASTM C 1064 - 86 (1993). "Test Method for Temperature of Freshly Mixed Portland Cement Concrete," *Annual Book of ASTM Standards, Volume 04.02, Concrete and Aggregates*. Philadelphia, PA: American Society for Testing and Materials. (Available from American Society for Testing and Materials, 1916 Race Street, Philadelphia, PA 19103-1187, 215/299-5400.)
- ASTM C 1077 - 95a. "Practice for Laboratories Testing Concrete and Concrete Aggregates for Use in Construction and Criteria for Laboratory Evaluation," *Annual Book of ASTM Standards, Volume 04.02, Concrete and Aggregates*. Philadelphia, PA: American Society for Testing and Materials. (Available from American Society for Testing and Materials, 1916 Race Street, Philadelphia, PA 19103-1187, 215/299-5400.)
- ASTM D 1556 - 90. "Test Method for Density and Unit Weight of Soil in Place by the Sand-Cone Method," *Annual Book of ASTM Standards, Volume 04.08, Soil and Rock*. Philadelphia, PA: American Society for Testing and Materials. (Available from American Society for Testing and Materials, 1916 Race Street, Philadelphia, PA 19103-1187, 215/299-5400.)
- ASTM D 2167 - 94. "Test Method for Density and Unit Weight of Soil in Place by the Rubber Balloon Method," *Annual Book of ASTM Standards, Volume 04.08, Soil and Rock*. Philadelphia, PA: American Society for Testing and Materials. (Available from American Society for Testing and Materials, 1916 Race Street, Philadelphia, PA 19103-1187, 215/299-5400.)

- ASTM D 2216 - 92. "Test Method for Laboratory Determination of Water (Moisture) Content of Soil and Rock," *Annual Book of ASTM Standards, Volume 04.08, Soil and Rock*. Philadelphia, PA: American Society for Testing and Materials. (Available from American Society for Testing and Materials, 1916 Race Street, Philadelphia, PA 19103-1187, 215/299-5400.)
- ASTM D 2922 - 91. "Test Methods for Density of Soil and Soil-Aggregate in Place by Nuclear Methods (Shallow Depth)," *Annual Book of ASTM Standards, Volume 04.08, Soil and Rock*. Philadelphia, PA: American Society for Testing and Materials. (Available from American Society for Testing and Materials, 1916 Race Street, Philadelphia, PA 19103-1187, 215/299-5400.)
- ASTM D 3017 - 88 (1993). "Test Method for Water Content of Soil and Rock in Place by Nuclear Methods (Shallow Depth)," *Annual Book of ASTM Standards, Volume 04.08, Soil and Rock*. Philadelphia, PA: American Society for Testing and Materials. (Available from American Society for Testing and Materials, 1916 Race Street, Philadelphia, PA 19103-1187, 215/299-5400.)
- ASTM D 4791 - 95. "Test Method for Flat or Elongated Particles in Coarse Aggregate," *Annual Book of ASTM Standards, Volume 04.03, Road and Paving Materials; Pavement Management Technologies*. Philadelphia, PA: American Society for Testing and Materials. (Available from American Society for Testing and Materials, 1916 Race Street, Philadelphia, PA 19103-1187, 215/299-5400.)
- ASTM E 534 - 91. "Test Methods for Chemical Analysis of Sodium Chloride," *Annual Book of ASTM Standards, Volume 15.05, Engine Coolants; Halogenated Organic Solvents; Industrial Chemicals*. Philadelphia, PA: American Society for Testing and Materials. (Available from American Society for Testing and Materials, 1916 Race Street, Philadelphia, PA 19103-1187, 215/299-5400.)
- Brodsky, N.S., F.D. Hansen, and T.W. Pfeifle. 1996. "Properties of Dynamically Compacted WIPP Salt," *4th International Conference on the Mechanical Behavior of Salt, Montreal, Quebec, June 17-18, 1996*. SAND96-0838C. Albuquerque, NM: Sandia National Laboratories. (Copy on file at the Technical Library, Sandia National Laboratories, Albuquerque, NM.)
- Brown, E.R. 1990. "Density of Asphalt Concrete--How Much is Needed?," *Transportation Research Record No. 1282*. Washington, DC: Transportation Research Board. 27-32. (Copy on file in the SWCF.)
- Callahan, G.D., M.C. Loken, L.D. Hurtado, and F.D. Hansen. 1996. "Evaluation of Constitutive Models for Crushed Salt," *4th International Conference on the Mechanical Behavior of Salt, Montreal, Quebec, June 17-18, 1996*. SAND96-0791C. Albuquerque, NM: Sandia National Laboratories. (Copy on file in the SWCF as WPO36449.)

- Cheung, S.C.H., M.N. Gray, and D.A. Dixon. 1987. "Hydraulic and Ionic Diffusion Properties of Bentonite-Sand Buffer Materials," *Coupled Processes Associated with Nuclear Waste Repositories, Proceedings of the International Symposium on Coupled Processes Affecting the Performance of a Nuclear Waste Repository, Berkeley, CA, September 18-20, 1985*. Ed. C-F. Tsang. Orlando, FL: Academic Press, Inc. 383-407. (Copy on file in the SWCF.)
- CRD-C 38 - 73. "Method of Test for Temperature Rise in Concrete," *Handbook for Concrete and Cement*. Vicksburg, MS: U.S. Army Corps of Engineers, Waterways Experiment Station. (Copy on file in the SWCF as WPO39656.)
- DOE (U.S. Department of Energy). 1995. *Waste Isolation Pilot Plant Sealing System Design Report*. DOE/WIPP-95-3117. Carlsbad, NM: U.S. Department of Energy, Waste Isolation Pilot Plant. (Copy on file in the SWCF as WPO29062.)
- EPA (Environmental Protection Agency). 1996a. *Criteria for the Certification and Re-Certification of the Waste Isolation Pilot Plant's Compliance with the 40 CFR Part 191 Disposal Regulations. Response to Comments Document for 40 CFR Part 194*. EPA 402-R-96-001. Washington, DC: Environmental Protection Agency, Office of Radiation and Indoor Air. (Copy on file in the Nuclear Waste Management Library, Sandia National Laboratories, Albuquerque, NM.)
- EPA (Environmental Protection Agency). 1996b. *Criteria for the Certification and Re-Certification of the Waste Isolation Pilot Plant's Compliance with the 40 CFR Part 191 Disposal Regulations. Background Information Document for 40 CFR Part 194*. EPA 402-R-96-002. Washington, DC: Environmental Protection Agency, Office of Radiation and Indoor Air. (Copy on file in the Nuclear Waste Management Library, Sandia National Laboratories, Albuquerque, NM.)
- Freeman, H.D., and R.A. Romine. 1994. *Hanford Permanent Isolation Barrier Program: Asphalt Technology Test Plan*. PNL-9336. Richland, WA: Pacific Northwest Laboratories. (Copy available from National Technical Information Service, 5285 Port Royal Road, Springfield, VA, 22161, 703/487-4650. Order number: DE94013454.)
- Gray, M.N. 1993. *OECD/NEA International Stripa Project. Overview Volume III: Engineered Barriers*. Stockholm, Sweden: SKB, Swedish Nuclear Fuel and Waste Management Company. (Copy on file in the Nuclear Waste Management Library, Sandia National Laboratories, Albuquerque, NM as TD898.2 .G73 1993.)
- Hansen, F.D., and E.H. Ahrens. 1996. "Large-Scale Dynamic Compaction of Natural Salt," *4th International Conference on the Mechanical Behavior of Salt, Montreal, Quebec, June 17-18, 1996*. SAND96-0792C. Albuquerque, NM: Sandia National Laboratories. (Copy on file in the SWCF as WPO39544.)
- IAEA (International Atomic Energy Agency). 1990. *Sealing of Underground Repositories for Radioactive Wastes*. STI/DOC/10/319. Technical Reports Series No. 319. Vienna, Austria: International Atomic Energy Agency; Lanham, MD: Unipub. (Copies on file at the Technical Library, Sandia National Laboratories, Albuquerque, NM and at Centennial Science and Engineering Library, University of New Mexico, Albuquerque, NM.)

- Kjartanson, B.H., N.A. Chandler, A.W.L. Wan, C.L. Kohle, and P.J. Roach. 1992. "Use of a Method Specification for In Situ Compaction of Clay-Based Barrier Materials," *High Level Radioactive Waste Management, Proceedings of the Third International Conference, Las Vegas, NV, April 12-16, 1992*. La Grange Park, IL: American Nuclear Society, Inc.; New York, NY: American Society of Civil Engineers. Vol. 1, 1129-1136. (Copy on file in the SWCF.)
- Knowles, M.K., and C.L. Howard. 1996. "Field and Laboratory Testing of Seal Materials Proposed for the Waste Isolation Pilot Plant," *Proceedings of the Waste Management 1996 Symposium, Tucson, AZ, February 25-29, 1996*. SAND95-2082C. Albuquerque, NM: Sandia National Laboratories. (Copy on file in the SWCF as WPO30945.)
- Mitchell, J.K. 1993. *Fundamentals of Soil Behavior*. 2nd ed. New York, NY: John Wiley & Sons, Inc.
- Myers, D.R., and D.A. Duranceau. 1994. *Prototype Hanford Surface Barrier: Design Basis Document*. BHI-00007, Rev. 00. Richland, WA: Bechtel Hanford, Inc. for the U.S. Department of Energy, Office of Environmental Restoration and Waste Management. (Copy on file at the Nuclear Waste Management Library, Sandia National Laboratories, Albuquerque, NM.)
- Nilsson, J. 1985. "Field Compaction of Bentonite-Based Backfilling," *Engineering Geology*. Vol. 21, no. 3-4, 367-376. (Copy on file in the SWCF.)
- Onofrei, M., M.N. Gray, W.E. Coons, and S.R. Alcorn. 1992. "High Performance Cement-Based Grouts for Use in a Nuclear Waste Disposal Facility," *Waste Management*. Vol. 12, no. 2/3, 133-154. (Copy on file in the SWCF.)
- Pfeifle, T.W., F.D. Hansen, and M.K. Knowles. 1996. "Salt-Saturated Concrete Strength and Permeability," *4th Materials Engineering Conference, ASCE Materials Engineering Division, Washington, DC, November 11-18, 1996*. Albuquerque, NM: Sandia National Laboratories.)
- Pusch, R. 1982. "Mineral-Water Interactions and Their Influence on the Physical Behavior of Highly Compacted Na Bentonite," *Canadian Geotechnical Journal*. Vol. 19, no. 3, 381-387. (Copy on file in the SWCF.)
- Pusch, R., and L. Börgesson. 1989. "Bentonite Sealing of Rock Excavations," *Sealing of Radioactive Waste Repositories, Proceedings of an NEA/CEC Workshop, Braunschweig, Germany, May 22-25, 1989*. EUR 12298. Paris: Organisation for Economic Co-Operation and Development. 297-308. (Copy on file in the SWCF.)
- Pusch, R., M. Gray, F. Huertas, M. Jorda, A. Barbreau, and R. Andre-Jehan. 1989. "Sealing of Radioactive Waste Repositories in Crystalline Rock," *Sealing of Radioactive Waste Repositories, Proceedings of an NEA/CEC Workshop, Braunschweig, Germany, May 22-25, 1989*. EUR 12298. Paris: Organisation for Economic Co-Operation and Development. 214-228. (Copy on file in the SWCF.)

Wakeley, L.D., P.T. Harrington, and F.D. Hansen. 1995. *Variability in Properties of Salado Mass Concrete*. SAND94-1495. Albuquerque, NM: Sandia National Laboratories. (Copy on file in the SWCF as WPO22744.)

Wing, N.R., and G.W. Gee. 1994. "Quest for the Perfect Cap," *Civil Engineering*. Vol. 64, no. 10, 38-41. (Copy on file in the SWCF as WPO21158.)

# **Appendix B**

## **Shaft Sealing Construction Procedures**

### **Appendix B Abstract**

This appendix describes equipment and procedures used to construct the shaft seals as specified in the main report. Existing or reasonably modified construction equipment is specified, standard mining practices are applied, and a general schedule is provided at the end of this appendix. This appendix describes the following activities:

- pre-sealing activities for the sub-surface and surface,
- construction and operation of a multi-deck stage,
- installation of special concrete (sumps, shaft station monoliths, and concrete plugs),
- installation of compacted clay columns,
- emplacement and dynamic compaction of WIPP salt,
- installation of neat asphalt and asphaltic mastic mix,
- grouting of concrete plugs and the country rock behind existing shaft liners,
- removal of portions of the existing shaft liners, and
- emplacement of compacted earthen fill.

Page intentionally blank.

## Contents

B1. INTRODUCTION.....	5
B2. PROJECT MOBILIZATION.....	6
B2.1 Subsurface.....	6
B2.2 Surface.....	6
B2.3 Installation of Utilities.....	7
B3. MULTI-DECK STAGE.....	7
B4. PLACEMENT OF SEALING MATERIALS.....	11
B4.1 Concrete.....	11
B4.1.1 Shaft Station Monolith.....	12
B4.1.2 Concrete-Asphalt Waterstops.....	13
B4.1.3 Concrete Plugs.....	13
B4.2 Clay.....	13
B4.2.1 Salado and Rustler Compacted Clay Column.....	13
B4.3 Asphalt.....	14
B4.3.1 Concrete-Asphalt Waterstops.....	14
B4.3.2 Asphaltic Mastic Mix Column.....	16
B4.4 Compacted Salt Column.....	17
B4.5 Grout.....	19
B4.6 Compacted Earthen Fill.....	22
B4.6.1 Lower Section.....	24
B4.6.2 Upper Section.....	24
B4.7 Schedule.....	24
B5 REFERENCES.....	51

## Figures

Figure B-1. Multi-deck stage illustrating dynamic compaction.....	9
Figure B-2. Multi-deck stage illustrating excavation for asphalt waterstop.....	10
Figure B-3. Typical fibercrete at top of asphalt.....	16
Figure B-4. Drop pattern for 6-m-diameter shaft using a 1.2-m-diameter tamper.....	20
Figure B-5. Plan and section views of downward spin pattern of grout holes.....	21
Figure B-6. Plan and section views of upward spin pattern of grout holes.....	23

Page intentionally blank.

## B1. INTRODUCTION

This appendix describes construction specifications for placement of shaft seal materials. Flexibility is incorporated in construction specifications to facilitate placement of several different material types. Engineering materials used to seal the full length of the shaft include earthen fill, compacted clay, tamped crushed salt, asphalt, concrete, and a combination of concrete and asphalt in concrete-asphalt waterstops. Appendix A of this report provides details of the materials. A full-length shaft seal of this type has never before been constructed; however, application of available technology and equipment, standard construction practices, and common materials provides confidence that the system can be placed to satisfy the design requirements.

A primary feature of the construction specification is development of a work platform from which seal materials are placed. Although the proposed multi-deck stage (galloway) proposed here is engineered specifically for shaft sealing operations, it is similar to stages used for construction of shafts. Inherently flexible, the multi-deck stage facilitates several construction methods required for the various materials specified for the shaft seal system. It provides an assembly of a slickline and header for transport of flowable materials from the surface to the placement horizon. A crane device is attached to the base of the stage to facilitate compaction, and an avenue through the stage provides a means to transport bulk material. It is understood that procedures specified here may change during the tens of years preceding construction as a result of equipment development, additional testing, or design changes. Further, it is acknowledged that the construction methods specified are not the only methods that could place the seal materials successfully.

A few assumptions are made for purposes of evaluating construction activities. These assumptions are not binding, but are included to assist discussion of general operational scenarios. For example, four multi-deck stages are specified, one for each shaft. This specification is based on shaft-sinking experience, which indicates that because of the wear encountered, it is advisable to replace rather than rebuild stages. However, much of the equipment on the multi-deck stage is reused. For scheduling purposes, it is assumed that sealing operations are conducted in two of the four shafts simultaneously. The Air Intake and Exhaust Shafts are sealed first, and the Waste and Salt Handling Shafts are sealed last. With this approach, shaft sealing will require about six and a half years, excluding related work undertaken by the WIPP Operating Contractor. Sealing the shafts sequentially would require approximately eleven and a half years. To facilitate discussion of scheduling and responsibilities, it is assumed that sealing operations will be conducted by a contractor other than the WIPP Operating Contractor.

Years from now, when actual construction begins, it is probable that alternatives may be favored. Therefore, construction procedures note alternative methods in recognition that changes are likely and that the construction strategy is sufficiently robust to accommodate alternatives. This appendix contains both general and very specific information. It begins with a discussion of general mobilization in Section 2. Details of the multi-deck construction stage are provided in Section 3. Section 4 contains descriptions of the construction activities. Information presented here is supplemented by several engineering drawings and sketches contained in Appendix E. The topical information and the level of provided detail substantiate the theory that reliable shaft seal construction is possible using available technology and materials.

## **B2. PROJECT MOBILIZATION**

The duty descriptions that follow are for discussion purposes. The discussions do not presuppose contractual arrangements, but simply identify tasks necessary for shaft seal construction.

### **B2.1 Subsurface**

Prior to initiation of sealing activities, the WIPP Operating Contractor will remove installations and equipment on the repository level. A determination of items removed will be made before construction begins. Such removal would include, but is not limited to, gates and fences at the shaft; equipment such as winches, ventilation fans, pipelines; and communication and power cables. Additionally, the following items will be removed from the shafts:

- cables, counterweights, and sheaves;
- existing waterlines; and
- electrical cables not required for sealing operations.

The following equipment will be stored near the shaft on the repository level by the Sealing Contractor prior to initiation of sealing activities:

- a concrete header, hopper, and pump;
- a concrete pump line to distribute concrete; and
- an auxiliary mine fan and sufficient flexible ventilation tubing to reach work areas required for installation of the shaft station concrete monolith.

The subsurface will be prepared adequately for placement of the shaft station monolith. Determination of other preparatory requirements may be necessary at the time of construction.

### **B2.2 Surface**

The Operating Contractor will remove surface facilities such as headframes, hoists, and buildings to provide clear space for the Sealing Contractor. Utilities required for sealing activities (e.g., air compressors, water, electrical power and communication lines) will be preserved. The Sealing Contractor will establish a site office and facilities required to support the construction crews, including a change house, lamp room, warehouse, maintenance shop, and security provisions. Locations will be selected and foundations constructed for headframes, multi-deck stage winches, man/equipment hoist, and exhaust fan. A drawing in Appendix E (Sketch E-4) depicts a typical headframe and associated surface facilities. The hoist and winches will be enclosed in suitable buildings; utilities and ventilation ducting will be extended to the shaft collar. The large ventilation fan located near the collar is designed to exhaust air through the rigid ventilation duct, resulting in the movement of fresh air down the shaft. Air flow will be sufficient to support eight workers to the depth of the repository level. The following facilities will be procured and positioned near the shaft collar:

- a concrete batch plant capable of weighing, batching, and mixing the concrete to design specifications;
- a crushing and screening plant to process WIPP salt and local soil;

- an insulated and heated pug mill, asphalt pump, asphalt storage tank, and other auxiliary equipment; and
- pads, silos, and structures to protect sealing materials from the weather.

The Sealing Contractor will construct a temporary structural steel bulkhead over the shaft at the surface. The bulkhead will be sufficiently strong to support the weight of the multi-deck stage, which will be constructed on it. When the multi-deck stage is completed, the headframe will be erected. The headframe (depicted in Appendix E, Sketch E-3) will be built around the multi-deck stage, and a mobile crane will be required during fabrication. When the headframe is completed, cables for hoisting and lowering the multi-deck stage will be installed. Cables will run from the three winches, over the sheaves in the headframe, down and under the sheaves on the multi-deck stage, and up to anchors in the headframe. The headframe will be sufficiently high to permit the multi-deck stage to be hoisted until the lowest component is 3.05 m (10 ft) above surface. This will facilitate slinging equipment below the multi-deck stage and lowering it to the work surface, as well as activities required at the collar during asphalt emplacement.

The multi-deck stage will be lowered to clear the collar, allowing the installation of compressed-air-activated steel shaft collar doors, which will serve as a safety device, permitting safe access to the man cage and bucket, while preventing objects from falling down the shaft. Following installation of these doors, workers will utilize the multi-deck stage to traverse the shaft from the collar to the repository horizon, inspecting it for safety hazards and making any necessary repairs. After this inspection, the multi-deck stage will return to the surface.

### **B2.3 Installation of Utilities**

In preparation for placement of shaft seal materials, requisite utilities will be outfitted for operations. The multi-deck stage will descend from the collar to the repository horizon. As added assurance against unwanted water, a gathering system similar to the one currently in place at the bottom of the concrete liner will be installed and moved upward as seal emplacement proceeds. Water collected will be hoisted to the surface for disposal. Additionally, any significant inflow will be located and minimized by grouting. After installation of the water gathering system, the following utilities will be installed from surface to the repository horizon by securely fastening them to the shaft wall:

- 5.1-cm steel waterline with automatic shut-off valves every 60 m;
- 10.2-cm steel compressed-air line;
- power, signal, and communications cables;
- 15.2 cm steel slickline and header; and
- a rigid, cylindrical, ventilation duct, which would range from 107 cm in diameter in the three largest shafts to 91 cm in diameter in the Salt Handling Shaft.

### **B3. MULTI-DECK STAGE**

The multi-deck stage (galloway) provides a work platform from which all sealing operations except placement of asphalt are conducted. The concept of using a multi-deck stage is derived from similar equipment commonly employed during shaft sinking operations. Plan and

section views of conceptual multi-deck stages are shown in Appendix E, Sketches E-1 and E-2. The construction decks specified here are modified from typical shaft sinking configurations in two important ways to facilitate construction. Conceptual illustrations of these two modifications are displayed in Figures B-1 and B-2. Figure B-1 illustrates the multi-deck performing dynamic compaction of salt. Figure B-2 illustrates the multi-deck stage configured for excavation of the kerf required for the asphalt waterstop in Salado salt.

A device called a polar crane mounted below the lower deck can be configured for either dynamic compaction or salt excavation. The crane can rotate 360° horizontally by actuating its geared track drive. Its maximum rotational speed will be approximately two revolutions per minute. The crane can be controlled manually or by computer (computerized control will swiftly position the tamper in the numerous drop positions required for dynamic compaction). When excavation for the concrete-asphalt waterstops is required, the tamper, electromagnet, and cable used for dynamic compaction will be removed, and a custom salt undercutter will be mounted on the polar crane trolley. Geared drives on the crane, trolley, and undercutter will supply the force required for excavation. In addition to the special features noted above and shown in Figures B-1 and B-2, the multi-deck stage has the following equipment and capabilities:

- Maximum hoisting/lowering speed is approximately 4.6 m (15 ft) per minute.
- A cable, electromagnet, and tamper will be attached to the polar crane during dynamic compaction. The cylindrical tamper consists of A-36 carbon steel plates bolted together with high-tensile-strength steel bolts. It is hoisted and dropped by the polar crane using the electromagnet. The tamper will be mechanically secured to the polar crane before personnel are allowed under it.
- Range-finding lasers will facilitate the accurate positioning of the multi-deck stage above the work surface and allow the operator to determine when the surface is sufficiently level. The distance indicated by each laser will be displayed on a monitor at the crane control station.
- Flood lights and remotely controlled closed-circuit television equipment will enable the crane operator to view operations below the multi-deck stage on a monitor.
- Fold-out floor extensions that accommodate the variance in shaft diameter between the unlined and lined portions of the shaft will be provided for safety.
- A cutout in each deck, combined with a removable section of the polar crane track, will permit stage movement without removal of the rigid ventilation duct (which is fastened to the shaft wall).

The multi-deck stage is equipped with many of the features found on conventional shaft sinking stages, such as:

- three independent hoisting/lowering cables,
- man and material conveyances capable of passing through the multi-deck stage and accessing the working surface below,
- a jib crane that can be used to service the working surface below,
- removable safety screens and railings, and
- centering devices.

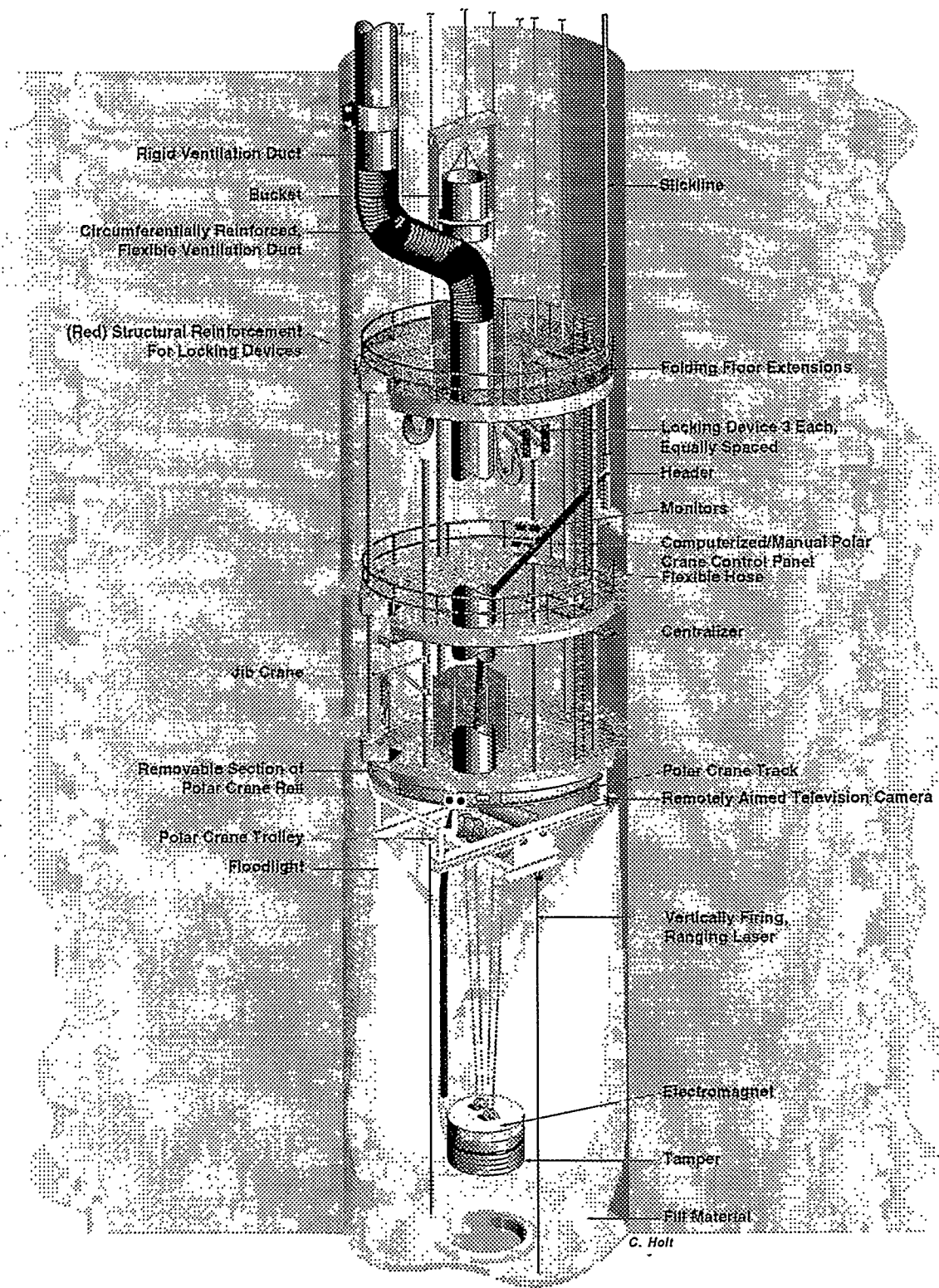


Figure B-1. Multi-deck stage illustrating dynamic compaction.

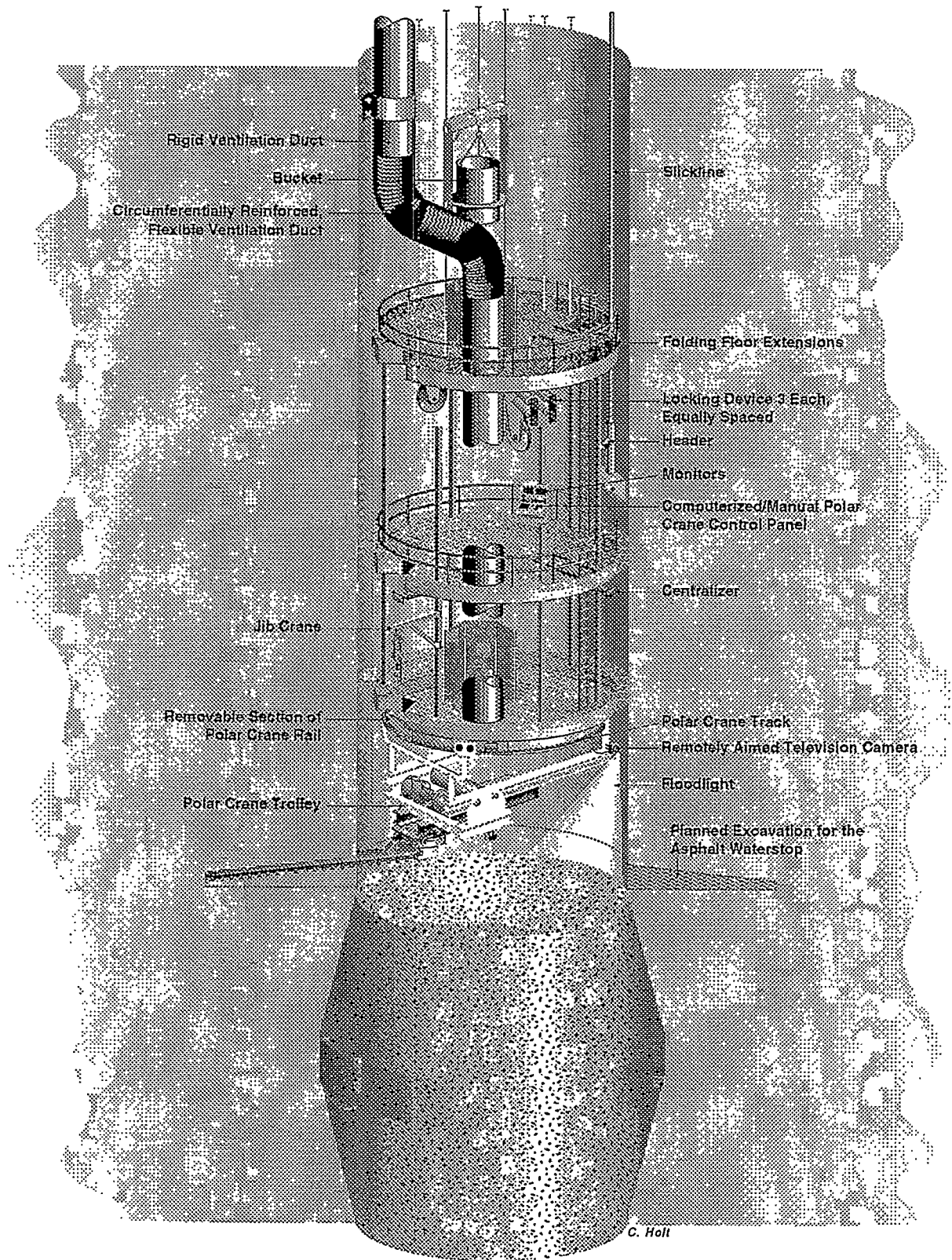


Figure B-2. Multi-deck stage illustrating excavation for asphalt waterstop.

Three sets of double locking devices are provided to secure the multi-deck stage to the shaft wall. A suitable factor of safety for these locking devices is judged to be 4. The area of the grips securing the deck is calculated from static principles:

$$FS = \mu (Co)(A) / W \quad (B-1)$$

where:

$FS$  = factor of safety

$\mu$  = steel/salt friction coefficient = 0.15 (see Table 20.1 in McClintock and Argon, 1966; and Van Sambeek, 1988)

$Co$  = compressive strength of WIPP salt, which varies from 172 kg/cm<sup>2</sup> to 262 kg/cm<sup>2</sup> (Van Sambeek, 1988)

$W$  = total vertical weight

$A$  = total gripper pad surface area.

Manipulating the equation to solve for required area, applying a factor of safety of 4, selecting the heaviest work stage (753,832 kg) and the minimum compressive strength value for salt (assuming that the locking pressure equals the minimum compressive strength of salt), the following gripper surface area ( $A$ ) is:

$$A = 4(753,832 \text{ kg}) / 0.15(172 \text{ kg/cm}^2) = 11,416.5 \text{ cm}^2, \text{ and each of the six gripper pads would be } 1902.8 \text{ cm}^2.$$

As designed, each gripper pad area is 2167.2 cm<sup>2</sup>, resulting in a factor of safety ( $FS$ ) of 4.56. Additionally, although tension in the hoisting cables is relaxed while the multi-deck stage is in the locked configuration, the cables are still available to hold the work-deck, should the locking devices fail.

## B4. PLACEMENT OF SEALING MATERIALS

Construction activities include placement of materials in three basic ways: (1) by slickline (e.g., concrete and asphalt), (2) by compaction (e.g., salt and earthen fill), and (3) by physical placement (e.g., clay blocks). Materials will be placed at various elevations using identical procedures. Because placement procedures generally are identical regardless of elevation, they will be described only once. Where differences occur, they will be identified and described. In general, placement of shaft seal elements is described from bottom to top.

### B4.1 Concrete

Concrete is used as a seal material for several different components, such as the existing sumps in the Salt Handling Shaft and the Waste Shaft, the shaft station monoliths, concrete plugs, and concrete-asphalt waterstops. Existing sumps are shown in Appendix E, Drawings SNL-007, Sheets 6 and 21. Shaft station monoliths are shown in Drawings SNL-007, Sheets 6, 11, 16, and 21. Concrete plugs are depicted on Drawings SNL-007, Sheets 4, 5, 9, 10, 14, 15, 19, and 20. Lower, middle, and upper concrete-asphalt waterstops are shown in Drawing

SNL-007, Sheet 22. Construction material for all concrete members will be Salado Mass Concrete (SMC).

As specified, all SMC will be mixed on surface to produce a product possessing the characteristics defined in Appendix A. Concrete will be transferred to its placement location within the shaft via slickline and header. The slickline (shown in Figure B-1) is a steel pipe fastened to the shaft wall. Vertical drops as great as 656 m to the repository horizon are required. Such concrete transport and construction are common in mining applications. For example, a large copper mine in Arizona is placing concrete at a depth of 797 m using this procedure. A header attached to the bottom of the slickline is designed to absorb kinetic energy generated by the falling material. The header, a steel pipe slightly larger in diameter than the slickline and made of thicker steel, diverts the flow 45°, absorbing most of the impact. Because the drop generates considerable force, the header will be securely supported by a reinforced steel shelf bolted to the shaft wall. A flexible hose, in sections approximately 3 m long and joined by quick-connect fittings, will be attached to the header.

#### **B4.1.1 Shaft Station Monolith**

Construction of the shaft station monoliths is preceded by filling two existing sumps with SMC. Initially, sufficient hose will be used to convey the concrete to the bottom of the sump. The discharge will remain below the concrete surface during placement to minimize air entrainment. Sections of hose will be withdrawn and removed as the SMC rises to the floor of the repository horizon in a continuous pour. Subsequent to filling the sump, arrangements will be made to place the concrete monolith.

A small mine fan will be located above the rigid suction-duct inlet to ensure a fresh air base. Masonry block forms will be constructed at the extremities of the shaft station monolith in the drifts leading from the station. Temporary forms, partially filling the opening, will be erected at the shafts to facilitate the placement of the outermost concrete. These temporary forms will permit access necessary to ensure adequate concrete placement. SMC will be transported via the slickline to the header, which will discharge into a hopper feeding the concrete pump, and the pump will be attached to the pumpcrete line. The pumpcrete line, suspended in cable slings near the back of the drifts, will be extended to the outer forms. A flexible hose, attached to the end of the pumpcrete line, will be used by workers to direct emplacement. The pumpcrete line will be withdrawn as emplacement proceeds toward the shaft.

When the concrete has reached the top of the temporary forms, they will be extended to seal the openings completely, and two 5-cm-diameter polyvinyl chloride (PVC) pipes will be incorporated in the upper portion of each form. Both pipes will be situated in a vertical plane oriented on the long axis of the heading and inclined away from the station at approximately 70° to the horizontal. The upper end of the top pipe will extend to just below the back, and the upper end of the lower pipe will be located just below that of the top pipe. SMC will be injected through the lower pipe until return is obtained from the upper pipe, ensuring that the heading has been filled to the back. The header will then be moved to a position in the shaft above the designed elevation at the top of the shaft station monolith and supported by a bracket bolted to the shaft wall. After the outer concrete has achieved stability, the temporary interior forms may be removed. Equipment no longer required will be slung below the multi-deck stage and hoisted

to surface for storage and later use. The station and shaft will be filled to design elevation with concrete via the slickline, header, and flexible hose. The slickline is cleaned with spherical, neoprene swabs ("pigs") that are pumped through the slickline, header, and hose.

#### **B4.1.2 Concrete-Asphalt Waterstops**

Lower, middle, and upper concrete-asphalt waterstops in a given shaft are identical and consist of two SMC sections separated by an asphalt waterstop. Before the bottom member of the lower concrete component is placed, the multi-deck stage will be raised into the headframe; the polar crane will be mounted below the lower deck; and the salt undercutter will be mounted on the crane trolley. The multi-deck stage will then return to the elevation of the concrete component. Two undercutter bars will be used to make the necessary excavations for upper, middle, and lower asphalt-concrete waterstops and the concrete plug above the Salado Formation. Notches for the plugs will be excavated using a short, rigid cutter bar (length less than half the radius). The kerf for the asphalt waterstop will be excavated using a long cutter bar that can excavate the walls to a depth of one shaft radius. These operations will be conducted as required as seal placement proceeds upward.

The lower concrete member (and all subsequent concrete entities) will be placed via the slickline, header, and flexible hose, using the procedure outlined for the shaft station monolith. Construction of vertical shaft seals provides the ideal situation for minimizing interface permeability between the rock and seal materials. Concrete will flow under its own weight to provide intimate contact. A tight cohesive interface was demonstrated for concrete in the small-scale seal performance tests (SSSPTs). The SSSPT concrete plugs were nearly impermeable without grouting. However, interface grouting is usually performed in similar construction, and it will be done here in the appropriate locations.

#### **B4.1.3 Concrete Plugs**

An SMC plug, keyed into the shaft wall, is situated a few meters above the upper Salado contact in the Rustler Formation. A final SMC plug is located a few meters below surface in the Dewey Lake Redbeds. This plug is emplaced within the existing shaft liner using the same construction technique employed for the concrete-asphalt waterstops.

### **B4.2 Clay**

#### **B4.2.1 Salado and Rustler Compacted Clay Column**

Blocks of sodium bentonite clay, precompacted to a density of 1.8 to 2.0 g/cm<sup>3</sup>, will be the sealing material. This density has been achieved at the WIPP using a compaction pressure of 492.2 kg/cm<sup>2</sup> in a machine designed to produce adobe blocks (Knowles and Howard, 1996). Blocks are envisioned as cubes, 20.8 cm on the edge, weighing approximately 18 kg, a reasonable weight for workers to handle. The bentonite blocks will be compacted at the WIPP in a new custom block-compacting machine and will be stored in controlled humidity to prevent desiccation cracking. Blocks will be transported from surface in the man cage, which will be sized to fit through the circular "bucket hole" in the multi-deck stage. The conveyance will be stacked with blocks to a height of approximately 1.8 m.

Installation will consist of manually stacking individual blocks so that all interfaces are in contact. Block surfaces will be moistened with a spray of potable water as the blocks are placed to initiate a minor amount of swelling, which will ensure a tight fit and a decrease in permeability. Peripheral blocks will be trimmed to fit irregularities in the shaft wall and placed as close to the wall as possible. Trimmed material will be manually removed with a vacuum. Dry bentonite will be manually tamped into remaining voids in each layer of blocks. This procedure will be repeated throughout the clay column. The multi-deck stage will, in all cases, be raised and utilities removed to the surface as emplacement of sealing materials proceeds upward.

Dynamic compaction construction is an alternative method of clay emplacement that could be considered in the detailed design. Dynamic compaction materials being considered are:

- sodium bentonite/fine silica sand, and
- highly compressed bentonite pellets.

Boonsinsuk et al. (1991) developed and tested a dynamic (drop hammer) method for a relatively large diameter (0.5-m) hole, simulated with a steel cylinder, that gave very good results on 1 : 1 dry mass mixtures of sodium bentonite and sand, at a moisture content of 17% to 19%. The alternatives have the advantages of simplifying emplacement.

### **B4.3 Asphalt.**

Asphalt, produced as a distillate of petroleum, is selected as the seal material because of its longevity, extremely low permeability, history of successful use as a shaft lining material, and its ability to heal if deformed. Shielded from ultraviolet radiation and mixed with hydrated lime to inhibit microbial degradation, the longevity of the asphalt will be great. Emplaced by tremie line at the temperature specified, the material will be fluid and self-leveling, ensuring complete contact with the salt.

Construction of an asphalt column using heated asphalt will introduce heat to the surrounding salt. The thermal shock and heat dissipation through the salt has not been studied in detail. Performance of the asphalt column may be enhanced by the introduction of the heat that results from acceleration of creep and healing of microfractures. If, upon further study, the thermomechanical effects are deemed undesirable or if an alternative construction method is preferred at a later date, asphalt can readily be placed as blocks. Asphalt can "cold flow" to fill gaps, or the seams between blocks can be filled with low-viscosity material.

#### **B4.3.1 Concrete-Asphalt Waterstops**

Electrically insulated, steel grated flooring will be constructed over the shaft at the surface. A second, similar flooring will be built in the shaft 3 m below the first. These floors will be used only during the emplacement of asphalt and asphaltic mastic mix (AMM) and will be removed at all other times. A 12.7-cm ID/14-cm OD, 4130 steel pipe (tremie line) in 3-m lengths will be electrically equipped for impedance heating, then insulated and suspended in the shaft from slips (pipe holding devices) situated on the upper floor. The tremie line cross-sectional area is smallest at the shoulder of the top thread, where tensional yield is 50,000 kg; the

line weight is 20.8 kg/m. Heavier weights are routinely suspended in this manner in the petroleum and mining industries.

Neat, AR-4000-graded petroleum-based asphalt cement will be the sealing material for asphalt waterstops. Neat asphalt from the refinery will be delivered to the WIPP at approximately 80°C in conventional, insulated refinery trucks and pumped into a heated and insulated storage tank located near the shaft. The multi-deck stage will be hoisted into the headframe and mechanically secured for safety. Asphalt, heated to 180°C ±5°, will be pumped down the shaft to the fill elevation through the heated tremie line. Viscosity of the neat asphalt for the waterstops will be sufficiently low to allow limited penetration of the DRZ. Installation of asphalt in each of the concrete-waterstops is identical.

As the pipe is lowered, workers on the lower deck will attach the wiring required for heating circuits and apply insulation. Workers on the top deck will install flanged and electrically insulated couplings as required (the opening in the slip bowl will be large enough to permit the passage of these couplings). Properly equipping and lowering the pipe should progress at the rate of one section every 10 minutes. The lower asphalt waterstop requires approximately 607 m of pipe for a casing weight of 12,700 kg. Additionally, electrical wire and insulation will weigh about 7250 kg for a total equipped tremie line weight of 20,000 kg. Therefore, the safety factor for the tremie line is 50,000 kg/20,000 kg, or 2.5.

To minimize air entrainment, the lower end of the tremie line will be immersed as much as 1 m during hot asphalt emplacement. Therefore, the lower 3 m of casing will be left bare (to simplify cleaning when emplacement has been completed).

Initially the tremie line will be lowered until it contacts the concrete plug (immediately underlying the excavation for the waterstop) and then raised approximately 0.3 m. Asphalt emplacement will proceed as follows:

- The impedance heating system will be energized, heating the tremie line to 180°C ±5°, and the asphalt in the storage tank will be heated to approximately 180°C ±5°.
- Heated, neat asphalt will be pumped down the tremie line at a rate approximating 13 L/min. This low rate will ensure that the asphalt flows across the plug from the insertion point, completely filling the excavation and shaft to the design elevation.
- The tremie line will be raised 3 m and cleaned by pumping a neoprene swab through it with air pressure. Impedance heating will be stopped, and the line will be allowed to cool. When cool, the line will be hoisted, stripped, cleaned, disassembled, and stored for future use.

Sealing operations will be suspended until the air temperature at the top of the asphalt has fallen to approximately 50°C for the comfort of the workers when they resume activity at the fill horizon. Temperature will be determined by lowering a remotely read thermometer to an elevation approximately 3 m above the asphalt at the center of the shaft. The temperature of the asphalt at the center of the shaft will be 50°C in about a month, but active ventilation should permit work to resume in about two weeks (see calculations in Appendix D).

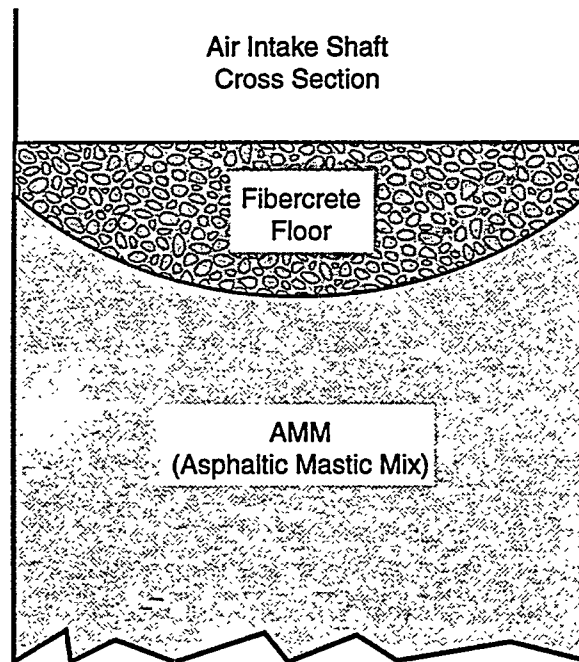
When sufficient cooling has occurred, workers will descend in the multi-deck stage and cover the hot asphalt with an insulating and structural material such as fiber-reinforced shotcrete,

as illustrated in Figure B-3. To accomplish this, they will spray cementitious shotcrete containing fibrillated polypropylene fibers (for added tensional strength), attaining a minimum thickness of approximately 0.6 m.

### B4.3.2 Asphaltic Mastic Mix Column

Asphaltic mastic mix (AMM) for the column will be prepared on surface in a pug mill. Viscosity of the AMM can be tailored to provide desired properties such as limited migration into large fractures.

- AMM will be prepared by mixing the ingredients in the pug mill, which has been heated to  $180^{\circ}\text{C} \pm 5^{\circ}$ . The mix will be pumped from the pug mill through the tremie line to the emplacement depth. AMM is self-leveling at this temperature, and its hydrostatic head will ensure intimate contact with the shaft walls.
- Pumping rate will be approximately 200 L/min for efficiency, because of the larger volume (approximately 1,224,700 L in the Air Intake Shaft). To facilitate efficient emplacement and avoid air entrainment, the tremie line will not be shortened until the mix has filled 6 vertical meters of the shaft. Back pressure (approximately  $0.84 \text{ kg/cm}^2$ ) resulting from 6 m of AMM above the discharge point will be easily overcome from surface by the hydraulic head.



TRI-6121-375-0

Figure B-3. Typical fibercrete at top of asphalt.

After 6 vertical meters of AMM have been placed:

- Impedance heating current will be turned off and locked out (the hot line will drain completely).
- To prevent excessive back pressure resulting from AMM above the insertion point, the line will be disconnected from the pump and hoisted hot. Two sections will be stripped, removed, cleaned with a "pig," and stacked near the shaft.
- Electrical feed will be adjusted (because of the decreased resistance of the shortened line).
- The tremie line will be reconnected to the pump.
- The impedance heating system will be energized.
- When the temperature of the line has stabilized at  $180^{\circ}\text{C} \pm 5^{\circ}$ , pumping will resume.

This procedure will be followed until the entire column, including the volume computed to counteract 0.9 m of vertical shrinkage (calculations in Appendix D), has been placed. The line will be disconnected from the pump and cleaned by pumping "pigs" through it with air pressure. It will then be hoisted, stripped, removed in 3-m sections, and stacked on surface for reuse.

Sealing operations will be suspended following removal of the tremie line, and ventilation will be continuous to speed cooling. The column will shrink vertically but maintain contact with the shaft walls as it cools. When the air temperature at 3 m above the asphalt has cooled sufficiently, workers will descend on the multi-deck stage and cover the hot asphalt with fibercrete as described for the concrete-asphalt waterstop (Section B4.3.1) and illustrated in Figure B-3.

Note: Near the top of the Salado Formation, portions of the concrete liner key, chemical seal rings, and concrete and steel shaft liners will be removed. Liner removal will occur before emplacement of AMM. For safety, exposed rock will be secured with horizontal, radial rock bolts and cyclone steel mesh. A range-finding device, fastened to the shaft wall approximately 3 m above the proposed top of the asphaltic column, will indicate when the hot AMM reaches the desired elevation. A remotely read thermometer, affixed to the shaft wall approximately 2 m above the proposed top of the column, will show when the air temperature has fallen sufficiently to resume operations. The intake of the rigid ventilation duct will be positioned approximately 3 m above the proposed top of the column, and ventilation will be continuous throughout emplacement and cooling of the asphaltic column. After the multi-deck stage has been hoisted into the headframe and mechanically secured for safety, emplacement of AMM will proceed.

#### **B4.4 Compacted Salt Column**

Crushed, mine-run salt, dynamically compacted against intact Salado salt, is the major long-term shaft seal element. As-mined WIPP salt will be crushed and screened to a maximum particle dimension of 5 mm. The salt will be transferred from surface to the fill elevation via the slickline and header. A flexible hose attached to the header will be used to emplace the salt, and a calculated weight of water will be added. After the salt has been nominally leveled, it will be dynamically compacted. Dynamic compaction consists of compacting material by dropping a tamper on it and delivering a specified amount of energy. The application of three times

Modified Procter Energy (MPE) to each lift (one MPE equals 2,700,000 Joules/m<sup>3</sup>) will result in compacting the salt to 90% of the density of in-place rock salt.

Approximately 170 vertical meters of salt will be dynamically compacted. Dynamic compaction was validated in a large-scale demonstration at Sandia National Laboratories during 1995. As-mined WIPP salt was dynamically compacted to 90% density of in-place rock salt in a cylindrical steel chamber simulating the Salt Handling Shaft (Ahrens and Hansen, 1995). Depth of compaction is greater than that achieved by most other methods, allowing the emplacement of thicker lifts. For example, dropping the 4.69 metric ton tamper 18 m (as specified below) results in a compaction depth of approximately 4.6 m, allowing emplacement of lifts 1.5-m high. Most other compaction methods are limited to lifts of 0.3 m or less. Lift thickness will be increased and drop height decreased for the initial lift above the concrete plug at the base of the salt column to ensure that the concrete is not damaged. Drop height for the second and third lifts will be decreased as well. Although the tamper impact is thereby reduced, three MPE will be delivered to the entire salt column.

If lifts are 1.5-m thick, the third lift below the surface will receive additional densification during compaction of overlying lifts, and this phenomenon will proceed up the shaft. Construction will begin by hoisting the multi-deck stage to the surface and attaching the cable, electromagnet, and tamper to the hoist on the polar crane. The multi-deck assembly will be lowered to the placement elevation, and moisture content of the crushed and screened salt will be calibrated. Then the salt will be conveyed at a measured rate via a weighbelt conveyor to a vibrator-equipped hopper overlying the 15.2-cm ID slickline. The salt will pass down the slickline and exit a flexible hose connected to the header. A worker will direct the discharge so that the upper surface of the lift is nominally level and suitable for dynamic compaction. A second worker will add potable water, in the form of a fine spray, to the salt as it exits the hose. Water volume will be electronically controlled and coordinated with the weight of the salt to achieve the desired moisture content.

The initial lift above the SMC will be 4.6 m, and drop height will be 6 m. This increased lift thickness and reduced drop height are specified to protect the underlying SMC plug from damage and/or displacement from tamper impact. Compaction depth for a drop height of 6 m is approximately 3.7 m. Ultimately, the tamper will be dropped six times in each position, resulting in a total of 132 drops per lift in the larger shafts. The drop pattern is shown in Figure B-4. A salt lift 1.5 m high will then be placed and leveled. Following compaction of the initial lift, the multi-deck stage will be positioned so the base of the hoisted tamper is 10 m above the surface of the salt.

The multi-deck stage will then be secured to the shaft walls by activating hydraulically powered locking devices. Hydraulic pressure will be maintained on these units when they are in the locked position; in addition, a mechanical pawl and ratchet on each pair will prevent loosening. The safety factor for the locking devices has been calculated to be approximately 4.5. After locking, tension in the hoisting cables will be relaxed, and centering rams will be activated to level the decks. Prior to positioning the stage, tension will be applied to the hoisting cables; the centering rams will be retracted; and the locking devices will be disengaged.

The work deck will be hoisted until the base of the retracted tamper is 23 m above the surface of the salt, where it will be locked into position and leveled as described above. This

procedure, repeated throughout the salt column, allows emplacement and compaction of three lifts (1.5-m thick) per multi-deck stage move. Depth of compaction for a drop height of 18 m is approximately 4.6 m. Therefore the third lift below the fill surface will receive a total of 9 MPE (274,560 m kg/m<sup>3</sup>), matching the energy applied in the successful, large-scale demonstration.

The compactive effect expands laterally as it proceeds downward from the base of the tamper and will effectively compact the salt into irregularities in the shaft wall, as demonstrated in the large-scale demonstration. Although other techniques could be used, dynamic compaction was selected because it is simple, can be used in the WIPP shafts, and has been demonstrated (Hansen and Ahrens, 1996).

The tamper will be dropped from the hoisted position by turning off the power to the electromagnet. Immediately upon release, the crane operator will "chase" the tamper by lowering the electromagnet at twice hoisting speed; the magnet will engage the tamper, allowing it to be hoisted for the subsequent drop. Initially, the tamper will be dropped in positions that avoid impact craters caused by preceding drops. The surface will then be leveled manually and the tamper dropped in positions omitted during the previous drop series.

Experience gained during the large-scale salt compaction demonstration indicated that a considerable volume of dust is generated during the emplacement of the salt, but not during dynamic compaction. However, because the intake of the rigid vent duct is below the multi-deck stage, workers below the stage will wear respirators during emplacement. They will be the only workers affected by dust during dynamic compaction.

The Air Intake Shaft will require 22 drop positions (Figure B-4). Application of one MPE requires six drops in each position, for a total of 132 drops per lift. Three MPE, a total of 396 drops per lift, will be applied to all salt. After each compaction cycle, the salt surface will be leveled manually and the tamper will be dropped in positions omitted in the preceding drop series. Two lifts, each 1.8 m high, will then be sequentially placed, leveled, and compacted with two MPE, using a 6-m drop height.

Dynamic compaction ensures a tight interface. Salt compacted during the large-scale dynamic compaction demonstration adhered so tenaciously to the smooth interior walls of the steel compaction chamber that grinders with stiff wire wheels were required for its removal.

#### **B4.5 Grout**

Ultrafine sulfate-resistant cementitious grout (Ahrens et al., 1996) is selected as the sealing material. Specifically developed for use at the WIPP, and successfully demonstrated in an in situ test, the hardened grout has a permeability of  $1 \times 10^{-21}$  m<sup>2</sup>. It has the ability to penetrate fractures smaller than 6-microns and is being used for the following purposes:

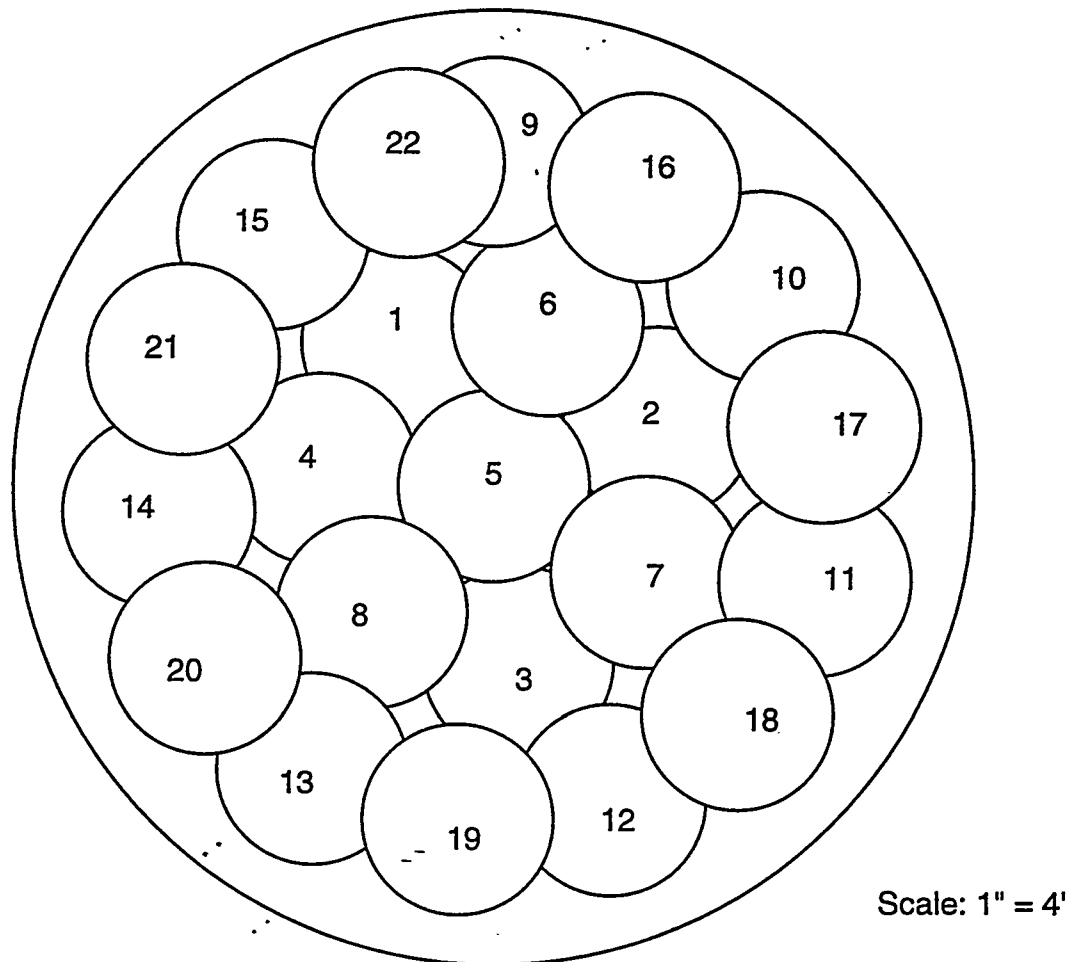
- to seal many of the microfractures in the DRZ and ensure a tight interface between SMC and the enclosing rock, and
- to solidify fractured rock behind existing concrete shaft liners, prior to removal of the liner (for worker safety).

The interface between concrete plugs in the Salado Formation (and one in the Rustler Formation, a short distance above the Salado) will be grouted. A 45° downward-opening cone of

reverse circulation diamond drill holes will be collared in the top of the plugs, drilled in a spin pattern (see Figure B-5), and stage grouted with ultrafine cementitious grout at  $3.5 \text{ kg/cm}^2$  below lithostatic pressure. Stage grouting consists of:

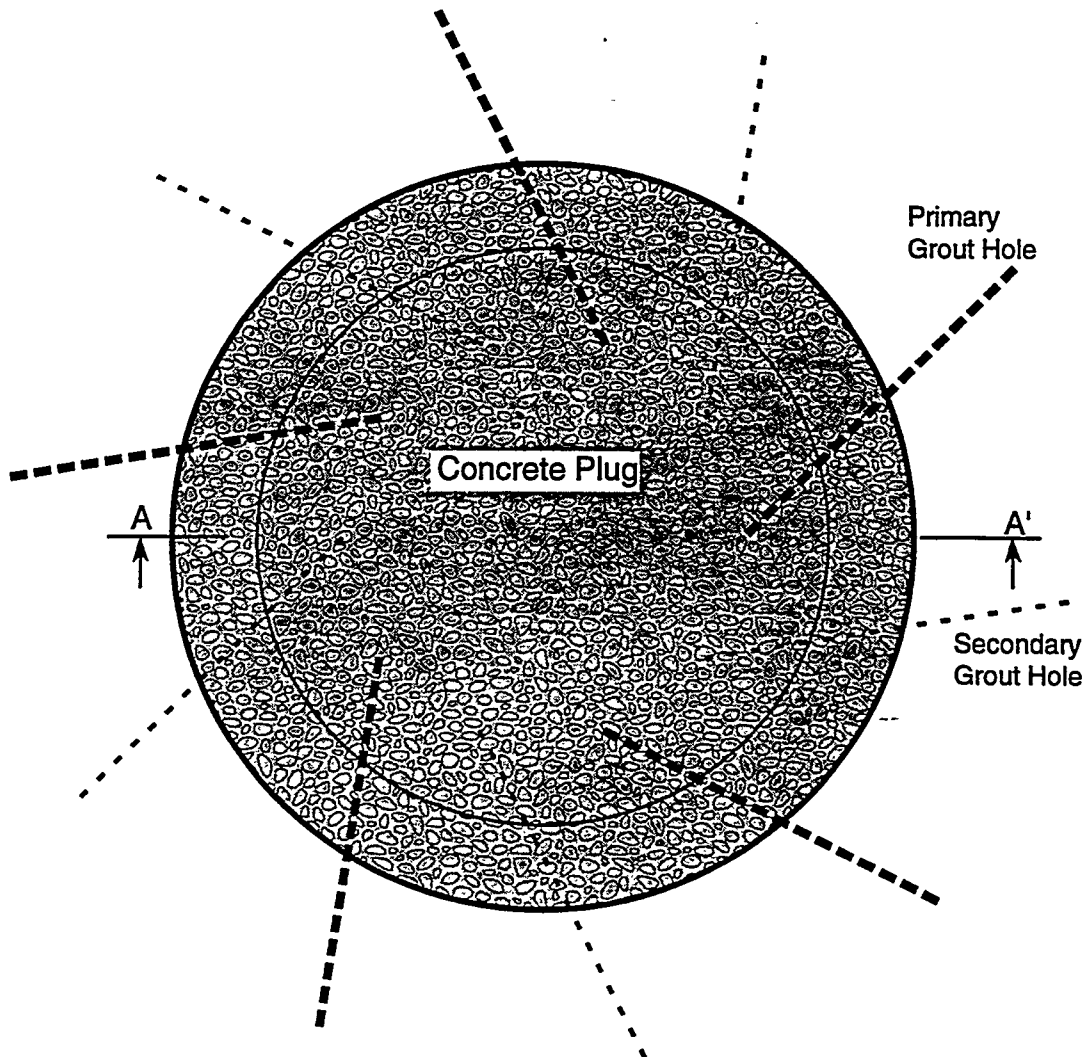
- drilling and grouting primary holes, one at a time;
- drilling and grouting secondary holes, one at a time, on either side of the primary holes that accepted grout; and
- (if necessary) drilling and grouting tertiary holes on either side of secondary holes that accepted grout.

Note: For safety, all liner removal tasks will be accomplished from the bottom deck. In areas where the steel liner is removed, it will be cut into manageable pieces with a cutting torch and hoisted to the surface for disposal. Mechanical methods will be employed to clean and roughen the existing concrete shaft liner before placing the Dewey Lake SMC plug in the shafts.

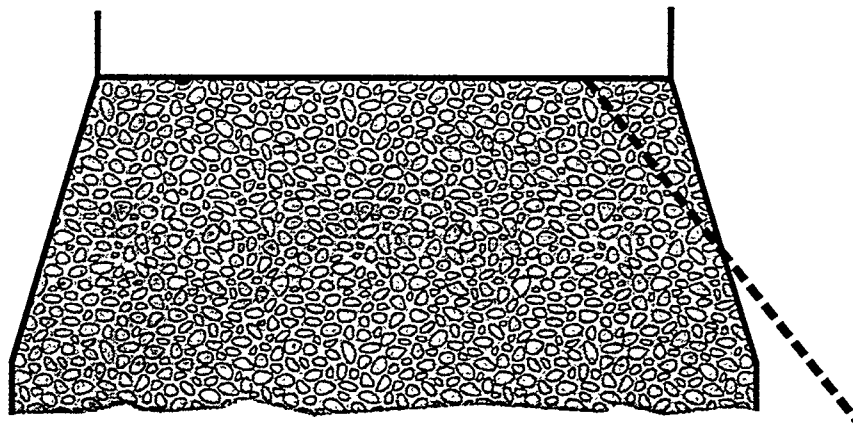


TRI-6121-376-0

Figure B-4. Drop pattern for 6-m-diameter shaft using a 1.2-m-diameter tamper.



Plan View of Grout Holes in Spin Pattern



Section A - A'

TRI-6121-373-0

Figure B-5. Plan and section views of downward spin pattern of grout holes.

The work sequence will start 3 m below the lower elevation of liner removal. A 45° upward-opening cone of grout injection holes, drilled in a "spin" pattern (Figure B-6), will be drilled to a depth subtending one shaft radius on a horizontal plane. These holes will be stage grouted as described in Section 4.5. Noncoring, reverse circulation, diamond drill equipment will be used to avoid plugging fractures with fine-grained diamond drill cuttings. Ultrafine cementitious grout will be mixed on the surface, transferred via the slickline to the upper deck of the multi-deck stage, and injected at 3.5 kg/cm<sup>2</sup> gage below lithostatic pressure to avoid hydrofracturing the rock. Grout will be transferred in batches, and after each transfer, a "pig" will be pumped through the slickline and header to clean them. Grouting will proceed upward from the lowest fan to the highest. Recent studies conducted in the Air Intake Shaft (Dale and Hurtado, 1996) show that this hole depth exceeds that required for complete penetration of the Disturbed Rock Zone (DRZ). Maximum horizontal spacing at the ends of the holes will be 3 m.

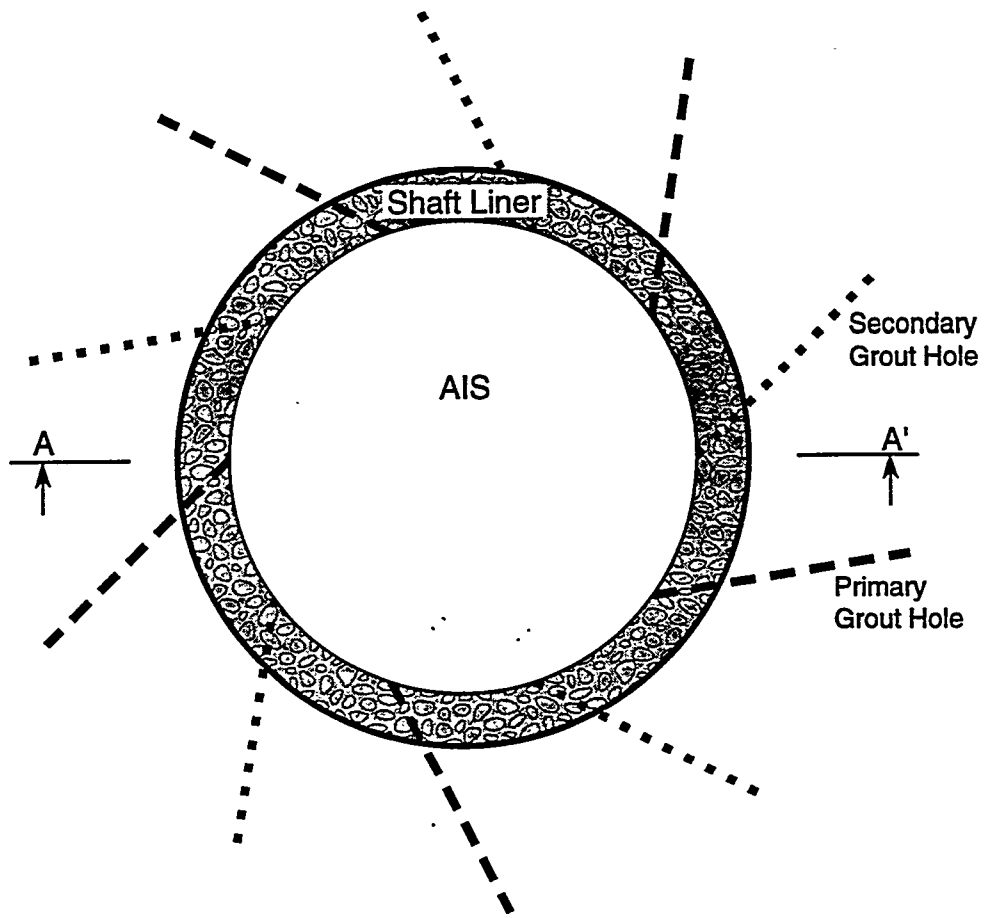
The multi-deck stage will then be raised 3 m and a second fan, identical to the first, will be drilled and grouted. This procedure will continue, with grout fans 3 m apart vertically, until the highest fan, located 3 m above the highest point of liner removal, has been drilled and grouted. Ultrafine cementitious grout was observed to penetrate more than 2 m in the underground grouting experiment conducted at the WIPP in Room L-3 (Ahrens and Onofrei, 1996).

When grouting is completed, the multi-deck stage will be lowered to the bottom of the liner removal section and a hole will be made through the concrete liner. This hole, approximately 30 cm in diameter, will serve as "free-face" to which the liner will be broken. Similar establishment and utilization of free face is a common practice in hard rock mining (e.g., the central drill hole in a series drilled into the rock to be blasted is left empty and used as free-face to which explosives in adjacent holes break the rock). Radial, horizontal percussion holes will be drilled on a 30-cm grid (or less, if required), covering the liner to be removed. Hydraulic wedges, activated in these holes, will then break out the liner, starting adjacent to the free face and progressing away from it, from the bottom up. Broken fragments of the concrete liner will fall to the fill surface below.

A mucking "claw," suspended from the trolley of the polar crane, will collect the broken concrete and place it in the bucket for removal to the surface. As many as three buckets can be used to speed this work.

#### **B4.6 Compacted Earthen Fill**

Local soil, screened to a maximum particle dimension of 13 mm, will be placed and compacted to inhibit the migration of surficial water into the shaft cross section. Such movement is further decreased by a 12-m high SMC plug at the top of the Dewey Lake Redbeds.



Plan View of Grout Holes in Spin Pattern



Section A - A'

TRI-6121-374-0

Figure B-6. Plan and section views of upward spin pattern of grout holes.

#### **B4.6.1 Lower Section**

Emplacement of the compacted earthen fill will proceed as follows:

- Moisture content of the screened soil will be determined.
- The soil will then be transferred via the slickline, header, and flexible hose from surface to the fill elevation. The moisture content optimal for compaction will be achieved using the same procedure as described for compacted salt (Section B4.4). The soil will be emplaced in lifts 1.2 m high (depth of compaction is approximately 3.7 m) and dynamically compacted using a drop height of 18.3 m.
- The fill will be dynamically compacted until its hydraulic conductivity to water is nominally equivalent to that of the surrounding formation.

This procedure will continue until the lower section has been emplaced and compacted. Care will be exercised at the top of the column to ensure that all soil receives sufficient compaction.

#### **B4.6.2 Upper Section**

The upper section contains insufficient room to employ dynamic compaction. Therefore the screened soil, emplaced as described above, will be compacted by vibratory-impact sheepsfoot roller, vibratory sheepsfoot roller, or a walk-behind vibratory-plate compactor. Because of the limited compaction depth of this equipment, lifts will be 0.3 m high. The top of the fill will be coordinated with the WIPP Operating Contractor to accommodate plans for decommissioning surface facilities and placing markers.

#### **B4.7 Schedule**

Preliminary construction schedules are included on the following pages. The first schedule is a concise outline of the total construction schedule. It is followed by individual schedules for each shaft. The first schedule in each shaft series is a truncated schedule showing the major milestones. The truncated schedules are followed by detailed construction schedules for each shaft. These schedules indicate that it will take approximately six and a half years to complete the shaft sealing operations, assuming two shafts are simultaneously sealed.

**SEALING SCHEDULE--ALL SHAFTS**



**SEALING SCHEDULE--AIR INTAKE SHAFT**

B-28

ID	Task Name	Duration	Year 1				Year 2				Year 3				Qtr 1			
			Qtr 1	Qtr 2	Qtr 3	Qtr 4	Qtr 1	Qtr 2	Qtr 3	Qtr 4	Qtr 1	Qtr 2	Qtr 3	Qtr 4				
1	Mobilization	4w	■															
3	Plant Set-up	12w	■	■														
5	Inspect & Scale Shaft-2151'	1w			■													
7	Install Construction Utilities	7.17w		■														
9	Drill & Grout Lining	11.5w			■	■												
11	Shaft Station Monolith-37'	4.78w				■												
15	Lower Salado Compacted Clay Column-93.5'	4.96w					■											
17	Lower Concrete-Asphalt Waterstop-50'	8.25w						■										
26	Compacted Salt Column-563.5'	23.58w						■	■									
28	Middle Concrete-Asphalt Waterstop-50'	8.25w							■									
37	Upper Salado Compacted Clay Column-344'	18.24w								■	■							
39	Upper Concrete-Asphalt Waterstop-50'	10.25w									■	■						
48	Asphalt Column-138.3'	19.41w										■	■					
56	Concrete Plug-20'	5.99w											■					
61	Remove Concrete Shaft Lining	5.71w												■				
63	Rustler Compacted Clay Column-234.7'	8.36w													■			
65	Compacted Earthen Fill-473'	7.59w														■		
67	Concrete Plug-40'	2.96w															■	
71	Compacted Earthen Fill-57'	0.65w																■
73	Demobilization	3.2w																■

Project: AIR INTAKE SHAFT SEALING SCHEDULE Date: Tue 7/9/96	Task	■	Summary	■	Rolled Up Progress	■
	Progress	■	Rolled Up Task			
	Milestone		Rolled Up Milestone	◇		

B-29

ID	Task Name	Duration	Year 1				Year 2				Year 3			
			Qtr 1	Qtr 2	Qtr 3	Qtr 4	Qtr 1	Qtr 2	Qtr 3	Qtr 4	Qtr 1	Qtr 2	Qtr 3	Qtr 4
1	Mobilization	4w	█											
2	Mobilize	4w	█											
3	Plant Set-up	12w	██████											
4	Plant Set-up	12w	██████											
5	Inspect & Scale Shaft-2151'	1w		█										
6	Inspect & Scale Shaft	1w		█										
7	Install Construction Utilities	7.17w		██████										
8	Install Utilities	7.17w		██████										
9	Drill & Grout Lining	11.5w			██████									
10	Drill & Grout Lining	11.5w			██████									
11	Shaft Station Monolith-37'	4.78w				█								
12	Construct Bulkheads	0.8w				█								
13	Pour Concrete (37' high)	0.98w				█								
14	Cure Concrete	3w				█								
15	Lower Salado Compacted Clay Column-93.5'	4.96w					█							
16	Emplace Bentonite Blocks (93.5' high)	4.96w					█							
17	Lower Concrete-Asphalt Waterstop-50'	8.25w						█						
18	Excavate for Lower Plug	1.67w						█						
19	Pour Concrete-Lower Plug (23' high typ.)	0.28w						█						
20	Excavate Waterstop	0.63w						█						
21	Place Asphalt (4' high typ.)	0.72w						█						
22	Cool-down Asphalt	1w						█						

Project: AIR INTAKE SHAFT  
SEALING SCHEDULE  
Date: Tue 7/9/96

Task ██████████  
Progress ██████████  
Milestone

Summary ██████████  
Rolled Up Progress ██████████  
Rolled Up Task  
Rolled Up Milestone ◇

B-30

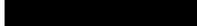
ID	Task Name	Duration	Year 1				Year 2				Year 3				
			Qtr 1	Qtr 2	Qtr 3	Qtr 4	Qtr 1	Qtr 2	Qtr 3	Qtr 4	Qtr 1	Qtr 2	Qtr 3	Qtr 4	Qtr 1
23	Excavate for Upper Plug	1.67w													
24	Pour Concrete-Upper Plug (23' high typ.)	0.28w													
25	Cure Concrete	2w													
26	Compacted Salt Column-563.5'	23.58w					■	■	■	■					
27	Emplace & Compact Crushed/Screened Salt	23.58w					■	■	■	■					
28	Middle Concrete-Asphalt Waterstop-50'	8.25w													
29	Excavate for Lower Plug	1.67w													
30	Pour Concrete-Lower Plug	0.28w													
31	Excavate Waterstop	0.63w													
32	Place Asphalt	0.72w													
33	Cool-down Asphalt	1w													
34	Excavate for Upper Plug	1.67w													
35	Pour Concrete-Upper Plug	0.28w													
36	Cure Concrete	2w													
37	Upper Salado Compacted Clay Column-344'	18.24w													
38	Emplace Bentonite Blocks	18.24w													
39	Upper Concrete-Asphalt Waterstop-50'	10.25w													
40	Excavate for Lower Plug	1.67w													
41	Pour Concrete-Lower Plug	0.28w													
42	Excavate Waterstop	0.63w													
43	Place Asphalt	0.72w													
44	Cool-down Asphalt	1w													

Project: AIR INTAKE SHAFT  
SEALING SCHEDULE  
Date: Tue 7/9/96

Task  Summary  Rolled Up Progress   
 Progress  Rolled Up Task  
 Milestone  Rolled Up Milestone

B-31

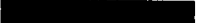
ID	Task Name	Duration	Year 1				Year 2				Year 3				Qtr 1
			Qtr 1	Qtr 2	Qtr 3	Qtr 4	Qtr 1	Qtr 2	Qtr 3	Qtr 4	Qtr 1	Qtr 2	Qtr 3	Qtr 4	
45	Excavate for Upper Plug	1.67w													
46	Pour Concrete-Upper Plug	0.28w													
47	Cure Concrete	4w													
48	Asphalt Column-138.3'	19.41w													
49	Remove Lining in Key	3.76w													
50	Remove Chemical Seal Rings	0.6w													
51	Mobilize to Emplace Asphalt	0.3w													
52	Asphalt in Salt Section	3.62w													
53	Asphalt in Lower Lined Section	1.93w													
54	Complete Asphalt Emplacement	2.77w													
55	Cool-down Asphalt	6.43w													
56	Concrete Plug-20'	5.99w													
57	Remove Concrete Lining & Rock	1.65w													
58	Remove Liner Plate	0.13w													
59	Pour Concrete(20' high)	0.21w													
60	Cure Concrete	4w													
61	Remove Concrete Shaft Lining	5.71w													
62	Remove 86' of lining--4 zones	5.71w													
63	Rustler Compacted Clay Column-234.7'	8.36w													
64	Emplace & Compact Bentonite(234.7' high)	8.36w													
65	Compacted Earthen Fill-473'	7.59w													
66	Emplace & Compact Earthen Fill(473' high)	7.59w													

<b>Project: AIR INTAKE SHAFT SEALING SCHEDULE</b> Date: Tue 7/9/96	<b>Task</b> 	<b>Summary</b> 	<b>Rolled Up Progress</b> 
	<b>Progress</b> 	<b>Rolled Up Task</b>	
	<b>Milestone</b>	<b>Rolled Up Milestone</b> 	

B-32

ID	Task Name	Duration	Year 1				Year 2				Year 3				
			Qtr 1	Qtr 2	Qtr 3	Qtr 4	Qtr 1	Qtr 2	Qtr 3	Qtr 4	Qtr 1	Qtr 2	Qtr 3	Qtr 4	Qtr 1
67	Concrete Plug-40'	2.96w													
68	Clean Existing Surface	0.6w													
69	Pour Concrete(40' high)	0.36w													
70	Cure Concrete	2w													
71	Compacted Earthen Fill-57'	0.65w													
72	Emplace & Compact Earthen Fill (57' high)	0.65w													
73	Demobilization	3.2w													
74	Demob	3.2w													

Project: AIR INTAKE SHAFT  
SEALING SCHEDULE  
Date: Tue 7/9/96

Task  Summary  Rolled Up Progress   
 Progress  Rolled Up Task  
 Milestone  Rolled Up Milestone 

**SEALING SCHEDULE--SALT HANDLING SHAFT**

B-34

ID	Task Name	Duration	Year 1				Year 2				Qtr 1		
			Qtr 1	Qtr 2	Qtr 3	Qtr 4	Qtr 1	Qtr 2	Qtr 3	Qtr 4			
1	Mobilization	4w	█										
3	Plant Set-up	12w	██████████										
5	Inspect & Scale Shaft-2164.5'	1.06w		█									
7	Install Construction Utilities	7.6w		██████									
9	Drill & Grout Lining	5.35w			█								
12	Shaft Station Monolith-37'	4.44w			█								
16	Lower Salado Compacted Clay Column-107'	3.06w			█								
18	Lower Concrete-Asphalt Waterstop-50'	8.74w				██████							
27	Compacted Salt Column-560'	12.67w					██████████						
29	Middle Concrete-Asphalt Waterstop-50'	6.74w						█					
38	Upper Salado Compacted Clay Column-335'	9.58w							██████				
40	Upper Concrete-Asphalt Waterstop-50'	8.74w								██████			
49	Asphalt Column-140'	15.33w									██████████		
57	Concrete Plug-20'	5.32w										█	
61	Remove Concrete Shaft Lining	1.9w											█
63	Rustler Compacted Clay Column-234'	4.81w											█
65	Compacted Earthen Fill-449'	3.65w											█
67	Concrete Plug-40'	2.45w											█
71	Compacted Earthen Fill-92.5'	0.65w											█
73	Demobilization	3w											█

Project: SALT HANDLING SHAFT SEALING SCHEDULE Date: Tue 7/9/96	Task	██████████	Summary	██████████	Rolled Up Progress	██████████
	Progress	██████████	Rolled Up Task			
	Milestone		Rolled Up Milestone	◇		

B-35

ID	Task Name	Duration	Year 1				Year 2				Qtr 1	
			Qtr 1	Qtr 2	Qtr 3	Qtr 4	Qtr 1	Qtr 2	Qtr 3	Qtr 4		
1	Mobilization	4w	■									
2	Mobilize	4w	■									
3	Plant Set-up	12w	■	■								
4	Plant Set-up	12w	■	■								
5	Inspect & Scale Shaft-2164.5'	1.06w										
6	Inspect & Scale Shaft	1.06w										
7	Install Construction Utilities	7.6w		■								
8	Install Utilities	7.6w		■								
9	Drill & Grout Lining	5.35w			■							
10	Drill Grout Holes	2.14w			■							
11	Grout Lining	3.21w			■							
12	Shaft Station Monolith-37'	4.44w			■							
13	Construct Bulkheads	0.8w			■							
14	Pour Concrete (37' high)	0.64w			■							
15	Cure Concrete	3w			■							
16	Lower Salado Compacted Clay Column-107'	3.06w			■							
17	Eplace Bentonite Blocks (107.0' high)	3.06w			■							
18	Lower Concrete-Asphalt Waterstop-50'	8.74w			■	■						
19	Excavate for Lower Plug	1.38w			■							
20	Pour Concrete-Lower Plug (23' high-ty)	0.17w			■							
21	Excavate Waterstop	0.34w			■							
22	Place Asphalt (4' high-ty)	0.3w			■							

<b>Project: SALT HANDLING SHAFT SEALING SCHEDULE</b> <b>Date: Tue 7/9/96</b>	<b>Task</b> ■■■■■	<b>Summary</b> ■■■■■	<b>Rolled Up Progress</b> ■■■■■
	<b>Progress</b> ■■■■■	<b>Rolled Up Task</b>	
	<b>Milestone</b>	<b>Rolled Up Milestone</b> ◇	

B-36

ID	Task Name	Duration	Year 1				Year 2				Qtr 1
			Qtr 1	Qtr 2	Qtr 3	Qtr 4	Qtr 1	Qtr 2	Qtr 3	Qtr 4	
23	Cool-down Asphalt	1w									
24	Excavate for Upper Plug	1.38w									
25	Pour Concrete-Upper Plug (23' high-ty)	0.17w									
26	Cure Concrete	4w									
27	Compacted Salt Column-560'	12.67w									
28	Emplace & Compact Crushed/Screened Salt	12.67w									
29	Middle Concrete-Asphalt Waterstop-50'	6.74w									
30	Excavate for Lower Plug	1.38w									
31	Pour Concrete-Lower Plug	0.17w									
32	Excavate Waterstop	0.34w									
33	Place Asphalt	0.3w									
34	Cool-down Asphalt	1w									
35	Excavate for Upper Plug	1.38w									
36	Pour Concrete-Upper Plug	0.17w									
37	Cure Concrete	2w									
38	Upper Salado Compacted Clay Column-335'	9.58w									
39	Emplace Bentonite Blocks	9.58w									
40	Upper Concrete-Asphalt Waterstop-50'	8.74w									
41	Excavate for Lower Plug	1.38w									
42	Pour Concrete-Lower Plug	0.17w									
43	Excavate Waterstop	0.34w									
44	Place Asphalt	0.3w									

Project: SALT HANDLING SHAFT SEALING SCHEDULE Date: Tue 7/9/96	Task		Summary		Rolled Up Progress	
	Progress		Rolled Up Task			
	Milestone		Rolled Up Milestone			

B-37

ID	Task Name	Duration	Year 1				Year 2				Qtr 1
			Qtr 1	Qtr 2	Qtr 3	Qtr 4	Qtr 1	Qtr 2	Qtr 3	Qtr 4	
45	Cool-down Asphalt	1w									
46	Excavate for Upper Plug	1.38w									
47	Pour Concrete-Upper Plug	0.17w									
48	Cure Concrete	4w									
49	Asphalt Column-140'	15.33w									
50	Remove Lining in Key	2.02w									
51	Remove Chemical Seal Rings	0.4w									
52	Mobilize to emplace asphalt	2w									
53	Asphalt in Salt Section	2.73w									
54	Asphalt in Lower Lined Section	0.25w									
55	Complete Asphalt Emplacement	1.5w									
56	Cool-down Asphalt	6.43w									
57	Concrete Plug-20'	5.32w									
58	Remove Concrete Lining & Rock	1.11w									
59	Pour Concrete (20' high)	0.21w									
60	Cure Concrete	4w									
61	Remove Concrete Shaft Lining	1.9w									
62	Remove 72' of lining-4 zones	1.9w									
63	Rustler Compacted Clay Column-234'	4.81w									
64	Emplace & Compact Bentonite (234' high)	4.81w									
65	Compacted Earthen Fill-449'	3.65w									
66	Emplace & Compact Earthen Fill (449' high)	3.65w									

<b>Project: SALT HANDLING SHAFT SEALING SCHEDULE</b> Date: Tue 7/9/96	Task	██████████	Summary	██████████	Rolled Up Progress	██████████
	Progress	██████████	Rolled Up Task			
	Milestone		Rolled Up Milestone	◇		

ID	Task Name	Duration	Year 1				Year 2				Qtr 1	
			Qtr 1	Qtr 2	Qtr 3	Qtr 4	Qtr 1	Qtr 2	Qtr 3	Qtr 4		
67	Concrete Plug-40'	2.45w										
68	Clean Existing Surface	0.34w										■
69	Pour Concrete	0.11w										
70	Cure Concrete	2w										
71	Compacted Earthen Fill-92.5'	0.65w										■
72	Emplace & Compact Earthen Fill (92.5'high)	0.65w										
73	Demoblization	3w										■
74	Demob	3w										■

B-38

Project: SALT HANDLING SHAFT  
SEALING SCHEDULE  
Date: Tue 7/9/96

Task   
Progress   
Milestone

Summary   
Rolled Up Task  
Rolled Up Milestone 

Rolled Up Progress 

**SEALING SCHEDULE--EXHAUST SHAFT**

B-40

ID	Task Name	Duration	Year 1				Year 2				Year 3		
			Qtr 1	Qtr 2	Qtr 3	Qtr 4	Qtr 1	Qtr 2	Qtr 3	Qtr 4	Qtr 1	Qtr 2	
1	Mobilization	4w	█										
3	Plant Set-up	12w	█	█									
5	Inspect & Scale Shaft-2159.5'	1w		█									
7	Install Construction Utilities	7.2w		█									
9	Drill & Grout Lining	8.26w			█	█							
12	Shaft Station Monolith-33'	3.69w				█							
16	Lower Salado Compacted Clay Column-98'	3.18w					█						
18	Lower Concrete-Asphalt Waterstop-50'	9.19w					█						
27	Compacted Salt Column-559'	14.37w						█					
29	Middle Concrete-Asphalt Waterstop-50'	7.19w							█				
38	Upper Salado Compacted Clay Column-340'	11.01w								█			
40	Upper Concrete-Asphalt Waterstop-50'	9.19w									█		
49	Asphalt Column-142.5'	18.43w										█	
57	Concrete Plug-20'	5.87w											█
61	Remove Concrete Shaft Lining	3.23w											█
63	Rustler Compacted Clay Column-234.5'	6.62w											█
65	Compacted Earthen Fill-486.4'	5.44w											█
67	Concrete Plug-40'	2.69w											█
71	Compacted Earthen Fill-56.1'	0.44w											█
73	Demobilization	3w											█

Project: EXHAUST SHAFT SEALING SCHEDULE Date: Tue 7/9/96	Task	█	Summary	█	Rolled Up Progress	█
	Progress	█	Rolled Up Task			
	Milestone		Rolled Up Milestone	◇		

B-41

ID	Task Name	Duration	Year 1				Year 2				Year 3		
			Qtr 1	Qtr 2	Qtr 3	Qtr 4	Qtr 1	Qtr 2	Qtr 3	Qtr 4	Qtr 1	Qtr 2	
1	Mobilization	4w	■										
2	Mobilize	4w	■										
3	Plant Set-up	12w	■	■									
4	Plant Set-up	12w	■	■									
5	Inspect & Scale Shaft-2159.5'	1w			■								
6	Inspect & Scale Shaft	1w			■								
7	Install Construction Utilities	7.2w		■	■								
8	Install Utilities	7.2w		■	■								
9	Drill & Grout Lining	8.26w			■	■							
10	Drill Grout Holes	3.3w			■								
11	Grout Lining	4.96w			■	■							
12	Shaft Station Monolith-33'	3.69w				■							
13	Construct Bulkheads	0.4w				■							
14	Pour Concrete (33' high)	0.29w				■							
15	Cure Concrete	3w				■							
16	Lower Salado Compacted Clay Column-98'	3.18w				■							
17	Emplace Bentonite Blocks (98' high)	3.18w				■							
18	Lower Concrete-Asphalt Waterstop-50'	9.19w					■	■					
19	Excavate for Lower Plug	1.45w					■						
20	Pour Concrete-Lower Plug (23' high-tp)	0.22w					■						
21	Excavate Waterstop	0.47w					■						
22	Place Asphalt (4' high-tp)	0.38w					■						

Project: EXHAUST SHAFT SEALING SCHEDULE Date: Tue 7/9/96	Task	■	Summary	■	Rolled Up Progress	■
	Progress	■	Rolled Up Task			
	Milestone		Rolled Up Milestone	◇		

B-42

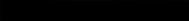
ID	Task Name	Duration	Year 1				Year 2				Year 3		
			Qtr 1	Qtr 2	Qtr 3	Qtr 4	Qtr 1	Qtr 2	Qtr 3	Qtr 4	Qtr 1	Qtr 2	
23	Cool-down Asphalt	1w				■							
24	Excavate for Upper Plug	1.45w				■							
25	Pour Concrete-Upper Plug (23' high-ty)	0.22w											
26	Cure Concrete	4w				■							
27	Compacted Salt Column-559'	14.37w				■	■	■	■	■			
28	Emplace & Compact Crushed/Screened Salt	14.37w				■	■	■	■	■			
29	Middle Concrete-Asphalt Waterstop-50'	7.19w						■	■	■			
30	Excavate for Lower Plug	1.45w						■					
31	Pour Concrete-Lower Plug	0.22w											
32	Excavate Waterstop	0.47w						■					
33	Place Asphalt	0.38w											
34	Cool-down Asphalt	1w						■					
35	Excavate for Upper Plug	1.45w						■					
36	Pour Concrete-Upper Plug	0.22w											
37	Cure Concrete	2w						■					
38	Upper Salado Compacted Clay Column-340'	11.01w						■	■	■			
39	Emplace Bentonite Blocks(340' high)	11.01w						■	■	■			
40	Upper Concrete-Asphalt Waterstop-50'	9.19w							■	■	■		
41	Excavate for Lower Plug	1.45w							■				
42	Pour Concrete-Lower Plug	0.22w											
43	Excavate Waterstop	0.47w							■				
44	Place Asphalt	0.38w											

Project: EXHAUST SHAFT SEALING SCHEDULE Date: Tue 7/9/96	Task	■	Summary	■	Rolled Up Progress	■
	Progress	■	Rolled Up Task			
	Milestone		Rolled Up Milestone	◇		

B-43

ID	Task Name	Duration	Year 1				Year 2				Year 3		
			Qtr 1	Qtr 2	Qtr 3	Qtr 4	Qtr 1	Qtr 2	Qtr 3	Qtr 4	Qtr 1	Qtr 2	
45	Cool-down Asphalt	1w											
46	Excavate for Upper Plug	1.45w											
47	Pour Concrete-Upper Plug	0.22w											
48	Cure Concrete	4w											
49	Asphalt Column-142.5'	18.43w											
50	Remove Lining in Key	3.15w											
51	Remove Chemical Seal Rings	0.5w											
52	Mobilize to Emplace Asphalt	2w											
53	Asphalt in Salt Section	2.64w											
54	Asphalt in Lower Lined Section	1.44w											
55	Complete Asphalt Emplacement	2.27w											
56	Cool-down Asphalt	6.43w											
57	Concrete Plug-20'	5.87w											
58	Remove Concrete Lining & Rock	1.7w											
59	Pour Concrete (20' high)	0.17w											
60	Cure Concrete	4w											
61	Remove Concrete Shaft Lining	3.23w											
62	Remove 84' of lining--4 zones	3.23w											
63	Rustler Compacted Clay Column-234.5'	6.62w											
64	Emplace & Compact Bentonite(234.5' high)	6.62w											
65	Compacted Earthen Fill-486.4'	5.44w											
66	Emplace & Compact Earthen Fill(486.4' high)	5.44w											

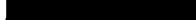
Project: EXHAUST SHAFT  
 SEALING SCHEDULE  
 Date: Tue 7/9/96

Task  Summary  Rolled Up Progress   
 Progress  Rolled Up Task  
 Milestone  Rolled Up Milestone 

ID	Task Name	Duration	Year 1				Year 2				Year 3		
			Qtr 1	Qtr 2	Qtr 3	Qtr 4	Qtr 1	Qtr 2	Qtr 3	Qtr 4	Qtr 1	Qtr 2	
67	Concrete Plug-40'	2.69w											
68	Clean Existing Surface	0.47w											■
69	Pour Concrete	0.22w											
70	Cure Concrete	2w											
71	Compacted Earthen Fill-56.1'	0.44w											■
72	Emplace & Compact Earthen Fill (56.1'high)	0.44w											
73	Demobilization	3w											
74	Demob	3w											■

B-44

Project: EXHAUST SHAFT  
SEALING SCHEDULE  
Date: Tue 7/9/96

Task  Summary  Rolled Up Progress   
Progress  Rolled Up Task  
Milestone Rolled Up Milestone 

**SEALING SCHEDULE--WASTE SHAFT**

B-46

ID	Task Name	Duration	Year 1				Year 2				Year 3				Year 4	
			Qtr 1	Qtr 2	Qtr 3	Qtr 4	Qtr 1	Qtr 2	Qtr 3	Qtr 4	Qtr 1	Qtr 2	Qtr 3	Qtr 4	Qtr 1	Qtr 2
1	Mobilization	4w	█													
3	Plant Set-up	12w	█	█												
5	Inspect & Scale Shaft-2159.5'	1w		█												
7	Install Construction Utilities	7.2w		█												
9	Drill & Grout Lining	11.21w			█											
12	Shaft Station Monolith-37'	5.17w				█										
16	Lower Salado Compacted Clay Column-96'	5.01w					█									
18	Lower Concrete-Asphalt Waterstop-50'	12.57w						█								
27	Compacted Salt Column-555.5'	22.87w							█							
29	Middle Concrete-Asphalt Waterstop-50'	10.57w								█						
38	Upper Salado Compacted Clay Column-351.5'	17.86w									█					
40	Upper Concrete-Asphalt Waterstop-50'	12.57w										█				
49	Asphalt Column-142.3'	20.71w											█			
57	Concrete Plug-20'	5.98w												█		
61	Remove Concrete Shaft Lining	5.07w													█	
63	Rustler Compacted Clay Column-234.7'	10.99w														█
65	Compacted Earthen Fill-447'	8.25w														█
67	Concrete Plug-40'	3.04w														█
71	Compacted Earthen Fill-61.5'	1.14w														█
73	Demobilization	3.5w														█

Project: WASTE HANDLING SHAFT SEALING SCHEDULE Date: Tue 7/9/96	Task	█	Summary	█	Rolled Up Progress	█
	Progress	█	Rolled Up Task			
	Milestone		Rolled Up Milestone	◇		

B-47

ID	Task Name	Duration	Year 1				Year 2				Year 3				Year 4	
			Qtr 1	Qtr 2	Qtr 3	Qtr 4	Qtr 1	Qtr 2	Qtr 3	Qtr 4	Qtr 1	Qtr 2	Qtr 3	Qtr 4	Qtr 1	Qtr 2
1	Mobilization	4w	■													
2	Mobilize	4w	■													
3	Plant Set-up	12w	■	■												
4	Plant Set-up	12w	■	■												
5	Inspect & Scale Shaft-2159.5'	1w														
6	Inspect & Scale Shaft	1w														
7	Install Construction Utilities	7.2w		■												
8	Install Utilities	7.2w		■												
9	Drill & Grout Lining	11.21w			■	■										
10	Drill Grout Holes	4.48w			■											
11	Grout Lining	6.73w			■											
12	Shaft Station Monolith-37'	5.17w				■										
13	Construct Bulkheads	1w				■										
14	Pour Concrete (37' high)	1.17w				■										
15	Cure Concrete	3w				■										
16	Lower Salado Compacted Clay Column-96'	5.01w				■										
17	Emplace Bentonite Blocks (96' high)	5.01w				■										
18	Lower Concrete-Asphalt Waterstop-50'	12.57w					■	■								
19	Excavate for Lower Plug	2.72w					■									
20	Pour Concrete-Lower Plug (23' high-ty)	0.27w					■									
21	Excavate Waterstop	0.84w					■									
22	Place Asphalt (4' high-ty)	0.75w					■									

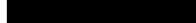
Project: WASTE HANDLING SHAFT SEALING SCHEDULE Date: Tue 7/9/96	Task	■	Summary	■	Rolled Up Progress	■
	Progress	■	Rolled Up Task			
	Milestone		Rolled Up Milestone	◇		

B-48

ID	Task Name	Duration	Year 1				Year 2				Year 3				Year 4	
			Qtr 1	Qtr 2	Qtr 3	Qtr 4	Qtr 1	Qtr 2	Qtr 3	Qtr 4	Qtr 1	Qtr 2	Qtr 3	Qtr 4	Qtr 1	Qtr 2
23	Cool-down Asphalt	1w														
24	Excavate for Upper Plug	2.72w														
25	Pour Concrete-Upper Plug (23' high-ty)	0.27w														
26	Cure Concrete	4w														
27	Compacted Salt Column-555.5'	22.87w														
28	Emplace & Compact Crushed/Screened Salt	22.87w														
29	Middle Concrete-Asphalt Waterstop-50'	10.57w														
30	Excavate for Lower Plug	2.72w														
31	Pour Concrete-Lower Plug	0.27w														
32	Excavate Waterstop	0.84w														
33	Place Asphalt	0.75w														
34	Cool-down Asphalt	1w														
35	Excavate for Upper Plug	2.72w														
36	Pour Concrete-Upper Plug	0.27w														
37	Cure Concrete	2w														
38	Upper Salado Compacted Clay Column-351.5'	17.86w														
39	Emplace Bentonite Blocks(351.5' high)	17.86w														
40	Upper Concrete-Asphalt Waterstop-50'	12.57w														
41	Excavate for Lower Plug	2.72w														
42	Pour Concrete-Lower Plug	0.27w														
43	Excavate Waterstop	0.84w														
44	Place Asphalt	0.75w														

Project: WASTE HANDLING SHAFT  
SEALING SCHEDULE  
Date: Tue 7/9/96

Task   
Progress   
Milestone

Summary   
Rolled Up Task  
Rolled Up Milestone 

Rolled Up Progress 

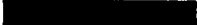
B-49

ID	Task Name	Duration	Year 1				Year 2				Year 3				Year 4	
			Qtr 1	Qtr 2	Qtr 3	Qtr 4	Qtr 1	Qtr 2	Qtr 3	Qtr 4	Qtr 1	Qtr 2	Qtr 3	Qtr 4	Qtr 1	Qtr 2
45	Cool-down Asphalt	1w														
46	Excavate for Upper Plug	2.72w														
47	Pour Concrete-Upper Plug	0.27w														
48	Cure Concrete	4w														
49	Asphalt Column-142.3'	20.71w														
50	Remove Lining in Key	3.8w														
51	Remove Chemical Seal Rings	0.6w														
52	Mobilize to emplace asphalt	0.3w														
53	Asphalt in Salt Section	4.01w														
54	Asphalt in Lower Lined Section	2.33w														
55	Complete Asphalt Emplacement	3.24w														
56	Cool-down Asphalt	6.43w														
57	Concrete Plug-20'	5.98w														
58	Remove Concrete Lining & Rock	1.73w														
59	Pour Concrete (20' high)	0.25w														
60	Cure Concrete	4w														
61	Remove Concrete Shaft Lining	5.07w														
62	Remove 84' of lining--4 zones	5.07w														
63	Rustler Compacted Clay Column-234.7'	10.99w														
64	Emplace & Compact Bentonite (234.7' high)	10.99w														
65	Compacted Earthen Fill-447'	8.25w														
66	Emplace & Compact Earthen Fill (447' high)	8.25w														

<b>Project: WASTE HANDLING SHAFT SEALING SCHEDULE</b> Date: Tue 7/9/96	Task		Summary		Rolled Up Progress	
	Progress		Rolled Up Task			
	Milestone		Rolled Up Milestone			

B-50

ID	Task Name	Duration	Year 1				Year 2				Year 3				Year 4	
			Qtr 1	Qtr 2	Qtr 3	Qtr 4	Qtr 1	Qtr 2	Qtr 3	Qtr 4	Qtr 1	Qtr 2	Qtr 3	Qtr 4	Qtr 1	Qtr 2
67	Concrete Plug-40'	3.04w														
68	Clean Existing Surface	0.64w														
69	Pour Concrete	0.4w														
70	Cure Concrete	2w														
71	Compacted Earthen Fill-61.5'	1.14w														
72	Emplace & Compact Earthen Fill (61.5' high)	1.14w														
73	Demobilization	3.5w														
74	Demob	3.5w														

Project: WASTE HANDLING SHAFT SEALING SCHEDULE Date: Tue 7/9/96	Task		Summary		Rolled Up Progress	
	Progress		Rolled Up Task			
	Milestone		Rolled Up Milestone			

## B5. REFERENCES

- Ahrens, E.H., and F.D. Hansen. 1995. *Large-Scale Dynamic Compaction Demonstration Using WIPP Salt: Fielding and Preliminary Results*. SAND95-1941. Albuquerque, NM: Sandia National Laboratories. (Copy on file in the Sandia WIPP Central Files, Sandia National Laboratories, Albuquerque, NM [SWCF] as WPO31104.)
- Ahrens, E.H., and M. Onofrei. 1996. "Ultrafine Cement Grout for Sealing Underground Nuclear Waste Repositories," *2nd North American Rock Mechanics Symposium (NARMS 96), Montreal, Quebec, June 19-21, 1996*. SAND96-0195C. Albuquerque, NM: Sandia National Laboratories. (Copy on file in the SWCF as WPO31251.)
- Ahrens, E.H., T.F. Dale, and R.S. Van Pelt. 1996. *Data Report on the Waste Isolation Pilot Plant Small-Scale Seal Performance Test, Series F Grouting Experiment*. SAND93-1000. Albuquerque, NM: Sandia National Laboratories. (Copy on file in the SWCF as WPO37355.)
- Boonsinsuk, P., B.C. Pulles, B.H. Kjartanson, and D.A. Dixon. 1991. "Prediction of Compactive Effort for a Bentonite-Sand Mixture," *44th Canadian Geotechnical Conference, Preprint Volume, Calgary, Alberta, September 29-October 2, 1991*. Paper No. 64. Waterloo, Ontario: Canadian Geotechnical Society. Pt. 2, 64/1 through 64/12. (Copy on file in the SWCF.)
- Dale, T., and L.D. Hurtado. 1996. "WIPP Air-Intake Shaft Disturbed-Rock Zone Study," *4th International Conference on the Mechanical Behavior of Salt, Montreal, Quebec, June 17-18, 1996*. SAND96-1327C. Albuquerque, NM: Sandia National Laboratories. (Copy on file in the SWCF.)
- Hansen, F.D., and E.H. Ahrens. 1996. "Large-Scale Dynamic Compaction of Natural Salt," *4th International Conference on the Mechanical Behavior of Salt, Montreal, Quebec, June 17-18, 1996*. SAND96-0792C. Albuquerque, NM: Sandia National Laboratories. (Copy on file in the SWCF as WPO39544.)
- Knowles, M.K., and C.L. Howard. 1996. "Field and Laboratory Testing of Seal Materials Proposed for the Waste Isolation Pilot Plant," *Proceedings of the Waste Management 1996 Symposium, Tucson, AZ, February 25-29, 1996*. SAND95-2082C. Albuquerque, NM: Sandia National Laboratories. (Copy on file in the SWCF as WPO30945.)
- McClintock, F.A., and A.S. Aragon. 1996. *Mechanical Behavior of Materials*. Reading MA: Addison-Wesley.
- Van Sambeek, L.L. 1988. *Considerations for the Use of Quarried Salt Blocks in Seal Components at the WIPP*. Topical Report RSI-0340. Rapid City, SD: RE/SPEC Inc. (Copy on file in the SWCF as WPO9233.)

Page intentionally blank.

# **Appendix C**

## **Fluid Flow Analyses**

### **Appendix C Abstract**

This appendix documents four models that were used to evaluate the performance of the proposed WIPP shaft seal system design in terms of fluid-flow (gas and brine) within the seal system components and surrounding Disturbed Rock Zone (DRZ). The common hydrogeologic framework used by the models is described in terms of a radially symmetric system centered on the Air Intake Shaft and extending from the repository level upward through the Salado and Rustler Formations. Properties that govern fluid flow within porous media are defined for the seal system components, the host lithologic units, and the DRZ. Laboratory, field, and mechanical modeling studies are utilized to develop a conceptualization of the DRZ, which includes a time-varying permeability within the Salado Formation dependent on depth and rigidity of adjacent seal components. Model 1 is a completely saturated numerical flow model and is used to evaluate brine flow down the shaft from the Rustler Formation to the compacted salt column component during the 200-year period immediately after seal emplacement. Model 2 is a two-phase (gas and brine) numerical flow model used to evaluate gas flow up from the repository to the compacted salt column as well as pressure within the compacted salt column during the same 200-year period. A compacted salt reconsolidation submodel is incorporated, which predicts crushed salt permeability as a function of time, pressure, and depth within the column. Model 3 is a fully saturated numerical flow model and is used to evaluate brine flow upward within the seal system during the time period from 400 to 10,000 years after seal emplacement under ambient formation pressure conditions. Model 4 utilizes simple analytical relationships to analyze the potential brine flow through the shaft seals attributable to a range of nonhydrostatic natural head conditions between the Magenta and Culebra, the two primary water-bearing members of the Rustler Formation. The seal-system performance models were used to examine fluid-flow sensitivity to various assumptions of DRZ continuity, the existence of asphalt within concrete-seal components, and different repository pressure loading scenarios.

Page intentionally blank.

## Contents

C1. INTRODUCTION.....	7
C2. DEFINITION OF PERFORMANCE MODELS .....	7
C3. HYDROGEOLOGIC FRAMEWORK .....	9
C3.1 Stratigraphy .....	9
C3.2 Observed Vertical Gradients .....	12
C3.3 Shaft Seal Material Properties.....	13
C3.3.1 Saturated Flow Parameters.....	15
C3.3.2 Two-Phase Flow Parameters.....	16
C3.4 Host-Rock Properties .....	17
C3.4.1 Permeability and Hydraulic Conductivity.....	17
C3.4.2 Porosity .....	23
C3.4.3 Formation Compressibility.....	23
C3.4.4 Two-Phase Properties of the Salado.....	24
C3.5 DRZ Properties.....	25
C3.5.1 Model for Calculating the Effective DRZ Permeability .....	27
C3.5.2 Model DRZ Effective Permeability .....	29
C4. FLOW DOWN FROM THE RUSTLER (MODEL 1) .....	31
C4.1 Statement of Problem.....	31
C4.2 Performance Model 1 Description .....	31
C4.2.1 Conceptual Model and Assumptions.....	31
C4.2.2 Numerical Method.....	36
C4.2.3 Model Geometry and Boundary Conditions .....	36
C4.2.4 Model Parameters.....	45
C4.3 Performance Model Results .....	45
C5. GAS MIGRATION AND CONSOLIDATION OF COMPACTED SALT COLUMN (MODEL 2).....	53
C5.1 Statement of Problem.....	53
C5.2 Performance Model 2 Description .....	53
C5.2.1 Conceptual Model and Assumptions.....	53
C5.2.2 Numerical Model.....	55
C5.2.3 Model Geometry and Boundary Conditions .....	56
C5.2.4 Model Parameters.....	63
C5.3 Performance Model Results .....	63
C6.0 FLOW UP FROM THE SALADO (MODEL 3) .....	72
C6.1 Statement of Problem.....	72
C6.2 Performance Model Description .....	73
C6.2.1 Conceptual Model and Assumptions.....	73
C6.2.2 Numerical Method.....	75
C6.2.3 Model Geometry and Boundary Conditions .....	75
C6.2.4 Model Parameters.....	76
C6.3 Performance Model Results .....	76
C7. INTRA-RUSTLER FLOW (MODEL 4) .....	78

C7.1 Statement of Problem .....	78
C7.2 Performance Model Description .....	78
C7.2.1 Conceptual Model and Assumptions.....	78
C7.2.2 Analytical Approach .....	80
C7.2.3 Model Parameters.....	81
C7.3 Performance Model Results .....	83
C8. REFERENCES.....	88

## Figures

Figure C-1. AIS field permeability results.....	28
Figure C-2. Log-linear model for the calculation of an effective permeability of the DRZ.....	29
Figure C-3a. Full shaft model grid (top).....	37
Figure C-3b. Full shaft model grid (bottom). .....	38
Figure C-4. Permeability fields for Run 1 (base case).....	46
Figure C-5. Permeability fields for Run 1 (base case).....	47
Figure C-6. Model 1 flow rates.....	48
Figure C-7. Cumulative flow at 200 years.....	50
Figure C-8. Pressure distributions for Run 1 (base case).....	51
Figure C-9. Pressure distributions for Run 1 (base case).....	52
Figure C-10. Conceptual diagram of compacted salt column performance model components. ....	54
Figure C-11. Grid used by the compacted salt column performance model.....	57
Figure C-12. Two specifications of pressure at the base of the shaft. ....	62
Figure C-13. Rate of change in log permeability (fractional density) with pressure and depth.....	64
Figure C-14. Reconsolidation surface for the best-fit permeability/fractional density predictor. ....	65
Figure C-15. Calculated pressure versus time after seal emplacement at the top, middle, and bottom of the compacted salt column (base case).....	67
Figure C-16. Calculated salt column permeability versus elevation within the column for several times following seal emplacement (base case). ....	68
Figure C-17. Calculated pressure versus time after seal emplacement at the top, middle, and bottom of the compacted salt column (Run 2).....	69
Figure C-18. Calculated salt column permeability versus elevation within the column for several times following seal emplacement (Run 2). ....	70
Figure C-19. Pressure contours at 75 years for base case and for 95% permeability/fractional density predictor (Run 2). ....	71
Figure C-20. Comparison of calculated pressure results for base case and continuous DRZ with no waterstops (Run 6). ....	73
Figure C-21. Calculated salt column permeability versus elevation within the column for several times following seal emplacement (Run 6: Rustler flow included, continuous DRZ, no waterstops).....	74
Figure C-22. Cumulative gas flow from the repository to the compacted salt column. ....	75

Figure C-23. Permeability fields for Runs 1 through 3 ( $t > 400$ years).....	77
Figure C-24. Intra-Rustler flow conceptual model.....	79
Figure C-25. Effect of an injection well on a unidirectional flow field.....	82
Figure C-26. Sensitivity of flow rate between Culebra and Magenta to head difference (base case).....	84
Figure C-27. Sensitivity of flow-field disturbance to head difference (base case).....	85
Figure C-28. Sensitivity of flow rate between Culebra and Magenta to DRZ radius (continuous DRZ). ....	86
Figure C-29. Sensitivity of flow-field disturbance to DRZ radius (continuous DRZ). ....	87

## Tables

Table C-1. Summary of Salado Stratigraphic Units Merged into Salado Model Combined Units.....	10
Table C-2. Freshwater Head Estimates in the Vicinity of the Air Intake Shaft.....	13
Table C-3. Bentonite Compacted Clay Parameters .....	13
Table C-4. Asphalt Parameters .....	14
Table C-5. Compacted Salt Parameters .....	14
Table C-6. Concrete Parameters .....	14
Table C-7. Earthen Fill Parameters.....	15
Table C-8. Capillary Pressure and Relative Permeability Model Parameters for Compacted Clay, Concrete, Reconsolidated Salt, and Earthen Fill.....	15
Table C-9. Summary of Permeability and Hydraulic Conductivity, Porosity, and Compressibility for the Rustler Modeled Lithologic Units .....	18
Table C-10. Summary of Permeability and Hydraulic Conductivity, Porosity, and Compressibility for the Salado Modeled Lithologic Units.....	18
Table C-11. Testing and Analysis Summary for Salado Halite.....	19
Table C-12. Salado Brine Seepage Intervals <sup>(1)</sup> .....	20
Table C-13. Testing Summary for Rustler Formation.....	22
Table C-14. Summary of Literature Values for Formation Porosities.....	23
Table C-15. Salado Two-Phase Properties .....	25
Table C-16. Model DRZ permeability for base-case conceptualization (corrected for model DRZ area).....	32
Table C-17. Full-Shaft Model Vertical Layers .....	39
Table C-18. Full-Shaft Model Radial Gridding.....	43
Table C-19. Performance Model 1 Simulations .....	45
Table C-20. Vertical Layers of the Compacted Salt Column Performance Model .....	58
Table C-21. Compacted Salt Column Performance Model Radial Gridding .....	60
Table C-22. Compacted Salt Column Performance Model Simulations .....	66
Table C-23. Performance Model 3 Simulations .....	76
Table C-24. Comparison of Flow Rates Up the Shaft/DRZ from Simulations that Incorporate the Measured Pressure Conditions.....	78
Table C-25. Regional Darcy Velocities for Culebra and Magenta Members of the Rustler Formation.....	83

Page intentionally blank.

## **C1. INTRODUCTION**

This appendix describes analyses conducted to quantify the fluid-flow performance of the WIPP shaft seal system design. The appendix is organized in the following manner. First, the statements of the problems to be solved are developed. The problem statements are introduced in terms of performance models. The analysis sections of this appendix are organized in terms of these performance models. For each performance model, the conceptual model is described along with a description of the quantitative method used. Each performance calculation is defined in terms of the relevant assumptions, parameters, and boundary conditions. Finally, results from each performance model are presented. The numerical codes SWIFT II (Version 2F) and TOUGH28W (Version 2.02) have been used in this appendix to quantitatively analyze fluid-flow performance for the WIPP shaft seal system.

The fluid-flow analyses presented in this appendix were performed using SI units. Dimensions, parameter values, and performance model results will be presented in SI units. However, graphical depiction of the models used will be presented in terms of feet above mean sea level (ft msl) to facilitate comparisons with seal system design drawings.

## **C2. DEFINITION OF PERFORMANCE MODELS**

Evaluation of the fluid-flow performance of the shaft seal system is facilitated through definition of relevant performance models. Each performance model is derived from performance measures that quantify migration of fluids within and through the system. This approach differs in scope from that of the assessment of the WIPP repository. In the latter case, a general system model is developed in an iterative manner. Physical processes that may result in contaminant release are systematically identified and evaluated through results of the system model simulations. The performance models defined in this appendix are specific to performance measures applicable to the shaft seal system. These models were developed through assessment of the physical characteristics of the WIPP shaft sealing system, the surrounding media, and the sealing functions that are described in detail in Section 4 of the main report.

Qualitative design guidance has been developed for the shaft seal system based on the function of the shaft seal system. This guidance seeks (1) to limit the migration of radiological or other hazardous constituents from the repository horizon to the regulatory boundary over a 10,000-year regulatory period and (2) to limit groundwater flow into and through the shaft sealing system. Additional qualitative design guidance arises from special requirements of the compacted salt column. The salt column requires reconsolidation, a process that can be adversely affected by significant pore pressures within the column. This guidance seeks (3) to limit both groundwater and repository-generated gas from flowing into the compacted salt column.

The primary potential source of significant groundwater flow to the shaft sealing system comes from the Rustler Formation. Because of the low permeability of the Salado Formation, it is isolated from active groundwater circulation. However, because the Salado is significantly over-pressured relative to the Rustler Formation (Beauehim et al., 1993), the Salado Formation

represents a possible source of long-term upward flow from the repository horizon through the seal system.

The motivations for limiting brine migration in the seal system are: (1) to limit brine migration from the Rustler to the repository during repressurization of the seal system; (2) to prevent significant pore pressures from building in the compacted salt column and potentially affecting reconsolidation; (3) to limit the interconnection of water-bearing strata in the Rustler; and (4) to limit brine migration upward from the Salado. Likewise, the motivations for limiting gas and brine migration up the seal system from the repository are: (5) to limit upward fluid flow to the accessible environment; and (6) to prevent significant pore pressures from building in the compacted salt column.

These motivations, together with the features and processes that underlie them, can be synthesized into four flow-performance models:

Model 1: Flow Down from the Rustler

Model 2: Gas Migration and Compacted Salt Column Consolidation

Model 3: Flow up from the Salado

Model 4: Intra-Rustler Flow

These performance models are coupled or interdependent. For example, flow from the Rustler (Model 1) could be affected by the consolidation (permeability) of the compacted salt column (Model 2). Likewise, Model 2 performance could be affected by the flow from the Rustler (Model 1). Model 1 will be evaluated first, followed by the analysis of Model 2. Models 3 and 4 will be evaluated separately.

Several analysis assumptions are shared among all the performance models and are listed below.

- Each analysis uses the Air Intake Shaft (AIS) as the shaft analyzed. It is assumed that the AIS analysis is representative of the three other WIPP shafts.
- The stratigraphy used in these performance calculations is consistent with the AIS stratigraphy as presented by Holt and Powers (1990) and as summarized by DOE (1995).
- A radial model geometry is assumed.
- Isothermal conditions are considered. This means that fluid flow driven by temperature gradients is assumed to be negligible.
- Each shaft can be considered independently. This means that it is assumed that no hydraulic interference exists between shafts.
- Flow is considered through the intact rocks, the seal materials, and the disturbed rock zone (DRZ).
- The DRZ can appropriately be described as having its largest permeability at the shaft/DRZ contact and approaching intact permeabilities at its outer extent. The permeability is assumed to vary log-linearly from the shaft/DRZ interface to the outer extent of the DRZ (intact rock).

- For Models 1 and 2, a preclosure period of 50 years is assumed. During the preclosure period, the shaft is held at atmospheric conditions.

The analyses presented in this appendix are deterministic and do not account for the full-range of potential outcomes that may be expected by performing a stochastic analysis allowing parameters to randomly vary across their respective uncertainty ranges. A stochastic analysis of the complete disposal system was conducted by WIPP PA for the 40 CFR 191 Compliance Certification Application of the WIPP (DOE, 1996). This analysis addressed the ranges of seal system parameters as applicable to the behavior of the disposal system. The analyses presented in this report address those parameters that are considered the most uncertain and to which the primary performance measures (flow rates) are most sensitive. These parameters include (1) the permeability of the DRZ, (2) the relationship between compacted salt density and permeability, and (3) the repository gas pressure applied at the base of the shaft seal system. The prediction of brine-flow migration down the shaft system (Model 1) is performed with a saturated flow model, which estimates the flow. In addition, a limited sensitivity analysis was performed, which provided a range in model predictions for variations in what are considered to be important processes. These processes are incorporated in model parameters that address (1) the vertical continuity of the DRZ, (2) the healing rate against the concrete-asphalt waterstops, (3) the relationship between compacted salt density and permeability, and (4) the repository gas pressure applied at the base of the shaft sealing system.

### **C3. HYDROGEOLOGIC FRAMEWORK**

This section discusses the hydrogeologic framework for the hydraulic analysis of the performance of the WIPP shaft seal system. The hydrogeologic framework includes (1) the stratigraphy of the host rocks and how it is conceptualized for the performance models; (2) the ambient fluid pressure profile within the host rocks; (3) and the hydraulic parameters describing the seal system, the host rocks, and the DRZ.

The properties that govern fluid flow within porous media are defined for the seal components, the host lithologic units, and the DRZ. Both single-phase (SWIFT II) and multi-phase (TOUGH28W) fluid flow codes were used in these calculations.

#### **C3.1 Stratigraphy**

The stratigraphy of the host rocks adjacent to the shaft from the repository horizon to the surface is composed of the Salado Formation, the Rustler Formation, the Dewey Lake Redbeds, and the surficial Santa Rosa and Gatuña Formations. Dune sand and caliche overlie the sediments at the surface. The primary water-bearing strata are confined to the Rustler and Salado Formations. Therefore, the discussion of stratigraphy will focus on the Salado and Rustler Formations.

The reference stratigraphy used to develop the performance models in this appendix is based on the shaft mapping of the AIS (Holt and Powers, 1990). The detailed stratigraphy of the Rustler and Salado Formations in the AIS is also summarized in Appendix A of DOE (1995). The detailed stratigraphy will not be discussed here.

The detailed modeling of the discrete stratigraphy present in the Rustler and Salado formations presents a challenge. Several Salado marker beds are very thin, with thicknesses less than 0.5 m in many instances. To reduce the total number of grid cells to a manageable level in the performance models, several individual stratigraphic units were merged into single model combined units. Units were merged together based on proximity, thickness, and lithology. Table C-1 lists the Salado Formation combined units and the individual beds that were merged to form them. Rock properties of the combined stratigraphic units were calculated based on the thickness-weighted arithmetic mean of the rock properties of individual beds composing the combined units. DRZ permeabilities of the combined stratigraphic units were calculated based on the thickness-weighted harmonic mean.

Table C-1. Summary of Salado Stratigraphic Units Merged into Salado Model Combined Units

Combined Unit Name	Combined Unit Thickness (m)	Stratigraphic Unit	Rock Type	Individual Unit Thickness (m)
Unit 1	5.79	MB103	Anhydrite <sup>(1) (2)</sup>	5.03
		MB104	Anhydrite	0.30
		MB105	Anhydrite	0.30
		MB106	Anhydrite	0.15
Unit 2	8.05	MB107	Polyhalite	0.15
		MB108	Polyhalite	0.15
		MB109	Anhydrite <sup>(1) (2)</sup>	7.74
Unit 3	3.57	MB110	Polyhalite	0.34
		MB111	Polyhalite	0.18
		MB112	Polyhalite	0.61
		MB113	Polyhalite	0.30
		MB114	Polyhalite	0.30
		MB115	Polyhalite	1.07
Unit 4	5.79	MB116	Polyhalite	0.76
		MB117	Polyhalite	0.46
		MB118	Polyhalite	0.79
		MB119	Polyhalite	0.61
		MB120	Polyhalite	0.27
		Zone A	Halite <sup>(1)</sup>	3.05

Table C-1. Summary of Salado Stratigraphic Units Merged into Salado Model Combined Units

Combined Unit Name	Combined Unit Thickness (m)	Stratigraphic Unit	Rock Type	Individual Unit Thickness (m)
		MB121	Polyhalite	0.30
		MB122	Polyhalite	0.30
Unit 5	4.72	MB123	Anhydrite	1.98
		MB124	Anhydrite <sup>(1)</sup>	2.74
Unit 6	3.96	Zone B	Halite <sup>(1)</sup>	0.91
		Zone C	Halite <sup>(1)</sup>	2.74
		MB126	Polyhalite	0.30
Unit 7	11.83	MB127	Polyhalite	0.79
		MB128	Polyhalite	1.07
		Zone D	Halite <sup>(1)</sup>	3.20
		Zone E	Halite <sup>(1)</sup>	0.61
		Zone F	Halite <sup>(1)</sup>	0.91
		Zone G	Halite <sup>(1)</sup>	0.61
		Zone H	Halite <sup>(1)</sup>	1.80
		MB129	Polyhalite <sup>(1)</sup>	0.46
		Zone I	Halite <sup>(1)</sup>	1.74
		MB130	Polyhalite	0.64
Unit 8	2.29	MB131	Polyhalite	0.30
		Zone J	Halite <sup>(1)</sup>	1.22
		MB132	Polyhalite	0.30
		MB133	Polyhalite	0.46
Unit 9	4.75	Unnamed	Anhydrite	0.76
		MB134	Anhydrite <sup>(2)</sup>	3.69
		MB135	Anhydrite	0.30

Table C-1. Summary of Salado Stratigraphic Units Merged into Salado Model Combined Units

Combined Unit Name	Combined Unit Thickness (m)	Stratigraphic Unit	Rock Type	Individual Unit Thickness (m)
Unit 10		MB136	Anhydrite <sup>(2)</sup>	4.30
		MB137	Anhydrite	0.40
Unit 11	0.49	MB138	Anhydrite	0.18
		Anhydrite A	Anhydrite	0.30

(1) Identified brine seepage interval.

(2) Anhydrite unit greater than 3 m in thickness.

### C3.2 Observed Vertical Gradients

Heads within the Rustler and between the Rustler and Salado formations are not in hydrostatic equilibrium. Mercer (1983) recognized that heads at the Rustler/Salado transition (referred to as the brine aquifer and not present in the vicinity of the WIPP shafts) indicate an upward hydraulic gradient from that zone to the Culebra. Later, with the availability of more head measurements within the Salado and Rustler, Beauheim (1987) provided additional insight into the potential direction of vertical fluid movement within the Rustler. He reported that the hydraulic data indicate an upward gradient from the Salado to the Rustler.

Formation pressures in the Salado Formation have been decreased in the near vicinity of the WIPP underground facility. The highest, and thought to be least disturbed, estimated formation fluid pressure from hydraulic testing is 12.55 MPa estimated from interpretation of testing within borehole SCP01 in MB139 just below the underground facility horizon (Beauheim et al., 1993). The freshwater head within MB139, based on the estimated static formation pressure of 12.55 MPa, is 1663.6 m (5458 ft) above mean sea level (msl).

Heads in the Rustler have also been impacted by the presence of the WIPP shafts. These impacts in the Culebra were significant in the 1980s, with a large drawdown cone extending away from the shafts in the Culebra (Haug et al., 1987). The undisturbed head of the Rustler/Salado contact in the vicinity of the AIS is estimated to be approximately 936.0 m (3071 ft) msl (Brinster, 1991). The undisturbed head in the Culebra is estimated to be approximately 926.9 m (3041 ft) msl in the vicinity of the AIS (LaVenue et al., 1990). The undisturbed head in the Magenta is estimated to be approximately 960.1 m (3150 ft) msl (Brinster, 1991).

The disturbed and undisturbed heads in the Rustler are summarized in Table C-2. Also included is the freshwater head of MB139 based on hydraulic testing in the WIPP underground. Consistent with the vertical flow directions proposed by previous investigators, estimated vertical gradients in the vicinity of the AIS before the shafts were drilled indicate a hydraulic gradient from the Magenta to the Culebra and from the Rustler/Salado contact to the Culebra. There is also the potential for flow from the Salado Formation to the Rustler Formation.

Table C-2. Freshwater Head Estimates in the Vicinity of the Air Intake Shaft

Hydrologic Unit	Freshwater Head (m asl)		Reference
	Undisturbed	Disturbed	
Magenta Member	960.1 <sup>(1)</sup>	948.8 <sup>(2)</sup>	Brinster (1991)
		(H-16)	Beauheim (1987)
Culebra Member	926.9 <sup>(1)</sup>	915.0 <sup>(2)</sup>	LaVenue et al. (1990)
		(H-16)	Beauheim (1987)
Lower Unnamed Member	—	953.4 <sup>(2)</sup>	Beauheim (1987)
		(H-16)	
Rustler/Salado Contact	936.0 - 940.0 <sup>(1)</sup>	—	Brinster (1991)
Salado MB139	1663.6 <sup>(2)</sup>	—	Beauheim et al. (1993)

(1) Estimated from contoured head surface plot based primarily on well data collected before shaft construction.

(2) Measured through hydraulic testing and/or long-term monitoring.

### C3.3 Shaft Seal Material Properties

The WIPP shaft seal system is composed of four primary materials: compacted clay, compacted salt, salt-saturated concrete, and asphalt. Eathern fill material is specified for the shafts in the near-surface regions. The performance models described in Section 2 require quantitative values for certain properties of the seal materials. These properties may be broadly divided into two categories: saturated flow parameters and two-phase flow parameters. Saturated flow parameters include intrinsic permeability, porosity, and compressibility of the materials, as well as the initial pore pressure of the components. Necessary parameters for two-phase flow will depend on the selection of an appropriate conceptual model for two-phase flow. The following sections describe the process used in the selection of saturated and two-phase flow parameters for the performance models presented in Sections C4, C5, and C6. Values for these parameters are summarized in Tables C-3 through C-8.

Table C-3. Bentonite Compacted Clay Parameters

Parameter	Value
Intrinsic Permeability (m <sup>2</sup> )	5×10 <sup>-19</sup>
Porosity (m <sup>3</sup> /m <sup>3</sup> )	0.24
Pore compressibility (1/Pa)-	
Upper Salado clay	1.81×10 <sup>-9</sup>
Lower Salado clay	1.59×10 <sup>-9</sup>
Rustler clay column	1.96×10 <sup>-9</sup>
Initial Pressure (Pa)	101356.5
Initial Water Saturation	0.79

Table C-4. Asphalt Parameters

Parameter	Value
Intrinsic Permeability (m <sup>2</sup> )	1×10 <sup>-20</sup>
Porosity (m <sup>3</sup> /m <sup>3</sup> )	0.01
Pore compressibility (1/Pa)	2.97×10 <sup>-8</sup>
Initial Pressure (Pa)	101356.5
Initial Water Saturation	0.0

Table C-5. Compacted Salt Parameters

Parameter	Value
Intrinsic Permeability (m <sup>2</sup> )	7.9×10 <sup>-13</sup> to 6.3×10 <sup>-21</sup> (1)
Porosity (m <sup>3</sup> /m <sup>3</sup> )	0.05
Pore compressibility (1/Pa)	8.5×10 <sup>-10</sup>
Initial Pressure (Pa)	101356.5
Initial Water Saturation	0.32

(1) Section C5.3.

Table C-6. Concrete Parameters

Parameter	Value
Intrinsic Permeability (m <sup>2</sup> )	
0 to 400 years	1.78×10 <sup>-19</sup>
400 to 10000 years	1.0×10 <sup>-14</sup>
Porosity (m <sup>3</sup> /m <sup>3</sup> )	0.0227
Pore compressibility (1/Pa)	2.64×10 <sup>-9</sup>
Initial Pressure (Pa)	101356.5
Initial Water Saturation	1.0

Table C-7. Earthen Fill Parameters

Parameter	Value
Intrinsic Permeability ( $m^2$ )	$1 \times 10^{-14}$
Porosity ( $m^3/m^3$ )	0.32
Pore compressibility (1/Pa)	$3.1 \times 10^{-8}$
Initial Pressure (Pa)	101356.5
Initial Water Saturation	0.8

Table C-8. Capillary Pressure and Relative Permeability Model Parameters for Compacted Clay, Concrete, Reconsolidated Salt, and Earthen Fill

Parameter	Value
Threshold Pressure (Pa)	$P_t = 5.6 \times 10^{-7} k^{-0.346}$
Lambda ( $\lambda$ )	0.94
Residual Water Saturation	0.2
Residual Gas Saturation	0.2

### C3.3.1 Saturated Flow Parameters

The simplest approximation of flow can be derived from Darcy's Law, an empirical relationship that demonstrates that flow through a porous material depends directly on the hydraulic gradient, fluid viscosity, and material permeability. The hydraulic gradient will depend on the physical system, as will fluid viscosity. For an engineered system such as the WIPP shaft sealing system, it is possible to limit flow by specifying very low material permeabilities. It is recognized that fluid flow through the WIPP shaft sealing system is complex and that a simple Darcy flow analysis will not suffice. Nonetheless, the importance of seal material permeability and the ability to engineer low-permeability materials can be justifiably retained in the performance analysis of the seal system. The specifications for seal materials are discussed in considerable detail in Appendix A. The analyses presented in this appendix focus on the expected behavior of the seal system within the context of each performance model. Because of uncertainty in the consolidation process for crushed salt, deterministic calculations are presented that capture this uncertainty. In all other cases, the selected permeability reflects confidence that the seal components will be constructed in a manner consistent with the specifications put forth in Appendix A. The most probable value for each material permeability was used for the analyses, except as noted otherwise in the text.

Unlike TOUGH28W, SWIFT II requires input of hydraulic conductivity rather than intrinsic permeability. The conversion from permeability to hydraulic conductivity in this report

will use a fluid density of  $1230 \text{ kg/m}^3$ , an acceleration of gravity of  $9.792 \text{ m/s}^2$ , and a fluid viscosity of  $1.8 \times 10^{-3} \text{ Pa} \cdot \text{s}$ . These fluid properties are representative of a WIPP saturated brine.

Material porosity and compressibility relate to the storage capacity of a porous media. Sensitivity studies conducted previously (WIPP PA, 1992–1993) have demonstrated that fluid flow is not significantly impacted by material storage capacity. With the exception of the crushed salt column permeability, the performance measures identified for the shaft seal system relate to fluid flow. As discussed in the previous paragraphs, the uncertainty in the salt column consolidation process is addressed in the relevant performance model. Variations in seal material porosity and compressibility were not included in these analyses. The most probable values for these parameters were selected for use in the performance models (DOE, 1996).

The pressure in the open shafts is atmospheric. It was assumed that the initial pore pressure for all seal materials was also atmospheric. Values for the saturated flow parameters and initial conditions for all seal materials are presented in Tables C-3 through C-7. These values are consistent with the most probable values listed in Appendix PAR of the WIPP Compliance Certification Application (DOE, 1996). Additional details regarding the uncertainty in these parameters are presented as appropriate later in the text.

### **C3.3.2 Two-Phase Flow Parameters**

Two conditions necessitate consideration of two-phase flow within the shaft seal system. The first is that the seal system will be partially saturated with respect to brine at the time of construction. The second relates to the possibility that gas will be generated by the waste forms, and this gas could migrate to the base of the sealed shafts. Modeling a system that has two phases requires knowledge of the two-phase properties, which are characterized by capillary pressure and relative permeability curves for each phase. Ideally, each material will have a set of characteristic curves derived from experimental data. In practice, however, these curves rarely exist for the precise materials being modeled. The curves can be estimated using functional relationships found in the literature (Brooks and Corey, 1966; van Genuchten, 1980; Parker et al., 1987). Webb (1996) performed a literature review of the relationships for determining two-phase characteristic curves. Based on those comparisons, he concluded that no single model best fits all the data, and he further recommended the use of two models for future modeling activities at the WIPP. He referred to these two models as the mixed Brooks and Corey model and the van Genuchten/Parker model. The van Genuchten/Parker model was implemented in the two-phase calculations presented in this appendix.

Based on literature searches, two-phase parameters for the Brooks and Corey model were derived. These parameters were applied to all seal materials, with the exception of asphalt. Parameters necessary for the van Genuchten/Parker model can be derived from those specified for the Brooks and Corey model. The necessary parameters are the threshold pressure, pore size distribution index ( $\lambda$ ), residual water saturation, and residual gas saturation. An empirically derived relationship between threshold pressure and permeability (Davies, 1991) is used for determining the threshold pressure. The values used for two-phase flow parameters are summarized in Table C-8.

The initial saturation condition must also be specified for the seal system. The initial liquid saturation state is derived from the following relationship:

$$S = w\gamma \frac{(1 - \phi)}{\phi} \quad (C-1)$$

where

- $S$  = the liquid saturation
- $\gamma$  = the specific gravity of the material
- $w$  = the moisture content of the material
- $\phi$  = the material porosity.

For all materials, the liquid was assumed to be brine. Porosity and moisture content are engineered parameters specified for each material (DOE, 1996).

The capillary pressure model for asphalt is the only exception to the parameters described above. Asphalt is a hydrophobic material. Using the parameters described for other seal materials and the low brine saturation of the asphalt, this seal component would develop a large suction pressure, attracting water. This behavior is not consistent with a hydrophobic material. Therefore, a linear capillary model is assumed for the asphalt. The model is defined by a zero capillary pressure at all brine saturations.

### **C3.4 Host-Rock Properties**

Because the permeability (or hydraulic conductivity) of the host-rock formations is the most important parameter characterizing the host formations, emphasis will be given to it. Porosity and compressibility used for each rock type will be summarized in tables, but discussion of these parameters and their sources will be limited.

#### **C3.4.1 Permeability and Hydraulic Conductivity**

The following sections discuss the permeability and hydraulic conductivity of the Salado evaporites and each member of the Rustler Formation. The values assumed for both the undisturbed and disturbed formation are presented. Tables C-9 and C-10 summarize the values of permeability and hydraulic conductivity for the Rustler and Salado Formations.

The reported disturbed formation permeabilities represent the permeability of the DRZ at the shaft/DRZ interface. These permeabilities will later be used to calculate the effective DRZ permeability.

Table C-9. Summary of Permeability and Hydraulic Conductivity, Porosity, and Compressibility for the Rustler Modeled Lithologic Units

Lithology	Undisturbed Permeability (m <sup>2</sup> )	Undisturbed Hydraulic Conductivity (m/s)	Disturbed Permeability (m <sup>2</sup> )	Disturbed Hydraulic Conductivity (m/s)	Porosity (fraction)	Rock Compressibility (Pa <sup>-1</sup> )	Pore-Volume Compressibility (Pa <sup>-1</sup> )
Anhydrite <sup>(1)</sup>	1.00×10 <sup>-19</sup>	6.69×10 <sup>-13</sup>	1.00×10 <sup>-19</sup>	6.69×10 <sup>-13</sup>	0.01	2.2×10 <sup>-11</sup>	2.2×10 <sup>-9</sup>
Mudstone 4	3.89×10 <sup>-16</sup>	2.60×10 <sup>-9</sup>	3.89×10 <sup>-13</sup>	2.60×10 <sup>-6</sup>	0.30	9.8×10 <sup>-10</sup>	3.3×10 <sup>-9</sup>
Magenta	1.49×10 <sup>-15</sup>	1.00×10 <sup>-8</sup>	1.49×10 <sup>-14</sup>	1.00×10 <sup>-7</sup>	0.16	1.1×10 <sup>-9</sup>	6.9×10 <sup>-9</sup>
Mudstone 3	1.49×10 <sup>-19</sup>	1.00×10 <sup>-12</sup>	1.49×10 <sup>-16</sup>	1.00×10 <sup>-9</sup>	0.30	9.8×10 <sup>-10</sup>	3.3×10 <sup>-9</sup>
Culebra	2.09×10 <sup>-14</sup>	1.40×10 <sup>-7</sup>	2.09×10 <sup>-13</sup>	1.40×10 <sup>-6</sup>	0.16	1.1×10 <sup>-9</sup>	6.9×10 <sup>-9</sup>
Anhydrite 1/ Mudstone 1	1.00×10 <sup>-19</sup>	6.69×10 <sup>-13</sup>	1.00×10 <sup>-19</sup>	6.69×10 <sup>-13</sup>	0.05	200×10 <sup>-11</sup>	4.5×10 <sup>-10</sup>
Transition/ Bioturbated Clastics	2.24×10 <sup>-18</sup>	1.50×10 <sup>-11</sup>	2.24×10 <sup>-15</sup>	1.50×10 <sup>-8</sup>	0.20	7.9×10 <sup>-11</sup>	3.9×10 <sup>-10</sup>

(1) Anhydrite 5, Anhydrite 4, Anhydrite 3, and Anhydrite 2.

Table C-10. Summary of Permeability and Hydraulic Conductivity, Porosity, and Compressibility for the Salado Modeled Lithologic Units

Lithology	Undisturbed Permeability (m <sup>2</sup> )	Undisturbed Hydraulic Conductivity (m/s)	Disturbed Permeability (m <sup>2</sup> )	Disturbed Hydraulic Conductivity (m/s)	Porosity (fraction)	Rock Compressibility (Pa <sup>-1</sup> )	Pore-Volume Compressibility (Pa <sup>-1</sup> )
Anhydrite >3 m thick	1.00×10 <sup>-19</sup>	6.69×10 <sup>-13</sup>	1.00×10 <sup>-19</sup>	6.69×10 <sup>-13</sup>	0.01	2.23×10 <sup>-11</sup>	2.23×10 <sup>-9</sup>
Anhydrite <3 m thick	1.00×10 <sup>-19</sup>	6.69×10 <sup>-13</sup>	1.00×10 <sup>-15</sup>	6.69×10 <sup>-9</sup>	0.01	2.23×10 <sup>-11</sup>	2.23×10 <sup>-9</sup>
Halite	1.00×10 <sup>-21</sup>	6.69×10 <sup>-15</sup>	1.00×10 <sup>-15</sup>	6.69×10 <sup>-9</sup>	0.01	8.05×10 <sup>-11</sup>	8.05×10 <sup>-9</sup>
Polyhalite	3.00×10 <sup>-21</sup>	2.01×10 <sup>-14</sup>	1.00×10 <sup>-15</sup>	6.69×10 <sup>-9</sup>	0.01	2.23×10 <sup>-11</sup>	2.23×10 <sup>-9</sup>
Vaca Triste	1.49×10 <sup>-19</sup>	1.00×10 <sup>-12</sup>	1.49×10 <sup>-16</sup>	1.00×10 <sup>-9</sup>	0.20	6.6×10 <sup>-10</sup>	3.3×10 <sup>-9</sup>

## Salado Formation

Table C-11 summarizes testing and analysis of test data for the Salado halite. In this appendix, the permeability of the undisturbed halite is assumed to have a value of  $1 \times 10^{-21} \text{ m}^2$ , and the permeability of the disturbed halite is assumed to have a value of  $1 \times 10^{-15} \text{ m}^2$ . The permeability for undisturbed halite is consistent with the cumulative probability distribution for the permeability of far field and depressurized halite given in Gorham et al. (1992). The permeability for disturbed halite was selected based on the probability density function for disturbed halite recommended to PA and included in Appendix D of this document. The basis for the disturbed halite permeability values is derived from field tests within the AIS (Dale and Hurtado, 1996) and other field test programs (Knowles et al., 1996; Stormont, 1990), which are discussed in Section C3.5. The disturbed halite distribution function recommended to PA is log-triangular with a maximum of  $1 \times 10^{-14} \text{ m}^2$  ( $6.7 \times 10^{-8} \text{ m/s}$ ) and a minimum of  $1 \times 10^{-17} \text{ m}^2$ . The permeability of  $1 \times 10^{-15} \text{ m}^2$  is consistent with the Salado disturbed permeability for halite previously used by PA.

The median permeability for undisturbed anhydrite, based on borehole testing, was  $1.0 \times 10^{-19} \text{ m}^2$  (DOE, 1996). The value for the disturbed permeability of the Salado anhydrites was assumed to be  $1 \times 10^{-15} \text{ m}^2$ , which is consistent with the disturbed anhydrite permeability reported by Sandia WIPP Project (WIPP PA, 1992–1993).

The undisturbed polyhalite permeability of  $3.0 \times 10^{-21} \text{ m}^2$  was taken from Lappin et al. (1989) and Saulnier and Avis (1988). Because there was no specific information concerning polyhalite disturbed permeability, it was assumed to be the same as that for halite and anhydrite.

Table C-11. Testing and Analysis Summary for Salado Halite

Lithology	Reference(s)	Permeability ( $\text{m}^2$ )	Hydraulic Conductivity (m/s)	Comments
Undisturbed Halite	Beauheim et al., 1991 Beauchim et al., 1993	$3 \times 10^{-18} - 10^{-21}$	$2 \times 10^{-11} - 6.7 \times 10^{-15}$	Underground testing at the WIPP from 1988 to 1992
	Gorham et al., 1992	$10^{-19} - 10^{-24}$	$6.9 \times 10^{-13} - 6.7 \times 10^{-18}$	Values recommended for PA calculation
Disturbed Halite	Gorham et al., 1992	$10^{-13} - 10^{-18}$	$6.7 \times 10^{-7} - 6.7 \times 10^{-12}$	Values recommended for 1992 PA calculation
	WIPP PA, 1992–1993	$10^{-15} - 10^{-22}$	$6.9 \times 10^{-9} - 6.7 \times 10^{-16}$	Range used for 1992 PA calculations
	Dale and Hurtado, 1996	$10^{-14} - 10^{-17}$	$6.9 \times 10^{-8} - 6.7 \times 10^{-11}$	Testing in the AIS during 1995

The lithology of the Vaca Triste is a halitic siltstone and mudstone. No hydraulic conductivity information was available for the Vaca Triste. In the absence of any specific information, the undisturbed permeability and the disturbed permeability for the Vaca Triste were assumed to be  $1.49 \times 10^{-19} \text{ m}^2$  ( $1.0 \times 10^{-12} \text{ m/s}$ ) and  $1.49 \times 10^{-16} \text{ m}^2$  ( $1.0 \times 10^{-9} \text{ m/s}$ ), respectively. These values are the same as those used for Mudstone 3 in the Rustler, which has a similar lithology.

Within the Salado formation, several brine seepage intervals were noted. Permeabilities for these zones were assigned values of 10 times the base value for each rock type. Porosities and compressibilities were not modified for the brine seepage zones. Table C-12 identifies which Salado stratigraphic units were treated as brine seepage intervals.

Table C-12. Salado Brine Seepage Intervals<sup>(1)</sup>

Stratigraphic Unit
Marker Bed 103
Marker Bed 109
Vaca Triste
Zone A
Marker Bed 121
Union Anhydrite
Marker Bed 124
Zone B
Zone C
Zone D
Zone E
Zone F
Zone G
Zone H
Marker Bed 129
Zone I
Zone J

(1) After US DOE, 1995.

### Rustler Formation

The Rustler Formation consists of five members, which from the oldest to youngest are: the unnamed lower member, the Culebra Dolomite Member, the Tamarisk Member, the Magenta Dolomite Member, and the Forty-niner Member. Many of the members are composed of informal lithologic units. The lower unnamed member has been hydraulically tested in the

vicinity of the AIS (see Table C-13) Because the tests reported in Beauheim (1987) most likely tested the most transmissive portions of the unnamed lower member (i.e., the transition and bioturbated clastic zones), the maximum measured hydraulic conductivity of  $1.5 \times 10^{-11}$  m/s was selected as the hydraulic conductivity for the transition and bioturbated zones units. The lower permeability units of the unnamed lower member, Anhydrite 1 and Mudstone 1, were assigned a permeability consistent with the anhydrite permeability of  $1.0 \times 10^{-19}$  m<sup>2</sup>. Mudstone 2, which underlies the Culebra, was tested in H-16 in the test interval that included the Culebra (Beauheim, 1987). For this reason, the model considers Mudstone 2 and the Culebra as a single unit. The hydraulic conductivity of this unit is discussed with the Culebra.

A disturbed permeability  $2.24 \times 10^{-15}$  m<sup>2</sup> was selected for the bioturbated clastic zone and the transition zone. This value represents a three order of magnitude increase in hydraulic conductivity over the undisturbed value. A disturbed permeability of  $1.0 \times 10^{-15}$  m<sup>2</sup> was assigned to Anhydrite 1 and Mudstone 1, which were considered as a single unit in the model. Rock mechanics calculations presented in Appendix D of this report evaluate DRZ development in the clay units of the Rustler Formation.

The hydraulic conductivity of the Culebra dolomite varies over a wide range (four orders of magnitude) at the WIPP site. This wide variation is due to the presence of both open and filled fractures within the Culebra. The hydraulic conductivity is lowest in regions where the fractures in the Culebra are filled and highest in regions where the fractures are open. The location of the WIPP shafts is in a region of relatively lower hydraulic conductivity.

A value of  $2.09 \times 10^{-14}$  m<sup>2</sup> was selected as the permeability for the Culebra. This value represents the highest site-specific hydraulic conductivity estimated from testing the Culebra in the vicinity of the AIS. The disturbed permeability for the Culebra was assigned a value of  $2.09 \times 10^{-13}$  m<sup>2</sup>. Mechanical calculations presented in Appendix D predict that Rustler dolomites will not develop a DRZ.

The Tamarisk Member of the Rustler Formation includes Anhydrite 2, which directly overlies the Culebra, Mudstone 3, and Anhydrite 3, which underlies the Magenta. Hydraulic testing of the Tamarisk was attempted at H-16 adjacent to the AIS but was unsuccessful (Beauheim, 1987). It was estimated that the transmissivity of the Tamarisk was one to two orders of magnitude lower than the least-transmissive unit successfully tested at H-16. This results in an estimated permeability ranging from  $4.63 \times 10^{-20}$  to  $4.63 \times 10^{-19}$  m<sup>2</sup>.

A value of  $1.0 \times 10^{-19}$  m<sup>2</sup> was selected for the undisturbed permeability of the anhydrite units (Anhydrite 3 and Anhydrite 2) of the Tamarisk. The value for the disturbed permeability of the anhydrite units was taken as  $1.0 \times 10^{-15}$  m<sup>2</sup>, which is consistent with the disturbed anhydrite permeability reported by Sandia WIPP Project (WIPP PA, 1992–1993). Rock mechanics calculations presented in Appendix D of this report predict that Rustler anhydrites do not develop a DRZ adjacent to the shaft. A value of  $1.49 \times 10^{-19}$  m<sup>2</sup> was selected for the undisturbed permeability of Mudstone 3, consistent with Brinster (1991). A disturbed permeability three orders of magnitude higher than the undisturbed value, or  $1.49 \times 10^{-16}$  m<sup>2</sup>, was assumed for Mudstone 3.

Table C-13. Testing Summary for Rustler Formation

Lithology	Reference(s)	Range (m <sup>2</sup> )	Conductivity (m/s)	Comments
Unnamed lower member: bioturbated clastic zone	Beauheim, 1987 Beauheim et al., 1993	$2.24 \times 10^{-18}$ – $1.84 \times 10^{-18}$	$1.5 \times 10^{-11}$ – $1.2 \times 10^{-11}$	Two build-up tests conducted over a 34.1-m interval
Silty mudstone at 238.4 m	Saulnier & Avis, 1988	$1.49 \times 10^{-20}$ – $1.49 \times 10^{-21}$	$1.0 \times 10^{-13}$ – $1.0 \times 10^{-14}$	Pulse testing in Waste Handling Shaft at discrete depth intervals
Silty claystone at 245.4 m	Saulnier & Avis, 1988	$7.47 \times 10^{-21}$ – $8.97 \times 10^{-22}$	$5.0 \times 10^{-14}$ – $6.0 \times 10^{-13}$	
Culebra Dolomite	Beauheim, 1987	$2.09 \times 10^{-14}$ – $1.18 \times 10^{-14}$	$1.0 \times 10^{-7}$ – $7.9 \times 10^{-8}$	Results of two drill-stem tests conducted in H-16
	Avis & Saulnier, 1990	$1.49 \times 10^{-14}$ – $2.84 \times 10^{-15}$	$1.0 \times 10^{-7}$ – $1.9 \times 10^{-8}$	Interpretation from fluid-pressure response in H-16 during drilling of AIS
Tamarisk Member	Avis & Saulnier, 1990	Response insufficient to estimate	Response insufficient to estimate	Interpretation from fluid-pressure response in H-16 during drilling of AIS
Magenta Member	Beauheim, 1987	$5.68 \times 10^{-16}$	$3.8 \times 10^{-9}$	Drill-stem test in H-16
	Avis & Saulnier, 1990	$1.49 \times 10^{-15}$	$1.0 \times 10^{-8}$	Interpretation from fluid-pressure response in H-16 during drilling of AIS
Forty-niner Member (Mudstone 4)	Beauheim, 1987	$2.84 \times 10^{-16}$ to $2.54 \times 10^{-16}$	$1.9 \times 10^{-9}$ – $1.7 \times 10^{-9}$	Testing at H-16
	Beauheim, 1987	$2.39 \times 10^{-15}$	$1.6 \times 10^{-18}$	Testing at H-14
	Avis & Saulnier, 1990	$3.89 \times 10^{-16}$	$2.6 \times 10^{-9}$	Interpretation from fluid-pressure response in H-16 during drilling of AIS

A value of  $1.49 \times 10^{-15} \text{ m}^2$  was selected as the undisturbed permeability for the Magenta. A value of  $1.49 \times 10^{-14} \text{ m}^2$  was selected for the disturbed permeability for the Magenta. This value is one order of magnitude greater than the undisturbed value.

The Forty-Niner member is composed of Anhydrite, Mudstone 4, and Anhydrite 6. At H-16, the permeability of the Forty-Niner Member is attached to Mudstone 4. Table C-3 summarizes hydraulic testing results for the Forty-Niner Member. Because the hydraulic conductivity value interpreted by Avis and Saulnier (1990) derived from a test that stressed a larger volume of rock, and because their hydraulic conductivity is larger than that determined for Mudstone 4 at H-16, a hydraulic conductivity of  $3.89 \times 10^{-16} \text{ m}^2$  was selected as the undisturbed permeability for Mudstone 4. The disturbed hydraulic conductivity for Mudstone 4 was assigned a value of  $3.89 \times 10^{-13} \text{ m}^2$ , which is three orders of magnitude greater than the undisturbed value. The undisturbed and disturbed permeability for the anhydrite units in the Forty-niner (Anhydrite 4 and Anhydrite 5) were assigned values of  $1.0 \times 10^{-19}$  and  $1.0 \times 10^{-15} \text{ m}^2$ , respectively.

### C3.4.2 Porosity

Hydraulic test analyses have been performed on the members of the Rustler Formation (Beauheim, 1987; Saulnier and Avis, 1988; and Avis and Saulnier, 1990). These investigators assumed porosity values consistent with clays and dolomites, which are considered to be the most permeable units within the Rustler. The porosity values for anhydrite and halite were derived primarily from underground testing at the WIPP. The primary references for the anhydrites and halite porosities are Beauheim et al. (1991), Sandia WIPP Project (1992), and Beauheim et al. (1993). The ranges in porosity values used by WIPP investigators are listed in Table C-14. Selected values for the formation porosities fell within the ranges listed in this table (Tables C-9 and C-10).

Table C-14. Summary of Literature Values for Formation Porosities

Information/Lithology	Reference(s)	Porosity Range
Salado Halite and Anhydrite	Peterson et al., 1987 Beauheim et al., 1991 WIPP PA, 1992–1993 Beauheim et al., 1993	0.001 to 0.01
Rustler clays and dolomites	Beauheim, 1987 Saulnier & Avis, 1988 Brinster, 1991 Freeze & Cherry, 1979	0.05 to 0.3

### C3.4.3 Formation Compressibility

The compressibility of the mudstone units and the transition/bioturbated clastic unit were calculated using Equation C-2 (Touloukian et al., 1981):

$$C_R = \frac{3(1-2\nu)}{E} \quad (\text{C-2})$$

where:

$C_R$  = rock compressibility, Pa<sup>-1</sup>

$\nu$  = Poisson's ratio, dimensionless

$E$  = Young's modulus, Pa<sup>-1</sup>.

Touloukian et al. (1981) give a Young's modulus of 2.83 GPa and a Poisson's ratio of 0.04 for claystone. These values were assumed to be representative of the mudstones in the Rustler Formation. Substituting these values into Equation C-2 yields a rock compressibility of  $9.8 \times 10^{-10}$  Pa<sup>-1</sup>. Dividing this value by the mudstone porosity of 0.30 results in a pore-volume compressibility of  $3.3 \times 10^{-9}$  Pa<sup>-1</sup>.

The lithology of the transition/bioturbated clastic unit can be described as sandstone, siltstone, and halite-cemented sandstone and siltstone. Compressibility data for this unit are not available; therefore Young's modulus and Poisson's ratio for sandstones and siltstones were taken from Touloukian et al. (1981). The average Young's modulus and Poisson's ratio were 19.0 and 0.24 GPa respectively for sandstone, and 25.2 and 0.18 GPa respectively for siltstone. The values for the two rock types were then averaged to obtain a Young's modulus of 22.1 GPa and a Poisson's ratio of 0.21, assumed to be representative of the transition/bioturbated clastic unit. Using Equation C-2 and the assumed porosity of 0.20 yields a rock compressibility of  $7.9 \times 10^{-11}$  Pa<sup>-1</sup> and a pore-volume compressibility of  $3.9 \times 10^{-10}$  Pa<sup>-1</sup> for this unit.

LaVenue et al. (1990) assumed a rock compressibility of  $1.1 \times 10^{-9}$  Pa<sup>-1</sup> for the Culebra in their regional groundwater flow model. This value was adopted for the rock compressibility of the Culebra and Magenta. Dividing this value by the assumed porosity of 0.16 yields a pore-volume compressibility of  $6.9 \times 10^{-9}$  Pa<sup>-1</sup> for these two units.

The median rock compressibility for anhydrite interpreted from borehole testing was  $2.23 \times 10^{-11}$  Pa<sup>-1</sup> (DOE, 1996), which converts to a pore-volume compressibility of  $2.23 \times 10^{-9}$  Pa<sup>-1</sup> for a porosity of 0.01. Because no information about polyhalite compressibility was available, a value equal to that determined for anhydrite was assumed. A value of  $8.05 \times 10^{-9}$  Pa<sup>-1</sup> was used for pore-volume compressibility for the Salado halite. Rock and pore-volume compressibilities for all lithologic units modeled are summarized in Tables C-9 and C-10.

#### C3.4.4 Two-Phase Properties of the Salado

Unsaturated flow properties for Salado halite and anhydrite marker beds were taken from Sandia WIPP Project (WIPP PA, 1992–1993) and are shown in Table C-15 in terms of parameter values for the Brooks-Corey equations for relative permeability and capillary pressure. The required parameters are threshold displacement pressure ( $P_t$ ), residual wetting phase saturation ( $S_{lr}$ ), residual gas saturation ( $S_{gr}$ ), and the pore size distribution parameter ( $\lambda$ ). Threshold displacement pressure ( $P_t$ ) is specified by using the correlation with permeability,  $k$ , suggested by Davies (1991) and documented in Sandia WIPP Project (WIPP PA, 1992–1993). The same parameters were used for both disturbed and undisturbed rock. For the compacted salt column

performance model, it was found that greater numerical stability could be achieved if the TOUGH28W implementations of the Van Genuchten-Parker equations were used for relative permeability and capillary pressure instead of the Brooks-Corey equations. Pressure parameter  $P_o$  in the Van Genuchten-Parker equation for capillary pressure was derived from the Brooks-Corey parameter  $P_c$  in Table C-15 by equating the two formulas at an effective saturation of 0.5.

Table C-15. Salado Two-Phase Properties

Parameter	Salado Halite and Polyhalite	Salado Anhydrite
$P_t$ (MPa)	$5.6 \times 10^{-7} [k(m^2)]^{-0.346}$	$2.6 \times 10^{-7} [k(m^2)]^{-0.346}$
$S_{lr}$	0.2	0.2
$S_{gr}$	0.0	0.0
$\lambda$	0.7	0.7

### C3.5 DRZ Properties

A disturbed rock zone (DRZ) forms around excavations in the bedded halite of the Salado Formation immediately upon passage of the mining tools, and progressively develops over time with the unloading of the formation as it creeps into excavations (Stormont, 1990). Van Sambeek et al. (1993) refer to the DRZ that forms upon mining as the "initial DRZ" and the DRZ that forms as a result of creep deformation and stress redistribution as the "secondary DRZ." The DRZ extends radially out from the shaft wall into the host formation. The DRZ is expected to have the following characteristics: (1) increased porosity resulting from micro- or macro-fracturing, (2) increased fluid (gas or liquid) permeability, (3) decreased brine saturation, (4) decreased load-bearing capacity, and (5) decreased lithostatic pressure (Stormont, 1990; Van Sambeek et al., 1993). Because of these properties, the DRZ could act as a vertical flow path for brine and gas around a shaft seal. It is important to characterize the extent of the DRZ around the shaft excavations and its time-dependent properties (especially permeability).

Laboratory, field, and modeling studies have been performed to determine the mechanics of DRZ development. DRZ development has been documented in almost all horizontal rectangular excavations of the WIPP underground facility through gas permeability testing (Stormont et al., 1987; Stormont, 1990), visual observations (Borns and Stormont, 1988), and by other methodologies (Holcomb, 1988). Laboratory testing of salt cores has also provided significant insight into DRZ development. Hansen and Mellegard (1979) found that dilatancy is favored by conditions of low confining stress and high deviatoric stress, which characterize the region near an excavation. Laboratory testing has shown that a halite DRZ is self-healing given the proper stress conditions; Brodsky (1990) showed that artificially damaged cores could be healed with certain confining pressures and time.

Two hydraulic testing programs have been conducted within WIPP shafts. The earliest hydraulic testing program was conducted in the Waste Handling Shaft (Saulnier and Avis, 1988). More recently, hydraulic testing was performed to determine the extent of the DRZ in the AIS.

Six boreholes, three at each of two levels, were used to determine both gas and brine permeabilities (Dale and Hurtado, 1996).

### Waste Handling Shaft Hydraulic Testing

The objective of the hydraulic testing conducted in the Waste Handling Shaft (Saulnier and Avis, 1988) was to identify the DRZ using permeability testing. This testing used a three-packer system capable of simultaneously testing the permeability in three zones at three different radial distances from the shaft. Four levels were tested, two in the unnamed lower member of the Rustler (depths 238.4 m [782 ft] and 245.4 m [805 ft] below ground surface [bgs], which coincide with the transition and bioturbated clastic zones), one just below the Rustler/Salado contact in halite (at a depth of 259.1 m [850 ft] bgs), and one in Salado halite, anhydrite, and polyhalite (at a depth of 402.3 m [1320 ft] bgs). The results from these tests showed no correlation between permeability and radial distance from the shaft at any level and did not identify the DRZ. A potential reason the DRZ was not clearly identified in the Waste Handling Shaft was the location of the test intervals. For three of the test intervals, the test closest to the shaft was located 1 m (3.2 ft) from the excavation. One test conducted in the Waste Handling Shaft (W850W) tested a zone located within 0.3 m (1 ft) of the shaft liner. The test zone closest to the shaft for test W850W extended from the outer edge of the shaft liner to a distance of 1.25 m (4.08 ft) from the shaft. This zone included the liner/DRZ interface and the DRZ. Saulnier and Avis (1988) report that testing of this zone proved futile because the zone could not be pressurized. They concluded that the test zone included an open fracture or a gap representing the liner/DRZ interface.

### Air Intake Shaft Hydraulic Testing

Permeability testing was conducted to determine the radial extent of the DRZ in the Salado Formation surrounding the AIS. Testing was conducted at two levels within the AIS (Level A at 345.9 m [1135 ft] and Level C at 626.4 m [2,055 ft] bgs). At each of the two levels tested, three 10-cm (4-in.) diameter boreholes were drilled at a spacing of 120° into the formation at a 6° angle below the horizontal. The boreholes were drilled to a depth of approximately 6 m (20 ft). All six boreholes were gas-flow tested prior to the performance of brine testing. It is expected that the regions of the DRZ closest to the shaft wall have the greatest dilation and are likely the most desaturated (i.e., have brine saturations significantly less than 1.0). As the permeability of the DRZ approaches the intact permeability at greater radial distances, it is expected that the brine saturation of the DRZ approaches unity. Gas-flow tests were performed to determine the extent of the desaturated region (and, in so doing, define the radius where brine testing can be performed), to identify the relative permeability to gas of the DRZ, and to bracket the DRZ threshold pressure.

The distance within the boreholes at which the brine-permeability tests were conducted was based on the results of the gas-permeability testing. For gas-flow testing, a four-packer test tool was initially set so that the first test zone started at 6 in. from the shaft wall and extended an additional 15 in. into the formation. If gas flow was observed at that depth, the test tool was inserted an additional 2 to 4 in. and another test was performed. The process was repeated until a test with no observable gas flow was obtained. Brine-flow testing was performed approximately 5 to 6 in. beyond the distance at which no gas flow was observed. The objective of the brine-

permeability tests was to bracket the Salado permeability as a function of radial distance away from the shaft face in brine-saturated portions of the Salado. It was assumed that if the gas-permeability estimate was above  $1.0 \times 10^{-21} \text{ m}^2$ , the formation was not completely saturated with respect to brine. Once the gas permeability decreased to less than or equal to  $1.0 \times 10^{-21} \text{ m}^2$ , the formation was assumed to be at high brine saturations. The intact salt permeability was assumed (based on repository horizon testing) to be approximately  $1.0 \times 10^{-21} \text{ m}^2$ . This order of magnitude value for intact permeability was confirmed with the brine testing in the AIS. The gas permeability testing system threshold was  $1.0 \times 10^{-23} \text{ m}^2$ .

### C3.5.1 Model for Calculating the Effective DRZ Permeability

From the results of the field testing in the AIS it was determined that the permeability of the Salado halite can vary over orders of magnitude across the DRZ. An effective permeability of the DRZ can be estimated through the definition of a functional relationship for the change in permeability as a function of radial distance in the DRZ. The AIS field data provide insight into the variation of permeability in the DRZ and the extent of the DRZ. Figure C-1 plots the AIS brine and gas permeability results along with several lines demonstrating potential relationships of DRZ permeability as a function of radial distance and the extent of the DRZ.

This interpretation is taken from Dale and Hurtado (1996); the details are not provided here. The AIS field data support the assumption that the DRZ permeability is greatest in the DRZ near the excavation face and decreases radially outward away from the shaft wall. Figure C-1 shows that a log-linear model of permeability as a function of radial distance is reasonable, based on the field results. A log-linear variation in permeability is also consistent with radial variation in dilatant strain predicted in the DRZ. Figure C-2 is a schematic of a shaft with a DRZ of inner radius  $r_i$  and outer radius  $r_o$ . It is assumed that the permeability  $k_i$  at  $r_i$  is several orders of magnitude higher than the intact undisturbed permeability  $k_o$  defined at  $r_o$ . A log-linear model is assumed to describe the DRZ permeability as a function of radial distance, and used to calculate an effective DRZ permeability. Field data are limited, and a precise functional relation for the radial change in permeability is not known. However, this model captures results of available field data and incorporates the largest calculated extent of the DRZ.

An equation was derived to calculate the effective DRZ permeability assuming that the change in permeability within the DRZ is log-linear. For a given  $r_i$ ,  $k_i$ ,  $r_o$ , and  $k_o$ , an effective DRZ permeability can be calculated that accounts for both the decrease in DRZ permeability and the increase in flow area as a function of radial distance away from the excavation. The equation for the effective DRZ permeability is:

$$k_{\text{DRZ}} = \frac{2}{r_o + r_i} \left[ \left( \frac{r_o [\ln(k_o) - \ln(k_i)] - \Delta r}{[\ln(k_o) - \ln(k_i)]^2} \right) k_o - \left( \frac{r_i [\ln(k_o) - \ln(k_i)] - \Delta r}{[\ln(k_o) - \ln(k_i)]^2} \right) k_i \right] \quad (\text{C-3})$$

where  $\Delta r$  is equal to the outer DRZ radius minus the inner DRZ radius.

Figure C-1 demonstrates that this relationship (dotted lines) provides a reasonable representation of the field permeability test results for both the upper and lower zones of the AIS.

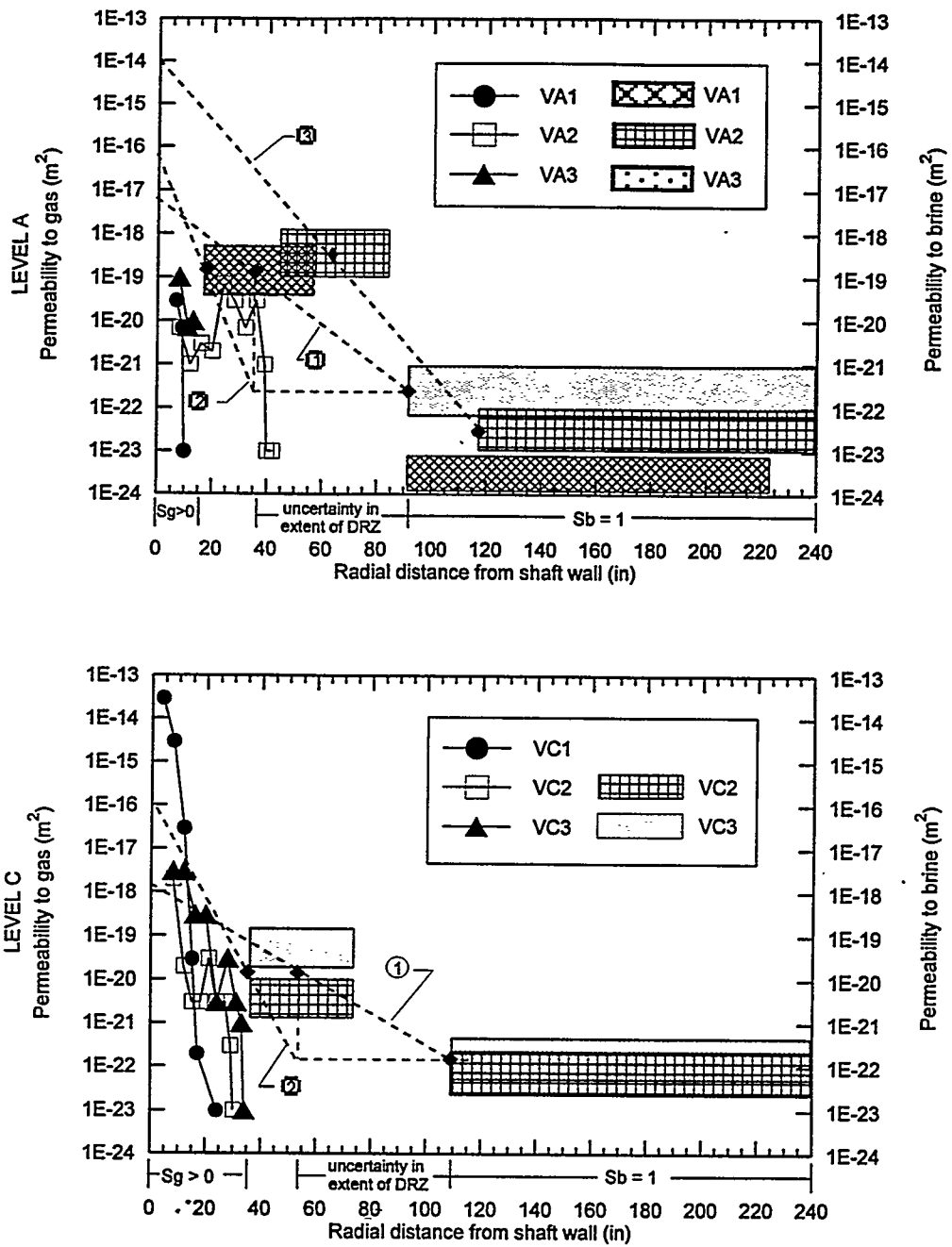
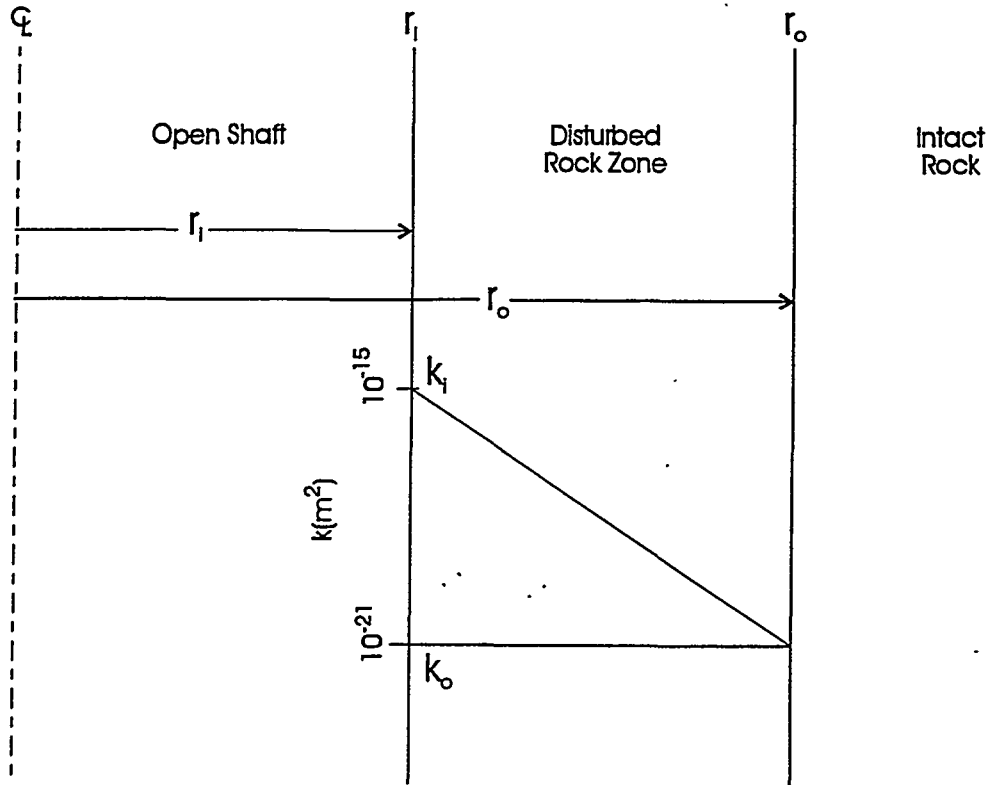


Figure C-1. AIS field permeability results.



- $k_i$  Represents Maximum Dilatation
- $k_o$  Represents Intact Conditions
- $r_1$  Excavation Face, Inner Radius of DRZ
- $r_o$  Outer Radius of DRZ

Figure C-2. Log-linear model for the calculation of an effective permeability of the DRZ.

### C3.5.2 Model DRZ Effective Permeability

Rock mechanics calculations have been performed to predict the DRZ extent in both the Rustler and Salado formations. These calculations are presented in Appendix D of this report. The extent of the DRZ within the Rustler Formation is a function of rock type and depth. Mechanical calculations presented in Appendix D indicate no DRZ for anhydrites and dolomites, and a DRZ extent that increases with shaft depth for mudstones. The DRZ extent for the Rustler mudstones was interpolated from values given in Appendix D. For the base case assumption, the anhydrites were assumed to have no DRZ, consistent with the mechanical calculations presented in Appendix D. However, for the base-case model conceptualization, the Magenta and Culebra dolomites were assigned a DRZ. This was done to account for the fact that both of these dolomites are naturally fractured and the mechanical calculations did not account for the

presence of fractures. The extent of the DRZ for dolomite was set equal to one shaft radius. The DRZ in the Rustler is assumed not to heal as a function of time.

The DRZ extent within the Salado halite is calculated as a function of depth, shaft seal material, and time. In the Salado, the halite DRZ is at a maximum at closure and heals as a function of time. Healing occurs quickest with increased depth of burial and increased stiffness (bulk modulus) of the shaft seal material. Calculations of the radial extent of the halite DRZ for times 0, 10, 25, 50, and 100 years after shaft closure are provided in Appendix D. Plots of the halite DRZ extent adjacent to the various seal materials are also shown in Appendix D.

For halite, the effective DRZ permeability was calculated with Equation C-3 using the extent of the halite DRZ from Appendix D and the disturbed halite permeability at the shaft/DRZ interface. The effective permeability of the DRZ, as calculated using Equation C-3, is controlled by the permeability at the shaft/DRZ interface ( $k_i$ ). For these calculations,  $k_i$  is assumed to remain constant and at its maximum value as long as a DRZ is predicted. In reality, it is expected that as the DRZ heals (halite),  $k_i$  will also decrease in magnitude. Therefore the calculation of the effective DRZ permeability is considered conservative.

Also presented in Appendix D are mechanical calculations that predict the DRZ in anhydrite Salado interbeds as a function of interbed thickness. These calculations show that for an anhydrite interbed thickness less than approximately 0.8 m, the anhydrite interbeds develop a DRZ approximately 1 m in extent. Previous estimates predicted that Salado anhydrite units with a thickness of less than 3 m have a DRZ extending 1 m from the shaft. For the base-case conceptualization, anhydrite units equal to or greater than 3 m in thickness were assigned no DRZ.

Because the anhydrite and polyhalite DRZs do not heal, the values calculated for DRZ extent do not change with time for these units. The DRZ extent for polyhalite for all times was assumed to be equal to the halite DRZ extent for the open shaft time period. Effective DRZ permeabilities based on Equation C-3 were adjusted for the difference between model DRZ areas, which do not vary (12% of shaft radius), and the variable DRZ areas described above.

Mechanical calculations predict that anhydrites within the Rustler and several within the Salado do not form a DRZ. These predictions do not account for damage induced during shaft construction, such as blasting damage. Because field data are not available for the DRZ in the Rustler members and Salado anhydrites, the models assume that the DRZ may be configured as "continuous" or "discontinuous." The discontinuous DRZ assumption utilizes only intact permeability values for Salado anhydrites and Rustler members. The continuous DRZ assumes these lithologies are damaged, and permeabilities are adjusted accordingly.

The model grids in this appendix do not include a discrete interface zone between shaft seal materials and the DRZ. This is because the model grids presented were based on the assumption that a continuous DRZ would be considered in all simulations. In the base-case conceptualization, a discontinuous DRZ is modeled consistent with mechanical predictions. However, in all cases the models are also run considering a continuous DRZ.

Mechanical calculations presented in Appendix D indicate that the DRZ surrounding the concrete-asphalt waterstops becomes discontinuous through healing of the salt within 2 years after emplacement. In the modeling in this appendix, it is assumed that the waterstops

effectively intersect the DRZ at 2 years after seal emplacement. Table C-16 gives the permeability values used for the base case conceptualization of the DRZ.

At the Rustler/Salado contact, unsaturated Rustler brine can potentially enter the Salado DRZ. Seepage of Rustler groundwater into the Salado DRZ could result in dissolution of Salado salt. It has been postulated that this type of dissolution would produce a direct conduit from the Rustler/ Salado contact to the lower Salado sealing system. Approximately  $1.4 \times 10^{-4} \text{ m}^3$  (0.3 kg) of salt are required to fully saturate  $10^{-3} \text{ m}^3$  (1 kg) of Culebra groundwater (Siegel et al., 1991). The potential for creation of such a conduit will be treated within Performance Model 1.

## **C4. FLOW DOWN FROM THE RUSTLER (MODEL 1)**

### **C4.1 Statement of Problem**

The shaft seal system is designed to limit migration of fluids within the sealed shaft. Using the approximation of a completely saturated seal system, this calculation examined the potential for flow and quantity of flow that migrates from the Rustler and Salado down the shaft during early times. The performance measures (results) from this model are brine flow rate and cumulative brine volume over a 200-year time frame after repository closure. These performance measures are presented at (1) the Rustler/Salado interface, (2) the top of the compacted salt column, and (3) the base of the compacted salt column.

### **C4.2 Performance Model 1 Description**

#### **C4.2.1 Conceptual Model and Assumptions**

To investigate the potential for vertical flow down from the Rustler through the shaft seal system, a full-shaft saturated-flow model was used. The focus of this calculation was to estimate the amount of brine flowing down through the shaft seal system to reach the top of the compacted salt column and, potentially, the repository.

Conceptually, flow down the seal system is an early-time issue. Over time, pressures at depth in the seal system will equilibrate to far-field pressures, which are significantly over-pressured with respect to the Rustler, and the downward driving force will reverse its direction. However, because the Rustler will repressurize more rapidly than the Salado, there is a potential for downward flow during the seal repressurization period. To characterize this period, the flow system has been conceptualized as a shaft seal system and an adjacent DRZ surrounded by host rocks. The primary assumptions are listed below:

- This calculation assumed that the primary water-producing zones above the Salado Formation are within the Rustler Formation. As a result, this calculation did not include supra-Rustler units.
- The calculation assumed brine-saturated flow conditions. This assumption (1) did not account for the time required or volume of liquid required to saturate the seal components and (2) overestimated brine transmissivities over the time period where the DRZ and seals would be variably saturated.

Table C-16. Model DRZ Permeability for Base-Case Conceptualization (Corrected for Model DRZ Area)

Row	Unit	Intrinsic Permeability (m <sup>2</sup> )					
		Time=0 Yr	Time=2 Yr	Time=10 Yr	Time=25 Yr	Time=50 Yr	Time=100 Yr
1	Anhydrite5	1.00×10 <sup>-19</sup>	1.00×10 <sup>-19</sup>	1.00×10 <sup>-19</sup>	1.00×10 <sup>-19</sup>	1.00×10 <sup>-19</sup>	1.00×10 <sup>-19</sup>
2	Anhydrite5	1.00×10 <sup>-19</sup>	1.00×10 <sup>-19</sup>	1.00×10 <sup>-19</sup>	1.00×10 <sup>-19</sup>	1.00×10 <sup>-19</sup>	1.00×10 <sup>-19</sup>
3	Mudstone4	5.99×10 <sup>-13</sup>	5.99×10 <sup>-13</sup>	5.99×10 <sup>-13</sup>	5.99×10 <sup>-13</sup>	5.99×10 <sup>-13</sup>	5.99×10 <sup>-13</sup>
4	Mudstone4	5.99×10 <sup>-13</sup>	5.99×10 <sup>-13</sup>	5.99×10 <sup>-13</sup>	5.99×10 <sup>-13</sup>	5.99×10 <sup>-13</sup>	5.99×10 <sup>-13</sup>
5	Anhydrite4	1.00×10 <sup>-19</sup>	1.00×10 <sup>-19</sup>	1.00×10 <sup>-19</sup>	1.00×10 <sup>-19</sup>	1.00×10 <sup>-19</sup>	1.00×10 <sup>-19</sup>
6	Magenta	6.06×10 <sup>-14</sup>	6.06×10 <sup>-14</sup>	6.06×10 <sup>-14</sup>	6.06×10 <sup>-14</sup>	6.06×10 <sup>-14</sup>	6.06×10 <sup>-14</sup>
7	Anhydrite3	1.00×10 <sup>-19</sup>	1.00×10 <sup>-19</sup>	1.00×10 <sup>-19</sup>	1.00×10 <sup>-19</sup>	1.00×10 <sup>-19</sup>	1.00×10 <sup>-19</sup>
8	Anhydrite3	1.00×10 <sup>-19</sup>	1.00×10 <sup>-19</sup>	1.00×10 <sup>-19</sup>	1.00×10 <sup>-19</sup>	1.00×10 <sup>-19</sup>	1.00×10 <sup>-19</sup>
9	Mudstone3	2.75×10 <sup>-16</sup>	2.75×10 <sup>-16</sup>	2.75×10 <sup>-16</sup>	2.75×10 <sup>-16</sup>	2.75×10 <sup>-16</sup>	2.75×10 <sup>-16</sup>
10	Anhydrite2	1.00×10 <sup>-19</sup>	1.00×10 <sup>-19</sup>	1.00×10 <sup>-19</sup>	1.00×10 <sup>-19</sup>	1.00×10 <sup>-19</sup>	1.00×10 <sup>-19</sup>
11	Anhydrite2	1.00×10 <sup>-19</sup>	1.00×10 <sup>-19</sup>	1.00×10 <sup>-19</sup>	1.00×10 <sup>-19</sup>	1.00×10 <sup>-19</sup>	1.00×10 <sup>-19</sup>
12	Culbera/Mudstone2	8.50×10 <sup>-13</sup>	8.50×10 <sup>-13</sup>	8.50×10 <sup>-13</sup>	8.50×10 <sup>-13</sup>	8.50×10 <sup>-13</sup>	8.50×10 <sup>-13</sup>
13	Anhydrite1/Mudstone1	1.00×10 <sup>-19</sup>	1.00×10 <sup>-19</sup>	1.00×10 <sup>-19</sup>	1.00×10 <sup>-19</sup>	1.00×10 <sup>-19</sup>	1.00×10 <sup>-19</sup>
14	Transition/Bioturbated Clastics	4.94×10 <sup>-15</sup>	4.94×10 <sup>-15</sup>	4.94×10 <sup>-15</sup>	4.94×10 <sup>-15</sup>	4.94×10 <sup>-15</sup>	4.94×10 <sup>-15</sup>
15	Transition/Bioturbated Clastics	4.94×10 <sup>-15</sup>	4.94×10 <sup>-15</sup>	4.94×10 <sup>-15</sup>	4.94×10 <sup>-15</sup>	4.94×10 <sup>-15</sup>	4.94×10 <sup>-15</sup>
16	Transition/Bioturbated Clastics	4.94×10 <sup>-15</sup>	4.94×10 <sup>-15</sup>	4.94×10 <sup>-15</sup>	4.94×10 <sup>-15</sup>	4.94×10 <sup>-15</sup>	4.94×10 <sup>-15</sup>
17	Transition/Bioturbated Clastics	4.94×10 <sup>-15</sup>	4.94×10 <sup>-15</sup>	4.94×10 <sup>-15</sup>	4.94×10 <sup>-15</sup>	4.94×10 <sup>-15</sup>	4.94×10 <sup>-15</sup>
18	Transition/Bioturbated Clastics	4.94×10 <sup>-15</sup>	4.94×10 <sup>-15</sup>	4.94×10 <sup>-15</sup>	4.94×10 <sup>-15</sup>	4.94×10 <sup>-15</sup>	4.94×10 <sup>-15</sup>
19	Transition/Bioturbated Clastics	4.94×10 <sup>-15</sup>	4.94×10 <sup>-15</sup>	4.94×10 <sup>-15</sup>	4.94×10 <sup>-15</sup>	4.94×10 <sup>-15</sup>	4.94×10 <sup>-15</sup>
20	Salado Halite	3.64×10 <sup>-16</sup>	3.64×10 <sup>-16</sup>	3.62×10 <sup>-16</sup>	3.59×10 <sup>-16</sup>	3.55×10 <sup>-16</sup>	3.49×10 <sup>-16</sup>
21	Salado Halite	3.68×10 <sup>-16</sup>	3.68×10 <sup>-16</sup>	1.10×10 <sup>-16</sup>	4.05×10 <sup>-17</sup>	1.00×10 <sup>-21</sup>	1.00×10 <sup>-21</sup>

Table C-16. Model DRZ Permeability for Base-Case Conceptualization (Corrected for Model DRZ Area)

Row	Unit	Intrinsic Permeability (m <sup>2</sup> )					
		Time=0 Yr	Time=2 Yr	Time=10 Yr	Time=25 Yr	Time=50 Yr	Time=100 Yr
22	Salado Halite	3.70×10 <sup>-16</sup>	3.70×10 <sup>-16</sup>	1.08×10 <sup>-16</sup>	3.88×10 <sup>-17</sup>	1.00×10 <sup>-21</sup>	1.00×10 <sup>-21</sup>
23	Salado Halite	3.72×10 <sup>-16</sup>	3.72×10 <sup>-16</sup>	1.07×10 <sup>-16</sup>	3.80×10 <sup>-17</sup>	1.00×10 <sup>-21</sup>	1.00×10 <sup>-21</sup>
24	Salado Halite	3.73×10 <sup>-16</sup>	3.73×10 <sup>-16</sup>	1.06×10 <sup>-16</sup>	3.72×10 <sup>-17</sup>	1.00×10 <sup>-21</sup>	1.00×10 <sup>-21</sup>
25	Salado Halite	3.74×10 <sup>-16</sup>	3.74×10 <sup>-16</sup>	3.72×10 <sup>-16</sup>	3.69×10 <sup>-16</sup>	3.65×10 <sup>-16</sup>	3.58×10 <sup>-16</sup>
26	Salado Halite	3.76×10 <sup>-16</sup>	3.76×10 <sup>-16</sup>	3.73×10 <sup>-16</sup>	3.70×10 <sup>-16</sup>	3.66×10 <sup>-16</sup>	3.60×10 <sup>-16</sup>
27	Salado Halite	3.78×10 <sup>-16</sup>	3.78×10 <sup>-16</sup>	3.76×10 <sup>-16</sup>	3.73×10 <sup>-16</sup>	3.69×10 <sup>-16</sup>	3.62×10 <sup>-16</sup>
28	Salado Halite	3.83×10 <sup>-16</sup>	3.83×10 <sup>-16</sup>	3.81×10 <sup>-16</sup>	3.78×10 <sup>-16</sup>	3.73×10 <sup>-16</sup>	3.66×10 <sup>-16</sup>
29	Salado Halite	3.86×10 <sup>-16</sup>	3.86×10 <sup>-16</sup>	9.75×10 <sup>-17</sup>	2.87×10 <sup>-17</sup>	1.00×10 <sup>-21</sup>	1.00×10 <sup>-21</sup>
30	Salado Halite	3.88×10 <sup>-16</sup>	3.88×10 <sup>-16</sup>	9.62×10 <sup>-17</sup>	2.74×10 <sup>-17</sup>	1.00×10 <sup>-21</sup>	1.00×10 <sup>-21</sup>
31	Salado Halite	3.90×10 <sup>-16</sup>	1.00×10 <sup>-20</sup>				
32	Salado Halite	3.91×10 <sup>-16</sup>	3.91×10 <sup>-16</sup>	9.47×10 <sup>-17</sup>	2.60×10 <sup>-17</sup>	1.00×10 <sup>-21</sup>	1.00×10 <sup>-21</sup>
33	Salado Halite	3.93×10 <sup>-16</sup>	3.93×10 <sup>-16</sup>	9.33×10 <sup>-17</sup>	2.47×10 <sup>-17</sup>	1.00×10 <sup>-21</sup>	1.00×10 <sup>-21</sup>
34	Combined Unit 1	1.15×10 <sup>-18</sup>	1.15×10 <sup>-18</sup>	1.15×10 <sup>-18</sup>	1.15×10 <sup>-18</sup>	1.15×10 <sup>-18</sup>	1.15×10 <sup>-18</sup>
35	Combined Unit 1	1.15×10 <sup>-18</sup>	1.15×10 <sup>-18</sup>	1.15×10 <sup>-18</sup>	1.15×10 <sup>-18</sup>	1.15×10 <sup>-18</sup>	1.15×10 <sup>-18</sup>
36	Salado Halite	4.00×10 <sup>-16</sup>	4.00×10 <sup>-16</sup>	2.92×10 <sup>-16</sup>	1.97×10 <sup>-16</sup>	1.01×10 <sup>-16</sup>	2.56×10 <sup>-17</sup>
37	Salado Halite	4.05×10 <sup>-16</sup>	4.05×10 <sup>-16</sup>	2.90×10 <sup>-16</sup>	1.91×10 <sup>-16</sup>	9.13×10 <sup>-17</sup>	1.81×10 <sup>-17</sup>
38	Salado Halite	4.13×10 <sup>-16</sup>	4.13×10 <sup>-16</sup>	2.86×10 <sup>-16</sup>	1.81×10 <sup>-16</sup>	7.85×10 <sup>-17</sup>	7.76×10 <sup>-18</sup>
39	Combined Unit 2	1.04×10 <sup>-18</sup>	1.04×10 <sup>-18</sup>	1.04×10 <sup>-18</sup>	1.04×10 <sup>-18</sup>	1.04×10 <sup>-18</sup>	1.04×10 <sup>-18</sup>
40	Salado Halite	4.25×10 <sup>-16</sup>	4.25×10 <sup>-16</sup>	2.75×10 <sup>-16</sup>	1.63×10 <sup>-16</sup>	6.00×10 <sup>-17</sup>	1.00×10 <sup>-21</sup>
41	Salado Halite	4.32×10 <sup>-16</sup>	4.32×10 <sup>-16</sup>	2.66×10 <sup>-16</sup>	1.51×10 <sup>-16</sup>	5.04×10 <sup>-17</sup>	1.00×10 <sup>-21</sup>
42	Salado Halite	4.37×10 <sup>-16</sup>	4.37×10 <sup>-16</sup>	2.61×10 <sup>-16</sup>	1.42×10 <sup>-16</sup>	4.37×10 <sup>-17</sup>	1.00×10 <sup>-21</sup>
43	Combined Unit 3	4.79×10 <sup>-16</sup>	4.79×10 <sup>-16</sup>	4.79×10 <sup>-16</sup>	4.79×10 <sup>-16</sup>	4.79×10 <sup>-16</sup>	4.79×10 <sup>-16</sup>
44	Salado Halite	4.41×10 <sup>-16</sup>	4.41×10 <sup>-16</sup>	2.55×10 <sup>-16</sup>	1.34×10 <sup>-16</sup>	3.73×10 <sup>-17</sup>	1.00×10 <sup>-21</sup>
45	Salado Halite	4.44×10 <sup>-16</sup>	4.44×10 <sup>-16</sup>	2.52×10 <sup>-16</sup>	1.29×10 <sup>-16</sup>	3.35×10 <sup>-17</sup>	1.00×10 <sup>-21</sup>
46	Salado Halite	4.47×10 <sup>-16</sup>	4.47×10 <sup>-16</sup>	2.49×10 <sup>-16</sup>	1.25×10 <sup>-16</sup>	3.00×10 <sup>-17</sup>	1.00×10 <sup>-21</sup>
47	Vaca Triste	1.40×10 <sup>-16</sup>	1.40×10 <sup>-16</sup>	1.40×10 <sup>-16</sup>	1.40×10 <sup>-16</sup>	1.40×10 <sup>-16</sup>	1.40×10 <sup>-16</sup>

Table C-16. Model DRZ Permeability for Base-Case Conceptualization (Corrected for Model DRZ Area)

Row	Unit	Intrinsic Permeability (m <sup>2</sup> )					
		Time=0 Yr	Time=2 Yr	Time=10 Yr	Time=25 Yr	Time=50 Yr	Time=100 Yr
48	Salado Halite	4.49×10 <sup>-16</sup>	4.49×10 <sup>-16</sup>	2.45×10 <sup>-16</sup>	1.20×10 <sup>-16</sup>	2.64×10 <sup>-17</sup>	1.00×10 <sup>-21</sup>
49	Salado Halite	4.50×10 <sup>-16</sup>	4.50×10 <sup>-16</sup>	2.45×10 <sup>-16</sup>	1.19×10 <sup>-16</sup>	2.55×10 <sup>-17</sup>	1.00×10 <sup>-21</sup>
50	Salado Halite	4.52×10 <sup>-16</sup>	4.52×10 <sup>-16</sup>	5.44×10 <sup>-17</sup>	2.94×10 <sup>-18</sup>	1.00×10 <sup>-21</sup>	1.00×10 <sup>-21</sup>
51	Salado Halite	4.53×10 <sup>-16</sup>	4.53×10 <sup>-16</sup>	5.32×10 <sup>-17</sup>	2.64×10 <sup>-18</sup>	1.00×10 <sup>-21</sup>	1.00×10 <sup>-21</sup>
52	Salado Halite	4.54×10 <sup>-16</sup>	1.00×10 <sup>-20</sup>				
53	Salado Halite	4.55×10 <sup>-16</sup>	4.55×10 <sup>-16</sup>	5.19×10 <sup>-17</sup>	2.30×10 <sup>-18</sup>	1.00×10 <sup>-21</sup>	1.00×10 <sup>-21</sup>
54	Salado Halite	4.57×10 <sup>-16</sup>	4.57×10 <sup>-16</sup>	5.07×10 <sup>-17</sup>	2.00×10 <sup>-18</sup>	1.00×10 <sup>-21</sup>	1.00×10 <sup>-21</sup>
55	Salado Halite	4.60×10 <sup>-16</sup>	4.60×10 <sup>-16</sup>	9.88×10 <sup>-17</sup>	7.89×10 <sup>-18</sup>	1.00×10 <sup>-21</sup>	1.00×10 <sup>-21</sup>
56	Salado Halite	4.65×10 <sup>-16</sup>	4.65×10 <sup>-16</sup>	9.40×10 <sup>-17</sup>	3.94×10 <sup>-18</sup>	1.00×10 <sup>-21</sup>	1.00×10 <sup>-21</sup>
57	Combined Unit 4	5.46×10 <sup>-16</sup>	5.46×10 <sup>-16</sup>	1.73×10 <sup>-16</sup>	9.66×10 <sup>-19</sup>	1.90×10 <sup>-20</sup>	1.90×10 <sup>-20</sup>
58	Salado Halite	4.71×10 <sup>-16</sup>	4.71×10 <sup>-16</sup>	8.65×10 <sup>-17</sup>	1.00×10 <sup>-21</sup>	1.00×10 <sup>-21</sup>	1.00×10 <sup>-21</sup>
59	Salado Halite	4.73×10 <sup>-16</sup>	4.73×10 <sup>-16</sup>	8.36×10 <sup>-17</sup>	1.00×10 <sup>-21</sup>	1.00×10 <sup>-21</sup>	1.00×10 <sup>-21</sup>
60	Union Anhydrite	3.86×10 <sup>-16</sup>	3.86×10 <sup>-16</sup>	3.86×10 <sup>-16</sup>	3.86×10 <sup>-16</sup>	3.86×10 <sup>-16</sup>	3.86×10 <sup>-16</sup>
61	Salado Halite	4.76×10 <sup>-16</sup>	4.76×10 <sup>-16</sup>	8.08×10 <sup>-17</sup>	1.00×10 <sup>-21</sup>	1.00×10 <sup>-21</sup>	1.00×10 <sup>-21</sup>
62	Salado Halite	4.78×10 <sup>-16</sup>	4.78×10 <sup>-16</sup>	7.80×10 <sup>-17</sup>	1.00×10 <sup>-21</sup>	1.00×10 <sup>-21</sup>	1.00×10 <sup>-21</sup>
63	Salado Halite	4.81×10 <sup>-16</sup>	4.81×10 <sup>-16</sup>	7.42×10 <sup>-17</sup>	1.00×10 <sup>-21</sup>	1.00×10 <sup>-21</sup>	1.00×10 <sup>-21</sup>
64	Combined Unit 5	3.37×10 <sup>-16</sup>	3.37×10 <sup>-16</sup>	3.37×10 <sup>-16</sup>	3.37×10 <sup>-16</sup>	3.37×10 <sup>-16</sup>	3.37×10 <sup>-16</sup>
65	Salado Halite	4.85×10 <sup>-16</sup>	4.85×10 <sup>-16</sup>	6.91×10 <sup>-17</sup>	1.00×10 <sup>-21</sup>	1.00×10 <sup>-21</sup>	1.00×10 <sup>-21</sup>
66	Salado Halite	4.88×10 <sup>-16</sup>	4.88×10 <sup>-16</sup>	6.62×10 <sup>-17</sup>	1.00×10 <sup>-21</sup>	1.00×10 <sup>-21</sup>	1.00×10 <sup>-21</sup>
67	Salado Halite	4.90×10 <sup>-16</sup>	4.90×10 <sup>-16</sup>	6.34×10 <sup>-17</sup>	1.00×10 <sup>-21</sup>	1.00×10 <sup>-21</sup>	1.00×10 <sup>-21</sup>
68	Combined Unit 6	5.91×10 <sup>-16</sup>	5.91×10 <sup>-16</sup>	7.93×10 <sup>-17</sup>	1.08×10 <sup>-20</sup>	1.08×10 <sup>-20</sup>	1.08×10 <sup>-20</sup>
69	Salado Halite	4.93×10 <sup>-16</sup>	4.93×10 <sup>-16</sup>	5.96×10 <sup>-17</sup>	1.00×10 <sup>-21</sup>	1.00×10 <sup>-21</sup>	1.00×10 <sup>-21</sup>
70	Salado Halite	4.95×10 <sup>-16</sup>	4.95×10 <sup>-16</sup>	5.67×10 <sup>-17</sup>	1.00×10 <sup>-21</sup>	1.00×10 <sup>-21</sup>	1.00×10 <sup>-21</sup>
71	Combined Unit 7	5.94×10 <sup>-16</sup>	5.94×10 <sup>-16</sup>	8.12×10 <sup>-17</sup>	1.33×10 <sup>-20</sup>	1.33×10 <sup>-20</sup>	1.33×10 <sup>-20</sup>
72	Salado Halite	5.03×10 <sup>-16</sup>	5.03×10 <sup>-16</sup>	4.77×10 <sup>-17</sup>	1.00×10 <sup>-21</sup>	1.00×10 <sup>-21</sup>	1.00×10 <sup>-21</sup>
73	Salado Halite	5.05×10 <sup>-16</sup>	5.05×10 <sup>-16</sup>	4.38×10 <sup>-17</sup>	1.00×10 <sup>-21</sup>	1.00×10 <sup>-21</sup>	1.00×10 <sup>-21</sup>

Table C-16. Model DRZ Permeability for Base-Case Conceptualization (Corrected for Model DRZ Area)

Row	Unit	Intrinsic Permeability (m <sup>2</sup> )					
		Time=0 Yr	Time=2 Yr	Time=10 Yr	Time=25 Yr	Time=50 Yr	Time=100 Yr
74	Salado Halite	5.06×10 <sup>-16</sup>	5.06×10 <sup>-16</sup>	4.15×10 <sup>-17</sup>	1.00×10 <sup>-21</sup>	1.00×10 <sup>-21</sup>	1.00×10 <sup>-21</sup>
75	Combined Unit 8	5.85×10 <sup>-16</sup>	5.85×10 <sup>-16</sup>	8.42×10 <sup>-17</sup>	1.88×10 <sup>-20</sup>	1.88×10 <sup>-20</sup>	1.88×10 <sup>-20</sup>
76	Salado Halite	5.08×10 <sup>-16</sup>	5.08×10 <sup>-16</sup>	3.89×10 <sup>-17</sup>	1.00×10 <sup>-21</sup>	1.00×10 <sup>-21</sup>	1.00×10 <sup>-21</sup>
77	Salado Halite	5.09×10 <sup>-16</sup>	5.09×10 <sup>-16</sup>	3.61×10 <sup>-17</sup>	1.00×10 <sup>-21</sup>	1.00×10 <sup>-21</sup>	1.00×10 <sup>-21</sup>
78	Salado Halite	5.11×10 <sup>-16</sup>	5.11×10 <sup>-16</sup>	3.31×10 <sup>-17</sup>	1.00×10 <sup>-21</sup>	1.00×10 <sup>-21</sup>	1.00×10 <sup>-21</sup>
79	Combined Unit 9	1.29×10 <sup>-19</sup>	1.29×10 <sup>-19</sup>	1.29×10 <sup>-19</sup>	1.29×10 <sup>-19</sup>	1.29×10 <sup>-19</sup>	1.29×10 <sup>-19</sup>
80	Combined Unit 9	1.29×10 <sup>-19</sup>	1.29×10 <sup>-19</sup>	1.29×10 <sup>-19</sup>	1.29×10 <sup>-19</sup>	1.29×10 <sup>-19</sup>	1.29×10 <sup>-19</sup>
81	Salado Halite	5.13×10 <sup>-16</sup>	5.13×10 <sup>-16</sup>	2.99×10 <sup>-17</sup>	1.00×10 <sup>-21</sup>	1.00×10 <sup>-21</sup>	1.00×10 <sup>-21</sup>
82	Salado Halite	5.13×10 <sup>-16</sup>	5.13×10 <sup>-16</sup>	5.53×10 <sup>-18</sup>	1.00×10 <sup>-21</sup>	1.00×10 <sup>-21</sup>	1.00×10 <sup>-21</sup>
83	Salado Halite	5.13×10 <sup>-16</sup>	5.13×10 <sup>-16</sup>	5.25×10 <sup>-18</sup>	1.00×10 <sup>-21</sup>	1.00×10 <sup>-21</sup>	1.00×10 <sup>-21</sup>
84	Salado Halite	5.14×10 <sup>-16</sup>	5.14×10 <sup>-16</sup>	4.95×10 <sup>-18</sup>	1.00×10 <sup>-21</sup>	1.00×10 <sup>-21</sup>	1.00×10 <sup>-21</sup>
85	Salado Halite	5.14×10 <sup>-16</sup>	1.00×10 <sup>-20</sup>				
86	Salado Halite	5.15×10 <sup>-16</sup>	5.15×10 <sup>-16</sup>	4.48×10 <sup>-18</sup>	1.00×10 <sup>-21</sup>	1.00×10 <sup>-21</sup>	1.00×10 <sup>-21</sup>
87	Salado Halite	5.16×10 <sup>-16</sup>	5.16×10 <sup>-16</sup>	4.08×10 <sup>-18</sup>	1.00×10 <sup>-21</sup>	1.00×10 <sup>-21</sup>	1.00×10 <sup>-21</sup>
88	Salado Halite	5.16×10 <sup>-16</sup>	5.16×10 <sup>-16</sup>	1.02×10 <sup>-16</sup>	1.91×10 <sup>-18</sup>	1.00×10 <sup>-21</sup>	1.00×10 <sup>-21</sup>
89	Combined Unit 10	1.09×10 <sup>-19</sup>	1.09×10 <sup>-19</sup>	1.09×10 <sup>-19</sup>	1.09×10 <sup>-19</sup>	1.09×10 <sup>-19</sup>	1.09×10 <sup>-19</sup>
90	Combined Unit 10	1.09×10 <sup>-19</sup>	1.09×10 <sup>-19</sup>	1.09×10 <sup>-19</sup>	1.09×10 <sup>-19</sup>	1.09×10 <sup>-19</sup>	1.09×10 <sup>-19</sup>
91	Salado Halite	5.18×10 <sup>-16</sup>	5.18×10 <sup>-16</sup>	9.66×10 <sup>-17</sup>	1.43×10 <sup>-18</sup>	1.00×10 <sup>-21</sup>	1.00×10 <sup>-21</sup>
92	Salado Halite	5.19×10 <sup>-16</sup>	5.19×10 <sup>-16</sup>	9.18×10 <sup>-17</sup>	1.01×10 <sup>-18</sup>	1.00×10 <sup>-21</sup>	1.00×10 <sup>-21</sup>
93	Salado Halite	5.21×10 <sup>-16</sup>	5.21×10 <sup>-16</sup>	8.76×10 <sup>-17</sup>	6.34×10 <sup>-19</sup>	1.00×10 <sup>-21</sup>	1.00×10 <sup>-21</sup>
94	Salado Halite	5.21×10 <sup>-16</sup>	5.21×10 <sup>-16</sup>	8.55×10 <sup>-17</sup>	4.47×10 <sup>-19</sup>	1.00×10 <sup>-21</sup>	1.00×10 <sup>-21</sup>
95	Salado Halite	5.22×10 <sup>-16</sup>	5.22×10 <sup>-16</sup>	8.44×10 <sup>-17</sup>	3.53×10 <sup>-19</sup>	1.00×10 <sup>-21</sup>	1.00×10 <sup>-21</sup>
96	Combined Unit 11	2.86×10 <sup>-16</sup>	2.86×10 <sup>-16</sup>	2.86×10 <sup>-16</sup>	2.86×10 <sup>-16</sup>	2.86×10 <sup>-16</sup>	2.86×10 <sup>-16</sup>
97	Salado Halite	5.22×10 <sup>-16</sup>	5.22×10 <sup>-16</sup>	5.22×10 <sup>-16</sup>	5.22×10 <sup>-16</sup>	5.22×10 <sup>-16</sup>	5.22×10 <sup>-16</sup>
98	Salado Halite	5.22×10 <sup>-16</sup>	5.22×10 <sup>-16</sup>	5.22×10 <sup>-16</sup>	5.22×10 <sup>-16</sup>	5.22×10 <sup>-16</sup>	5.22×10 <sup>-16</sup>
99	Salado Halite	5.23×10 <sup>-16</sup>	5.23×10 <sup>-16</sup>	5.23×10 <sup>-16</sup>	5.23×10 <sup>-16</sup>	5.23×10 <sup>-16</sup>	5.23×10 <sup>-16</sup>

- The model was initialized at hydrostatic conditions based on heads in the Rustler Formation.
- The base of the shaft, at the repository horizon, was held at atmospheric conditions. The pressure at the repository horizon will increase after closure in response to far-field pressures and waste-generated gas. This assumption maintains a large downward potential gradient.

Assumptions relevant to all numerical calculations in this appendix are listed in Section C2.

Except for isolated regions, the Rustler Formation will likely resaturate the DRZ and adjacent rock surrounding the shaft liner in a relatively short period. However, performance models show that the lower-shaft seal system will not resaturate with brine and repressurize to ambient pressures for at least 100 years. Under variably saturated conditions along the shaft, brine flow rates are expected to be less than those provided in this analysis.

#### **C4.2.2 Numerical Method**

The modeling for this investigation was conducted using SWIFT II (Sandia Waste Isolation, Flow, and Transport Code), Version 2F. SWIFT II is a fully transient three-dimensional, finite-difference code that solves the coupled equations for single-phase flow and transport in porous and fractured geologic media. SWIFT II was selected because it is versatile and has been extensively verified against analytical results.

SWIFT II is supported by comprehensive documentation and an extensive testing history. Reeves et al. (1986a) discuss the theory and implementation of the code and basic limitations of the methodology. A guide to the input data is provided by Reeves et al. (1986b). Comparisons of the results from SWIFT II to analytical solutions appear in Finley and Reeves (1981), Reeves et al. (1987), and Ward et al. (1984).

#### **C4.2.3 Model Geometry and Boundary Conditions**

The full-shaft model was implemented with the cylindrical grid shown in Figures C-3a and C-3b. This grid extends vertically from the shaft station monolith at elevation 387.4 m (1271.0 ft) msl up through the Rustler Formation to an elevation of 872.6 m (2862.7 ft) msl. The grid extends radially from the center of the shaft out to an outer radius of 30.9 m (101.4 ft). It is composed of 19 radial columns and 99 vertical layers. Tables C-14 and C-15 provide details of the grid representing various seal components and host rock units.

Layer thicknesses (Table C-17) and column widths (Table C-18) are chosen so that they will adequately resolve the flow field within each seal component and each unit of the host formation without unduly compromising computational efficiency. Consistent with the first-order analysis of Van Sambeek et al. (1993), the total DRZ width (0.370 m) represents approximately 12% of the shaft radius (3.09 m).

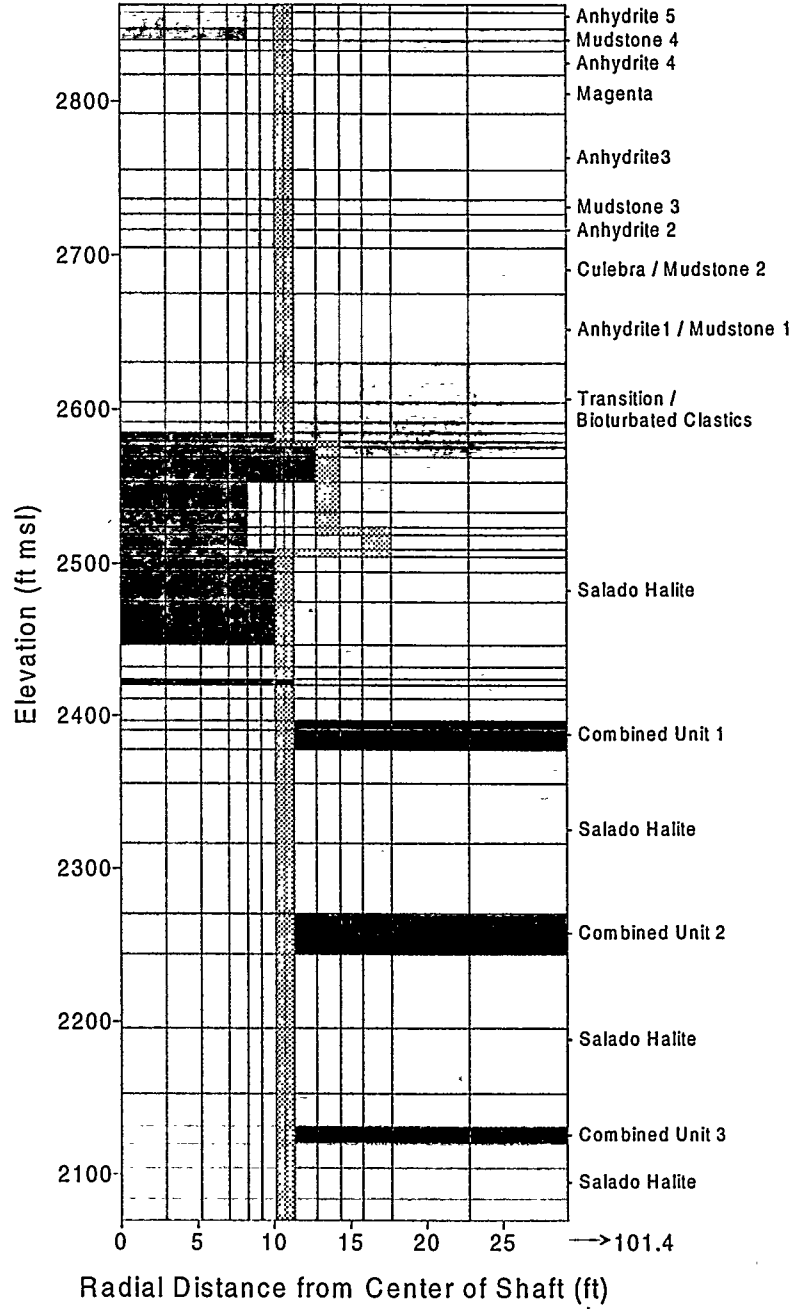
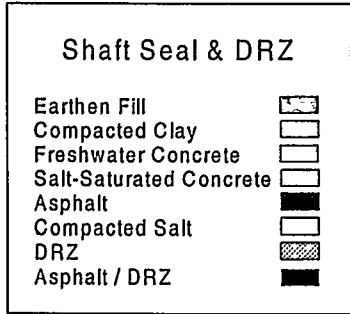


Figure C-3a. Full shaft model grid (top).



Table C-17. Full-Shaft Model Vertical Layers

Layer Number	Layer Thickness (m)	Shaft Seal Component	Host Formation Unit
1 (TOP)	1.52	Earthen Fill	Anhydrite 5
2	3.11	Earthen Fill	Anhydrite 5
3	2.29	Earthen Fill	Mudstone 4
4	2.13	Rustler Compacted Clay Column	Mudstone 4
5	4.69	Rustler Compacted Clay Column	Anhydrite 4
6	7.82	Rustler Compacted Clay Column	Magenta
7	11.26	Rustler Compacted Clay Column	Anhydrite 3
8	5.80	Rustler Compacted Clay Column	Anhydrite 3
9	2.90	Rustler Compacted Clay Column	Mudstone 3
10	3.15	Rustler Compacted Clay Column	Anhydrite 2
11	3.41	Rustler Compacted Clay Column	Anhydrite 2
12	8.99	Rustler Compacted Clay Column	Culbera/Mudstone 2
13	13.72	Rustler Compacted Clay Column	Anhydrite 1/Mudstone 1
14	7.76	Rustler Compacted Clay Column	Transition/Bioturbated Clastics
15	4.02	Concrete Plug	Transition/Bioturbated Clastics
16	2.07	Concrete Plug	Transition/Bioturbated Clastics
17	1.72	Asphalt Column	Transition/Bioturbated Clastics
18	1.02	Asphalt Column	Transition/Bioturbated Clastics
19	2.04	Asphalt Column	Transition/Bioturbated Clastics
20	4.97	Asphalt Column	Salado Halite
21	5.86	Asphalt Column	Salado Halite

Table C-17. Full-Shaft Model Vertical Layers

Layer Number	Layer Thickness (m)	Shaft Seal Component	Host Formation Unit
22	3.00	Asphalt Column	Salado Halite
23	1.50	Asphalt Column	Salado Halite
24	2.90	Asphalt Column	Salado Halite
25	1.50	Asphalt Column	Salado Halite
26	3.00	Asphalt Column	Salado Halite
27	6.00	Asphalt Column	Salado Halite
28	8.55	Asphalt Column	Salado Halite
29	4.57	Upper Concrete Plug	Salado Halite
30	2.44	Upper Concrete Plug	Salado Halite
31	1.22	Asphalt Waterstop	Salado Halite
32	2.71	Upper Concrete Plug	Salado Halite
33	4.30	Upper Concrete Plug	Salado Halite
34	1.93	Upper Salado Compacted Clay Column	Combined Unit 1
35	3.86	Upper Salado Compacted Clay Column	Combined Unit 1
36	6.76	Upper Salado Compacted Clay Column	Salado Halite
37	11.92	Upper Salado Compacted Clay Column	Salado Halite
38	14.08	Upper Salado Compacted Clay Column	Salado Halite
39	8.05	Upper Salado Compacted Clay Column	Combined Unit 2
40	14.74	Upper Salado Compacted Clay Column	Salado Halite
41	13.00	Upper Salado Compacted Clay Column	Salado Halite
42	6.50	Upper Salado Compacted Clay Column	Salado Halite
43	3.57	Upper Salado Compacted Clay Column	Combined Unit 3

Table C-17. Full-Shaft Model Vertical Layers

Layer Number	Layer Thickness (m)	Shaft Seal Component	Host Formation Unit
44	4.87	Upper Salado Compacted Clay Column	Salado Halite
45	6.13	Upper Salado Compacted Clay Column	Salado Halite
46	4.27	Upper Salado Compacted Clay Column	Salado Halite
47	2.44	Upper Salado Compacted Clay Column	Vaca Triste
48	1.22	Upper Salado Compacted Clay Column	Salado Halite
49	1.52	Upper Salado Compacted Clay Column	Salado Halite
50	3.90	Middle Concrete Plug	Salado Halite
51	3.12	Middle Concrete Plug	Salado Halite
52	1.22	Asphalt Waterstop	Salado Halite
53	2.44	Middle Concrete Plug	Salado Halite
54	4.57	Middle Concrete Plug	Salado Halite
55	7.65	Compacted Salt Column	Salado Halite
56	9.69	Compacted Salt Column	Salado Halite
57	5.79	Compacted Salt Column	Combined Unit 4
58	9.49	Compacted Salt Column	Salado Halite
59	4.57	Compacted Salt Column	Salado Halite
60	2.29	Compacted Salt Column	Union Anhydrite
61	4.57	Compacted Salt Column	Salado Halite
62	9.17	Compacted Salt Column	Salado Halite
63	9.45	Compacted Salt Column	Salado Halite
64	4.72	Compacted Salt Column	Combined Unit 5
65	6.41	Compacted Salt Column	Salado Halite
66	8.17	Compacted Salt Column	Salado Halite
67	5.24	Compacted Salt Column	Salado Halite
68	3.96	Compacted Salt Column	Combined Unit 6
69	6.00	Compacted Salt Column	Salado Halite

Table C-17. Full-Shaft Model Vertical Layers

Layer Number	Layer Thickness (m)	Shaft Seal Component	Host Formation Unit
70	8.33	Compacted Salt Column	Salado Halite
71	11.83	Compacted Salt Column	Combined Unit 7
72	12.97	Compacted Salt Column	Salado Halite
73	8.00	Compacted Salt Column	Salado Halite
74	4.25	Compacted Salt Column	Salado Halite
75	2.29	Compacted Salt Column	Combined Unit 8
76	4.88	Compacted Salt Column	Salado Halite
77	9.95	Compacted Salt Column	Salado Halite
78	6.52	Compacted Salt Column	Salado Halite
79	3.11	Compacted Salt Column	Combined Unit 9
80	1.65	Compacted Salt Column	Combined Unit 9
81	0.82	Compacted Salt Column	Salado Halite
82	1.65	Lower Concrete Plug	Salado Halite
83	3.23	Lower Concrete Plug	Salado Halite
84	2.13	Lower Concrete Plug	Salado Halite
85	1.22	Asphalt Waterstop	Salado Halite
86	3.63	Lower Concrete Plug	Salado Halite
87	3.38	Lower Concrete Plug	Salado Halite
88	1.13	Lower Salado Compacted Clay Column	Salado Halite
89	1.52	Lower Salado Compacted Clay Column	Combined Unit 10
90	3.18	Lower Salado Compacted Clay Column	Combined Unit 10
91	6.33	Lower Salado Compacted Clay Column	Salado Halite
92	8.66	Lower Salado Compacted Clay Column	Salado Halite
93	4.39	Lower Salado Compacted Clay Column	Salado Halite
94	2.19	Lower Salado Compacted Clay Column	Salado Halite

Table C-17. Full-Shaft Model Vertical Layers

Layer Number	Layer Thickness (m)	Shaft Seal Component	Host Formation Unit
95	1.10	Lower Salado Compacted Clay Column	Salado Halite
96	0.49	Shaft Station Monolith	Combined Unit 11
97	1.16	Shaft Station Monolith	Salado Halite
98	2.19	Shaft Station Monolith	Salado Halite
99 (BOTTOM)	3.78	Shaft Station Monolith	Salado Halite

Table C-18. Full-Shaft Model Radial Gridding

Column Number	Radius to Outer Grid Column Boundary (m)	Model Component(s)
1	0.90	Seal
2	1.60	Seal
3	2.15	Seal
4	2.53	Seal
5	2.80	Liner, Seal
6	3.09	Liner, Seal
7	3.27	DRZ, Liner, Seal
8	3.46	DRZ, Liner, Seal
9	3.90	Host Rock, Liner, DRZ, Seal
10	4.37	Host Rock, Liner, DRZ
11	4.81	Host Rock, Liner, DRZ
12	5.39	Host Rock, DRZ
13	6.94	Host Rock
14	8.90	Host Rock
15	11.42	Host Rock
16	14.66	Host Rock
17	18.81	Host Rock
18	24.14	Host Rock
19	30.9	Host Rock

Because the outer boundary condition accurately characterizes an infinite aquifer, it is unnecessary to extend the radial grid to large distances. The radial boundary was fixed at 30.9 m (10 shaft radii), a distance sufficient to capture any vertical flow components that may arise in the host rock during the shaft resaturation process. Beyond the outermost extent of the seal components (4.81 m), a node-distributed grid is used because it is most appropriate for a radially converging flow field. Here coordinates of the nodal points increase in geometric progression, as recommended by Aziz and Settari (1979, p. 87).

Grid sensitivities are not expected. For liquid flow, flow rates are sufficiently small that the chosen level of refinement can resolve pressure gradients. It is important to resolve such gradients because they control the rates at which groundwater moves downward through seal components and radially inward through host rock.

For gas flow as simulated with a similar grid in Model 2, the situation is quite different. Within seal components lying below the lower seal, gas pressurization times are sufficiently small in comparison to the time required for salt-column reconsolidation that it is unnecessary to resolve gradients in the pressure front with either spatial or temporal discretization. Rather, grid refinement must be focused on the critical lower seal components and the DRZ that surrounds them. Here it is essential to resolve pressure gradients.

After DRZ healing, permeabilities of these components are sufficiently small so that long-term pressure gradients can be maintained, thus limiting gas pressurization of the salt columns as desired. Current results of two-phase simulations indicate that this grid is sufficiently refined to show substantially limited gas flows. Although some level of grid sensitivity could be present for gas flow within the lower seal components and surrounding DRZ, further refinement would yield only steeper pressure gradients and even smaller gas flow rates into the salt column.

For the model to accurately represent formation conditions at the time of closure, a pre-closure period was simulated. Therefore the modeling was conducted in two stages. The pre-closure period extended from the time of shaft excavation to the time of shaft closure. The duration was assumed to be 50 years. The shaft was considered to be instantaneously excavated, and development of the DRZ was considered to occur instantaneously after shaft excavation. The initial pressure conditions, in the portions of the system other than the open shaft, were represented by hydrostatic equilibrium based on an undisturbed head of 927 m msl at the center of the Culebra and a single-density fluid of  $1230 \text{ kg/m}^3$ . The pressure in the open shaft was held at 1 atm for the duration of the pre-closure simulation. No-flow boundary conditions were imposed at the top and bottom of the model. Infinite aquifer boundary conditions were set at the outer edge of the modeled region. The model components for the pre-closure simulation were the open shaft, the existing shaft liner, the DRZ, and the undisturbed formation.

The purpose of pre-closure modeling was to develop the pressure distribution in the formations created by the open shaft. For the post-closure period, the shaft was sealed and the initial grid-block pressures were set equal to the final grid-block pressures of the pre-closure simulation. Sealing of the shaft was considered to occur instantaneously. To maximize the driving force between the Rustler Formation and the bottom of the shaft, atmospheric pressure was maintained at the bottom of the shaft and DRZ. Otherwise, no-flow boundary conditions were imposed at the bottom and top of the model and along the vertical boundary at the center of

the shaft. Infinite aquifer boundary conditions were set at the outer edge of the modeled region. The model components for the post-closure simulation were the earthen fill, freshwater concrete, salt-saturated concrete, asphalt, compacted clay, crushed salt, the existing shaft liner, the DRZ, and the undisturbed formation. Freshwater concrete was assigned properties identical to those specified for salt-saturated concrete.

#### C4.2.4 Model Parameters

The model parameters were discussed in detail in Section C3. As reported in that section, permeabilities within the compacted salt column and within the Salado DRZ are transient (see Tables C-5 and C-16). Figures C-4 and C-5 illustrate the model permeabilities for the base-case simulation during the open-shaft period, at closure ( $t = 0$  years), at 2 years ( $t = 2$ ), and at 200 years ( $t = 200$ ). These figures demonstrate the transient nature of the DRZ and compacted salt column permeabilities. These figures offer a method to integrate all of the permeability information provided in the tables in Section C3.

The base-case simulation assumed that the anhydrites in the Rustler Formation and anhydrites greater than 3 m thick in the Salado Formation had no DRZ (based on mechanical modeling results presented in Appendix D). This condition results in a discontinuous DRZ at the time of closure (see Figure C-4, second panel), as discussed in Section C3.5.1. Although this case could be realistic, a second case (Run 2) was considered to allow assessment of the impact of the discontinuous DRZ. The relationship developed for the Salado DRZ (Equation C-3) was applied to all lithologies for Run 2, resulting in a continuous DRZ along the shaft wall. Run 2 included concrete-asphalt waterstops that completely healed the adjacent DRZ after two years.

Run 3 was a sensitivity simulation to examine the impact of the concrete-asphalt waterstops. Run 3 incorporated a continuous DRZ at the time of shaft closure, as in Run 2. However, in contrast to Run 2, the DRZ adjacent to the concrete-asphalt waterstops was allowed to heal at the same rate as the DRZ adjacent to the concrete of the plugs, rather than in two years. Table C-19 summarizes the three simulations, highlighting the principal differences among them.

Table C-19. Performance Model 1 Simulations

Run	DRZ	Waterstops
1 (Base-Case)	Discontinuous	Yes
2	Continuous	Yes
3	Continuous	No

#### C4.3 Performance Model Results

Simulation results for Performance Model 1 are presented in terms of brine flow rates ( $m^3/yr$ ), cumulative flow ( $m^3$ ), and pressure distribution plots. Figure C-6 shows calculated brine flow rates for Runs 1 through 3 measured at the Rustler/Salado contact and at the top and bottom of the compacted salt column. Although the simulations continued out to 1000 years after shaft closure, the brine flow values were plotted to only 50 years because flow rates diminished to less than  $0.03 m^3/yr$  by that time.

C-46

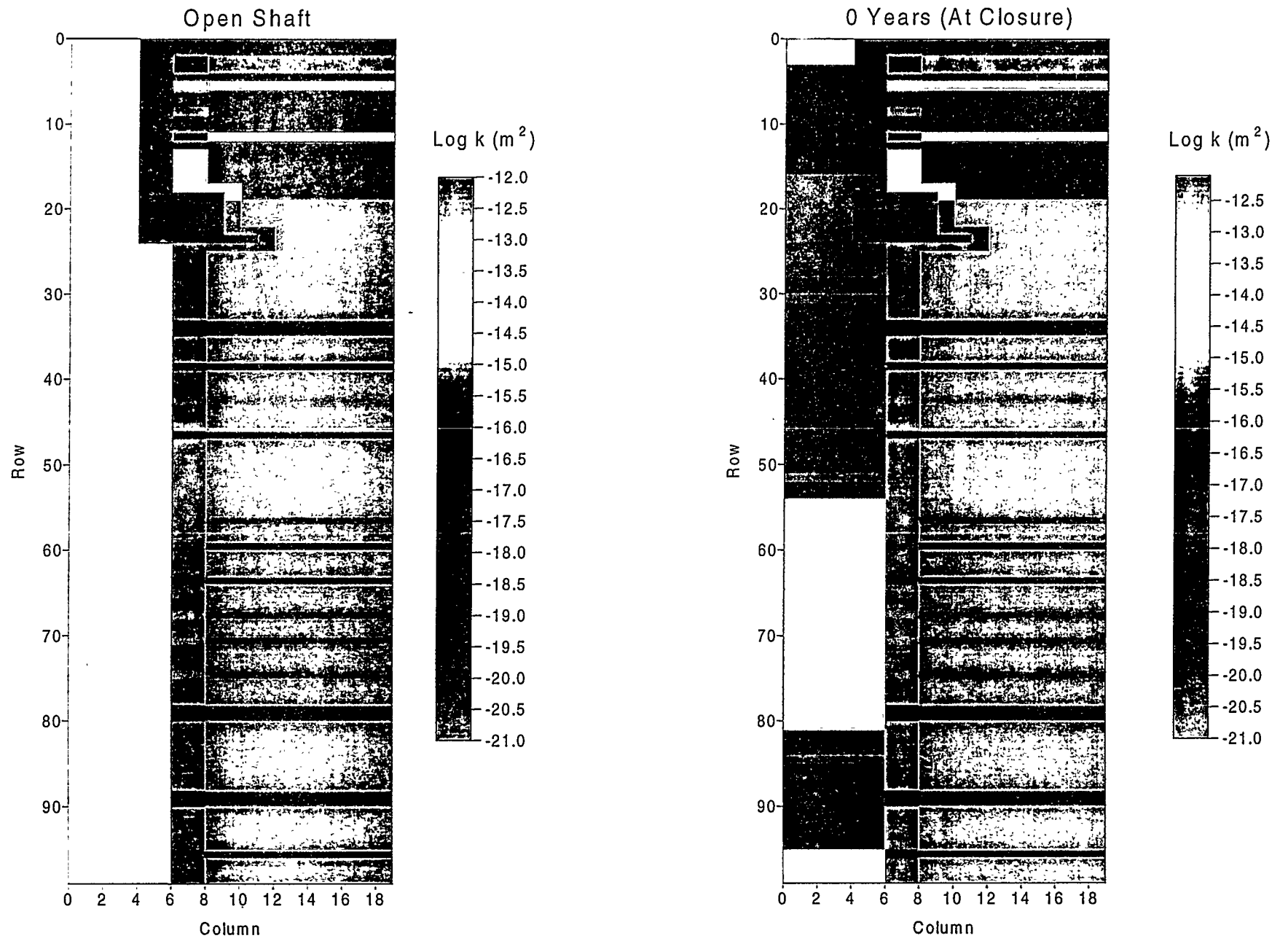


Figure C-4. Permeability fields for Run 1 (base case).

C-47

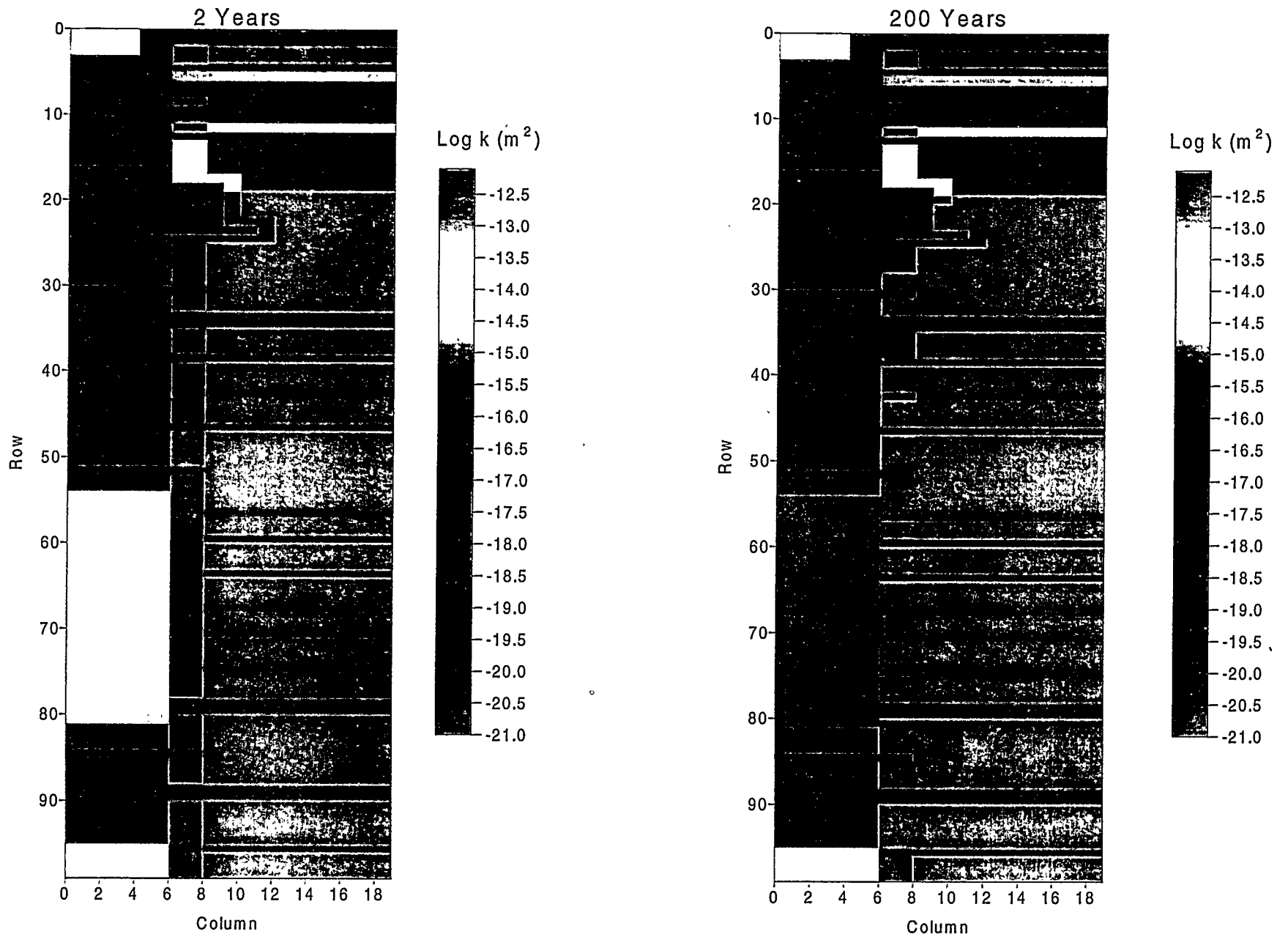


Figure C-5. Permeability fields for Run 1 (base case).

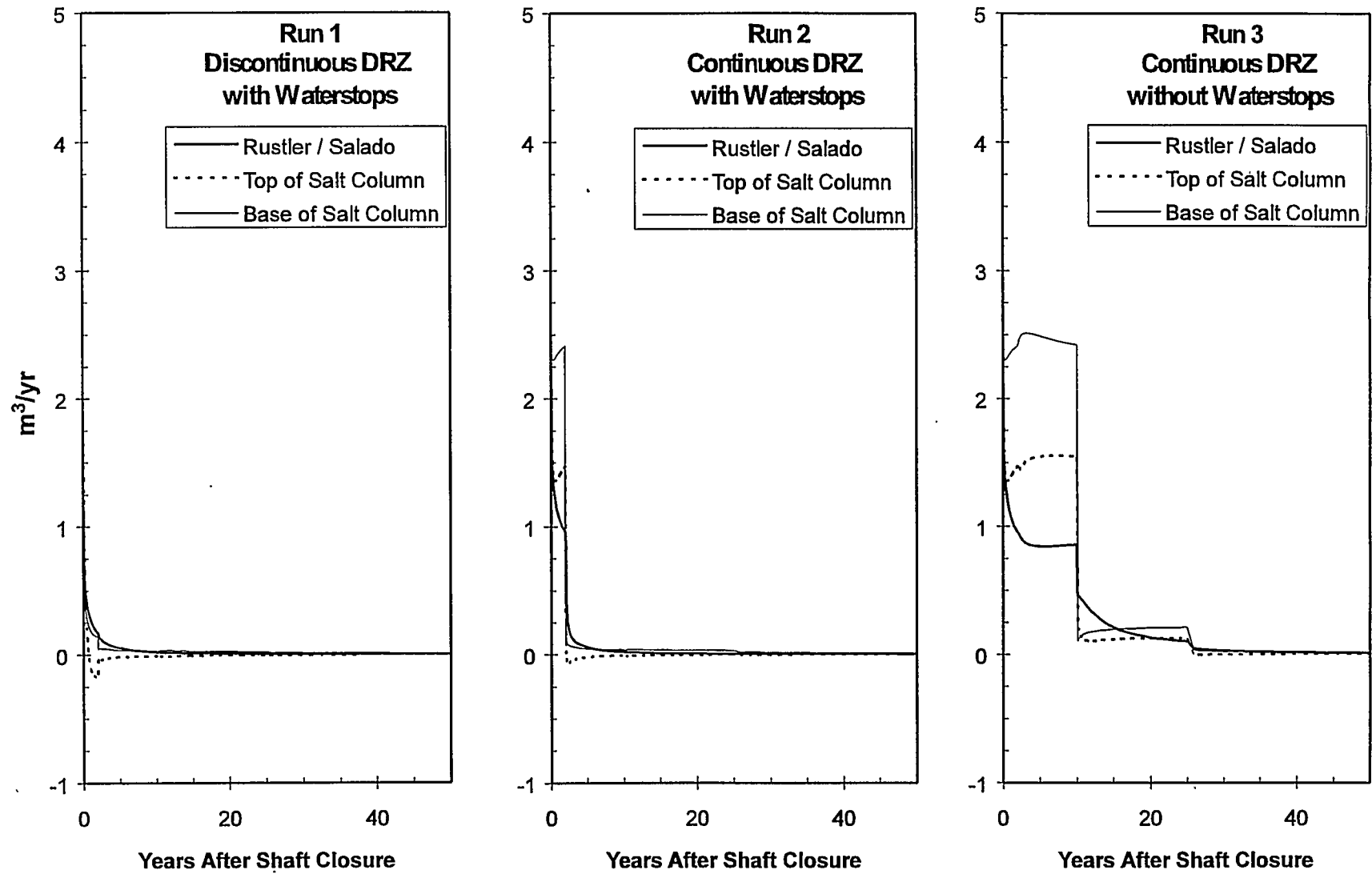


Figure C-6. Model 1 flow rates.

Figure C-7 shows the cumulative flow at 200 years measured at the Rustler/Salado contact and the top and bottom of the compacted salt column. Flow for each level for each run was divided into three components: flow through the shaft seal materials, flow through the DRZ, and flow through the intact host rock out to a radial distance of 10 shaft radii. As expected, flow through the intact rock was minimal for all cases. In Runs 2 and 3, where the DRZ is continuous, the amount of flow moving down through the seal system increased as a function of depth. This was a product of the model boundary conditions that direct formation fluids through the base of the shaft. In Run 1, the combination of a discontinuous DRZ and the waterstops created a pressure sink within and adjacent to the upper Salado compacted clay column. The small amount of flow moving down across the Rustler/Salado contact was used to repressurize the sink and did not migrate past the top of the compacted salt column.

The flow volumes predicted by Model 1 provided an estimate of the number of seal component pore-volumes that will pass through a given seal component. This exercise provides a useful method of quantifying flow estimates and is useful in the evaluation of seal material longevity. The total volume passing across the Rustler/Salado contact, the top of the compacted salt column, and the bottom of the compacted salt column was estimated for a 10,000-year period. Because the simulation did not extend for 10,000 years, the last simulated flow rate was used as a constant for times greater than the simulation time. As discussed in Section C4.2.1, the flow direction will reverse as the system equilibrates. The estimated flow volumes presented here are therefore maximum values.

The flow volumes were estimated for the top of the Salado concrete seal components and the compacted clay components. These flow volumes were then converted to total number of pore-volumes for a given seal component. The largest number of pore volumes predicted to flow through any Salado concrete component was 4. This calculation does not account for the volume of the asphalt waterstop. The largest number of pore volumes that flowed through any Salado compacted clay column was 0.4 for the lower Salado compacted clay column.

Figures C-8 and C-9 illustrate the change in pressure distribution with time for Run 1 (Discontinuous DRZ with Waterstops). All pressures are referenced to the elevation at the base of the model. The first panel of Figure C-8 shows the pressure drawdown at the end of the open shaft period just before shaft closure. The second panel shows the pressure profile just prior to activation of the waterstops. The first of the two panels shown in Figure C-9 illustrates the effect of the waterstops. The final panel in this sequence shows that most of the model has been repressurized by 200 years after shaft closure.

The potential for dissolution of salt in the Salado DRZ was introduced in Section C3.5. The results of Model 1 can be used to estimate the volume of salt that could be dissolved. Run 1 of the performance model predicts a maximum of about 1000 kg ( $1 \text{ m}^3$ ) of groundwater will migrate into the Salado DRZ. A maximum of about  $0.14 \text{ m}^3$  of salt could be dissolved in this quantity of groundwater. The DRZ adjacent to the asphalt column contains approximately  $1700 \text{ m}^3$  of salt. Dissolution of  $0.14 \text{ m}^3$  of salt constitutes less than 0.01% of the DRZ volume. Therefore the probability that dissolutions will impact performance is exceedingly low.

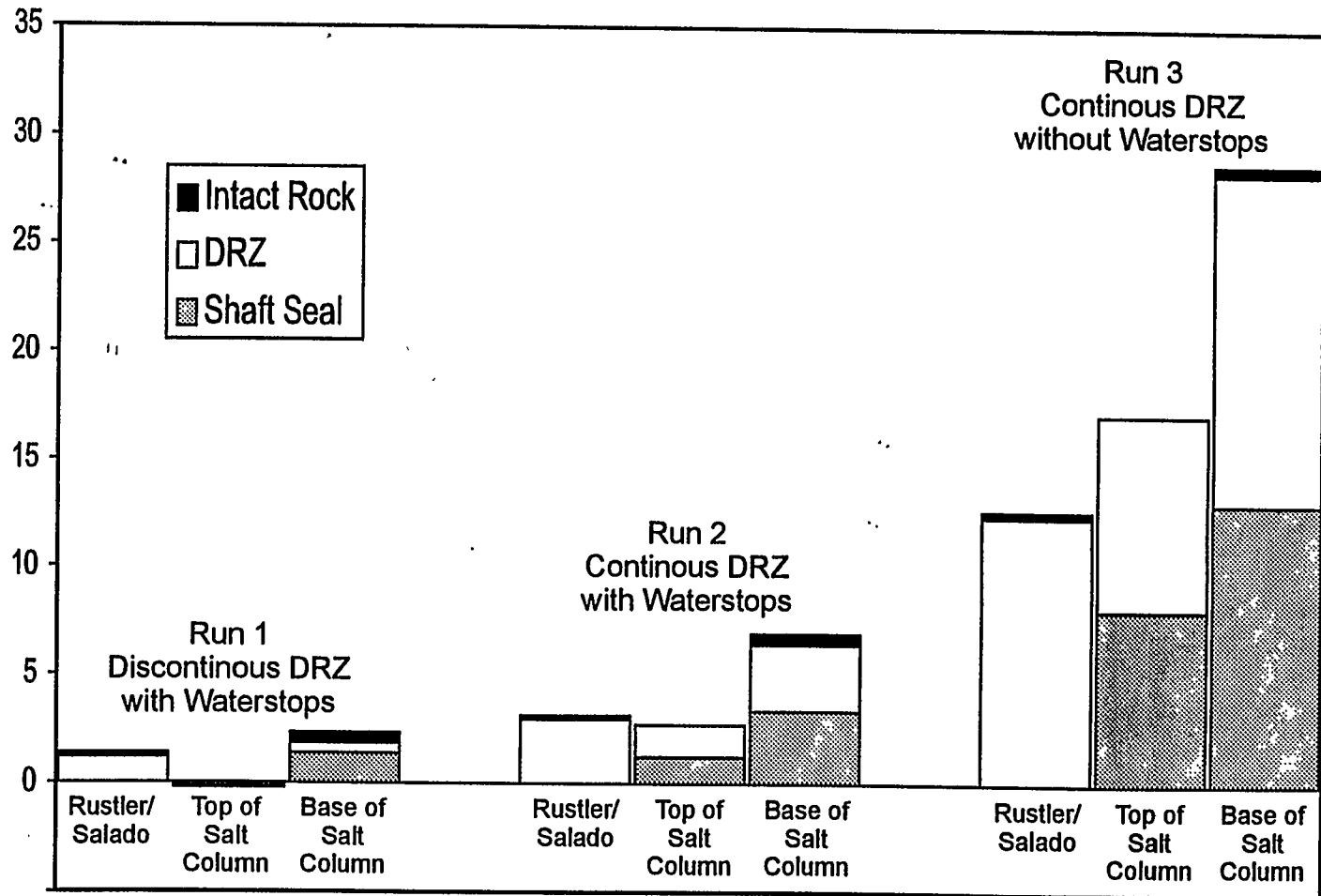


Figure C-7. Cumulative flow at 200 years.

C-51

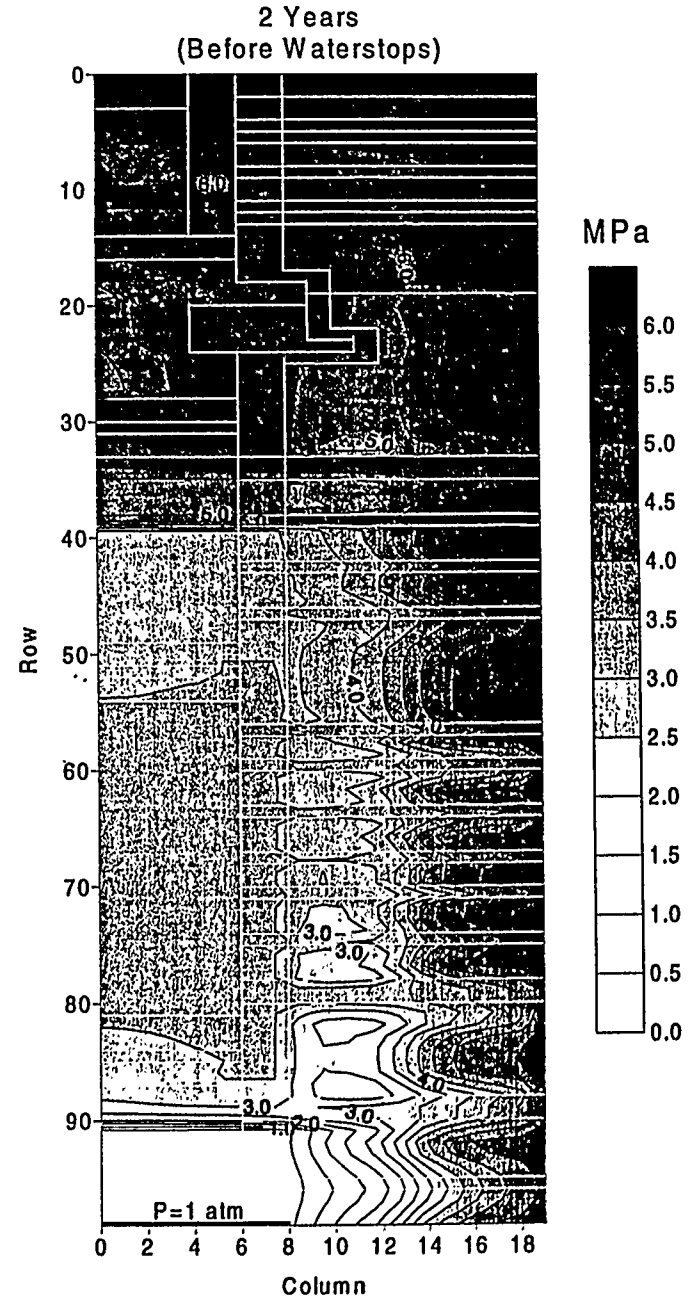
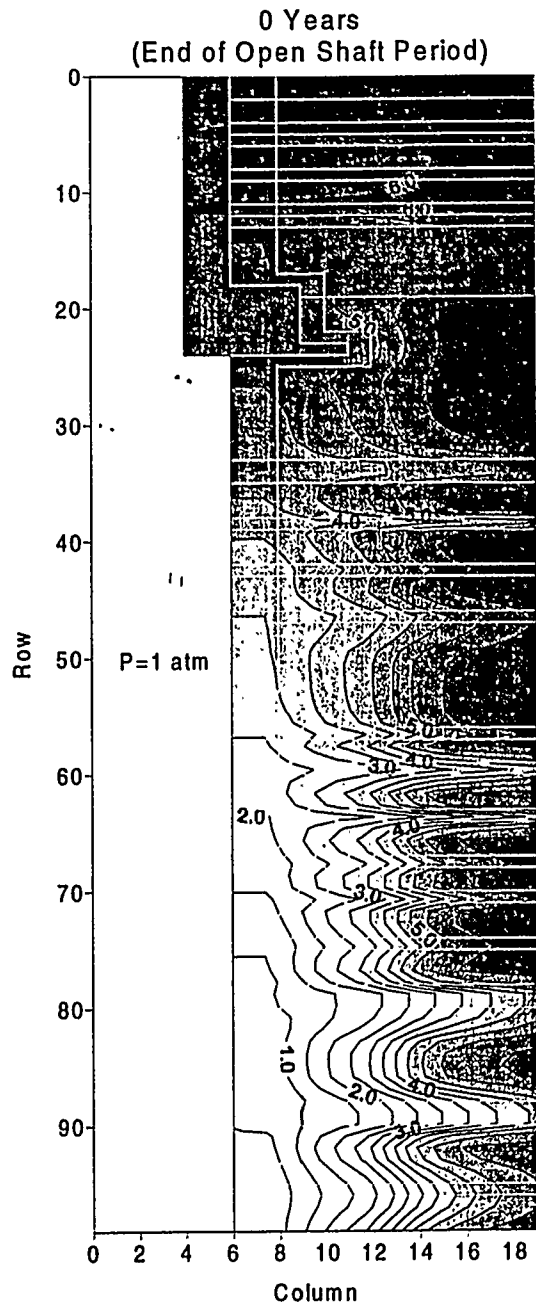


Figure C-8. Pressure distributions for Run 1 (base case).

C-52

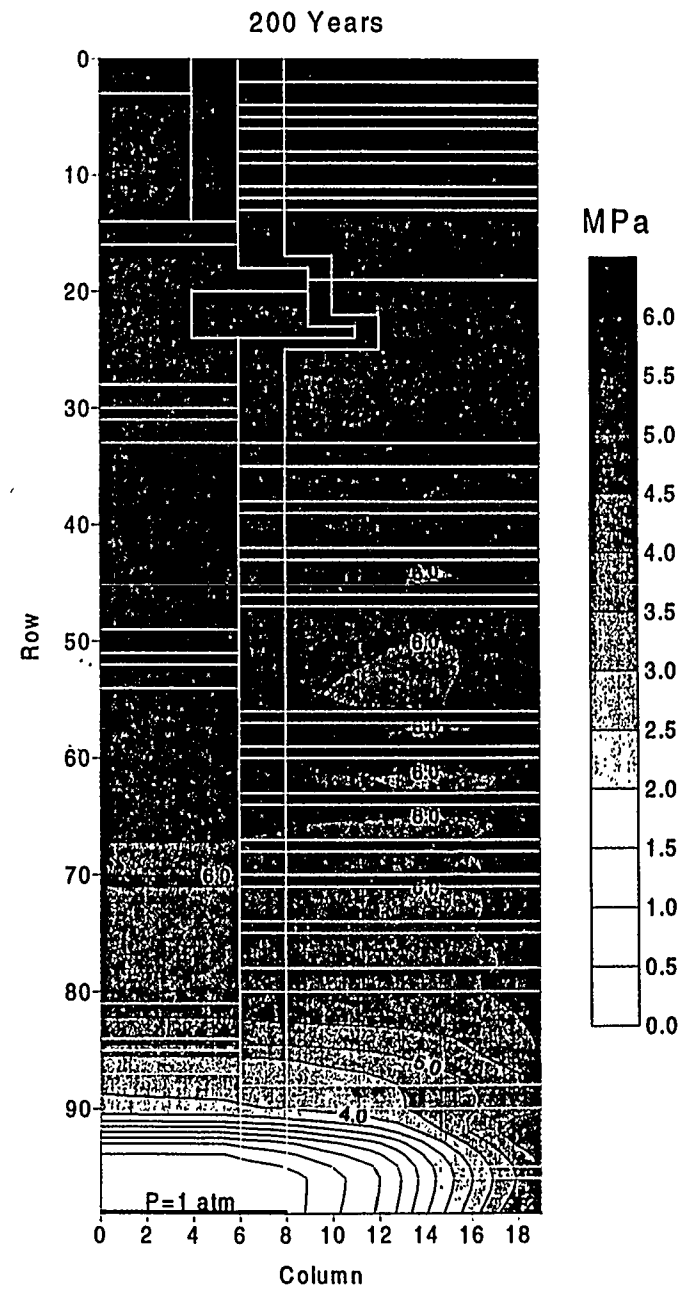
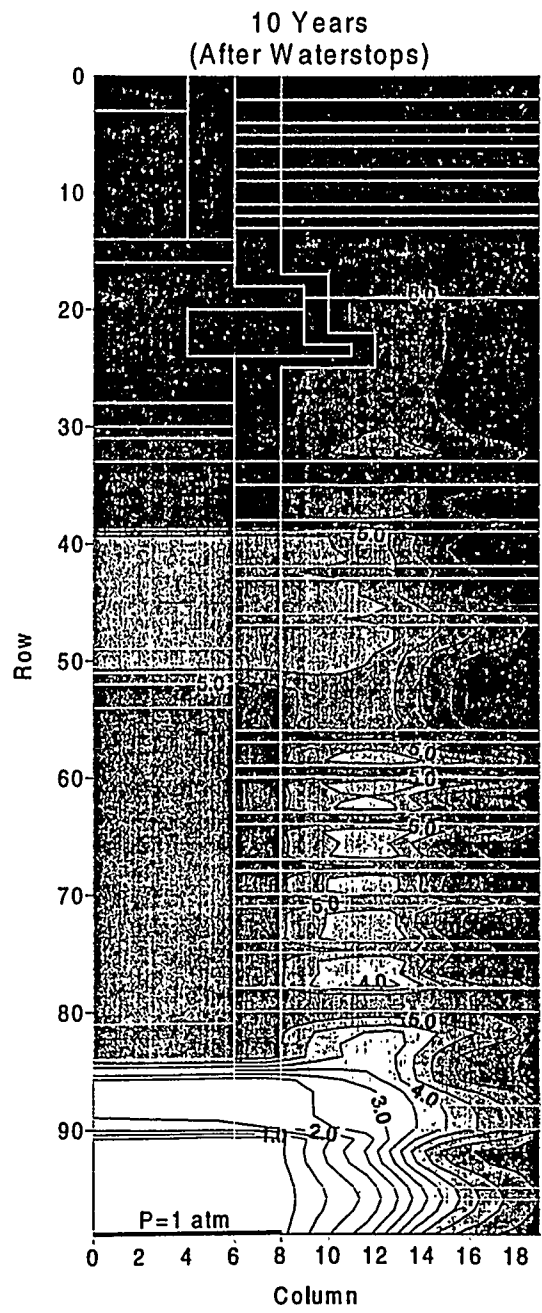


Figure C-9. Pressure distributions for Run 1 (base case).

## **C5. GAS MIGRATION AND CONSOLIDATION OF COMPACTED SALT COLUMN (MODEL 2)**

### **C5.1 Statement of Problem**

The compacted salt column seal component is approximately 172 m (563 ft) long and located between elevations 439 m (1440 ft) msl and 611 m (2003 ft) msl in the proposed seal system design. This seal system component is composed of compacted crushed Salado salt, initially partially saturated with small amounts of water. After closure, as the host formation creeps inward, the crushed salt is expected to consolidate to a density and permeability condition comparable to that of the Salado host rock, thus creating a permanent, chemically compatible, low permeability seal component. The consolidation process can potentially be affected by pore pressures in the salt column. The purpose of this analysis was to predict the effect of pressure increases due to fluid (brine or gas) movement within the lower shaft seal system on compacted salt column permeability during the early time period when consolidation is occurring.

Fluid movement into the salt column could occur from three different sources: (1) brine flow down the shaft from the Rustler Formation above, (2) gas flow up the shaft from the repository below, and (3) brine flow towards the shaft from the host Salado formation due to pressure gradients created during the period the shaft is open to atmospheric pressure. Relationships developed for salt column fractional density (Appendix D) as a function of depth, pressure, and time were combined with estimates for crushed salt permeability as a function of fractional density and used in the analysis to provide an estimate of salt column permeability as a function of depth and time during the first 200 years after seal emplacement. In addition to salt column permeability, model outputs to be analyzed include pressure in the salt column and gas flow from the repository past the lower concrete component into the salt column.

### **C5.2 Performance Model 2 Description**

#### **C5.2.1 Conceptual Model and Assumptions**

The schematic diagram in Figure C-10 shows the conceptualization of the flow system in the lower shaft region and the model components implemented by the compacted salt column performance model. The three sources of fluid flow that could contribute to pressure increases in the compacted salt column are shown in the diagram of the conceptual model (i.e., brine from the Rustler, brine from the host formation, and gas from the repository). Model components include the lower shaft seal components from the repository horizon to the top of the Vaca Triste interbed in the Salado Formation, a DRZ surrounding the shaft, and various anhydrite marker beds within the Salado Formation from the Vaca Triste to the repository horizon.

As discussed in Section C3, the DRZ was assumed to have progressively lower permeability as healing occurs with time after seal emplacement. The crushed salt of the compacted salt column was assumed to consolidate and achieve lower permeability with time at differing rates depending on depth within the column and the amount of pore-pressure back stress within the column.

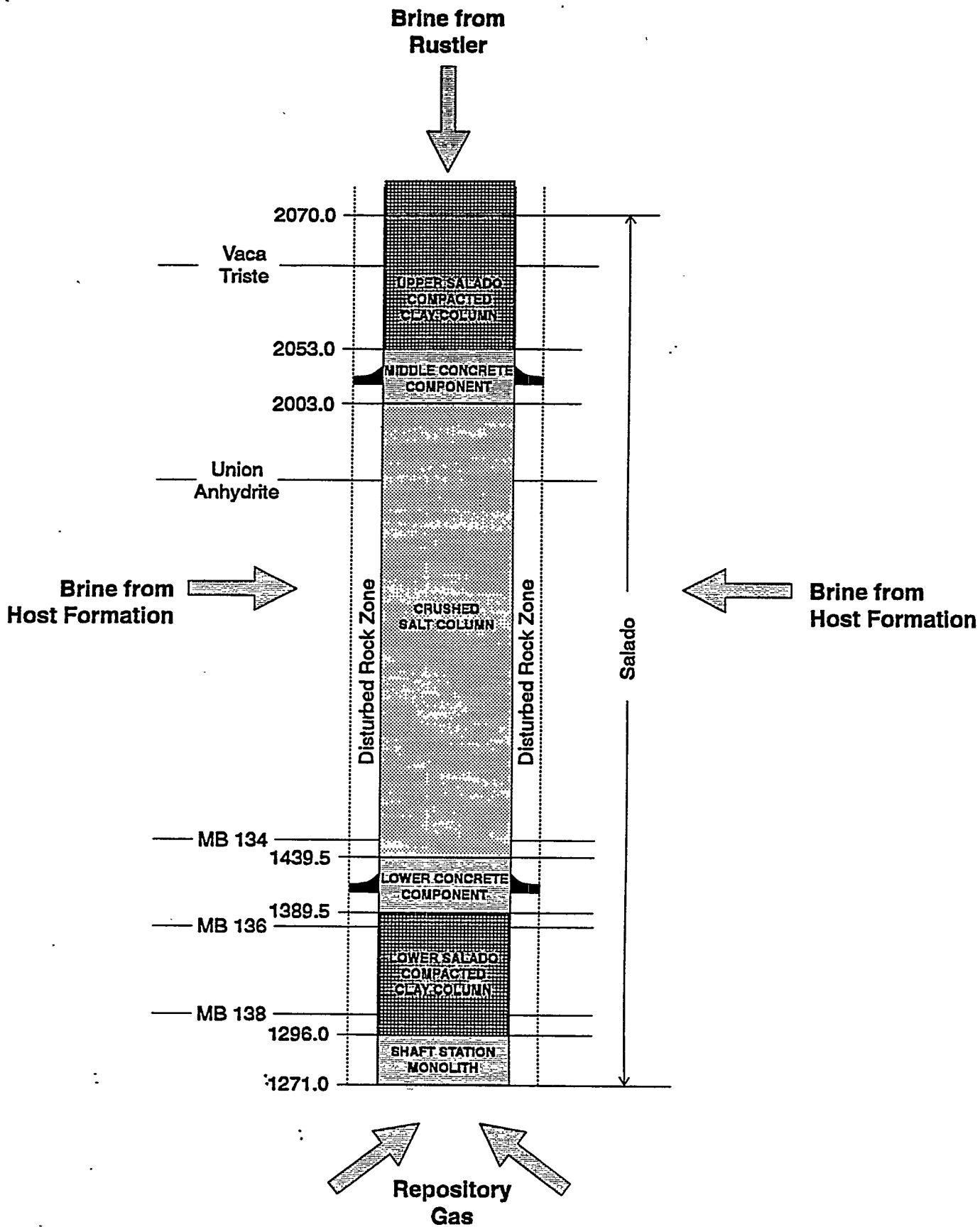


Figure C-10. Conceptual diagram of compacted salt column performance model components.

Results obtained from the full-shaft saturated flow model discussed in Section C4 indicate no brine flow down the shaft into the compacted salt column from the Rustler Formation for the case of a discontinuous DRZ, 2.7 m<sup>3</sup> for a continuous DRZ with waterstops, or 17.2 m<sup>3</sup> for the case of a continuous DRZ without waterstops. This volume of fluid was accounted for in the compacted salt column performance model by including it in the initial brine saturation of the crushed salt. The Rustler flow was distributed evenly throughout the entire pore space of the column by making an appropriate adjustment to initial salt column liquid saturation.

Pressure increase resulting from gas generation within the repository was simulated by applying an increasing gas pressure boundary condition at the base of the shaft. The repository pressure was assumed to increase to 7 MPa in 100 years in one case and 14 MPa in 200 years in a second case. Additional assumptions included in the compacted salt column performance model are discussed in Section C2.

### **C5.2.2 Numerical Model**

The computer code used to implement the compacted salt column performance model is TOUGH28W, Version 2.02 (TOUGH2). TOUGH28W is a numerical simulation program for multi-dimensional coupled fluid and heat flows of multi-phase, multi-component fluid mixtures in porous and fractured media. This code was developed by Karsten Pruess at Lawrence Berkeley National Laboratory and has been used extensively in studies of high-level nuclear waste isolation in partially saturated geologic media (Pruess, 1991). TOUGH28W includes a number of fluid property equation-of-state modules. These modules make the code applicable to a variety of subsurface flow systems, including groundwater aquifers, unsaturated zones, and geothermal reservoirs. The version of the code used for this study incorporates the equation-of-state module EOS8W, which allows for simulation of the three phases water, air, and oil. This version includes a feature which optionally allows for specification of fluid properties representative of WIPP brine instead of water and hydrogen instead of air.

Version 2.02 includes a modification that permits specification of permeability as a function of time for specific model regions. This feature was included to simulate the reduction in permeability of the DRZ around the shaft attributable to healing after seal emplacement. The feature was implemented by allowing the user to provide as input a table specifying permeabilities at different values of the time variable and a rock type (i.e., region) to which the table applies. At each calculational time-step, the code will interpolate a permeability value from the table and apply that value to the specified region.

Version 2.02 also includes a modification to allow specification of permeability as a function of depth and pressure. This feature was included in order to simulate reconsolidation of the compacted salt column at differing rates depending on depth within the column and pore-pressure back stress. This feature was implemented by allowing the user to provide a table as input specifying the rate of change of permeability at different values of pore pressure and elevation for a specific rock type (i.e., region) to which the table applies. At each time-step for each grid element in the specified region, the rate of change in permeability obtained from the table is multiplied by the step size and applied to that grid element subject to specified minimum and maximum permeability values.

### C5.2.3 Model Geometry and Boundary Conditions

The compacted salt column performance model was implemented with the radially symmetric cylindrical grid shown in Figure C-11. The modeled region extends in the vertical direction from the base of the shaft at elevation 387 m (1271 ft) up to the top of the Vaca Triste unit at elevation 631 m (2070 ft). The modeled region extends in the radial direction from the center of the shaft to the outer radial boundary at 282 m (925 ft).

The radial extent of Figure C-11 is truncated at 100 ft in order to show shaft detail. The grid contains 25 columns of grid cells in the radial direction and 59 layers in the vertical direction. The innermost four columns of grid cells represent the shaft and associated seal materials, and the next two columns radially outward represent a DRZ surrounding the shaft. Seal components represented in the model include, from top to bottom:

- a small portion of the upper Salado compacted clay column,
- the middle concrete component including asphalt waterstop,
- the compacted salt column,
- the lower concrete component including asphalt waterstop,
- the lower Salado compacted clay column, and
- the shaft station concrete monolith.

Although the last component is represented in the model grid, no “credit” is taken for its sealing properties; thus the model permeability of the shaft station monolith was set relatively high ( $1 \times 10^{-14} \text{ m}^2$ ) when compared to other model permeabilities.

The host Salado Formation was modeled as layers of halite separated by several layers of anhydrite marker beds. Some of the interbeds that occur close together are combined in the model into single layers, as discussed in Section C3. Table C-20 provides details of the model grid layers representing the various seal components and host formation units. Table C-21 provides details of model gridding in the radial direction.

The leftmost model boundary was considered to be no-flow since this is the line of symmetry at the center of the shaft. The rightmost model boundary (i.e. the outer radial boundary) was assumed to be a constant pressure boundary at hydrostatic equilibrium relative to 12.5 MPa in MB139 near the base of the repository. A boundary radius of 282 m (926 ft) was determined by conducting a series of one-dimensional sensitivity runs to determine at what distance pressure response in the shaft was not sensitive to boundary location. The top and bottom model boundaries were assumed to be no-flow boundaries. This is a reasonable assumption for the time period considered in this model since pressure gradients are primarily directed radially inward because of the open-shaft condition during the repository operational period.

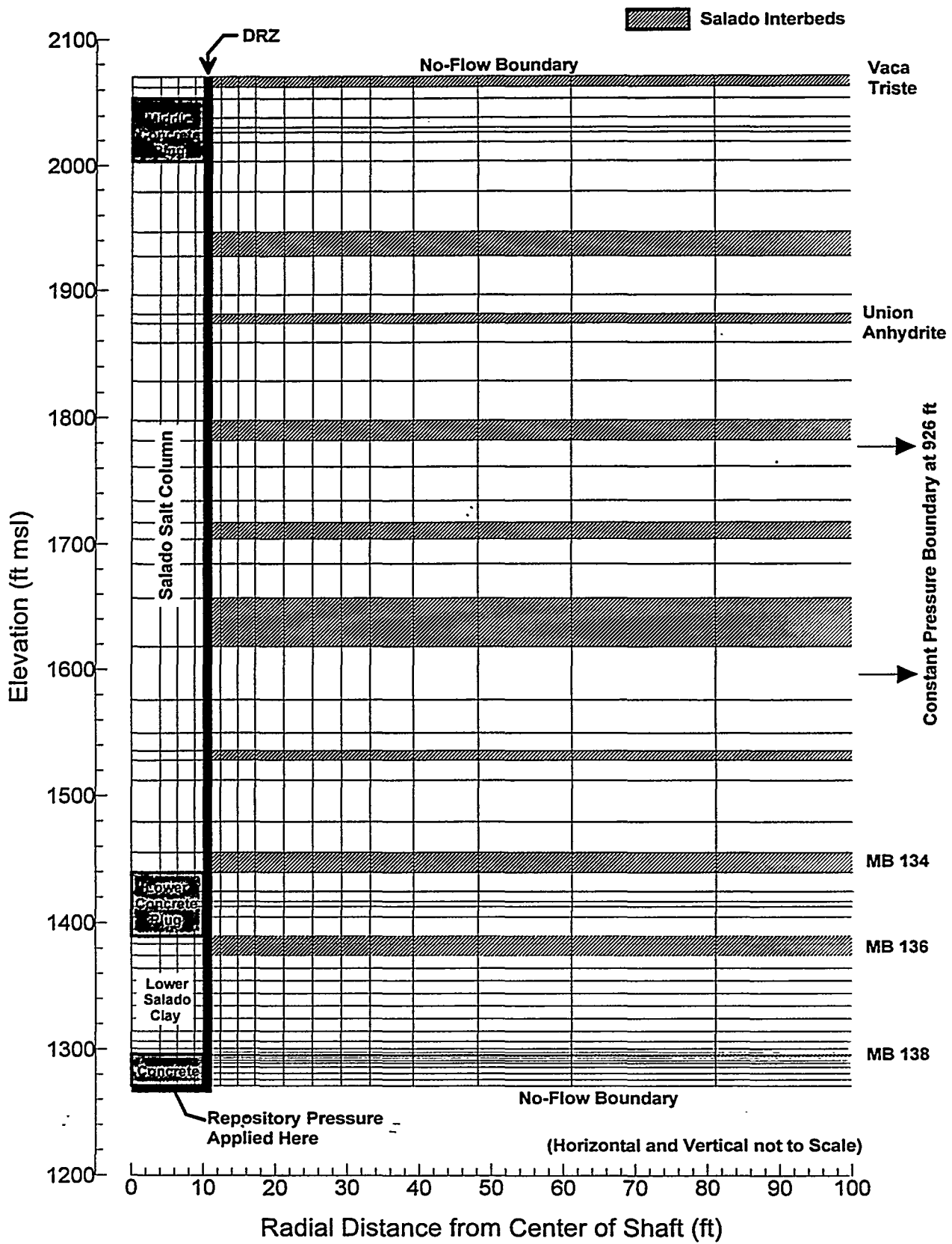


Figure C-11. Grid used by the compacted salt column performance model.

Table C-20. Vertical Layers of the Compacted Salt Column Performance Model

Layer Number	Layer Thickness (m)	Shaft Seal Component	Host Formation Unit
1 (TOP)	2.44	Upper Salado Compacted Clay Column	Vaca Triste
2	2.74	Upper Salado Compacted Clay Column	Salado Halite
3	4.57	Middle Concrete Plug	Salado Halite
4	2.44	Middle Concrete Plug	Salado Halite
5	1.22	Asphalt Waterstop	Salado Halite
6	2.44	Middle Concrete Plug	Salado Halite
7	4.57	Middle Concrete Plug	Salado Halite
8	7.65	Compacted Salt Column	Salado Halite
9	9.69	Compacted Salt Column	Salado Halite
10	5.79	Compacted Salt Column	Combined MB117 - MB122 and Zone A
11	9.49	Compacted Salt Column	Salado Halite
12	4.57	Compacted Salt Column	Salado Halite
13	2.29	Compacted Salt Column	Union Anhydrite
14	4.57	Compacted Salt Column	Salado Halite
15	9.17	Compacted Salt Column	Salado Halite
16	9.45	Compacted Salt Column	Salado Halite
17	4.72	Compacted Salt Column	Combined MB123 - MB124
18	6.41	Compacted Salt Column	Salado Halite
19	8.17	Compacted Salt Column	Salado Halite
20	5.24	Compacted Salt Column	Salado Halite
21	3.96	Compacted Salt Column	Combined Zone B - C and MB126
22	6.00	Compacted Salt Column	Salado Halite
23	8.33	Compacted Salt Column	Salado Halite
24	11.83	Compacted Salt Column	Combined MB127 - MB130 and Zones D - I
25	12.97	Compacted Salt Column	Salado Halite
26	8.00	Compacted Salt Column	Salado Halite

Table C-20. Vertical Layers of the Compacted Salt Column Performance Model

Layer Number	Layer Thickness (m)	Shaft Seal Component	Host Formation Unit
27	4.25	Compacted Salt Column	Salado Halite
28	2.29	Compacted Salt Column	Combined MB131 - MB133 and Zone J
29	4.88	Compacted Salt Column	Salado Halite
30	9.95	Compacted Salt Column	Salado Halite
31	7.35	Compacted Salt Column	Salado Halite
32	4.75	Compacted Salt Column	Combined MB134 - MB135
33	4.57	Lower Concrete Plug	Salado Halite
34	2.44	Lower Concrete Plug	Salado Halite
35	1.22	Asphalt Waterstop	Salado Halite
36	2.44	Lower Concrete Plug	Salado Halite
37	4.57	Lower Concrete Plug	Salado Halite
38	0.61	Lower Salado Compacted Clay Column	Combined MB136-MB137
39	1.22	Lower Salado Compacted Clay Column	Combined MB136-MB137
40	2.87	Lower Salado Compacted Clay Column	Combined MB136-MB137
41	3.05	Lower Salado Compacted Clay Column	Salado Halite
42	3.05	Lower Salado Compacted Clay Column	Salado Halite
43	3.05	Lower Salado Compacted Clay Column	Salado Halite
44	3.05	Lower Salado Compacted Clay Column	Salado Halite
45	3.05	Lower Salado Compacted Clay Column	Salado Halite
46	3.05	Lower Salado Compacted Clay Column	Salado Halite
47	2.32	Lower Salado Compacted Clay Column	Salado Halite
48	1.83	Lower Salado Compacted	Salado Halite

Table C-20. Vertical Layers of the Compacted Salt Column Performance Model

Layer Number	Layer Thickness (m)	Shaft Seal Component	Host Formation Unit
		Clay Column	
49	0.91	Lower Salado Compacted Clay Column	Salado Halite
50	0.46	Lower Salado Compacted Clay Column	Salado Halite
51	0.23	Shaft Station Monolith	Combined MB138 and Anhydrite A/B
52	0.23	Shaft Station Monolith	Combined MB138 and Anhydrite A/B
53	0.46	Shaft Station Monolith	Salado Halite
54	0.61	Shaft Station Monolith	Salado Halite
55	0.61	Shaft Station Monolith	Salado Halite
56	0.91	Shaft Station Monolith	Salado Halite
57	1.52	Shaft Station Monolith	Salado Halite
58	1.52	Shaft Station Monolith	Salado Halite
59 (BOTTOM)	1.52	Shaft Station Monolith	Salado Halite

Table C-21. Compacted Salt Column Performance Model Radial Gridding

Column Number	Radius to Outer Grid Column Boundary (m)	Model Component
1	1.22	Shaft
2	1.95	Shaft
3	2.68	Shaft
4	3.05	Shaft
5	3.23	DRZ
6	3.41	DRZ
7	3.78	Host Formation
8	4.51	Host Formation
9	5.24	Host Formation
10	6.46	Host Formation

Table C-21. Compacted Salt Column Performance Model Radial Gridding

Column Number	Radius to Outer Grid Column Boundary (m)	Model Component
11	7.68	Host Formation
12	8.90	Host Formation
13	10.12	Host Formation
14	11.95	Host Formation
15	14.69	Host Formation
16	18.65	Host Formation
17	24.75	Host Formation
18	33.89	Host Formation
19	47.61	Host Formation
20	68.95	Host Formation
21	99.43	Host Formation
22	145.15	Host Formation
23	190.87	Host Formation
24	236.59	Host Formation
25	282.31	Host Formation

Two exceptions to the no-flow top and bottom model boundaries were considered. First, the possibility of brine flow down the shaft from the Rustler Formation was considered by increasing the initial crushed-salt brine saturation as discussed above. Second, gas flow up from the repository was simulated by applying a time varying pressure boundary condition at the base of the shaft. The waste forms in the repository may generate gas (WIPP PA, 1992–1993). Model 2 does not explicitly model the generation of gas in the repository. Rather, it indirectly incorporates repository gas generation by applying a time-varying gas pressure boundary condition at the base of the shaft. Two pressure specifications were considered in the gas flow analysis. In one, the pressure increased to 7 MPa in 100 years and then remained constant for the remaining simulation time (200 years total). In the second, the pressure at the base of the shaft increased steadily for the 200-year simulation period to 14 MPa. These two specifications are representative of results obtained for pressure at the base of the shaft by WIPP PA in the No Migration Variance Petition (NMVP) simulations. The time-varying pressure boundary conditions were chosen to correspond to the quickest pressure increase (i.e., highest gas generation rates) simulated in the NMVP simulations. Figure C-12 shows the pressure condition applied at the base of the shaft in the model runs for these two specifications. Because of limitations in implementing the time-varying boundary condition at the base of the shaft in TOUGH28W, the pressure was “stepped up” to final values in a series of consecutive restarted simulations.

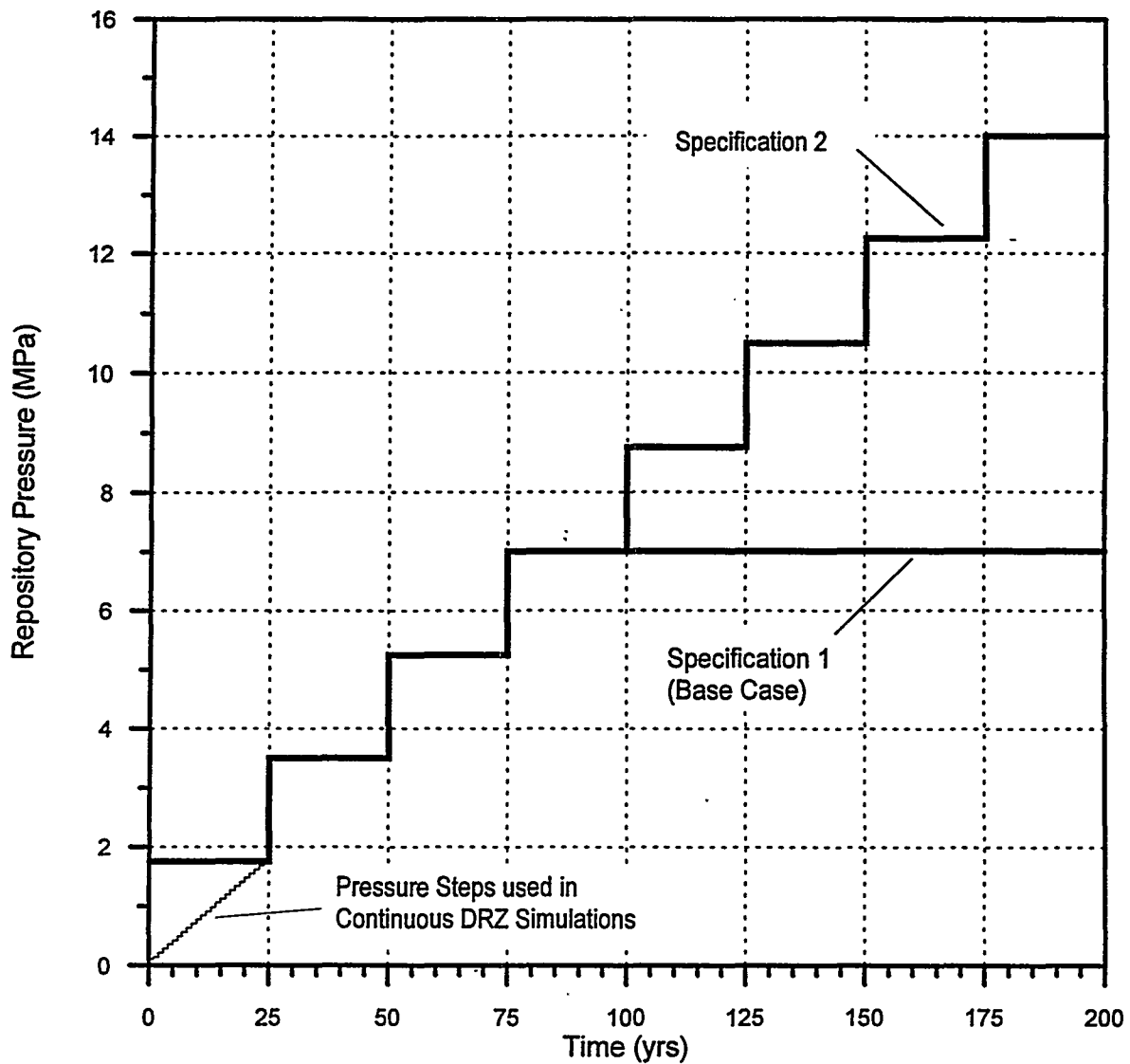


Figure C-12. Two specifications of pressure at the base of the shaft.

: For most of the simulations presented here, the pressure was increased in 1.75-MPa steps at 25-year intervals. For continuous DRZ simulations, however, the 1.75 MPa repository pressure at time zero was considered an unrealistic boundary condition to apply to the pre-healed DRZ around the lower concrete component seal. For these cases, the boundary pressure was increased in 1-year steps of 0.07 MPa each. The lighter line between 0 and 25 years in Figure C-12 represents the repository pressure boundary condition used for continuous DRZ simulations.

#### **C5.2.4 Model Parameters**

Model parameters for the compacted salt column performance model include material properties for shaft seal components, fluid properties, two-phase flow properties, and material properties for Salado halite and anhydrite marker beds. The properties used in this model are discussed in detail in Section C3. Also discussed in Section C3 are the time-varying permeabilities of the DRZ zones surrounding the shaft.

An additional process that must be modeled for the compacted salt column performance model was the consolidation behavior of the crushed salt column. Curves showing salt column fractional density as a function of time at three different depths (430, 515, and 600 m) and three different pore pressures (0, 2, and 4 MPa) are presented in Appendices A and D. The data are replotted in Figure C-13 in terms of the average rate of change in fractional density (on the right axis) versus pressure for the three depths. A relationship has also been developed between crushed salt fractional density and permeability. To account for uncertainty in the permeability versus fractional density relationship, a best fit line through the data, as well as lines through 95th and 5th percentiles, were developed. Using the best fit line between fractional density and permeability, the left axis of Figure C-13 gives the average rate of change for the log of permeability as a function of pressure at the three depths. As shown in the figure, several points were extrapolated from the data to provide model data points up to 10 MPa. The consolidation rate at these higher pressures is not significant to model performance, but the data were required because it was anticipated that salt column pressures could reach these values during late model times.

The “consolidation surface” shown in Figure C-14 was developed by interpolating between the data points shown in Figure C-13. This surface provides the relationship between the rate of change in permeability and depth and pressure within the compacted salt column. In tabular form, this surface is required as input to the compacted salt column performance model. The general shape of this surface shows that the greatest magnitude of the rate of permeability change (i.e., the highest consolidation rate) occurs at the greatest depth (lowest elevation) and lowest pore pressure.

#### **C5.3 Performance Model Results**

Six simulations were run with the compacted salt column performance model, a base-case and five additional runs, to examine the sensitivity of the model to variations in repository pressure, the crushed-salt permeability-fractional density relationship, flow down the shaft from the Rustler Formation, and continuous DRZ with and without waterstops.

Table C-22 summarizes the six simulations and provides information about the combination of parameters used for each. The “Repository Pressure” column in the table refers to the pressure specifications defined in Figure C-12. The “Permeability/Fractional Density Predictor” column in the table refers to either the best fit or the 95th percentile lines through the permeability versus fractional density data. The primary difference between these two permeability specifications is the starting and ending points for salt column permeability. For the best fit line, crushed salt permeability starts at  $2.5 \times 10^{-15} \text{ m}^2$  (90% fractional density) and achieves a minimum possible value of  $6.3 \times 10^{-21} \text{ m}^2$  (100% fractional density). For the “95%” predictor line, crushed salt permeability starts at  $7.9 \times 10^{-13} \text{ m}^2$  and achieves a minimum possible

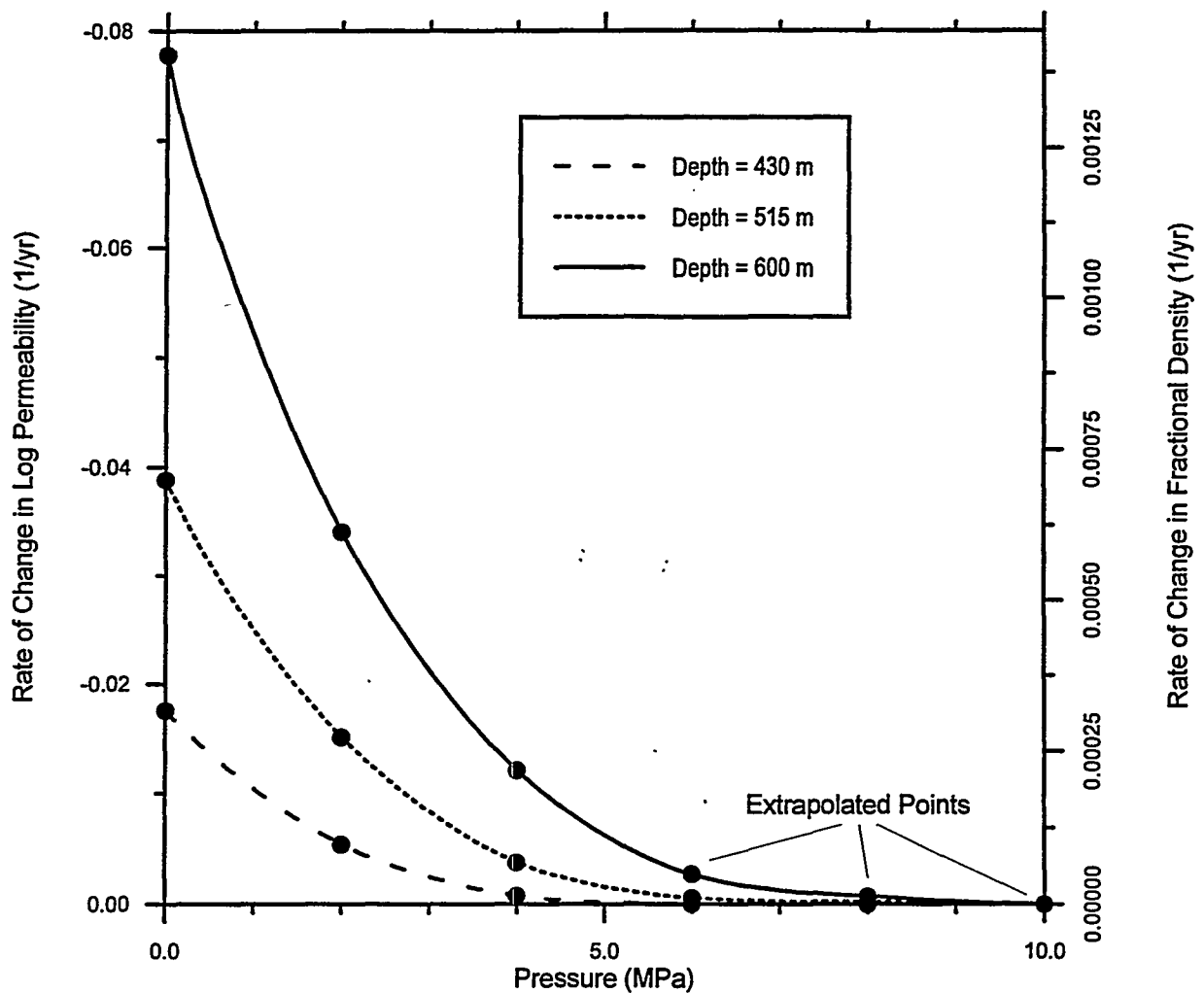


Figure C-13. Rate of change in log permeability (fractional density) with pressure and depth.

value of  $2.0 \times 10^{-18} \text{ m}^2$ . The “Rustler Flow” column in the table indicates the amount by which the salt column initial liquid saturation was increased to account for brine flow down the shaft from the Rustler Formation, predicted by the full-shaft saturated flow model for the case of a continuous DRZ with and without waterstops.

Identical initial pressure conditions were used for each simulation and were established in two steps. First, all grid elements were assigned an initial pressure based on hydrostatic pressure referenced to 12.5 MPa at the elevation of MB139. Next, a conditioning simulation was run in which the shaft was considered to be open to atmospheric pressure for 50 years. Grid-element pressures were captured at the end of this 50-year simulation and used to initialize each of the performance calculations.

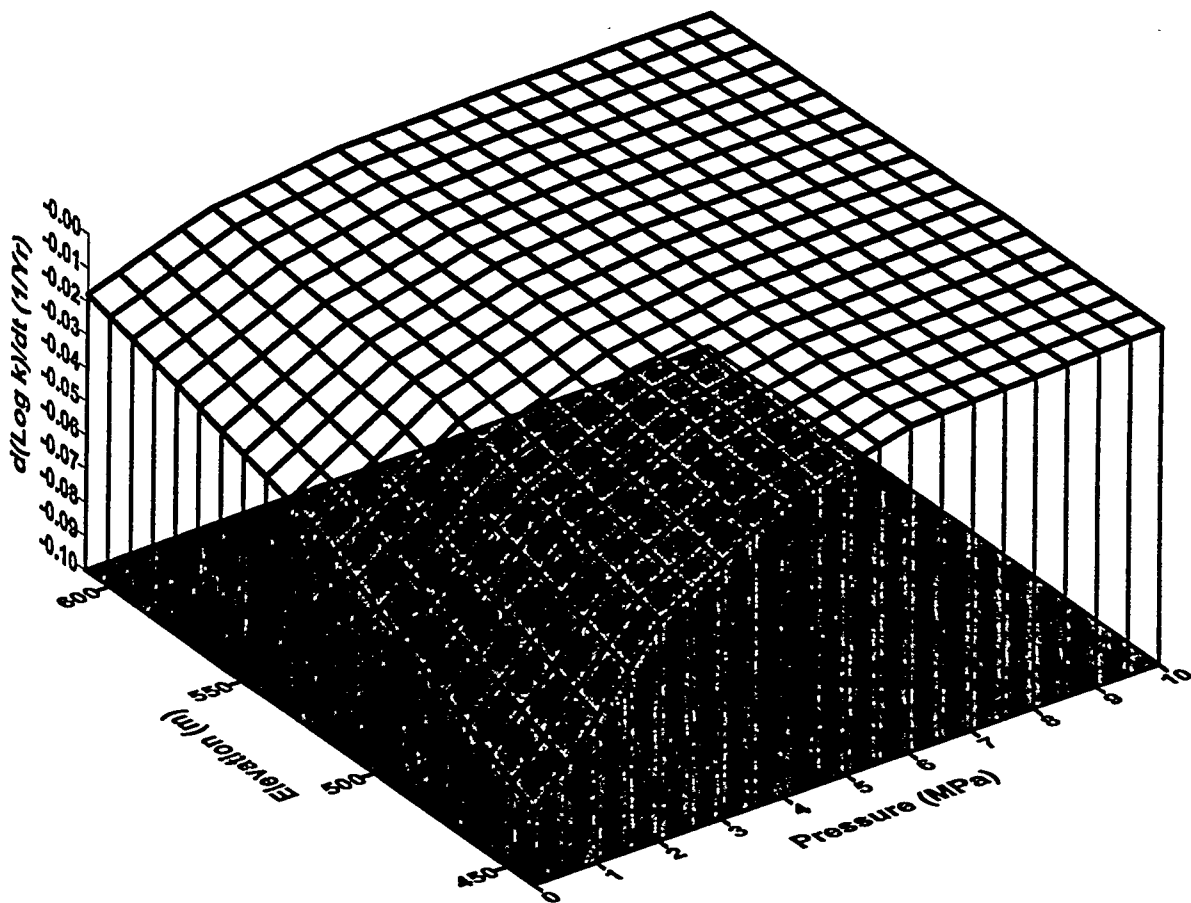


Figure C-14. Reconsolidation surface for the best-fit permeability/fractional density predictor.

Simulation results are presented here in terms of pressure in the compacted salt column, gas flow past the lower concrete component into the compacted salt column, and predicted permeability of the compacted salt column. For the base case of 7 MPa at the repository horizon, Figure C-15 shows calculated pressure in the compacted salt column versus time after seal emplacement at three locations near the top, middle, and bottom of the salt column. The figure shows pressure increased most rapidly at the bottom of the column. Pressure began to increase rapidly at the bottom of the salt column approximately 30 years after seal emplacement. The fact that the pressure in Figure C-15 increased to levels greater than the maximum pressure at the

Table C-22. Compacted Salt Column Performance Model Simulations

Run	Repository Pressure*	Permeability/ Fractional Density Predictor	Rustler Flow (m <sup>3</sup> )	Continuous DRZ	Water Stops
1 (Base Case)	7 MPa in 100 Years	Best Fit	0.00	No	Yes
2	7 MPa in 100 Years	95%	0.00	No	Yes
3	14 MPa in 200 Years	Best Fit	0.00	No	Yes
4	14 MPa in 200 Years	95%	0.00	No	Yes
5	7 MPa in 100 Years (Linear First 25 Years)	Best Fit	2.70	Yes	Yes
6	7 MPa in 100 Years (Linear First 25 Years)	Best Fit	17.20	Yes	No

\* Source: NMVP calculations.

base of the shaft (7 MPa) indicates that the far-field pressure boundary was the primary source driving the pressure increase. Figure C-16 shows calculated permeability profiles in the compacted salt column at several points in time following seal emplacement. This figure shows that permeability has decreased to a minimum value of  $6.3 \times 10^{-21} \text{ m}^2$  over a portion of the base of the salt column in 100 years and shows little further reduction of permeability over the period from 100 to 200 years. The figure generally shows lower permeability near the bottom of the salt column where the consolidation rate is higher, and relatively higher permeability near the top of the salt column where the consolidation rate is lower. After 100 years, pressure increases throughout the column have almost completely stopped the consolidation process.

A small region, from elevation 439 m (1440 ft) to about elevation 457 m (1500 ft), at the base of the salt column showed less reconsolidation at times ranging from 50 to 200 years than the region immediately above it due to the pressure influence of the repository. Figure C-16 also shows that for times greater than about 50 years, consolidation in the upper half of the salt column was significantly slowed because of repressurization through the relatively high permeability Union Anhydrite ( $1.0 \times 10^{-18} \text{ m}^2$ ).

The results of Run 2, in terms of pressure and permeability in the compacted salt column, are shown in Figures C-17 and C-18, respectively. Parameter specification for this run was identical to Run 1 except that the 95% permeability-fractional density correlation was used (i.e., the assumed salt column permeability was higher for a given fractional density). These results show that pressurization in the salt column occurred at later times than for the base case. The permeability profiles in Figure C-18 show that, in contrast to the base case, very little crushed salt reconsolidation occurred in the lower half of the salt column after about 75 years. This outcome occurs because the pressure increased throughout the vertical extent of the salt column

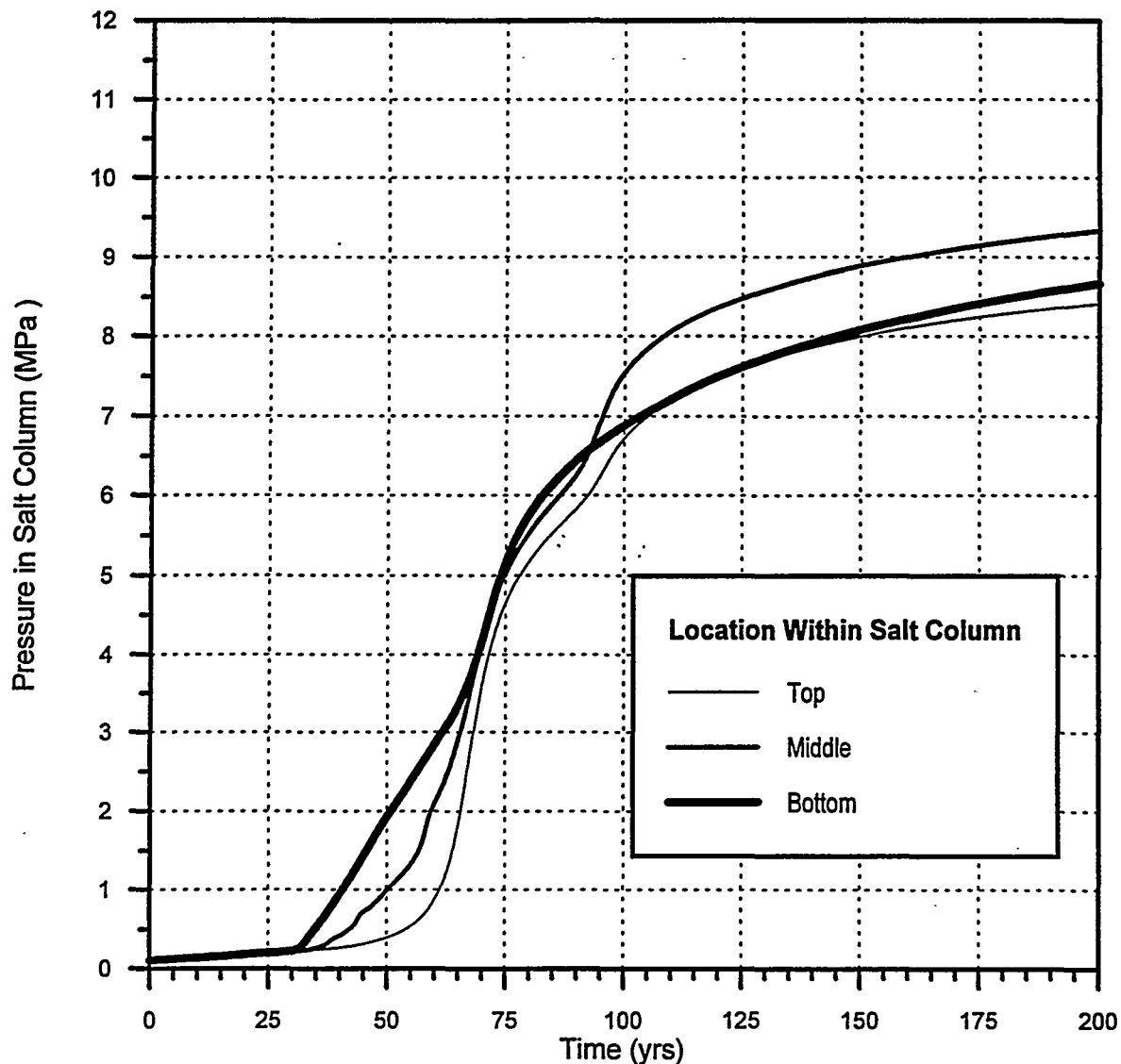


Figure C-15. Calculated pressure versus time after seal emplacement at the top, middle, and bottom of the compacted salt column (base case).

at 75 years in this case, whereas the base case, because of lower permeability of the salt column, retained a region of lower pressure near the base of the column. This can be seen in Figure C-19, which shows pressure contours at 75 years for the base case and for Run 2. In both cases, pressure increases in the salt column due to the influence of the outer pressure boundary through the Union Anhydrite (and to a lesser extent the other interbeds). In the base case, the lower permeability of the reconsolidating crushed salt isolated the area at the base of the column from the Union Anhydrite. For the base case, Figure C-19 shows an area near the base of the column where pressure remained less than 1 MPa at 75 years. In Run 2, the relatively higher permeability of the consolidating crushed salt allowed the pressure to equilibrate along the entire

length of the column, thereby inhibiting consolidation even in the lower half of the column after 75 years.

Runs 3 and 4 in Table C-22 are identical to Runs 1 and 2, respectively, except that the repository pressure was increased from 7 MPa to 14 MPa in the period from 100 to 200 years (see Figure C-12). The results of these two runs in terms of pressure and permeability in the salt column are nearly identical to the results of Runs 1 and 2, and additional plots are not shown. Like those of Runs 1 and 2, these results indicate that, after 100 years, the compacted salt column was sufficiently isolated that salt reconsolidation is not significantly affected by repository-pressure increases.

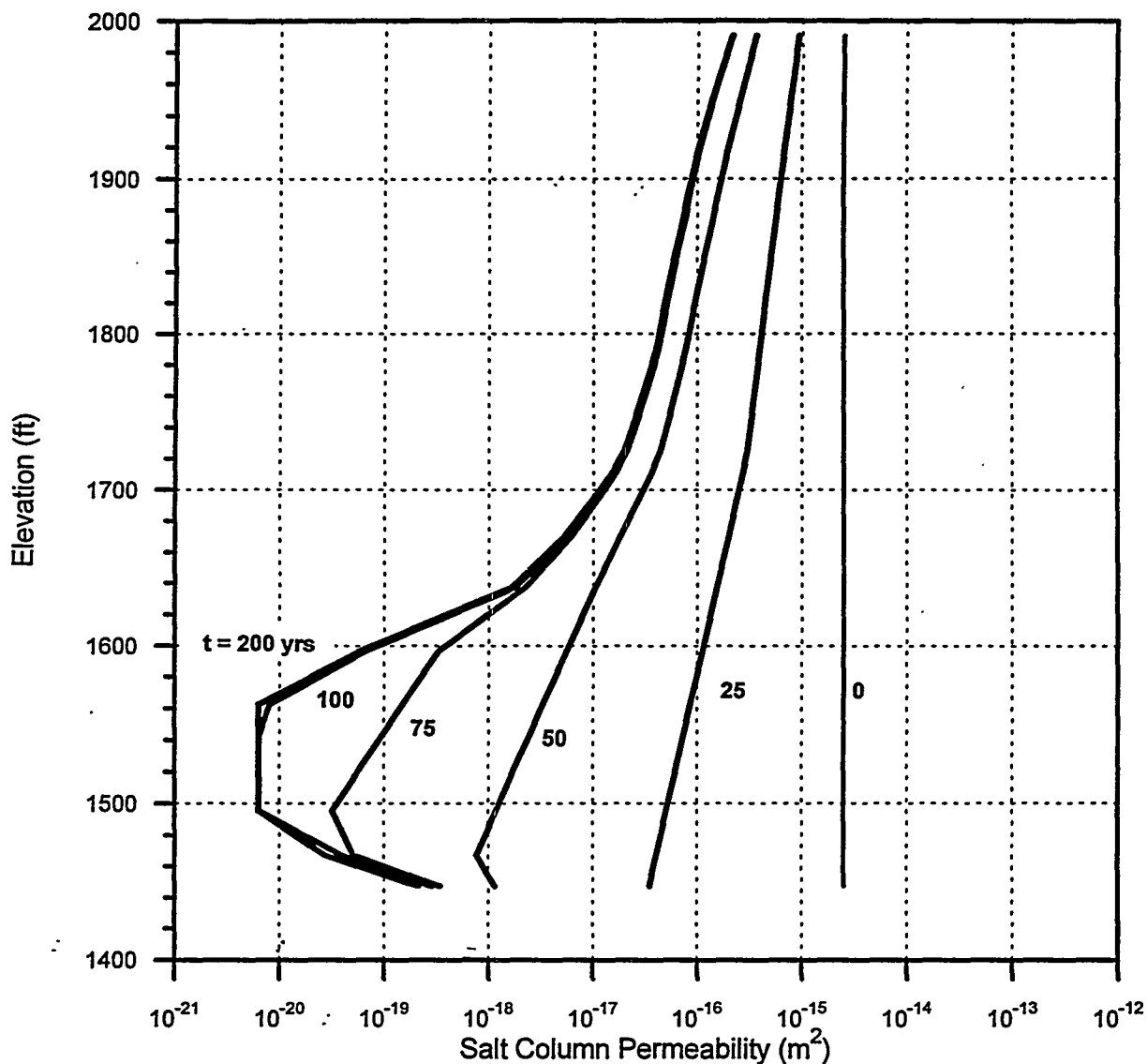


Figure C-16. Calculated salt column permeability versus elevation within the column for several times following seal emplacement (base case).

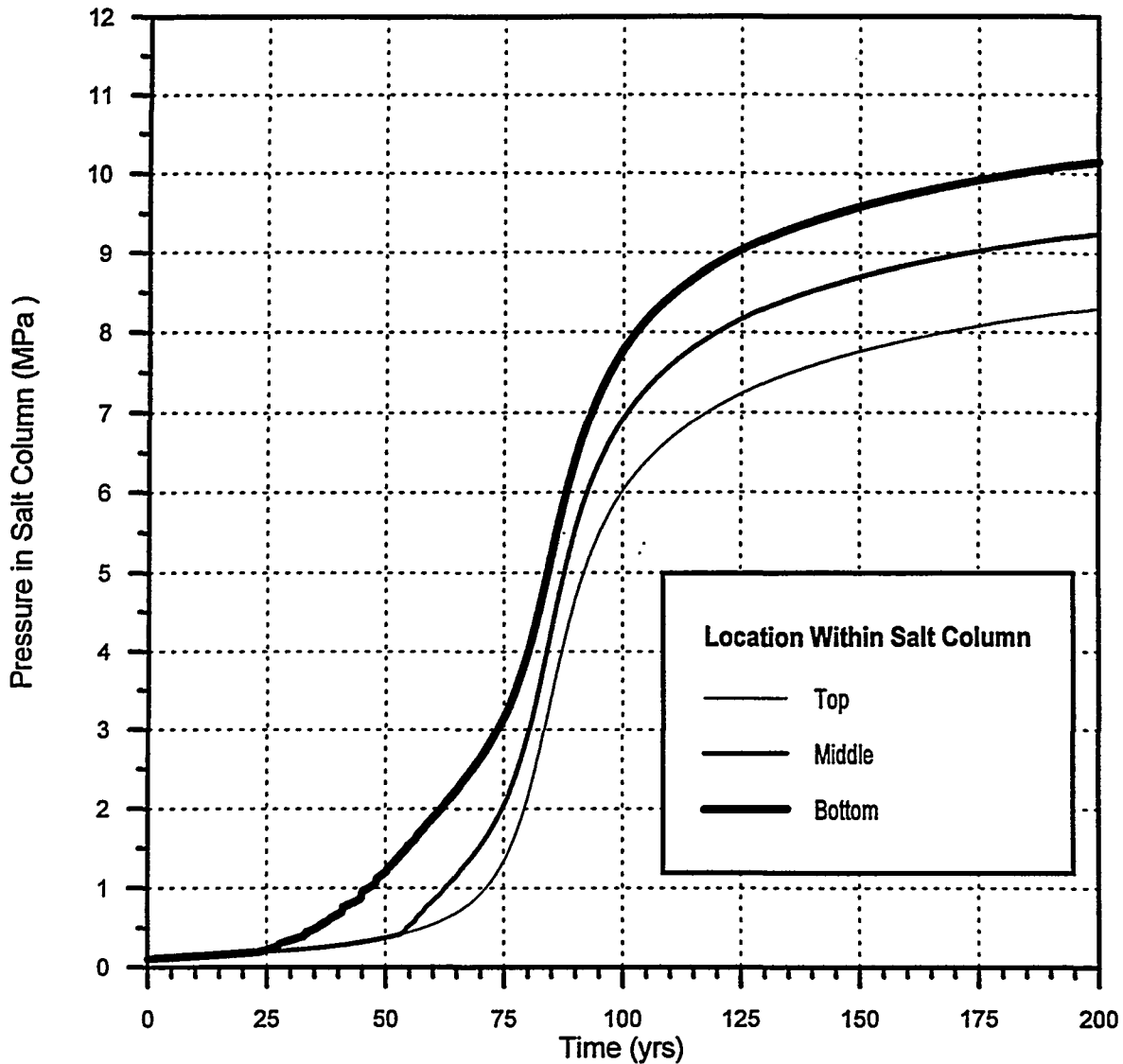


Figure C-17. Calculated pressure versus time after seal emplacement at the top, middle, and bottom of the compacted salt column (Run 2).

Two additional runs (Runs 5 and 6 in Table C-22) were made in which brine flow down the shaft from the Rustler Formation calculated by the full-shaft saturated flow model was included in the initial brine saturation of the compacted salt column. For these two simulations, the permeability of the DRZ adjacent to the shaft at the level of MB134, MB135, MB136, and MB137 was increased to  $2.9 \times 10^{-16} \text{ m}^2$ , thus creating a continuous (prior to healing) DRZ from the gas source at the repository level to the salt column. In the previous simulations, these DRZ units were assumed to be mostly unfractured, with permeability more like the undisturbed host anhydrite of the associated marker beds ( $1.0 \times 10^{-19} \text{ m}^2$ ).

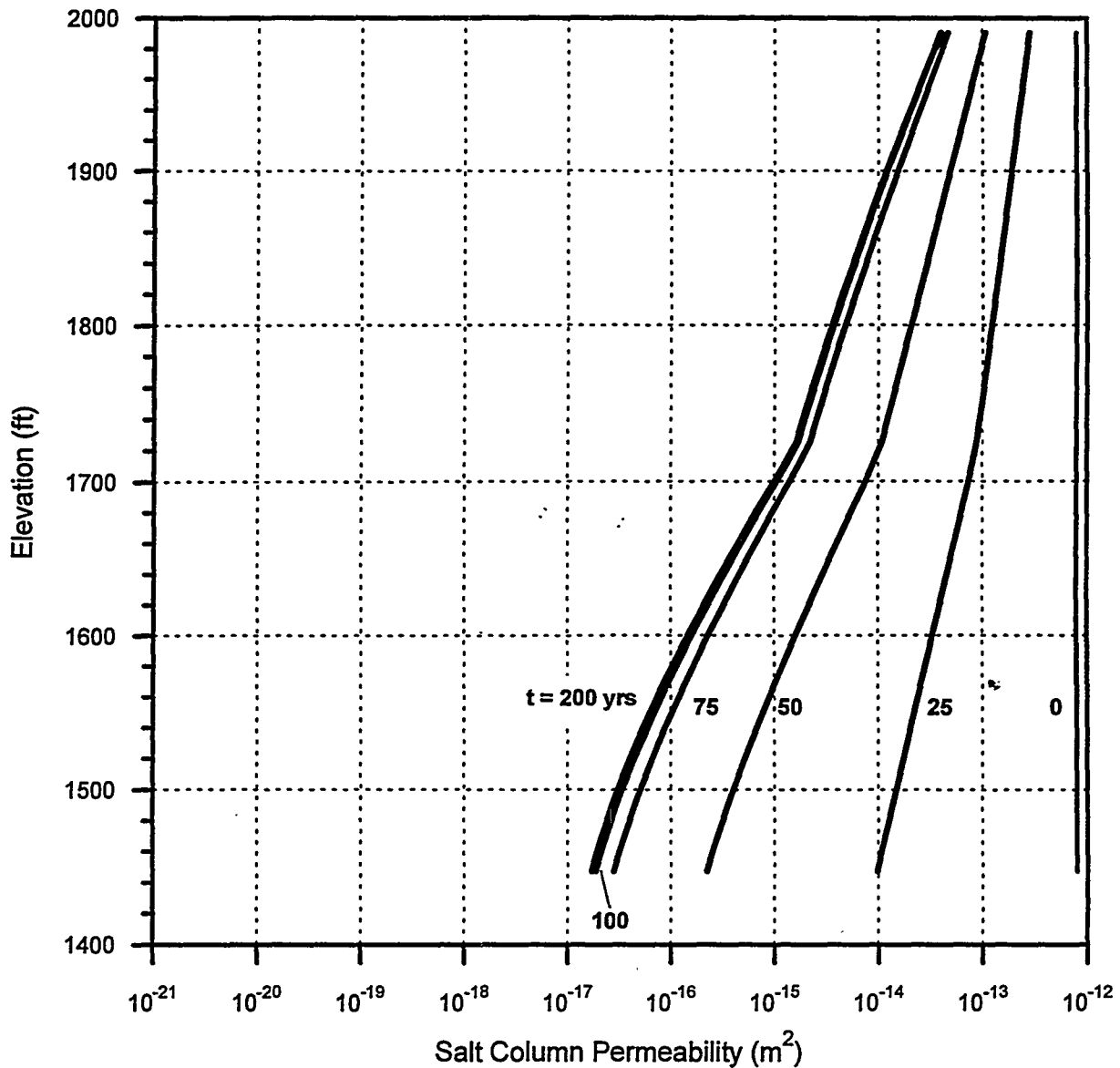


Figure C-18. Calculated salt column permeability versus elevation within the column for several times following seal emplacement (Run 2).

In Run 5 the asphalt waterstops were assumed to be in place as in the previous runs; however, in Run 6 the asphalt waterstops were excluded. The initial brine saturation of the salt column was increased by  $2.7 \text{ m}^3$  and  $17.2 \text{ m}^3$  for the two runs, respectively, to account for Rustler flow predicted by the full-shaft saturated flow model for these two cases. For the continuous DRZ assumption, with the increased communication between the base of the shaft and the compacted salt column prior to DRZ healing around the rigid concrete components, it was thought that stepping the repository pressure up to 1.75 MPa at time zero would provide unrealistic results. Therefore, for these two runs, the repository boundary pressure was

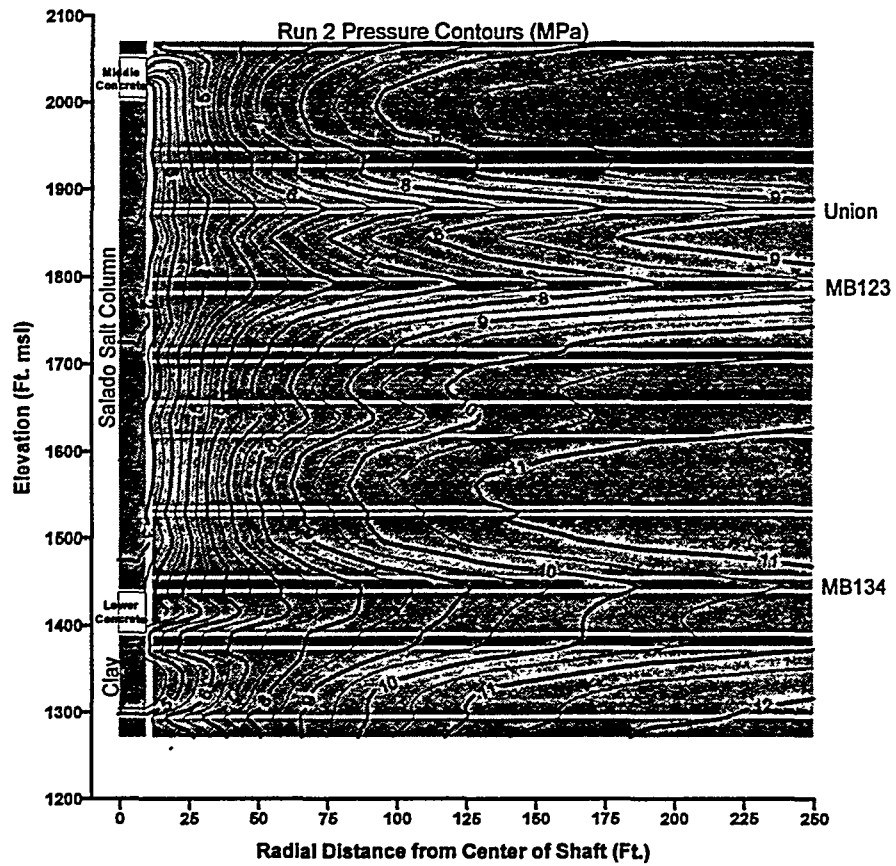
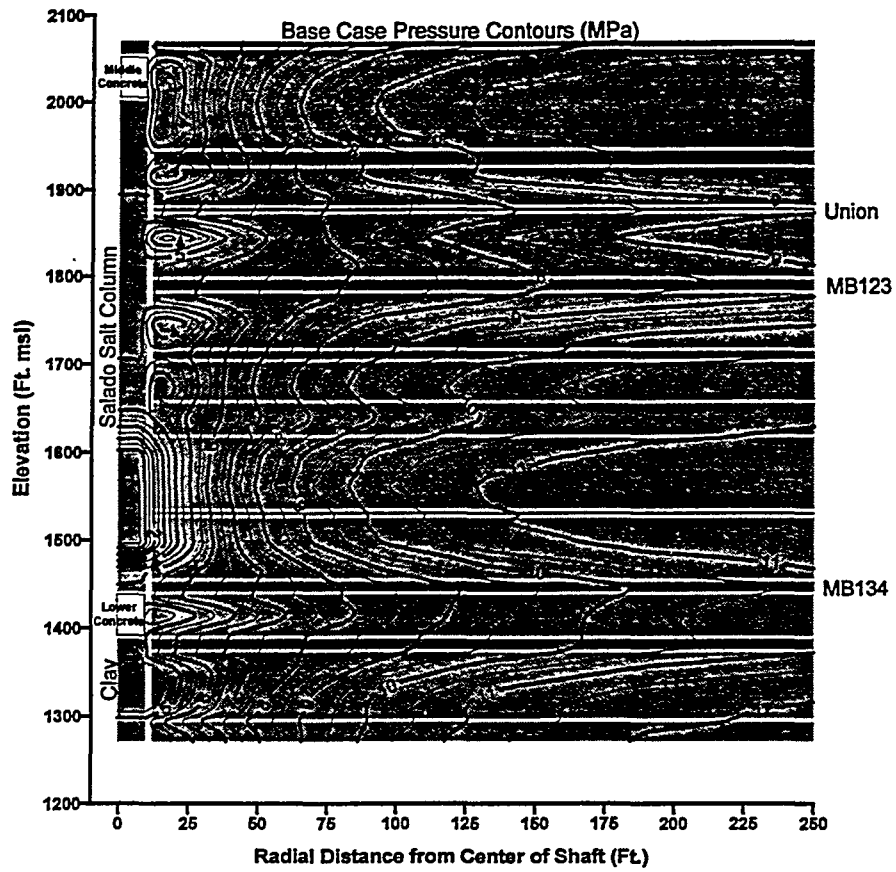


Figure C-19. Pressure contours at 75 years for base case and for 95% permeability/fractional density predictor (Run 2).

increased in 0.07-MPa increments at one-year time intervals (see Figure C-12). This rate of pressure increase is the same for all simulations; however, it is applied in smaller time increments in Runs 5 and 6.

The pressure and permeability results of Run 5 are nearly identical to the results of the base case (Run 1) shown in Figures C-15 and C-16, indicating no sensitivity to the inclusion of a DRZ adjacent to MB134 through MB137. The results of Run 6 do, however, show some sensitivity to the absence of the asphalt waterstops. Figure C-20 shows pressure versus time at the top, middle, and bottom of the salt column for the base case and for Run 6. This figure shows that pressure rose faster than for the base case at early times before the DRZ had fully healed around the lower concrete seal at 25 years. As a result of the faster pressure increase in the salt column, the calculated permeability profiles shown in Figure C-21 for this run show less crushed-salt reconsolidation at 100 years than in the base case shown in Figure C-16. Figure C-21 shows that, without concrete-asphalt waterstops, permeability at the bottom of the salt column for the case does not reach the minimum value of  $6.3 \times 10^{-21} \text{ m}^2$ .

Figure C-22 shows cumulative gas flow up the shaft from the repository past the lower concrete seal for each run. The right axis in the figure gives cumulative mass of gas flow in kg and the left axis translates this mass to a cumulative volume of flow in  $\text{m}^3$  at standard conditions ( $20^\circ\text{C}$  and atmospheric pressure). This figure shows that cumulative gas flow up from the repository was less than  $100 \text{ m}^3$  for all runs, except for Run 6 in which the concrete-asphalt waterstops were omitted. Run 6 predicted that approximately  $600 \text{ m}^3$  of gas reached the salt column in the first 25 years.

The lower Salado compacted clay column provides an effective barrier in shaft cross-section because of its low permeability and its relatively high brine saturation, thus forcing most of the gas to flow through the DRZ. The compacted clay column was initialized at an initial brine saturation of nearly 80%. For all simulations performed, it resaturated to near 100% at top and bottom over the 200-year simulation time.

## **C6.0 FLOW UP FROM THE SALADO (MODEL 3)**

### **C6.1 Statement of Problem**

This calculation examined the potential for brine flow and quantity of brine flow that may be expected to migrate upward through the shaft seal system in response to the ambient pressure conditions that will be present several hundred years after closure. Pressures measured in the Salado at the repository horizon are significantly over-pressured with respect to hydrostatic conditions and to the Rustler (see Table C-2). Because the Salado is very impermeable, any natural component of vertical flow from the Salado upward must be very low. However, with the connection of the Salado and the Rustler Formations through the shaft seal system, the potential for upward flow exists. The performance measure (result) for this model is the steady-state brine flow rate. The performance measure will be provided for the Rustler/Salado contact, the top of the compacted salt column, and the top of combined Unit 8 (composed of MB131, Zone J, MB132, and MB133).

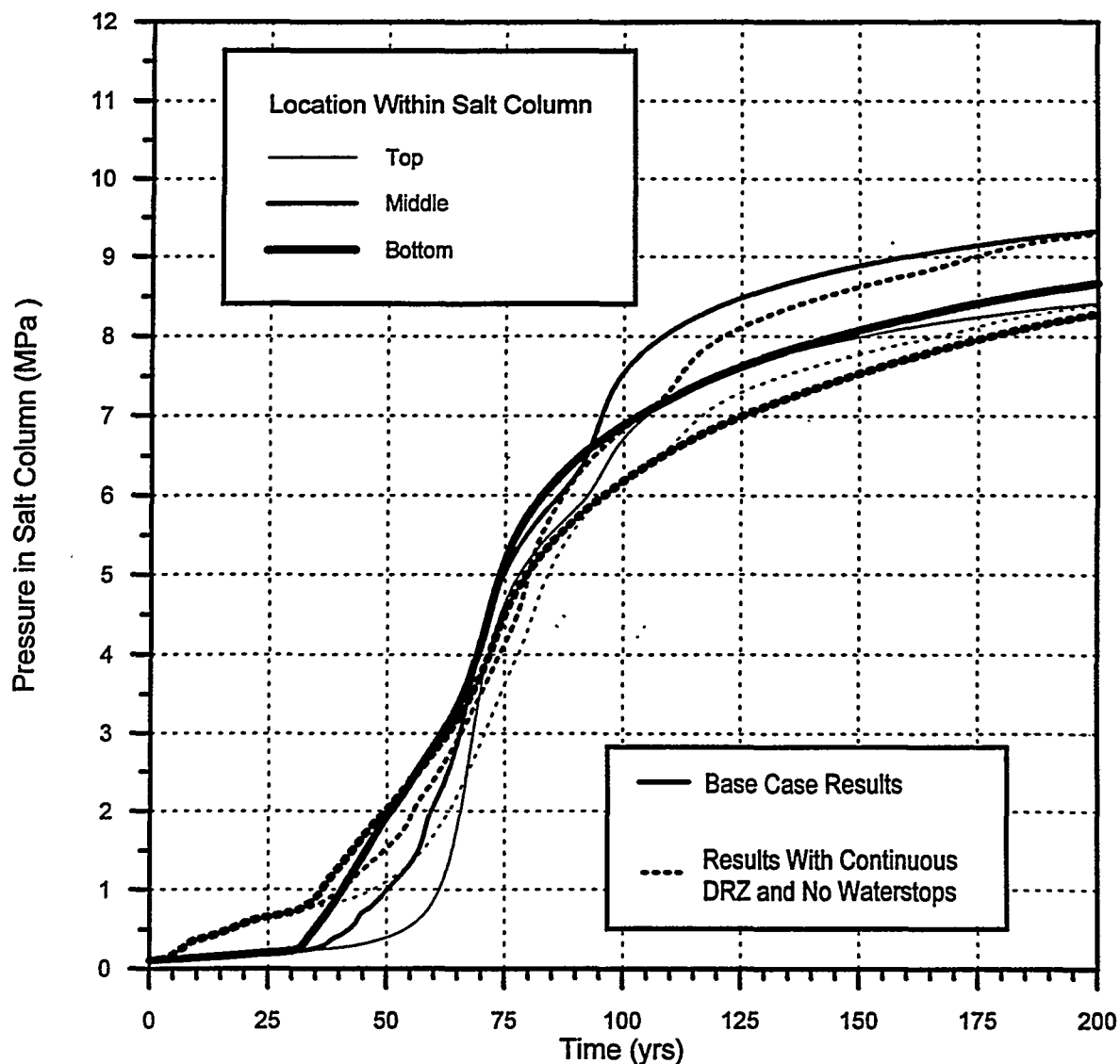


Figure C-20. Comparison of calculated pressure results for base case and continuous DRZ with no waterstops (Run 6).

## C6.2 Performance Model Description

### C6.2.1 Conceptual Model and Assumptions

The model grid and simulation code (SWIFT II) used in this model are identical to those used in Model 1. The primary difference in the conceptual model between Model 1 and Model 3 is the time frame over which this calculation is considered relevant. Model 1 predicted brine flow down the shaft. The Model 1 calculation is considered an early-time calculation before far-field pressures gradients reestablish in the vicinity of the shaft. The Model 1 calculation runs from shaft closure forward to 400 years post-closure. Model 3 assumed that equilibrium pressure gradients have reestablished in the vicinity of the shaft and DRZ healing has taken place within the Salado halite.

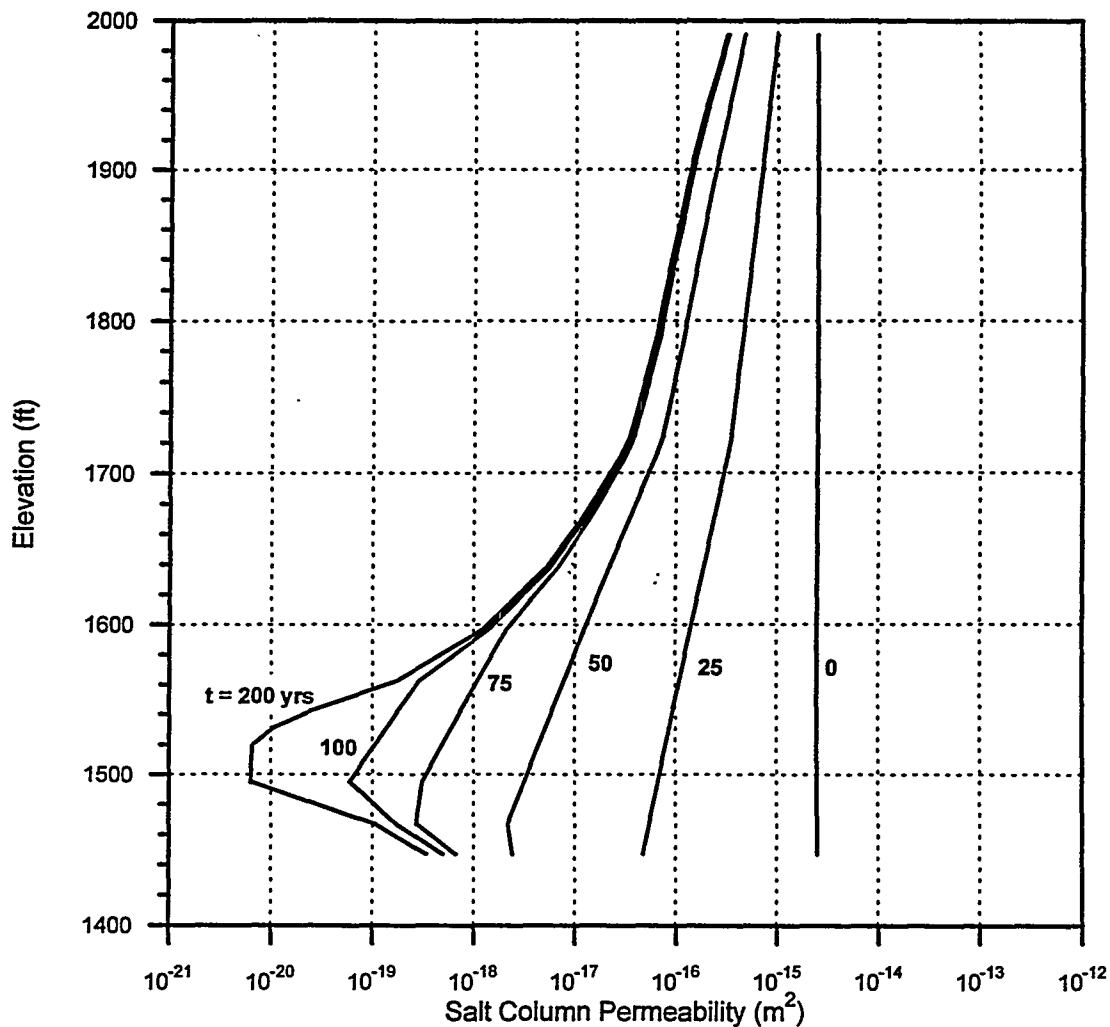


Figure C-21. Calculated salt column permeability versus elevation within the column for several times following seal emplacement (Run 6: Rustler flow included, continuous DRZ, no waterstops).

In Section C2, the primary assumptions common to all numerical calculations in this appendix are listed. In addition to those listed in Section C2, the following list summarizes the primary assumptions specific to Model 3:

- The calculation assumed brine-saturated flow conditions.
- The model is initialized at nonhydrostatic conditions based on undisturbed heads in the Rustler Formation and the maximum estimated formation pressure measured in the Salado Formation (see Table C-2).
- Seal system and DRZ permeabilities are representative of times greater than or equal to 400 years after closure.

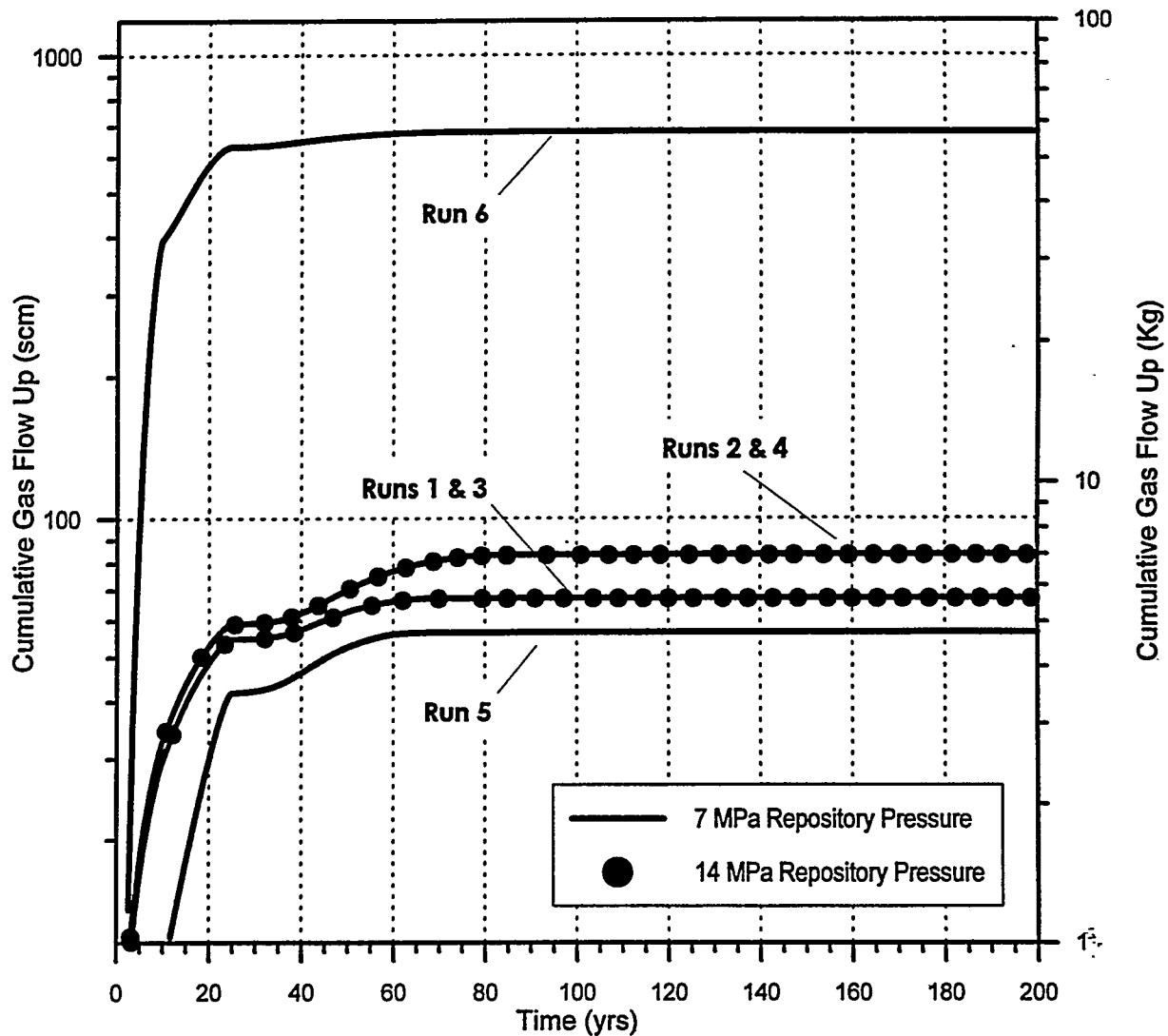


Figure C-22. Cumulative gas flow from the repository to the compacted salt column.

### C6.2.2 Numerical Method

The numerical code used in Model 3 is SWIFT II. This code was also used in Model 1; see Section C4.2.2 for a complete description.

### C6.2.3 Model Geometry and Boundary Conditions

The model geometry and grid are the same as that used in Model 1; see Section C4.2.3 for a complete description. However, the initial conditions and boundary conditions differ from those of Model 1. For Model 3, the shaft is completely sealed, and the DRZ and the compacted salt column permeabilities are no longer transient and have achieved their lowest values. This permeability field was held constant in Model 3.

The lateral boundary and initial grid-block pressures were initialized at nonhydrostatic conditions consistent with the undisturbed heads reported for the Magenta, the Culebra, the Rustler/Salado contact, and MB139 (see Table C-2). No-flow boundary conditions were imposed at the top and bottom of the model. Infinite aquifer boundary conditions were set at the outer edge of the modeled region. The model components for the simulation are concrete, asphalt, compacted clay, crushed salt, shaft liner, DRZ, and undisturbed formation.

#### C6.2.4 Model Parameters

Best case model parameters as specified for Model 1 for the host-rock and seal system have been used. Table C-23 summarizes the three simulations performed in Model 3, highlighting the principal differences among them. This suite of runs is similar to the runs simulated in Model 1.

The base-case simulation (Run 1) assumed that the anhydrites in the Rustler Formation, and anhydrites greater than 3 m thick in the Salado Formation, have no DRZ (based on mechanical modeling results presented in Appendix D). This condition results in a discontinuous DRZ, which is discontinuous initially and remains so throughout the simulations. The second simulation (Run 2) assumes that Rustler members and Salado anhydrites are damaged, and allows healing to occur only in the Salado halite. Runs 1 and 2 include waterstops. The third simulation (Run 3) is a sensitivity simulation to examine the impact of the asphalt waterstops. It is the same as Run 2 except that the concrete-asphalt waterstops were not incorporated into the model. Figure C-23 depicts the permeabilities used in these three simulations.

Table C-23. Performance Model 3 Simulations

Run	Rustler and Anhydrite DRZ	Waterstops
1 (Base-Case)	No	Yes
2	Yes	Yes
3	Yes	No

#### C6.3 Performance Model Results

Results are presented in terms of brine flow rates ( $m^3/s$ ). Because the vertical gradient is directed upward, the flow rates reported are also upward. Table C-24 provides the steady-state upward flow rates measured at the Rustler/Salado contact, the top of the compacted salt column, and the top of combined Unit 8 of the model. The difference between the results of Runs 1 and 2 derives from the increased DRZ permeabilities assumed for the anhydrite units. The lack of a difference between the results of Runs 2 and 3 denotes the negligible effect of the waterstops on long-term saturated flow.

The waterstops were included in the seal system design as an immediate seal for the DRZ. Therefore, their inclusion in Runs 1 and 2 was not really appropriate. However, based on the results from Run 3, it can be concluded that their presence in Runs 1 and 2 did not affect the predicted performance measure of upward steady-state flow rate for these simulations.

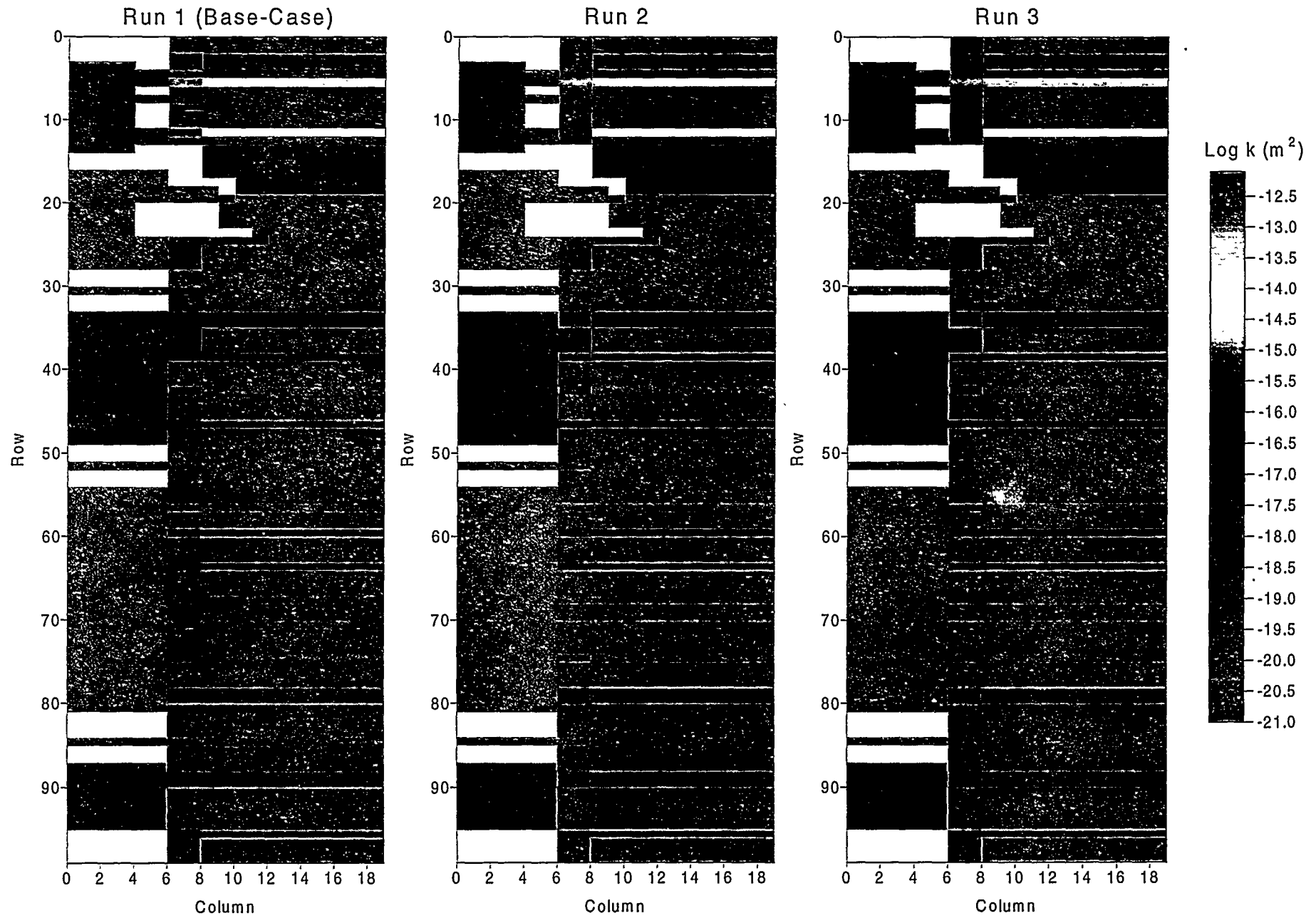


Figure C-23. Permeability fields for Runs 1 through 3 ( $t > 400$  years).

Table C-24. Comparison of Flow Rates Up the Shaft/DRZ from Simulations that Incorporate the Measured Pressure Conditions

Run	Combined Unit 8	Top of Compacted Salt Column	Rustler/Salado Contact
Flow Rate up the Shaft and DRZ (m <sup>3</sup> /yr)			
1 (base-case)	4.76×10 <sup>-5</sup>	1.68×10 <sup>-4</sup>	8.27×10 <sup>-4</sup>
2	4.76×10 <sup>-5</sup>	1.71×10 <sup>-4</sup>	9.68×10 <sup>-4</sup>
3	4.76×10 <sup>-5</sup>	1.71×10 <sup>-4</sup>	9.68×10 <sup>-4</sup>

## C7. INTRA-RUSTLER FLOW (MODEL 4)

### C7.1 Statement of Problem

The shaft seal system is designed to limit migration of fluids within the sealed shaft. The natural heads within the Rustler Formation are nonhydrostatic indicating the potential for vertical flow (Beauheim, 1989). This calculation examined the potential for, and quantity of brine flow, which, after closure, could be expected to migrate between the Magenta and the Culebra, the two primary water-bearing members of the Rustler Formation.

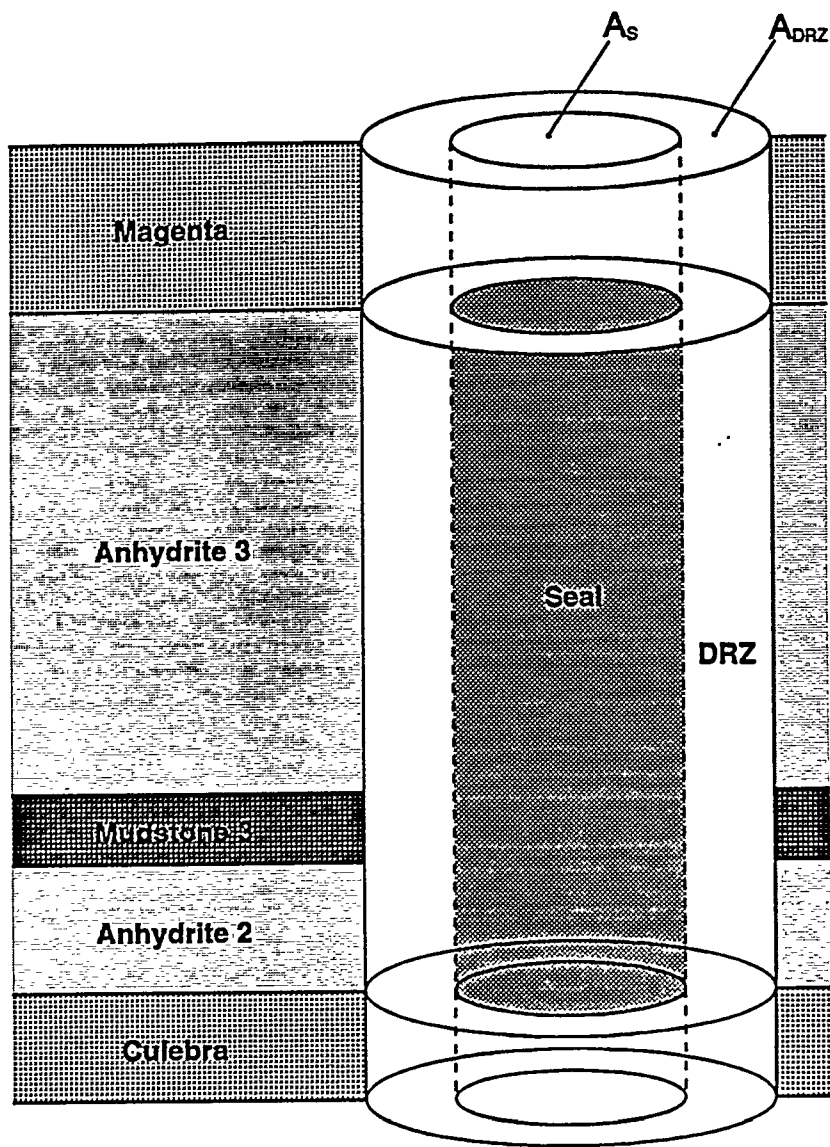
### C7.2 Performance Model Description

The previous models have used sophisticated numerical flow models. This performance model employed simple analytical relationships. The calculation assumptions yielded a relatively simple conceptual model and estimates of intra-Rustler flow rates. The conceptual model, relevant assumptions, and the analysis approach are discussed below.

#### C7.2.1 Conceptual Model and Assumptions

Non-hydrostatic conditions exist within the Rustler Formation based on estimated undisturbed or measured disturbed head differences between the various members of the Rustler Formation (see Table C-1). Relatively low undisturbed permeabilities of the mudstone and anhydrite units separating the Culebra and the Magenta naturally limit crossflow. However, the construction and subsequent closure of the shaft provide a potential permeable vertical conduit connecting water bearing units. In this calculation, the hydraulic conductance of the shaft seal system was used to estimate flow rates between the Magenta and Culebra under various assumptions. Figure C-24 schematically shows the conceptual model for calculating intra-Rustler flow rates. From Figure C-24 one can see that flow was considered through the seal and through the DRZ consistent with Models 1 through 3. The primary assumptions for this analysis are listed below:

- Saturated flow was assumed under isothermal and constant fluid-density conditions.
- Flow-rates were calculated using the steady-state version of Darcy's Law for saturated flow.



Hydraulic Conductance of the Seal

$$\frac{k_s A_s}{L} \left( \frac{\rho g}{\mu} \right)$$

Combined Hydraulic Conductance of the Seal Plus DRZ

$$\frac{k_s A_s + k_{DRZ} A_{DRZ}}{L} \left( \frac{\rho g}{\mu} \right)$$

Figure C-24. Intra-Rustler flow conceptual model.

- Resistance to flow was assumed to be only a function of the seal material and DRZ permeabilities. The resistance provided by the geologic members is assumed to be much larger, and the resulting natural vertical crossflow was not considered.
- The driving force (head difference) between water-bearing strata was assumed to be constant and unchanged as a result of flow between units.

### C7.2.2 Analytical Approach

A simple analytical model was used to estimate the potential for brine migration between Rustler members. When two hydraulic units are hydraulically connected and at different heads, flow will occur from the unit with the highest head to the unit with the lowest head. Flow is governed by Darcy's Law, which under the assumptions of single-phase steady-state fluid flow through a porous medium can be expressed as

$$Q = -kA \frac{\Delta h \rho g}{\Delta l \mu} \quad (C-4)$$

where

- $Q$  = volumetric flow rate with units of (m<sup>3</sup>)
- $k$  = the intrinsic permeability of the porous medium (m<sup>2</sup>)
- $\rho$  = the fluid density (kg/m<sup>3</sup>)
- $g$  = the acceleration of gravity (m/s<sup>2</sup>)
- $\mu$  = the fluid viscosity (Pa • s)
- $\Delta h$  = the head difference between these two units (m)
- $\Delta l$  = the separation of the Culebra and the Magenta (m)
- $A$  = the seal plus DRZ cross-sectional area normal to the flow direction (m<sup>2</sup>).

Equation C-4 above can be simplified by using the concept of the hydraulic conductance of a porous medium. The hydraulic conductance of a porous medium is composed of area, length, intrinsic permeability, and the fluid viscosity and density. The hydraulic conductance is the inverse of the hydraulic resistance.

The hydraulic conductance defined in terms of intrinsic permeability can be expressed as

$$C = \frac{kA \rho g}{\Delta l \mu} \quad (C-5)$$

where  $C$  is the hydraulic conductance (m<sup>2</sup>/s).

In this case Darcy's Law above can be expressed as

$$Q = C \Delta h \quad (C-6)$$

where  $C$  is the effective hydraulic conductance of the seal and DRZ materials separating the Culebra and the Magenta.

Figure C-24 shows the conceptual model for intra-Rustler flow. An effective hydraulic conductance of the seal and DRZ system between the Magenta and the Culebra members can be calculated by analogy to electrical circuit theory. The effective hydraulic conductance is composed of the properties of the DRZ and the seal combined. The seal and DRZ act in parallel, and therefore the hydraulic conductance of these two regions can be directly added to get their combined conductance:

$$C = \frac{k_s A_s + k_{DRZ} A_{DRZ}}{\Delta l} \frac{\rho g}{\mu} \quad (C-7)$$

Because the DRZ permeability is a function of rock type, the effective seal plus DRZ hydraulic conductance must also be combined vertically in series between the Magenta and the Culebra. Using the hydraulic conductance of the seal system and the DRZ, a volumetric flow rate can be estimated from the potential head difference.

To put the calculated volumetric flow rates into perspective, the flow rate can be used to calculate the width of the hydraulic disturbance which is created in the water-bearing unit receiving the interflow. Figure C-25 depicts the case of a point injection into a linear flow field. The injected fluid displaces a certain volume of the receiving aquifer fluid and this volume can be expressed as the maximum plume width (measured in plan view, Figure C-25). Within this maximum plume width, the fluid in the receiving aquifer is composed entirely of injected fluid. Outside of this width, the fluid is composed of the resident aquifer fluid. The equation describing the half plume width is:

$$W = \frac{Q_w}{2u_o b} \quad (C-8)$$

where

$Q_w$  = the intra-Rustler fluid flow rate

$u_o$  = the Darcy velocity of the stratigraphic unit being injected into

$b$  = the thickness of the stratigraphic unit being injected into.

### C7.2.3 Model Parameters

Model parameters having to do with the seal system and the Rustler rocks have been previously defined (Section C3). Using the base case seal and DRZ conceptualization and parameters, the flow rate between the Magenta and the Culebra was calculated considering a range of head differences. The calculated flow rates are used to estimate plume half widths in both the Culebra or the Magenta. The flow rate between the Magenta and the Culebra was also calculated considering a continuous DRZ of variable normalized radius and considering a constant head difference of similar magnitude to that which is currently estimated for undisturbed conditions (see Table C-2).

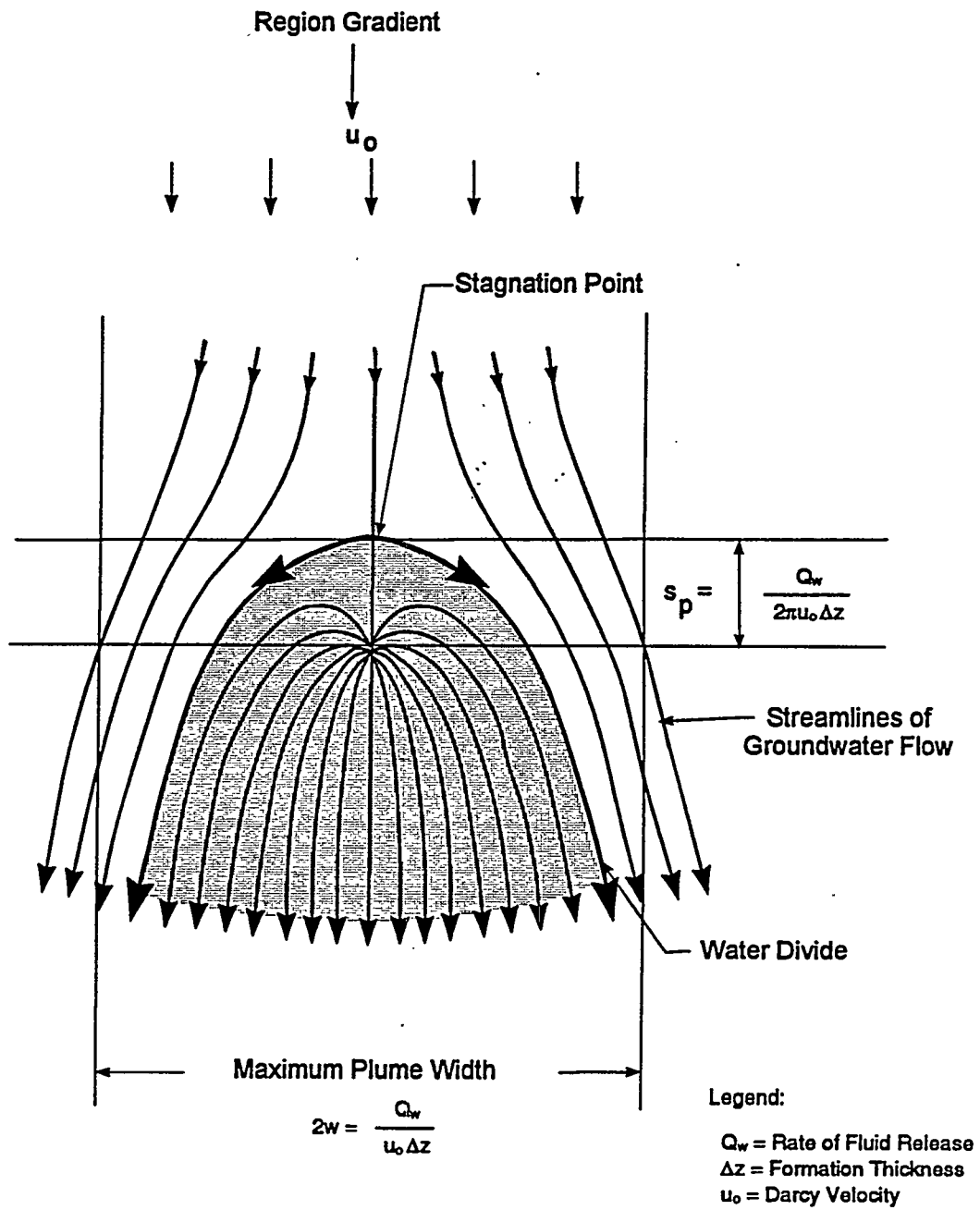


Figure C-25. Effect of an injection well on a unidirectional flow field.

The only parameters unique to Model 4 are the Darcy velocities in the Magenta and the Culebra. These velocities were calculated assuming steady-state Darcy flow and using the minimum regional hydraulic gradient for the Culebra and a regional hydraulic gradient for the Magenta reported by Lambert (1996). The Culebra Darcy velocity was chosen to predict the largest plume half width for a given flow rate (see Equation C-8 above). Table C-25 lists the gradients and Darcy velocities calculated from them using the Culebra and Magenta hydraulic conductivities reported in Section C3.

Table C-25. Regional Darcy Velocities for Culebra and Magenta Members of the Rustler Formation

Rustler Member	Hydraulic Gradient <sup>(1)</sup>	Darcy Velocity (m/s)
Magenta	0.003788	$3.788 \times 10^{-11}$
Culebra	0.001894	$2.652 \times 10^{-10}$

(1) After Lambert, 1996.

### C7.3 Performance Model Results

Table C-2 shows that the approximate undisturbed head difference between the Magenta and the Culebra is 33.2 m (109 ft). Presently, this head difference would direct flow from the Magenta to the Culebra. However, the true head difference is uncertain, especially temporally. Using the base case conceptualization for the DRZ, the flow-rate between the Magenta and the Culebra was calculated for head differences ranging from 3.1 to 121.9 m (10 to 400 ft). Figure C-26 plots the resulting flow rates, which range from 0.002 to 0.096 m<sup>3</sup>/yr. Figure C-27 plots the resulting plume-half width assuming flow was directed into either the Magenta or the Culebra. As can be seen in Figure C-27, the plume half width did not extend past one shaft radius for head differences less than approximately 76 m (250 ft).

The base-case conceptualization assumed that no anhydrite DRZ exists in the Rustler. The next calculation examined the sensitivity of interflow to a continuous DRZ (in both anhydrite and mudstone) for the estimated undisturbed head difference between the Magenta and Culebra.

Figure C-28 plots the flow rate between the Magenta and the Culebra assuming a head difference of 33.5 m (110 ft) and assuming the DRZ is continuous and has a normalized radius of extent varying from 1.0 (no DRZ) to 3.0 (three shaft radii). Flow rates range from 0.003 to 2.93 m<sup>3</sup>/yr. Figure C-29 plots the calculated plume half-width for these flow rates assuming flow is directed into either the Magenta or the Culebra. For a continuous DRZ normalized radius of less than 1.5, the hydraulic disturbance caused by Culebra-Magenta interflow is minimal. Because the flow-rate and plume half-width are linearly correlated to the head difference, results from Figures C-28 and C-29 can be easily scaled to consider any head difference of interest.

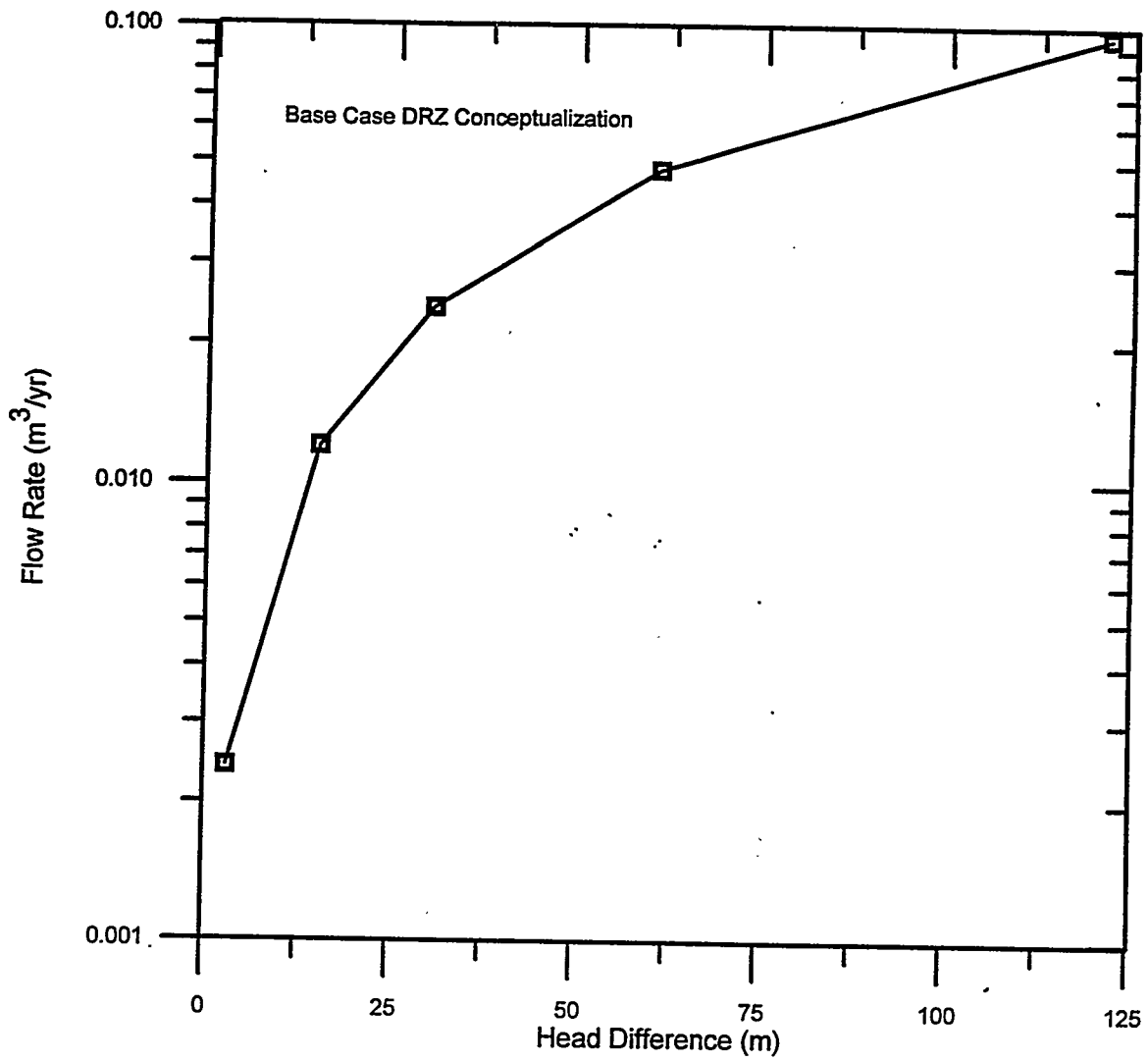


Figure C-26. Sensitivity of flow rate between Culebra and Magenta to head difference (base case).

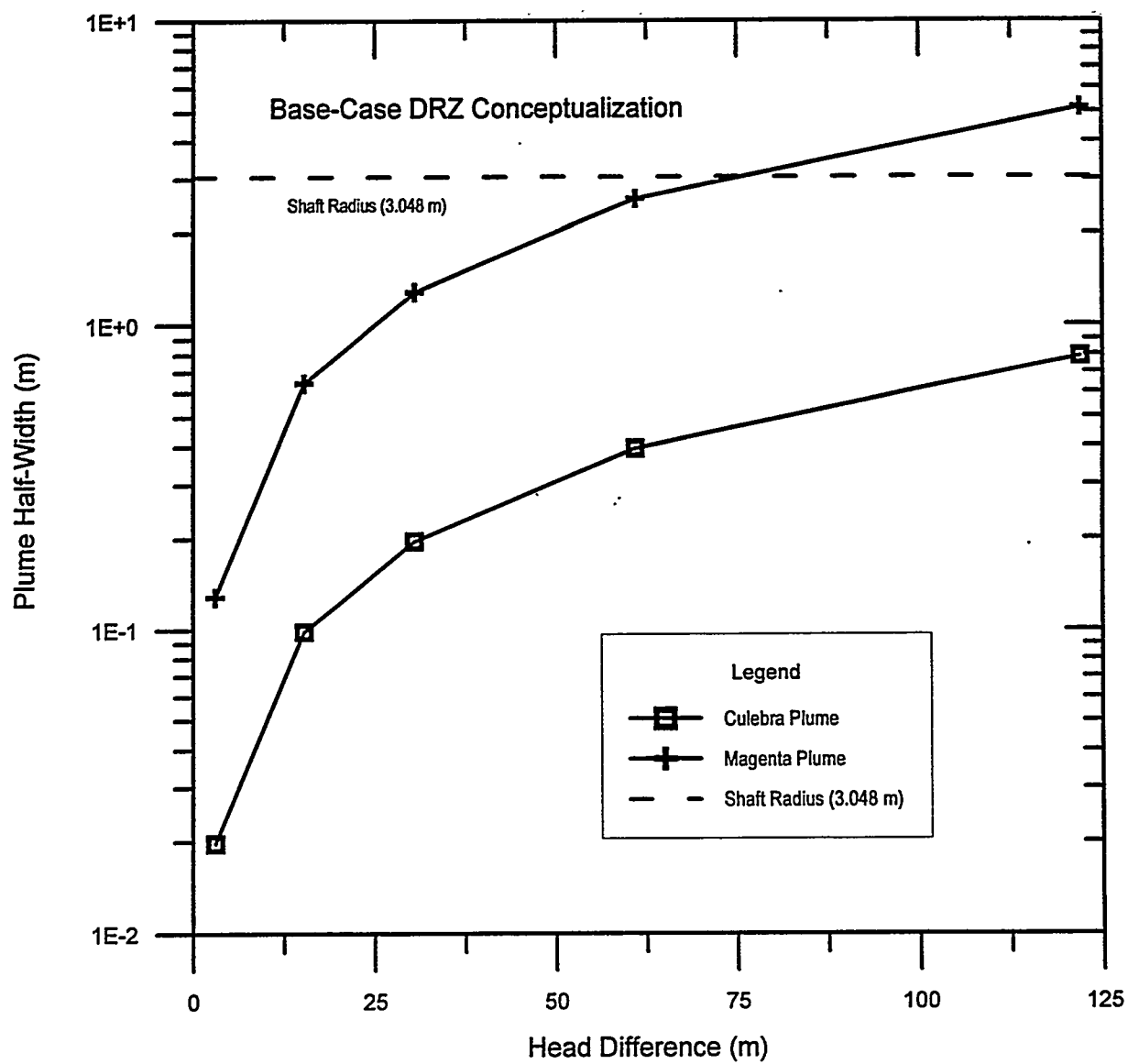


Figure C-27. Sensitivity of flow-field disturbance to head difference (base case).

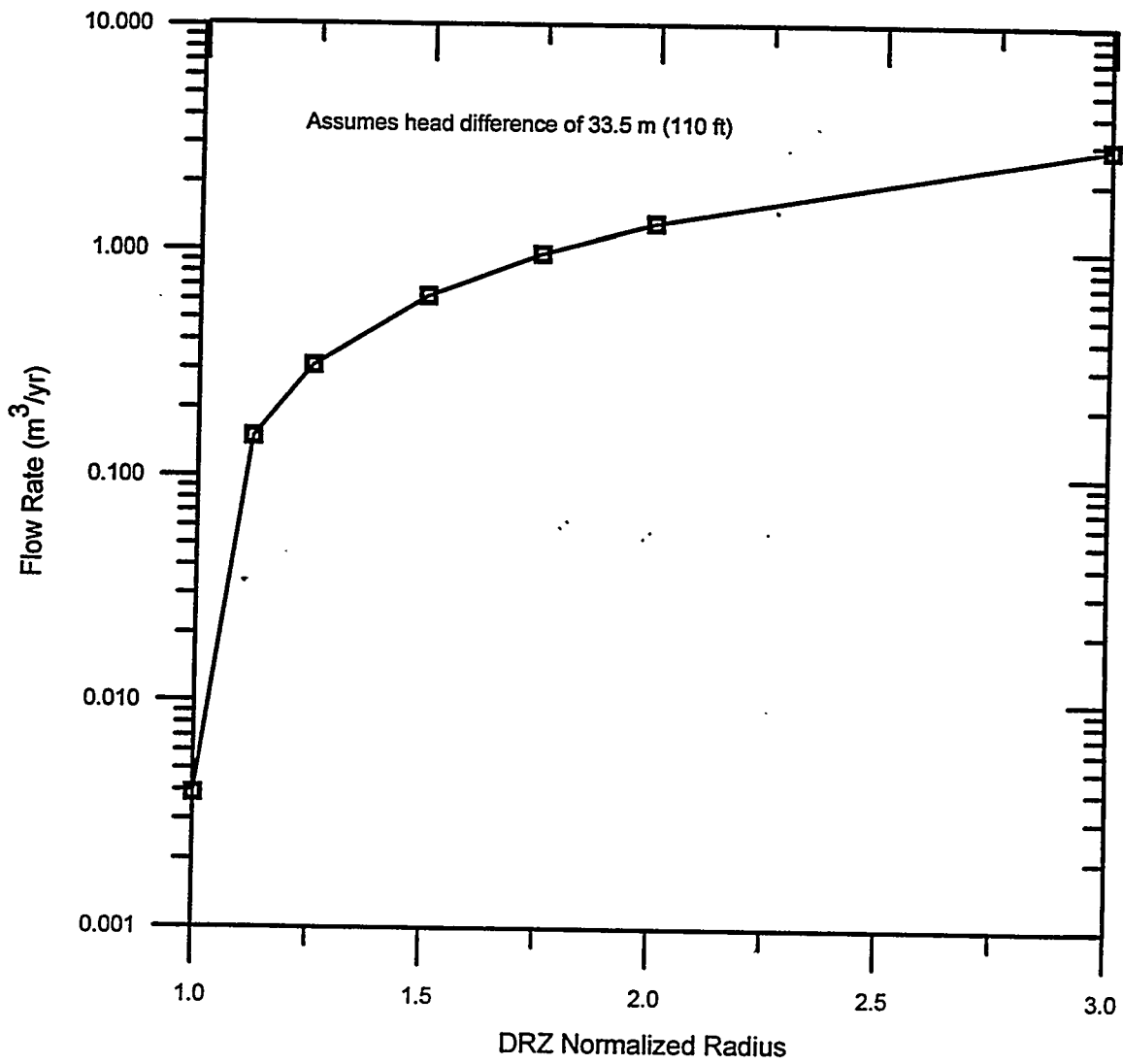


Figure C-28. Sensitivity of flow rate between Culebra and Magenta to DRZ radius (continuous DRZ).

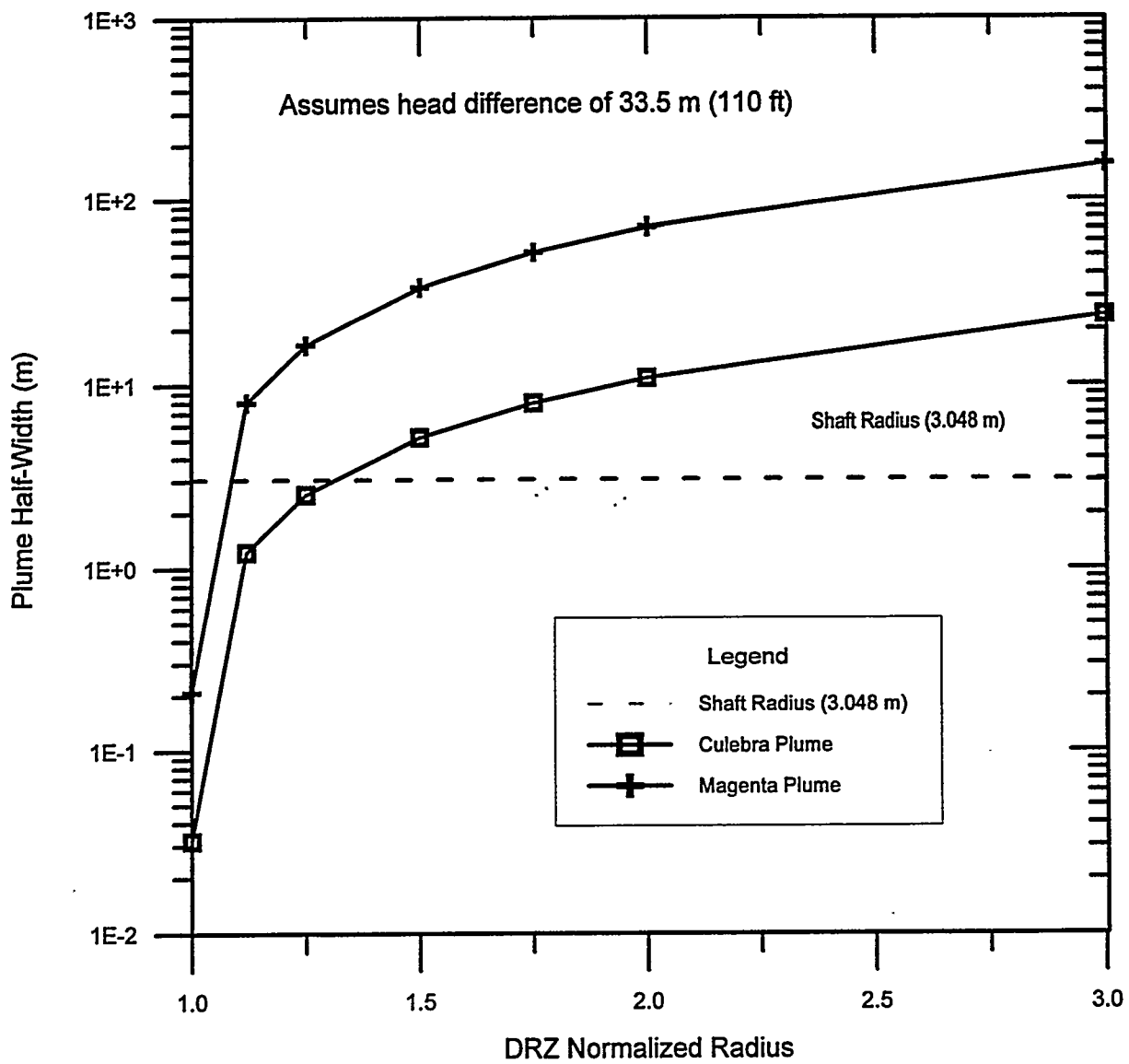


Figure C-29. Sensitivity of flow-field disturbance to DRZ radius (continuous DRZ).

## C8. REFERENCES

- Avis, J.D., and G.J. Saulnier, Jr. 1990. Analysis of the Fluid-Pressure Responses of the Rustler Formation at H-16 to the Construction of the Air-Intake Shaft at the Waste Isolation Pilot Plant (WIPP) Site. SAND89-7067. Albuquerque, NM: Sandia National Laboratories. (Copy on file in the Sandia WIPP Central Files, Sandia National Laboratories, Albuquerque, NM [SWCF] as WPO24168.)
- Aziz, K., and A. Settari. 1979. Petroleum Reservoir Simulation. New York, NY: Elsevier Applied Science Publishers.
- Beauheim, R.L. 1987. Interpretations of Single-Well Hydraulic Tests Conducted at and Near the Waste Isolation Pilot Plant (WIPP) Site, 1983-1987. SAND87-0039. Albuquerque, NM: Sandia National Laboratories. (Copy on file in the SWCF as WPO27679.)
- Beauheim, R.L. 1989. Interpretation of H-11b4 Hydraulic Tests and the H-11 Multipad Pumping Test of the Culebra Dolomite at the Waste Isolation Pilot Plant (WIPP) Site. SAND89-0536. Albuquerque, NM: Sandia National Laboratories. (Copy on file in the SWCF as WPO24154.)
- Beauheim, R.L., G.J. Saulnier, Jr., and J.D. Avis. 1991. Interpretation of Brine-Permeability Tests of the Salado Formation at the Waste Isolation Pilot Plant Site: First Interim Report. SAND90-0083. Albuquerque, NM: Sandia National Laboratories. (Copy on file in the SWCF as WPO26003.)
- Beauheim, R.L., R.M. Roberts, T.F. Dale, M.D. Fort, and W.A. Stensrud. 1993. Hydraulic Testing of Salado Formation Evaporites at the Waste Isolation Pilot Plant Site: Second Interpretive Report. SAND92-0533. Albuquerque, NM: Sandia National Laboratories. (Copy on file in the SWCF as WPO23378.)
- Borns, D.J., and J.C. Stormont. 1988. An Interim Report on Excavation Effect Studies at the Waste Isolation Pilot Plant: The Delineation of the Disturbed Rock Zone. SAND87-1375. Albuquerque, NM: Sandia National Laboratories. (Copy on file in the SWCF as WPO24694.)
- Brinster, K.F. 1991. Preliminary Geohydrologic Conceptual Model of the Los Medaños Region Near the Waste Isolation Pilot Plant for the Purpose of Performance Assessment. SAND89-7147. Albuquerque, NM: Sandia National Laboratories. (Copy on file in the SWCF as WPO27781.)
- Brodsky, N.S. 1990. Crack Closure and Healing Studies in WIPP Salt Using Compressional Wave Velocity and Attenuation Measurements: Test Methods and Results. SAND90-7076. Albuquerque, NM: Sandia National Laboratories. (Copy on file in the SWCF as WPO25755.)
- Brooks, R.H., and A.T. Corey. 1966. "Properties of Porous Media Affecting Fluid Flow," Journal of the Irrigation and Drainage Division, Proceedings of the American Society of Civil Engineers (ASCE). Vol. 92, no. IR2, 61-88. (Copy on file in the SWCF.)

- Dale, T., and L.D. Hurtado. 1996. "WIPP Air-Intake Shaft Disturbed-Rock Zone Study," 4th International Conference on the Mechanical Behavior of Salt, Montreal, Quebec, June 17-18, 1996. SAND96-1327C. Albuquerque, NM: Sandia National Laboratories. (Copy on file in the SWCF.)
- Davies, P.B. 1991. Evaluation of the Role of Threshold Pressure in Controlling Flow of Waste-Generated Gas into Bedded Salt at the Waste Isolation Pilot Plant. SAND90-3246. Albuquerque, NM: Sandia National Laboratories. (Copy on file in the SWCF as WPO26169.)
- DOE (U.S. Department of Energy). 1995. Waste Isolation Pilot Plant Sealing System Design Report. DOE/WIPP-95-3117. Carlsbad, NM: U.S. Department of Energy, Waste Isolation Pilot Plant. (Copy on file in the SWCF as WPO29062.)
- DOE (U.S. Department of Energy). 1996. Compliance Certification Application for the Waste Isolation Pilot Plant. DOE/CAO-96-2184. Carlsbad, NM: U.S. Department of Energy, Carlsbad Area Office.
- Finley, N.C., and M. Reeves. 1981. SWIFT Self-Teaching Curriculum: Illustrative Problems to Supplement the User's Manual for the Sandia Waste-Isolation Flow and Transport Model (SWIFT). SAND81-0410. Albuquerque, NM: Sandia National Laboratories. (Copy on file in the SWCF as WPO30254.)
- Freeze, R.A., and J.A. Cherry. 1979. Groundwater. Englewood Cliffs, NJ: Prentice-Hall, Inc. (Copy on file in the Nuclear Waste Management Library, Sandia National Laboratories, Albuquerque, NM as GB1003.2 .F73 1979.)
- Gorham, E., R. Beauheim, P. Davies, S. Howarth, and S. Webb. 1992. "Recommendations to PA on Salado Formation Intrinsic Permeability and Pore Pressure for 40 CFR 191 Subpart B Calculations," Preliminary Performance Assessment for the Waste Isolation Pilot Plant, December 1992. Volume 3: Model Parameters. Sandia WIPP Project. SAND92-0700/3. Albuquerque, NM: Sandia National Laboratories. A-47 through A-66. (In Appendix A of SAND92-0700/3, which is on file in the SWCF as WPO23529.)
- Hansen, F.D., and K.D. Mellegard. 1979. Creep Behavior of Bedded Salt from Southeastern New Mexico at Elevated Temperature. SAND79-7030; RSI-0062. Albuquerque, NM: Sandia National Laboratories. (Copy on file in the SWCF as WPO27369.)
- Haug, A., V.A. Kelley, A.M. LaVenue, and J.F. Pickens. 1987. Modeling of Ground-Water Flow in the Culebra Dolomite at the Waste Isolation Pilot Plant (WIPP) Site: Interim Report. SAND86-7167. Albuquerque, NM: Sandia National Laboratories. (Copy on file in the SWCF as WPO28486.)
- Holcomb, D.J. 1988. "Cross-Hole Measurements of Velocity and Attenuation to Detect a Disturbed Zone in Salt at the Waste Isolation Pilot Plant," Key Questions in Rock Mechanics, Proceedings of the 29th U.S. Symposium, University of Minnesota, Minneapolis, MN, June 13-15, 1988. Eds. P.A. Cundall, R.L. Sterling, and A.M. Starfield. SAND87-3016C. Brookfield, VT: A.A. Balkema. 633-640. (Copy on file in the SWCF as WPO29992.)

- Holt, R.M., and D.W. Powers. 1990. Geologic Mapping of the Air Intake Shaft at the Waste Isolation Pilot Plant. DOE-WIPP 90-051. Carlsbad, NM: Westinghouse Electric Corporation. (Copy on file in the Nuclear Waste Management Library, Sandia National Laboratories, Albuquerque, NM.)
- Knowles, M.K., D. Borns, J. Fredrich, D. Holcomb, R. Price, D. Zeuch, T. Dale, and R.S. Van Pelt. 1996. "Testing the Disturbed Zone Around a Rigid Inclusion in Salt," 4th Conference on the Mechanical Behavior of Salt, Montreal, Quebec, June 17-18, 1996. SAND95-1151C. Albuquerque, NM: Sandia National Laboratories. (Copy on file in the SWCF.)
- Lambert, S.J. In preparation. Sources of Natural Brines at the Waste Isolation Pilot Plant and Implications for the Seal System. SAND94-0091. Albuquerque, NM: Sandia National Laboratories. (Copy on file in the SWCF.)
- Lappin, A.R., R.L. Hunter, D.P. Garber, and P.B. Davies, eds. 1989. Systems Analysis, Long-Term Radionuclide Transport, and Dose Assessments, Waste Isolation Pilot Plant (WIPP), Southeastern New Mexico; March 1989. SAND89-0462. Albuquerque, NM: Sandia National Laboratories. (Copy on file in the SWCF as WPO24125.)
- LaVenue, A.M., T.L. Cauffman, and J.F. Pickens. 1990. Ground-Water Flow Modeling of the Culebra Dolomite. Volume I: Model Calibration. SAND89-7068/1. Albuquerque, NM: Sandia National Laboratories. (Copy on file in the SWCF as WPO24085.)
- Mercer, J.W. 1983. Geohydrology of the Proposed Waste Isolation Pilot Plant Site, Los Medanos Area, Southeastern New Mexico. Water-Resources Investigations Report 83-4016. Albuquerque, NM: U.S. Geological Survey, Water Resources Division. (Copy on file in the SWCF.)
- Parker, J.C., R.L. Lenhard, and T. Kuppusamy. 1987. "A Parametric Model for Constitutive Properties Regarding Multiphase Flow in Porous Media," Water Resource Research, Vol. 23, no. 4.
- Peterson, E.W., P.L. Lagus, and K. Lie. 1987. Fluid Flow Measurements of Test Series A and B for the Small Scale Seal Performance Tests. SAND87-7041. Albuquerque, NM: Sandia National Laboratories. (Copy on file in the SWCF as WPO24430.)
- Pruess, K. 1991. TOUGH2 - A General-Purpose Numerical Simulator for Multiphase Fluid and Heat Flow. LBL-29400. Berkeley, CA: Earth Sciences Division, Lawrence Berkeley Laboratory. (Copy on file in the SWCF.)
- Reeves, M., D.S. Ward, N.D. Johns, and R.M. Cranwell. 1986a. Theory and Implementation for SWIFT II, The Sandia Waste-Isolation Flow and Transport Model for Fractured Media, Release 4.84. SAND83-1159; NUREG/CR-3328. Albuquerque, NM: Sandia National Laboratories. (Copy on file in the SWCF as WPO28363.)
- Reeves, M., D.S. Ward, N.D. Johns, and R.M. Cranwell. 1986b. Data Input Guide for SWIFT II, The Sandia Waste-Isolation Flow and Transport Model for Fractured Media, Release 4.84. SAND83-0242, NUREG/CR-3162. Albuquerque, NM: Sandia National Laboratories. (Copy on file in the SWCF as WPO29686.)

- Reeves, M., D.S. Ward, P.A. Davis, and E.J. Bonano. 1987. SWIFT II Self-Teaching Curriculum: Illustrative Problems for the Sandia Waste-Isolation Flow and Transport Model for Fractured Media. SAND84-1586 Revision, NUREG/CR-3925. Albuquerque, NM: Sandia National Laboratories. (Copy on file in the SWCF as WPO30179.)
- Sandia WIPP Project. 1992. Preliminary Performance Assessment for the Waste Isolation Pilot Plant, December 1992. Volume 3: Model Parameters. SAND92-0700/3. Albuquerque, NM: Sandia National Laboratories. (Copy on file in the SWCF as WPO20910.)
- Saulnier, G.J., Jr., and J.D. Avis. 1988. Interpretation of Hydraulic Tests Conducted in the Waste-Handling Shaft at the Waste Isolation Pilot Plant (WIPP) Site. SAND88-7001. Albuquerque, NM: Sandia National Laboratories. (Copy on file in the SWCF as WPO24164.)
- Siegel, M.D., S.J. Lambert, and K.L. Robinson, eds. 1991. Hydrogeochemical Studies of the Rustler Formation and Related Rocks in the Waste Isolation Pilot Plant Area, Southeastern New Mexico. SAND88-0196. Albuquerque, NM: Sandia National Laboratories. (Copy on file in the SWCF as WPO25624.)
- Stormont, J.C. 1990. Summary of 1988 WIPP Facility Horizon Gas Flow Measurements. SAND89-2497. Albuquerque, NM: Sandia National Laboratories. (Copy on file in the SWCF as WPO24044.)
- Stormont, J.C., E.W. Peterson, and P.L. Lagus. 1987. Summary of and Observations About WIPP Facility Horizon Flow Measurements Through 1986. SAND87-0176. Albuquerque, NM: Sandia National Laboratories. (Copy on file in the SWCF as WPO24698.)
- Touloukian, Y.S., C.Y. Ho, W.R. Judd, and R.F. Roy. 1981. Physical Properties of Rocks and Minerals. McGraw-Hill/Cindas Data Series on Material Properties ; Vol. II-2. New York, NY: McGraw-Hill. (Copies available at Technical Library, Sandia National Laboratories, Albuquerque, NM and at Centennial Science and Engineering Library, University of New Mexico, Albuquerque, NM.)
- van Genuchten, M. Th. 1980. "A Closed-Form Equation for Predicting the Hydraulic Conductivity of Unsaturated Soils," Soil Science Society of America Journal. Vol. 44, no. 5, 892-898. (Copy on file in the SWCF.)
- Van Sambeek,, L.L., D.D. Luo, M.S. Lin, W. Ostrowski, and D. Oyenuga. 1993. Seal Design Alternatives Study. SAND92-7340. Albuquerque, NM: Sandia National Laboratories. (Copy on file in the SWCF as WPO23445.)
- Ward, D.S., M. Reeves, and L.E. Duda. 1984. Verification and Field Comparison of the Sandia Waste-Isolation Flow and Transport Model (SWIFT). SAND83-1154, NUREG/CR-3316. Albuquerque, NM: Sandia National Laboratories. (Copy on file in the SWCF as WPO29695.)
- Webb, S. W. 1996. Review of Two-Phase Characteristic Curves for Porous Media and Application to the WIPP. SAND93-3912. Albuquerque, NM: Sandia National Laboratories. (WPO# 37539)

WIPP PA. 1992-1993. Preliminary Performance Assessment for the Waste Isolation Pilot Plant, December 1992. SAND92-0700. Albuquerque, NM: Sandia National Laboratories. (Vol. 1 on file in the SWCF as WPO20762; Vol. 2 filed as WPO20805; Vol. 3 filed as WPO20910; Vol. 4 filed as WPO20958; Vol. 5 filed as WPO20929.)

# **Appendix D**

## **Structural Analyses**

### **Appendix D Abstract**

The seals for the shafts at the WIPP are comprised of columns of compacted earthen fill, compacted clay, asphalt, and compacted crushed salt, separated by concrete seals. The structural behavior of these columns and the concrete components is the primary focus of the calculations presented in this appendix. The development (and subsequent healing) of the disturbed rock zone that forms in the rock mass surrounding the shafts is a significant concern in the seal design, and these issues are also addressed in this appendix. In addition, several structural calculations are included that were used as input to the hydrological calculations reported in Section 8 and Appendix C. Complexity of the calculations ranged from solving a simple equation to rigorous finite-element modeling encompassing both thermal and structural elements.

Page intentionally blank.

## Contents

D1. INTRODUCTION .....	7
D2. ANALYSES METHODS .....	8
D2.1 SPECTROM-32 .....	9
D2.2 SPECTROM-41 .....	9
D2.3. SALT_SUBSID .....	10
D3. MATERIAL CHARACTERIZATION.....	10
D3.1 Shaft Seal Components .....	10
D3.1.1 Salado Mass Concrete.....	10
D3.1.2 Crushed Salt.....	14
D3.1.3 Compacted Clay.....	19
D3.1.4 Asphalt.....	19
D3.2 In Situ Materials.....	21
D3.2.1 Salado Salt.....	21
D3.2.2 Salado Anhydrite and Polyhalite.....	26
D3.2.3 Near Surface and Rustler Formations .....	28
D3.3 Models for the Disturbed Rock Zone within Salt .....	29
D3.3.1 Stress-Invariant Criterion.....	29
D3.3.2 Damage-Stress Criterion.....	30
D3.3.3 Evaluation of DRZ Models.....	30
D4. SHAFT SEAL COMPONENT ANALYSES .....	33
D4.1 Salado Mass Concrete Seals .....	33
D4.1.1 Thermal Analysis of Concrete Seals.....	33
D4.1.2 Structural Analysis of Concrete Seals.....	33
D4.1.3 Thermal Stress Analysis of Concrete Seals .....	42
D4.1.4 Effect of Dynamic Compaction on Concrete Seals.....	43
D4.1.5 Effect of Clay Swelling Pressures on Concrete Seals.....	44
D4.2 Crushed Salt Seal .....	44
D4.2.1 Structural Analysis of Crushed Salt Seal .....	44
D4.2.2 Effect of Fluid Pressure on the Reconsolidation of Crushed Salt Seals .....	47
D4.3 Compacted Clay Seals .....	51
D4.3.1 Structural Analysis of Compacted Clay Seals .....	51
D4.4 Asphalt Seals.....	51
D4.4.1 Thermal Analysis of Asphalt Seals.....	51
D4.4.2 Structural Analysis of Asphalt Seals.....	54
D4.4.3 Shrinkage Analysis of Asphalt Seals .....	54
D5. DISTURBED ROCK ZONE CONSIDERATIONS.....	59
D5.1 General Discussion .....	59
D5.1.1 Salt Damage Models .....	60
D5.1.2 Salt Healing Models.....	60
D5.2 Disturbed Rock Zone Analyses.....	62
D5.2.1 Analysis of the Disturbed Rock Zone in Salado Salt.....	62
D5.2.2 Salado Anhydrite Beds.....	70

D5.2.3 Near Surface and Rustler Formations .....	73
D6. OTHER ANALYSES .....	74
D6.1 Asphalt Waterstops .....	74
D6.2 Shaft Pillar Backfilling.....	76
D7. REFERENCES .....	83

## Figures

Figure D-1. Heat generation of Salado Mass Concrete mixture.....	12
Figure D-2. Comparison of calculated results using damage-stress and stress-invariant DRZ models with measured AIS results.....	32
Figure D-3. Axisymmetric model used in the SMC thermal analysis.....	34
Figure D-4. Temperature histories of SMC center and SMC/salt interface.....	35
Figure D-5. Isotherms surrounding SMC seal at 0.02 year.....	36
Figure D-6. Seal system conceptual design for the WIPP air intake shaft.....	38
Figure D-7. Axisymmetric model configuration of upper concrete shaft seal.....	39
Figure D-8. Axisymmetric model configuration of middle concrete shaft seal.....	40
Figure D-9. Axisymmetric model configuration of lower concrete shaft seal.....	41
Figure D-10. Swelling pressures as a function of time for a brine-saturated bentonite specimen with a density of 1,800 kg/m <sup>3</sup> .....	45
Figure D-11. "Pineapple slice" axisymmetric models.....	46
Figure D-12. Consolidation of crushed salt in a shaft at depths of 430, 515, and 600 m using the modified Sjaardema-Krieg, Spiers, and Zeuch models.....	48
Figure D-13. Crushed-salt fractional density as a function of time for a fluid pressure of 2 MPa and using the modified Sjaardema-Krieg creep consolidation model.....	50
Figure D-14. WIPP shaft seal design showing asphalt components.....	52
Figure D-15. Models used in thermal analysis of asphalt seal.....	53
Figure D-16. Temperature histories in asphalt (Point A, Figure D-15a) and salt (Point B, Figure D-15a).....	55
Figure D-17. Comparison of asphalt center temperatures for different waterstop configurations.....	56
Figure D-18. Pressure buildup in the upper, middle, and lower shaft seal waterstops.....	57
Figure D-19. Normalized DRZ radius as a function of shaft seal stiffness at various depths within the Salado Formation at time = 0 year after emplacement.....	64
Figure D-20. Normalized DRZ radius as a function of shaft seal stiffness at various depths within the Salado Formation at time = 10 years after emplacement.....	65
Figure D-21. Normalized DRZ radius as a function of shaft seal stiffness at various depths within the Salado Formation at time = 25 years after emplacement.....	66
Figure D-22. Normalized DRZ radius as a function of shaft seal stiffness at various depths within the Salado Formation at time = 50 years after emplacement.....	67
Figure D-23. Normalized DRZ radius as a function of shaft seal stiffness at various depths within the Salado Formation at time = 100 years after emplacement.....	68
Figure D-24. Factor of safety in polyhalite beds at 50 years.....	71

Figure D-25. Factor of safety in anhydrite beds at 50 years. ....	72
Figure D-26. Normalized DRZ radius for strength reduction factor of 4 and horizontal stress factor of 1.5. ....	75
Figure D-27. Salt DRZ around the lower shaft seal at 50 years (prior to seal construction). ....	77
Figure D-28. Salt DRZ around the lower shaft seal at 50.1 years (after excavations but before seal construction). ....	78
Figure D-29. Salt DRZ around the lower shaft seal at 20 years after seal construction. ....	79
Figure D-30. Mining blocks used to represent WIPP underground workings. ....	81
Figure D-31. Surface subsidence profiles over shaft area. ....	82

### Tables

Table D-1. Salado Mass Concrete Thermal Properties. ....	11
Table D-2. Heat of Hydration Model Parameters. ....	13
Table D-3. Summary of Creep Data (from Wakeley et al., 1994). ....	13
Table D-4. Variation of Elastic Modulus of SMC as a Function of Time (from Wakeley et al., 1994). ....	13
Table D-5. Nonlinear Elastic Material Parameters for WIPP Crushed Salt. ....	15
Table D-6. Creep Consolidation Parameters for Crushed Salt (after Sjaardema and Krieg, 1987). ....	16
Table D-7. Revised Sjaardema-Krieg, Zeuch, and Spiers Creep Consolidation Parameter Values. ....	18
Table D-8. Nonlinear Elastic Material Parameters for Compacted Clay. ....	20
Table D-9. Asphalt Thermal Properties. ....	20
Table D-10. Asphalt Elastic Properties. ....	20
Table D-11. Salado Salt Thermal Properties. ....	21
Table D-12. Munson-Dawson Parameter Values for Argillaceous Salt (after Munson et al., 1989). ....	27
Table D-13. Damage Model Parameters for Argillaceous Salt. ....	28
Table D-14. Anhydrite and Polyhalite Elastic and Drucker-Prager Parameter Values. ....	28
Table D-15. Rock Types and Properties. ....	29
Table D-16. Normalized DRZ Radius Surrounding the AIS. ....	30
Table D-17. Initial Temperature and Stress Conditions within Salado Formation. ....	42
Table D-18. Normalized DRZ Radius—Concrete. ....	69
Table D-19. Normalized DRZ Radius—Crushed Salt. ....	69
Table D-20. Normalized DRZ Radius—Compacted Clay. ....	69
Table D-21. Normalized DRZ Radius—Asphalt. ....	70

Page intentionally blank.

## D1. INTRODUCTION

The seals for the shafts at the WIPP are comprised of columns of compacted earthen fill, compacted clay, asphalt, and compacted crushed salt, separated by concrete seals. Within the Salado Formation each shaft seal includes: (1) an asphalt column extending from above the Rustler/ Salado interface down into the Salado salt, (2) an upper Salado compacted clay column, (3) a long compacted crushed salt column, and (4) a lower Salado compacted clay column. Each of these columns is separated by specially designed salt-saturated concrete components. The structural behavior of the various columns and the concrete components is the initial focus of the calculations presented in this appendix.

The development (and subsequent healing) of a disturbed rock zone (DRZ) that forms in the rock mass surrounding the WIPP shafts is a significant concern in the seal design. It is well known that an initial DRZ will develop in the rock adjacent to the shaft immediately after excavation. Moreover, the DRZ within the Salado Formation continues to develop because of salt creep. Shaft seal emplacement will cause the DRZ to heal with time because of restraint to creep closure by the seal materials and the subsequent reduction in the stress differences in the surrounding intact salt. Within the formations above the Salado, the DRZ is assumed to be time-invariant, since the behavior of the rock masses encountered there is predominantly elastic. The calculation of the temporal and spatial extent of the DRZ along the entire shaft length is the second focus of this appendix.

This appendix provides a collection of calculations pertaining to the above mentioned structural concerns. The purpose of each calculation varied; however, the calculations generally addressed one or more of the following issues (1) stability of the component, (2) influences of the component on hydrological properties of the seal and surrounding rock, or (3) construction issues. Stability issues that were addressed in these calculations included:

- potential for thermal cracking of concrete seals, and.
- structural failure of concrete seal components because of loads resulting from (1) creep of surrounding salt, (2) dynamic compaction and gravity loads of overlying seal material, (3) repository generated gas pressures, and (4) clay swelling pressures.

Structural calculations were also used to define input conditions to the hydrological calculations reported in Section 8, including:

- spatial extent of the DRZ within the Salado Formation surrounding the shafts as a function of depth, time, and seal material type,
- fracturing and DRZ development within Salado Formation interbeds,
- compacted-salt fractional density as a function of depth and time,
- shaft-closure induced consolidation of compacted-salt seals, and
- impact of pore pressures on consolidation of compacted-salt seals.

The construction issues that were addressed included:

- emplacement and structural performance of asphalt waterstops, and
- potential benefits from backfilling shaft stations.

Complexity of the calculations ranged from solving a simple equation to rigorous finite-element modeling encompassing both thermal and structural elements. All calculations are presented in a similar format, having approximately the same detail. Each calculation is described in terms of its objectives, problem statement, assumptions, and results.

Calculations were performed concurrently with development of the shaft seal design. Consequently, in some instances calculations reported here do not exactly match particular component dimensions shown in the design drawings (Appendix E) because of later changes in the design. Conclusions drawn from the results of these earlier calculation would not, however, change simply because of dimensional changes or emplacement conditions. In some instances a single calculation (e.g., a finite-element analysis of the concrete seal) was used to evaluate the structural behavior of more than one seal component. For example, the finite-element analysis of the asphalt waterstops was used to calculate both the DRZ development in the Salado salt and the time-dependent stresses in the concrete seals. Additionally, some results are drawn from previous similar analyses that are still generally applicable to the current design.

For convenience, the presentation of structural analyses in this appendix is divided into five sections, describing:

- analyses methods,
- material models,
- structural behavior of the shaft seal components,
- DRZ development (and healing) in intact rock surrounding the shaft, and
- analyses related to construction issues.

More specifically, analyses methods and computer programs used in performing these analyses are presented in Section D2. The analyses methods include finite element modeling and analytical techniques. Section D3 describes the models used in characterizing material behavior of shaft seal components, the intact rock mass, and the DRZ. Material models included thermal properties, deformational behavior, and strength properties for the four shaft seal materials and the in situ materials. Also included is a description of the models used to characterize the DRZ. A summary of the structural analyses of the four shaft seal materials is presented in Section D4. Analyses of the shaft seal components are presented by material type, i.e., concrete, compacted crushed salt, compacted clay, and asphalt. The behavior of the DRZ within the intact rock mass surrounding the shaft is described in Section D5. The DRZ was evaluated within Salado salt, Salado interbeds, and overlying nonsalt formations. Finally, analyses of asphalt waterstops and shaft station backfilling are discussed in Section D6.

## **D2. ANALYSES METHODS**

Finite-element modeling and subsidence modeling were the primary methodologies used in evaluating the structural performance of the shaft seals and the surrounding intact rock mass. The finite element programs SPECTROM-32 and SPECTROM-41 were used in the structural and thermal calculations, respectively. The program SALT\_SUBSID was used in the subsidence modeling. These programs are described below.

## **D2.1 SPECTROM-32**

The finite-element structural modeling program SPECTROM-32 (Callahan, 1994) was used in performing structural calculations. These calculations included creep deformation of the host rock, consolidation of shaft seal material, and development (and subsequent healing) of the DRZ within salt. This thermomechanical program was designed specifically for simulation of underground openings and structures. SPECTROM-32 has the capability to model the elastic-plastic response, commonly associated with brittle rock types, and has been used extensively to simulate the time-dependent viscoplastic behavior observed in intact salt. In addition, creep consolidation material behavior (e.g., crushed salt) can be modeled using SPECTROM-32. Specific features and capabilities of SPECTROM-32 required for numerical simulations include:

- capabilities for plane-strain and axisymmetric geometries,
- kinematic and traction boundary conditions,
- Multimechanism Deformation Coupled Fracture (MDCF) (Chan, 1993) constitutive model for modeling creep behavior of salt and estimating the DRZ in salt,
- creep consolidation models for time-dependent densification of crushed salt,
- nonlinear elastic behavior for modeling time-independent deformational behavior of crushed salt and compacted clay,
- capability to represent arbitrary in situ stress and temperature fields, and
- capability to simulate shaft excavation and seal material emplacements.

Most of the structural analyses were performed using Version 4.06 of this program. Analyses using recently developed creep consolidation models and for calculating the effects of pore pressure on consolidation of crushed-salt seal were performed using Version 4.08 of the program.

## **D2.2 SPECTROM-41**

The finite-element program SPECTROM-41 (Svalstad, 1989) was used in performing thermal calculations. This program has been designed and used to solve heat transfer problems resulting from the storage of heat-generating material in geologic formations for the past 15 years. The program has been documented to satisfy the requirements and guidelines outlined in NUREG-0856 (Silling, 1983). Specific features and capabilities of SPECTROM-41 that were required for the numerical simulations include:

- capabilities for two-dimensional and axisymmetric geometries,
- multimaterial behavior,
- specified initial temperature conditions,
- specified temperature or flux boundary conditions,
- temperature-dependent thermal properties,
- time-dependent volumetric heat generation, and
- transient and/or steady-state solutions.

### D2.3. SALT\_SUBSID

SALT\_SUBSID (Nieland, 1991) is a PC-based subsidence modeling software used to evaluate surface subsidence over underground openings in salt. The computer program has the capability of developing a site-specific subsidence model which can be used for predicting the future subsidence over a new or existing mining plan. The computer program can also predict stresses and strains along the shaft height resulting from subsidence. Subsidence calculations can be performed on either solution mines or dry mines in salt or potash. The analytical model is based on the solution for ground movement above a closing displacement discontinuity in an isotropic material and includes a time-dependent function to account for the viscoplastic nature of salt. SALT\_SUBSID is commercially available software from the Solution Mining Research Institute (SMRI).

## D3. MATERIAL CHARACTERIZATION

This section describes models used in characterizing material behavior of the WIPP shaft seal components, intact rock mass, and DRZ. Structural models used to characterize the four shaft seal materials are discussed in Section D3.1. The structural models include thermal properties, deformational behavior, and strength characteristics. Seal materials include concrete, crushed salt, compacted clay, and asphalt. Structural models for intact rock are presented in Section D3.2. These materials include Salado salt, Salado anhydrite and polyhalite, and the rock types encountered in the near-surface and Rustler Formations. Models used in characterizing the DRZ within the intact rock mass surrounding the shaft are presented in Section D3.3.

### D3.1 Shaft Seal Components

The shaft seal components include Salado Mass Concrete (SMC), crushed salt, compacted clay, and asphalt. Thermal, deformational, and strength characteristics of these four materials that were required in the structural analyses are given in the following sections.

#### D3.1.1 Salado Mass Concrete

Thermal, deformational, and strength characteristics of SMC were required in these structural analyses. These properties are discussed in the following subsections.

*Thermal Properties.* Required thermal properties include thermal conductivity, specific heat, density, and volumetric heat generation rate (Table D-1). Values of thermal conductivity, specific heat, and density are based on laboratory tests performed at Waterways Experimental Station (WES) (Wakeley et al., 1994).

Heat of hydration of SMC is illustrated in Figure D-1 which shows heat generation (Btu/lb<sub>cem</sub>) as a function of time (hr), where the subscript "cem" refers to the total weight of cementitious material. The curve was digitized and fit to the functional form,

$$Q(t) = Q_{\infty} \exp\left[-(\tau_e / t)^{\alpha}\right] \quad (D-1)$$

which was suggested by the Andersen et al. (1992) for describing the heat of hydration for concrete pavements, where  $Q_\infty$ ,  $\tau_e$  and  $\alpha$  are the model parameters and  $t$  is time (hr).

These model parameters were determined using the statistical program BMDP/386 and are listed in Table D-2. The volumetric heat generation rate ( $dQ/dt$ ) of the concrete is required in performing the thermal analyses. Differentiating Equation D-1 with respect to time results in:

$$dQ(t)/dt = Q(t)(\tau_e/t)^\alpha (\alpha/t) \quad (D-2)$$

The conversion of units from Btu/lb<sub>cem</sub> to W-hr/m<sup>3</sup><sub>con</sub>, where m<sup>3</sup><sub>con</sub> refers to cubic meters of concrete, is given as follows:

$$[1 \text{ Btu/lb}_{\text{cem}}] [1055 \text{ J/Btu}] [2.2 \text{ lb/kg}] [2280 \text{ kg/m}^3] [1 \text{ W-s/J}] [1 \text{ hr/3600 s}] [0.16 \text{ lb}_{\text{cem}}/\text{lb}_{\text{con}}] \\ = 235 \text{ W-hr/m}^3_{\text{con}}$$

*Deformational Properties.* SMC is assumed to behave as a viscoelastic material, based on experimental data for several mixes of SMC. The WES (Wakeley et al., 1994) creep data are summarized in Table D-3. An isothermal form of the Norton (power) creep law was fit to long-term laboratory creep-test data and resulted in the following:

$$\dot{\epsilon}_{ss} = A\sigma^n \quad (D-3)$$

where:

- $\dot{\epsilon}_{ss}$  = steady-state strain rate
- $\sigma$  = deviatoric stress
- $A$  = fitted model parameter =  $0.11(10^{-6})/\text{day}$
- $n$  = fitted model parameter = 0.54.

Table D-1. Salado Mass Concrete Thermal Properties

Property	Units	Value
Thermal Conductivity	W/m-K	2.145
Specific Heat	J/kg-K	971.
Density	kg/m <sup>3</sup>	2,280
Heat of Hydration Rate	W/m <sup>3</sup>	(Equation D-2)

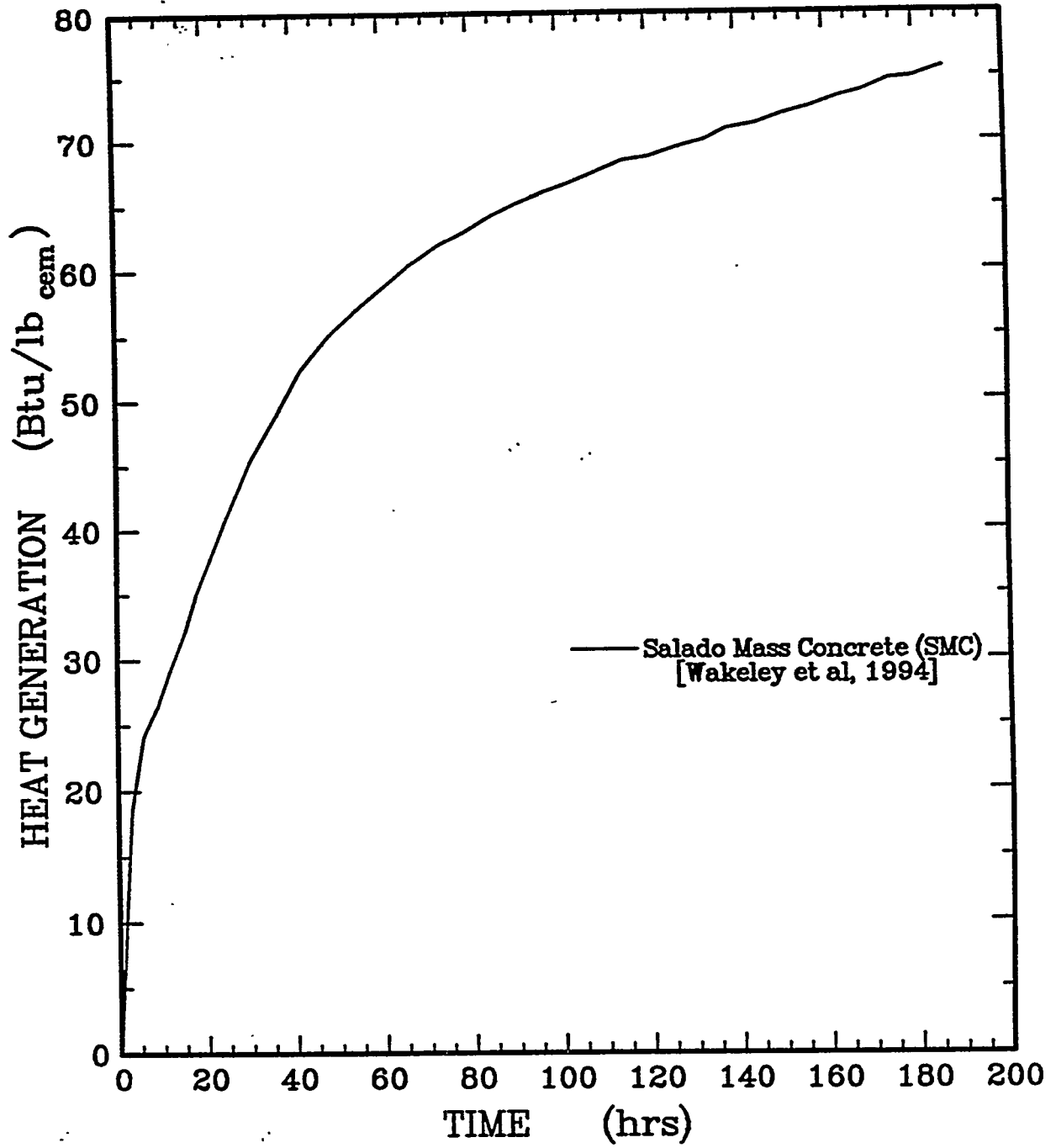


Figure D-1. Heat generation of Salado Mass Concrete mixture.

Table D-2. Heat of Hydration Model Parameters

Parameter	Units	SMC
$Q_{\infty}$	Btu/lb <sub>cem</sub> (W-hr/m <sup>3</sup> <sub>con</sub> )	173.7 (40,837)
$\tau_c$	hr	89.8
$\alpha$	—	0.264

Table D-3. Summary of Creep Data (from Wakeley et al., 1994)

Test Number	Uniaxial Stress (MPa)	Steady-State Strain Rate (10 <sup>-6</sup> /day)
1	2.5	0.175
2	5.9	0.265
3	7.8	0.333

The elastic modulus of SMC is assumed to be age-dependent, based on experimental data reported by WES (Wakeley et al., 1994). These data are given in Table D-4. A functional form shown in Equation D-4 was used to represent the age-dependence of the elastic modulus of SMC as it sets (increases in stiffness):

$$E(t) = E_{\max} \left( \frac{t}{t + t_0} \right) \quad (D-4)$$

where:

- $E(t)$  = modulus at time  $t$
- $t$  = time (days)
- $E_{\max}$  = ultimate stiffness.

Table D-4. Variation of Elastic Modulus of SMC as a Function of Time (from Wakeley et al., 1994)

Time (days)	Elastic Modulus 10 <sup>6</sup> (psi)
0	0
28	4.00
90	5.77
230	6.34

The model parameters derived from experimental results given in Table D-4 are:

$$E_{\max} = 6.7 (10^6) \text{ psi}$$

$$t_0 = 16.75 \text{ days.}$$

Poisson's ratio of SMC was assumed to be 0.19 and is consistent with literature values for concretes. The thermal expansion of SMC is  $11.9 (10^{-6})/^{\circ}\text{C}$  based on test data from WES (Wakeley et al., 1994).

*Strength Properties.* The design specification for concrete is a 28-day unconfined compressive strength of 4,500 psi (31 MPa) (Appendix A). Recent laboratory tests indicate that SMC has an unconfined compressive strength of about 6,000 psi (40 MPa) (Wakeley et al., 1994).

### D3.1.2 Crushed Salt

The total strain rate for the crushed-salt constitutive model is assumed to consist of three components. These components include nonlinear elastic ( $\dot{\epsilon}_{ij}^e$ ), creep consolidation ( $\dot{\epsilon}_{ij}^c$ ), and creep ( $\dot{\epsilon}_{ij}^i$ ) contributions, and the total strain rate ( $\dot{\epsilon}_{ij}$ ) can be written as:

$$\dot{\epsilon}_{ij} = \dot{\epsilon}_{ij}^e + \dot{\epsilon}_{ij}^c + \dot{\epsilon}_{ij}^i \quad (\text{D-5})$$

Both the nonlinear elastic and creep consolidation portions of the model describe the material behavior in bulk (volumetric deformation) and in shear (deviatoric deformation). However, the creep portion of the crushed-salt model only describes deviatoric behavior. In fact, the creep portion of the crushed-salt model is the same as that of intact salt, i.e., the Munson-Dawson model described in Section D3.2.1. Nonlinear elastic and creep consolidation models used for crushed salt are described in the next sections.

*Nonlinear Elastic Model for Crushed Salt.* Elastic strain,  $\epsilon_{ij}^e$ , is the contribution from the stress field given by Hooke's law, which, in terms of the bulk modulus and shear modulus, is written as:

$$\epsilon_{ij}^e = \frac{\sigma_m}{3K} \delta_{ij} + \frac{S_{ij}}{2G} \quad (\text{D-6})$$

where:

- $\sigma_m$  =  $\frac{\sigma_{kk}}{3}$ , mean stress
- $S_{ij}$  =  $\sigma_{ij} - \sigma_m \delta_{ij}$ , deviatoric stress
- $\delta_{ij}$  = Kronecker delta
- $K$  = bulk modulus
- $G$  = shear modulus.

Sjaardema and Krieg (1987) propose bulk and shear moduli as exponential functions of the current density,  $\rho$ :

$$\begin{aligned} K &= K_0 e^{K_1 \rho} \\ G &= G_0 e^{G_1 \rho} \end{aligned} \tag{D-7}$$

where  $K_0$ ,  $K_1$ ,  $G_0$ , and  $G_1$  are material constants. The current density ( $\rho$ ) is written in terms of the total volumetric strain,  $\epsilon_v$ , using the relation:

$$\rho = \frac{\rho_0}{1 + \epsilon_v} \tag{D-8}$$

where  $\rho_0$  is the density of the material before the volumetric strain is imposed. The moduli are capped at values consistent with moduli for intact salt when the current density equals intact salt's density.

Table D-5 lists material parameters of the nonlinear elastic model for WIPP crushed salt. The terms  $K_0$  and  $G_0$  are the leading coefficients defining the bulk and shear moduli, respectively as the density approaches zero. The terms  $K_1$  and  $G_1$  are identical in magnitude and describe the density dependence in Equation D-7. Exponential function parameters are from Sjaardema and Krieg (1987). Intact crushed-salt constants ( $K_f$ ,  $G_f$ , and  $\rho_f$ ) are based on recent measurements on WIPP salt.

Table D-5. Nonlinear Elastic Material Parameters for WIPP Crushed Salt

Parameter	Units	Value
$K_0$	MPa	0.01760
$K_1$	$\text{m}^3/\text{kg}$	0.00653
$G_0$	MPa	0.0106
$G_1$	$\text{m}^3/\text{kg}$	0.00653
$K_f$	MPa	23,504
$G_f$	MPa	14,156
$\rho_f$	$\text{kg}/\text{m}^3$	2,160

*Creep Consolidation Models for Crushed Salt.* Four constitutive laws were used to describe the creep consolidation portion of the crushed-salt model:

- Sjaardema-Krieg
- Revised Sjaardema-Krieg
- Zeuch
- Spiers.

The first model is based on the work of Sjaardema and Krieg (1987) with a deviatoric component added (Callahan and DeVries, 1991). In this study, this model is referred to as the original S-K model. This model can be expressed mathematically as:

$$\dot{\epsilon}_{ij}^c = \frac{(1 + \epsilon_v)^2}{\rho_0} B_0 (1 - e^{-B_1 \sigma_e}) e^{A\rho} \left\{ \frac{\delta_{ij}}{3} - \frac{S_{ij}}{\sigma_e} \right\} \quad (D-9)$$

where:

- $\epsilon_v$  =  $\epsilon_{kk}$  total volumetric strain
- $\sigma_e$  = average effective stress measure
- $B_0, B_1, A$  = material constants.

Because Equation D-9 allows for unlimited consolidation, a cap is introduced that eliminates further consolidation when the intact material density ( $\rho_f$ ) is reached. Thus, when the condition

$$|\epsilon_v| \geq \left| \frac{\rho_0}{\rho_f} - 1 \right| \quad (D-10)$$

is satisfied, no further creep consolidation occurs.

Table D-6 gives values of the crushed-salt parameters for the original S-K model.

Table D-6. Creep Consolidation Parameters for Crushed Salt (after Sjaardema and Krieg, 1987)

Parameter	Units	Value
$B_0$	$\text{kg/m}^3 \cdot \text{s}^{-1}$	$1.3 \times 10^8$
	$\text{kg/m}^3 \cdot \text{yr}^{-1}$	$4.10 \times 10^{15}$
$B_1$	$\text{MPa}^{-1}$	0.82
$A$	$\text{m}^3/\text{kg}$	$-1.73 \times 10^{-2}$

The second creep consolidation model used in this study is a revised Sjaardema-Krieg model, reported originally by Callahan et al. (1995) and recently updated to include a more general formulation and an updated database by Callahan et al. (1996). The mathematical form of this model is:

$$\dot{\epsilon}_{ij}^c = \dot{\epsilon}_{eq}^c (\sigma_{eq}^f) \frac{\partial \sigma_{eq}}{\partial \sigma_{ij}} \quad (D-11)$$

where  $\dot{\epsilon}_{eq}^c$  and  $\sigma_{eq}^f$  are the power-conjugate equivalent inelastic strain measure and equivalent stress measure for creep consolidation, respectively, and  $\sigma_{eq}$  is an equivalent stress measure that provides a nonassociative formulation in governing the magnitude of the volumetric strain.

With these considerations, the equivalent stress measures can be written as:

$$\begin{aligned}\sigma_{eq}^f &= \eta |\sigma_m|^{\eta_2} - \frac{|\sigma_1 - \sigma_3|^{m_1}}{\sigma_{r_1}^{m_1-1}} \\ \sigma_{eq} &= \kappa |\sigma_m|^{\kappa_2} - \frac{|\sigma_1 - \sigma_3|^{m_1}}{\sigma_{r_2}^{m_1-1}}\end{aligned}\tag{D-12}$$

where:

$$\eta = \eta_0 (1 - \Omega)^{\eta_1}$$

$$\kappa = \kappa_0 (1 - \Omega)^{\kappa_1}$$

$$\Omega = \begin{cases} D_t, & 0 < D < D_t \\ D, & D_t < D < 1 \end{cases}$$

$D_t$  = transitional fractional density

$D$  = fractional density

$\sigma_1$  and  $\sigma_3$  = principal stresses

$\sigma_{r_1}$  and  $\sigma_{r_2}$  = reference stresses

$\eta_0, \eta_1, \eta_2,$

$\kappa_0, \kappa_1, \kappa_2,$

$m_1, m_2$  = material parameters.

The kinetic equation as described by the revised Sjaardema-Krieg model can be written as:

$$\dot{\varepsilon}_{eq}^c = \frac{B_0 (1 + \varepsilon_v)^2}{\rho_0 d^p} \exp\left(\frac{A \rho_0}{1 + \varepsilon_v}\right) [1 + a_1 (1 - e^{-a_2 w})] e^{\frac{-Q_c}{RT}}\tag{D-13}$$

where:

$d$  = grain diameter

$w$  = percent moisture by weight

$T$  = absolute temperature

$R$  = universal gas constant

$B_0, A, p,$

$a_1, a_2, Q_c$  = material parameters.

The revised Sjaardema-Krieg creep consolidation model has a total of 17 parameters, which are listed in Table D-7.

Table D-7. Revised Sjaardema-Krieg, Zeuch, and Spiers Creep Consolidation Parameter Values

Parameter	Units	Modified Material Models			Reference Values
		Sjaardema-Krieg	Zeuch	Spiers	
$\eta_0$	MPa <sup>1-<math>\eta_2</math></sup>	-1.437	-42.33	-2.91(10 <sup>-6</sup> )	—
$\eta_1$	—	2.594	2.740	0.108	—
$\eta_2$	—	3.623	3.049	5.523	—
$m_1$	—	0.731	0.605	0.174	—
$\sigma_{r_1}$	MPa	3.535	18.33	0.019	—
$D_t$	—	0.867	0.888	0.881	—
$a_1$	—	17.00	20.10	71.10	—
$a_2$	—	47.50	96.60	0.626	—
$Q_c/R$	K	4.01(10 <sup>3</sup> )	9.26(10 <sup>-17</sup> )	1.8(10 <sup>2</sup> )	—
$p$	—	0.564	0.396	3.22(10 <sup>-5</sup> )	—
$B_0$	kg • m <sup>p-3</sup> /(MPa • s)	6.459(10 <sup>7</sup> )			—
$A$	m <sup>3</sup> /kg	-1.307(10 <sup>-2</sup> )			-1.72(10 <sup>-2</sup> )
$b_2$	—		4.469		1/3
$b_3$	—		5.722		1/2
$b_7$	m <sup>p</sup> /(MPa • s)		6.54(10 <sup>-14</sup> )		—
$b_8$	m <sup>p</sup> /(MPa • s)		9.05(10 <sup>-19</sup> )		—
$n$	—		9.991		4.9
$r_1$	m <sup>p</sup> /(MPa • s)			1.02(10 <sup>-7</sup> )	—
$r_3$	—			9.770	1/3
$r_4$	—			0.806	2
$n$	—			3.190	4.15

The third model used for the creep consolidation is the Zeuch model, which is based on the kinetics of isostatic pressing. Similar to the revised Sjaardema-Krieg model, the Zeuch model was modified to account for a more general formulation. The Zeuch model is divided into two stages, depending on the fractional density. The kinetic equation describing the modified Zeuch model is:

For Stage 1 ( $D_0 \leq D \leq 0.9$ ):

$$\epsilon_{eq}^c = \frac{\rho_0 b_7}{\rho d^p} D_0^{b_2} D^{2(b_2-n)-1} \left( \frac{D-D_0}{1-D_0} \right)^{b_3-n} [1 + a_1(1 - e^{-a_2 w})] \exp\left(-\frac{Q_c}{RT}\right) \quad (D-14)$$

For Stage 2 ( $0.9 < D \leq 1$ ):

$$\dot{\varepsilon}_{eq}^c = \frac{\rho_0 b_8}{\rho d^p} \frac{(1-D)}{\{1-(1-D)^{1/n}\}^n} [1 + a_1(1 - e^{-a_2 w})] \exp\left(e - \frac{Q_c}{RT}\right) \quad (D-15)$$

where  $D = D_0/(1+\varepsilon_v)$  and  $b_2, b_3, b_7, b_8, n, a_1, a_2$ , and  $Q_c$  are model parameters (Table D-7).

The fourth model was developed by Spiers and coworkers based on pressure solutioning as the consolidation mechanism. The Spiers model was also modified to account for a more general formulation and an updated database by Callahan et al. (1996). The modified Spiers model is:

$$\dot{\varepsilon}_{eq}^c = \frac{r_1}{d^p} [1 + a_1(1 - e^{-a_2 w})] e^{-\frac{Q_c}{RT}} \left( \frac{(1 + \varepsilon_v)^{r_2}}{|\varepsilon_v|^{r_3}} \right) \Gamma \quad (D-16)$$

where:

$$\Gamma = \begin{cases} 1 & \text{small strain } (\varepsilon_v > -15\%) \\ \left[ \frac{\varepsilon_v + \phi_0}{\phi_0(\varepsilon_v + 1)} \right]^n & \text{large strain } (\varepsilon_v < -15\%) \end{cases} \quad (D-17)$$

and  $\phi_0$  is the initial porosity and  $r_1, r_2, r_3, n, a_1, a_2, p$ , and  $Q_c$  are material parameters (Table D-7).

### D3.1.3 Compacted Clay

The clay used in the WIPP shaft seal design is assumed to behave according to a nonlinear elastic model. The form of this model is identical to the nonlinear elastic portion of the crushed-salt model, in which the bulk and shear moduli are expressed as exponential functions of the current density:

$$\begin{aligned} K &= K_0 e^{K_1 \rho} \\ G &= G_0 e^{G_1 \rho} \end{aligned} \quad (D-18)$$

The parameters for the volumetric (bulk) behavior of clay are based on consolidation data reported in Lambe and Whitman (1969). These parameters are listed in Table D-8. The intact shear modulus ( $G$ ) was calculated from the bulk modulus, assuming a Poisson's ratio of 0.25.

### D3.1.4 Asphalt

Thermal properties of solidified asphalt are given in Table D-9. These properties are taken from the literature (Yoder and Witczak, 1975). Asphalt was assumed to behave elastically. The elastic (primarily bulk) response of the asphalt is considered most important to seal application. Because the asphalt is emplaced in a confined volume and the expected stresses that develop (as a result of creep of the surrounding salt and weight of the overlying seal materials) are compressive in nature, the volumetric behavior of the material is important to characterize.

The shear and time-dependent behavior of the asphalt are secondary effects. Young's modulus and Poisson's ratio of asphalt are listed in Table D-10. These properties are taken from Yoder and Witczak (1975) and are highly sensitive to temperature. The values shown in Table D-10 are representative of the WIPP repository horizon temperature of 27°C. Asphalt stiffness is assumed to be zero before it solidifies; i.e., it behaves as a fluid.

Although it is recognized that the behavior of asphalt is certainly time-dependent, the creep effects of this material were not considered in this modeling effort. As noted above, the predominant structural behavior of the seals is highly dependent on the behavior of surrounding materials, primarily creep of surrounding salt. Elastic behavior is assumed to be the predominant behavior because the asphalt is confined and will be volumetrically compressed. Because of confinement, there is little opportunity for creep flow of asphalt. In addition, the primary mechanism for creep (shear stress) of the asphalt is not expected to occur.

Table D-8. Nonlinear Elastic Material Parameters for Compacted Clay

Parameter (Equation D-18)	Units	Value
$K_0$	MPa	2.26(10 <sup>-6</sup> )
$K_1$	m <sup>3</sup> /kg	0.0096
$G_0$	MPa	1.36(10 <sup>-8</sup> )
$G_1$	m <sup>3</sup> /kg	0.0096
$K_f$	MPa	20,824
$G_f$	MPa	12,494
$\rho_f$	kg/m <sup>3</sup>	2,390

Table D-9. Asphalt Thermal Properties

Property	Units	Value
Thermal Conductivity	W/m-K	1.45
Specific Heat	J/kg-K	712
Density	kg/m <sup>3</sup>	2000

Table D-10. Asphalt Elastic Properties

Property	Units	Value
Young's Modulus	MPa	3034
Poisson's Ratio	—	0.35

## D3.2 In Situ Materials

The in situ materials include Salado salt, Salado interbeds (anhydrite and polyhalite), and rock types encountered in the near-surface and Rustler Formations. Thermal, deformational, and strength characteristics of these materials required for structural analyses are given in the following subsections.

### D3.2.1 Salado Salt

*Thermal Properties.* Thermal properties of Salado salt are given in Table D-11. These values are reported by Krieg (1984). Thermal conductivity of Salado salt is temperature dependent, expressed mathematically as:

$$k(T) = k_{300}(300/T)^\lambda \quad (D-19)$$

where:

- $k(T)$  = thermal conductivity of salt as a function of temperature
- $T$  = temperature (K)
- $k_{300}$  = thermal conductivity at reference temperature ( $T = 300$  K) = 5.0 W/m-K
- $\lambda$  = exponent describing temperature dependence = 1.14.

Table D-11. Salado Salt Thermal Properties

Property	Units	Value
Thermal Conductivity	W/m-K	(Equation D-19)
Specific Heat	J/kg · K	971
Density	kg/m <sup>3</sup>	2160

*Deformational Characteristics.* Intact salt was assumed to be argillaceous salt that is governed by the Multimechanism Deformation Coupled Fracture (MDCF) model (Chan et al., 1995a). This model is an extension of the well-documented Munson-Dawson (M-D) creep model (Munson et al., 1989) to include a calculation of damage. The evolutionary equations for the MDCF model are:

$$\dot{\epsilon}_{ij}^i = \dot{\epsilon}_{ij}^c + \dot{\epsilon}_{ij}^d + \dot{\epsilon}_{ij}^h \quad (D-20)$$

The first inelastic strain rate represents climb-controlled creep, which is described by the following kinetic equation:

$$\dot{\epsilon}_{ij}^c = \dot{\epsilon}_{eq}^c \frac{\partial \sigma_{eq}^c}{\partial \sigma_{ij}} \quad (D-21)$$

where  $\sigma_{eq}^c$  and  $\dot{\epsilon}_{eq}^c$  are power-conjugate equivalent stress measure and equivalent inelastic strain rate for the climb-controlled creep deformation mechanisms, respectively. The second inelastic

strain rate represents damage accumulation in the model. Two kinetic equations describe the damage model, one for shear-induced damage and one for cleavage fracture. These kinetic equations are additive to give the total inelastic damage strain rate as follows:

$$\dot{\epsilon}_{ij}^d = \dot{\epsilon}_{eq}^{\omega_s} \frac{\partial \sigma_{eq}^{\omega_s}}{\partial \sigma_{ij}} + \dot{\epsilon}_{eq}^{\omega_t} \frac{\partial \sigma_{eq}^{\omega_t}}{\partial \sigma_{ij}} \quad (D-22)$$

where  $\{\sigma_{eq}^{\omega_s}$  and  $\sigma_{eq}^{\omega_t}\}$  and  $\{\dot{\epsilon}_{eq}^{\omega_s}$  and  $\dot{\epsilon}_{eq}^{\omega_t}\}$  are power-conjugate equivalent stress measures and equivalent inelastic strain rates for the damage mechanisms, respectively. The third inelastic strain rate represents healing in the model. For calculations performed in support of the shaft seal design, healing was not operative, i.e.,  $\dot{\epsilon}_{ij}^h = 0$ .

### Climb-Controlled Creep

The equivalent inelastic strain rate is assumed to consist of a multiplicative transient function on the steady-state creep rate, viz.:

$$\dot{\epsilon}_{eq}^c = F \dot{\epsilon}_s \quad (D-23)$$

The steady-state strain rate consists of three mechanisms that describe dislocation climb, an undefined mechanism, and dislocation glide.

$$\dot{\epsilon}_s = \sum_{i=1}^3 \dot{\epsilon}_{s_i} \quad (D-24)$$

$$\dot{\epsilon}_{s_1} = A_1 \left( \frac{\sigma_{eq}^c}{(1-\omega)\mu} \right)^{n_1} \exp\left(-\frac{Q_1}{RT}\right) \quad (D-25)$$

$$\dot{\epsilon}_{s_2} = A_2 \left( \frac{\sigma_{eq}^c}{(1-\omega)\mu} \right)^{n_2} \exp\left(-\frac{Q_2}{RT}\right) \quad (D-26)$$

$$\dot{\epsilon}_{s_3} = \left[ B_1 \exp\left(-\frac{Q_1}{RT}\right) + B_2 \exp\left(-\frac{Q_2}{RT}\right) \right] \times \sinh \left[ q \frac{\left( \frac{\sigma_{eq}^c}{(1-\omega)\mu} - \sigma_0 \right)}{\mu} \right] H \left( \frac{\sigma_{eq}^c}{(1-\omega)\mu} - \sigma_0 \right) \quad (D-27)$$

The transient function,  $F$ , describes work-hardening, equilibrium, and recovery branches:

$$F = \begin{cases} \exp\left[\Delta\left(1 - \frac{\zeta}{\varepsilon_i^*}\right)^2\right] & \zeta < \varepsilon_i^* \\ 1 & \zeta = \varepsilon_i^* \\ \exp\left[-\delta\left(1 - \frac{\zeta}{\varepsilon_i^*}\right)^2\right] & \zeta > \varepsilon_i^* \end{cases} \quad (\text{D-28})$$

with an internal variable,  $\xi$ , described in terms of an evolutionary equation as:

$$\dot{\zeta} = (F - 1)\dot{\varepsilon}_s \quad (\text{D-29})$$

and the transient strain limit is defined by:

$$\varepsilon_i^* = K_0 \exp(cT) \left( \frac{\sigma_{eq}^c}{(1-\omega)\mu} \right)^m \quad (\text{D-30})$$

with the hardening parameter,  $\Delta$ , given by:

$$\Delta = \alpha + \beta \log\left(\frac{\sigma_{eq}^c}{(1-\omega)\mu}\right) \quad (\text{D-31})$$

where:

- $R$  = universal gas constant
- $\mu$  = normalizing parameter
- $q$  = activation volume
- $\sigma_0$  = stress limit of dislocation slip mechanism
- $A_1, A_2, B_1,$   
 $B_2, n_1, n_2,$   
 $Q_1, Q_2, q,$   
 $K_0, c, m,$
- $\alpha, \beta, \delta$  = experimental constants
- $H(\cdot)$  = Heaviside step function.

The maximum shear stress (Tresca) is chosen as the conjugate stress measure for climb-controlled creep:

$$\sigma_{eq}^c = 2\sqrt{J_2}\Psi \quad (\text{D-32})$$

where:

$$\begin{aligned}
J_2 &= \frac{1}{2} s_{ij} s_{ji} \\
s_{ij} &= \sigma_{ij} - \sigma_m \delta_{ij} \\
\sigma_m &= \frac{\sigma_{kk}}{3}, \text{ mean stress} \\
\delta_{ij} &= \text{Kronecker delta} \\
\Psi &= \frac{1}{3} \sin^{-1} \left[ \frac{-3\sqrt{3} J_3}{2 J_2^{3/2}} \right] \left( -\frac{\pi}{6} \leq \Psi \leq \frac{\pi}{6} \right) \\
J_3 &= \frac{1}{3} s_{ij} s_{jk} s_{ki}
\end{aligned} \tag{D-33}$$

### Damage Induced Flow

The damage strain rate in Equation D-22 is examined next with the two terms representing shear-induced damage and tension-induced damage considered separately (Chan et al., 1992; Chan, 1994a, 1994b; Chan et al., 1995b):

$$\dot{\epsilon}_{ij}^{\omega_s} = \dot{\epsilon}_{eq}^{\omega_s} \frac{\partial \sigma_{eq}^{\omega_s}}{\partial \sigma_{ij}}, \text{ and } \dot{\epsilon}_{ij}^{\omega_t} = \dot{\epsilon}_{eq}^{\omega_t} \frac{\partial \sigma_{eq}^{\omega_t}}{\partial \sigma_{ij}} \tag{D-34}$$

The equations describing the shear-induced (*s*) and tension-induced (*t*) damage are similar in form. Thus, the subscript *i* is used to represent *s* and *t*. The equivalent inelastic strain rate is given by:

$$\dot{\epsilon}_{eq}^{\omega_i} = F^{\omega_i} \dot{\epsilon}_s^{\omega_i} \tag{D-35}$$

with:

$$F^{\omega_s} = F \exp \left[ \frac{c_4 (\sigma_{eq}^{\omega_s} - c_5)}{\sigma_0 (1 - \rho)} \right] \tag{D-36}$$

$$F^{\omega_t} = F \exp \left[ \frac{c_4 (\sigma_{eq}^{\omega_t} - c_5)}{\sigma_0 (1 - \rho)} \right] \tag{D-37}$$

and:

$$\dot{\epsilon}_s^{\omega_i} = c_1 \omega_0 \exp(c_3 \omega) \left[ \sinh \left( \frac{\dot{c}_2 \sigma_{eq}^{\omega_i} H[\sigma_{eq}^{\omega_i}]}{[1 - \omega][1 - \rho] \mu} \right) \right]^m \tag{D-38}$$

and  $c_1$  is defined by:

$$c_1 = c_0 \left[ B_1 \exp\left(-\frac{Q_1}{RT}\right) + B_2 \exp\left(-\frac{Q_2}{RT}\right) \right] \quad (D-39)$$

where  $c_0$ ,  $c_2$ ,  $c_3$ ,  $c_4$ ,  $c_5$ , and  $n_3$  are material constants and  $\omega_0$  is the initial damage. The power-conjugate equivalent stress measures are given by:

$$\sigma_{eq}^{\omega_s} = |\sigma_1 - \sigma_3| + f_p x_2 x_7 \operatorname{sgn}(I_1 - \sigma_3) \left( \frac{I_1 - \sigma_3}{3 x_7 \operatorname{sgn}(I_1 - \sigma_3)} \right)^{x_6} \quad (D-40)$$

$$\sigma_{eq}^{\omega_t} = x_1 \sigma_1 H(\sigma_1) \quad (D-41)$$

where  $x_1$ ,  $x_2$ ,  $x_6$ , and  $x_7$  are material constants of the damage model,  $I_1$  is the first stress invariant, and  $\sigma_1$  and  $\sigma_3$  are the maximum and minimum principal stresses, respectively, with compression assumed to be negative. The material parameter  $f_p$  is related to the impurity content by:

$$f_p = 1 - p_1 \rho \quad (D-42)$$

where  $\rho$  is the impurity (clay) content and  $p_1$  is a material parameter, which is analogous to a local stress intensity factor.

The preceding equations include the damage ( $\omega$ ), which is described in terms of an evolutionary equation. The damage evolution equation is taken as:

$$\dot{\omega} = \dot{\omega}_s + \dot{\omega}_t - h(\omega, \sigma_{eq}^h) \quad (D-43)$$

where the damage rate components for the shear-induced and tension-induced damage are given by:

$$\dot{\omega}_s = \frac{x_4}{t_0} \omega \left[ \ln\left(\frac{1}{\omega}\right) \right]^{\frac{x_4+1}{x_4}} \left[ \frac{\sigma_{eq}^{\omega_s} H(\sigma_{eq}^{\omega_s})}{(1-\rho) \xi_s} \right]^{x_3} \quad (D-44)$$

$$\dot{\omega}_t = \frac{x_4}{t_0} \omega \left[ \ln\left(\frac{1}{\omega}\right) \right]^{\frac{x_4+1}{x_4}} \left[ \frac{\sigma_{eq}^{\omega_t} H(\sigma_{eq}^{\omega_t})}{(1-\rho) \xi_t} \right]^{x_3} \quad (D-45)$$

where  $x_4$ ,  $x_3$ ,  $x_4$ ,  $\xi_s$ ,  $\xi_t$ , and  $t_0$  are material constants. The parameter  $\xi_s$  may have different values according to the magnitude of the effective shear-induced damage stress; i.e.,:

$$\begin{aligned} \xi_s &= \xi_s^1 \text{ for } \sigma_{eq}^{\omega_s} / (1-\omega) > \sigma_0 \\ \xi_s &= \xi_s^2 \text{ for } \sigma_{eq}^{\omega_s} / (1-\omega) \leq \sigma_0 \end{aligned} \quad (D-46)$$

The healing term in Equation D-43,  $h(\omega, \sigma_{eq}^h)$ , was assumed to be zero for these calculations.

The shear-induced inelastic damage flow is assumed to be nonassociative. The flow potential power-conjugate stress measure for shear-induced damage is given by (cf. Equation D-42):

$$\sigma_{eq}^{\omega_s} = |\sigma_1 - \sigma_3| + \frac{x_2 x_8}{3} (I_1 - \sigma_3) \quad (D-47)$$

where  $x_8$  is a material constant.

The flow potential power-conjugate stress measure for tension-induced damage is given by:

$$\sigma_{eq}^{\omega_t} = x_1 \sigma_1 H(\sigma_1) \quad (D-48)$$

where  $x_1$  is a material constant.

The Munson-Dawson creep parameter values for argillaceous WIPP salt are listed in Table D-12. The damage parameters are given in Table D-13.

### D3.2.2 Salado Anhydrite and Polyhalite

Salado anhydrite and polyhalite interbeds were assumed to behave elastically. Elastic constants for anhydrite and polyhalite are given in Table D-14. These values have been used in previous similar WIPP analyses (Morgan et al., 1987).

DRZ development was assessed using a Drucker-Prager strength criterion. Damage to the interbeds is assumed to occur when the peak material strength of the rock is exceeded. The material strength of brittle rocks can be described by a Drucker-Prager type yield:

$$F = aI_1 + \sqrt{J_2} - C \quad (D-49)$$

where:

- $I_1$  = first invariant of the total stress tensor
- $J_2$  = second invariant of the deviatoric stress tensor
- $a$  and  $C$  = material constants.

Values for the Drucker-Prager material constants presented by Morgan et al. (1987) for anhydrite and polyhalite are given in Table D-14. The material is elastic when  $F < 0$  and will fracture and dilate if  $F \geq 0$ . The potential for fracture development can be expressed as a factor of safety given by the ratio of the strength measure to the stress measure. The factor of safety as used in this appendix is based on the following equation:

$$\text{Factor of Safety} = \frac{|aI_1 - C|}{\sqrt{J_2}} \quad (D-50)$$

Table D-12. Munson-Dawson Parameter Values for Argillaceous Salt  
(after Munson et al., 1989)

Parameter	Units	Value
Elastic Parameter Values		
$E$	MPa	31,000
$\nu$	—	0.25
Munson-Dawson Creep Parameter Values		
$A_1$	$\text{yr}^{-1}$ $\text{s}^{-1}$	$4.437 \times 10^{30}$ $1.407 \times 10^{23}$
$A_2$	$\text{yr}^{-1}$ $\text{s}^{-1}$	$4.144 \times 10^{20}$ $1.314 \times 10^{13}$
$Q_1/R$ $Q_1$	K cal/mol	12,581 25,000
$Q_2/R$ $Q_2$	K cal/mol	5032 10,000
$n_1$	—	5.5
$n_2$	—	5.0
$B_1$	$\text{yr}^{-1}$ $\text{s}^{-1}$	$2.838 \times 10^{14}$ $8.998 \times 10^6$
$B_2$	$\text{yr}^{-1}$ $\text{s}^{-1}$	$1.353 \times 10^6$ $4.289 \times 10^{-2}$
$q$	—	$5.335 \times 10^3$
$\sigma_0$	MPa	20.57
$m$	—	3
$K_0$	—	$2.47 \times 10^6$
$c$	$\text{K}^{-1}$	$9.198 \times 10^{-03}$
$\alpha$	—	-14.96
$\beta$	—	-7.738
$\delta$	—	0.58

Table D-13. Damage Model Parameters for Argillaceous Salt

Parameter	Units	Value
$x_1$	—	0.0
$x_2$	—	9.0
$x_3$	—	5.5
$x_4$	—	3.0
$x_5$	(MPa) <sup><math>x_3-s</math></sup>	$10^{13}; \sigma_1 - \sigma_3 > \sigma_0$ $10^{14}; \sigma_1 - \sigma_3 < \sigma_0$
$x_6$	—	0.75
$x_7$	MPa	1
$x_8$	—	0.1
$c_0$	—	34.0
$c_2$	—	850.0
$c_3$	—	10.0
$c_4$	—	6.0
$n_3$	—	3
$\omega_0$	—	$10^{-4}$
$p_1$	—	28
$\rho_0$	—	0.029

Table D-14. Anhydrite and Polyhalite Elastic and Drucker-Prager Parameter Values

Material	$E$ (MPa)	$\nu$	$C$ (MPa)	$a$
Anhydrite	75,100	0.35	1.35	0.450
Polyhalite	55,300	0.36	1.42	0.473

### D3.2.3 Near Surface and Rustler Formations

Failure of the rock within the near-surface and Rustler formations is assumed to be time independent and can be estimated according to two common failure criteria: Tresca and Coulomb criteria. The Tresca criterion for failure is based strictly on the difference between minimum and maximum principal stresses:

$$\sigma_3 - \sigma_1 \geq C_0 \tag{D-51}$$

where  $C_0$  is uniaxial compressive strength. The von Mises criterion is a modification of the Tresca criterion wherein  $C_0$  is replaced by  $2C_0/\sqrt{3}$ .

The Coulomb criterion accounts for the beneficial effect of confinement and says failure occurs whenever:

$$\begin{aligned} \sigma_1 - \sigma_3 &\geq C_0 + \sigma_3(\tan\beta - 1) \\ \tan\beta &= \frac{1 + \sin\phi}{1 - \sin\phi} \end{aligned} \quad (D-52)$$

where  $\phi$  is the angle of internal friction.

Strength parameters of rock types encountered in near-surface and Rustler formations are given in Table D-15.

Table D-15. Rock Types and Properties

Rock Type	Depth (m)	Strength Properties		
		$C_0$ (MPa)	$T_0$ (MPa)	$\phi$ (Deg)
Mudstone	0-165, 223-260	16.8	1	34.4
Anhydrite	165-183, 192-213	92.6	5.72	44.8
Dolomite	183-192, 213-223	107.3	4	41.9

### D3.3 Models for the Disturbed Rock Zone within Salt

Two different models were used to evaluate the development and extent of the DRZ within the intact salt. The first approach is based on the ratio between two stress invariants: i.e.,  $\sqrt{J_2}/I_1$ . This criterion has been used to characterize the potential of salt damage or healing in related WIPP studies. The second approach uses the damage stress ( $\sigma_{eq}^w$ ) according to the MDCF constitutive model for WIPP salt. These criteria are discussed in the following subsections.

#### D3.3.1 Stress-Invariant Criterion

The stress-invariant criterion is based on the separation of stress conditions that do or do not cause dilatancy in WIPP salt when plotted in  $I_1 - \sqrt{J_2}$  stress space.  $I_1$  is the first invariant of the stress tensor and represents the mean stress.  $\sqrt{J_2}$  is the second invariant of the deviatoric stress tensor and represents the shear stress. Taken together,  $I_1$  and  $\sqrt{J_2}$  provide a damage factor that indicates the potential for dilatancy and fracture. The functional form of the stress-invariant criterion is:

$$\frac{\sqrt{J_2}}{I_1} \begin{cases} \geq 0.27; \text{damage occurs} \\ < 0.27; \text{remains intact} \end{cases} \quad (\text{D-53})$$

where:

$$\sqrt{J_2} = \sqrt{\frac{1}{6} [(\sigma_1 - \sigma_2)^2 + (\sigma_2 - \sigma_3)^2 + (\sigma_3 - \sigma_1)^2]}$$

$$I_1 = \sigma_1 + \sigma_2 + \sigma_3$$

$\sigma_1, \sigma_2, \sigma_3$  = principal stresses

This criterion is based on experimental evidence of dilation in tested samples of WIPP salt. Other investigators have observed similar stress-invariant criteria for dilatancy in other salts as documented by Van Sambeek et al. (1993b).

### D3.3.2 Damage-Stress Criterion

Using the MDCF model (Chan, 1993), the potential level of damage can be evaluated by the power-conjugate equivalent stress measure (the damage stress,  $\sigma_{eq}^{\omega}$ ). The damage stress for shear-induced damage is given by Chan (1993):

$$\sigma_{eq}^{\omega} = |\sigma_1 - \sigma_3| + (1 - p_1 \rho) \left[ \frac{I_1 - \sigma_3}{3 \text{sgn}(I_1 - \sigma_3)} \right]^{x_6} \quad (\text{D-54})$$

The MDCF damage model constants are given in Table D-13 for argillaceous halite.

### D3.3.3 Evaluation of DRZ Models

An evaluation of the stress-invariant (Equation D-53) and damage-stress (Equation D-54) models was performed using the air intake shaft (AIS) permeability testing results reported in Section 3.5 of Appendix C. In this testing, permeability was measured as a function of radius into the surrounding intact salt at two depths (346 m and 626 m) within the Salado Formation. The results of this testing are shown in Figure C-1 of Appendix C. This figure was used to estimate the range in the radial extent of the DRZ. The minimum and maximum normalized DRZ radii at the two depths are given in Table D-16. The term "normalized DRZ radius" is defined as the radial extent of the DRZ into the Salado Formation divided by the AIS shaft radius.

Table D-16. Normalized DRZ Radius Surrounding the AIS

Depth (m)	Minimum	Maximum
346	1.31	1.77
626	1.45	1.92

An estimation of the state of stress surrounding the AIS can be made using the steady-state analytical solution for a circular opening in an infinite domain that has an initial lithostatic stress state (Van Sambeek, 1986). The material is assumed to be governed by a simple Norton creep law and a von Mises flow rule. The solution is given in terms of the radial ( $\sigma_r$ ) tangential ( $\sigma_{\theta\theta}$ ), and axial ( $\sigma_z$ ) stresses as:

$$\begin{aligned}\sigma_1 = \sigma_r &= P_0 \left[ (a/r)^{2/n} - 1 \right] \\ \sigma_3 = \sigma_{\theta\theta} &= P_0 \left[ (1 - 2/n)(a/r)^{2/n} - 1 \right] \\ \sigma_2 = \sigma_z &= (\sigma_r + \sigma_{\theta\theta}) / 2 \\ &= P_0 (a/r)^{2/n} \left[ (1 - 1/n) - 1 \right]\end{aligned}\tag{D-55}$$

where:

- $\sigma_1, \sigma_2, \sigma_3$  = maximum, intermediate, and minimum principal stresses, respectively
- $a$  = radius of AIS = 3.05 [m]
- $r$  = arbitrary radius (note:  $r \geq a$ )
- $P_0$  = magnitude of preexisting stress in surrounding salt  
=  $5.8 + 0.0225(d - 250)$  [MPa]
- $d$  = depth [m]
- $n$  = exponent of effective stress in Norton creep law  
= 5.0 (steady-state, time =  $\infty$ )  
= 1.0 (elastic, time = 0).

The normalized DRZ radius ( $r/a$ ) was calculated as a function of depth by substituting Equation D-55 into Equation D-53 (stress-invariant model) and Equation D-54 (damage-stress model). The results of these calculations are shown in Figure D-2. Superposed on this figure are the AIS field test results (Table D-16). The following conclusions can be made regarding this calculation:

- The stress-invariant model (Equation D-53) substantially underpredicts the measured DRZ.
- The damage-stress model (Equation D-54) provides a conservative estimate (overprediction) of the measured DRZ.

Based on the results of this simple exercise, the damage-stress model was used to estimate the behavior of the DRZ in all subsequent structural calculations.

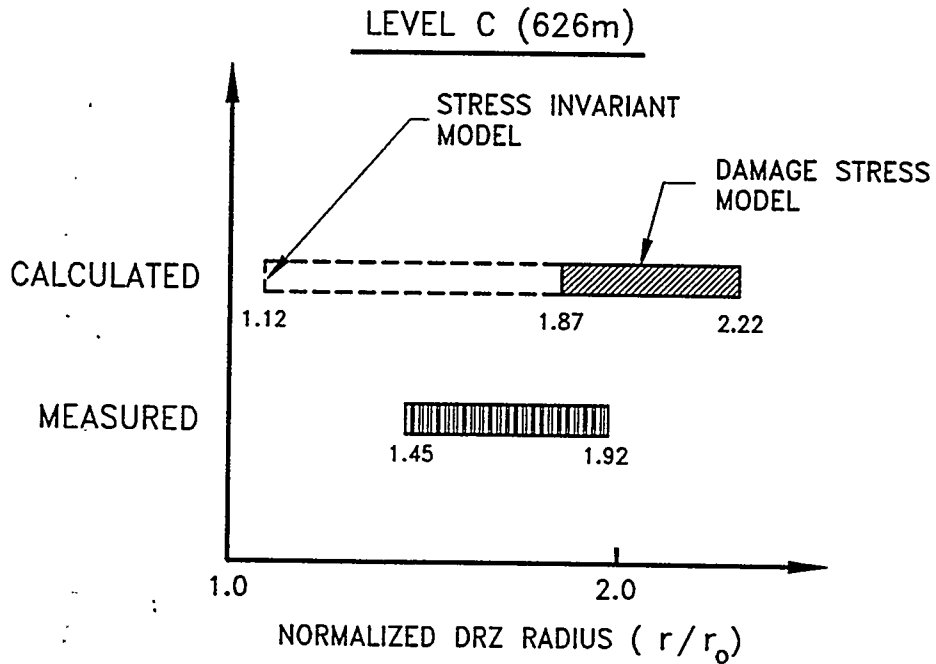
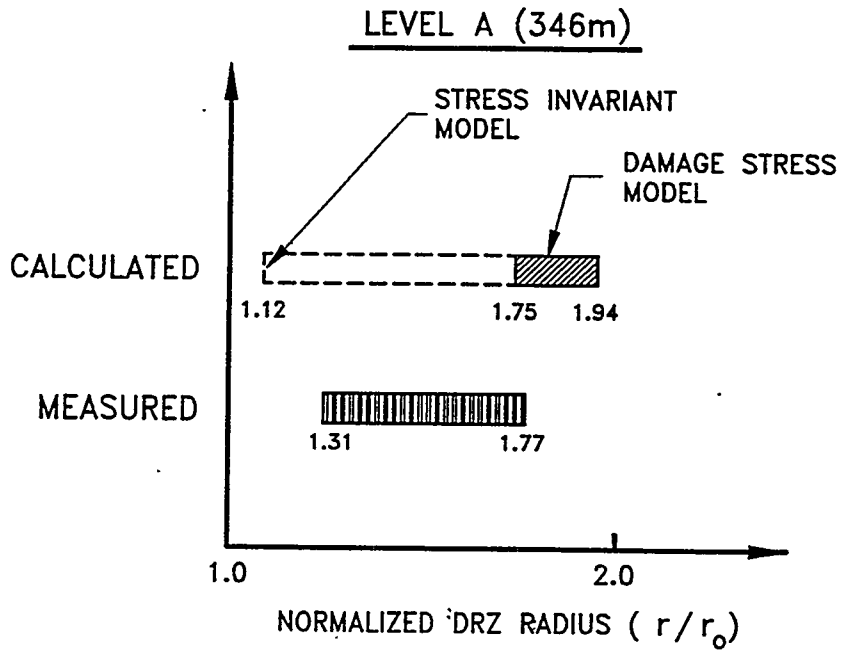


Figure D-2. Comparison of calculated results using damage-stress and stress-invariant DRZ models with measured AIS results.

## **D4. SHAFT SEAL COMPONENT ANALYSES**

### **D4.1 Salado Mass Concrete Seals**

#### **D4.1.1 Thermal Analysis of Concrete Seals**

##### **Objective**

The objective of this calculation was to determine the expected temperatures within (and surrounding) an SMC emplacement attributable to its heat of hydration.

##### **Problem Description**

An axisymmetric representation of the SMC seal, the open shaft, and the surrounding Salado salt is shown in Figure D-3. The left vertical boundary is the centerline of the shaft and is a line of symmetry. The lower horizontal boundary is a plane of symmetry located at the midheight of the SMC seal. The upper horizontal and right vertical boundaries are beyond the thermal influence of the heat-generating SMC seal throughout the simulation period of 1 year. The modeled height of the SMC seal was 6.08 m (20 ft). The radius of the shaft was modeled as 3.04 m. A simulation period of 1 year was determined to be of sufficient duration for the SMC and Salado salt temperatures to reach maximums.

##### **Assumptions**

- The SMC seal is placed instantaneously at time = 0 year and generates heat in accordance with Equation D-2.
- The initial temperature of the surrounding salt is 27°C.
- The variations in stratigraphy within the Salado Formation are ignored in this calculation. The in situ material surrounding the shaft was assumed to be entirely Salado salt.
- The seal and shaft are thermally isolated from other seals and other shafts; i.e., the domain surrounding the seal is assumed to be infinite in extent.

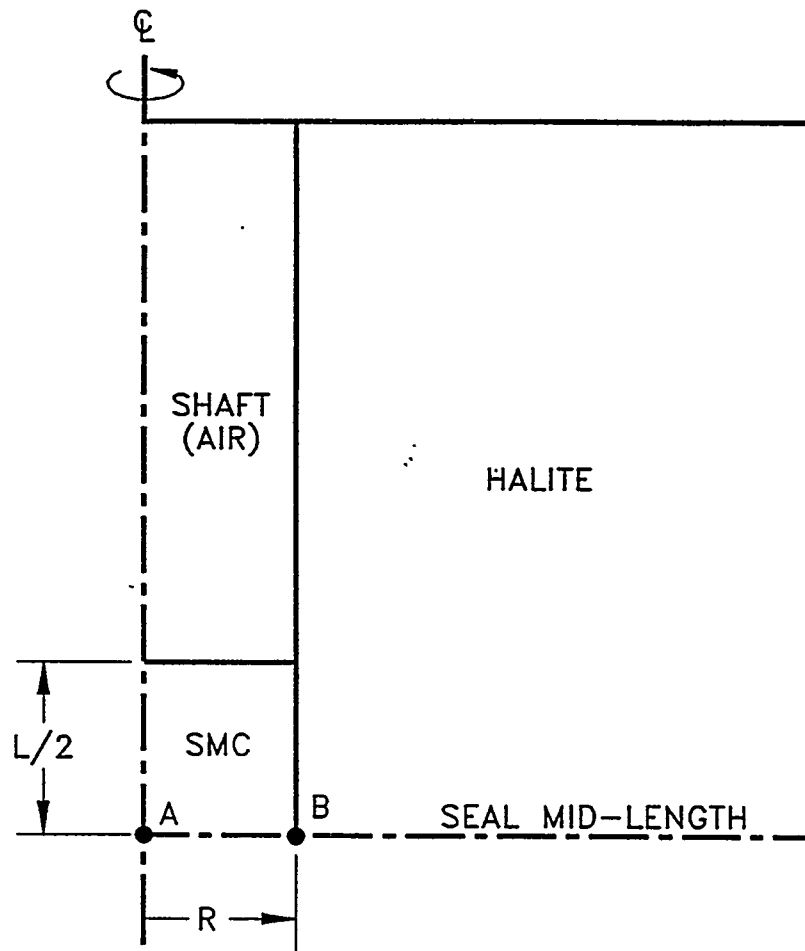
##### **Results**

Calculated temperatures from this analysis are shown in Figures D-4 and D-5. Figure D-4 shows that locations in the SMC increase in temperature from ambient (27°C) to a maximum of 53°C at 0.02 year after SMC placement. The maximum temperature in the surrounding salt is 38°C at approximately the same time. Figure D-5 shows isotherms within and surrounding the seal at 0.02 year. The thermal gradient within the concrete is approximately 1.5°C/m. This figure also shows that at a radial distance of 2.0 m into the surrounding salt, the temperature rise is less than 1°C.

#### **D4.1.2 Structural Analysis of Concrete Seals**

##### **Objective**

The objective of this calculation was to determine stresses within the concrete seals resulting from creep of the surrounding salt and the weight of the overlying seal material.



POINT A = SMC Midpoint  
 POINT B = SMC/Salt Interface  
 $L$  = Seal Length (20 ft)  
 $R$  = Shaft Radius = (10 ft)

Figure D-3. Axisymmetric model used in the SMC thermal analysis.

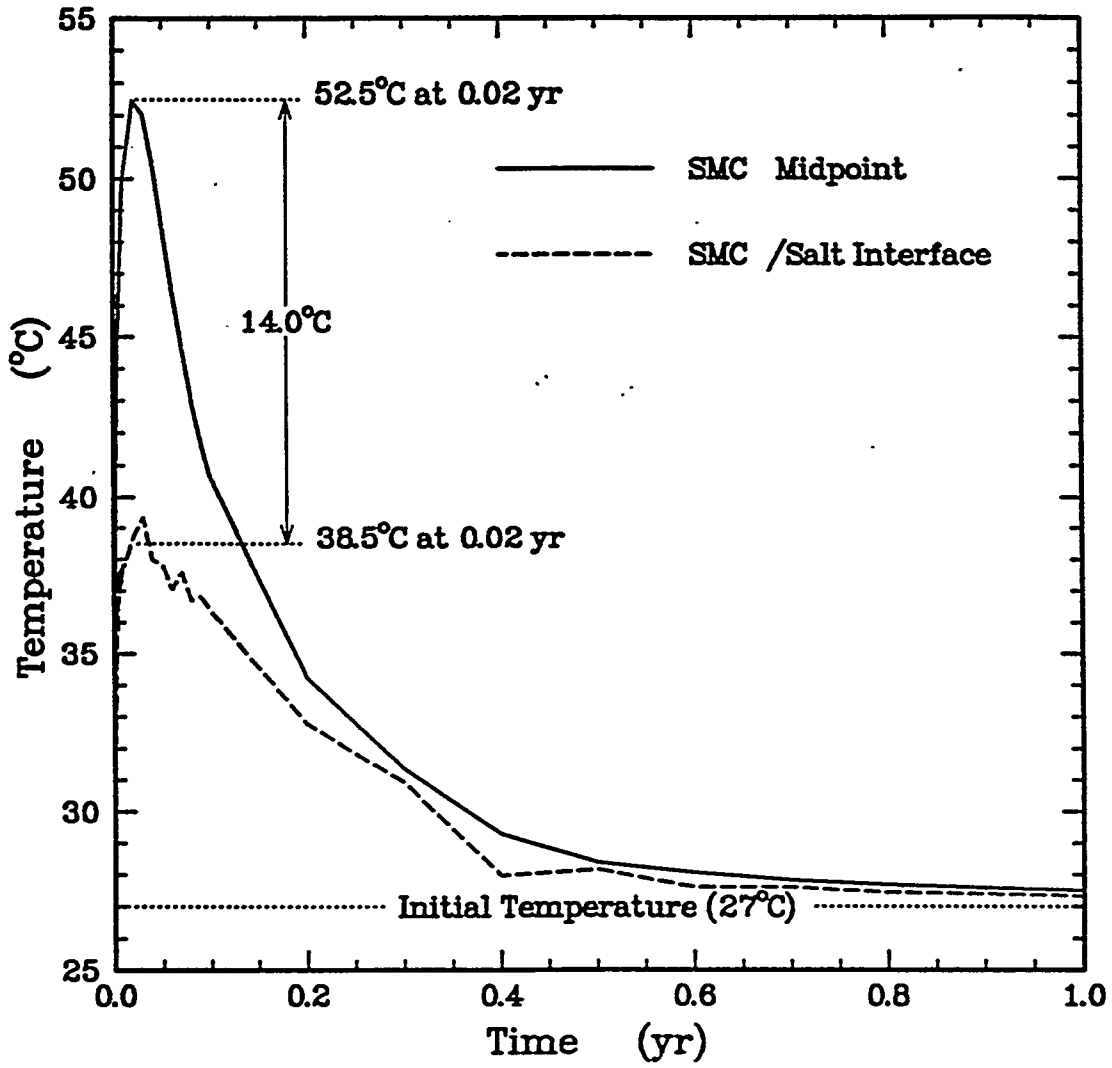


Figure D-4. Temperature histories of SMC center and SMC/salt interface.

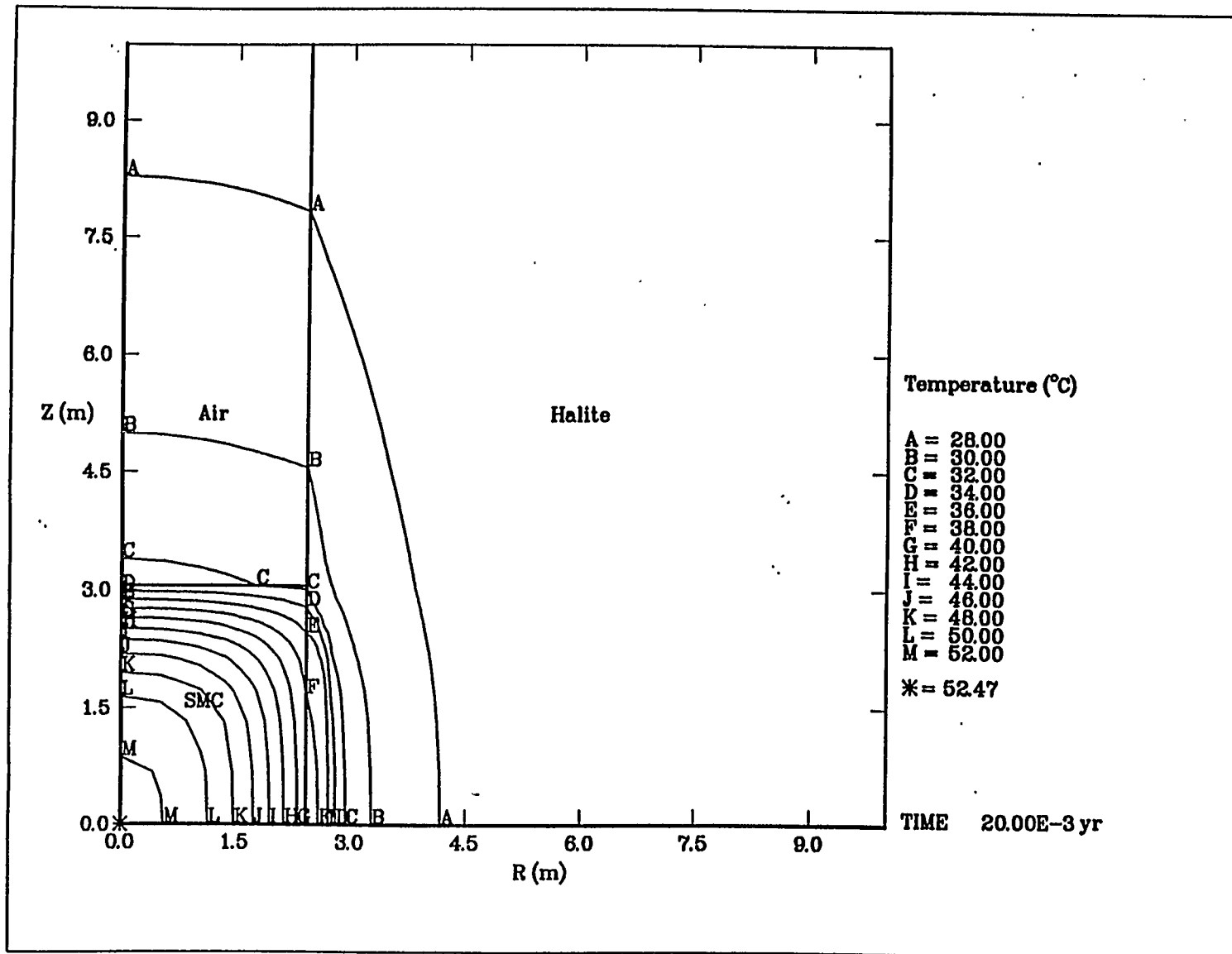


Figure D-5. Isotherms surrounding SMC seal at 0.02 year.

## Problem Description

The concrete seal components in the shaft seal were modeled using the Air Intake Shaft (AIS) geometry (see Figure D-6). The bottoms of the concrete components are located in good quality halite at depths of 308 m, 429 m, and 616 m for the upper, middle, and lower concrete seals, respectively. Each of the three concrete components was analyzed independently.

As shown in Figures D-7 through D-9, sealing of the shaft and installation of seal system components were simulated from bottom to top of the modeled region in arbitrary increments of 0.1 year for each stage. The response of the seal components and extent of the DRZ were simulated to 100 years. The following marker beds (MBs) were included in the calculation model: MB101, MB103, MB115, MB116, MB117, MB134, MB136, and the Vaca Triste.

## Assumptions

- Axisymmetric conditions are applicable, and a condition of axially restrained displacements exists with respect to the vertical direction at a moderate distance from the seal system.
- The shaft is instantaneously excavated at time  $t = 0$ . Excavations for the concrete seal wings and waterstop occur instantaneously at time  $t = 50$  years.
- Each seal emplacement operation occurs instantaneously.
- The shaft has a uniform initial diameter of 6.1 m.
- The shaft is sufficiently isolated from other excavations that the response of the shaft is unaffected by other underground workings at the WIPP.
- Anhydrite, siltstone, and polyhalite beds exhibit elastic behavior only. Marker beds MB104, MB105, MB118, and MB137 were not modeled in this study because these relatively thin members are not structurally important and would not significantly affect the results.
- Beds comprised predominately of halite are assumed to be argillaceous salt, as defined by the MDCF model, with a clay content of 2.9%.
- Elastic properties of all materials are independent of temperature within the range of interest.
- Inelastic behavior, such as creep, yielding, or cracking, was not modeled for concrete.
- Tension-induced creep damage of salt is ignored.
- Damage stress can be used to indicate if a region within the salt is accumulating damage or healing.
- Initial temperature and stress conditions are listed in Table D-17.

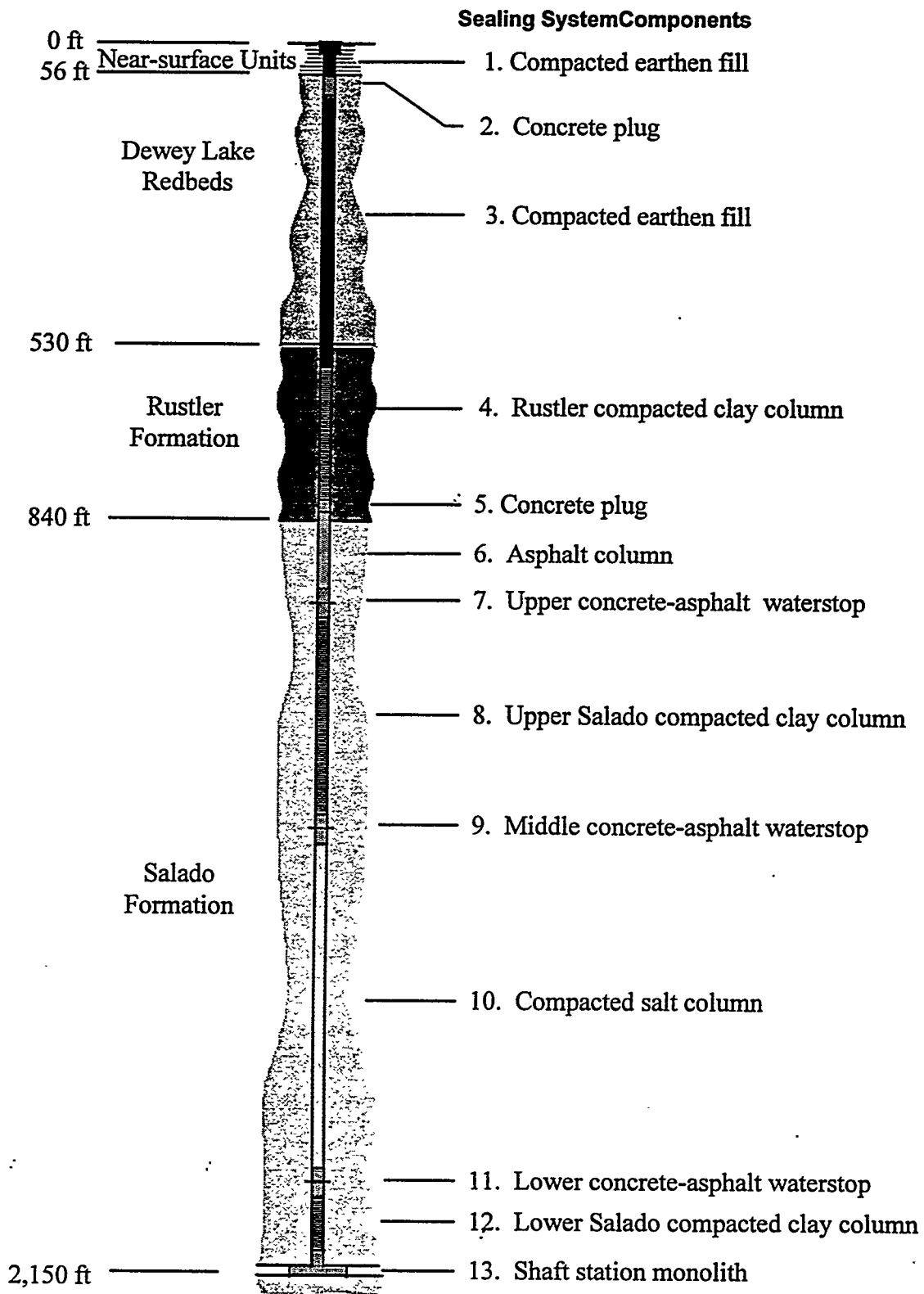


Figure D-6. Seal system conceptual design for the WIPP Air Intake Shaft (DOE, 1995).

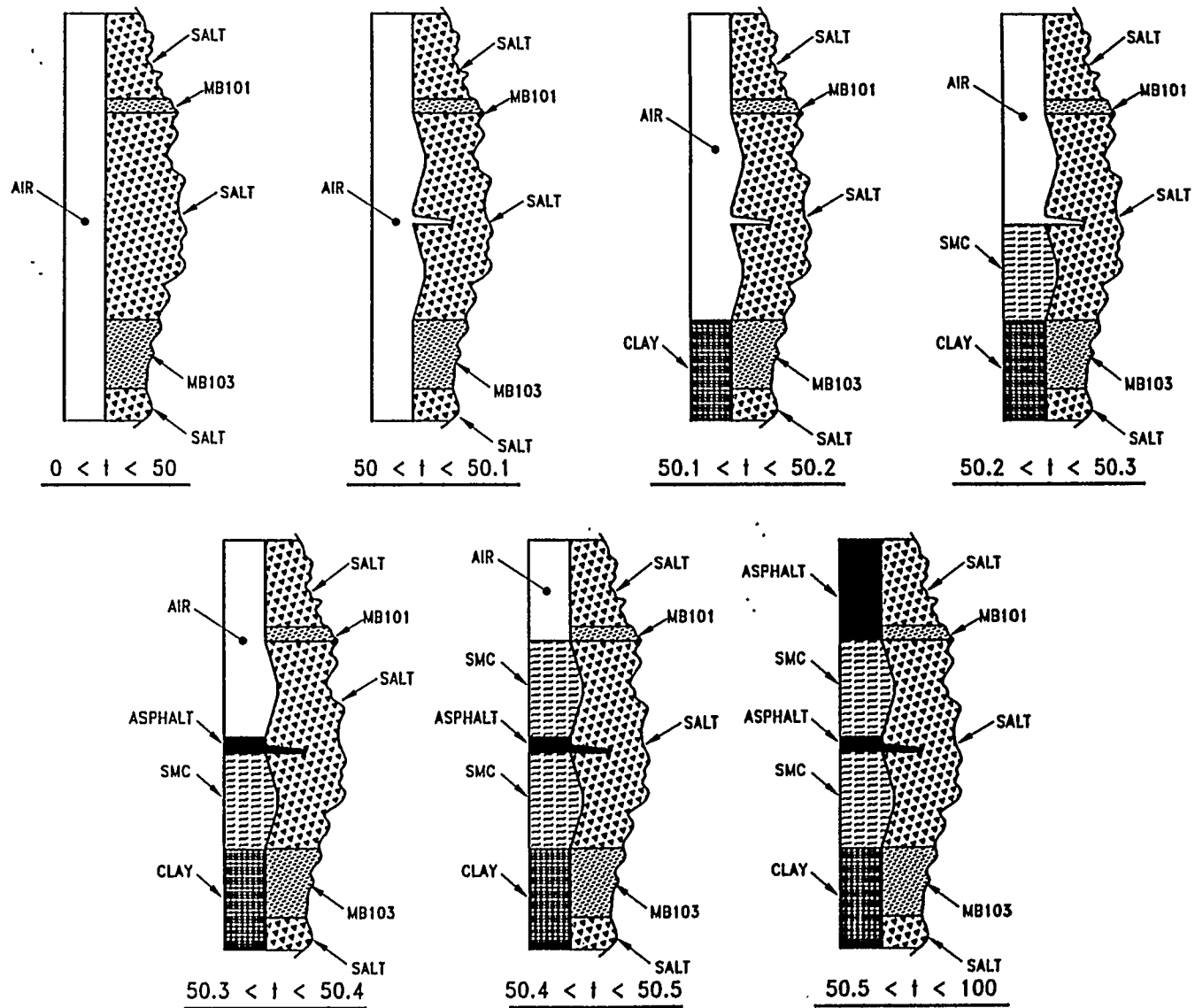


Figure D-7. Axisymmetric model configuration of upper concrete shaft seal.

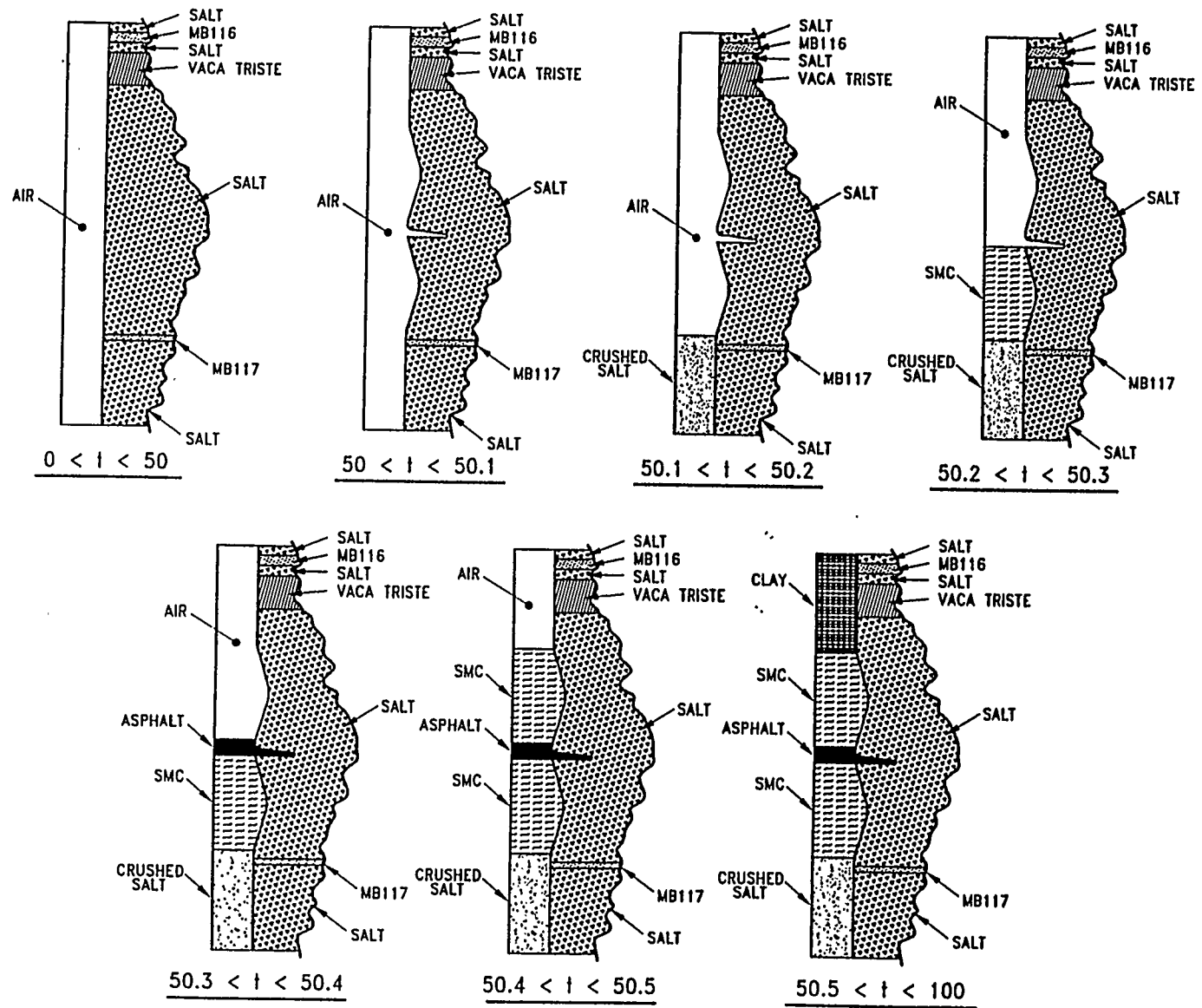


Figure D-8. Axisymmetric model configuration of middle concrete shaft seal.

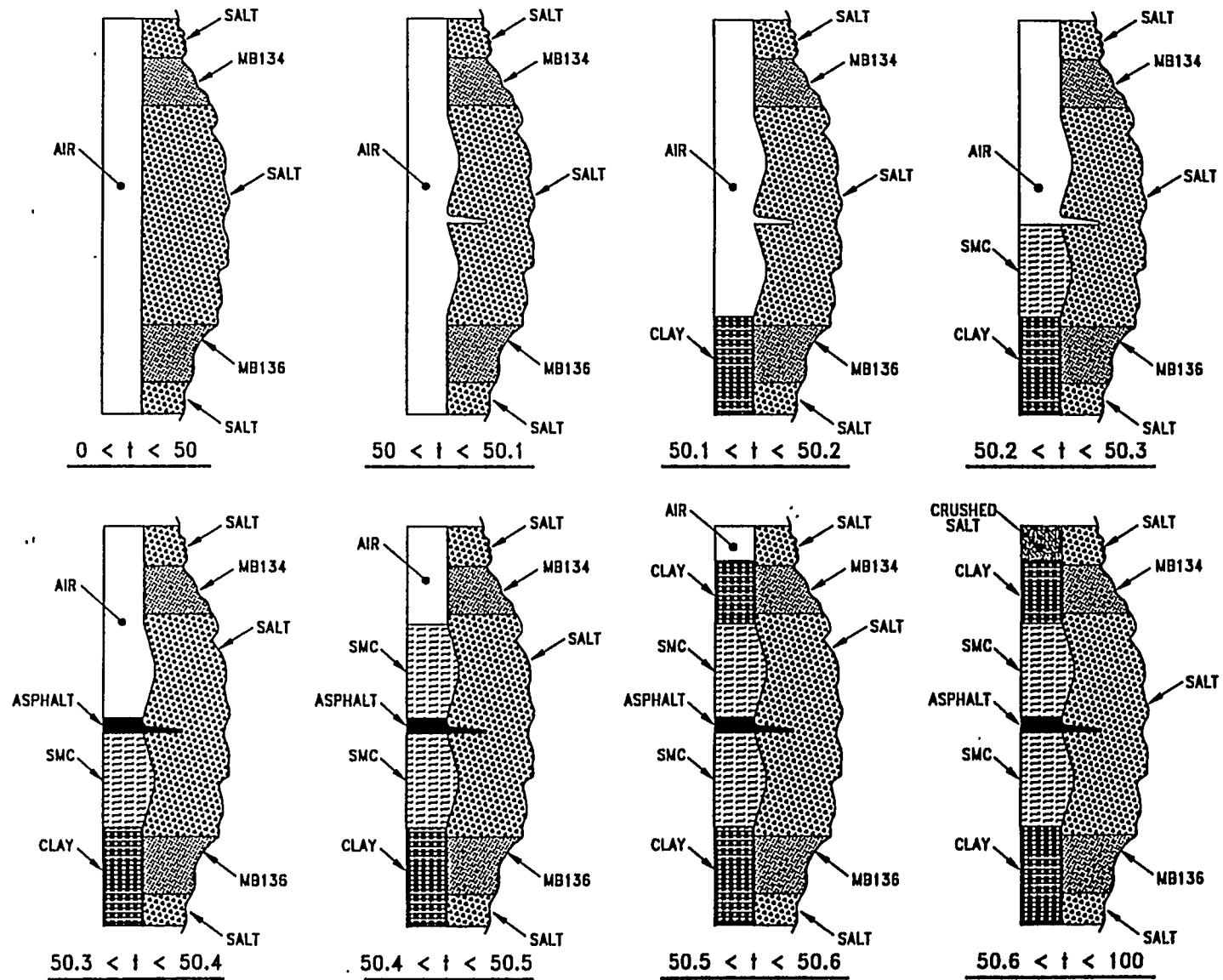


Figure D-9. Axisymmetric model configuration of lower concrete shaft seal.

Table D-17. Initial Temperature and Stress Conditions within Salado Formation

Location Within Salado Formation	Depth (m)	Initial Conditions	
		Temperature <sup>(1)</sup> (°C)	Stress <sup>(2)</sup> (MPa)
Upper	301	23.5	6.95
Middle	421	24.7	9.65
Lower	608	26.6	13.86

(1) Based on temperature of 27°C at 650-m depth and a geothermal gradient of 10°C/km (Sass et al., 1971).

(2) Based on in situ stress of 14.8 MPa at 650-m depth and an average overburden density of 2,300 kg/m<sup>3</sup> (Krieg, 1984, p. 14).

## Results

Throughout the calculations, the salt surrounding the shaft creeps toward and into the shafts. This creep causes radial loading on the shaft components when the creep is restrained. In turn, the radial loading induces radial stress in the components. In the upper concrete component, the average radial stress increases from zero at time of emplacement ( $t = 0$ ) to 2.5 MPa at  $t = 50$  years. Similarly, the radial stress in the middle concrete component ranges from 3.5 to 4.5 MPa and in the lower concrete component the radial stress ranges from 4.5 to 5.5 MPa at  $t = 50$  years.

To determine the axial loading on the shaft components, it was assumed that each concrete component must support the weight of the overlying seal material between it and the next concrete component. Using an average vertical stress gradient of 0.02 MPa/m, the calculated vertical stresses on the upper, middle, and lower concrete components from the weight of the overlying seal material are 7.0, 2.4, and 3.8 MPa, respectively. The specified design strength of the concrete material is 31.0 MPa.

### D4.1.3 Thermal Stress Analysis of Concrete Seals

#### Objectives

The objectives of this calculation were (1) to determine the stresses in the concrete as a result of its heat of hydration and (2) to determine the thermal impact on the creep of the surrounding salt.

#### Problem Description

Compressive stresses develop within the concrete as a result of thermal expansion of the concrete and restrained creep of the surrounding salt. Thermal stresses within the concrete were calculated using the formula:

$$\sigma_T = E \alpha \Delta T \quad (D-56)$$

where:

- $\sigma_T$  = thermal stress (for a fully confined condition)
- $E$  = Young's modulus
- $\alpha$  = linear coefficient of thermal expansion
- $\Delta T$  = temperature increase.

Thermal results indicate that the concrete will heat to approximately 53°C at approximately 0.02 year after placement (see Section D4.1.1) from an ambient temperature of 27°C. The surrounding salt heats to a maximum of 38°C at approximately the same time.

## Results

The thermoelastic stresses in the concrete were calculated based on a maximum temperature increase of 26°C (Figure D-4) and assuming a fully confined condition. The calculation results indicate that short-term thermal stresses in the concrete are less than 9.2 MPa.

As shown in Figure D-4, the maximum salt temperature will be approximately 38°C at 0.02 year of the emplacement. While it is understood that elevated temperatures do increase the creep rate of salt, the small magnitude and short duration of the thermal pulse in the salt had negligible effect on increasing stresses in concrete through enhanced salt creep.

### D4.1.4 Effect of Dynamic Compaction on Concrete Seals

#### Objective

The objective of this simple calculation was to determine a thickness of seal layer above each of the concrete components to reduce the impact of dynamic compaction.

#### Problem Description

As shown in Figure D-6, compacted clay and salt columns are included in the shaft seal design directly above the three concrete components. These seal materials may be dynamically compacted as they are emplaced.

The compacted depth ( $D$ ) was calculated using the equation:

$$D = n (WH)^{1/2} \tag{D-57}$$

where:

- $W$  = tamper weight = 5.14 (metric tons)
- $H$  = drop height = 6.1 (m)
- $n$  = material coefficient.

This equation is taken from a construction reference manual and is based on a functional fit to field measurements. The material coefficient ( $n$ ) is given as 0.5 for all soil deposits and was used in the calculation for crushed salt. For clay, this coefficient ranges from 0.35 to 0.40 for decreasing moisture content. A higher value of  $n$  results in a larger compactive depth.

## Results

Using Equation D-57 and the design inputs, the compacted depths for crushed salt and clay are 9.2 feet and 7.2 feet, respectively. The calculations indicate that the provided thickness for crushed salt (12 ft) and clay (10 ft) are greater than the compacted depth.

### D4.1.5 Effect of Clay Swelling Pressures on Concrete Seals

#### Objectives

The objectives of this analysis were to determine the potential for failing the concrete components as a result of clay swelling pressures and the potential for fracturing the salt where the swelling pressure acts directly on the shaft wall.

#### Problem Description and Results

In order to fail the concrete seals, the applied swelling pressures must exceed the compressive strength of the concrete (4,500 psi = 31.0 MPa). Test measurements on confined bentonite at a density of  $1.8 \text{ g/c}^3$  (Pfeifle and Brodsky, 1991) indicate that the maximum swelling pressures are on the order of 3.5 MPa (Figure D-10). These test results were used to approximate the induced stresses on the concrete seals from clay swelling pressures.

## D4.2 Crushed Salt Seal

### D4.2.1 Structural Analysis of Crushed Salt Seal

#### Objective

The objective of this calculation was to determine the fractional density of the crushed salt seal as a function of time and depth within the shaft.

#### Problem Description

The analysis performed is illustrated schematically in Figure D-11, which also shows the model geometry. The model is an axisymmetric representation of the shaft and host rock at a prescribed depth. For time  $t < -50$  years, the shaft is not present and a self-equilibrating initial lithostatic (hydrostatic) stress field exists in the salt such that the three principal stresses are identical. At time  $t = -50$  years, the cylindrical shaft is "excavated," and the surrounding salt is allowed to creep for 50 years, i.e., the operational period. At time  $t = 0$ , crushed salt is compacted in the shaft with an initial density of  $1.944 \text{ Mg/m}^3$  (90% of the intact salt density). Salt surrounding the shaft continues to creep inward and consolidates the crushed salt until the crushed-salt seal reaches the intact density of salt. At that time, the model describing crushed salt is changed to the model for intact salt. Crushed salt was modeled using the candidate models discussed in Section D3.1.2. A simulation time of 450 years after emplacement was used, which is sufficient to allow the compacted crushed salt, even at the shallowest depth, to achieve a fractional density greater than 99% of the density of intact salt for each of the three crushed-salt models.

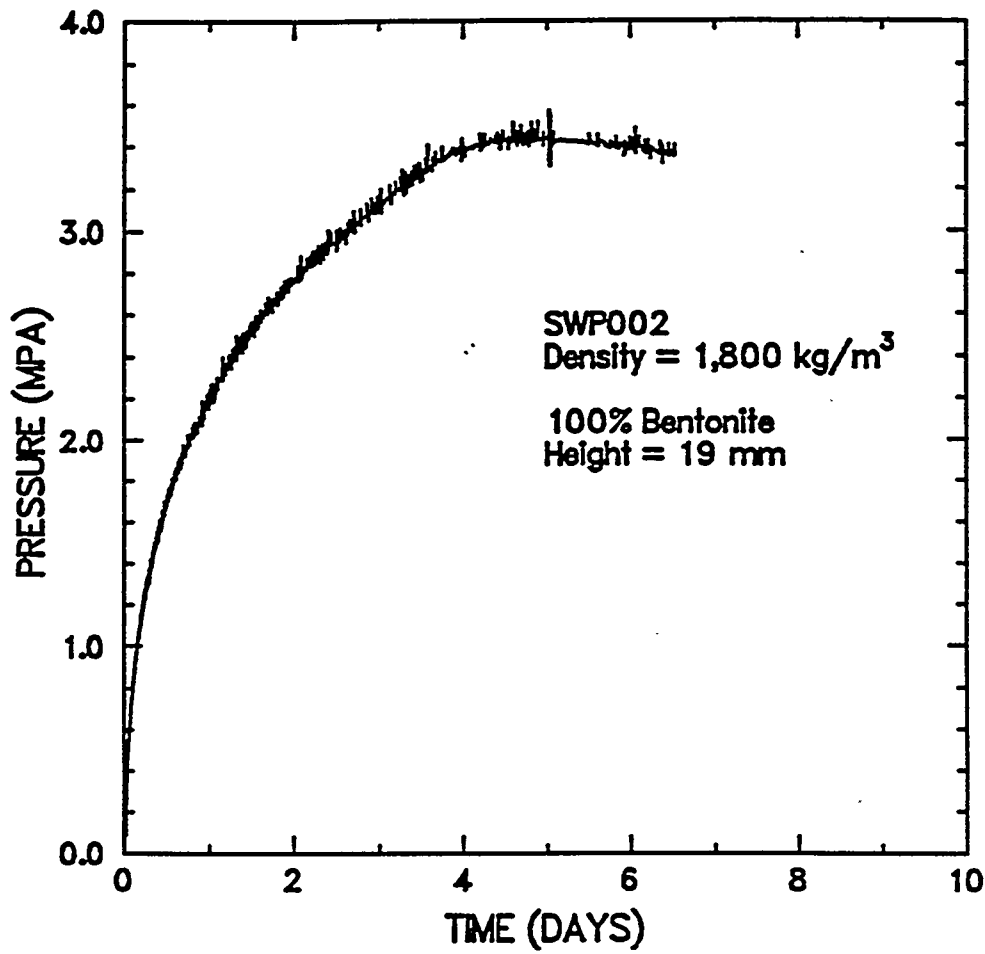


Figure D-10. Swelling pressures as a function of time for a brine-saturated bentonite specimen with a density of 1,800 kg/m<sup>3</sup>.

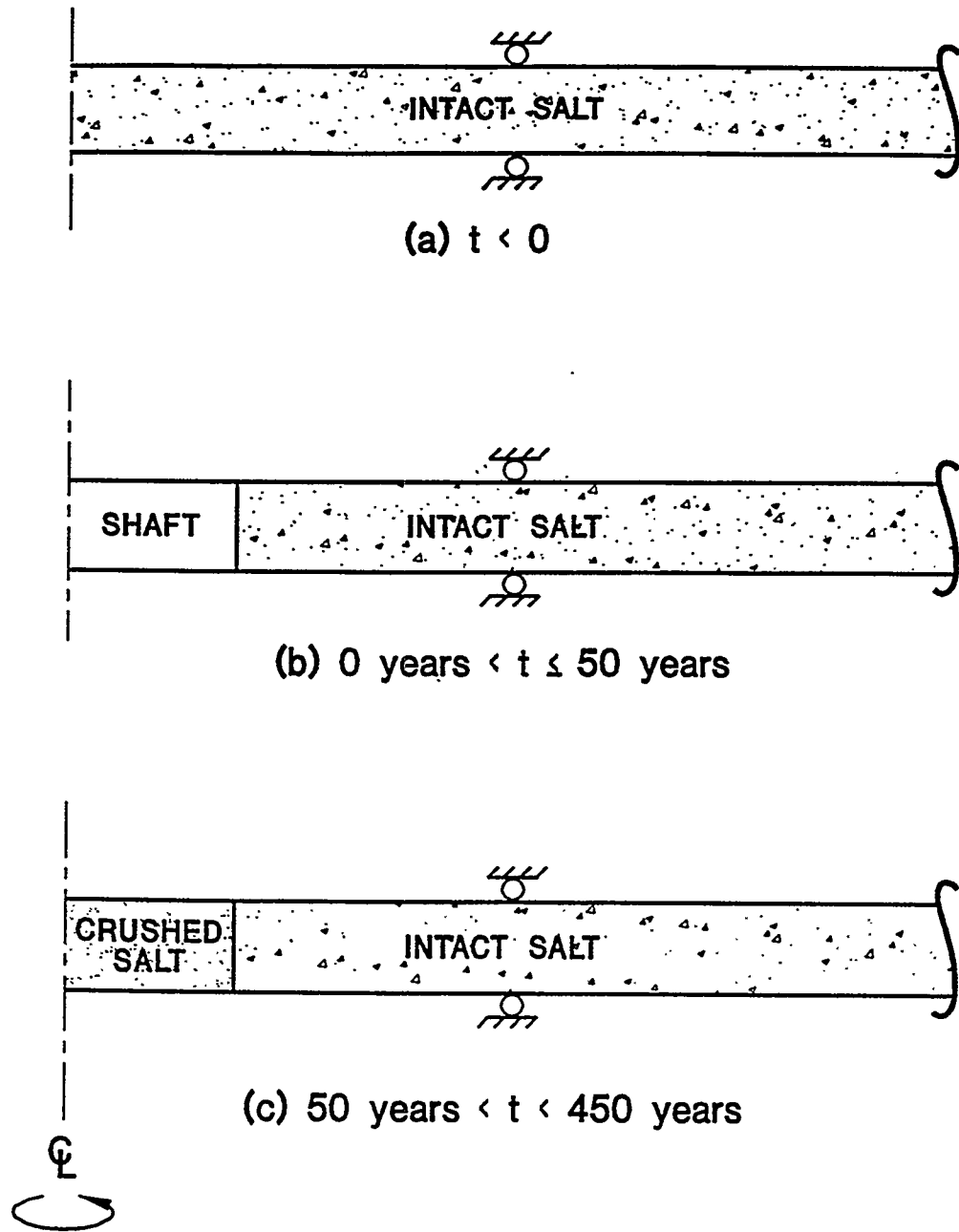


Figure D-11. "Pineapple slice" axisymmetric models.

## Assumptions

- Axisymmetric conditions exist around the shaft, and plane-strain conditions are appropriate with respect to the axial (vertical) direction.
- Vertical variations in stratigraphy are ignored. Intact salt is modeled exclusively as argillaceous salt governed by the MDCF model.
- The initial stress state and temperature vary with depth within the Salado Formation as given in Table D-17.
- The modified creep consolidation models of Zeuch, Spiers, and Sjaardema-Krieg were used. These models include the development of mean stresses in the crushed salt and restraint to creep closure.

## Results

The fractional densities of crushed-salt seal at the top (depth = 430 m), middle (depth = 515 m), and bottom (depth = 600 m) of the salt column are shown in Figure D-12 as a function of time for the three consolidation models. The models predict essentially the same behavior for fractional densities ranging from 90 to 95%. The times required to achieve a fractional density of 95% are approximately 40, 80, and 120 years at the bottom, middle, and top of the seal, respectively. Only the modified Sjaardema-Krieg creep consolidation model mathematically allows full consolidation. The times required to theoretically reconsolidate the crushed salt to 100% fractional density are 70 years, 140 years, and 325 years at the bottom, middle, and top of the salt column, respectively.

### D4.2.2 Effect of Fluid Pressure on the Reconsolidation of Crushed Salt Seals

#### Objective

The objective of this calculation was to determine the effect of fluid pressure on the reconsolidation of the crushed-salt seal. The results of this calculation were used as input conditions to the fluid-flow analyses described in Appendix C. Because creep of intact salt is an exponential function of stress, fluid pressure applied to the shaft wall would significantly reduce the closure rate of the shaft and, consequently, the reconsolidation rate of the crushed salt.

#### Problem Description

In this analysis, three models representative of different depths were used. These models are axisymmetric representations of the AIS and the surrounding intact salt. The reconsolidation rate depends on the depth, fluid pressure, time, and creep rate of the surrounding intact salt. Representative models used in this analysis are shown schematically in Figure D-11. The initial stress and temperature conditions were obtained as described in the notes to Table D-17.

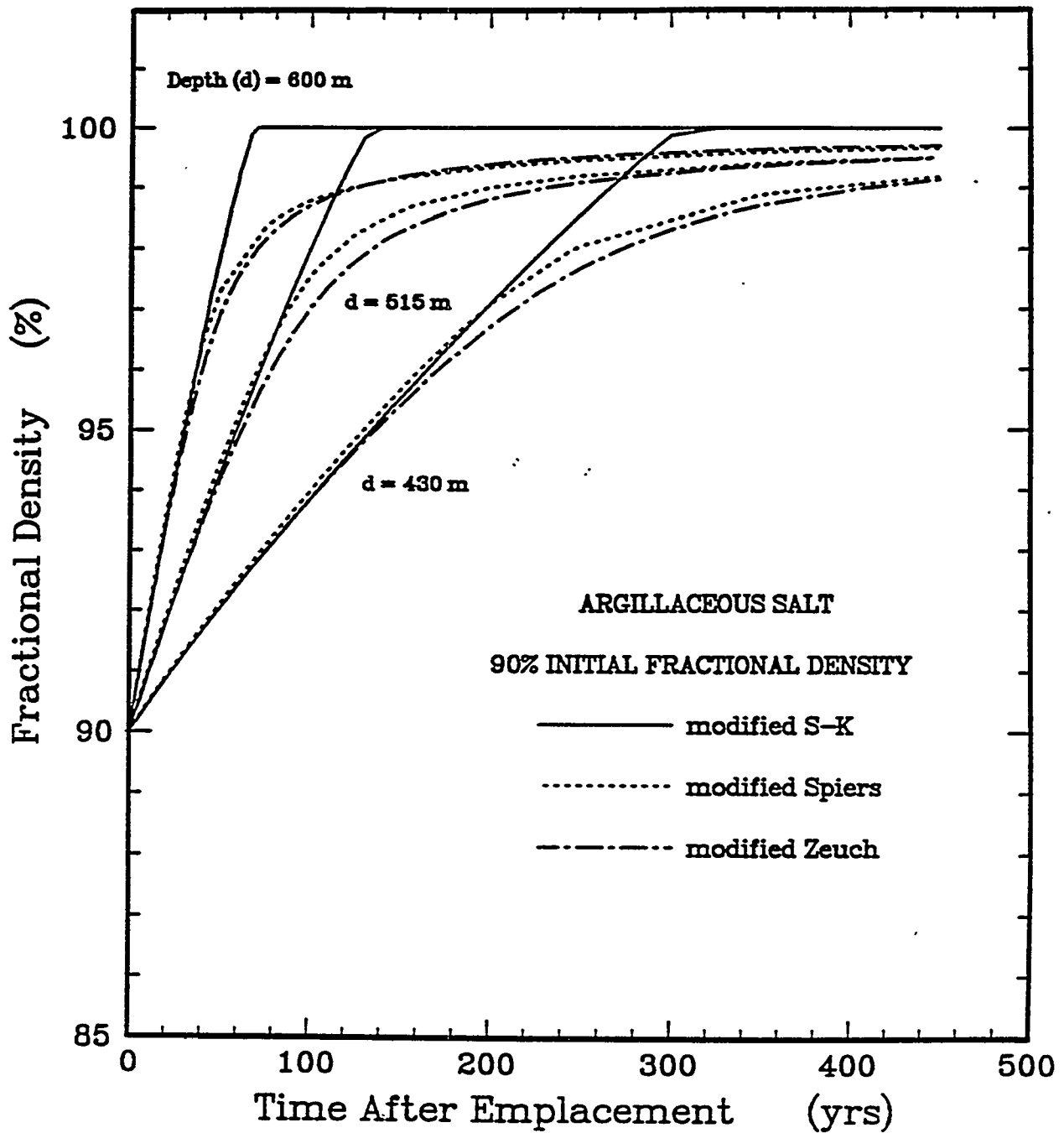


Figure D-12. Consolidation of crushed salt in a shaft at depths of 430, 515, and 600 m using the modified Sjaardema-Krieg, Spiers, and Zeuch models.

Three depths were considered: 430 m, 515 m, and 600 m, which are representative of the top, middle, and bottom of the compacted-salt seal. The fluid in the crushed salt was assumed to behave as a linear elastic material, in which the fluid pressure is related to the volumetric strain through the bulk modulus as:

$$P = \text{MIN}\{P_0 + K(1 - V/V_0), P_{\text{max}}\} \quad (\text{D-58})$$

where:

- $P$  = fluid pressure
- $P_0$  = initial fluid pressure
- $K$  = fluid bulk modulus
- $V$  = current volume of crushed salt
- $V_0$  = initial volume (based on 90% fractional density)
- $P_{\text{max}}$  = maximum fluid pressure.

Maximum fluid pressures ( $P_{\text{max}}$ ) considered are 0, 2, and 4 MPa. These values encompass the allowable range in fluid pressures in terms of salt reconsolidation. Based on the results of this calculation, fluid pressures greater than 4 MPa effectively prevent reconsolidation over a 1000-year time frame.

### Assumptions

- The fractional densities of the crushed-salt seal were calculated through 500 years using the modified Sjaardema-Krieg consolidation model.
- The fractional density of the crushed salt after compaction is 90%, i.e.,  $\rho_0 = 0.90$ .
- The shaft remains open for 50 years, then is instantaneously filled with compacted crushed salt.
- The initial fluid pressures are applied instantaneously at time = 50 years. This is a conservative assumption because it provides an immediate restraint to creep closure and results in longer reconsolidation times.
- Vertical variations in stratigraphy and material properties are neglected. Intact salt is modeled exclusively as argillaceous salt governed by the MDCF model.

### Results

Results for 0 MPa are shown in Figure D-12; results for 2 MPa are shown in Figure D-13. These results indicate that, as expected, the time required to consolidate the crushed salt increases substantially as the fluid pore pressure increases. For fluid pressures of 4 MPa or greater, reconsolidation times are increased to the point where the crushed salt does not achieve a fractional density of 96% until substantially beyond 1000 years. For zero fluid pressure, times of about 40 years, 70 years, and more than 150 years are required. For a fluid pressure of 2 MPa, the times required to achieve a fractional density of 96% are about 90 years, 200 years, and 560 years at the bottom, middle, and top of the crushed-salt column, respectively.

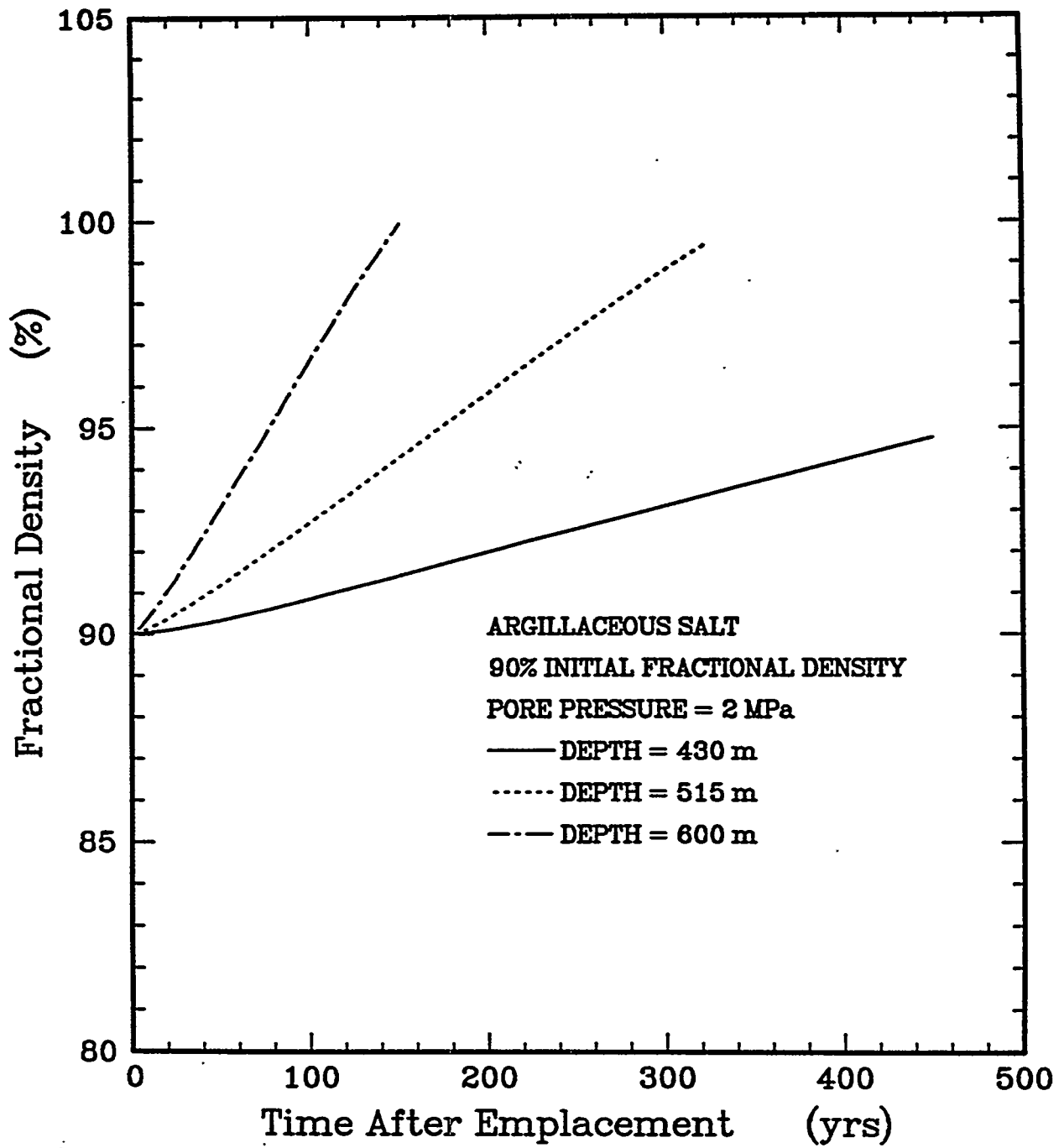


Figure D-13. Crushed-salt fractional density as a function of time for a fluid pressure of 2 MPa and using the modified Sjaardema-Krieg creep consolidation model.

## **D4.3 Compacted Clay Seals**

### **D4.3.1 Structural Analysis of Compacted Clay Seals**

#### **Objective**

The objective of this calculation was to determine the stresses in the upper and lower Salado compacted clay columns as a result of creep of the surrounding salt. These stresses may increase the loads imposed on the concrete seal components. The problem description and assumptions used in performing this calculation are the same as those presented in Section 4.1.2. The results of this calculation indicate that after 50 years the compressive stress in the upper Salado compacted clay column ranges from 0.6 MPa at the top to 0.8 MPa at the bottom of the column. Similarly, after 50 years, the mean stresses in the lower Salado compacted clay column are approximately 2.6 MPa.

## **D4.4 Asphalt Seals**

### **D4.4.1 Thermal Analysis of Asphalt Seals**

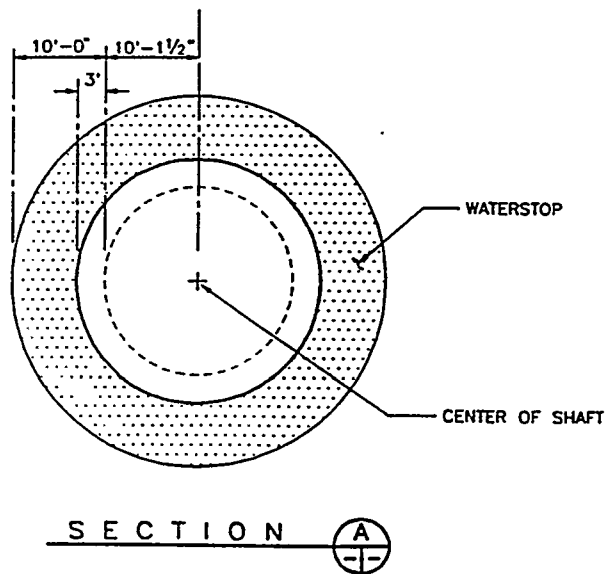
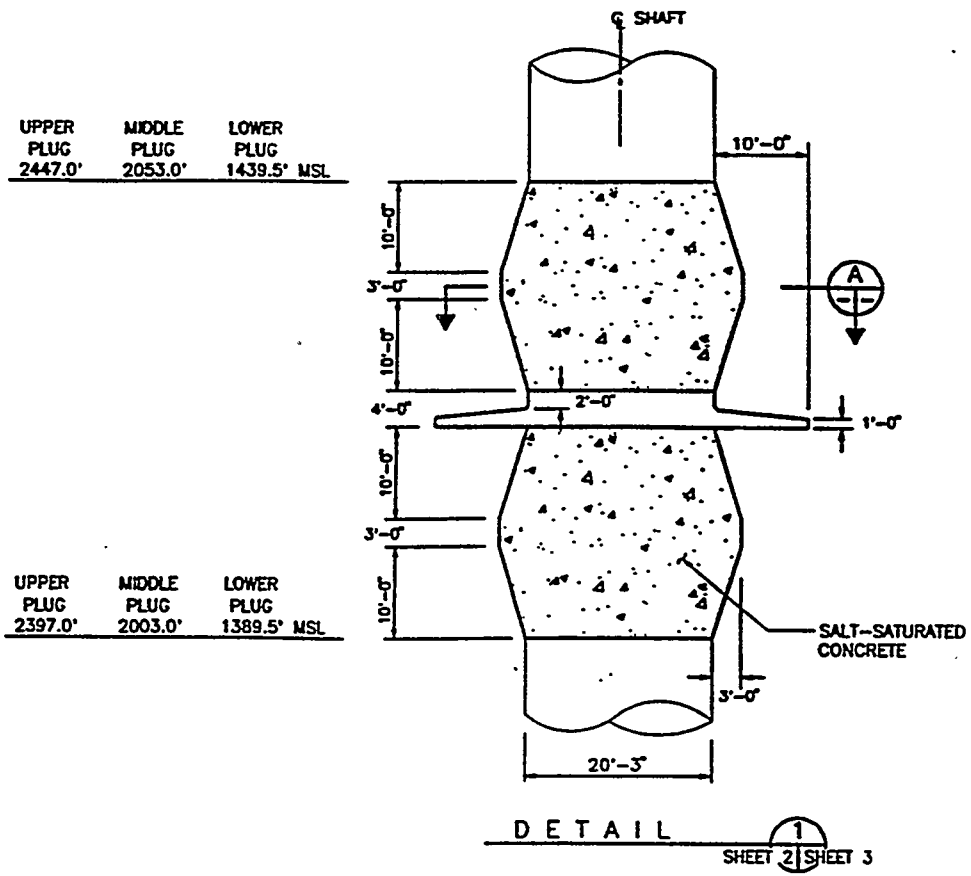
#### **Objectives**

The objectives of this calculation were (1) to determine the temperature histories within the asphalt seal and the surrounding salt and (2) to determine the thermal effects which depend on the length of the waterstop.

#### **Problem Description**

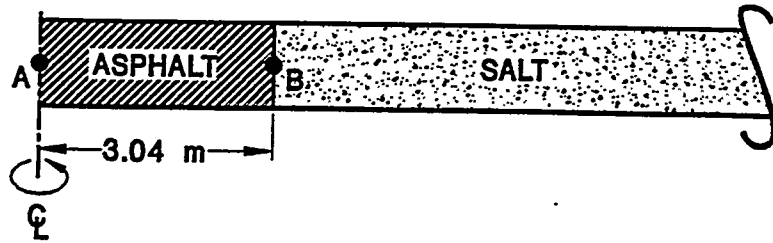
A schematic diagram of the AIS seal showing the asphalt components is given in Figure D-14. The AIS is approximately 6.1 m (20 feet) in diameter. The asphalt seal through the Rustler/Salado interface is more than 36 m (119 feet) in height (Figure D-6). The waterstops are 1.22 m (4 feet) in height and, as shown in Figure D-14, extend radially 3.05 m (10 feet) into the surrounding salt.

Two geometrical models were used to calculate thermal results. The first model, shown in Figure D-15(a), represents an asphalt seal of infinite length and can be used to approximate thermal conditions within the asphalt at the Rustler/Salado interface. This model was used to calculate the maximum asphalt (Point A) and salt (Point B) temperatures. The right boundary was extended laterally (100 shaft radii) to be beyond the thermal influence of the asphalt for 10 years. The left vertical boundary represents the shaft centerline and is a line of symmetry. The second model, shown in Figure D-15(b), is referred to as a "quarter-symmetry model." It is used to represent thermal conditions near the asphalt waterstops and to calculate the thermal effects of the radial extent of the waterstop into the salt. The left and lower boundaries are lines of symmetry located at the shaft centerlines and waterstop midheight, respectively. The modeled height of the asphalt is 0.61 m (2 ft). The radial extent of the waterstop as shown in Figure D-15(b) is 3.05 m (10 ft) or equivalently 1 shaft radius into the salt. The right and upper boundaries are extended 100 m from the waterstop center; beyond the thermal influence of the asphalt through 10 years following emplacement. The temperatures at the asphalt center (Point A in Figure D-15) were calculated as a function of time for two cases: (1) no waterstop and (2) full waterstop.

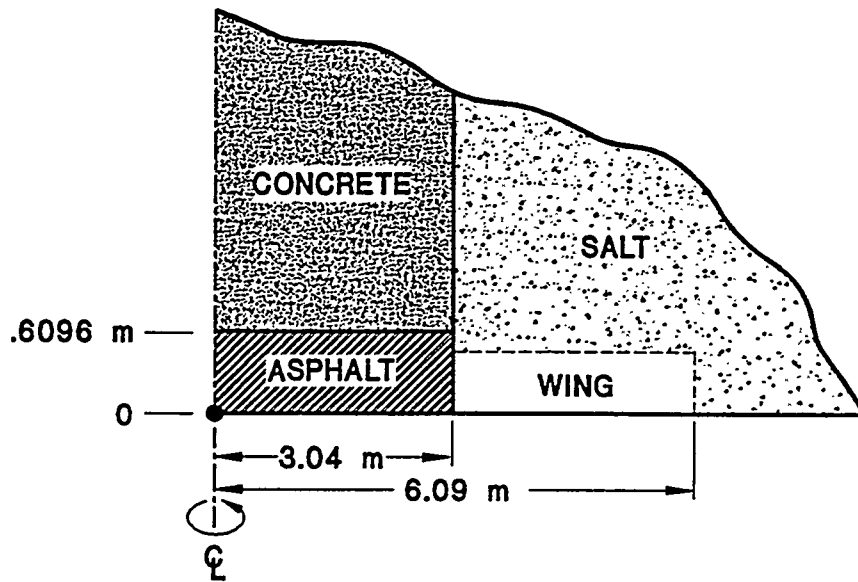


TYPICAL SALADO MASS CONCRETE PLUG  
WITH WATERSTOP (3 LOCATIONS)

Figure D-14. WIPP shaft seal design showing asphalt components.



(a) Pineapple-Slice Model



(b) Quarter-Symmetry Model

Figure D-15. Models used in thermal analysis of asphalt seal.

## Assumptions

- The initial formation temperature is 23°C everywhere along the length of the seal.
- The AIS is thermally isolated from the remaining shafts; i.e., the domain surrounding the AIS is assumed to be infinite in extent.
- The stratigraphy can be neglected; i.e., the domain is assumed to be homogeneous (salt).
- The heat of hydration of the concrete is ignored.
- All seal materials are emplaced simultaneously at time = 0.
- All boundaries are adiabatic.
- The asphalt is emplaced at 180°C.

## Results

The results of this analysis are shown in Figures D-16 through D-18. Figure D-16 shows temperature histories of the asphalt and surrounding salt near the seal midheight. These results indicate that the asphalt center cools from its emplaced temperature of 180°C to 83°C, 49°C, 31°C, and 26°C at times 0.1 year, 0.2 year, 0.5 year, and 1.0 year, respectively. Similarly, the asphalt/salt interface temperatures at the same times are 47°C, 38°C, 29°C, and 26°C.

Figure D-17 shows the temperature histories in the asphalt waterstop. The time required to cool the waterstop is significantly less than that required to cool the asphalt column. Specifically, the waterstop center has cooled to temperatures of 38°C, 29°C, 24°C, and 23°C at times 0.1 year, 0.2 year, 0.5 year, and 1.0 year, respectively.

### D4.4.2 Structural Analysis of Asphalt Seals

The objective of this analysis was to calculate the pressures in the asphalt as a result of creep of surrounding salt to evaluate stresses induced on concrete seal components. The problem description and assumptions used in performing this calculation are the same as those presented in Section 4.1.2. The results of this calculation are shown in Figure D-19, which shows the calculated pressure in the upper, middle, and lower asphalt waterstops as a function of time after emplacement. These results indicate that after 100 years, the pressures in the waterstop are 1.8 MPa, 2.5 MPa, and 3.2 MPa for the upper, middle, and lower waterstops, respectively.

### D4.4.3 Shrinkage Analysis of Asphalt Seals

#### Objective

The objective of this analysis was to determine the shrinkage of the asphalt column as it cools from its emplaced temperature to an acceptable working environment temperature.

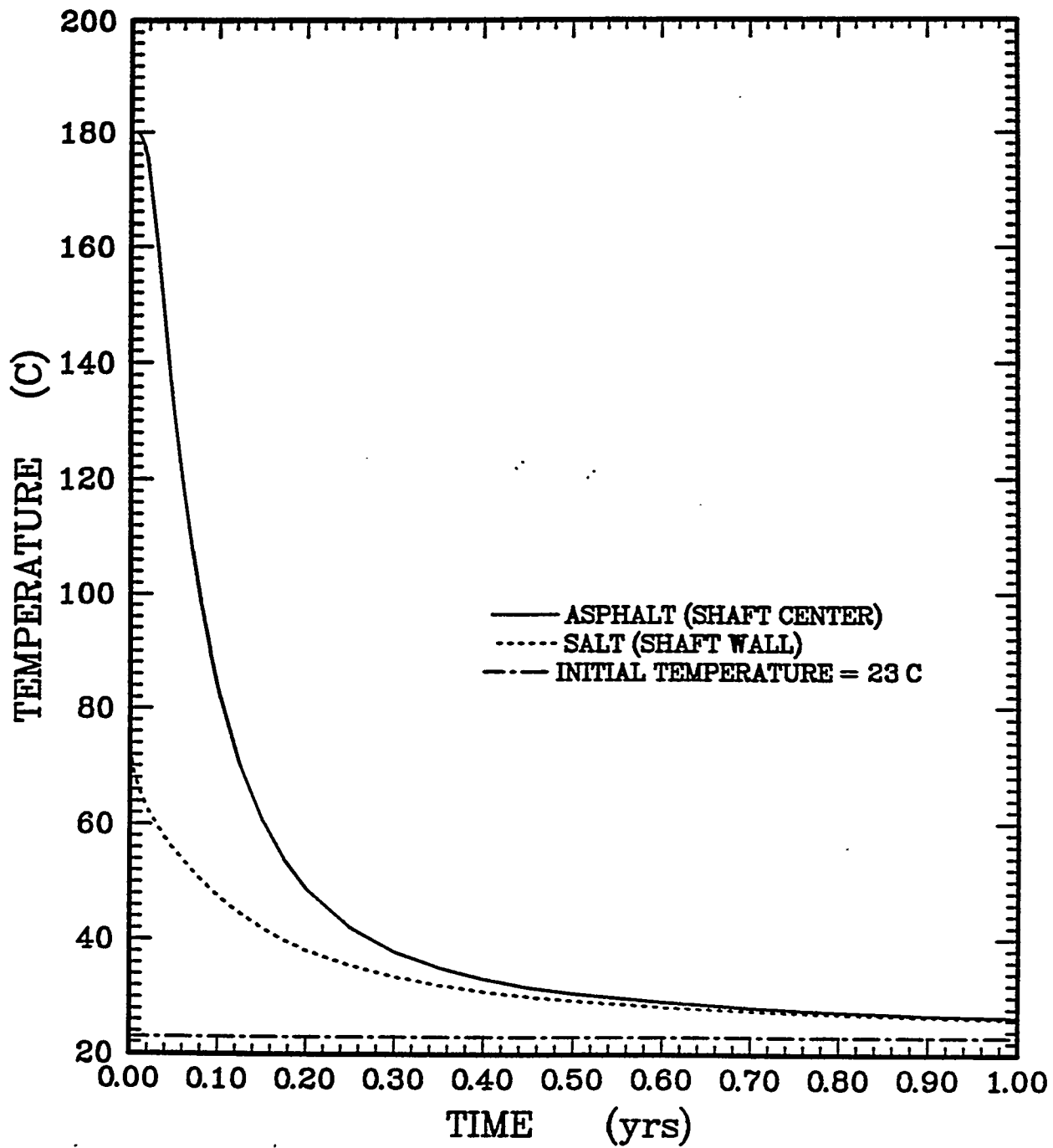


Figure D-16. Temperature histories in asphalt (Point A, Figure D-15a) and salt (Point B, Figure D-15a).

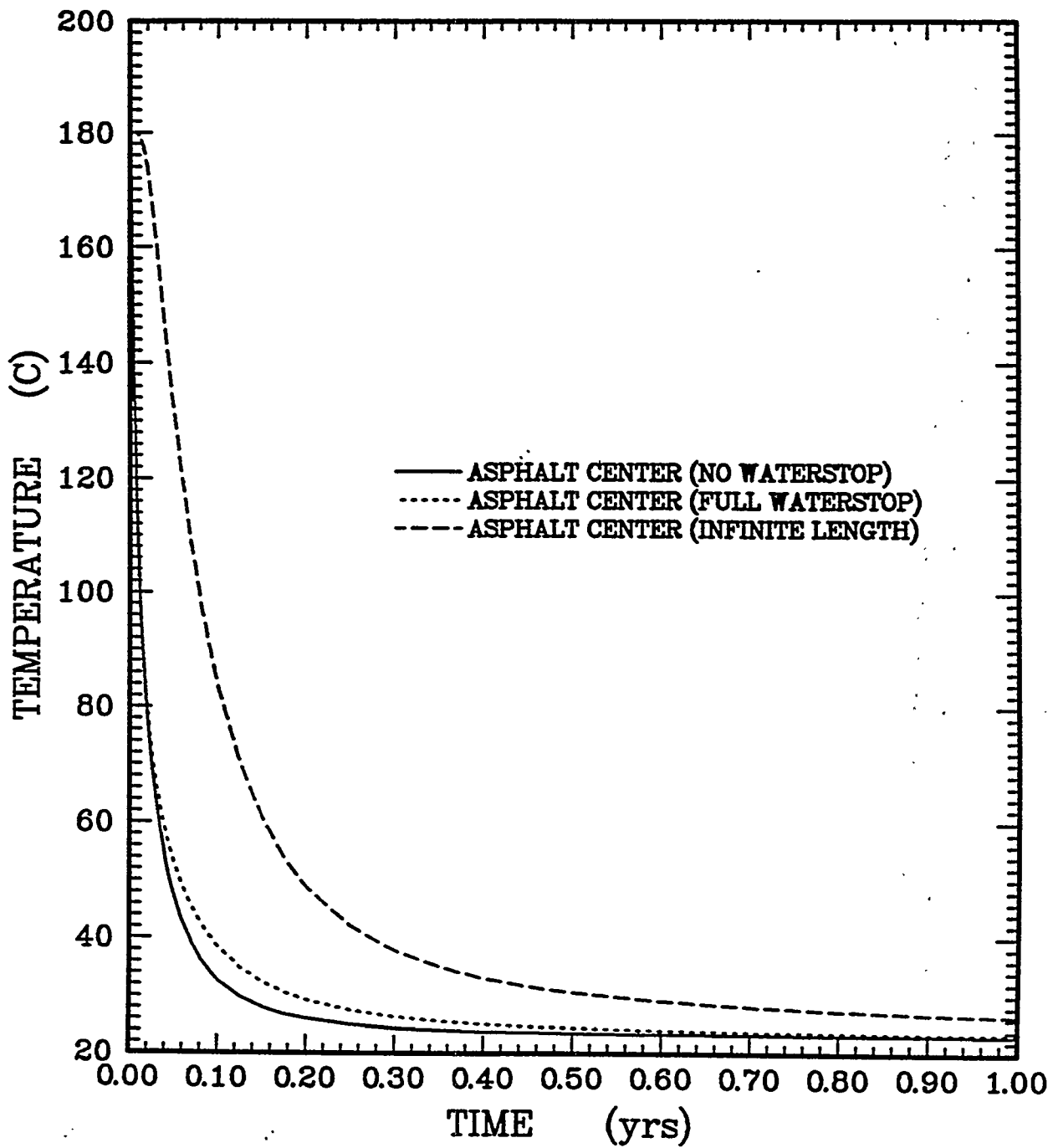


Figure D-17. Comparison of asphalt center temperatures for different waterstop configurations.

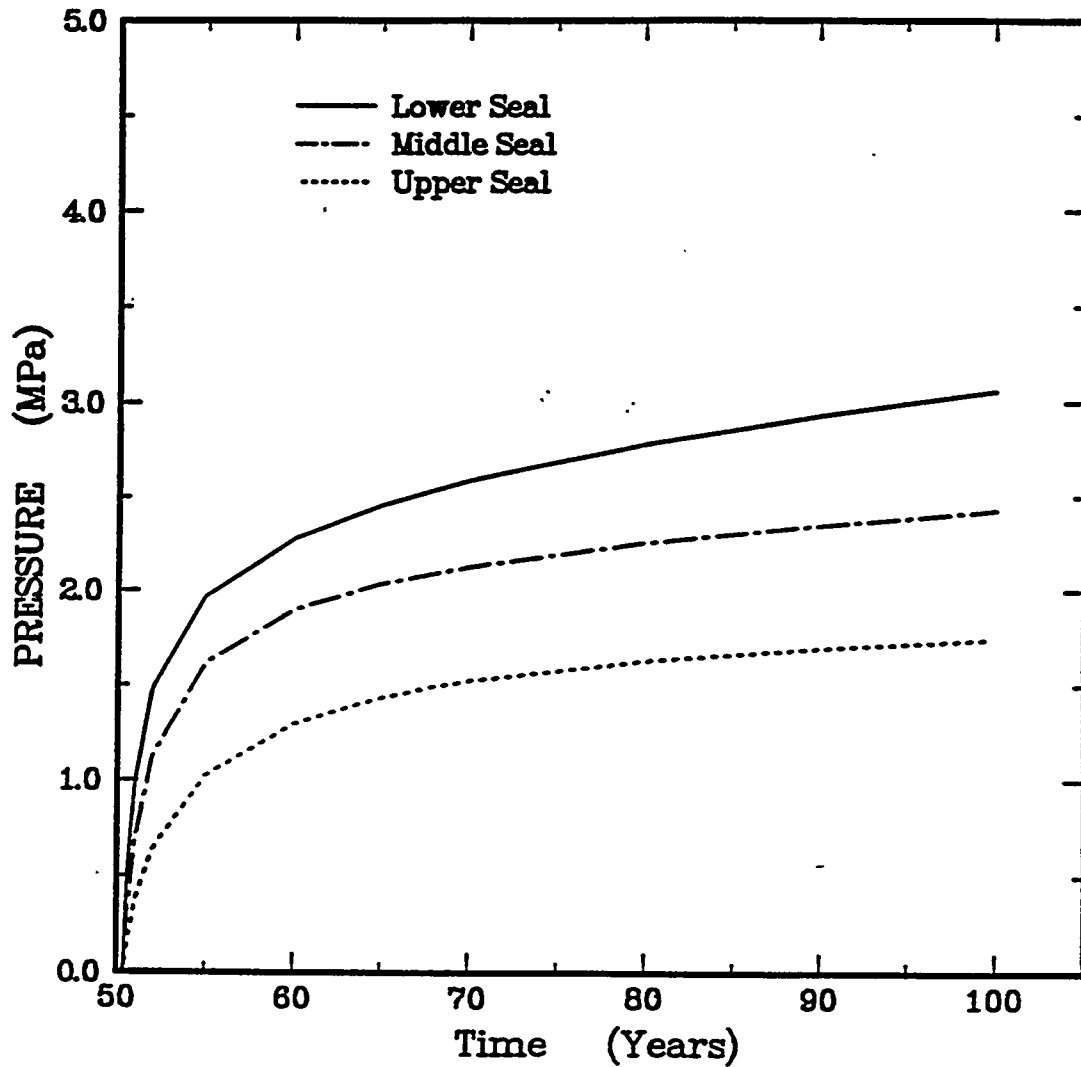


Figure D-18. Pressure buildup in the upper, middle, and lower shaft seal waterstops.

## Problem Description

The height of the asphalt column is 138 ft. The volumetric coefficient of thermal expansion for asphalt is  $0.00035/^\circ\text{F}$ .<sup>1</sup> The linear coefficient of thermal expansion for sandstone aggregate is  $0.000005/^\circ\text{F}$ ; the corresponding volume coefficient is about three times the linear coefficient, or  $0.000015/^\circ\text{F}$ . Within the column, sand and lime comprise 80% of the volume and asphalt comprises 20%. Thermal contraction can be calculated for each constituent or an equivalent coefficient can be calculated. The equivalent coefficient is:

$$\begin{aligned}\alpha_{\text{mix}} &= 0.8\alpha_{\text{sand}} + 0.2\alpha_{\text{asphalt}} \\ &= 0.8(0.000015) + 0.2(0.00035) \\ &= 0.00008/^\circ\text{F}\end{aligned}\tag{D-59}$$

## Assumptions

It is assumed that the asphalt mastic mixture will retain enough mobility that all “voids” caused by shrinkage will occur at the top of the emplacement only. That is, the mixture will flow downward as it shrinks. Accelerated creep closure of the shaft because of heating is ignored in calculating the shaft volume.

## Results

The change in height of the asphalt column is given by:

$$\begin{aligned}\Delta h &= \frac{\Delta V}{\pi r^2} = \frac{V\alpha\Delta T}{\pi r^2} = \frac{H\pi r^2\alpha\Delta T}{\pi r^2} = h\alpha\Delta T \\ &= (42.09 \text{ m})(1.44 \times 10^{-4}/^\circ\text{C})(180 - 37.78^\circ\text{C}) \\ &= 0.89 \text{ m}\end{aligned}\tag{D-60}$$

where:

- $\Delta h$  = change in height of asphalt column (m)
- $\Delta V$  = change in volume of asphalt column ( $\text{m}^3$ )
- $r$  = shaft radius (m)
- $\alpha$  = volumetric coefficient of thermal expansion ( $^\circ\text{C}$ )
- $\Delta T$  = temperature change from emplacement ( $T = 180^\circ\text{F}$ ) to cooled state ( $T = 37.78^\circ\text{C}$ ).

---

<sup>1</sup> *Standard Practice for Determining Asphalt Volume Correction to a Base Temperature*, ASTM Designation: D 4311-83, Section 3.3.

## D5. DISTURBED ROCK ZONE CONSIDERATIONS

### D5.1 General Discussion

A DRZ develops around virtually every underground excavation. The DRZ can be defined as that region near an excavation (in salt or nonsalt rock) that experiences a change in hydrological or mechanical properties. The DRZ is generally assumed to have the following characteristics:

1. dilational deformation resulting from micro- or macrofracturing,
2. decreased load-bearing capacity (loss of strength), and
3. increased fluid permeability (increase in interconnected porosity).

Characterization of the DRZ in salt requires both spatial and temporal considerations. For that purpose, the DRZ can be divided into four regimes: (1) initial creation of the DRZ resulting from stress perturbations brought on by the excavation, (2) changes in rock properties caused by "weathering" of exposed rock, (3) later changes in the DRZ extent that may occur with time as the salt creeps, and (4) a decrease in the DRZ extent (and eventual elimination) that occurs through healing of the micro- and macrofracturing when salt creep is restrained. Remediation of the DRZ may also be possible by engineering fixes such as grouting.

In situ fluid flow and permeability measurements performed in boreholes drilled from excavations in the WIPP provide a geometrical delineation of the DRZ and a measure of the hydrological properties for the DRZ. In general, the disturbance, as reflected by enhanced permeability, is restricted to about one-half the effective radius of the excavation. Within this region the permeability will increase from  $10^{-22}$  to  $10^{-23}$   $m^2$  (undisturbed permeability) at the edge of the DRZ to about  $10^{-14}$  to  $10^{-15}$   $m^2$  near the excavation surface (Knowles et al., 1996). Although this discussion relates to underground measurements in the WIPP drifts, a similar delineation of the DRZ around the AIS was observed by Dale and Hurtado (1996).

Underground observations and measurements are consistent with the description of the DRZ extending to less than one excavation radius and having permeabilities that are largest near the excavation boundary and lowest (decreasing by several orders of magnitude to salt's undamaged value) at the edge of the DRZ. Stress states around excavations, whether the instantaneous elastic distributions or the creep-induced stationary distributions, follow a similar trend. Shear stresses are largest near the excavation and become smaller at greater distances from the excavation. This similarity in trends suggests a conclusion that the DRZ can be defined in terms of the stress states existing in the salt. Laboratory testing data from independent laboratories using three different test types also support a conclusion that the onset of damage in salt (dilatant behavior) is predictable based on the stress state imposed on the salt (Van Sambeek et al., 1993a). Other laboratory testing data support a conclusion that damage within a salt specimen can be healed (in fact, healed quite rapidly) by applying favorable stress states to the damaged specimen (e.g., Costin and Wawersik, 1980; Brodsky, 1990). From these results, a conceptual model for the DRZ is developed where (1) the maximum extent of the DRZ is strictly a function of the most severe stress state ever to exist around the excavation and (2) the current extent of the DRZ is defined by the current stress state around the excavation. Implicit is that the

disturbed salt will heal “instantaneously” as the stress state is slowly changed from unfavorable (damage inducing) to favorable.

### D5.1.1 Salt Damage Models

Two salt damage models are used to define the DRZ for the WIPP seals design: the stress-invariant ratio and the damage stress criterion (Section D.3.2) model. The stress-invariant ratio states that salt will incur damage whenever the ratio between the shear stress (as measured by the second invariant of the deviatoric stress tensor) and the confining pressure (as measured by the first invariant of the stress tensor) exceeds a critical value of 0.27. Mathematically, this is:

$$\frac{\sqrt{J_2}}{I_1} \geq 0.27 \quad (D-61)$$

where  $\sqrt{J_2}$  is the shear stress measure and  $I_1$  is the confining stress measure. The relationship is based on laboratory testing data from numerous creep and quasi-static tests on WIPP and Avery Island salts. In general, the relationship seems to represent both different salts and different test types as described by Van Sambeek et al. (1993b).

The MDCF model tracks the development of porosity as result of strain-induced damage within the salt, as described in Section D3.2.1. The dominant deformation mechanism governing the dilational behavior of salt is the time-dependent microfracturing mechanism (Chan et al., 1992). This mechanism is operable for a limited range in stress states (i.e., high shear stresses relative to a low mean stress). The stress states causing microfracturing are typically most severe in the salt immediately adjacent the excavation and less severe deeper into the salt. At some depth, the mean stress increases enough and the shear stresses decrease enough that microfracturing stops; this depth defines the DRZ boundary.

Definition of the DRZ by the MDCF model is preferred over the stress-invariant ratio from a scientific viewpoint because it directly connects the variables of stress, strain, and damage (including damage reversal or healing) in one relationship, albeit a complex relationship. The stress-invariant ratio can only indicate where damage is likely to occur and when healing can begin based on changes in the stress-invariant ratio. The stress-invariant ratio provides no quantitative information about the degree of damage or the significance of the damage in terms of enhanced permeability. The stress-invariant ratio is, however, simpler to apply to engineering problems.

### D5.1.2 Salt Healing Models

Healing of damaged salt within the DRZ will occur whenever stress states no longer cause damage. This condition is reached by (1) reducing shear stress, (2) increasing the mean stress, or (3) doing both. The most practical way to achieve a more favorable stress state is to restrain the natural creep of salt by forming a barrier to closure at the free surface of the shaft. By doing so, the stress parallel to the creep deformation direction will increase in compressive magnitude. As this stress increases, the shear stress decreases and the mean stress increases, which is the situation required to reverse the damaging stress condition. Once the damaging stress state is reversed, healing of damage can begin.

Evidence for reversing damaging stress states into healing stress states can be found in (1) natural analogues, (2) laboratory tests (Costin and Wawersik, 1980), (3) in situ seal tests in the WIPP (Knowles et al., 1996), and (4) bulkheads in salt and potash mines. The physical process for healing the microfracture-damaged salt is primarily fluid-assisted pressure solution and redeposition. In addition, dislocation motion of the solid state allows further deformation of crystals to occupy space. Both mechanisms operate effectively at stresses and temperatures applicable to the DRZ around the WIPP shafts.

*Natural Analogues.* Salt formations are universally considered to have very low permeabilities, which is why salt formations are an ideal storage medium. The Salado salt formation originated as precipitate in oversaturated brines. The original porosity was huge because the salt mass was comprised of loose hopper crystals. With time and superincumbent pressure from additional salts and other sediments, the salt became impermeable, possessing essentially no voids. From this analog, suturing of grain boundaries under natural conditions is demonstrated. The geologic time available for healing is admittedly long; however, the natural stresses and temperatures for the healing process are similar to conditions expected around the WIPP shaft.

*Laboratory Test Evidence.* Brodsky (1990) and Brodsky and Munson (1994) present test results for the healing of damaged salt under isostatic stress. This work is particularly significant because the salt specimens used in the healing tests had been intentionally damaged in constant-strain-rate tests where the dilatant behavior (volumetric strain) was measured. Thus damage was quantified before the healing phase of the test. The ultrasonic velocity degradation and recovery were monitored during the damage and healing phases. The healing rate, as reflected by ultrasonic velocity recovery, depends on the original damage level, applied pressure, and temperature. The times to full recovery are short, based on the 20-day tests at a 20°C to 70°C range of test temperatures. Therefore, once the seal components restrain the creep of salt and cause confining stresses to develop in the salt, crack closure and healing in the DRZ will be rapid.

*In Situ Seal Tests.* Tests at the WIPP known as Small-Scale Seal Performance Tests (SSSPTs) have shown that large-diameter borehole seals constructed of bentonite and concrete provide nearly impermeable barriers to fluid flow. These seals were emplaced in boreholes drilled into the ribs and floor of a 5.5-m-square room. Thus the boreholes were drilled into a DRZ surrounding the room, and the borehole created a supplementary DRZ around itself. The time lapse between drilling the borehole and emplacing the seal was several months, so ample time was allowed for the DRZ to develop. Testing of the borehole seals 9 years after emplacement revealed no leakage through the DRZ. The DRZ must therefore have been healed because the borehole seal caused a stress state to reestablish that was conducive to healing.

*Bulkheads in Salt and Potash Mines.* The Rocanville potash mine in Saskatchewan provides one compelling case history for healing of a salt DRZ. An exploratory drift in the mine entered a barren salt zone (devoid of sylvite, so the surrounding rock was halite) and sustained a brine inflow. Within about a month, a concrete bulkhead was built in the drift, including construction grouting of the interface between the bulkhead and the salt. After sealing the drift, the brine pressure behind the bulkhead reached a near hydrostatic pressure greater than 8 MPa and remained at that pressure for more than 10 years. There is no evidence of leakage through either the bulkhead or the salt DRZ surrounding the drift. Although the drift was blocked at an early

age, a DRZ must have formed instantaneously with the excavation of the drift. To be consistent with the observations, this DRZ must have been healed to avoid leakage during a 10-year time span. This bulkhead remains accessible and continues to function perfectly.

## **D5.2 Disturbed Rock Zone Analyses**

### **D5.2.1 Analysis of the Disturbed Rock Zone in Salado Salt**

#### **Objective**

The objective of this calculation was to determine the spatial extent of the DRZ in the intact salt surrounding the shaft for each of the four shaft seal materials (i.e., concrete, crushed salt, compacted clay, and asphalt). This information was used to define the input parameters to the fluid-flow calculations reported in Section 8 of the main report.

#### **Problem Description**

The radial extent of the DRZ within the intact salt was determined using a series of "pineapple-slice" models. Each model corresponds to a depth (and its associated initial temperature and stress conditions). Figure D-11 shows the schematic model geometry, which includes an axisymmetric representation of the shaft and surrounding host rock at a fixed depth. The outer (right) boundary is located 50 shaft radii from the axis of symmetry, the shaft centerline. The boundary condition at the outer boundary is maintained at the initial stress magnitude, i.e., the lithostatic stress.

Five depths were chosen to be representative of conditions along the length of the shaft within the Salado Formation. Specifically, depths of 250, 350, 450, 550, and 650 m were considered in this analysis. The initial stress and temperature conditions for these depths were determined as shown by the notes to Table D-17. Four moduli of elasticity were considered to approximate the seal materials of asphalt, compacted clay, crushed salt, and salt-saturated concrete. Five depths are considered adequate to determine a functional relationship between the DRZ radial extent and depth for each seal material type.

In the analysis for times  $t < 0$  year, the shaft is not present, and an initial lithostatic stress field exists in the salt. At time  $t = 0$  year, the cylindrical shaft is excavated, and the surrounding salt is allowed to creep for 50 years, i.e., the operational period. At time  $t = 50$  years, the shaft is sealed. In the analyses, salt surrounding the shaft continues to creep against the seal material and consolidates the seal material (if applicable) for an additional 100 years. The time-dependent radial extent of the DRZ was calculated for each model (depth) and seal material-type. The damage-stress criterion for argillaceous salt (see Section D3.3.2) was used to estimate the spatial extent of the DRZ as a function of time for each of the models considered.

#### **Assumptions**

- The stratigraphy surrounding the AIS is modeled as being entirely argillaceous salt.
- The initial stress state prior to excavation is lithostatic.
- The modeled region remains isothermal.

- The shaft excavation and seal material emplacement are performed instantaneously at times of 0 and 50 years, respectively.
- The shaft is sufficiently isolated from other excavations so that only the shaft is considered in the analysis. Axisymmetric conditions are, therefore, applicable and a condition of plane strain exists with respect to the axial (vertical) direction.
- The calculations are based on finite deformation solutions.
- The damage stress criterion can be used to define the spatial extent of the DRZ.
- Short-term thermally enhanced salt creep is ignored.
- Pore pressure effects are not incorporated.
- A Tresca flow rule was used for intact salt.

## Results

The results of this calculation are shown in Figures D-19 through D-23 in terms of the normalized DRZ radius as a function of backfill stiffness (i.e., elastic modulus) at various depths within the Salado Formation at times 0, 10, 25, 50, and 100 years after emplacement, respectively. The normalized DRZ radius is defined as the ratio of the radius to the DRZ boundary and the shaft radius. The radius to the DRZ boundary is defined as the location where the damage stress (Equation D-54) is equal to zero. For all backfill types, the most conservative (i.e., largest) estimate of the extent of the DRZ was calculated using the minimum value of the material's stiffness.

The concrete seals are located at approximate depths of 301, 420, and 608 m. An elastic modulus of 30 GPa was used for concrete, corresponding to the 28-day stiffness according to Equation D-4. Using the results shown in Figures D-19 through D-23, the normalized DRZ radii surrounding the three concrete seals are summarized in Table D-18 for times of 0, 10, 25, 50, and 100 years after emplacement.

The compacted-salt column is located at depths ranging from 420 to 600 m. A minimum elastic modulus of 7.5 GPa was used for compacted crushed salt, corresponding to the emplaced fractional density of 90% using Equation D-7. Using the results shown in Figures D-19 through D-23, the normalized DRZ radii surrounding the compacted crushed salt seal are summarized in Table D-19 at the top (429 m), middle (515 m), and bottom (600 m) of the column at times 0, 10, 25, 50, and 100 years following emplacement.

Compacted clay is used as a shaft seal in two locations within the Salado Formation. The upper Salado compacted clay column is located at depths between 307 and 413 m. The lower Salado compacted clay column is located at depths between 617 and 643 m. An elastic modulus of 1.2 GPa was assumed for compacted clay, corresponding to a fractional density of 90% according to Equation D-18. Using the results shown in Figures D-19 through D-23, the normalized DRZ radii surrounding the compacted clay seals are summarized in Table D-20 at the top and bottom of the upper and lower Salado compacted clay columns at times 0, 10, 25, 50, and 100 years following emplacement.

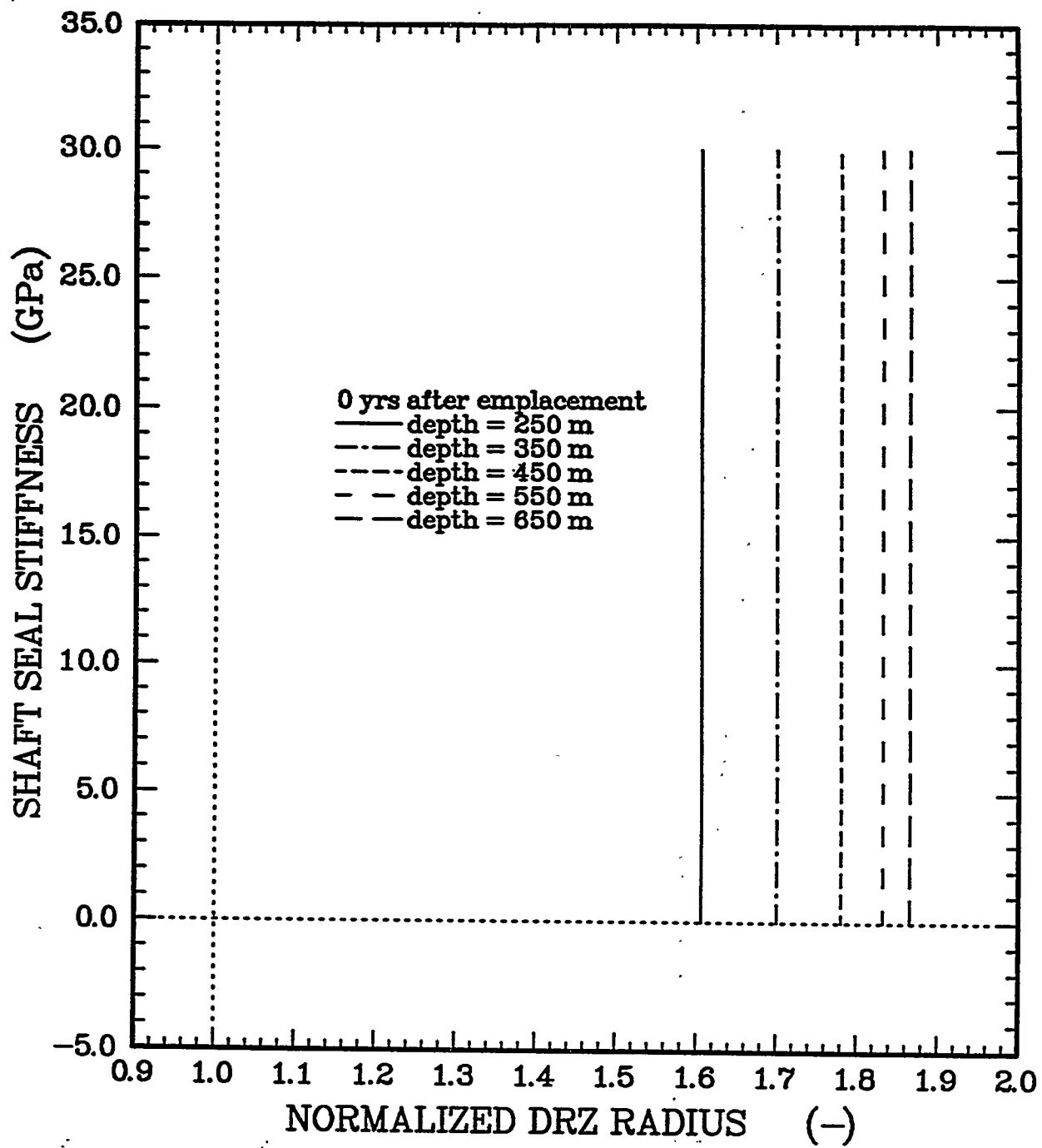


Figure D-19. Normalized DRZ radius as a function of shaft seal stiffness at various depths within the Salado Formation at time = 0 year after emplacement.

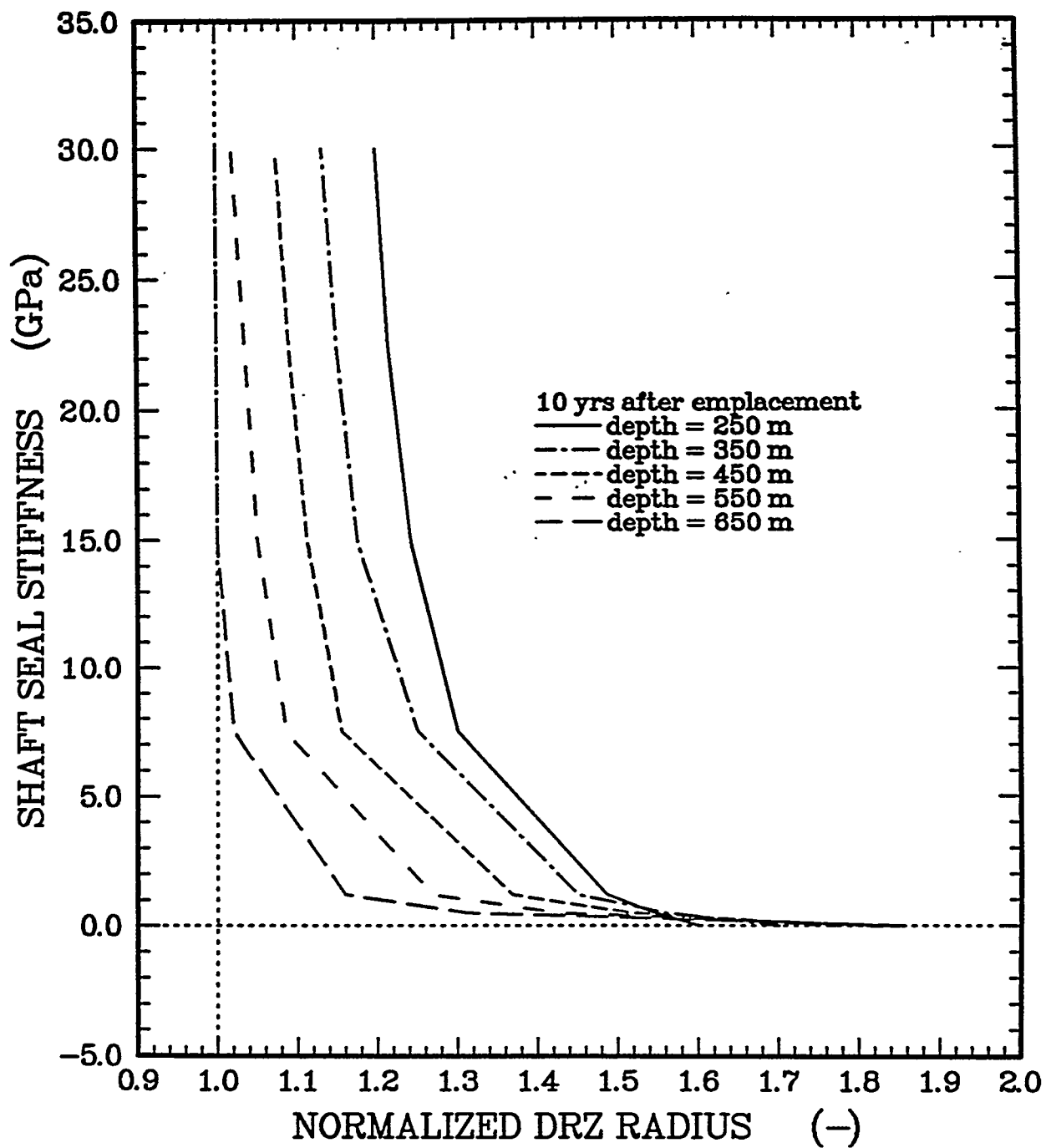


Figure D-20. Normalized DRZ radius as a function of shaft seal stiffness at various depths within the Salado Formation at time = 10 years after emplacement.

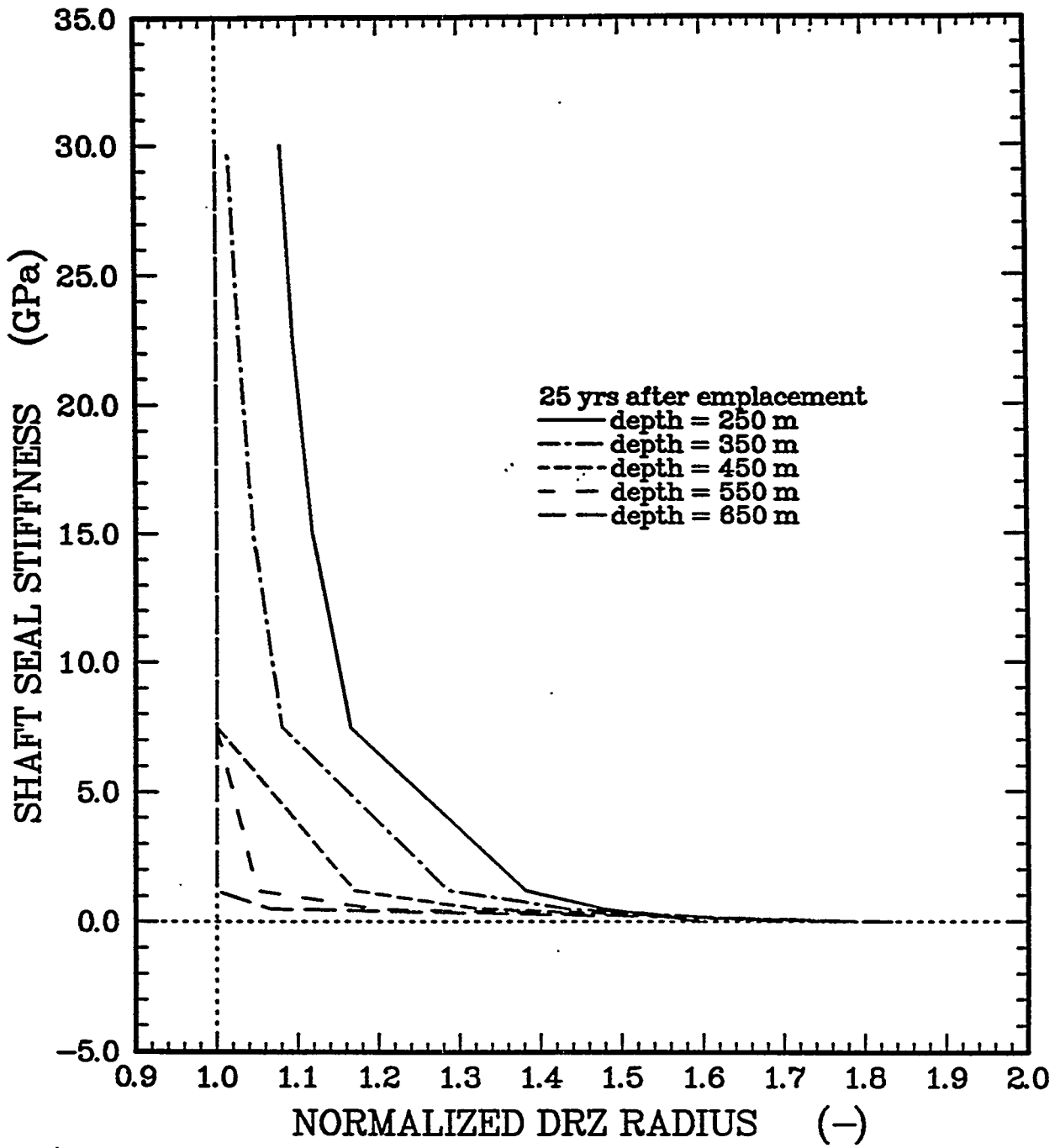


Figure D-21. Normalized DRZ radius as a function of shaft seal stiffness at various depths within the Salado Formation at time = 25 years after emplacement.

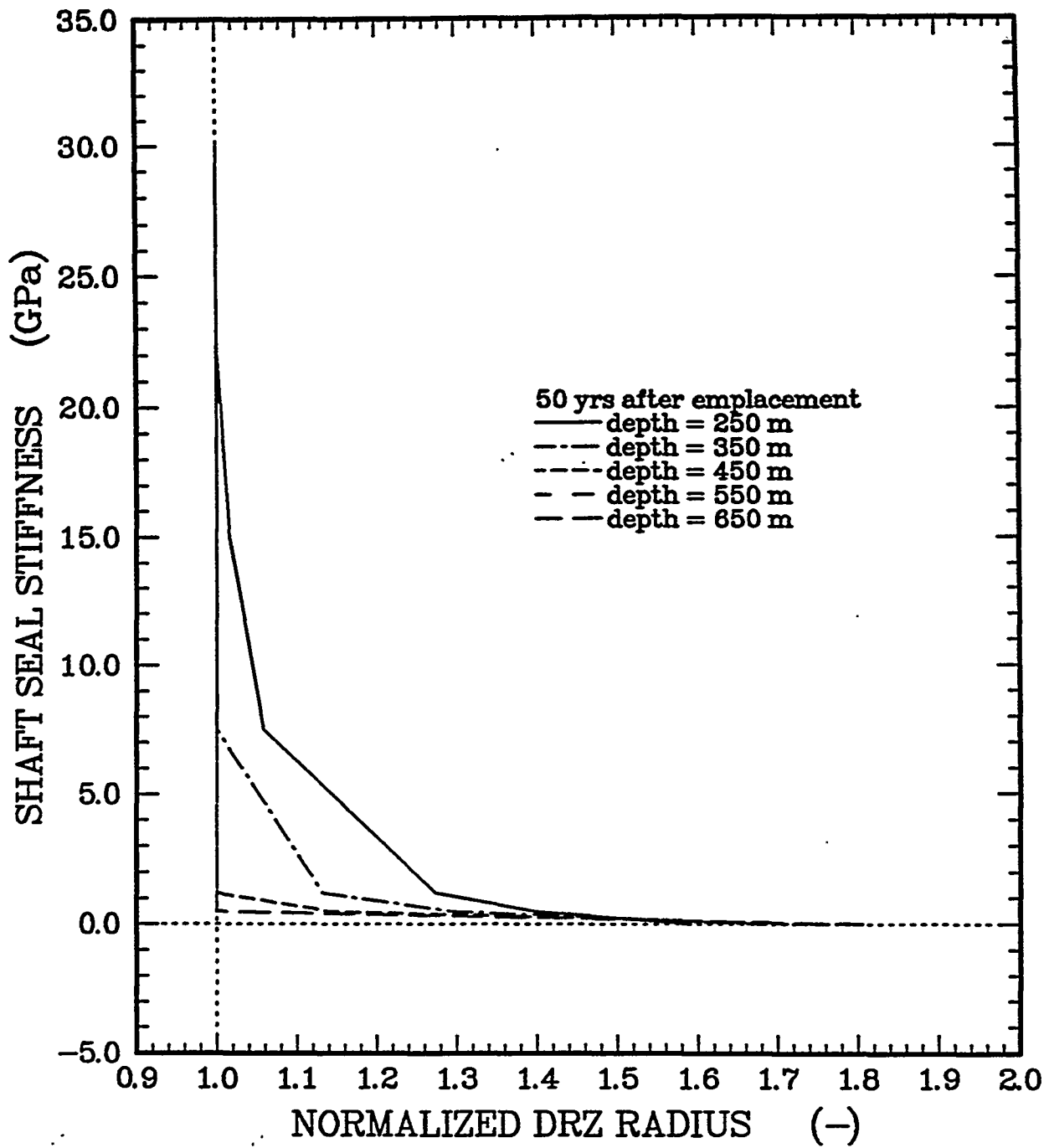


Figure D-22. Normalized DRZ radius as a function of shaft seal stiffness at various depths within the Salado Formation at time = 50 years after emplacement.

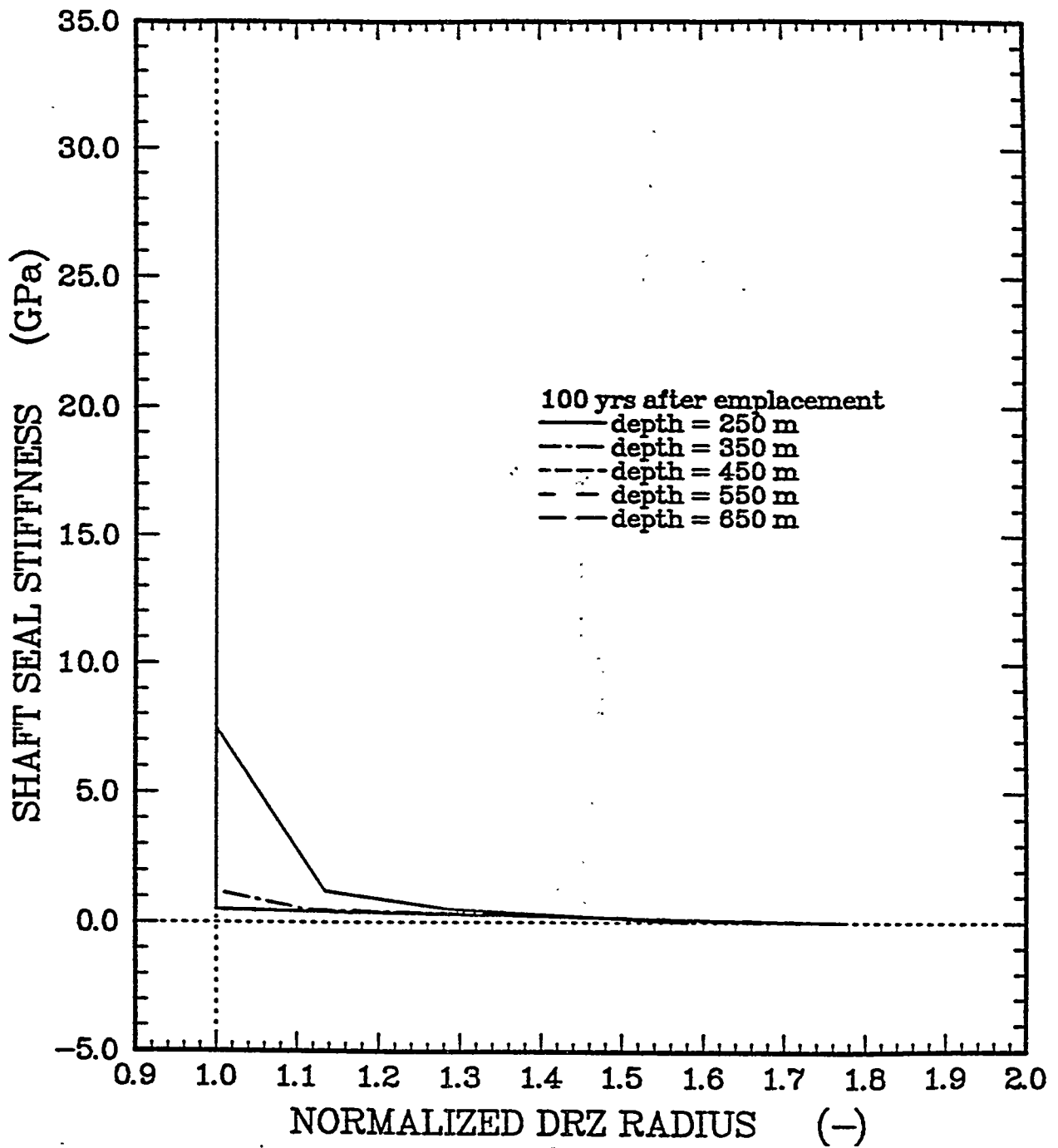


Figure D-23. Normalized DRZ radius as a function of shaft seal stiffness at various depths within the Salado Formation at time = 100 years after emplacement.

Table D-18. Normalized DRZ Radius—Concrete

Concrete Component	Time After Emplacement (yrs)				
	0	10	25	50	100
Upper (d = 301 m)	1.65	1.16	1.05	1.00	1.00
Middle (d = 421 m)	1.76	1.09	1.01	1.00	1.00
Lower (d = 608 m)	1.85	1.01	1.00	1.00	1.00

Table D-19. Normalized DRZ Radius—Crushed Salt

Depth	Time After Emplacement (yrs)				
	0	10	25	50	100
Upper (d = 429 m)	1.77	1.20	1.02	1.00	1.00
Middle (d = 510 m)	1.82	1.11	1.01	1.00	1.00
Lower (d = 600 m)	1.85	1.05	1.00	1.00	1.00

Table D-20. Normalized DRZ Radius—Compacted Clay

Depth	Time After Emplacement (yrs)				
	0	10	25	50	100
Top of USCCC (d = 308 m)	1.66	1.47	1.32	1.19	1.06
Bottom of USCCC (d = 413 m)	1.75	1.40	1.21	1.05	1.00
Top of LSCCC (d = 616 m)	1.85	1.22	1.03	1.00	1.00
Bottom of LSCCC (d = 643 m)	1.86	1.20	1.02	1.00	1.00

USCCC = upper Salado compacted clay column; LSCCC = lower Salado compacted clay column.

Asphalt is used as a shaft seal material from the Rustler/Salado interface to the top of the upper concrete component (depths between 256 and 293 m). A minimum elastic modulus of 0 GPa was assumed for asphalt, corresponding to its unsolidified stiffness.

Using the results shown in Figures D-19 through D-23, the normalized DRZ radii surrounding the asphalt seal are summarized in Table D-21 at the top and bottom of the column at times 0, 10, 25, 50, and 100 years after emplacement.

Table D-21. Normalized DRZ Radius—Asphalt

Depth	Time After Emplacement (yrs)				
	0	10	25	50	100
Top (d = 256 m)	1.61	1.61	1.60	1.59	1.58
Bottom (d = 293 m)	1.65	1.65	1.64	1.63	1.62

### D5.2.2 Salado Anhydrite Beds

The material behavior of the interbeds within the Salado Formation is assumed to be elastic (time-invariant); in contrast, the salt creeps (time-dependent). Therefore the interbeds will tend to inhibit creep closure of the shaft. In addition, the salt creep that does occur will tend to increase the potential for fracturing within the interbeds because of shear tractions that develop along the interface. The thickness of the interbeds relative to the thickness of the salt above and below the interbeds determines which of the two behaviors will dominate. That is, the thicker the interbeds, the less salt creep will occur; and the thicker the salt bed layer, the greater the potential for fracturing the interbeds.

#### Objective

The objective of this calculation is to determine the extent of the DRZ within the Salado anhydrite and polyhalite interbeds as a result of the creep of the surrounding salt. The definition of the DRZ within these interbeds was used in the fluid-flow consolidations reported in Appendix C.

#### Problem Description

The problem description and assumptions used in performing this calculation are the same as those presented in Section D4.1.2. The marker bed locations relative to the concrete seal components are shown in Figures D-7 and D-9. The deformational and strength properties of the anhydrite and polyhalite materials are given in Table D-15.

#### Results

The results are summarized in Figures D-24 and D-25, which show a calculated factor of safety against failure for the various anhydrite and polyhalite layers as a function of radial distance from the shaft after the shaft has been left open for 50 years.

For all interbeds, the factor of safety increases as the distance from the shaft wall increases. Further, with the exception of MB117, the factor of safety is greater than one (no DRZ) for all interbeds. For MB117, the failure (DRZ) is localized to within 1 m of the shaft wall.

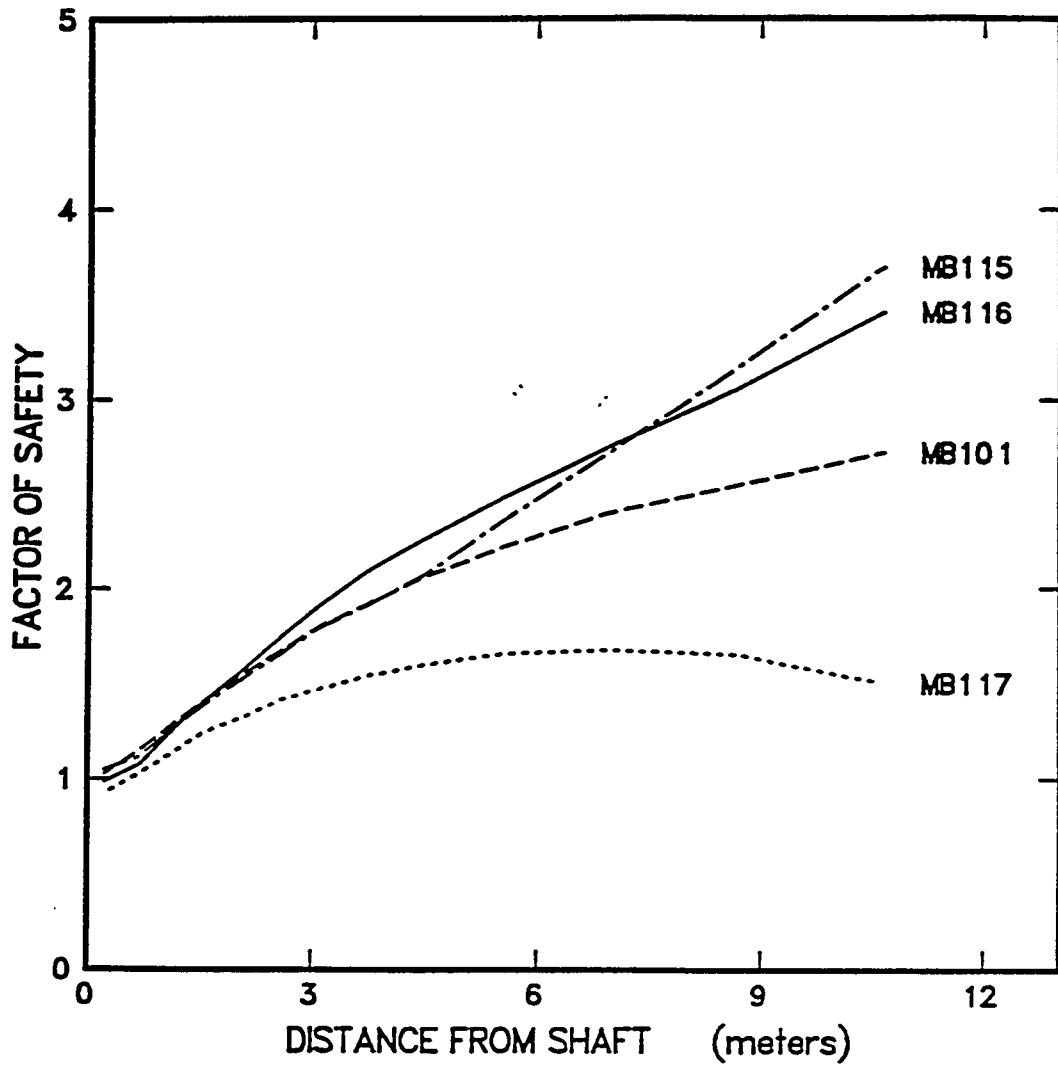


Figure D-24. Factor of safety in polyhalite beds at 50 years.

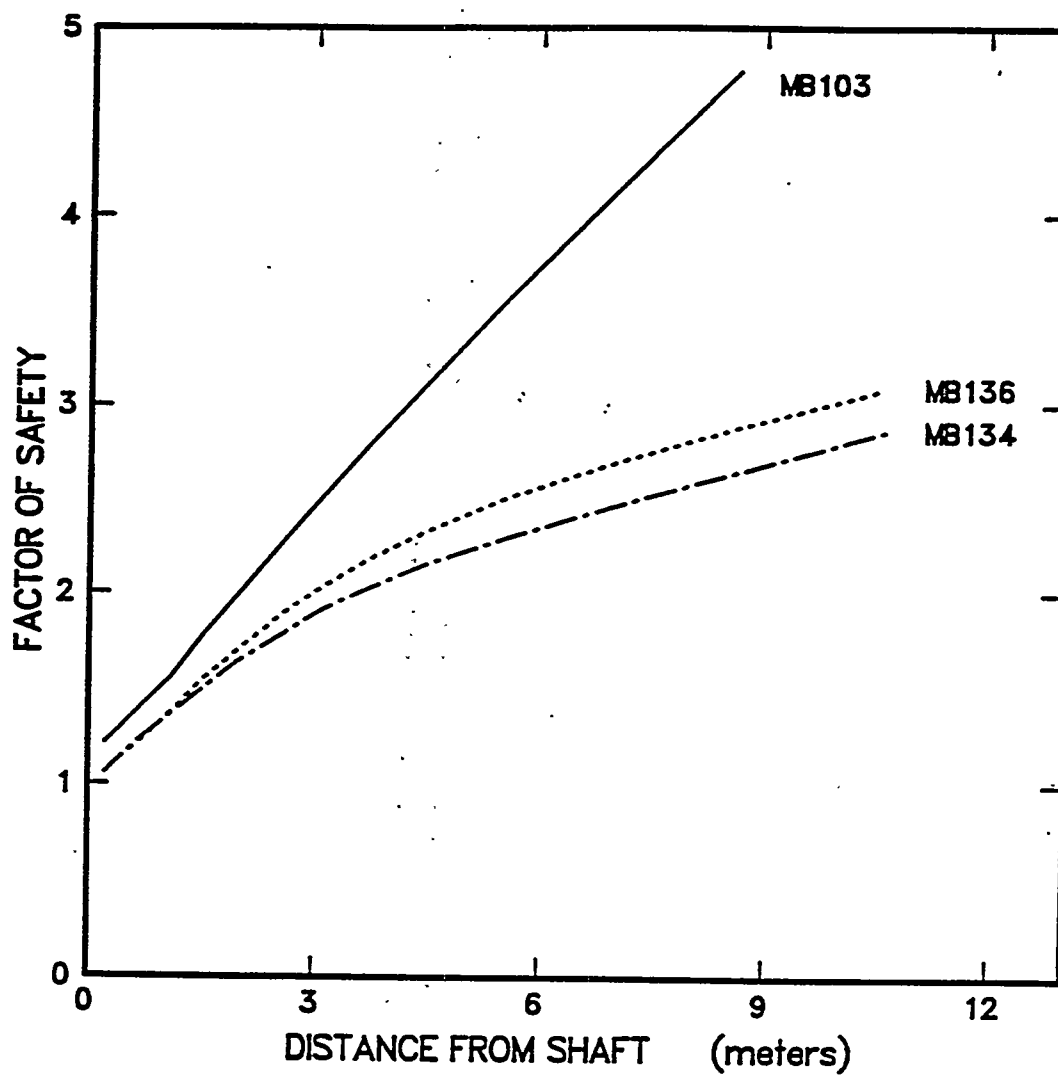


Figure D-25. Factor of safety in anhydrite beds at 50 years.

### D5.2.3 Near Surface and Rustler Formations

The DRZ around a circular opening (such as a shaft) was estimated using analytical means. The extent of the DRZ in the formations above the Salado was calculated based on two criteria for rock failure. The shaft excavation superimposes an increment of damage or disturbance on any natural preexisting disturbance in the host rock. In the near-surface and Rustler formations at the WIPP, the development of the DRZ is assumed to be time-invariant; rock behavior is observed to be elastic.

#### Objective

The objective of this calculation is to determine the extent of the DRZ surrounding the shafts in the near-surface and Rustler formations. The rock types that compose these formations are anhydrite, dolomite, and mudstone and exhibit time-invariant behavior.

#### Problem Description

The rock surrounding the shafts can be divided into two regions: the DRZ region in which the rock fails (plastic region) and a region that behaves elastically. The geometry of the regions is defined as:

$$\begin{aligned} \text{DRZ region: } & a \leq r \leq R \\ \text{Elastic region: } & R \leq r \leq \infty \end{aligned} \tag{D-62}$$

where  $a$  is the shaft radius and  $R$  is the radius to the interface between the plastic and elastic regions. The radius  $R$  can be calculated so that the radial stress distribution is continuous across the interface and satisfies the boundary conditions at the shaft wall and the far field. Similarly, stress distributions in the plastic zone are assumed to just satisfy the failure criterion.

The Coulomb failure criterion accounts for the beneficial effect of confinement and says failures occur whenever:

$$\begin{aligned} \sigma_1 - \sigma_3 &\geq C_0 + \sigma_3(\tan\beta - 1) \\ \tan\beta &= \frac{1 + \sin\phi}{1 - \sin\phi} \end{aligned} \tag{D-63}$$

where  $\phi$  is the angle of internal friction (Table D-16). The radius to the elastic/plastic interface based on the Coulomb failure criterion (Ladanyi, 1974) is:

$$\text{Coulomb: } R/a = \left[ \frac{P_0 + T_0 - mC_0}{T_0} \right]^{1/(\tan\beta - 1)} \tag{D-64}$$

where:

- $P_0$  = far-field stress magnitude
- $T_0$  = tensile strength =  $S_0 / \tan\phi$  (Table D-15)
- $C_0$  = cohesion (Table D-15).

Because of scale effects, rock is seldom as strong in situ as laboratory strength tests indicate. This scale effect is shown, for example, by Goodman (1980), who suggests a factor of safety (strength reduction factor) of five for foundation designs. The in situ strength of the rock was determined by reducing the matrix strength (based on a literature survey of laboratory tested strengths) by a factor ranging from three to five. To span the uncertainty in the horizontal stress magnitude, the in situ (far-field) stress was taken to be a multiple of between one to two times the vertical stress. The intermediate value for each parameter was used as the likely parameter value for southeastern New Mexico. These parameters should result in a conservative estimate of the DRZ within these formations.

## Results

The results of this calculation are shown in Figure D-26, which shows the radial extent of the DRZ as a function of depth. These results indicate that the DRZ is not present at depths less than 50 m and for the depth interval from 165 m to 213 m (principally, an anhydrite and dolomite interval). For the mudstones between 50 and 165 m and between 223 and 260 m, the radial extent of the DRZ increases with depth, reaching a maximum of 2.6 shaft radii at a depth of 260 m. The results of this analysis were used to define the initial conditions to the fluid-flow calculations predicted in Section 8.

## D6. OTHER ANALYSES

This section discusses two supplementary analyses performed to support the shaft seal design: (1) the DRZ created by asphalt waterstops and (2) potential benefits from shaft station backfilling.

### D6.1 Asphalt Waterstops

The DRZ is potentially a major contributor to fluid flows past a shaft seal, regardless of which seal materials are emplaced within the shaft. Therefore, to increase the confidence in the overall shaft seal system, low permeability layers (termed radial waterstops) intersect the DRZ surrounding the shaft to impede fluid flow. These waterstops are emplaced to alter the flow direction either inward toward the shaft seal or outward toward the intact salt. The waterstop effectively blocks the full cross section of the shaft and DRZ using a virtually impermeable material (asphalt). The waterstop is thin so that its height is small relative to its width (radius); a small ratio between height and width will concentrate the new DRZ at the edge of the waterstop. The extent of the new DRZ is small, so the area for fluid leakage past the waterstop is also small.

### Objectives

The objectives of this calculation were (1) to estimate the additional damage introduced by excavating the radial slot in the shaft wall and (2) to analyze the potential for healing this induced DRZ.

**Strength Reduction = 4.0**  
**Horizontal Stress Factor = 1.5**

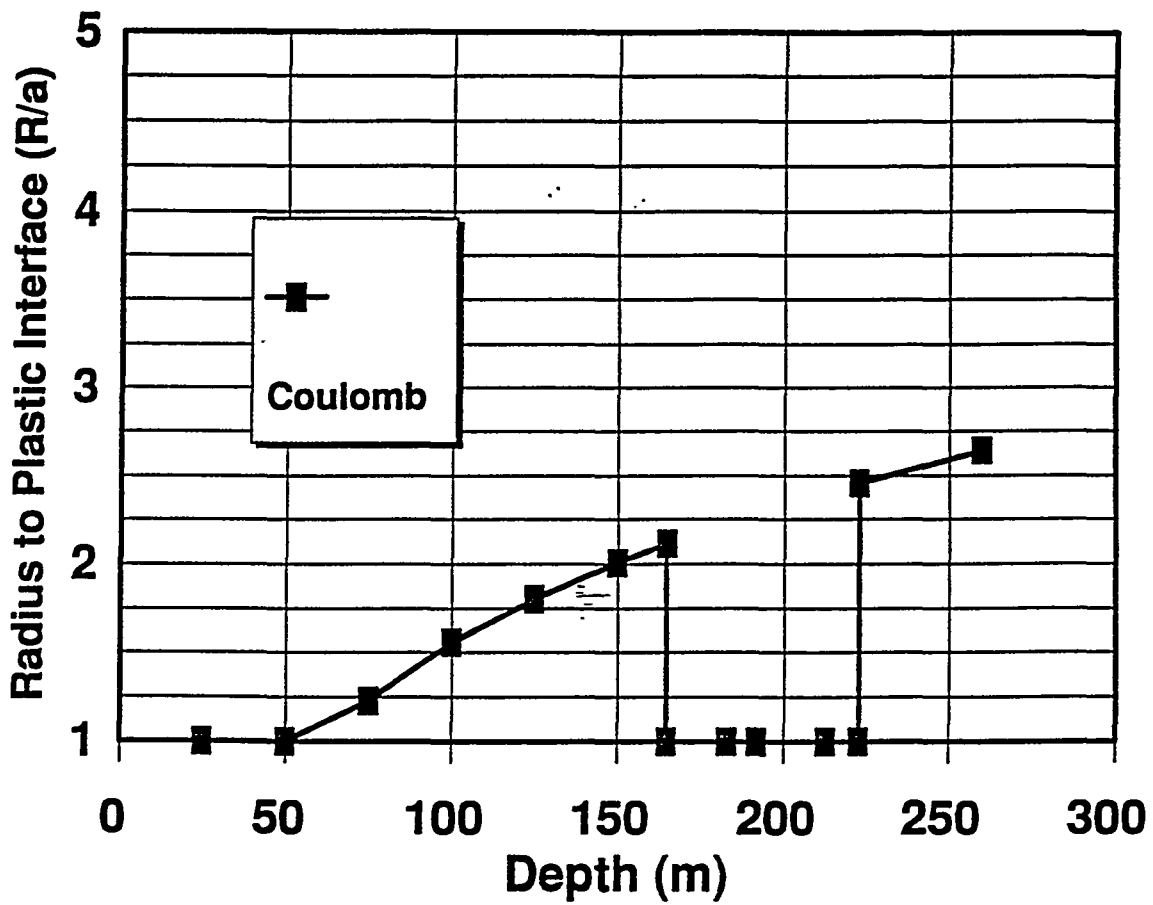


Figure D-26. Normalized DRZ radius for strength reduction factor of 4 and horizontal stress factor of 1.5.

## Problem Description

The problem description and assumptions used in performing this calculation are the same as those presented in Section 4.1.2. The damage-stress criterion was used to indicate the spatial extent of the DRZ; i.e., zones with positive damage stress were assumed to be damaged and zones with negative damage stress were assumed to be either undamaged or healed. The rate of healing was assumed to be instantaneous; i.e., zones where the damage stress changed from positive to negative were assumed to be healed immediately.

## Results

The results from analysis of the lower concrete component waterstop are presented here; the structural behavior of the other two waterstops is similar. Figures D-27, D-28, and D-29 show contours of damage stress surrounding the lower concrete component waterstop just before excavation of the waterstop, immediately after excavation, and 20 years after emplacement of the asphalt and concrete seals. Figure D-27 indicates that the DRZ before excavating the waterstop is contained spatially within the salt to a radial distance of less than one shaft radius (about 3 m). Figure D-28 indicates that the DRZ extends radially to approximately 1.4 shaft radii (4.3 m) into the salt as a result of the waterstop excavation. This extension of the DRZ is localized within the span of the concrete seals and approaches the waterstop kerf edge. The results shown in Figure D-29 indicate that the DRZ has reduced substantially in size as a result of emplacement of the concrete and asphalt seals and 20 years creep of the surrounding salt. After 20 years, the spatial extent of the DRZ is localized near the asphalt/concrete interface, extending spatially into the salt a distance of less than 2 m. For input to the fluid-flow calculations, a time of 2 years was estimated for the asphalt waterstop to become effective in terms of sealing off flow through the DRZ.

### D6.2 Shaft Pillar Backfilling

The underground portion of the WIPP is quite small when compared to most salt and potash mines. Nonetheless, subsidence will occur as the underground openings close because of creep in the salt. The amount of subsidence depends on the volume of space remaining in the repository at the time of closure. The volume of space (void) will consist of empty access drifts, backfilled entries, and filled waste rooms. The waste rooms are expected to have a 63.8% porosity after accounting for the voids in the waste containers, voids between containers, and headspace in the room (Callahan and DeVries, 1991). Similarly, backfilled entries are expected to retain a porosity of about 40% following mechanical placement of salt backfill (backfill fractional density of 0.6). Subsidence of the ground around the shafts could conceivably disturb the shaft seals. Backfilling the entries in the shaft pillar would reduce the eventual subsidence.

### Objective

The objective of this calculation was to assess the benefits of backfilling the shaft pillar in terms of reducing the subsidence of the shaft seal and therefore decreasing the potential for differential settlement within the seal.

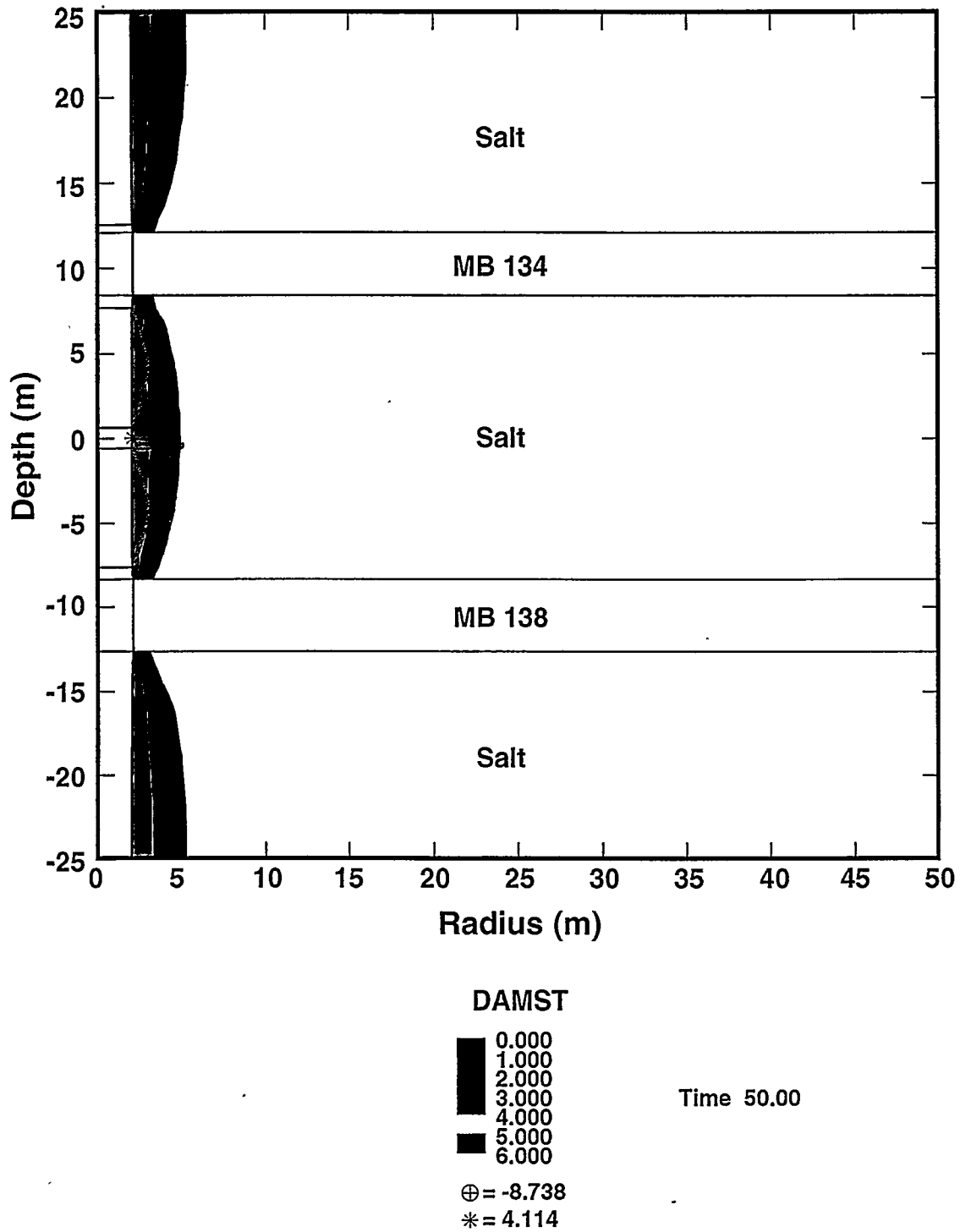


Figure D-27. Salt DRZ around the lower shaft seal at 50 years (prior to seal construction).

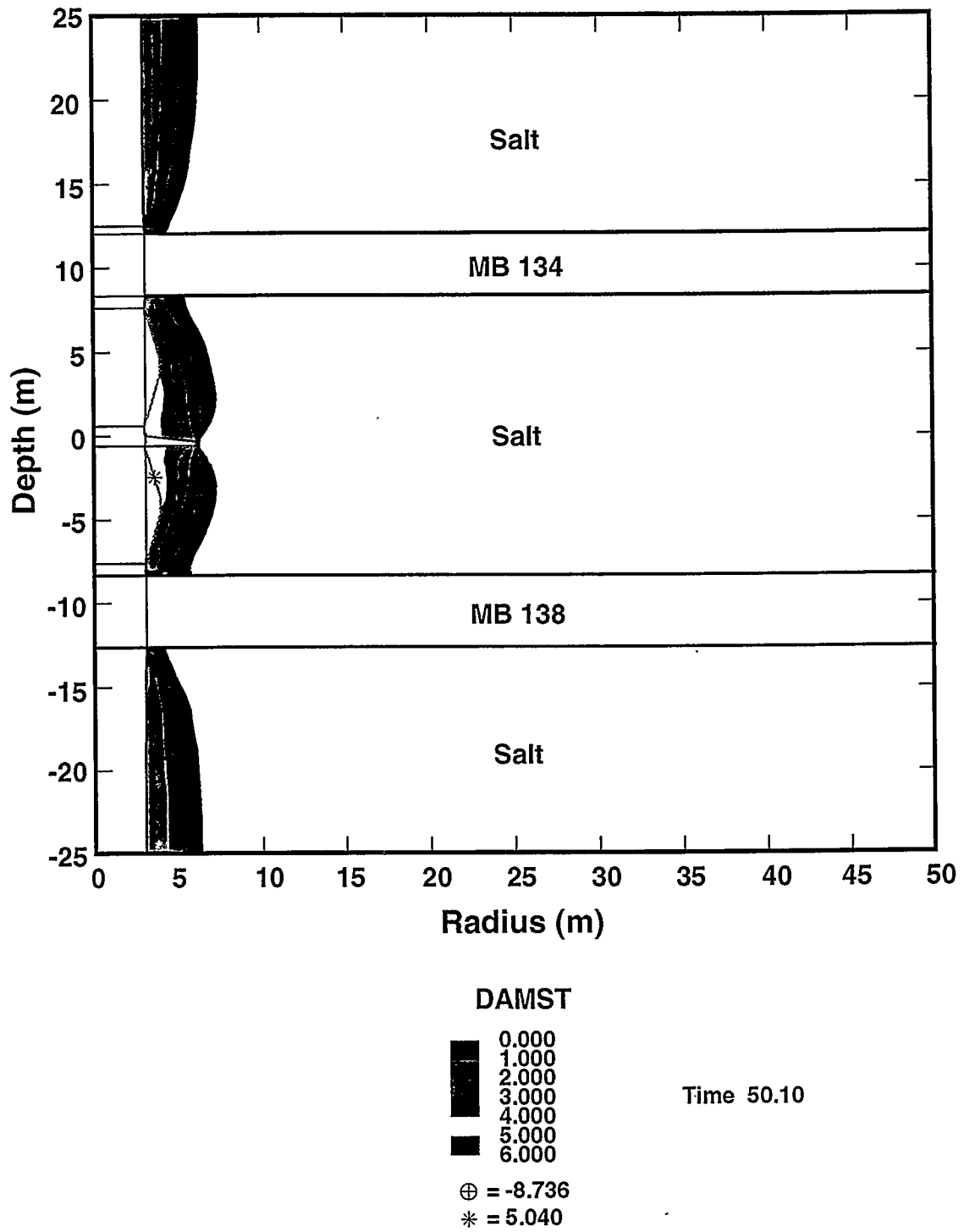


Figure D-28. Salt DRZ around the lower shaft seal at 50.1 years (after excavations but before seal construction).

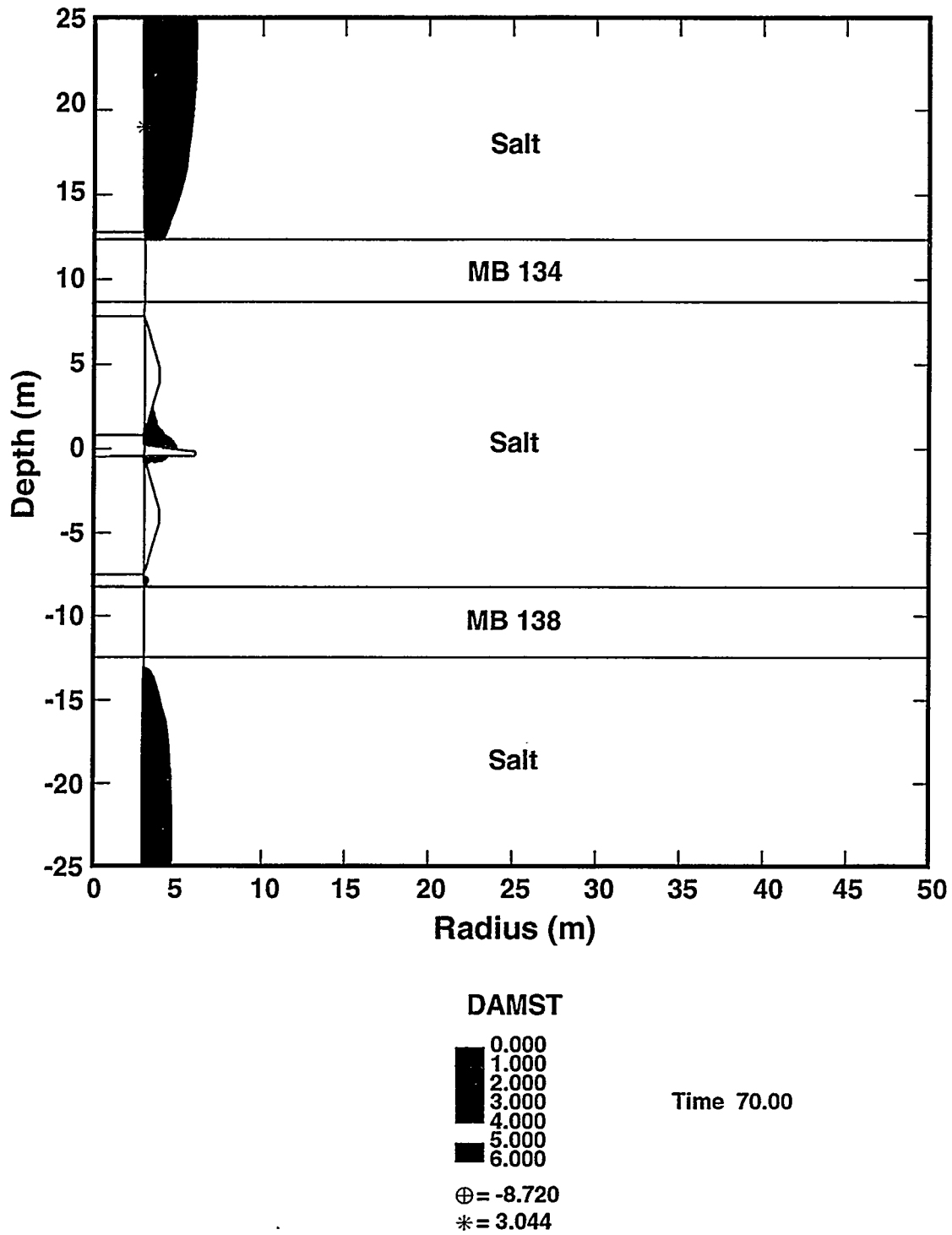


Figure D-29. Salt DRZ around the lower shaft seal at 20 years after seal construction.

## Problem Description

The subsidence analysis for this calculation was performed using the computer program SALT\_SUBSID, which is distributed by the Solution Mining Research Institute (Nieland, 1991). Mathematically, the numerical model is represented by:

$$S(x, y) = \sum_j F(x_j, y_j, D, A_j, V_j) \quad (\text{D-65})$$

where  $S$  is the ultimate subsidence at the  $x, y$  coordinates of a point on the surface after total closure of the underground openings. The function  $F(x_j, y_j, D, A, V_j)$  describes the spatial variation of ultimate subsidence for individual mining areas with centers at  $x_j, y_j$ , at depth  $D$ , of rectangular area  $A_j$ , and volume  $V_j$ . The spatial function,  $F$ , is based on the displacement discontinuity solution for the surface displacement after the closure of a rectangular prismatic opening in an elastic half space. The theoretical basis for the function was obtained from papers by Davis (1983).

The primary input to SALT\_SUBSID is the underground opening geometries. The coordinates of the entries and rooms were taken from an AutoCad rendering of the WIPP site. The mining blocks used as input to the analysis are shown in Figure D-30. (The representation is sufficiently accurate for purposes of this calculation but not accurate to the extent that the individual coordinates can be relied on for any other purposes.)

Eight panels of waste rooms were represented in the subsidence model. The height of the waste rooms was set to 8.29 ft based on an excavated height of 13 ft and a filled waste-room porosity of 63.8%. The waste rooms are close enough to affect the surface subsidence at the shaft collars; they probably are not close enough to affect subsurface subsidence at the shaft seal locations.

Two backfilled areas were considered: backfilled areas of either 200 or 300-ft radius around each of the four shafts. To account for backfilling, the entry height was adjusted for any portion of the entries within the circular area around each shaft. The adjusted height was 4.33 ft based on an assumed backfill porosity of 30% and a nominal 1-ft headspace for the originally 12-ft-tall entries. For each scenario, the ultimate subsidence was calculated. This subsidence results from total closure of the shaft pillar workings.

## Results

The ultimate subsidence was calculated for the three scenarios: no backfill in the shaft area, 61-m (200-ft) radius backfilled areas, and 91-m (300-ft) radius backfilled areas around the shafts. Over the shaft area, the ultimate surface subsidence is about 0.15 m (0.5 ft) or less depending on the backfill situation. Figure D-31 shows profiles of the ultimate subsidence over the shaft area; the profile is north-to-south, centered on the salt-handling shaft. The ultimate surface subsidence in the shaft area is reduced from 0.15 m (0.5 ft) for the no backfill condition to 0.13 m (0.44 ft) and 0.12 m (0.41 ft) by backfilling to 61 m and 91 m radii, respectively. As a matter of interest, the maximum subsidence for WIPP is centered over the waste panel area with a magnitude of 0.26 m (0.85 ft). The restriction in subsidence is not considered to be enough that it warrants backfilling the shaft pillar area.

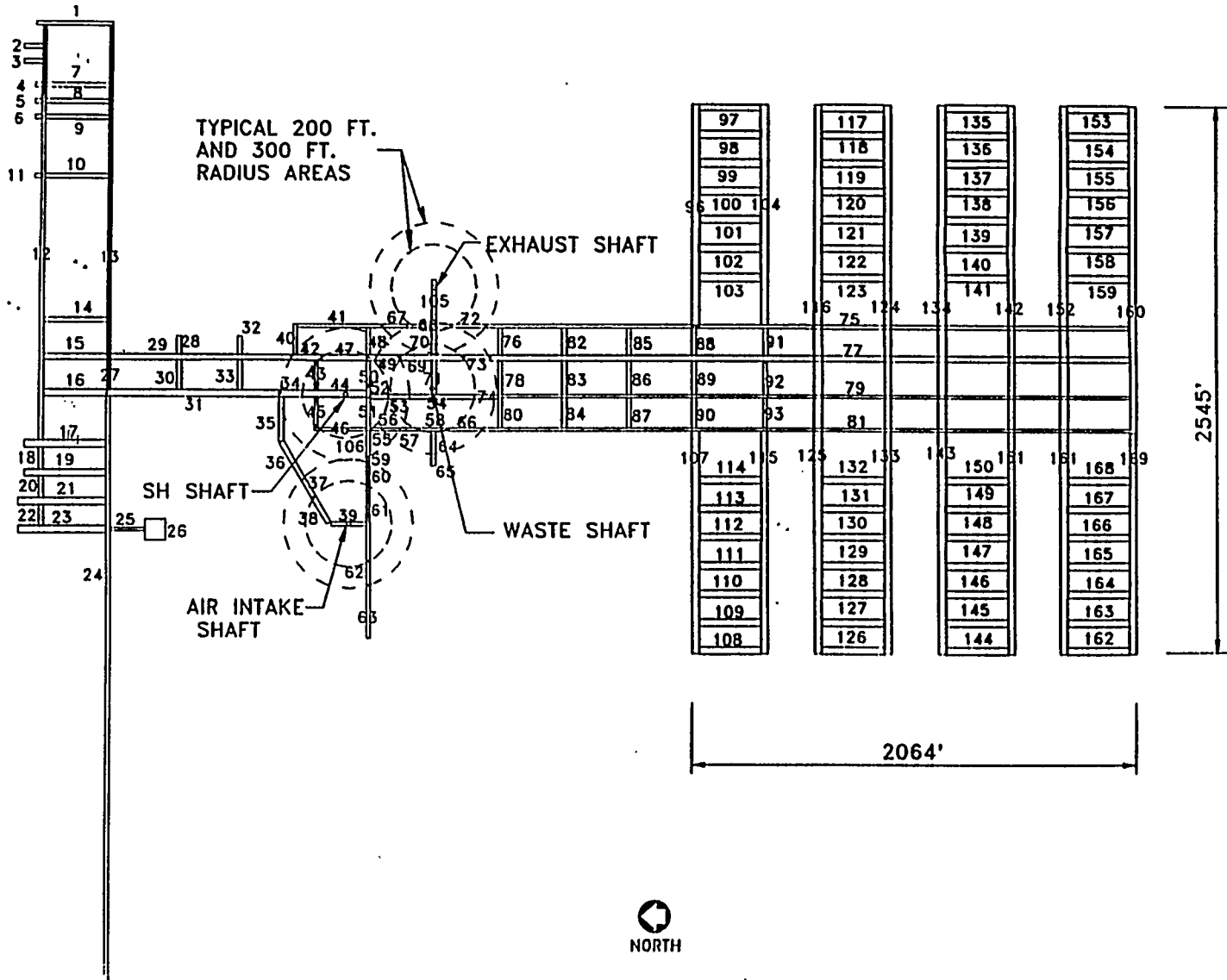


Figure D-30. Mining blocks used to represent WIPP underground workings.

### West-to-East Profile Thru Salt Shaft

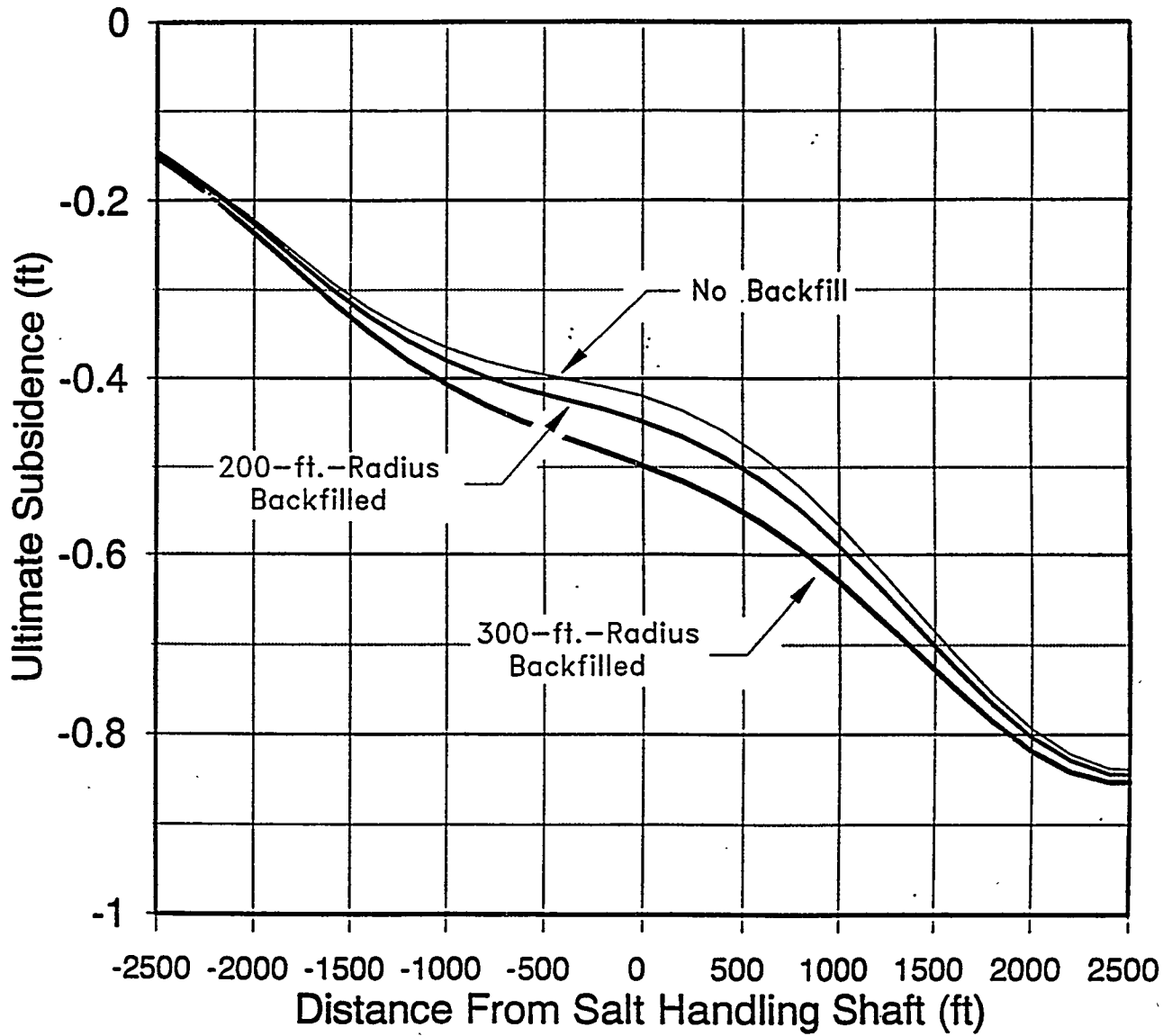


Figure D-31. Surface subsidence profiles over shaft area.

## D7. REFERENCES

- Andersen, P.J., M.E. Andersen, and D. Whiting. 1992. *A Guide to Evaluating Thermal Effects in Concrete Pavements*. SHRP-C/FR-92-101. Washington, DC: Strategic Highway Research Program, National Research Council.
- ASTM D 4311 - 83 (R 1990). "Standard Practice for Determining Asphalt Volume Correction to a Base Temperature (R 1990)," *Annual Book of ASTM Standards, Volume 04.03, Road and Paving Materials; Pavement Management Technologies*. Philadelphia, PA: American Society for Testing and Materials. (Available from American Society for Testing and Materials, 1916 Race Street, Philadelphia, PA 19103-1187, 215/299-5400.)
- Brodsky, N.S. 1990. *Crack Closure and Healing Studies in WIPP Salt Using Compressional Wave Velocity and Attenuation Measurements: Test Methods and Results*. SAND90-7076. Albuquerque, NM: Sandia National Laboratories. (Copy on file in the Sandia WIPP Central Files, Sandia National Laboratories, Albuquerque, NM [SWCF] as WPO25755.)
- Brodsky, N.S., and D.E. Munson. 1994. "Thermomechanical Damage Recovery Parameters for Rocksalt From the Waste Isolation Pilot Plant," *Rock Mechanics, Models and Measurements, Challenges from Industry: Proceedings of the 1st North American Rock Mechanics Symposium, University of Texas at Austin, Austin, TX, June 1-3, 1994*. Eds. P.P. Nelson and S.E. Laubach. Brookfield, VT: A.A. Balkema. 731-738. (Copy on file in the SWCF as WPO27175.)
- Callahan, G.D. 1994. *SPECTROM-32: A Finite Element Thermomechanical Stress Analysis Program Version 4.06*. Topical Report RSI-0531. Rapid City, SD: RE/SPEC Inc. (Copy on file in the SWCF as WPO36814.)
- Callahan, G.D., and K.L. DeVries. 1991. *Analyses of Backfilled Transuranic Wastes Disposal Rooms*. SAND91-7052. Albuquerque, NM: Sandia National Laboratories. (Copy on file in the SWCF as WPO23990.)
- Callahan, G.D., M.C. Loken, L.L. Van Sambeek, R. Chen, T.W. Pfeifle, J.D. Nieland, and F.D. Hansen. 1995a. *Evaluation of Potential Crushed-Salt Constitutive Models*. SAND95-2143. Albuquerque, NM: Sandia National Laboratories. (Copy on file in the SWCF as WPO31068.)
- Callahan, G.D., M.C. Loken, L.D. Hurtado, and F.D. Hansen. 1996. "Evaluation of Constitutive Models for Crushed Salt," *4th International Conference on the Mechanical Behavior of Salt, Montreal, Quebec, June 17-18, 1996*. SAND96-0791C. Albuquerque, NM: Sandia National Laboratories. (Copy on file in the SWCF as WPO36449.)
- Chan, K.S. 1993. "Time Dependent Interface of Bed Separation Fracture Process in Bedded Natural Salt Deposits," *Monthly Technical Report No. FY 93-6*. Prepared by Southwest Research Institute, San Antonio, TX for Sandia National Laboratories, Albuquerque, NM. (Copy on file in SWCF as WPO21030.)

- Chan, K.S. 1994a. "Further Development of Fracture Constitutive Model for Rock Salt," *Monthly Technical Report No. FY 93-12*. Prepared by Southwest Research Institute, San Antonio, TX, for Sandia National Laboratories, Albuquerque, NM, January 15, 1993[sic]. (Copy on file in the SWCF as WPO21086.)
- Chan, K.S. 1994b. "Further Development of Fracture Constitutive Model for Rock Salt," *Monthly Technical Report No. FY 94-1*. Prepared by Southwest Research Institute, San Antonio, TX, for Sandia National Laboratories, Albuquerque, NM, February 14, 1993[sic]. (Copy on file in the SWCF as WPO21087.)
- Chan, K.S., S.R. Bodner, A.F. Fossum, and D.E. Munson. 1992. "A Constitutive Model for Inelastic Flow and Damage Evolution in Solids Under Triaxial Compression," *Mechanics of Materials*. Vol. 14, no. 1, 1-14. (Copy on file in the SWCF as WPO29289.)
- Chan, K.S., S.R. Bodner, A.F. Fossum, and D.E. Munson. 1995a. "Constitutive Representation of Damage Healing in WIPP Salt," *Rock Mechanics, Proceedings of the 35<sup>th</sup> U.S. Symposium, University of Nevada, Reno, NV, June 5-7, 1995*. Eds. J.J.K. Daemen and R.A. Schultz. Brookfield, VT: A.A. Balkema. 485-490. (Copy on file in the SWCF as WPO23774.)
- Chan, K.S., D.E. Munson, A.F. Fossum, and S.R. Bodner. 1995b. "Inelastic Flow Behavior of Argillaceous Salt," *International Journal of Damage Mechanics*. SAND94-3017J. Albuquerque, NM: Sandia National Laboratories. (Copy on file in the SWCF as WPO22199.)
- Costin, L.S., and W.R. Wawersik. 1980. *Creep Healing of Fractures in Rock Salt*. SAND80-0392. Albuquerque, NM: Sandia National Laboratories. (Copy on file in the SWCF as WPO26748.)
- Dale, T., and L.D. Hurtado. 1996. "WIPP Air-Intake Shaft Disturbed-Rock Zone Study," *4th International Conference on the Mechanical Behavior of Salt, Montreal, Quebec, June 17-18, 1996*. SAND96-1327C. Albuquerque, NM: Sandia National Laboratories. (Copy on file in the SWCF.)
- Davis, P.M. 1983. "Surface Deformation Associated With a Dipping Hydrofracture," *Journal of Geophysical Research*. Vol. 88, no. B7, 5826-5834. (Copy on file in the SWCF.)
- DOE (U.S. Department of Energy). 1995. *Waste Isolation Pilot Plant Sealing System Design Report*. DOE/WIPP-95-3117. Carlsbad, NM: U.S. Department of Energy, Waste Isolation Pilot Plant. (Copy on file in the SWCF as WPO29062.)
- Goodman, R.E. 1980. *Introduction to Rock Mechanics*. New York, NY: John Wiley & Sons. 85-88, 310-311. (Copy on file in the SWCF as microfilm NNA.910315.0132.)
- Knowles, M.K., D. Borns, J. Fredrich, D. Holcomb, R. Price, D. Zeuch, T. Dale, and R.S. Van Pelt. 1996. "Testing the Disturbed Zone Around a Rigid Inclusion in Salt," *4th Conference on the Mechanical Behavior of Salt, Montreal, Quebec, June 17-18, 1996*. SAND95-1151C. Albuquerque, NM: Sandia National Laboratories. (Copy on file in the SWCF.)

- Krieg, R.D. 1984. *Reference Stratigraphy and Rock Properties for the Waste Isolation Pilot Plant (WIPP) Project*. SAND83-1908. Albuquerque, NM: Sandia National Laboratories. (Copy on file in the SWCF as WPO24519.)
- Ladanyi, B. 1974. "Use of the Long-Term Strength Concept in the Determination of Ground Pressure on Tunnel Linings," *Advances in Rock Mechanics, Proceedings of the Third Congress of the International Society for Rock Mechanics, Denver, CO, September 1-7, 1974*. Washington, DC: National Academy of Sciences. Vol. 2, pt. B, 1150-1156. (Copy on file in the SWCF.)
- Lambe, T.W., and R.V. Whitman. 1969. *Soil Mechanics*. New York, NY: John Wiley & Sons. (Copy on file in the SNL Technical Library.)
- Morgan, H.S., M. Wallner, and D.E. Munson. 1987. *Results of an International Parallel Calculations Exercise Comparing Creep Responses Predicted with Three Computer Codes for Two Excavations in Rock Salt*. SAND87-2125. Albuquerque, NM: Sandia National Laboratories. (Copy on file in the SWCF as WPO24110.)
- Munson, D.E., A.F. Fossum, and P.E. Senseny: 1989. *Advances in Resolution of Discrepancies Between Predicted and Measured In Situ WIPP Room Closures*. SAND88-2948. Albuquerque, NM: Sandia National Laboratories. (Copy on file in the SWCF as WPO27882.)
- Nieland, J.D. 1991. "SALT\_SUBSID: A PC-Based Subsidence Model, User's Manual." Topical Report RSI-0389. Prepared for the Solution Mining Research Institute, Woodstock, IL. Rapid City, SD: RE/SPEC Inc. (Copy on file in the SWCF.)
- Pfeifle, T.W., and N.S. Brodsky. 1991. *Swelling Pressure, Water Uptake, and Permeability of 70/30 Crushed Salt/Bentonite*. SAND91-7070. Albuquerque, NM: Sandia National Laboratories. (Copy on file in the SWCF as WPO25438.)
- Sass, J.H., A.H. Lachenbruch, R.J. Munroe, G.W. Greene, and T.H. Moses, Jr. 1971. "Heat Flow in the Western United States," *Journal of Geophysical Research*. Vol. 76, no. 26, 6376-6413. (Copy on file in the SWCF.)
- Silling, S.A. 1983. *Final Technical Position on Documentation of Computer Codes for High-Level Waste Management*. NUREG-0856. Washington, D.C.: Division of Waste Management, Office of Nuclear Material Safety and Safeguards, U.S. Nuclear Regulatory Commission. (Copy on file in the SWCF.)
- Sjaardema, G.D., and R. D. Krieg. 1987. *A Constitutive Model for the Consolidation of WIPP Crushed Salt and Its Use in Analyses of Backfilled Shaft and Drift Configurations*. : SAND87-1977. Albuquerque, NM: Sandia National Laboratories. (Copy on file in the SWCF as WPO27693.)
- Svalstad, D.K. 1989. *Documentation of SPECTROM-41: A Finite Element Heat Transfer Analysis Program; Revision 0*. DOE/CH/10378-1, RSI-0266. Prepared by RE/SPEC Inc., Rapid City, SD. Argonne, IL: U.S. Department of Energy, Chicago Operations Office. (Copy available from National Technical Information Service, 5285 Port Royal Road, Springfield, VA, 22161, 703/487-4650. Order number: DE90000683/XAB.)

- Van Sambeek, L.L. 1986. "Creep of Rock Salt Under Inhomogeneous Stress Conditions." Ph.D. dissertation. Golden, CO: Colorado School of Mines. (Dissertation available from Colorado School of Mines Library, Golden, CO.)
- Van Sambeek, L.L., D.D. Luo, M.S. Lin, W. Ostrowski, and D. Oyenuga. 1993a. *Seal Design Alternatives Study*. SAND92-7340. Albuquerque, NM: Sandia National Laboratories. (Copy on file in the SWCF as WPO23445.)
- Van Sambeek, L.L., J.L. Ratigan, and F.D. Hansen. 1993b. "Dilatancy of Rock Salt in Laboratory Tests," *International Journal of Rock Mechanics and Mining Sciences & Geomechanics Abstracts, Rock Mechanics in the 1990s, 34th U.S. Symposium on Rock Mechanics, University of Wisconsin, Madison, WI, June 27-30, 1993*. Vol. 30, no. 7, 735-738. (Copy on file in the SWCF.)
- Wakeley, L.D., J.J. Ernzen, B.D. Neeley, and F.D. Hansen. 1994. *Salado Mass Concrete: Mixture Development and Preliminary Characterization*. SAND93-7066. Albuquerque, NM: Sandia National Laboratories. (Copy on file in the SWCF as WPO10671.)
- Yoder, E.J., and M.W. Witczak. 1975. *Principles of Pavement Design*. 2nd ed. New York, NY: John Wiley & Sons.

**WIPP  
UC721 Distribution List**

**Federal Agencies**

US Department of Energy (4)  
Office of Civilian Radioactive Waste Mgmt.  
Attn: Deputy Director, RW-2  
Acting Director, RW-10  
Office of Human Resources & Admin.  
Director, RW-30  
Office of Program Mgmt. & Integ.  
Director, RW-40  
Office of Waste Accept., Stor., & Tran.  
Forrestal Building  
Washington, DC 20585

Attn: Project Director (2)  
Yucca Mountain Site Characterization Office  
Director, RW-3  
Office of Quality Assurance  
101 Convention Center Drive, Suite #P-110  
Las Vegas, NV 89109

US Department of Energy  
Albuquerque Operations Office  
Attn: National Atomic Museum Library  
P.O. Box 5400  
Albuquerque, NM 87185-5400

US Department of Energy  
Research & Waste Management Division  
Attn: Director  
P.O. Box E  
Oak Ridge, TN 37831

US Department of Energy (8)  
Carlsbad Area Office  
Attn: G. Dials  
D. Galbraith (3)  
M. Matthews  
M. McFadden  
R. Lark  
J. A. Mewhinney  
P.O. Box 3090  
Carlsbad, NM 88221-3090

US Department of Energy  
Office of Environmental Restoration and  
Waste Management  
Attn: J. Lytle, EM-30  
Forrestal Building  
Washington, DC 20585-0002

US Department of Energy (3)  
Office of Environmental Restoration and  
Waste Management  
Attn: M. Frei, EM-34, Trevion II  
Washington, DC 20585-0002

US Department of Energy  
Office of Environmental Restoration and  
Waste Management  
Attn: S. Schneider, EM-342, Trevion II  
Washington, DC 20585-0002

US Department of Energy (2)  
Office of Environment, Safety & Health  
Attn: C. Borgstrom, EH-25  
R. Pelletier, EH-231  
Washington, DC 20585

US Department of Energy (2)  
Idaho Operations Office  
Fuel Processing & Waste Mgmt. Division  
785 DOE Place  
Idaho Falls, ID 83402

US Environmental Protection Agency (2)  
Radiation Protection Programs  
Attn: M. Oge  
ANR-460  
Washington, DC 20460

**Boards**

Defense Nuclear Facilities Safety Board  
Attn: D. Winters  
625 Indiana Ave. NW, Suite 700  
Washington, DC 20004

Nuclear Waste Technical Review Board (2)  
Attn: Chairman  
S. J. S. Parry  
1100 Wilson Blvd., Suite 910  
Arlington, VA 22209-2297

**State Agencies**

Attorney General of New Mexico  
P.O. Drawer 1508  
Santa Fe, NM 87504-1508

Environmental Evaluation Group (3)  
Attn: Library  
7007 Wyoming NE, Suite F-2  
Albuquerque, NM 87109

Metropolitan Water District of Southern Calif.  
Attn: J. Narvaiz  
P.O. Box 54153  
Los Angeles, CA 90071-3123

NM Energy, Minerals, and Natural  
Resources Department  
Attn: Library  
2040 S. Pacheco  
Santa Fe, NM 87505

NM Environment Department (3)  
Secretary of the Environment  
Attn: Mark Weidler  
1190 St. Francis Drive  
Santa Fe, NM 87503-0968

NM Bureau of Mines & Mineral Resources  
Socorro, NM 87801

NM Environment Department  
WIPP Project Site  
Attn: P. McCasland  
P.O. Box 3090  
Carlsbad, NM 88221

#### Laboratories/Corporations

Battelle Pacific Northwest Laboratories (2)  
Attn: R. E. Westerman  
R. Romine, MS P8-38  
P.O. Box 999  
900 Battelle Blvd.  
Richland, WA 99352

Brookhaven National Laboratory  
Attn: P. D. Moskowitz  
Environmental & Waste Technology  
Center  
Building 830  
Upton, NY 11973

Harnischfeger Corp.  
Phonex Engineering Services :  
Attn: R. Luebke  
2969 S. Chase Avenue  
Milwaukee, WI 53207-6408

Ian Clelland  
6656 N. Amdahl Dr.  
Tucson, AZ 85704

INTERA, Inc.  
Attn: G. A. Freeze  
1650 University Blvd. NE, Suite 300  
Albuquerque, NM 87102

INTERA, Inc. (6)  
Attn: J. F. Pickens  
V. Kelley  
M. Reeves  
W. Statham  
J. Beach  
D. Fryar  
INTERA WIPP Library  
6850 Austin Center Blvd., Suite 300  
Austin, TX 78731

INTERA, Inc.  
Attn: J. Lee, YMP PA Dept.  
1261 Town Center Drive  
Las Vegas, NV 89134

INTERA, Inc.  
Attn: W. Stensrud  
P.O. Box 2123  
Carlsbad, NM 88221

Istasca Consulting Group, Inc.  
Attn: John Tinucci  
Thresher Square East  
708 South Third Street, Suite 310  
Minneapolis, MI 55415

Los Alamos National Laboratory  
Attn: B. Erdal, INC-12  
P.O. Box 1663  
Los Alamos, NM 87544

Morton International, Morton Salt  
Attn: H. W. Diamond  
Morton International Building  
100 N. Riverside Plaza,  
Randolph Street at the River  
Chicago, IL 60606-1597

Parsons Brinckerhoff Energy Services, Inc.  
Attn: W. S. Roman  
One Penn Plaza  
New York, NY 10119

Parsons Brinckerhoff Energy Services, Inc. (2)  
Attn: B. W. Lawerance  
C. D. Mann  
M. S. Lin  
303 Second Street  
Suite 850 North  
San Francisco, CA 94107

Parsons Brinckerhoff International, Inc.  
Attn: Mary Ann Novak  
700 11th Street, NW, Suite 710  
Washington, DC 20001

Phillips Mining, Geotechnical & Grouting  
Attn: Stephen Phillips  
8640 North Glenhurst Place  
Tucson, AZ 85704

RE/SPEC, Inc. (5)  
Attn: L. Van Sambeek (3)  
G. Callahan  
M. Loken  
J. Ratigan  
T. Pfeifle  
3824 Jet Drive  
P.O. Box 725  
Rapid City, SD 57709

RE/SPEC, Inc  
Attn: Angus Robb  
4775 Indian School NE, Suite 300  
Albuquerque, NM 87110-3927

Science Applications International Corp.  
Attn: W. Thompson  
15000 W. 6th Avenue, Suite 202  
Golden, CO 80401

Tech Reps, Inc. (3)  
Attn: J. Chapman (1)  
L. Robledo (2)  
5000 Marble NE, Suite 222  
Albuquerque, NM 87110

Westinghouse Electric Corporation (5)  
Attn: Library  
J. Epstein  
J. Lee  
B. A. Howard  
R. Kehrman  
P.O. Box 2078  
Carlsbad, NM 88221

S. Cohen & Associates  
Attn: Bill Thurber  
1355 Beverly Road  
McLean, VA 22101

National Academy of Sciences,  
WIPP Panel

Howard Adler  
Oxyrase, Incorporated  
7327 Oak Ridge Highway  
Knoxville, TN 37931

Bob Andrews  
Board of Radioactive Waste Management  
GF456  
2101 Constitution Ave.  
Washington, DC 20418

Rodney C. Ewing  
Department of Geology  
University of New Mexico  
Albuquerque, NM 87131

Charles Fairhurst  
Department of Civil  
and Mineral Engineering  
University of Minnesota  
500 Pillsbury Dr. SE  
Minneapolis, MN 55455-0220

B. John Garrick  
PLG Incorporated  
4590 MacArthur Blvd., Suite 400  
Newport Beach, CA 92660-2027

Leonard F. Konikow  
US Geological Survey  
431 National Center  
Reston, VA 22092

Carl A. Anderson, Director  
Board of Radioactive Waste Management  
National Research Council  
HA 456  
2101 Constitution Ave. NW  
Washington, DC 20418

Christopher G. Whipple  
ICF Kaiser Engineers  
1800 Harrison St., 7th Floor  
Oakland, CA 94612-3430

John O. Blomeke  
720 Clubhouse Way  
Knoxville, TN 37909

Sue B. Clark  
University of Georgia  
Savannah River Ecology Lab  
P.O. Drawer E  
Aiken, SC 29802

Konrad B. Krauskopf  
Department of Geology  
Stanford University  
Stanford, CA 94305-2115

Della Roy  
Pennsylvania State University  
217 Materials Research Lab  
Hastings Road  
University Park, PA 16802

David A. Waite  
CH<sub>2</sub> M Hill  
P.O. Box 91500  
Bellevue, WA 98009-2050

Thomas A. Zordon  
Zordan Associates, Inc.  
3807 Edinburg Drive  
Murrysville, PA 15668

#### Universities

Harvey Mudd College  
Attn: M. Cardenas  
Department of Engineering  
Claremont, CA 91711

New Mexico State University  
Waste-management Education & Research  
Corporation.  
Attn: R. Bhada  
P.O. Box 3001  
Las Cruces, NM 88003-8001

University of California  
Department of Mechanical and Environmental  
Engineering  
Attn: E. Marschall  
University of California  
Santa Barbara, CA 93106

University of Nevada-Reno  
Department of Mining Engineering  
Mackay School of Mines  
Attn: J. Daamen  
Reno, NV 89557

University of New Mexico  
Center for Radioactive Waste Management  
Attn: W. Lutze  
209 Faris Engineering Building  
Albuquerque, NM 87131-1341

University of New Mexico  
Department of Civil Engineering  
Attn: J. C. Stormont  
Albuquerque, NM 87131-1351

University of New Mexico  
Geology Department  
Attn: Library  
141 Northrop Hall  
Albuquerque, NM 87131

University of Washington  
College of Ocean & Fishery Sciences  
Attn: G. R. Heath  
583 Henderson Hall, HN-15  
Seattle, WA 98195

#### Libraries

Thomas Brannigan Library  
Attn: D. Dresp  
106 W. Hadley St.  
Las Cruces, NM 88001

Government Publications Department  
Zimmerman Library  
University of New Mexico  
Albuquerque, NM 87131

New Mexico Junior College  
Pannell Library  
Attn: R. Hill  
Lovington Highway  
Hobbs, NM 88240

New Mexico State Library  
Attn: N. McCallan  
325 Don Gaspar  
Santa Fe, NM 87503

New Mexico Tech  
Martin Speere Memorial Library  
Campus Street  
Socorro, NM 87810

WIPP Public Reading Room  
Carlsbad Public Library  
101 S. Halagueno St.  
Carlsbad, NM 88220

#### Foreign Addresses

Atomic Energy Canada Ltd. (5)  
Whiteshell Laboratory  
Attn: Neil Chandler  
Glenn McCrank  
B. Goodwin.  
Malcolm Gray  
Maria Onefrei  
Pinawa Manitoba, CANADA ROE 1L0

Francois Chenevier (2)  
ANDRA  
Route de Panorama Robert Schumann  
B. P. 38  
92266 Fontenay-aux-Roses, Cedex  
FRANCE

Claude Sombret  
Centre d'Etudes Nucleaires  
de la Vallee Rhone  
CEN/VALRHO  
S.D.H.A. B.P. 171  
30205 Bagnols-Sur-Ceze, FRANCE

Commissariat a L'Energie Atomique  
Attn: D. Alexandre  
Centre d'Etudes de Cadarache  
13108 Saint Paul Lez Durance Cedex  
FRANCE

Bundesanstalt fur Geowissenschaften und  
Rohstoffe (2)  
Attn: M. Langer  
M. Wallner  
Postfach 510 153  
D-30631 Hannover, GERMANY

Bundesministerium fur Forschung und  
Technologie  
Postfach 200 706  
5300 Bonn 2, GERMANY

Forschungszentrum Karlsruhe GmbH  
Institut für Nukleare Entsorgungstechnik  
Attn: E. Korthaus  
Postfach 3640, D-76021 Karlsruhe  
Bundesrepublik Deutschland  
GERMANY

Gesellschaft fur Anlagen und Reaktorsicherheit  
(GRS)  
Attn: B. Baltes  
Schwertnergasse 1  
D-50667 Cologne, GERMANY

Grundbau Und Felsbau GmbH  
Attn: W. Wittke  
Henricistraße 50  
52072 Aachen, GERMANY

Institut Für Gebirgsmechanik  
Attn: W. Minkley  
Friederikenstraße 60  
04279 Leipzig, GERMANY

Institut Für Tieflagerung  
Attn: K. Kuhn  
Theodor-Heuss-Strasse 4  
D-3300 Braunschweig, GERMANY  
Shingo Tashiro  
Japan Atomic Energy Research Institute  
Tokai-Mura, Ibaraki-Ken, 319-11  
JAPAN

Netherlands Energy Research Foundation ECN  
Attn: J. Prij  
3 Westerduinweg  
P.O. Box 1  
1755 ZG Petten  
THE NETHERLANDS

Universiteit Utrecht  
Department of Geology (HPT-lab)  
Attn: C. J. Spiers  
PO Box 80021  
NL-3508 TA Utrech  
Budapestlaan 4  
THE NETHERLANDS

Svensk Karnbransleforsorjning AB  
Attn: F. Karlsson  
Project KBS (Karnbranslesakerhet)  
Box 5864  
S-102 48 Stockholm  
SWEDEN

Nationale Genossenschaft fur die Lagerung  
Radioaktiver Abfalle (2)  
Attn: S. Vomvoris  
P. Zuidema  
Hardstrasse 73  
CH-5430 Wettingen  
SWITZERLAND

AEA Technology  
Attn: J. H. Rees  
D5W/29 Culham Laboratory  
Abington, Oxfordshire OX14 3DB  
UNITED KINGDOM

AEA Technology  
Attn: W. R. Rodwell  
044/A31 Winfrith Technical Centre  
Dorchester, Dorset DT2 8DH  
UNITED KINGDOM

AEA Technology  
Attn: J. E. Tinson  
B4244 Harwell Laboratory  
Didcot, Oxfordshire OX11 0RA  
UNITED KINGDOM

### Internal

MS	Org.	
0483	5165	R. E. Stinebaugh
0706	6113	J. K. Linn
1320	6719	E. J. Nowak
1322	6121	J. R. Tillerson (10)
1322	6121	E. H. Ahrens (2)
1322	6121	A. W. Dennis (10)
1322	6121	F. D. Hansen
1322	6121	L. D. Hurtado
1322	6121	M. K. Knowles
1324	6115	P. B. Davies
1325	6852	L. S. Costin
1325	6852	R. E. Finley
1328	6749	D. R. Anderson
1328	6741	H. N. Jow
1328	6849	M. F. Fewell
1328	6849	P. Vaughn
1335	6705	M. Chu
1341	6748	J. T. Holmes
1395	6800	L. Shephard
1395	6707	M. Marietta
1395	6841	V. H. Slaboszewicz
1330	6752	B. J. Pierson (2)
1330	6752	NWM Library (100)
9018	8523-2	Central Technical Files
0899	4414	Technical Library (5)
0619	12630	Review and Approval Desk, For DOE/OSTI (2)